TECTONIC, MAGMATIC AND METALLOGENIC EVOLUTION OF THE CAJAMARCA MINING DISTRICT, NORTHERN PERU

Thesis submitted by
Richard Charles Idris Davies B.Sc. (Hons)

in December, 2002,
for the degree of Doctor of Philosophy
in the School of Earth Sciences,
James Cook University,
Australia

STATEMENT OF ACCESS

I, the undersigned Richard Davies, author of this thesis, understand that the following restriction placed by me on this thesis will not extend beyond the date specified:

"I wish to place restriction of access on this thesis for a period of one year."

After this period has elapsed, James Cook University will make this thesis available for use within the University Library and, by microfilm or other means, allow access to users in other approved libraries. All users consulting this thesis will have to sign the following statement:

"In consulting this thesis, I agree not to copy or closely paraphrase it in whole or in part without written consent of the author, and make proper written acknowledgements for any assistance which I have obtained from it."

Richard Davies	December 2002

STATEMENT OF SOURCES

I, the undersigned, declare that this thesis is my own work and has not been submitted in any form from another degree, diploma or study at any university or other institution of tertiary education. Information derived from the published or unpublished work of others has been acknowledged in the text and a list of references is given.

Richard Davies	December 2002

ABSTRACT

In the Cajamarca region of northern Peru periods of peak Tertiary magmatism had a close association with orogenic episodes and high plate convergence rates. New $^{40}Ar/^{39}Ar$ dates show magmatism in the region had commenced by late Palaeocene times, some 15 m.y. earlier than suggested by previous geochronological studies. Palaeogene (57-43 Ma) intrusive and volcanic rocks are intermediate in composition with flat REE profiles and primitive isotope compositions. These magmas were derived from an immature sub-Andean mantle dominated by pyroxene and olivine. This magmatic interval coincided with development of an early fold-thrust fabric in deformed sedimentary rocks.

Early Miocene onset of high plate convergence rates triggered the generation of oxidised hydrous melts from the breakdown of a sub-Andean amphibole-rich upper mantle to lower crust. These melts rose into large magma ponds deep within the crust. Sr, Nd and Pb isotope compositions indicate synmineralisation magmas and metals were derived from a common deep source and that magmas underwent minimal upper crustal contamination. During brief changes in the tectonic stress, primitive hydrous-rich magmas were released from these chambers and ascended rapidly along deeply tapping faults. Dioritic intrusions with HREE-depleted profiles were emplaced during periods of extension in a highly fractured upper crust. New $^{40}Ar/^{39}Ar$ dates indicate this occurred from 23.2 to 16.5 Ma. Mineralised stocks are commonly located in the hanging wall of a regional thrust fault and situated at structural intersections, such as oblique secondary structures superimposed on pre-existing regional-scale faults. Mineralisation-controlling structures, e.g. fault, vein and fracture arrays, at the porphyry deposits have subparallel NNW and NE-NNE trends that suggest they were directly controlled by a regionally extensive stress regime. The physiochemical conditions that prevailed during early stage hypogene mineralisation strongly influenced the Au enrichment at the various porphyry deposits. Au-rich deposits are typically hosted in carbonates, tend to have well-developed potassic alteration zones, high temperature and oxygen fugacity hypogene sulphide mineral assemblages (bornite + chalcopyrite) and abundant hydrothermal magnetite. In contrast, mineralised stocks in contact with fractured quartzites ± carbonates are Cu-Au-Mo deposits with lower temperature hypogene sulphide assemblages of chalcopyrite and pyrite, and potassic alteration zones overprinted by low-grade pyritic phyllic alteration.

Late Miocene high-sulphidation deposits (~11 Ma) near Cajamarca formed during the cessation of intense crustal thickening and uplift that was associated with shallowing of the slab dip angle. Location of ore bodies at the Yanacocha mine was largely controlled by WNW structures, indicating rotation of the dominant fault orientation from NNE-NNW to WNW with time. A mineralised dioritic-tonalitic intrusion beneath the Yanacocha high-sulphidation system has a steep HREE-depleted profile and more evolved radiogenic Sr-Nd isotope compositions than the early Miocene intrusions. However, a pyrite Pb isotope composition from this intrusion is significantly less radiogenic than sulphides from early Miocene deposits. These features indicate late Miocene magmas were formed beneath a thickened crust, similar to that at the present day, and require a higher garnet content in the source.

ACKNOWLEDGEMENTS

Firstly, I would like to thank the people from North Ltd and Rio Tinto for creating, supporting and encouraging this project. Without the financial and ground support of these companies this study would have never been possible. Special thanks to Tim Moody from Rio Tinto for his continued support and patience. I would also like to express gratitude to all the people in Cajamarca and Peru that assisted and supported me during my time in Cajamarca. Their hospitality and generosity will always be remembered. Cesar Vidal, Dick Sillitoe, Carl Schnell and Javier Veliz are especially thanked for their time and knowledge.

I cannot thank enough my supervisors, Pat Williams and Tim Baker, for allowing me the freedom to design and mould this project. Thank you Pat and Tim for inspiring and helping me to develop my own thoughts and ideas. I am greatly indebted to you both. Extreme gratitude goes to Pat for reading so many of my drafts. I'm sure no supervisor should have to endure such pain as that. I must also express thanks to all the people at JCU for their ideas, encouragement and support throughout the duration of the study. Roger Buick and Graham Bradley are also thanked for their inspiration and encouragement. To the guys from the AAC, thank you for assistance and making lab work both enjoyable and educational. Roland Maas is also thanked for his knowledge and patience in helping me to develop a plan for the Sr-Nd isotope part of the study. To Dick Tosdal and the people at UBC, a huge thanks for kindly running the Pb isotope analyses. You guys are truly legends.

To my best friends Gregg, Jay and Dom, thank you for allowing me to lose the plot and escape from reality during difficult times. To Chris and Tre, *mi casa es su casa siempre*. You guys rock. To Nick Timms, never before has a person opened my mind and inspired me to be has creative and have a lust for life that you have. Special thanks are extended to all my friends in Townsville that made life up here so rich and enjoyable. Particular thanks goes to the TECC crew, plus Marc and Cathy. Finally, to the endless love and support provided by the two loveliest and most caring girls in my life – thank you toni and polli.

This thesis is dedicated to my mum and dad, and my three sisters.

TABLE OF CONTENTS

SECTION C C1-C46

Geochemistry of igneous suites from the Cajamarca district, northern Peru: Implications for magmatic controls on the formation of porphyry Cu-Au deposits.

SECTION D D1-D47

Geology of the El Galeno and Michiquillay Cu-Au-Mo deposits and a comparison with the Au-rich Minas Conga porphyry deposit in the Cajamarca mining district, northern Peru.

SECTION E E1-E15

Controls on formation of Miocene porphyry and high-sulphidation deposits in the Cajamarca Au District, northern Peru

REFERENCES R1-R19

APPENDICES

LIST OF FIGURES AND TABLES

SECTION A

SECTION B

SECTION C

SECTION D

SECTION E

THESIS INTRODUCTION

The Cajamarca district of northern Peru hosts an unusually high number of Tertiary Au-rich porphyry and high-sulphidation deposits for the Andean metallogenic belt. Despite extensive mineral exploration and recent development of the world class Yanacocha Au mine, the tectonic and magmatic understanding of the Cajamarca region has been poorly documented compared to other Au-rich regions in the Andes, such as the 27^o to 30^{o}S central Andean transect (e.g. Gustafson and Hunt, 1975; Vila and Sillitoe, 1991; Lindsay *et al*., 1995; Sasso and Clark, 1998; Kay *et al*., 1999; Richards *et al*., 2001).

This thesis investigates tectonic, magmatic and deposit geology controls on the formation of Tertiary mineralised centres in the Cajamarca district. The thesis consists of five sections written in journal format that are intended for future publication. The sections are arranged a logical progression that follow on from the previous section. The first four sections present new geochronological, structural and geochemical data, and a geological description of two porphyry-related deposits. The final section incorporates these results with findings from previous studies in the region and other mining districts in the Andes to develop a comprehensive tectonomagmatic model for the formation of Miocene hydrothermal deposits in the Cajamarca district.

Section A

The first section of the thesis presents a geological introduction to the Cajamarca region. This includes a brief summary and petrological description of the major magmatic units that crop out throughout the region. Ten new $^{40}Ar/^{39}Ar$ dates are also presented for selected magmatic and hydrothermal centres. The section concludes with discussion of the relationship between magmatic-hydrothermal events and tectonic episodes.

Section B

The second section addresses the structural evolution of the Cajamarca region. Data presented are derived from field and aerial photo studies of deformed Cretaceous sedimentary rocks and various mineralised centres. Fault, fracture and vein arrays at the porphyry-related deposits are used to assess the influence of the regional stress field on the formation of these deposits. The section documents a temporal change in the principal fault-fractures trend with time and links these changes to plate convergence direction.

Section C

The third section focuses on petrographical and geochemical data (major, trace, rare earth element and radiogenic isotope compositions) of the magmatic rocks in the region. Different igneous suites are identified and compared. A comparison between mineralised and unmineralised porphyry intrusions is also addressed. Selected samples are modelled using REE and trace element models to estimate possible changes in the residual mineralogy of a developing magmatic arc. The section concludes with a geochemical comparison with mineralised porphyry deposits in Chile and magmatic model for Tertiary igneous rocks in the Cajamarca region.

Section D

Section four gives geological descriptions of two mineralised intrusive-related centres in the Cajamarca district, i.e. the El Galeno and Michiquillay Cu-Au-Mo deposits. The study documents the intrusive history at the deposits, as well as the alteration and mineralisation paragenesis. A geological model for the formation of these centres is proposed. New sulphide Pb isotope compositions from four of the mineralised deposits are also presented. Finally, these porphyry deposits are compared with the well-documented Au-rich Minas Conga prospect and generalised models for porphyry Cu deposits.

Section E

The final section of this thesis unifies new geochronological and geochemical data with structural observations and deposit geology to develop a top-to-bottom tectonomagmatic model for the formation of Miocene porphyry-related and high-sulphidation deposits in the Cajamarca region.

SECTION A

New $^{40}Ar/^{39}Ar$ age constrains on the geological evolution of the Cajamarca mining district

Section A. New $^{40}Ar/^{39}Ar$ age constrains on the geological evolution of the Cajamarca mining district.

A.1 Abstract

New $^{40}Ar/^{39}Ar$ incremental-heating dates were determined for ten samples from intrusive and volcanic rocks in the Cajamarca mining district of northern Peru. A revised magmatic and hydrothermal history of the region is presented based on these new dates. A microdiorite stock east of the Minas Conga (Au-Cu) prospect was the oldest igneous rock dated (57 ± 3 Ma) and suggests magmatism in the region initiated at least during late Palaeocene times. An intrusion from Cerro Montana (47 ± 3 Ma) and a volcanic rock from the La Carpa region (42.55 ± 0.12 Ma) were also dated as middle Palaeogene in age. Hornblende phenocrysts from a mafic dyke yielded a plateau date of 29.4 ± 1.4 Ma.

Magmatic biotite from a synmineralisation intrusion at the Michiquillay porphyry Cu-Au-Mo deposit yielded a $^{40}Ar/^{39}Ar$ plateau date at 19.77 ± 0.05 Ma. This is slightly younger than hornblende phenocrysts from a barren intrusion to the north (20.60 ± 0.14 Ma). Two other barren intrusions from the region, Aurora Patricia (21.30 ± 0.80 Ma) and La Carpa (17.85 ± 0.06 Ma) returned similar early Miocene ages. Main stage alteration and mineralisation at the El Galeno Cu-Au-Mo deposit are dated at 17.50 ± 0.30 Ma (hydrothermal biotite), whilst a late- to post-mineralisation intrusion at the same deposit yielded a date of 16.53 ± 0.18 Ma (magmatic biotite).

Results from this and previous studies indicate periods of magmatic and hydrothermal activity in the Cajamarca region were temporally associated with high plate convergence rates. Hydrothermal activity occurred over both prolonged (~7 m.y.) and short periods (~1 m.y.). Whilst mineralisation events did not necessarily coincide with the major orogenic events, intense or peak magmatism may be linked with significant plate tectonic and orogenic episodes.

A.2 Introduction

The Cajamarca mining district lies between 2,300 and 4,400 m elevation in the Western Cordillera of the northern Peruvian Andes, approximately 685 km north of Lima (Fig. 1). The Cajamarca-Hualgayoc region has long been recognised as an important metalliferous area (von Humboldt, 1927; Orton, 1874). Mining in the district extends back to the Spanish colonial times, and possibly even to the Inca period, when Cu and Au were mined from hillsides near Hualgayoc (Macfarlane and Petersen, 1990). Today, the Cajamarca mining district (Fig. 1) is known to host a number of significant mineralised centres that include Yanacocha (Au), Minas Conga (Au-Cu), Minas Carpa (Au-Cu), Michiquillay (Cu-Au-Mo) and El Galeno (Cu-Au-Mo). Other mineralised centres in the region include Sipán (Au), La Zanja (Au) and the polymetallic Hualgayoc region (Fig. 1). These mineralised centres predominantly include high-sulphidation and porphyry Cu deposits, although minor mantos and skarn deposits have been recognised.

Previous geological descriptions and regional mapping of the Cajamarca district includes studies by Benavides (1956), Reyes (1980), Cobbing *et al*. (1981), Wilson (1985a, 1985b) and Noble *et al*. (1990). In addition, numerous deposit-related studies have further contributed to the geological understanding of the district (Hollister and Sirvas, 1974; Macfarlane and Petersen, 1990; Macfarlane *et al*., 1994; Llosa *et al*., 1996; Turner, 1997; James, 1998; Cordova and Hoyos, 2000; Sillitoe, 2000a). Based on these studies, the region is largely characterised by deformed Cretaceous sedimentary rocks intruded and overlain by Tertiary calc-alkaline magmatic rocks (Fig. 2). The Cretaceous sedimentary rocks were deformed by several compressional events termed the Incaic (I-IV) and Quechua (I-II) orogenic phases (Benavides, 1999). The Tertiary igneous rocks vary from basic to acidic in composition (Section C) and range in age from late Palaeocene to late Miocene (Llosa *et al*., 1996; Turner, 1997; this study). Published and unpublished U-Pb, K-Ar, Rb-Sr and $^{40}Ar/^{39}Ar$ dates (Fig. 3, Table 1) of these igneous units have focussed on rocks from the Yanacocha district (Turner, 1997), Minas Conga (Llosa *et al*., 1996), Michiquillay (Laughlin *et al*., 1968) and the Hualgayoc region (Borredon, 1982; Macfarlane *et al*., 1994; James, 1998). Limited high precision age dates exist for regional barren intrusions and most of the mineralised porphyry centres. Upper and lower age limits for volcanic sequences in the region (Noble *et al*., 1990; Llosa *et al*., 1996; Turner, 1997) are also poorly constrained largely.

Fig. 1. Map of Peru displaying the major tectonic units (modified from Benavides, 1999). Also shown are the significant mineralised centres in Cajamarca (defined by the black square, see Fig. 2) and nearby regions.

Fig. 2. Simplified geological map of the Cajamarca area showing the location of the major igneous units and samples used for $^{40}Ar/^{39}Ar$ dates (filled triangles). Map modified from Reyes (1980). Open triangles: previous dates at mineralised centres, 1 = Laughlin *et al*. (1968); 2 = Llosa *et al*., (1996), 3 = Turner (1997).

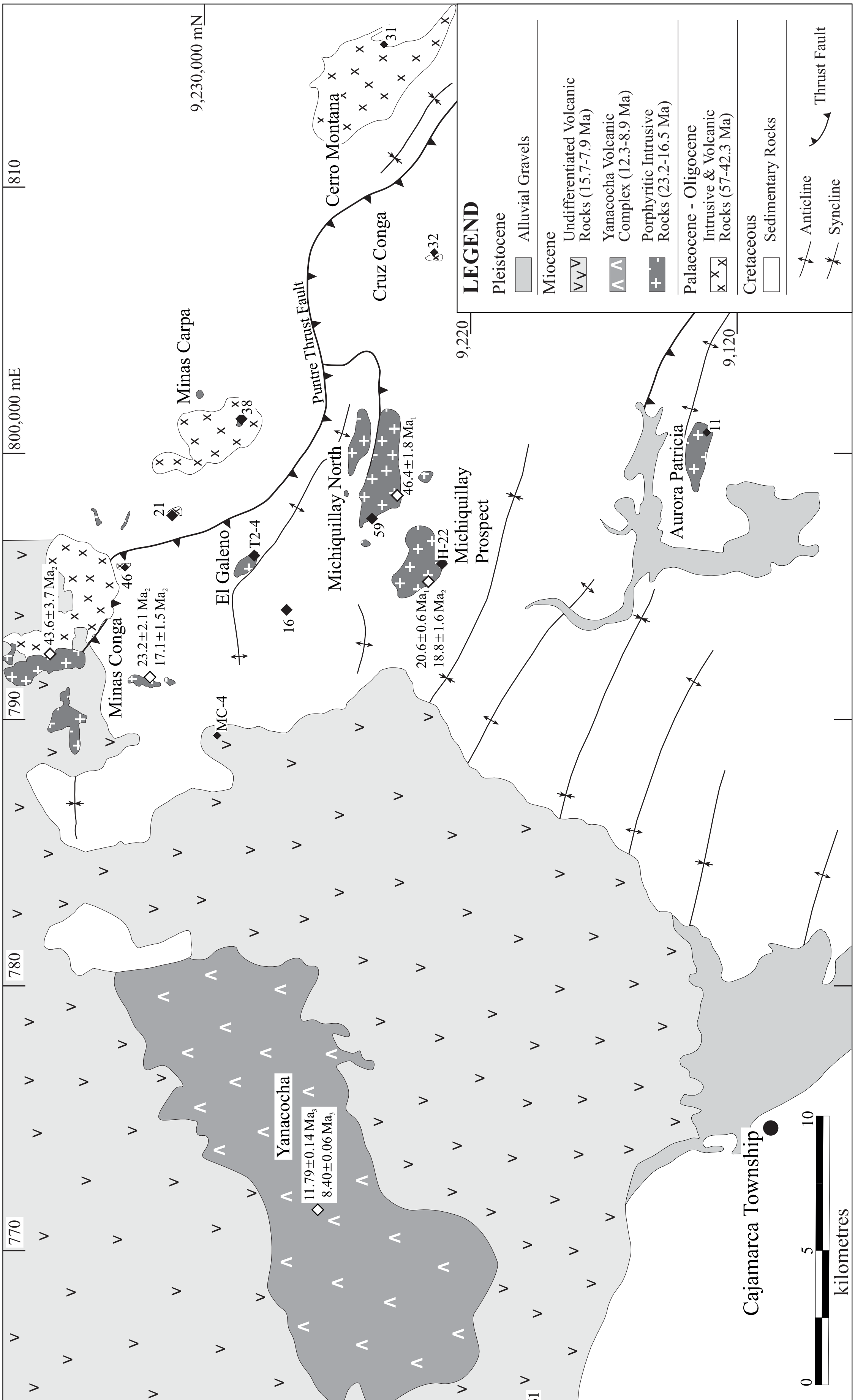

LEGEND
Pleistocene
Alluvial Gravels
Miocene
Undifferentiated Volcanic Rocks (15.7-7.9 Ma)
Yanacocha Volcanic Complex (12.3-8.9 Ma)
Porphyritic Intrusive Rocks (23.2-16.5 Ma)
Palaeocene - Oligocene
Intrusive & Volcanic Rocks (57-42.3 Ma)
Cretaceous
Sedimentary Rocks
Anticline
Syncline
Thrust Fault
9,230,000 mN
9,220
9,120
770
780
790
800,000 mE
810
Cerro Montana
Cruz Conga
Minas Carpa
Puntre Thrust Fault
Minas Conga
El Galeno
Michiquillay North
Michiquillay Prospect
Aurora Patricia
Yanacocha
Cajamarca Township
43.6±3.7 Ma
23.2±2.1 Ma
17.1±1.5 Ma
46.4±1.8 Ma
20.6±0.6 Ma
18.8±1.6 Ma
11.79±0.14 Ma
8.40±0.06 Ma
MC-4
T2-4
H-22
0
5
10
kilometres

Fig. 3. Previous radiogenic isotope dates from the Cajamarca and Hualgayoc districts (refer to Table 1). The shaded area defines the magmatic hiatus in the Cajamarca region. B = Borroden (1982); J = James (1998); LD = Laughlin *et al*. (1968); L = Llosa *et al*. (1996); M = Macfarlane *et al*. (1994); N = Noble *et al*. (1990); T = Turner (1997).

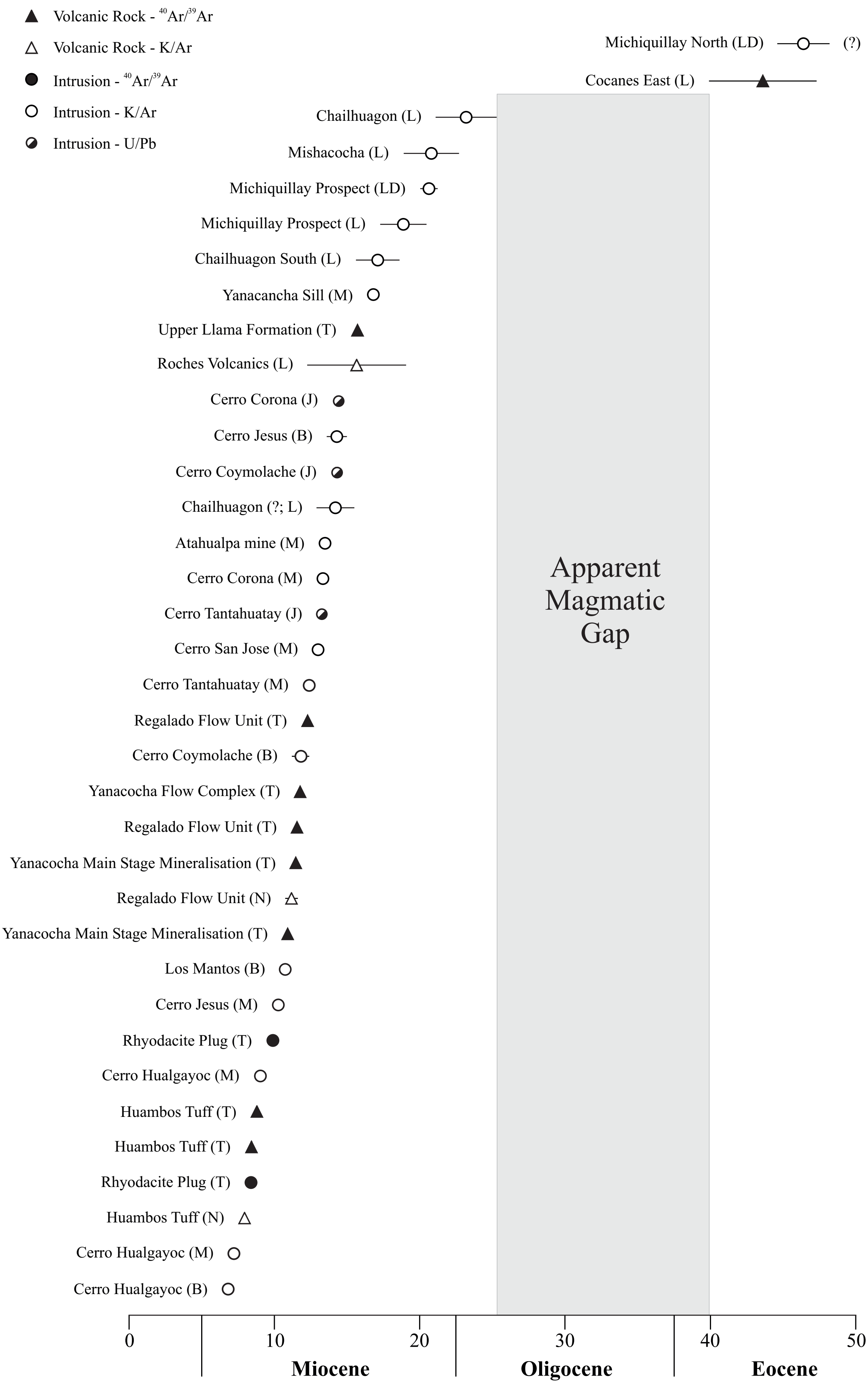
Volcanic Rock - 40Ar/39Ar
Volcanic Rock - K/Ar
Intrusion - 40Ar/39Ar
Intrusion - K/Ar
Intrusion - U/Pb
Michiquillay North (LD)
(?)
Cocanes East (L)
Chailhuagon (L)
Mishacocha (L)
Michiquillay Prospect (LD)
Michiquillay Prospect (L)
Chailhuagon South (L)
Yanacancha Sill (M)
Upper Llama Formation (T)
Roches Volcanics (L)
Cerro Corona (J)
Cerro Jesus (B)
Cerro Coymolache (J)
Chailhuagon (?; L)
Atahualpa mine (M)
Cerro Corona (M)
Cerro Tantahuatay (J)
Cerro San Jose (M)
Cerro Tantahuatay (M)
Regalado Flow Unit (T)
Cerro Coymolache (B)
Yanacocha Flow Complex (T)
Regalado Flow Unit (T)
Yanacocha Main Stage Mineralisation (T)
Regalado Flow Unit (N)
Yanacocha Main Stage Mineralisation (T)
Los Mantos (B)
Cerro Jesus (M)
Rhyodacite Plug (T)
Cerro Hualgayoc (M)
Huambos Tuff (T)
Huambos Tuff (T)
Rhyodacite Plug (T)
Huambos Tuff (N)
Cerro Hualgayoc (M)
Cerro Hualgayoc (B)
Apparent Magmatic Gap
0
10
20
30
40
50
Miocene
Oligocene
Eocene

Table 1. Previous radiogenic isotope dates from the Cajamarca and Hualgayoc regions.

Sample	Location / Rock Unit	Sample Type	Mineral Analysed	Date (Ma)	Reference	Method
Cajamarca Region						
YC-1	Upper Llama Formation	Rhyodacite	Biotite	15.78 ± 0.17	Turner (1997)	Ar-Ar
PL-36	Regalado Flow Unit	Andesite flow	Hornblende	12.26 ± 0.12	Turner (1997)	Ar-Ar
MM-165	Regalado Flow Unit	Andesite flow	Hornblende	11.58 ± 0.18	Turner (1997)	Ar-Ar
PL-48	Yanacocha Flow Complex	Andesite	Hornblende	11.79 ± 0.14	Turner (1997)	Ar-Ar
QU-114	Main Alteration (Yanacocha)	Crystalline Alunite	Alunite	11.46 ± 0.15	Turner (1997)	Ar-Ar
CA-SUR	Main Alteration (Yanacocha)	Crystalline Alunite	Alunite	10.92 ± 0.09	Turner (1997)	Ar-Ar
MM-11	Huambos Tuff	Rhyodacite	Biotite	8.42 ± 0.05	Turner (1997)	Ar-Ar
MM-11	Huambos Tuff	Rhyodacite	Hornblende	8.79 ± 0.08	Turner (1997)	Ar-Ar
YA	Rhyodacite Plug	Rhyodacite intrusion	Biotite	9.90 ± 0.05	Turner (1997)	Ar-Ar
YS-2	Rhyodacite Plug	Rhyodacite intrusion	Biotite	8.40 ± 0.06	Turner (1997)	Ar-Ar
Y63	Cocanes East	Diorite	Hornblende	43.6 ± 3.7	Llosa *et al*. (1996)	K-Ar
Y52	Chailhuagon (non-minl zone)	Diorite	Hornblende	23.2 ± 2.1	Llosa *et al*. (1996)	K-Ar
Y41a	Mishacocha (E Maqui-Maqui)	Intrusion	Hornblende	20.8 ± 1.9	Llosa *et al*. (1996)	K-Ar
Y75	Michiquillay Prospect	Diorite	Biotite	18.8 ± 1.6	Llosa *et al*. (1996)	K-Ar
Y501	Chailhuagon South	Diorite	Biotite	17.1 ± 1.5	Llosa *et al*. (1996)	K-Ar
Y4	W Yanacocha (Location?)	Ignimbrites	Biotite	15.7 ± 3.4	Llosa *et al*. (1996)	K-Ar
Y52	Chailhuagon (non-minl zone)	Diorite	Feldspar	14.2 ± 1.3	Llosa *et al*. (1996)	K-Ar
PED-2a-66	Michiquillay North	Hornblende Granodiorite	Hornblende	46.4 ± 1.8	Laughlin *et al*. (1968)	K-Ar
PED-2b-66	Michiquillay Prospect	Altered sulfide-bearing rock	Biotite (hydrothermal)	20.6 ± 0.6	Laughlin *et al*. (1968)	K-Ar
POR-1	Llama (Llama Fm)	Rhyodacite	Plagioclase	54.8 ± 1.8	Noble *et al*. (1990)	K-Ar
YML-4	Huambos (Llama Fm)	Rhyodacitic Ash-Flow Tuff	Sanidine	44.2 ± 1.2	Noble *et al*. (1990)	K-Ar
HMB-1	Huambos (Huambos Fm)	Basal Ash-Flow	Sanidine	39.3 ± 1.0	Noble *et al*. (1990)	Ar-Ar
HMB-4	Huambos (Huambos Fm)	Basal Ash-Flow	Sanidine	36.4 ± 1.0	Noble *et al*. (1990)	K-Ar
UHM-2	Huambos (Huambos Fm)	Overlying Dacite Tuff	Plagioclase	35.4 ± 1.2	Noble *et al*. (1990)	K-Ar
CHB-1	Late Volcanic Rock in Cajamarca	Ash-Flow Tuff	Hornblende	11.4 ± 0.6	Noble *et al*. (1990)	K-Ar
BMC-3	Late Volcanic Rock in Bambamarca	Ash-Flow Tuff	Sanidine	8.2 ± 0.2	Noble *et al*. (1990)	K-Ar

Sample	Location / Rock Unit	Sample Type	Mineral Analysed	Date (Ma)	Reference	Method
Hualgayoc District						
96D-LG	La Granja	Monzonite	Muscovite	13.8 ± 0.4	Noble and McKee (1999)	K-Ar
TANTAD	Tantahuatay	Dacitic Dyke	Biotite	8.5 ± 0.3	Noble and McKee (1999)	K-Ar
TANTAD	Tantahuatay	Dacitic Dyke	Biotite	8.7 ± 0.3	Noble and McKee (1999)	K-Ar
87009	Yanacancha Sill	Propylytized Andesite	K-Feldspar	16.8 ± 0.4	Macfarlane *et al* . (1994)	K-Ar
86027	Cerro Hualgayoc	Rhyodacite	Biotite (magmatic)	9.05 ± 0.21	Macfarlane *et al* . (1994)	K-Ar
	Cerro Corona	Potassic altered felsic pluton	Biotite (hydrothermal)	13.35 ± 0.27	Macfarlane *et al* . (1994)	K-Ar
86039	Cerro San Jose	Seriticized Andesite	Muscovite	13.00 ± 0.4	Macfarlane *et al* . (1994)	K-Ar
85019	Atahualpa mine	Argillically altered sill	Muscovite	13.48 ± 0.19	Macfarlane *et al* . (1994)	K-Ar
86011	Cerro Jesus	Argillically altered andesite	Muscovite	10.29 ± 0.20	Macfarlane *et al* . (1994)	K-Ar
87007	Cerro Tantahuatay	Acid-sulphate alteration	Coarse hypogene alunite	12.4 ± 0.4	Macfarlane *et al* . (1994)	K-Ar
	Cerro Hualgayoc	Rhyodacite	Biotite (magmatic)	7.9 ± 0.3	Macfarlane *et al* . (1994)	K-Ar
9602	Cerro Corona	Quartz Diorite	Zircon	14.4 ± 0.1	James, 1998	U-Pb
9605	Cerro Coymolache	Andesite	Zircon	14.3 ± 0.1	James, 1998	U-Pb
9699	Cerro Tantahuatay	Andesite	Zircon	13.2 ± 0.2	James, 1998	U-Pb
	Cerro Jesus	Argillically altered andesite	Whole-rock	14.3 ± 0.7	Borredon (1982)	K-Ar
	Cerro Coymolache	Propylytized Andesite	Whole-rock	11.8 ± 0.6	Borredon (1982)	K-Ar
	Los Mantos	Argillically altered andesite	Whole-rock	10.5 ± 0.5	Borredon (1982)	K-Ar
	Cerro Hualgayoc	Rhyodacite	Whole-rock	7.2 ± 0.35	Borredon (1982)	K-Ar

Hbl = Hornblende; Bt = Biotite

This section introduces the main magmatic units that crop out in the Cajamarca region and presents new $^{40}Ar/^{39}Ar$ dates for magmatic and hydrothermal minerals. These new dates are used to address to the duration of magmatic-hydrothermal intervals in the region, as well as their association with large-scale tectonic events. The results show short and prolonged magmatic-hydrothermal intervals may be linked to certain tectonic processes.

A.3 Magmatic Centres – Intrusive Rocks

A.3.1 Aurora Patricia

The Aurora Patricia intrusion is located *ca*. 26 km east of Cajamarca (Fig. 2). It is elongate, 2.6 km in length and 0.8 km wide, with the long axis oriented in a near E-W direction. The intrusion is hosted in deformed Upper Cretaceous rocks and located in a hanging wall anticline that plunges gently to the east. The porphyritic intrusion comprises plagioclase and hornblende phenocrysts set in a light grey feldspathic groundmass. The majority of outcropping intrusion has a strong clay alteration, although unaltered rock was observed in the northeastern section. Weak quartz stockwork and pyrite veinlets are evident in outcrop. Previous drilling indicates the Aurora Patricia intrusion is a poorly mineralised hornblende diorite (Jesus Cordova, *pers. commun*., 2000).

A.3.2 Cerro Montana

Cerro Montana is a strongly altered porphyritic intrusive complex *ca*. 42 km ENE of Cajamarca. The elongate complex (7 km by 3.5 km) has a general NW orientation and is located in the footwall of a regionally-extensive thrust fault, termed the Puntre Thrust Fault (Fig. 2). Its core is characterised by an intense clay alteration that has destroyed most primary igneous textures. Towards the periphery on the northeastern side, the intrusion displays only weak propylitic and argillic alteration. The intrusion contains abundant plagioclase and minor hornblende phenocrysts set in a grey feldspathic groundmass. On the eastern side of the complex, the intrusion has a crowded porphyritic texture with plagioclase, clinopyroxene and hornblende phenocrysts. The groundmass is feldspathic and greenish light grey in colour suggesting weak propylitic alteration.

A.3.3 La Carpa

The La Carpa region, *ca*. 35 km to the NE of Cajamarca (Fig. 2), contains both intrusive and extrusive rocks. Several porphyritic intrusions intrude both the deformed limestone and La Carpa volcanic rocks (see below). Mineralogically, these stocks contain plagioclase, hornblende, biotite and rounded quartz phenocrysts set in a light grey feldspathic groundmass. The intrusive rocks have a lower abundance of hornblende phenocrysts compared to the volcanic rocks. From field and petrographic observations, it is suggested that the intrusions are slightly altered hornblende-biotite quartz diorite stocks. The exact age dates of the intrusions and volcanic rocks are unknown. However, geochemical trends suggest the intrusions are considerably younger (Section C).

A.3.4 Michiquillay North

The Michiquillay North intrusive complex situated ~28 km ENE of Cajamarca consists of numerous medium- to small-sized stocks (Fig. 2). The porphyritic intrusive suite is generally homogeneous and composed of plagioclase, hornblende, biotite and quartz phenocrysts within a feldspathic groundmass. Quartz grains are rounded and may contain minor embayments. Rounded quartzite xenoliths, approximately 10 cm in size, occur within some of the intrusions. The intrusions display a weak to moderate chlorite-carbonate-muscovite-pyrite (propylitic) alteration assemblage. Disseminated fine-grained pyrite occurs in some intrusions, but no veins or stockwork are evident. These propylitically altered stocks are interpreted as hornblende ± biotite diorites. A previous K-Ar date from one of these intrusions by Laughlin *et al*. (1968) yielded a date of 46.4 ± 1.8 Ma from hornblende grains.

A.3.5 Michiquillay Deposit

The Michiquillay Cu-Au-Mo prospect is located *ca*. 4 km SW of the barren stocks (Fig. 2). A comprehensive discussion of the prospect is given in Section D. At the prospect, the most common rock type is a crowded porphyry with plagioclase, hornblende, biotite and rounded quartz phenocrysts. The groundmass is feldspathic. This medium-grained porphyry has previously been referred to as the 'quartz-biotite monzonite' (Hollister and Sirvas, 1974). However, petrographic studies (Appendix A1, Section C and D) show this intrusion contains no primary alkali feldspars and igneous hornblende phenocrysts have been replaced by hydrothermal biotite due to hydrothermal alteration. These features indicate this intrusion is a hornblende-biotite diorite. This Michiquillay intrusive phase has similar petrologic textures and mineralogy to the barren intrusions to the north. Previous K-Ar studies yielded dates of 20.6 ± 0.6 Ma (hydrothermal biotite, Laughlin *et al*., 1968) and 18.8 ± 1.8 Ma (magmatic biotite, Llosa *et al*., 1996).

A.3.6 El Galeno Deposit

El Galeno is a Cu-Au-Mo porphyry complex located *ca*. 30 km NE of Cajamarca (see Section D.5). The earliest and main intrusive body (P1) is roughly 1.25 km by 0.6 km, oriented in a NW direction and has been intruded by up to three later intrusive phases. The P1 porphyry and the second oldest intrusion (P2 porphyry) are mineralogically and texturally similar with medium-grained plagioclase, hornblende, biotite and quartz phenocrysts. The synmineralisation P1 and P2 porphyries have a moderate to well-developed quartz stockwork and are inferred to be of similar age (Section D.5.4). P3 porphyries intrude the earlier porphyries and contain coarse-grained plagioclase, hornblende, quartz and biotite phenocrysts. P3 porphyries have both lower metal grades and stockwork density than the P1 and P2 porphyries. This phase is inferred to be a series of late to synmineralisation dykes. The final intrusion (MBx porphyry) is a late- to post-mineralisation stock containing plagioclase, biotite and hornblende phenocrysts. This contains a poorly developed stockwork and is weakly mineralised.

A.3.7 Minas Conga Deposit

The Minas Conga complex is situated *ca*. 25 km NNE of Cajamarca and comprises several intrusive units (Fig. 2). Previous mapping by Llosa *et al*. (1996) and Llosa and Veliz (2000) has defined two mineralised centres, i.e. Chailhuagon and Cerro Perol. These centres are characterised by porphyritic intrusions with plagioclase, hornblende, biotite and rounded quartz phenocrysts. Both mineralised centres are intruded by late barren intrusions. Hornblende from the Chailhuagon intrusion yielded a date of 23.2 ± 2.1 Ma from K-Ar, whilst younger ages from the same intrusive complex were obtained from biotite (17.1 ± 1.5 Ma) and plagioclase (14.2 ± 1.3 Ma; Llosa *et al*., 1996).

A.3.8 Cerro Perol East

Unmineralised volcanic and intrusive rocks are exposed east of the Minas Conga complex. An altered volcanic to subvolcanic complex east of the Cerro Perol deposit is dominantly located in the footwall of the Puntre Thrust Fault (Fig. 2). Both rock-types contain acicular hornblende (some of them up to 20 mm), as well as plagioclase and pyroxene phenocrysts. The groundmass is feldspathic. In outcrop, these rock types range from intense propylitic to argillic altered. In zones of strong alteration, hornblende grains display intense chloritisation and calcite has partially replaced plagioclase phenocrysts. Chlorite, carbonate and epidote alteration is widespread throughout the volcanic sequence. Llosa *et al*. (1996) dated hornblende from an intrusion in this region which yielded a date of 43.6 ± 1.7 Ma.

Southeast of the Cerro Perol deposit, outcropping intrusive rocks are less altered and several discrete intrusive phases were observed. The least altered rock is holocrystalline and composed of plagioclase and hornblende phenocrysts, plus fine-grained euhedral pyroxene and magnetite. Petrographic and geochemical results (Section C) indicate this rock a hornblende microdiorite (Appendix D1). Randomly-oriented plagioclase- and hornblende-rich dykes crosscut the diorite. The dykes are pink in colour and range in thickness from millimetres to tens of centimetres. Minor epidote alteration and pyrite mineralisation are associated with the pink dykes, although the majority of the host rock is unaltered.

A.4 Mafic Dykes

Outcropping mafic dykes were predominantly observed within the northern part of the field area, particularly within 10 km of El Galeno. They are generally <5 m wide and black to dark greyish green in colour. They generally contain two size populations of plagioclase grains, i.e. phenocryst (1-3 cm) and microphenocryst (<1 cm). Two of the dykes also contain hornblende phenocrysts. The majority have calcite amygdales and strong to moderate chlorite-muscovite alteration. Petrographically, the dykes in the region exhibit consistent features, which include:

- Weakly porphyritic textures with a very low abundance of plagioclase and pyroxene phenocrysts. Plagioclase phenocrysts typically lack zoning textures but may display some twinning.
- A trachytic groundmass consisting of feldspar and quartz grains.
- Abundant very fine-grained opaque minerals, dominantly magnetite.
- Absence of quartz phenocrysts.
- Where less-altered, the dykes contain pyroxene.

These textural and field observations suggest that the emplacement of the dykes occurred at high levels. These dykes range from gabbros to hornblende diorites dykes.

A.5 Volcanic Rocks

Volcanic rocks are mostly exposed north and northwest of Cajamarca (Fig. 2). To date, there has been no comprehensive study of the regional volcanic sequences.

A.5.1 Llama Formation

The Llama Formation belongs to the lower part of the Tertiary Llama-Calipuy Volcanic Sequence (54.8-15.8 Ma) as defined by Noble *et al*. (1990) and Turner (1997). Reyes (1980) mapped equivalent rocks, the Tembladera Formation, in the Cajamarca region and defined the units as avalanche-type breccias and tuffs. Noble *et al*. (1990) described the Llama Formation as rhyolitic ashflow tuffs and dacitic volcanic sequences. Mapping by Turner (1997) of the Yanacocha Volcanic Complex (YVC) and adjacent volcanic rocks identified both the Tembladera and Llama Formation in the Cajamarca region. Turner (1997) dated primary biotite from rhyodacitic tuff using $^{40}Ar/^{39}Ar$ and yielded a date of 15.78 ± 0.34 Ma. Based on this age, he assigned this unit to the upper part for the Llama Formation.

In the Cajamarca region, some units of the Calipuy-Llama sequence crop out in the northeastern part of the study area, near Cruz Conga and La Carpa (Fig. 2). South of Cruz Conga, porphyritic volcanic rocks unconformably overly deformed Cretaceous rocks. They contain hornblende, clinopyroxene, and plagioclase phenocrysts set in a feldspathic matrix that has a trachytic texture. Based on mineralogy and geochemical evidence (Section C), these volcanic rocks from the Cruz Conga region are inferred to be basaltic andesites.

Volcanic rocks in the La Carpa region unconformably overlie deformed Cretaceous limestone units. They consist of a plagioclase, clinopyroxene and hornblende phenocrysts set in a light grey feldspathic matrix. The abundance of amphibole varies at outcrop scale and grains may exceed 3 cm in length. La Carpa volcanic rocks have a light green colour and display weak chlorite-carbonate (propylitic) alteration. Field and petrographical evidence suggests these rocks are propylitic-altered hornblende andesites.

A.5.2 Regalado Volcanic Rocks

According to Turner (1997), middle to late Miocene (12.3–8.2 Ma) volcanic rocks in the Cajamarca region include the Regalado Volcanic Rocks (RVR) and the Huambos Formation. He distinguished the RVR units from the Huambos rocks based on the absence of quartz phenocrysts. Field mapping and petrographic evidence (Appendix A1) indicates biotite phenocrysts may also be applied in this description. The RVR (~12.3-11.4 Ma) comprises andesitic lavas and tuffs (Noble *et al*., 1990; Turner, 1997). Petrographically, the rocks have a crowded porphyritic texture containing abundant plagioclase, clinopyroxene, acicular hornblende and magnetite phenocrysts. Most hornblende grains are rimmed by hematite. Quartz and biotite are notably absent. These units are greenish brown in colour and thin sections indicate weakly propylitic alteration. The matrix is feldspathic and glassy to trachytic in appearance.

A.5.3 Huambos Formation

Rocks of the Huambos Formation (8.8–8.2 Ma, Noble *et al*., 1990; Turner, 1997) are distinguished from the older RVR by the presence of quartz and biotite phenocrysts. Another distinguishing feature is an increase in hornblende and noticeable decrease in pyroxene compared the older Regalado units (Fig. 3 in Section C). The Huambos rocks are andesitic to dacitic ash flow tuffs with plagioclase, hornblende, quartz, biotite, magnetite and clinopyroxene phenocrysts. Quartz grains have corroded rims and minor embayments. Biotite and hornblende phenocrysts contain small inclusions of plagioclase and magnetite.

A.6 Radiometric Dating

Samples selected for $^{40}Ar/^{39}Ar$ studies were chosen based on a variety of factors. Several igneous units in the region had not been dated prior to this study, or had previously been dated using K-Ar and yielded significant errors (Table 2). Field mapping and petrographic studies (Appendix A1; Section C.5) showed mineralogical variations between the different igneous units. Geochemical analyses (major, trace and REE; Appendix C2) further highlighted these variations (Section C.6-C.8). Petrographic evidence combined with electron microprobe analyses (Appendix C1) and electron microscope images were then used on selected samples and minerals to determine the least altered, or otherwise most suitable samples for dating.

A.6.1 Analytical Procedures

Thirteen samples were used for $^{40}Ar/^{39}Ar$ dating, consisting of two samples from the La Carpa region (S-38 and S-21), two from El Galeno (T2 and T4), one from SW of El Galeno, and one each from the Michiquillay deposit (S-H22 176), Michiquillay north (S-59), Cerro Montana (S-31), Cruz Conga (S-32), Aurora Patricia (S-11), Cerro Perol East (S-46), south of Minas Conga (S-MC4) and west of Yanacocha (S-61). Three of these samples (S-21, S-38 and S-59) were analysed at the New Mexico Geochronological Research Laboratory (NMGRL). Inverse isochron ages, $^{40}Ar/^{39}Ar$ intercept and the mean square of weighted deviates (MSWD) were calculated for these samples. The remaining ten samples were analysed at the Argon Geochronology Laboratory at the University of Queensland and only plateau ages are presented. Mineral sample preparation and analytical techniques for both laboratories are provided in Appendix A2.

Table 2. Summary of reason why the various samples were selected for $^{40}Ar/^{39}Ar$ analyses

Sample No.	Location	Lithology	Previous Dates	Reason for Sample Selected
S-21	La Carpa	Hbl Andesite	N/A	Slightly altered volcanic unit unconformably overlying limestone, geochemically significant
S-31	Cerro Montana	Hbl Diorite	N/A	No available radiogenic age, least altered intrusion, geochemically significant
S-16	Sth Galeno	Hbl Gabbro	N/A	No available radiogenic age, least altered dyke observed
S-59	Michiquillay North	Hbl-Bt Diorite	43.6 ± 3.7 Ma$_1$	Previous age date considered unreliable
S-H22 (176)	Michiquillay Prospect	Hbl-Bt Diorite	20.6 ± 0.6 Ma$_1$ 18.8 ± 1.6 Ma$_2$	Previous age dates have high uncertainties
S-38	La Carpa	Hbl-Qtz Diorite	N/A	No available radiogenic age
S-T2	El Galeno	Hbl-Bt Diorite	N/A	No available radiogenic age, early mineralised intrusive phase
S-T4	El Galeno	Hbl-Bt Diorite	N/A	No available radiogenic age, final intrusive phase at centre
S-11	Aurora Patricia	Hbl Diorite	N/A	No available radiogenic age
S-61	West Yanacocha	Hbl Bas Andesite	N/A	Fresh volcanic rock, poorly constrained age
S-MC4	Sth Minas Conga	Hbl-Bt Andesite	N/A	Volcanic overlying deformed limestone, poorly constrained age, geochemically significant
S-46	East Minas Conga	Hbl Microdiorite	N/A	No available radiogenic age, geochemically significant
S-32	Cruz Conga	Hbl Basaltic Andesite	N/A	No available radiogenic age, previously unmapped unit, geochemically significant

Hbl = Hornblende; Bt = Biotite; Qtz = Quartz
N/A = not available; 1 = Laughlin *et al*., 1968; 2 = Llosa *et al*., 1996

A.7 $^{40}Ar/^{39}Ar$ Results

Most of the samples released high amounts of ^{40}Ar during the initial steps suggesting extraneous argon. However, the majority of grains yielded good plateau during later heating steps. Three samples, S-61, S-MC4 and S-32, released insufficient amounts of ^{39}Ar and no meaningful plateaux or spectrums were obtained (Table 3).

Hornblende from a microdiorite (S-46) in the Cerro Perol East region yielded a disturbed spectrum with the majority of ^{39}Ar (~90%) degassed over four heating steps (steps B-E). The final heating steps yielded a complex age spectrum and have a varying K/Ca ratio that suggests alteration (Fig. 4). A plateau age of 57 ± 3 Ma was deduced from steps B-E. This plateau age is considerably younger than the integrated or total gas age of 87 ± 4 Ma. There is low degree of confidence in the total gas age. Phenocrysts of hornblende in S-31, an intrusion from the Cerro Montana region, yielded a disturbed age spectrum during the initial and final heating steps (Fig.4). A plateau age of 47 ± 3 Ma (steps B-F) was obtained from the central portion of the spectrum (~95% of gas released). This plateau age is indistinguishable from the integrated age of 47 ± 2 Ma.

Hornblende from a volcanic rock in the La Carpa region (S-21) yielded a flat spectrum for nearly 85% of the ^{39}Ar released during the step heating (Fig. 5). The calculated weighted mean age for this plateau is 42.55 ± 0.12 Ma (steps B-H), which agrees within error of an inverse isochron age (42.58 ± 0.14 Ma). The last 15% of ^{39}Ar released yielded significant decreases in apparent age. This probably represents degassing of feldspar mineral inclusions observed within the hornblende phenocryst. Slightly altered hornblende grains from a mafic dyke (S-16) in the Galeno region yielded a near plateau age spectrum from ~80% of the gas released (Fig. 5). This sample has low K/Ca ratios for both the initial and final heating steps that correspond to a disturbed age spectrum. These steps suggest the grains have been slightly altered. An age of 29.4 ± 1.4 Ma was obtained from the near plateau (steps C-H). This age is ~5 m.y. older than the integrated age of 24.6 ± 1.2 Ma.

Hornblende from S-11, an intrusion in the Aurora Patricia region, yielded a disturbed age spectrum. High apparent ages were obtained during the initial and final

Table 3. Summary of $^{40}Ar/^{39}Ar$ results

Sample No.	Location	Lithology	Mineral Analysed	Date (Ma)	Error (2σ)	$^{40}Ar/^{36}Ar_i$	MSWD	Quality	Method
S-46	Cerro Perol East	Hbl Microdiorite	Hornblende	57	3			Disturbed	Ar-Ar (UQ)
S-31	Cerro Montana	Hbl Diorite	Hornblende	47	3			Disturbed	Ar-Ar (UQ)
S-21	La Carpa	Hbl Andesite	Hornblende	42.55	0.12	293 ± 7	0.90	Near Plateau	Ar-Ar (NMGRL)
S-16	Sth Galeno	Hbl Gabbro	Hornblende	29.40	1.40			Near Plateau	Ar-Ar (UQ)
S-59	Michiquillay North	Hbl-Bt Diorite	Hornblende	20.60	0.14	294 ± 22	1.70	Plateau	Ar-Ar (NMGRL)
S-11	Aurora Patricia	Hbl Diorite	Hornblende	21.30	0.80			Near Plateau	Ar-Ar (UQ)
S-H22 (176)	Michiquillay Deposit	Hbl-Bt Diorite	Biotite	19.77	0.05			Plateau	Ar-Ar (UQ)
S-38	La Carpa	Hbl-Qtz Diorite	Hornblende	17.85	0.06	296.9 ± 3.4	1.20	Plateau	Ar-Ar (NMGRL)
S-T2	El Galeno Deposit	Hbl-Bt Diorite	Biotite (hydrothermal)	17.50	0.30			Plateau	Ar-Ar (UQ)
S-T4	El Galeno Deposit	Hbl-Bt Diorite	Biotite	16.53	0.18			Plateau	Ar-Ar (UQ)
S-61	West Yanacocha	Hbl Basaltic Andesite	Hornblende	N/A				No Plateau	Ar-Ar (UQ)
S-MC4	Sth Minas Conga	Hbl-Bt Andesite	Hornblende	N/A				No Plateau	Ar-Ar (UQ)
S-32	Cruz Conga	Hbl Basaltic Andesite	Hornblende	N/A				No Plateau	Ar-Ar (UQ)

N/A = No meaningful plateau obtained
Hbl = Hornblende; Bt = Biotite; Qtz = Quartz
NMGRL = New Mexico Geochronology Research Lab, UQ = University of Queensland

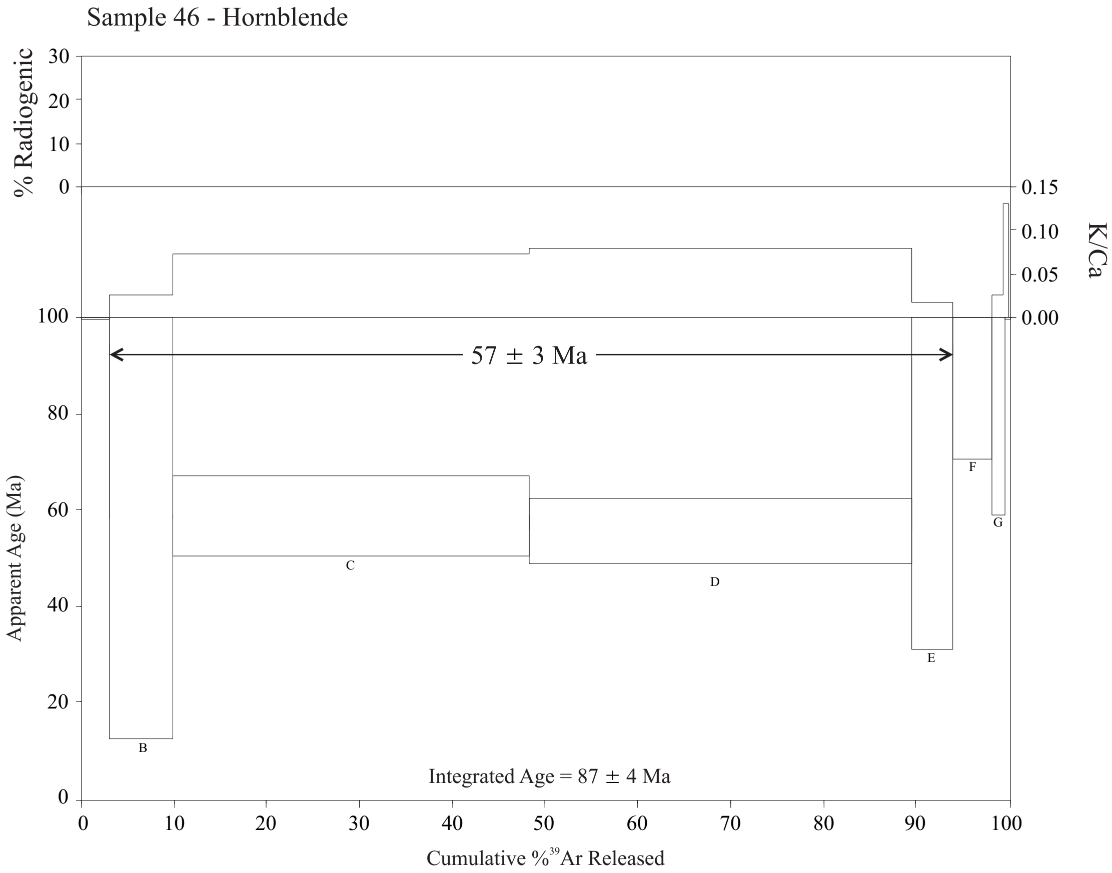

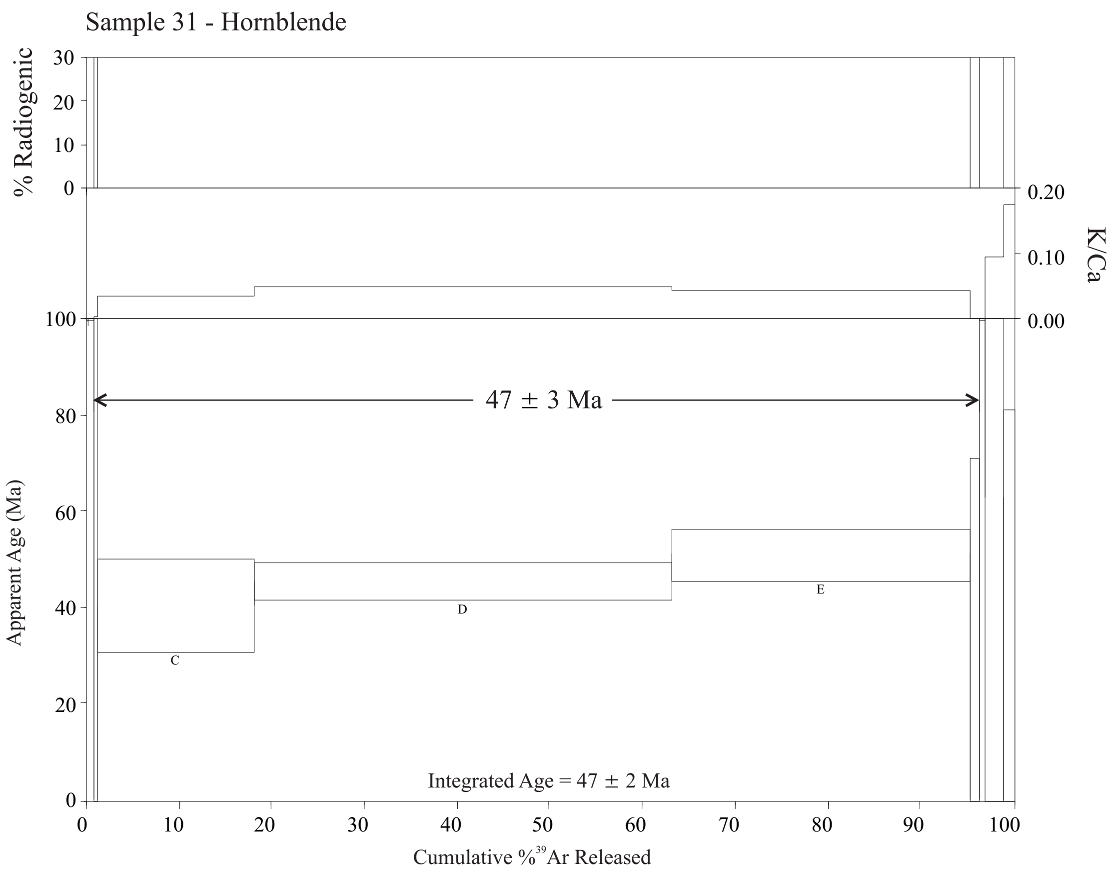

Fig. 4. $^{40}Ar/^{39}Ar$ apparent age spectra of intrusive rocks from the east Cerro Perol region and the Cerro Montana region analysed by incremental step heating.

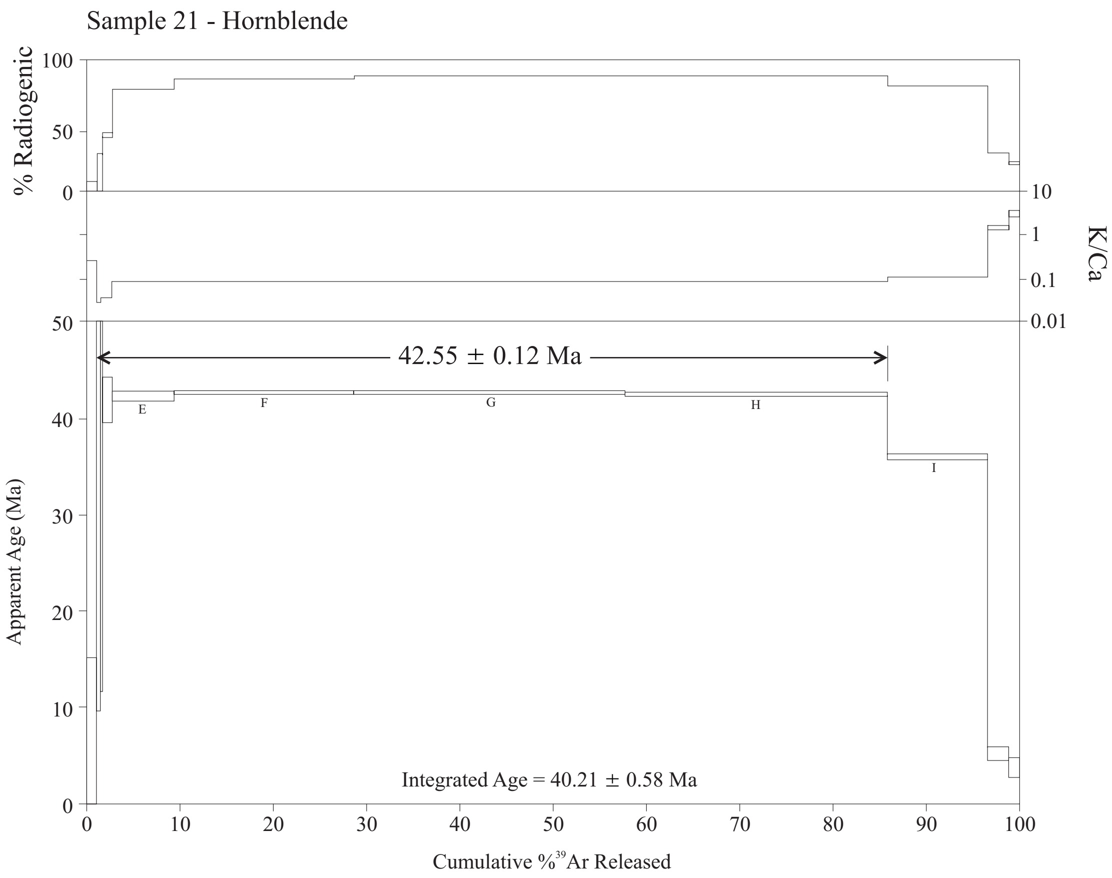

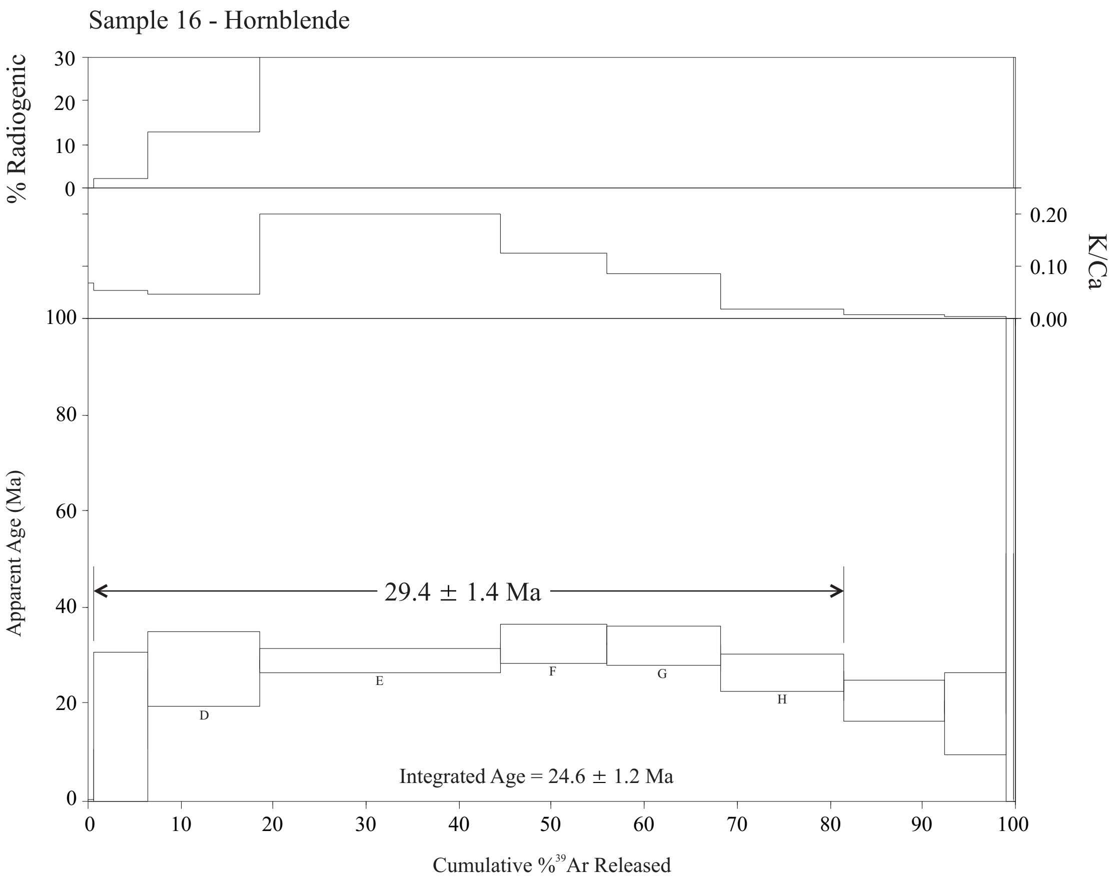

Fig. 5. $^{40}Ar/^{39}Ar$ apparent age spectra for a volcanic rock from the La Carpa region and mafic dyke near El Galeno region analysed by incremental step heating.

heating steps. This suggests either the presence of excess argon or minor alteration. A plateau age of 21.3 ± 0.8 Ma was calculated from ~99% of the gas released (Fig. 6, steps A-F). Hornblende from an intrusive rock (S-38) in the La Carpa region yielded an undisturbed age spectrum with a weighted mean age of 17.85 ± 0.06 Ma (steps A-H, Fig. 6) from ~99% of the ^{39}Ar released. This date is concordant with an inverse isochron age (17.83 ± 0.06 Ma) that produced a ^{40}Ar/^{39}Ar intercept (296.9 ± 3.4) within error of the atmospheric ratio.

Hornblende from a barren intrusive rock from Michiquillay North (S-59) yielded young apparent ages for the first 5% of ^{39}Ar released that possibly suggests minor alteration. The remaining portion (~95%) of the spectrum yields a weighted mean age of 20.61 ± 0.14 Ma (steps C-J, Fig. 7), that is concordant with an inverse isochron analysis (20.66 ± 0.64 Ma). Magmatic biotite from a synmineralisation stock at the Michiquillay prospect (S-H22) yielded old apparent dates for the initial nine heating steps suggesting extraneous ^{40}Ar (Fig. 7). The remaining spectrum (~80%) yielded a nearly undisturbed plateau giving a date of 19.77 ± 0.05 Ma.

Hydrothermal biotite from an early intrusive phase (S-T2) at El Galeno yielded a nearly undisturbed age spectrum with the initial two steps producing firstly younger then older apparent ages (Fig. 8). The remaining 96% of ^{39}Ar released yields a plateau age of 17.5 ± 0.3 Ma (steps C-I). This date is indistinguishable from the integrated age of the spectra (17.5 ± 0.3 Ma). A post-mineralisation intrusion (S-T4) from the same deposit produced a slight saddle-shaped age spectrum with the initial steps having an apparent date of *ca*. 25 Ma. The remaining 86% of the spectrum for the magmatic biotite yields a plateau age of 16.53 ± 0.18 Ma (steps D-K; Fig. 8).

A.8 Interpretation of ^{40}Ar/^{39}Ar Dates

level of analytical precision (within 2σ values) and are consistent with standard criterion for classification of plateaux as defined by Dalrymple and Lanphere (1974). Therefore, these results are considered reliable. S-46 yielded a disturbed spectrum and a ‘plateau’

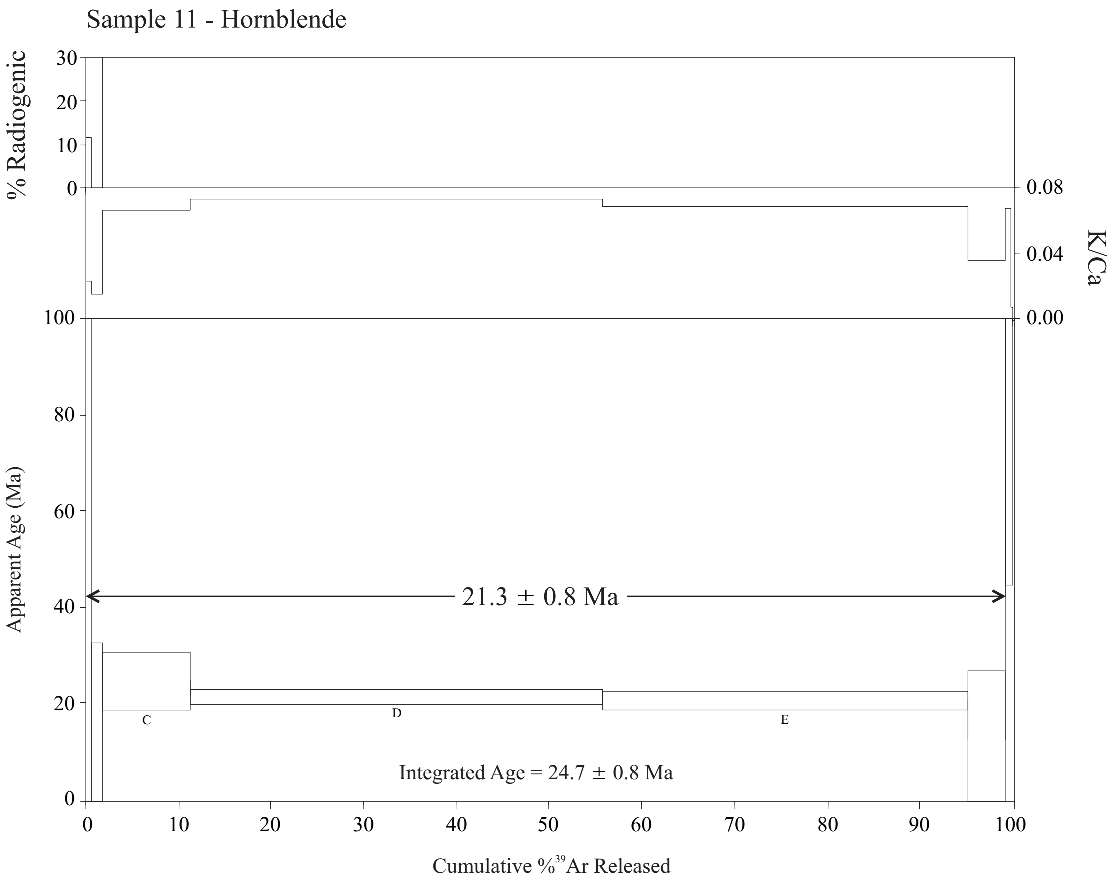

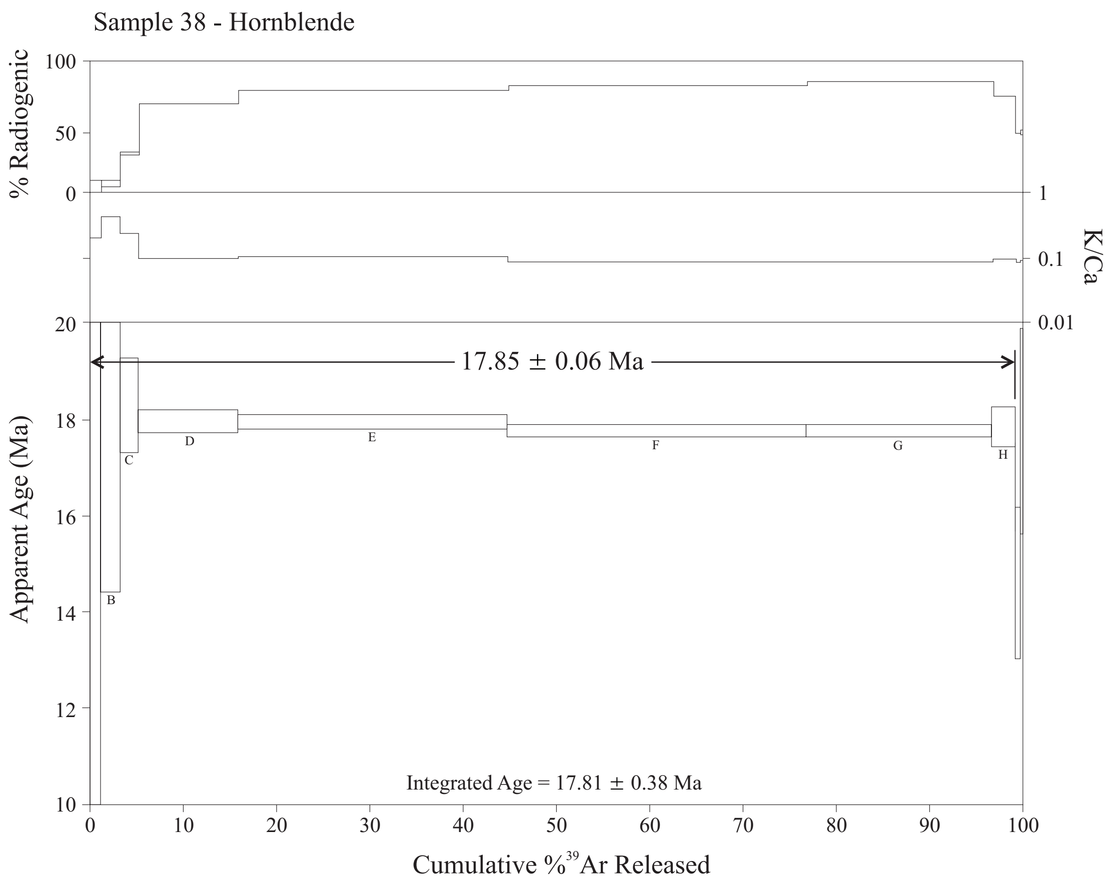

Fig. 6. $^{40}Ar/^{39}Ar$ apparent age spectra of intrusive samples from the Aurora Patricia and La Carpa regions analysed by incremental step heating.

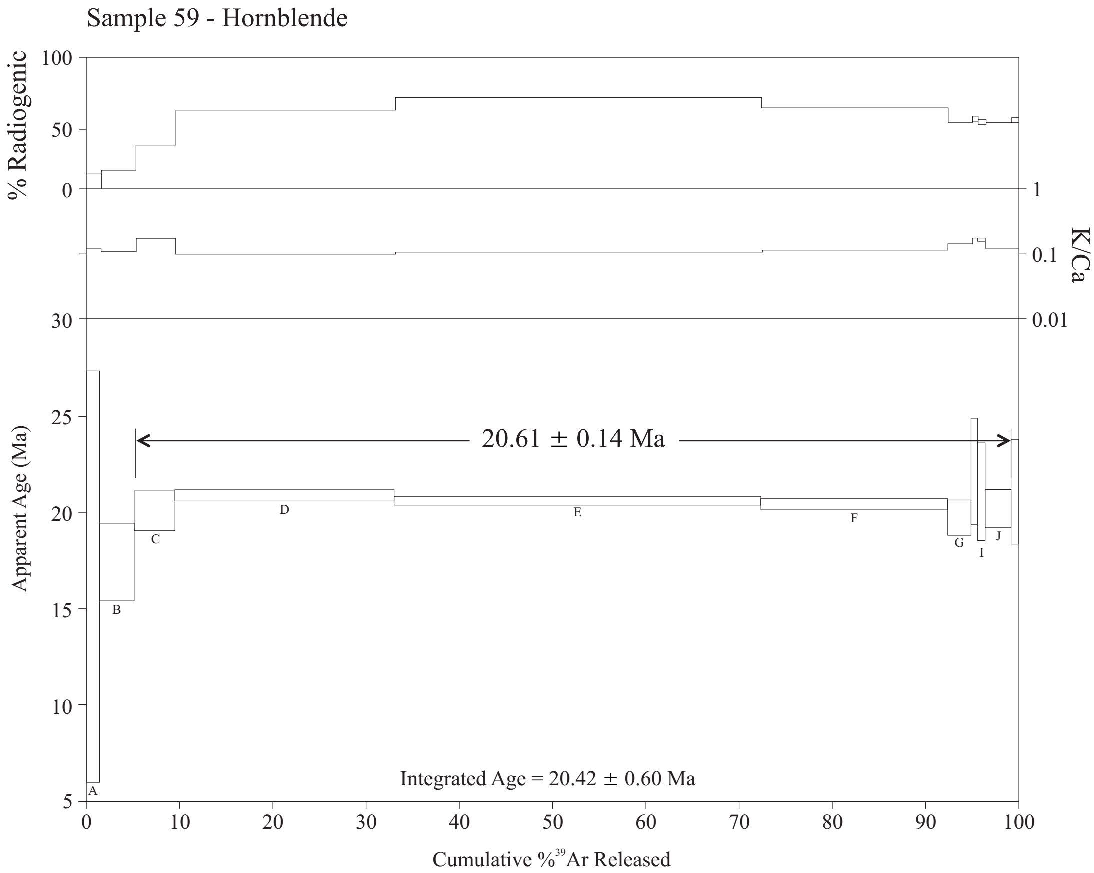

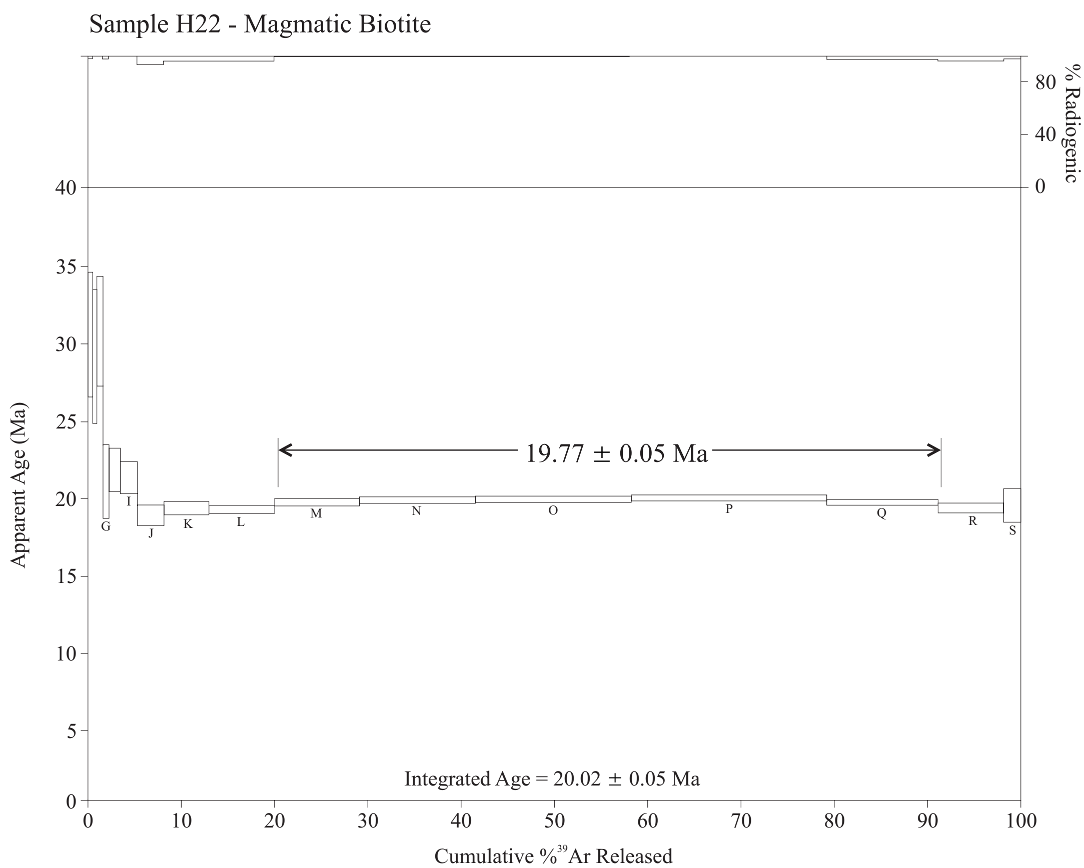

Fig. 7. $^{40}Ar/^{39}Ar$ apparent age spectra for samples from intrusions in the Michiquillay region analysed by incremental step heating.

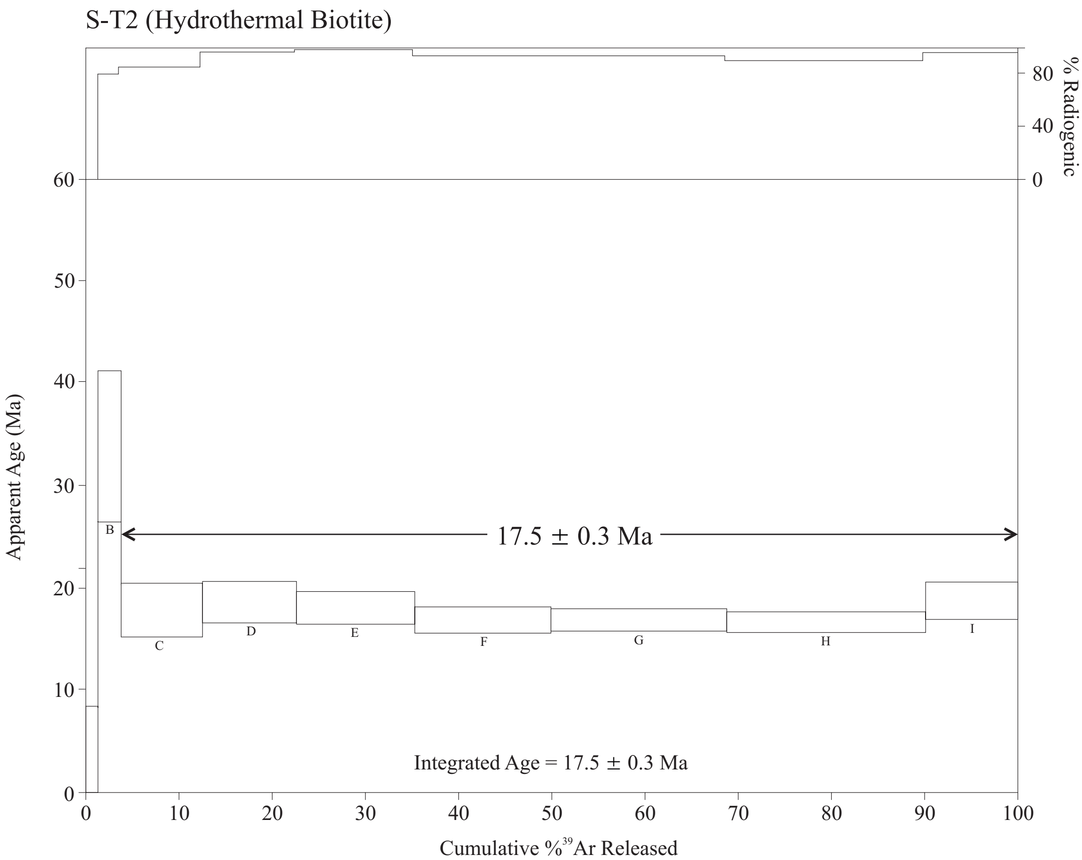

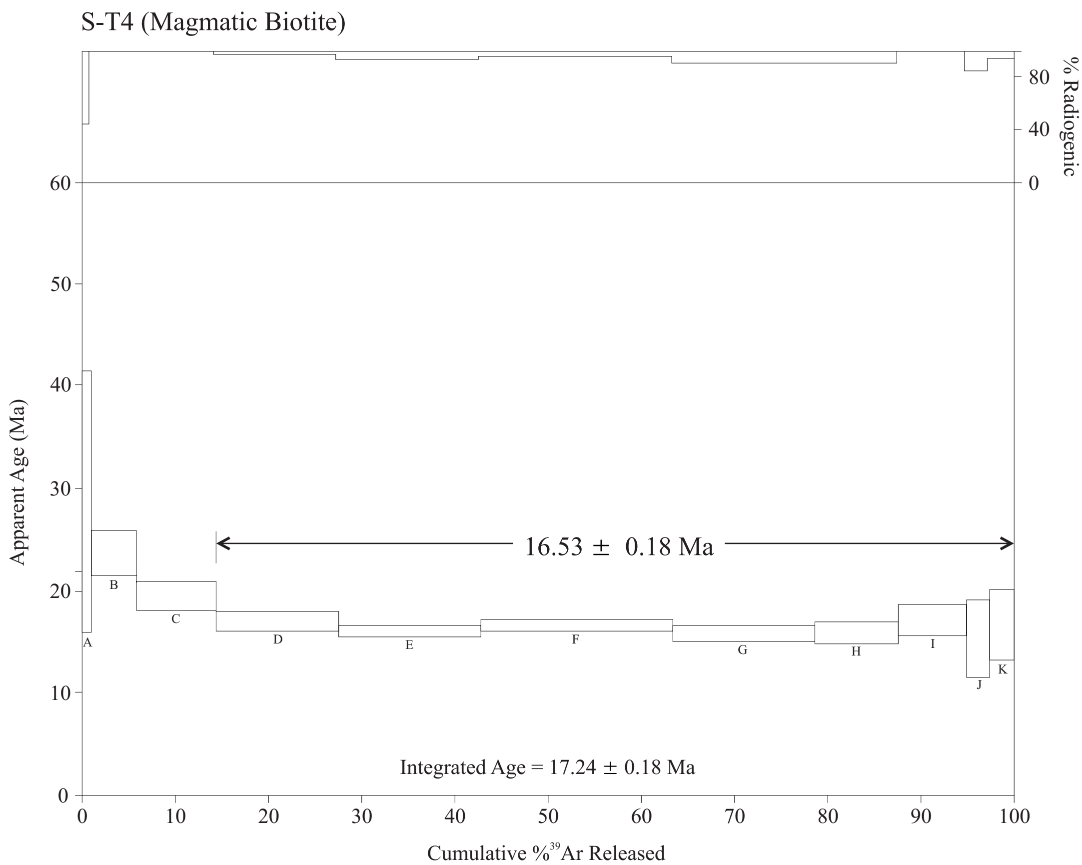

Fig. 8. $^{40}Ar/^{39}Ar$ incremental heating age spectra for a hydrothermal biotite from a synmineralisation intrusion and a magmatic biotite from a late-mineralisation stock at El Galeno.

age of 57 ± 3 Ma from step four heating steps. A second hornblende grain analysed from this sample yielded an apparent date of 59 ± 4 Ma from a disturbed plateau. Therefore, the age of this intrusion is cautiously interpreted at *ca*. 57 Ma. The following paragraphs will compare the reliable dates from this study with previous geochronology dates from the region.

Few dates exist for Palaeocene igneous rocks in the Cajamarca-Hualgayoc region (Laughlin *et al*., 1968; Macfarlane *et al*., 1994; Llosa *et al*., 1996) and prior to this study dates had only been obtained on intrusive rocks using the K-Ar or Rb-Sr systems. Llosa *et al*. (1996) dated an intrusion from Cocanes East at Minas Conga at 43.6 ± 3.7 Ma, whilst the Coymolache intrusion from Hualgayoc has been dated at 45 ± 3.4 Ma (Rb-Sr mineral isochron, Macfarlane *et al*., 1994). Recently however, James (1998) dated zircons from the Coymolache intrusion at 14.3 ± 0.1 Ma (U-Pb) indicating the Rb-Sr date is unreliable (Macfarlane, *pers commun*., 2002). New $^{40}Ar/^{39}Ar$ dates for S-46 (57 ± 3 Ma) and S-31 (47 ± 3 Ma) are the oldest igneous rocks dated in the region. These dates indicate that magmatic and intrusive activity in the Cajamarca commenced some 13 m.y. earlier than previous analyses suggested. Noble *et al*. (1990) dated several volcanic rocks of Palaeogene age (54.8–35.4 Ma) in the Llama and Huambos region, some 100 km NW of Cajamarca. S-21, an andesitic rock from La Carpa (42.55 ± 0.12 Ma), is also the first Palaeogene volcanic rock dated in the Cajamarca district. It is assigned to the Lower Llama Formation based on this date.

Intrusions from both Michiquillay north (46.4 ± 1.8 Ma) and the Michiquillay deposit (20.6 ± 0.6 Ma) were previously dated by Laughlin *et al*. (1968). These authors concluded that the apparent Eocene age of the Michiquillay north intrusion was unreliable and resulted from excess ^{40}Ar. They suggest this intrusion was more likely to have been emplaced around the same time as the intrusion from the Michiquillay deposit, i.e. ~20 Ma. A weighted mean age of 20.61 ± 0.14 Ma calculated for hornblende phenocrysts from S-59 confirms this suggestion and indicates these barren propylitically altered intrusions are early Miocene. Hornblende from a barren unaltered intrusion at Aurora Patricia, S-11, yielded a slightly older $^{40}Ar/^{39}Ar$ date at 21.3 ± 0.8 Ma. Previous K-Ar dates from the Michiquillay deposit include 20.6 ± 0.6 Ma (hydrothermal biotite, Laughlin *et al*., 1968) and 18.8 ± 1.6 Ma (magmatic biotite, Llosa *et al*., 1996). These dates have high uncertainties. A $^{40}Ar/^{39}Ar$ weighted mean age for magmatic biotite (S-H22 176) from a synmineralisation intrusion constrains the age of crystallisation at the Michiquillay deposit to 19.77 ± 0.05 Ma. These results also suggest mineralisation at the Michiquillay deposit occurred slightly later than the emplacement of barren Michiquillay north intrusions.

Hornblende phenocrysts from a barren La Carpa intrusion yield a weighted mean age of 17.85 ± 0.06 Ma. This result is similar to a K-Ar date (17.1 ± 1.5 Ma; Llosa *et al*., 1996) from a Chailhuagon South intrusion at Minas Conga and a $^{40}Ar/^{39}Ar$ date of hydrothermal biotite (17.50 ± 0.30 Ma) from the second intrusive phase (P2 porphyry) at El Galeno. These results suggest a temporal link between these three intrusions and the main P1 porphyry at El Galeno. This is supported by similar geochemical trends in the La Carpa and El Galeno intrusions (Section C).

Magmatic biotite in a late- to post-mineralisation intrusion (16.53 ± 0.18 Ma) at El Galeno crystallised about one million years after main stage alteration at the deposit and *ca*. 800,000 years before deposition of the Upper Llama Formation (15.78 ± 0.17 Ma; Turner, 1997). The next youngest intrusion dated in the district is from the Yanacocha deposit and has a $^{40}Ar/^{39}Ar$ date of 9.90 ± 0.05 Ma (Turner, 1997). Despite intense magmatic and hydrothermal activity in the Hualgayoc region throughout middle Miocene times (16.8–7.2 Ma), this stock at El Galeno is inferred to represent the last intrusive rock emplaced during early to middle Miocene times in the Cajamarca region. If this is assumed, emplacement and formation of most recognised porphyry-related deposits in the Cajamarca region occurred over an approximately 7 m.y. period, spanning from 23.2 to 16.5 Ma.

A.9 Discussion

Noble *et al*. (1990) recognised a close association between Tertiary tectonism and magmatism in the Central Andes. They inferred this association was directly linked to large-scale tectonic events, such as relative motion of major lithospheric plates and rate of plate convergence. This assumption appears to be partially true based on results from this and other age dating studies (Fig. 9). Between 50 and 42 Ma the western margin of the South American plate was characterised by high convergence rates (~150 mm/year, Pardo-Casas and Molnar, 1987). This interval roughly corresponds with widespread deposition of Llama-Calipuy Volcanic rocks (~54-43 Ma) in the northern Peruvian Andes (Benavides, 1999). The dates of four igneous rocks from the Cajamarca-Llama region fit within this interval of high convergence. Three of these four dates are toward the end of the interval and coincide with the Incaic II (43-42 Ma) tectonic event. Two igneous rocks predate this interval, with a crystallisation age of the oldest igneous rock (S-46 at 57 Ma) corresponding with the Incaic I orogenic event (59-55 Ma, Benavides, 1999).

This period of high convergence rates was followed by low convergence rates, from 36 to 24 Ma (Pardo-Casas and Molnar, 1987), during which some volcanic rocks were erupted (39.3-35.4 Ma, Noble *et al*., 1990) and high-level mafic dykes were emplaced (*ca*. 29.5 Ma). This age coincides with the onset of the Quechua III tectonic event (30-27 Ma, Benavides, 1999). A strong link between low convergence and magmatism quiescence is evident in northern Peru where few Oligocene igneous rocks have been documented or dated (Noble and McKee, 1999).

Magmatic activity recommenced around the early Miocene (*ca*. 23 Ma) and was temporally linked with the Incaic IV orogenic pulse (22 Ma, Benavides, 1999), clockwise rotation of the Nazca Plate and an increase in plate convergence rate (Fig. 9, Pardo-Casas and Molnar, 1987). Early Miocene magmatism near Cajamarca resulted in formation of numerous porphyry-related Cu ± Au deposits including Minas Conga (23.2-17.1 Ma), Michiquillay (19.8 Ma), El Galeno (17.5-16.5 Ma) and possibly Minas Carpa (~17.5 Ma?). Several similar-aged barren intrusions also crop out in the region, such as intrusions at Aurora Patricia (21.3 Ma), Michiquillay north (20.6 Ma) and La Carpa (17.9 Ma). Results from this study indicated early Miocene porphyry-related deposits formed over a 7 m.y. period. Noble and McKee (1999) and Petersen (1999) both suggested magmatic and metallogenic provinces in central and northern Peru formed over short time intervals. Noble and McKee (1999) further concluded prolonged magmatic-hydrothermal intervals (5–10 m.y.), such as documented in the Potrerillos district of Chile (Marsh *et al*., 1997), are favourable for formation of giant porphyry deposits. Therefore, the absence of giant deposits in central and northern Peru is

Fig. 9. Diagram illustrating the timing of magmatic-hydrothermal events in the Cajamarca (bold), Hualgayoc and Llama-Huambos regions (refer to Tables 1 and 3) with recognised orogenic pulses (Benavides, 1999) and changes in the rate of convergence between the South America and Nazca plates (Pardo-Casas and Molnar, 1987). Shaded regions define periods of mineralisation in the Cajamarca and Hualgayoc regions. Dates considered or shown to be unreliable, such as Michiquillay North by Laughlin *et al*. (1968), have been omitted from this diagram.

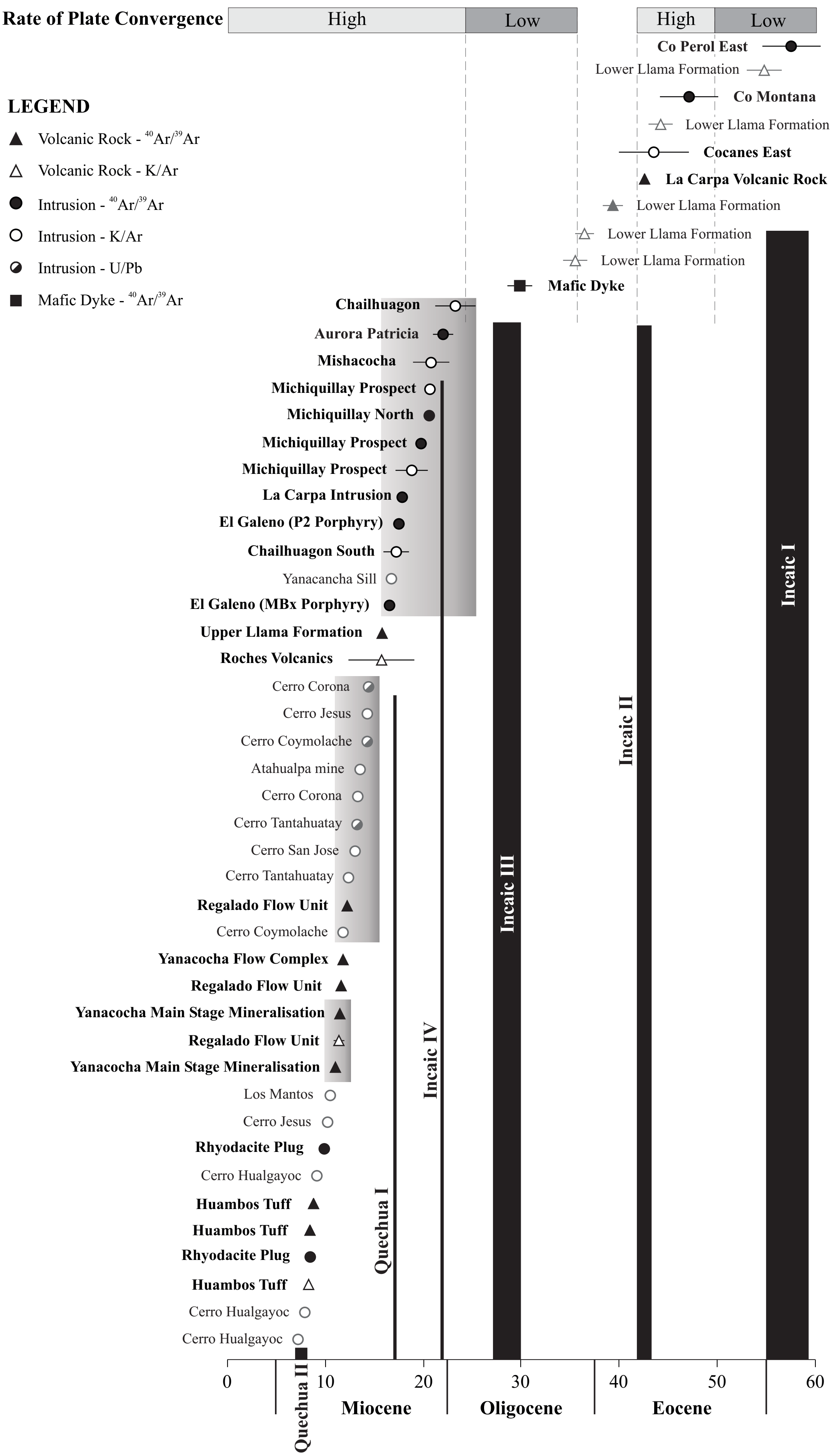
Rate of Plate Convergence
High
Low
High
Low
LEGEND
Volcanic Rock - 40Ar/39Ar
Volcanic Rock - K/Ar
Intrusion - 40Ar/39Ar
Intrusion - K/Ar
Intrusion - U/Pb
Mafic Dyke - 40Ar/39Ar
Co Perol East
Lower Llama Formation
Co Montana
Lower Llama Formation
Cocanes East
La Carpa Volcanic Rock
Lower Llama Formation
Lower Llama Formation
Lower Llama Formation
Mafic Dyke
Chailhuagon
Aurora Patricia
Mishacocha
Michiquillay Prospect
Michiquillay North
Michiquillay Prospect
Michiquillay Prospect
La Carpa Intrusion
El Galeno (P2 Porphyry)
Chailhuagon South
Yanacancha Sill
El Galeno (MBx Porphyry)
Upper Llama Formation
Roches Volcanics
Cerro Corona
Cerro Jesus
Cerro Coymolache
Atahualpa mine
Cerro Corona
Cerro Tantahuatay
Cerro San Jose
Cerro Tantahuatay
Regalado Flow Unit
Cerro Coymolache
Yanacocha Flow Complex
Regalado Flow Unit
Yanacocha Main Stage Mineralisation
Regalado Flow Unit
Yanacocha Main Stage Mineralisation
Los Mantos
Cerro Jesus
Rhyodacite Plug
Cerro Hualgayoc
Huambos Tuff
Huambos Tuff
Rhyodacite Plug
Huambos Tuff
Cerro Hualgayoc
Cerro Hualgayoc
Incaic I
Incaic II
Incaic III
Incaic IV
Quechua I
Quechua II
0
10
20
30
40
50
60
Miocene
Oligocene
Eocene

possibly explained by the lack of prolonged magmatic intervals. However, results from this study indicate prolonged magmatic-hydrothermal activity has occurred in the Cajamarca region. Whilst no giant porphyry deposits developed during this interval, a number of significant Au-rich (Minas Conga and Minas Carpa) and Cu-Au-Mo (Michiquillay and El Galeno) porphyry deposits did form. A cluster of dates between 17.85 and 16.53 Ma (Fig. 9) suggests early Miocene magmatism peaked and terminated contemporaneously with Quechua I tectonic event (17 Ma; Benavides, 1999). This magmatic interval appears to have been followed by an approximately three million year magmatic hiatus.

The timing of magmatic and hydrothermal activity in the polymetallic Hualgayoc region has been well documented (Fig. 9, Borredon, 1982; Macfarlane *et al*., 1994; James, 1998). The oldest igneous rock dated in this region, the Yanacancha Sill, was emplaced at *ca*. 16.8 Ma (Macfarlane *et al*., 1994) and followed by the Cerro Corona and Cerro Coymolache intrusions at ~14.4 Ma (James, 1998). A Tantahuatay intrusion yielded a slightly younger date of 13.2 ± 0.2 Ma (James, 1998) that concurs with hydrothermal activity at Cerro Corona, Cerro San Jose and the Atahualpa mine (Macfarlane *et al*., 1994). Despite later sporadic hydrothermal activity and emplacement of rhyodacitic stocks in the region (Fig. 9; Borredon, 1982; Macfarlane *et al*., 1994), intense magmatism largely ceased after *ca*. 12.5 Ma. The cause of this apparent change in focus of Miocene magmatic-hydrothermal activity between the Cajamarca and Hualgayoc districts is unclear. This possibly reflects a bias in sampling and the number of igneous rocks dated. High precision $^{40}Ar/^{39}Ar$ dates from Turner (1997) indicate eruption of andesitic to rhyodacitic rocks (12.3-8.4 Ma) and formation of the Yanacocha high-sulphidation deposit (11.46-10.92 Ma) characterises middle to late Miocene magmatic activity in the Cajamarca region. Termination of magmatism in both Cajamarca and Hualgayoc occurred during the Quechua II orogenic event (7-8 Ma, Benavides, 1999).

In summary, the ages of Tertiary igneous rocks in the Cajamarca and Hualgayoc regions further support the association between periods of magmatic activity, tectonism and high convergence rates proposed by Noble *et al*. (1990). Palaeocene-Eocene magmatism appears to have peaked during the Incaic II orogenic event and towards the end of a period of high convergence rate. Oligocene times were characterised by a lack of magmatic activity and low plate convergence rates. Intense Miocene magmatism commenced shortly after the Incaic IV compressional event, which was associated with a change to high convergence and rotation in plate motion (Pardo-Casas and Molnar, 1987). Significantly, periods of Miocene mineralisation in the Cajamarca-Hualgayoc region did not necessarily coincide with orogenic intervals or changes in plate subduction angle.

A.10 Conclusion

New $^{40}Ar/^{39}Ar$ dates further constrain the timing of magmatic and hydrothermal events in the Cajamarca region. These high precision results combined with previous age dating studies suggest the following magmatic-hydrothermal history:

1. Palaeogene magmatism (57-35 Ma) was characterised by both deposition of the Upper Llama Volcanic Formation and emplacement of felsic intrusions.
2. Several mafic dykes were possibly emplaced around middle Oligocene times. However, the Oligocene appears to have been characterised by a lack of volcanic and intrusive activity.
3. Formation of porphyry-related deposits occurred over a 7 m.y. interval during the early to middle Miocene (23.2 – 16.5 Ma) and coincided with emplacement of coeval barren intrusions. Thus far, no volcanic rocks have been dated during this 7 m.y. interval.
4. Deposition of the Lower Llama Volcanic Formation *ca*. 15.8 occurred following formation of the porphyry deposits.
5. Deposition of middle to Lower Miocene volcanic rocks (~12.3 Ma) occurred after an apparent 3.5 m.y. magmatic hiatus.
6. Formation of the Yanacocha district and main stage Au mineralisation between 11.5 and 10.9 Ma.
7. Cessation of magmatic activity in the Cajamarca region during late Miocene times (8.4 Ma).

The new $^{40}Ar/^{39}Ar$ dates suggest magmatic events in the Cajamarca region may have occurred over longer intervals than previously suggested. At present, a high concentration of age dates for magmatic-hydrothermal events in the Cajamarca-Hualgayoc region are from known mineralised centres, such as Yanacocha, Minas Conga, Michiquillay and El Galeno. This has created a bias towards understanding the age of mineralised centres. Further dates of barren igneous rocks are required to fully constrain the duration of regional magmatism so we understand to the timing of mineralisation events relative to magmatic intervals. Furthermore, a number of previous age dates were determined using the K-Ar system. Compared to the high precision $^{40}Ar/^{39}Ar$ results, previous K-Ar dates of igneous rocks in the region have high uncertainties or represent unreliable dates.

SECTION B

Structural evolution of the Cajamarca region, northern Peru: Implications for development of mineralised centres

Section B: Structural evolution of the Cajamarca region, northern Peru: Implications for development of mineralised centres.

B.1 Abstract

The oldest structural features identified in the Cajamarca region of northern Peru are a series of low-angle thrust faults and near E-W trending folds in Cretaceous sedimentary rocks. The dominant faults in the deformed sedimentary rocks are NE-trending and likely to have developed contemporaneously with the early fold-thrust phase. A series of subvertical Miocene(?) normal faults are superimposed on these older structures. These range from NE- to NW-trending, plus minor near E-trending. Early to middle Miocene intrusive rocks are mostly located in the hanging wall of a regional-scale thrust and are spatially associated with secondary oblique structures. Structural investigations at mineralised porphyry systems reveal that the deposits are typically characterised by NNW fault-fracture trends and subordinate NE-trending structures. Two of the porphyry Cu complexes, Minas Conga and Michiquillay, contain N to NNW deposit-controlling fault-vein arrays that were influenced by tectonic stress. In contrast, the third mineralised porphyry, El Galeno, has both magmatic- and tectonic-controlled fracture arrays. NW deposit-controlling faults and an overall NE district trend characterise the late Miocene Yanacocha high-sulphidation Au district. NE-trending faults throughout the region display dextral movement, whereas NW faults have sinistral displacement. Both of these fault trends also show evidence of late vertical displacement.

Structural investigations in the Cajamarca region suggest the location and formation of Miocene mineralised centres resulted from younger tectonic events superimposed on pre-existing structures. Fault and fracture trends in the region display a counterclockwise rotation in orientation with time, i.e. NE-trending structures in older units compared to NW-trending in the younger units. These changes in fault orientation are temporally linked with clockwise rotation of the Nazca plate. Cretaceous sedimentary rocks preserve a dominant NE fault-fracture trend that formed during NNE-directed oblique plate convergence along the western margin of the South American plate. A near orthogonal plate convergence direction predominated

throughout the Miocene, during which N- to NW-striking faults formed. These oblique to orthogonal fault trends superposed on pre-existing regional structures significantly influenced the emplacement of diorite stocks. Early- to middle Miocene porphyry Cu centres contain N- to NNW deposit-controlling faults, whereas the late Miocene high-sulphidation deposit was controlled by NW- and E-W striking faults. Faults at these Miocene mineralised centres display both horizontal and vertical displacement. This suggests rotation of the principal stress direction occurred during formation of these deposits. Changes in the principal stress direction and observed NW to NE conjugate trends at mineralised Miocene centres provided important dilatant channelways for ascending hydrothermal fluids.

B.2 Introduction

Porphyry Cu deposits are commonly spatially associated with regional structures or lineaments (Tosdal and Richards, 2001). The orientation and timing of activation or reactivation of these structures is largely controlled by major tectonic events and can significantly influence mineralisation at a deposit (Sibson, 2001). Fault-fracture networks focus ascending magmatic and hydrothermal fluids at porphyry Cu deposits, as well as preserving important information on structural controls of these deposits and regional stress fields. Previous studies and discussions on structural controls at porphyry Cu deposits and districts include work by Gustafson and Hunt (1975), Titley and Heidrick (1978), Heidrick and Titley (1982), Titley *et al*. (1986), Lindsay *et al*. (1995) Richards *et al*. (2001) and Chernicoff *et al*. (2002).

The Cajamarca mining district in northern Peru (Fig. 1a) is characterised by deformed marine Cretaceous sedimentary rocks that have been intruded and overlain by Tertiary porphyritic intrusive and volcanic units. Based on lineaments observed from satellite images, Quiroz (1997) proposed that mineralised systems in the region are restricted to a NE-trending feature, termed the Chicama-Yanacocha structural corridor (Fig. 1a). This incorporates the southern part of the Huancabamba Deflection zone and the world-class Yanacocha epithermal Au deposits. Several mineralised intrusive-related deposits such as Minas Conga (Au-Cu), Michiquillay (Cu-Au) and El Galeno (Cu-Au-Mo) are also located within this corridor (Fig. 1b). Previous regional geological

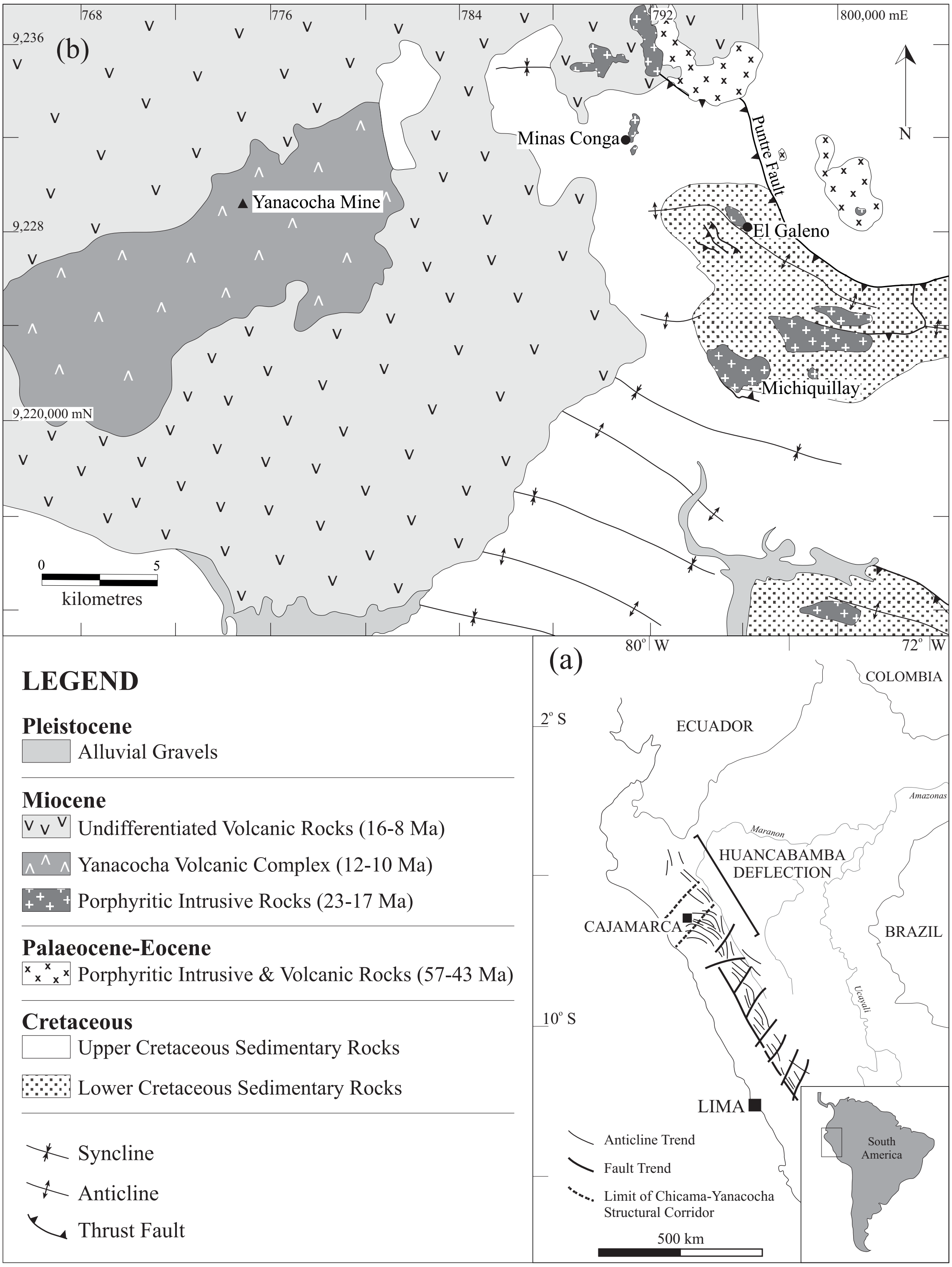

Fig. 1. (a) The Cajamarca district, located in southern part of Huancabamba deflection of northern Peru (modified from Benavides, 1999). (b) The district consists of deformed Cretaceous sediment intruded and unconformably overlaid by Tertiary igneous rocks (modified from Reyes, 1980).

mapping of the Cajamarca district (Reyes, 1980; Wilson, 1985a, 1985b; Bellier *et al*., 1989; Quiroz, 1997) and detailed geological studies at various mineralised centres (Hollister and Sirvas, 1974; Macfarlane and Petersen, 1990; Llosa *et al*., 1996; Turner, 1997; James, 1998; Longo, 2000), combined with palaeomagnetic studies (Laj *et al*., 1989: Mitourad *et al*., 1992) define a complex and protracted tectonic, magmatic, hydrothermal and mineralisation history.

The structural framework of the Cajamarca district during Tertiary times, especially with regards to formation of mineralised complexes is poorly understood. This section presents new fault and fracture data for the deformed Cretaceous sedimentary rocks and Miocene mineralised intrusive centres in the Cajamarca mining district. Structural data were compiled from field mapping, aerial photo interpretation and combined with previously unpublished and published material (MMA, 1975; Longo, 2000; Llosa and Veliz, 2000). A model for the structural evolution of the region, with emphasis on regional influences for formation of Miocene mineralised complexes, is also presented.

B.3 Tectonic Framework of Northern Peru

The Cajamarca mining district is located in the northern Peruvian Andes at altitudes from 2700m to 4300m where the Huancabamba Deflection marks a significant change in the structural grain from the dominant NW Andean trend to near E-W (Fig. 1a). Cretaceous marine and non-marine sedimentary rocks in northern Peru were deposited in the Western Peruvian Trough (WPT) in a Mariana-type subduction regime (Mégard, 1984). The WPT became the Western Cordillera after later folding and subsequent uplift. From early Tertiary time, a change to Andean-type subduction was marked by repeated episodes of compression, intense magmatism, crustal thickening and uplift (Benavides, 1999; Fig. 2).

B.3.1 Cretaceous History

During late Triassic to late Cretaceous times, northern Peru was the depositional site of a major marine sequence and characterised by an extensional regime that caused crustal attenuation or Mariana-type subduction (Benavides, 1999). The

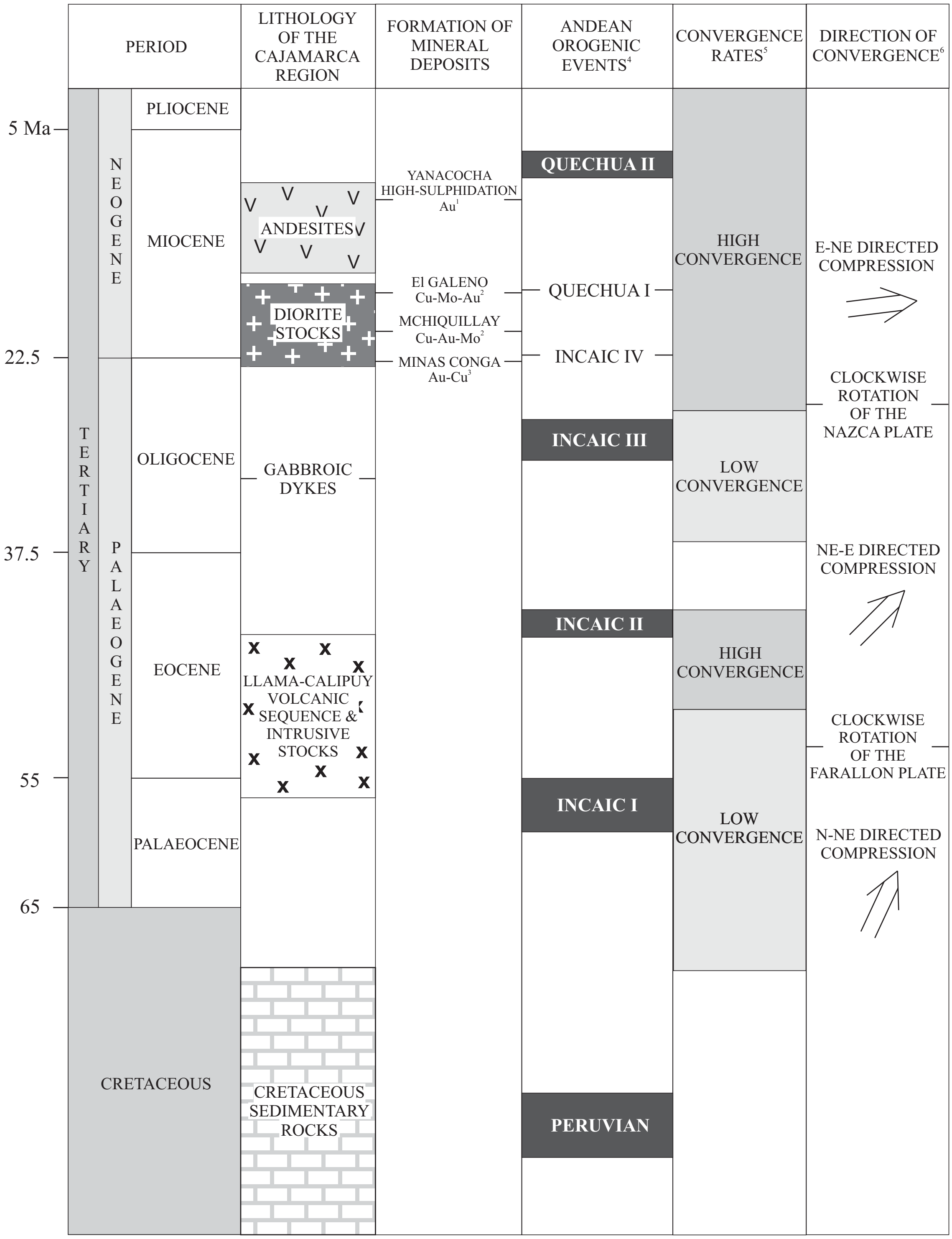

Fig. 2. Tectonic framework of the northern Peruvian Andes and the Cajamarca district. [1] Turner (1997), [2] Section A, [3] Llosa *et al*., (1996), [4] Megard (1984), [5] Pardo-Casas and Molnar (1987), [6] Pilger (1984).

oldest rocks in the Cajamarca region are Lower Cretaceous quartzite, siltstone and shale units (Benavides, 1956). These are overlain by an Upper Cretaceous shallow water marine marl – limestone sequence. Between 90 and 55 Ma, northern Peru underwent a period of weak deformation that was associated with a significant decrease in subsidence rates and resulted in the development of disconformities (Jaillard and Soler, 1996). The first widespread deformation phase observed in Peru is the Peruvian Orogeny that led to the emergence of both the WPT and Eastern Peruvian Trough (Mégard, 1984). In the WPT, this late Cretaceous orogenic event resulted in the emergence of the marine sedimentary rocks, continental red-beds were deposited and initial development of the Western Cordillera occurred. Pardo-Casas and Molnar (1987) suggest a slow plate convergence rate (55 ± 28 mm/a) between the Farallon and South American plates occurred from 70 to 50 Ma.

B.3.2 Tertiary History

Andean-type subduction has occurred along the western margin of the South American plate from the end of the Cretaceous period to the present day. Intense fold and thrust development in the Cretaceous sedimentary rocks is the oldest evidence for Andean-type subduction in the Cajamarca region. This compressional event is known as Incaic I orogenic pulse (Noble *et al*., 1985) and occurred from 59 to 55 Ma. The Llama-Calipuy Volcanic Sequence (54-43 Ma) unconformably overlies the folded Incaic I deformed sedimentary rocks (Noble *et al*., 1985). It is comprised of subaerial basaltic to rhyolitic rocks, but dominated by basalts and andesites. Atherton *et al*. (1985) observed that the Llama-Calipuy volcanic rocks are the most voluminous and characteristic Andean volcanic association. Several intrusive rocks were emplaced contemporaneously with these volcanic rocks (57-43 Ma, Llosa *et al*., 1996; Section A). Peak Eocene magmatism roughly coincided with the first of two major periods of rapid plate convergence (Section A). This occurred between 49.5 and 42.0 Ma at an estimated rate of 154 ± 58 mm/a and corresponded with a clockwise rotation of the subducting Farallon Plate in the northern Andes (Pilger, 1984; Pardo-Casas and Molnar, 1987). Soler and Bonhomme (1990) proposed that a decrease in the dip of the subducting slab resulted in arching, uplift, extension and volcanism in the overriding plate.

The cessation of both rapid plate convergence and deposition of the Llama-Calipuy Volcanic Sequence was marked by the second deformation phase, known as the

Incaic II phase, from 43 to 42 Ma (Benavides, 1999). Folds that developed during the Incaic orogenic events are generally upright, gentle to open, and within the Huancabamba Deflection plunge WNW or ESE. Thrust faults that developed during the same orogenic pulses generally dip SSW. Structures produced during the Incaic phases suggest NE-SW directed compression (Wilson, 2000). Some authors (Benavides, 1999; Mitourad *et al*., 1990; Kissel *et al*., 1992) have suggested that the Cajamarca structural bend and the N-S compression in the Cajamarca region resulted from counterclockwise rotation block movement and oblique convergence. Another characteristic of the Incaic Belt is a series of strike-slip faults trending NE or E-W, with significant vertical and lateral movements that are probably related to basement tectonics (Vidal and Noble, 1994). During Oligocene times (36-24 Ma), the convergence rate decreased to 50 ± 30 mm/a (Pardo-Casas and Molnar, 1987) and there was apparently a lull in magmatic activity in northern Peru. Since late Oligocene times the Peruvian Andes have been subjected to compressional tectonics with shortening occurring in the lowlands and extension restricted to high topographical regions in the Andes (Sebrier and Soler, 1991).

The second phase of rapid convergence (110 ± 8 mm/a) identified by Pardo-Casas and Molnar (1987) occurred from 26 Ma onwards, with possibly higher convergence rates between 20 and 10 Ma. Pardo-Casas and Molnar (1987) suggested rapid convergence coincided with the break-up of the Farallon plate (into the Nazca and Cocos plates) and a clockwise rotation of the subducting plates. Furthermore, Mitourad *et al*. (1992) proposed that the Peruvian margin underwent late Oligocene to early Miocene counterclockwise rotation of the order of 20^{o}. Renewed magmatic arc activity following the Incaic IV (22 Ma) orogenic pulse involved emplacement of intermediate, calc-alkaline intrusive stocks and development of mineralised porphyry centres (Llosa *et al*., 1996; Section A). The compressive Quechua I (17 Ma) pulse and extinction of the Pacific-Farallon spreading centre (~18 Ma) appears to have marked the end of this magmatic episode within the Cajamarca region (Benavides, 1999). After the Quechua I pulse, intra-cordillera graben basins developed in the highlands in response to gravitational extension (Benavides, 1999).

North of Cajamarca, major magmatic-hydrothermal activity occurred in the Hualgayoc district between 14 and 10 Ma (Macfarlane *et al*., 1994; James, 1998).

Deposition of andesitic lava flows near Yanacocha represents the initiation of middle- to late Miocene magmatic activity (12.3 Ma, Turner, 1997). Main stage alteration at Yanacocha took place at *ca*. 11 Ma (Turner, 1997), which roughly corresponds to termination of major uplift in the Peruvian Andes (Noble *et al*., 1990). The last magmatic activity in the Cajamarca region involved deposition of rhyodacite tuffs (8 Ma, Turner, 1997) and coincided with the Quechua II orogenic pulse (8-7 Ma) proposed by Mégard (1984). South of Cajamarca, Bellier *et al*. (1989) identified a series of late Miocene to Quaternary extensional and compressional events that were interpreted to reflect changes in the subduction angle.

B.4 Structural Observations

The regional structural analysis of the Cajamarca district presented in this section has been compiled from field mapping, aerial photo interpretation and previously unpublished studies from other sources. The data include fault, fracture and joint orientations observed in a variety of lithological units that range in age from Upper Cretaceous to late Miocene. The data are presented in three main sections that relate to the age of the lithological units in which structural features were observed. These include the Cretaceous sedimentary rocks, early- to middle Miocene mineralised intrusions and late Miocene volcanic rocks.

B.4.1 Cretaceous Sedimentary Rocks

Structural mapping of the deformed Cretaceous sedimentary rocks involved field mapping and aerial photograph interpretation. Analysis of the sedimentary rocks covered an area of ~1250 km^2 (Fig. 3). In general, these are characterised by small-scale extensional faults superposed on a regional-scale fold and thrust fabric. Bedding planes throughout the area have an average orientation of near NW-SE (23^o→213^o; Fig. 3).

Puntre Thrust Fault: The Puntre Thrust Fault is defined by Lower Cretaceous quartzites in the hanging wall juxtaposed against Middle-Upper Cretaceous limestones indicating several hundred metres of reverse offset. In the study area, the fault changes from near E-W trending and shallowly-dipping to NW-trending and steeply-dipping

Fig. 3. Structural map and cross section of the northeastern Cajamarca district displaying the major structural features in the deformed Cretaceous sedimentary rocks. Insert: Stereoplots and rose diagrams of folds, faults and bedding planes from field mapping. Fault trends picked from aerial photos have also been plotted.

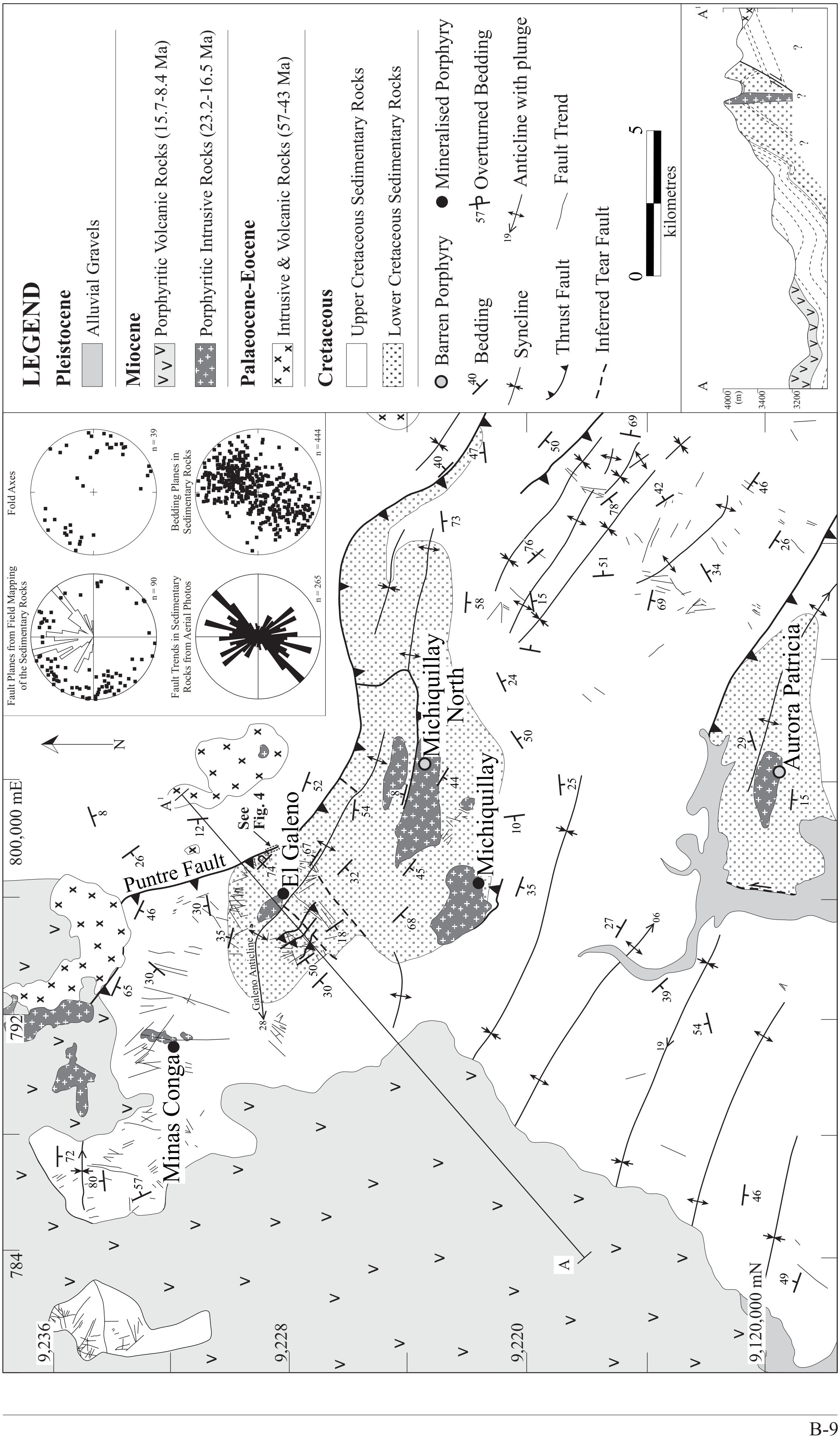
LEGEND
Pleistocene
Alluvial Gravels
Miocene
Porphyritic Volcanic Rocks (15.7-8.4 Ma)
Porphyritic Intrusive Rocks (23.2-16.5 Ma)
Palaeocene-Eocene
Intrusive & Volcanic Rocks (57-43 Ma)
Cretaceous
Upper Cretaceous Sedimentary Rocks
Lower Cretaceous Sedimentary Rocks
Barren Porphyry
Mineralised Porphyry
Bedding
Overturned Bedding
Syncline
Anticline with plunge
Thrust Fault
Fault Trend
Inferred Tear Fault
0
5
kilometres
Fault Planes from Field Mapping of the Sedimentary Rocks
n = 90
Fold Axes
n = 39
Fault Trends in Sedimentary Rocks from Aerial Photos
n = 265
Bedding Planes in Sedimentary Rocks
n = 444
N
800,000 mE
784
792
9,236
9,228
9,220
9,120,000 mN
Puntre Fault
Minas Conga
El Galeno
See Fig. 4
Galeno Anticline
Michiquillay North
Michiquillay
Aurora Patricia
A
A'
4000 (m)
3400
3200

(Section D.5.2). To the northeast of El Galeno, argillic altered limestones situated within the NW-trending zone of the thrust display polyphase deformation (Fig. 4). The earliest structures observed in the altered limestone are small-scale folds (50 cm amplitude) that dominantly have fold axes at $23^o \rightarrow 304^o$ and subvertical axial planes (Fig. 4). Early planar veins with calcite infill (V_1) have a general orientation of $30^o \rightarrow 268^o$. However, some minor veins have crenulate vein walls. These early structures are crosscut by subvertical normal faults that displace and disrupt early V_1 veins (Fig. 4). The fault planes have an average strike of 342^o and dip steeply (83^o) to the east. Steeply-dipping calcite veins (V_2) crosscut the early flat lying V_1 veins. Weak pyrite mineralisation was observed in the fault breccia matrix of the extensional faults.

Folds: Regional-scale folds are upright and have a wavelength >5 km (Fig. 3). Quartzite units commonly define hanging wall anticlines (Fig. 3) due to detachment occurring along competency boundaries, such as between quartzite and limestone units. Fold axes display a dominant ESE-WNW orientation with modes near $16^o \rightarrow 115^o$ and $19^o \rightarrow 295^o$ (Fig. 3). Some large-scale folds in the southern sector of the study area have a moderate plunge (>40^o) to the SW. Minor, small-scale folds (wavelengths of a few metres) that have NE and SE trends were also observed. The abundance of these folds is low and possibly represents different stress fields on a localised scale.

Normal Faults: Faults in the Cretaceous sedimentary rocks are mostly subvertical and contain cataclastic rocks with oxidised breccia textures. The majority display normal displacement ranging from a few, to tens of metres. A stereoplot (Fig. 3) indicates these subvertical faults have three dominate orientations, namely, (a) 175/77E, (b) 045/78SE and (c) 109/71S. Faults identified during aerial photo analysis over an area of ~1250 km^2 were mostly within deformed Cretaceous sedimentary units (Davies, 2000). The faults range from NE- to NW-striking, have an average strike of between 010^o-015^o and a mode of 040^o-045^o. The ages of the majority of faults identified in the field and aerial photo analysis are poorly constrained due to a lack of crosscutting relationships.

Fig. 4. Outcrop sketch of deformed limestone and quartzite rocks located in the Puntre Thrust Fault to the NE of El Galeno. In the limestones, flat calcite veins (V1) and upright small-scale folds are crosscut by steeply dipping calcite veins (V2) and normal faults that contain minor pyrite mineralisation.

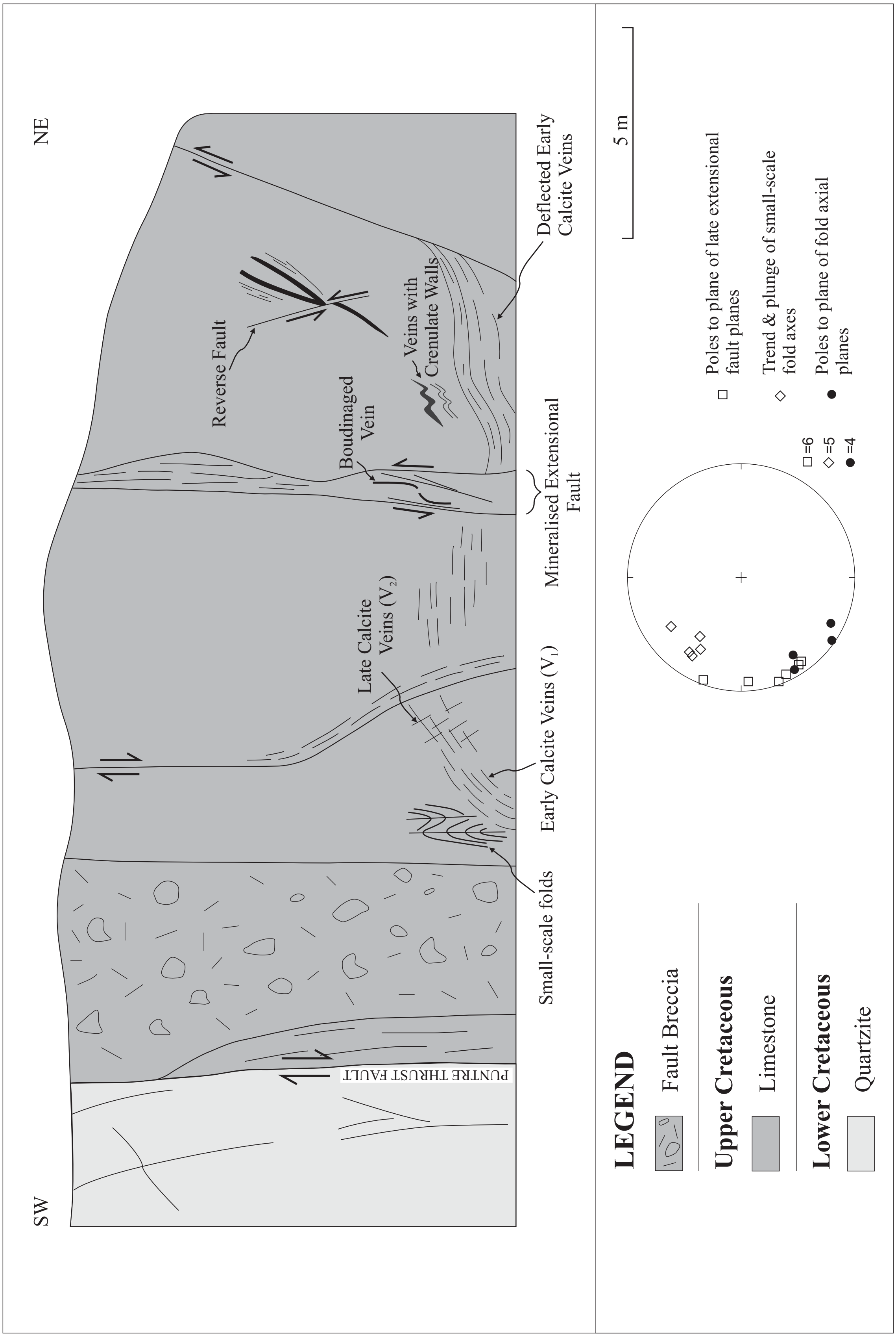
NE
SW
Deflected Early Calcite Veins
Reverse Fault
Veins with Crenulate Walls
Boudinaged Vein
Mineralised Extensional Fault
Late Calcite Veins (V_2)
Early Calcite Veins (V_1)
Small-scale folds
PUNTRE THRUST FAULT
5 m
LEGEND
Fault Breccia
Upper Cretaceous
Limestone
Lower Cretaceous
Quartzite
Poles to plane of late extensional fault planes
Trend & plunge of small-scale fold axes
Poles to plane of fold axial planes
□=6
◇=5
●=4

B.4.2 Cretaceous Sedimentary Rocks Summary

Thrust faults have near E-W trends and contain hanging wall anticlines with similar orientations. Regional-scale folds also have a near E-W trend that suggests fold and thrust structures developed contemporaneously. The geometries of both folds and thrusts suggest the structures developed during subhorizontal, N-NE directed compression. This is consistent with early NNE-SSW compression during the Eocene fold-thrust event (Incaic I) proposed by Wilson (2000). It is inferred that initial development of regional-scale folds and thrusts occurred during the same compressional event.

The deformed Cretaceous basement rocks are intruded and overlain by Tertiary diorite stocks and andesite volcanic rocks. The oldest magmatic rock dated in the Cajamarca region was emplaced *ca*. 57 Ma (Section A). Recent $^{40}Ar/^{39}Ar$ age data indicate major Eocene magmatism in the region ceased *ca*. 42.5 Ma (Section A). This age also possibly marks the end of the Palaeogene fold-thrust events in the region.

B.5. Early Miocene Mineralised Centres

Early to middle Miocene magmatism (23.2 to 16.5 Ma) produced a number of barren and mineralised diorite intrusive rocks with steep contacts (Llosa *et al*., 1996; Section A), as well as the upper Llama Formation volcanic rocks (15.8 Ma; Turner, 1997). The Minas Conga, El Galeno and Michiquillay porphyry systems have related Cu-Au-Mo mineralisation. Fault, fracture and/or vein data from these mineralised systems are presented and used to help determine stress conditions that prevailed during this 7 m.y. interval. Field mapping was conducted at El Galeno, whilst previous mapping at the Minas Conga by Llosa and Veliz (2000) and Michiquillay by the Metal Mining Agency (MMA) plus Japan International Cooperation Agency (1975) is presented in combination with structural features observed from the both aerial photo analyses and field mapping.

B.5.1 El Galeno

El Galeno is a Cu-Au-Mo porphyry centre hosted in multiple diorite stocks (Cordova and Hoyos, 2000; Section D.5). In outcrop, the main porphyry body is approximately 1.25 km by 0.6 km, oval in shape and has a general NW trend (Fig. 5). The diorite porphyry complex is hosted within folded Lower Cretaceous sedimentary rocks and was emplaced in the NW-trending El Galeno Anticline (Fig. 5). The porphyry stock is located at the intersection of the El Galeno Anticline and a NE-striking tear fault, which displays an overall dextral shear sense. Local folds and faults are inferred to have controlled localisation of the porphyry complex (Section D.5.2). Emplacement, alteration and mineralisation of the porphyry complex occurred between 17.5 and 16.5 Ma (Section A).

Southwest of the mineralised complex, several gabbroic dykes have intruded fault and bedding planes in the quartzite units (Fig. 5). The dykes intruded the deformed quartzite units prior to emplacement of the El Galeno porphyry system (29.4 Ma; Section A). The dykes are commonly located along fault planes that are subvertical and NNW- to N -trending. One of the dykes contains a series of cooling joints that are mostly subvertical (~80^{o}) and have a dominant trend of 028/80E with a subordinate 120/83NE to 150/84NE trend (Fig. 5). The average orientation of the cooling joints (010/81E) is oblique to the geometry of the host fault plane (167/80W).

Fracture orientations in the El Galeno intrusive complex were measured to assess the degree of magmatic versus tectonic stress during cooling and solidification of the complex. The fractures offset early quartz veins and in turn are crosscut by later quartz veins. Some fracture planes also display post-alteration movement with steep slickenlines, thereby indicating fractures were active both during and following alteration. A stereoplot (Fig. 5) shows the fractures display a large amount of scatter with orientations ranging from E- to WNW-striking and dip varying from subhorizontal to subvertical. The average orientation of the fractures in the intrusive complex is approximately 003/57E. Overall, fractures display a random orientation across the entire intrusive complex and no spatial trends were observed. However, a rose plot of the fracture data suggests three common fracture trends, which include 045^{o}-055^{o}, 170^{o}-140^{o} and 115^{o}-105^{o}.

In the southwestern part of the intrusive complex, crosscutting fracture sets were observed in the upper part of the exposed P1 intrusion (Fig. 6). The earliest fracture set (F_1) has strongly oxidised planes that are planar to slightly undulose. These fractures are

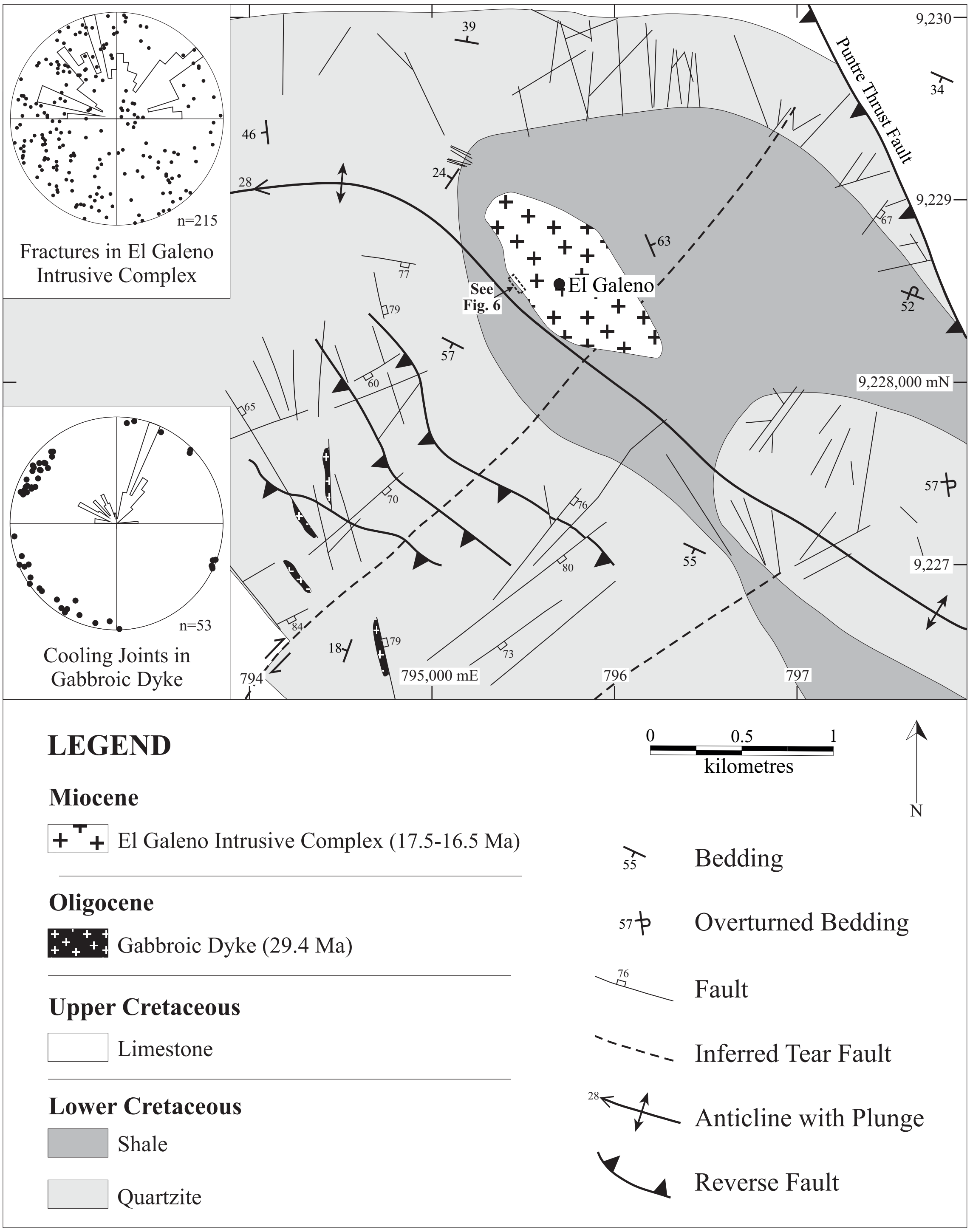

Fig. 5. Structural geology of the El Galeno prospect. Stereoplots and top-half rose diagrams of the subvertical cooling joints in Oligocene dykes display a dominant N-NE trends, whereas fractures in the Miocene El Galeno intrusive complex have a random orientation. However, the most common fractures have NE and NNW-NW trends.

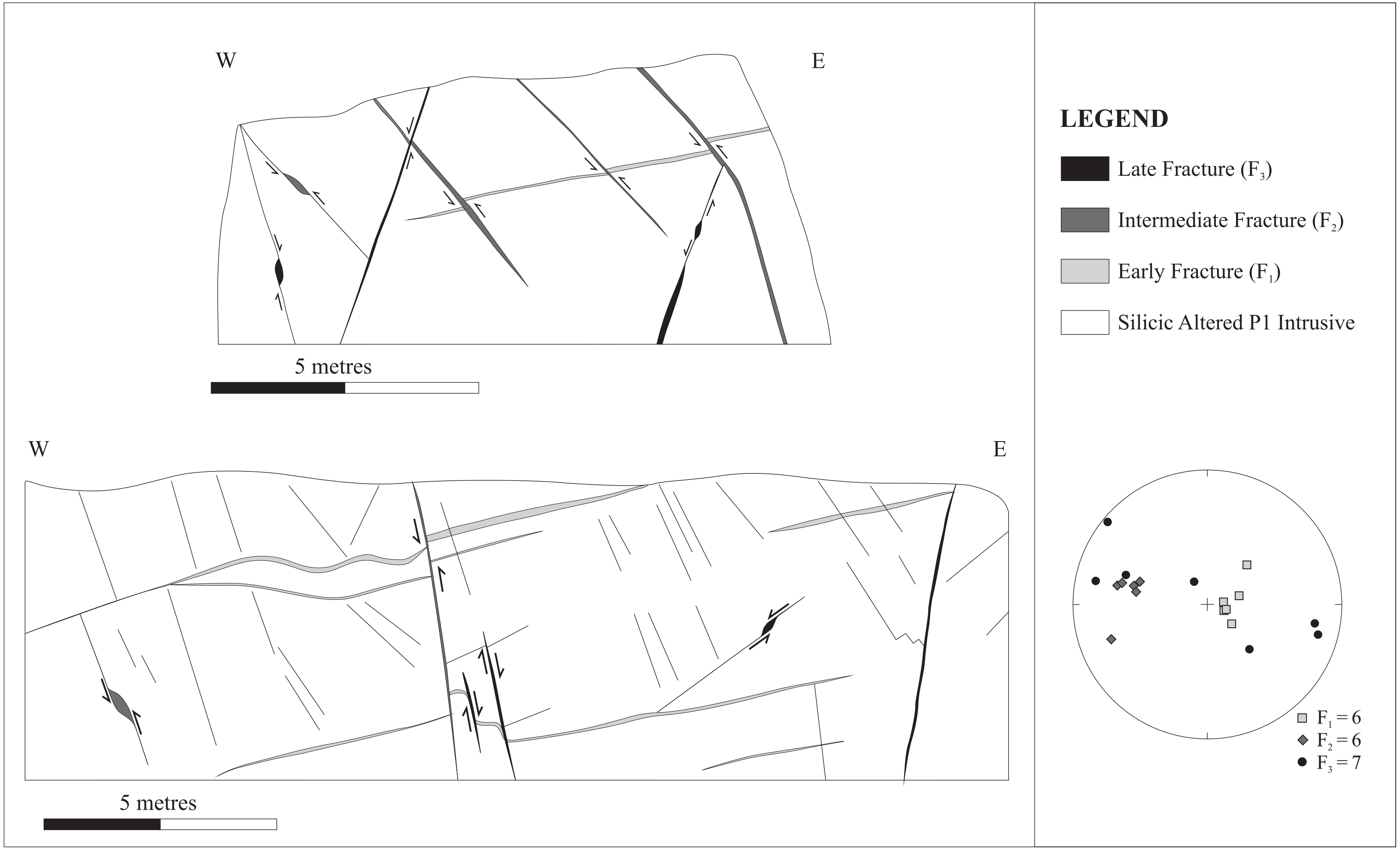

Fig. 6. Fracture patterns in the southwestern part of the El Galeno intrusive complex (location shown in Fig. 5). Early flat fractures (F_1) are crosscut by steep F_2 fractures that have a reverse movement. Steep extensional F_3 fractures postdate both of these

flat-lying and have a predominant N-S strike (174/15W). The flat-lying fractures are crosscut by a second set (F_2) of near N-striking, moderate-dipping planar fractures (008/51E) that display reverse displacement. F_2 fractures contain both strong oxidisation and clay alteration along the planes. The third fracture set (F_3) crosscuts both of these, has a NNE strike and is moderately- to steeply-dipping (022/65E). F_3 fractures are planar and also contain clay minerals. The wide range in fracture orientations and crosscutting relationships observed at El Galeno are typically of porphyry copper deposits characterised by multiple phases of intrusive and hydrothermal activity (Tosdal and Richards, 2001).

B.5.2 Michiquillay

Michiquillay is a diorite Cu-Au-Mo porphyry system and was previously mapped by Metal Mining Agency (MMA, 1975). The intrusive complex is elongate, ~5 km in length by 1.5 km wide, and roughly parallel to the local NW structural trend (Fig. 7). Intrusions were emplaced in the hanging wall of a NW-trending back-thrust, the Michiquillay Fault, that dips moderately (~60^o) to the NE. Hollister and Sirvas (1974) suggest the Michiquillay complex is located the intersection of the Michiquillay and the NE-trending Encanada faults. Laughlin *et al*. (1968) used the K-Ar method to date biotite from a quartz-biotite monzonite at the Michiquillay prospect and obtained an age of 20.6 ± 0.6 Ma. Llosa *et al*. (1996) dated biotite from the Michiquillay prospect at 18.8 ± 1.6 Ma also using the K-Ar method. New $^{40}Ar/^{39}Ar$ age dates indicate barren intrusions (20.6 ± 0.1 Ma) to the north of the Michiquillay region were emplaced slightly prior to the Michiquillay mineralised porphyry (19.8 ± 0.05 Ma; Section A).

Prospect-scale faults that crosscut the Michiquillay mineralised centre were previously mapped by MMA (1975) and were reviewed in this study. The faults dominantly occur toward the centre of the intrusive system and were recognised by an increased density of fractures toward the central part of the fault zones. Very few kinematic indicators were identified along fault planes, but where observed these displayed late steeply-plunging slickenlines (Fig. 16 in Section D). The prospect-scale faults have a dominant NNW-NW trend and a subordinate NNE-NE trend (Fig. 7). The faults have an average NNW strike and dip steeply to the E (167/79E). NNW-trending faults that crosscut both the Michiquillay Fault and mineralised intrusive complex have

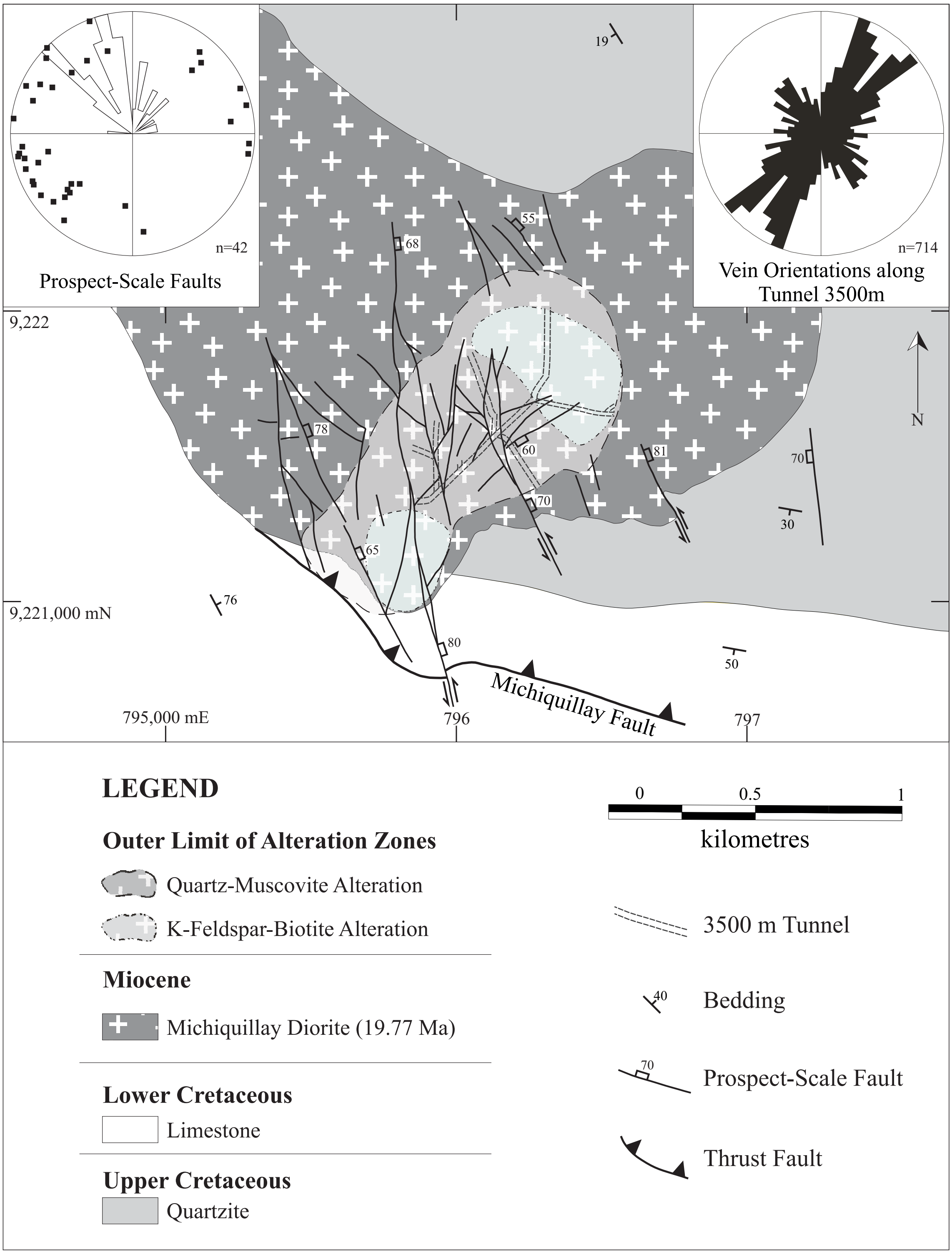

Fig. 7. Structural map of the Michiquillay prospect showing prospect-scale faults and the trend of the alteration zones (MMA, 1975). Top left insert, stereoplot illustrates the preferred NNW to NW trend of the subvertical prospect-scale faults. This is further highlighted by the top-half of a rose diagram. Top right, rose diagram showing veins have a dominant NE trend and a weak secondary NW trend. Note the oblique relationship of the vein and alteration trends compared to the prospect-scale fault trend.

a sinistral displacement (Fig. 7). In outcrop and drill core, K-feldspar-biotite and quartz-muscovite alteration assemblages display a NE trend. Metal grades are spatially associated with these alteration zones (Section D.6.3). The prospect-scale faults define the outer limit of strong quartz-muscovite alteration and divide K-silicate alteration zones in the NE and SW of the system. It is inferred that the NNW-trending faults controlled the distribution of quartz-muscovite alteration and possibly mineralisation.

Vein trends along the presently abandoned Tunnel 3500 m have been compiled from previously data (MMA, 1975) with the objective to compare variations between vein and prospect-scale fault trends. The vein data incorporate measurements from the central quartz-muscovite and northern K-feldspar-biotite alteration zones. These data display a very strong 020^{o}-055^{o} trend and a subordinate trend of 150^{o}-140^{o} (Fig. 7). The veins have a dominant NE strike that is roughly parallel to the NE alteration trend, but oblique to near orthogonal with the major NNW-striking prospect-scale faults.

B.5.3 Minas Conga

The Minas Conga (Au-Cu) prospect comprises two mineralised centres, known as Chailhuagon and Cerro Perol, with only the former being discussed in this paper. Previous mapping by Llosa *et al*. (1996) and Llosa and Veliz (2000) has defined the elongate Chailhuagon porphyry as a microdiorite stock that in plan is oriented N-S and 2 km long by 0.5 km wide (Fig. 8a). K-Ar age dating of hornblende from the Chailhuagon main intrusive body yielded an age of 23.2 ± 2.1 Ma (Llosa *et al*., 1996). The porphyry complex located at the intersection of a N-S trending fault and a NW-striking fault that has an apparent sinistral sense of shear. Fault trends observed from aerial photo analysis of the Minas Conga region have a dominant N and NW strike (Fig. 8b). Llosa and Veliz (2000) documented three major vein trends that strongly influenced mineralisation at Chailhuagon. These include 005^{o}-020^{o}, 140^{o}-120^{o} and an E-W trend. In outcrop, veins are predominantly subvertical (~75-80^{o}) and sheeted (Fig. 8c).

Fig. 8. (a) Structural map of the Minas Conga prospect (modified from Llosa and Veliz, 2000). (b) The Chailhuagon centre is hosted in deformed limestone rocks that contain NNE and NNW faults, as illustrated in the rose diagram. (c) Outcrop photo of vein stockwork illustrating three dominant trends N-S, NW and E-W.

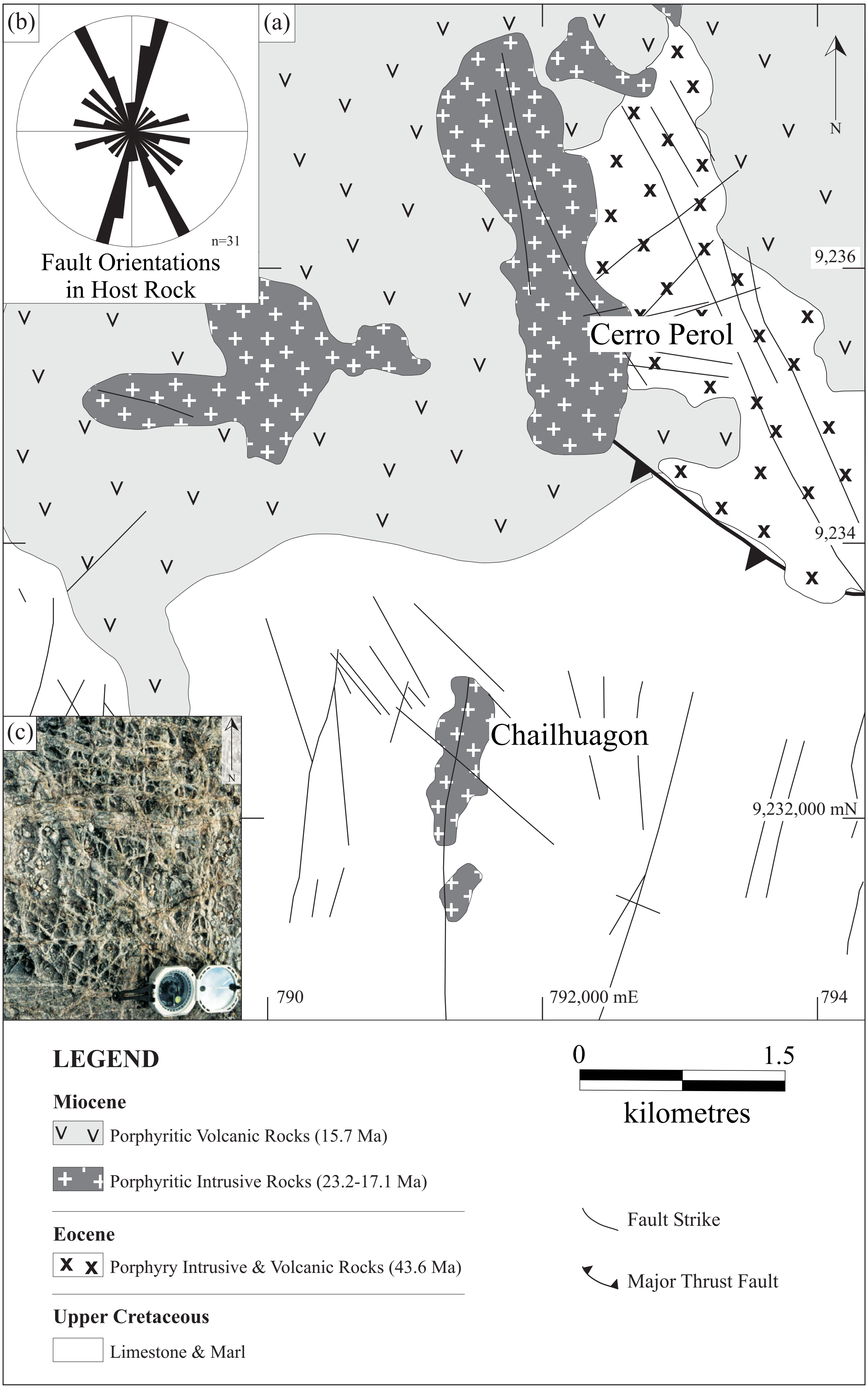
(b)
Fault Orientations in Host Rock
n=31
(a)
N
Cerro Perol
Chailhuagon
9,236
9,234
9,232,000 mN
790
792,000 mE
794
(c)
N
LEGEND
Miocene
Porphyritic Volcanic Rocks (15.7 Ma)
Porphyritic Intrusive Rocks (23.2-17.1 Ma)
Eocene
Porphyry Intrusive & Volcanic Rocks (43.6 Ma)
Upper Cretaceous
Limestone & Marl
0
1.5
kilometres
Fault Strike
Major Thrust Fault

B.6 Late Miocene Mineralised Centre

The late Miocene magmatic interval was characterised by deposition of andesitic volcanic rocks and formation of the Yanacocha epithermal system. Structural features that developed or were reactivated during this interval have been recognised at the Yanacocha mine.

B.6.1 Yanacocha

The Yanacocha high-sulphidation Au deposit is located within a complex N60^{o}E trending structural corridor that is defined by the alignment of deposits and alteration in the Yanacocha Volcanic Complex (YVC; Harvey *et al*., 1999). Andesitic rocks that form the YVC were initially deposited at 11.8 Ma (Turner, 1997). Main stage alteration took place shortly afterwards, between 11.5 and 10.9 Ma (Turner, 1997). Previous work by Harvey *et al*. (1999) and Longo (2000) documented the major deposit-controlling faults at the mine (Fig. 9). A rose diagram of these faults illustrates the major fault trends define the Yanacocha mine are 140-130^{o}, 045-050^{o} and 080-090^{o} (Fig. 9). Harvey *et al*. (1999) documented that several deposits were located at the intersection of NE and NW structural zones, and NW-trending structures spatially related to other deposits. Longo (2000) suggested sinistral displacement occurred along some of the NW- and N-trending faults, and dextral sense of shear along the NE-trending faults. Late N- and W-trending fracture zones appear to postdate the major structural trends. All structural trends are associated with late normal displacement or lateral movement, although the overall displacement along the faults in the mine is unknown (Turner, 1997; Longo, 2000).

B.7 Structural Evolution of the Cajamarca Region

The Cretaceous sedimentary rocks are the oldest exposed rocks in the Cajamarca district and are structurally the most complex (Table 1). The earliest deformation phase manifests as a fold-thrust fabric related to the Incaic I (59-55 Ma) orogenic event. Regional-scale fold axes are dominantly horizontal or plunge gently to the W-NW or ESE. Thrust faults mostly strike ENE and dip SSW. Anticlines located in the hanging wall of thrusts indicate folds and thrust faults developed contemporaneously. It is

Fig. 9. Geological map of the late Miocene Yanacocha district showing the major lithological units, ore deposits and faults identified at the mine (modified from Longo, 2000). The mine is characterised by an overall NE trend, although individual deposits are mostly controlled by NW-oriented faults.

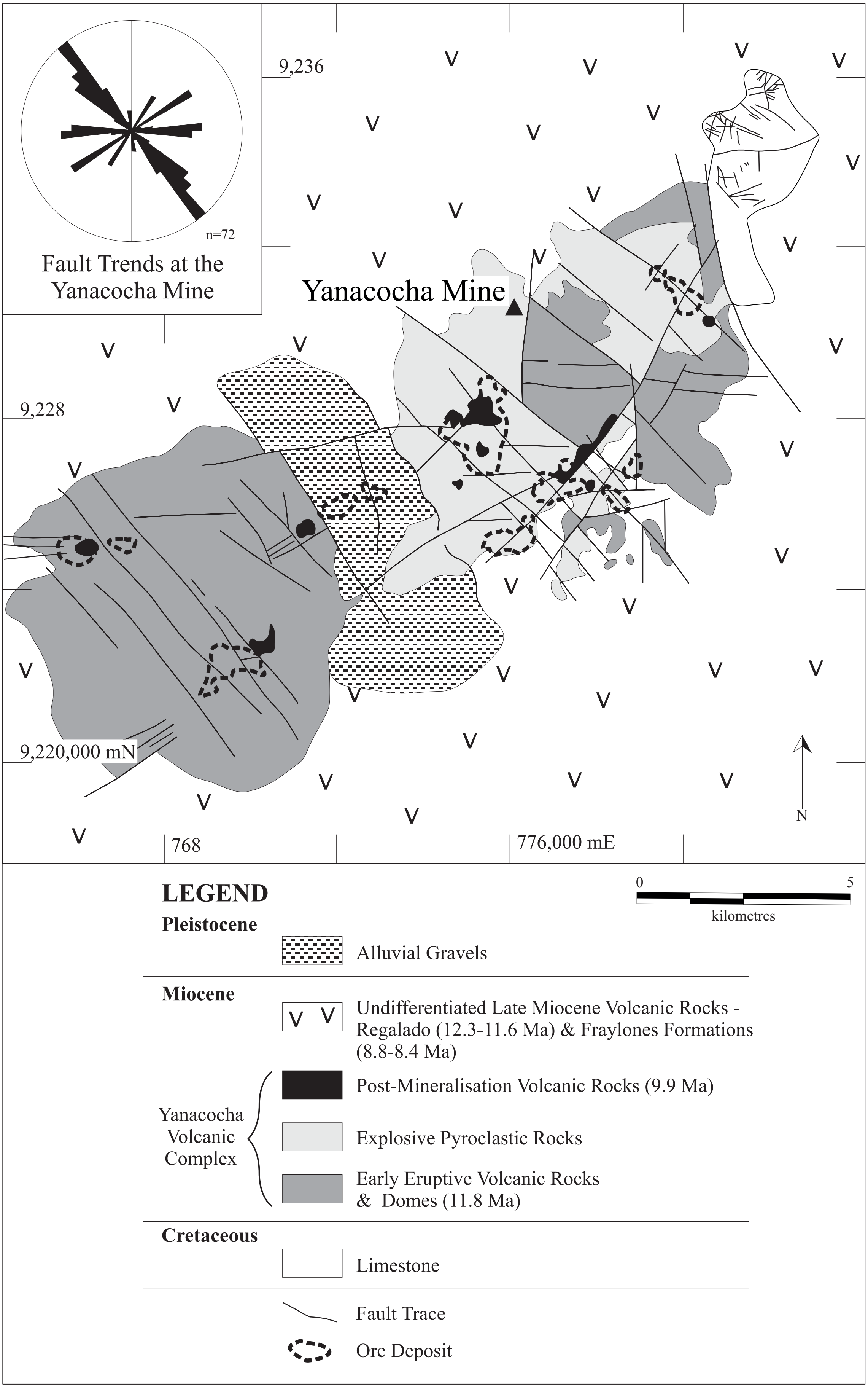

n=72
Fault Trends at the Yanacocha Mine
9,236
Yanacocha Mine
9,228
9,220,000 mN
768
776,000 mE
N
0
5
kilometres
LEGEND
Pleistocene
Alluvial Gravels
Miocene
Undifferentiated Late Miocene Volcanic Rocks - Regalado (12.3-11.6 Ma) & Fraylones Formations (8.8-8.4 Ma)
Yanacocha Volcanic Complex
Post-Mineralisation Volcanic Rocks (9.9 Ma)
Explosive Pyroclastic Rocks
Early Eruptive Volcanic Rocks & Domes (11.8 Ma)
Cretaceous
Limestone
Fault Trace
Ore Deposit

Table 1. Compilation of structural data from this study and previous work. [1] Pardo-Casas and Molnar (1987)

Location	Age of Complex (Ma)	Trend of Magmatic Complex	Alteration Trend	Faults		Fractures	Fault/ Fracture Plots	Veins	Rose Diagram of Vein Trends	Reference	Plate Convergence Direction[1]
				Major	*Minor*						
Yanacocha	12-10	NE	Fault Controlled	140°-130°	045-050°, 080-090°	Late N-S & E-W	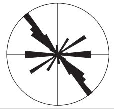	-	-	Harvey *et al*. (1999), Longo (2000)	
Sipan (La Zanja District)	13(?)	WNW	NE	NE				-	-	Turner (1999)	
El Galeno	17.5-16.5	NW	-	NE-striking Tear Fault	-	040°-055°, 170°-140°, 115°-105°	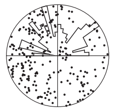	-	-	This study	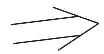
Michiquillay	19.8	NW	NE	170°-160°	140°-135°, 005°-010°		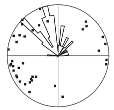	020°-055°, 150°-140°		MMA (1975), this study	
Minas Conga (Chailhuagon)	23-17	N-S	-	N-S, 145°-140°	-		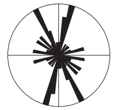	005°-020°, 140°-120°, E-W	-	Llosa *et al*. (1996), Llosa and Veliz (2000)	
Gabbroic Dykes (El Galeno)	29.4	NNW	-	010°-015°		**Cooling Joints** 020°-025°	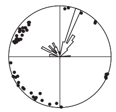	-	-	This study	
Cretaceous Sedimentary Rocks							**Faults from Aerial-photo Analysis**	**Folds**	**Stereoplot of Folds**		
Field & Aerial Photo	120-80	-	-	045°-050°	170°-165°, 120°-115°, 000°-005°	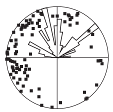	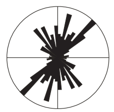	16°–>115°, 19°–>295°	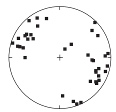	This study	

inferred that NNE-directed compression took place during development of the early fold-thrust fabric. These orientations are consistent with a NNE-directed oblique plate convergence direction proposed by Pilger (1984).

Observed NE-trending faults in all lithological units generally display dextral displacement, whereas N- to NW-trending faults have a dominant sinistral sense of shear. Fault planes in Cretaceous rocks display the largest range of fault orientations for all lithological units, ranging from NE- to NW-striking. The exact age of faults in these rocks is difficult to constrain due to a lack of overprinting or crosscutting relationships. The dominant fault orientation observed in the sedimentary rocks is steeply dipping and NE-striking, whereas NE-striking faults are rarely observed in the younger lithological units. It is inferred that the NE-striking faults initially developed as tensional faults contemporaneous with the early fold-thrust fabric. Tear faults observed near El Galeno have a NE-trend, display dextral displacement and inferred to have developed during the fold-thrust event. In the south of the study area, a N-S striking tear fault near the Aurora Patricia intrusion (Fig. 3) has a sinistral sense of displacement.

Most Palaeogene magmatic rocks in the Cajamarca region were deposited or emplaced during a change in the plate convergence rate, from low to high, and following a change in the direction of plate convergence (Fig. 2; Pardo-Casas and Molnar, 1987; Section A). This magmatic interval was characterised by widespread volcanism and emplacement of minor intrusive stocks. The majority of Palaeogene magmatic rocks in the region are spatially associated with the Puntre Thrust Fault and mostly located within the footwall of this thrust (Fig. 3). No secondary structures that may have influenced the location of these rocks were observed. At El Galeno, gabbroic dykes of middle Oligocene age (29.5 Ma) intruded subvertical NW-trending fault and bedding planes. Despite emplacement of these dykes, Oligocene times appear to have been mostly characterised by a lack of significant deformation and magmatism.

Renewed magmatic activity in the Cajamarca region during early to middle Miocene times (23.2-15.8 Ma) is represented by numerous diorite stocks and minor volcanic sequences. Initiation of major uplift (Noble *et al*., 1990) and formation of porphyry Cu deposits also occurred during this period. Most Miocene intrusions are spatially associated with the same regional-scale structure as the Palaeogene units, i.e.

the Puntre Thrust Fault, but dominantly located within its hanging wall. Field relationships indicate that most Miocene stocks were emplaced at structural intersections, commonly between a major fault and oblique secondary fault(s), such as El Galeno (Section D.5.2). In plan view, mineralised stocks are generally elliptical in shape with the long axis roughly parallel to the local structural fabric. El Galeno and Michiquillay intrusive complexes have NW orientations, whilst Chailhuagon (Minas Conga) has a N-S trend. The Chailhuagon and Michiquillay mineralised systems both contain NNW- to NW-striking faults that display sinistral displacement. Fracture and vein trends at these mineralised centres have a dominant NE, N-S or NW strike. In contrast, El Galeno is characterised by numerous fracture arrays of varying orientation and timing. However, faults in the host sedimentary rock and fractures in the El Galeno intrusive complex display a dominant NNW and NE trend.

Major uplift in the Andes had ceased by middle to late Miocene times (Noble *et al*., 1990). In the Cajamarca region, this time was marked by renewed volcanic activity (12-8 Ma) and the formation of the Yanacocha high-sulphidation Au deposit. A NE-striking structural fabric defines the Yanacocha district, but conjugate NW-striking faults are the dominant deposit-controlling structures (Harvey *et al*., 1999). At the mine, NW-striking faults display a sinistral sense of shear as opposed to NE-trending faults that have a dextral slip component (Longo, 2000). Recent work by Turner (1999) suggested a WNW-trending structural corridor controlled known mineralisation at the La Zanja deposit, with Sipán being located at the southeastern end of the structural corridor (Fig. 10). At the Sipán deposit, mineralisation was localised along a NE-striking fault that is nearly orthogonal to the WNW structural corridor (Compañia Minera Sipán, unpubl. data).

B.8 Discussion

At the current level of exposure, magmatic episodes in the Cajamarca region appear to have been characterised by either a high or low volcanic/intrusive ratio. Palaeogene and late Miocene magmatic intervals were characterised by widespread volcanism and minor subvolcanic stocks, whereas emplacement of abundant diorite stocks and porphyry Cu formation largely defines early Miocene magmatism.

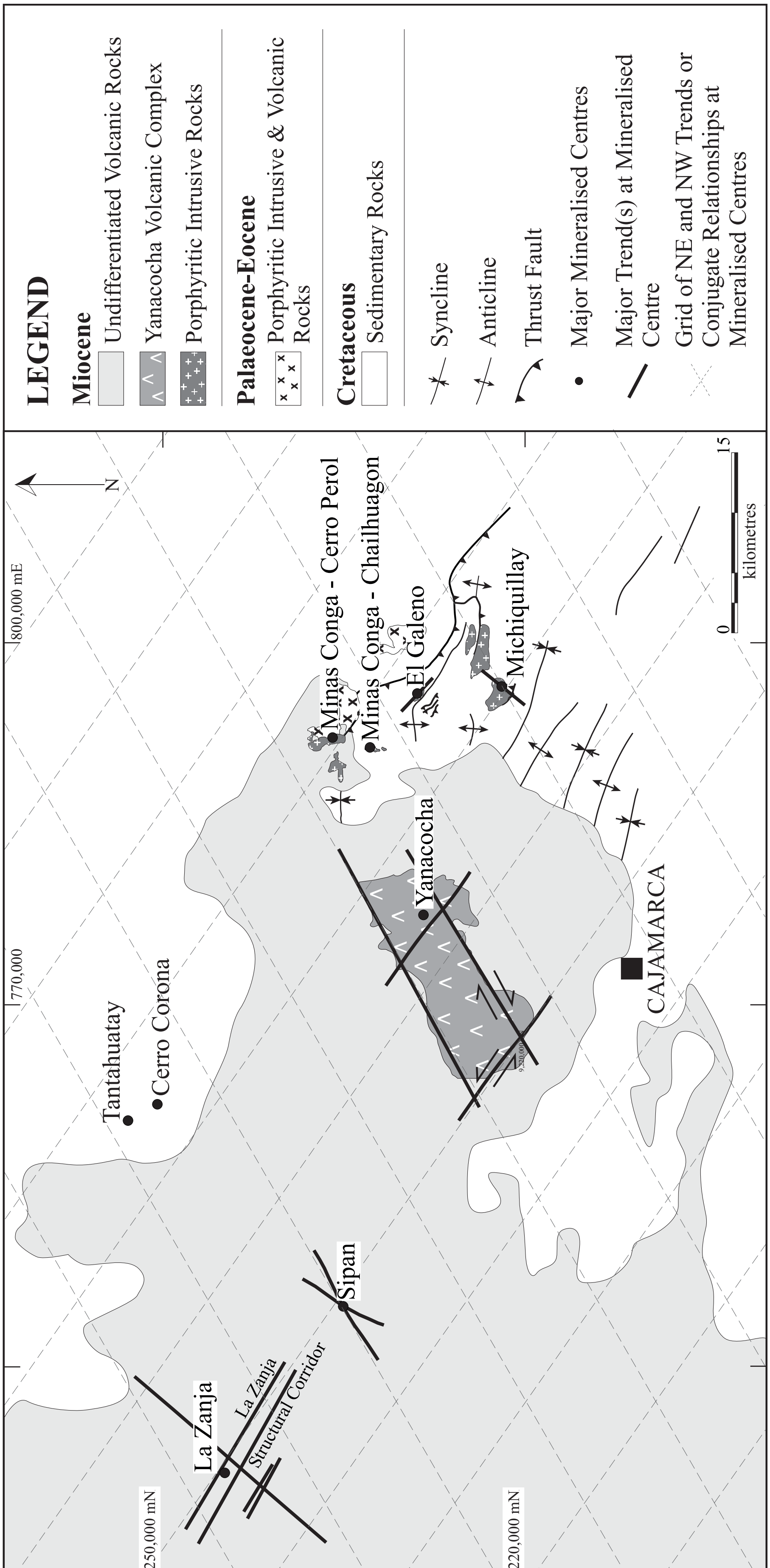

Fig. 10. Simplified geological map of the Cajamarca district displaying the major mineralised centres and the dominant structural trends (thick black lines) observed at the centres. The NE and NW trends identified at deposit-scale for most of the centres also trends to the regional-scale with the spatial location of the deposits. The deposits are roughly aligned in a NE and NW trend with respect to the other centres.

Numerous hypotheses have been proposed to explain periods dominated by volcanism or plutonism in magmatic arcs (Glazner, 1991; Takada, 1994; McNulty *et al*., 1998). In the Cordillera Blanca region of central Peru, coeval Miocene plutonic and volcanic activity occurred during periods of high convergence rates and transtensional tectonics (Petford and Atherton, 1992). Glazner (1991) and McNulty *et al*. (1998) suggest volcanism dominates during orthogonal convergence or compressional pulses within a magmatic arc, whereas strike-slip partitioning due to oblique convergence favours plutonism. Furthermore, Takada (1994) proposed that widespread volcanism and minor plutonism occurs during periods of large differential horizontal stress and high to intermediate magma input rates. Additionally, Tosdal and Richards (2001) suggested that near-surface magma chambers related to porphyry Cu centres result from intermediate to large magma input rates combined with small to intermediate differential horizontal stress. A low volcanic/intrusive ratio would dominate during such conditions.

Palaeogene igneous rocks in the Cajamarca region are mostly located within the footwall of the Puntre Fault. The volcanic-dominated interval occurred during periods of both low and high plate convergence rates, plus between two major orogenic compressive episodes, i.e. Incaic I and II, and within an oblique convergent setting (Mégard, 1984; Pardo-Casas and Molnar, 1987). Sebrier and Soler (1991) proposed that since late Oligocene times the high topographic regions in the Peruvian Andes have been dominated by extensional tectonics due to topographic forces. Therefore, Palaeogene magmatic rocks are proposed to have formed within a horizontal maximum principal stress regime, where σ_1 was probably parallel to the plate convergence direction, i.e. N-NE directed (Fig. 11a-b).

Miocene porphyry Cu centres and barren stocks of similar age (23.2 to 16.5 Ma) are also spatially associated with the Puntre Fault, but these igneous rocks are dominantly situated within the hanging wall of the thrust fault. The majority of Miocene stocks were emplaced between two orogenic episodes, i.e. the Incaic IV (22 Ma) and Quechua I (17 Ma), during high to moderate-high plate convergence with an E-NE direction (Fig. 11a; Mégard, 1984; Pardo-Casas and Molnar, 1987). Based on current data, no coeval volcanic rocks have been identified or dated between the 23.2 and 16.5 Ma intrusive interval. The mineralised porphyry stocks at Michiquillay, El Galeno and

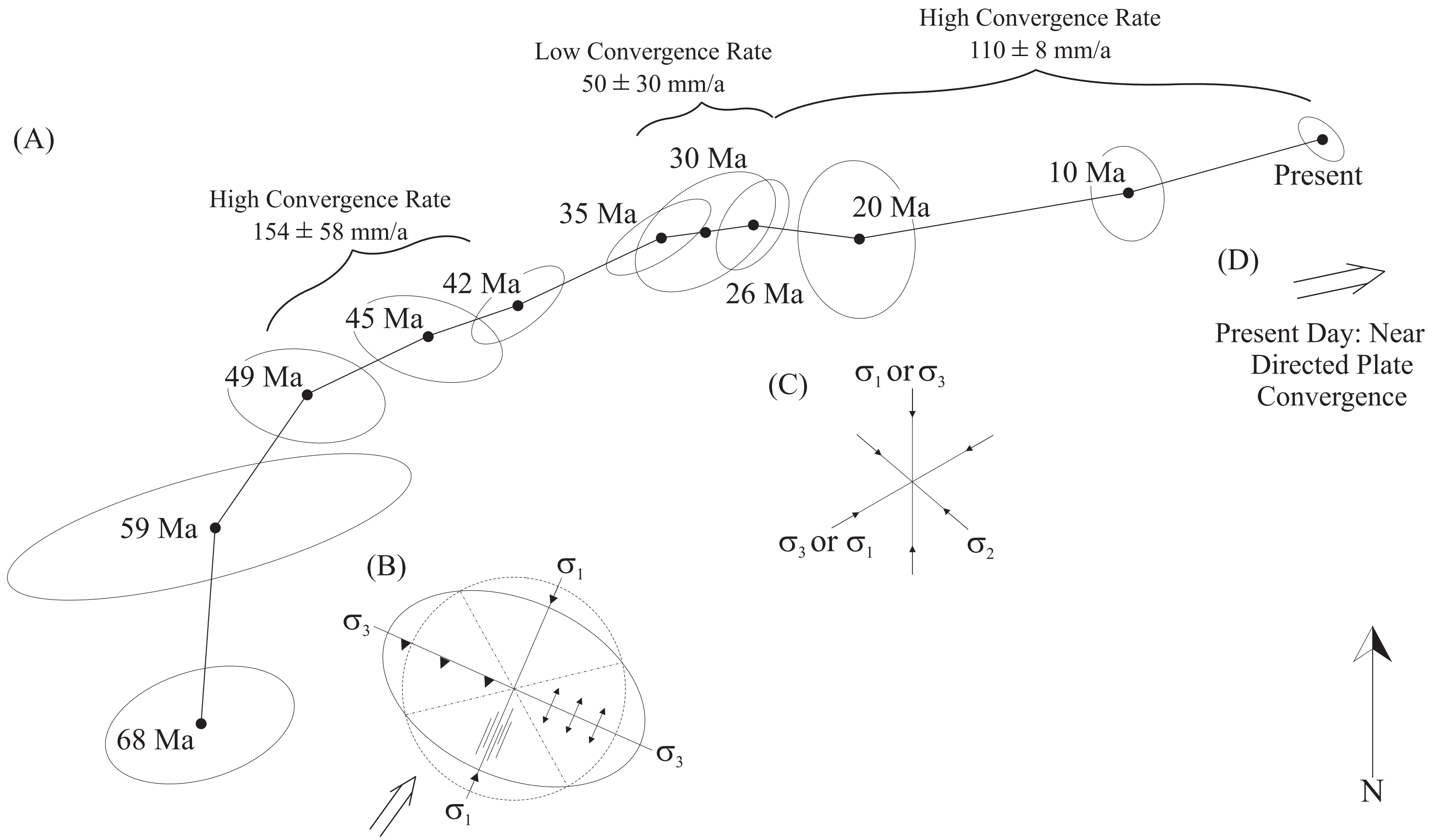

Fig. 11. (A) Plate motion direction of the Nazca Plate (Pardo-Casas and Molnar, 1987). (B) Horizontal principal stress directions for development of the fold-thrust fabric and tensional NE-trending faults during NE directed compression of the Incaic orogenic events (59-42 Ma). (C) Principle stress directions in the Andean Highlands since Late Oligocene (ca 26 Ma) to present day with possible rotations of σ_1 and σ_3 between horizontal and vertical. (D) Direction of the present day plate convergence along the South Amercian western margin .

Minas Conga are located at structural intersection zones defined by large-scale faults crosscut by second-order faults. To the NE of El Galeno, the Puntre Fault is crosscut by steep extensional faults that contain minor pyrite mineralisation. This suggests reactivation with normal movement along the regional-scale structure possibly took place during ascent of magmatic and hydrothermal fluids associated with the El Galeno complex. In plan view, the Miocene stocks are elliptical with the long axes roughly parallel to local large-scale structure(s). Similar alignment of pre-existing local structures and the long axes of elliptical intrusions suggest that the stocks intruded highly fractured, anisotropic crust with a high to possibly intermediate differential horizontal stress (Nakamura, 1977; Takada, 1994). Plate tectonic data combined with observed field relations indicate Miocene stocks were emplaced during periods of extension in the upper crust and localised at the intersection of large-scale faults crosscut by oblique subordinate faults.

Large-scale, deeply penetrating conduits or faults that are favourably oriented for dilation provide channelways for ascending fluids (Sibson, 1985; Petford *et al*., 1994; Pitcher, 1997). The close spatial association between the deposits and regional scale faults indicate that ascending early to middle Miocene melts and hydrothermal fluids were preferentially channelled along structural intersection zones. Field- and geophysical-based studies in Chile and Argentina have also documented significant magmatic and hydrothermal centres located at the loci of major structural intersections (Abels and Bischoff, 1999; Richards *et al*., 2001; Chernicoff *et al*., 2002). These authors also suggest porphyry Cu formation was optimised during periods of arc relaxation. This is supported by numerical models for deformation and fluid-flow in a subvolcanic compressive environment that indicate structural intersections are dilatant permeable zones that are favourable for porphyry emplacement (Gow and Ord, 1999).

.

Following initial solidification of the porphyry stock, the outer shell of the intrusion and its host rocks undergo brittle fracturing as a result of resurgent hydrothermal-magmatic activity or tectonic stresses (Fournier, 1999; Tosdal and Richards, 2001). In porphyry Cu deposits, regionally- and/or localised tectonically-influenced stresses result in linear fracture arrays, whereas concentric and radial fracture arrays are a product of magmatically-influenced stresses (Tosdal and Richards, 2001). The Minas Conga and Michiquillay mineralised systems are both characterised by deposit-controlling NNW- to NW-striking faults with sinistral displacement. Fracture and vein trends at the mineralised centres have a dominant NE, N-S or NW strike. These similar trends imply a regional stress field largely influenced fault-fracture-vein trends at these centres. In contrast, El Galeno is characterised by numerous fracture patterns of varying orientation and timing. It is inferred that the various fracture patterns at El Galeno were mostly influenced by magmatic stresses. However, faults in the host rock and fractures in the El Galeno intrusive complex display similar trends to those at Minas Conga and Michiquillay, i.e. dominantly NNW- and NE-trending. This suggests fractures at El Galeno formed in response to both magmatic and tectonic stresses, as well as indicating a regional control of fault-fracture systems. Elsewhere, regionally-extensive, systematic fracture patterns in plutons and their wall rocks in the Laramide region of North America have been related to regional stress fields (Heidrick and Titley, 1982).

Middle to late Miocene volcanism and formation of the Yanacocha Au deposit coincided with high convergence rates, near orthogonal E-NE directed convergence (Fig. 11d) and termination of major uplift. Longo (2000) argued subvertical NW-striking faults display sinistral movement, whereas NE faults are dextral (Fig. 10). Faults may also display vertical movement that is dominantly late. This implies the maximum principal stress direction has changed, possibly numerous times between horizontal E-directed (strike-slip) and vertical (extension) during formation of the deposit (Fig. 11c). Such episodic rotations of the regional stress field are unlikely during the short time span in which the Yanacocha deposit formed (<1 m.y.). Tosdal and Richards (2001) suggested rotations in the stress direction imposed on subvolcanic stocks during hydrothermal activity result from a low-differential stress field and fluctuating fluid pressures.

Tectonically-influenced fault-fracture arrays display both temporal and spatial relationships with various lithological units. The Cretaceous sedimentary rocks have a preferred NE fault trend that is inferred to have developed during Eocene SW-directed compression. NNW- and NE-trending faults characterise early Miocene mineralised stocks, whilst the late Miocene Yanacocha district is defined by NW and NE trends. Conjugate relationships between NW and NE structural trends are observed at the majority of mineralised Miocene deposits in the Cajamarca district, as well as to the north in the La Zanja district. The conjugate NE and NW structural trends at Yanacocha are broadly similar to trends observed at Michiquillay where NNW faults with a sinistral sense of shear are near orthogonal to the NE trend of alteration zones and the dominant vein orientation. Similar conjugate shear zones, with NE dextral and W-NW sinistral fault patterns, are observed in many regions and mining districts throughout the Peruvian Andes, e.g. Cerro de Pasco, Marcona and Toquepala (Petersen and Vidal, 1996). Intersections of conjugate zones are highly dilatant and act as channelways that both draw fluids up from a plutonic source (magmatic fluids), and meteoric fluids down during periods of intense horizontal compression in subvolcanic environments (Gow and Ord, 1999).

The dominant orientation of fault arrays in the Cajamarca district display a progressive rotation with time, i.e. early Miocene NNW and late Miocene NW dip-slip faults are superimposed on Eocene NE tensional faults. Two possible scenarios may explain the cause for the change in fault orientation with time. Firstly, counterclockwise rotation of the Cajamarca region in late Oligocene to early Miocene times (Mitourad *et al*., 1992) may have caused the apparent change in preferred fault orientation. Or alternatively, proposed clockwise rotations of the subducting Farallon/Nazca plate throughout Tertiary times (Fig. 11a, Pilger, 1984; Pardo-Casas and Molnar, 1987) are roughly consistent with the changes of the dominant fault orientation. Changes in the direction of plate convergence would induce a rotation in the horizontal principal stress fields from SW-directed during most of the Palaeogene to near E-directed since early Miocene times. This later scenario is consistent with work by Petersen and Vidal (1996) who suggested conjugate shear zones throughout the Peruvian Andes are a result of near E-directed plate convergence along western Peruvian margin. Despite these temporal relationships, structural evidence suggests both of these dominate fault trends (i.e. NE and NW) were active during Miocene times and strongly influenced the development of mineralised centres in the Cajamarca district.

B.9 Conclusion

Based on results from this study and previous work, several important structural relationships are inferred to have strongly influenced the development of the Cajamarca district and mineralised centres:

- An apparent counterclockwise rotation of the dominant fault orientation occurred with time.
- During changes in the tectonic stress or periods of relaxation structural intersection zones were focal points or favourable channelways for ascending magma and subsequent hydrothermal fluids. On a deposit-scale, periods of extension or rotations of the principal stress direction may have been facilitated by low-differential stress or fluid flow along fault planes.
- Faults and fracture data indicate two of the porphyry Cu complexes contain fault-vein patterns that were controlled by tectonic/regional stress fields, whereas the third mineralised porphyry complex has both magmatic and tectonic influenced fracture arrays.
- Conjugate structural relationships are evident at most of the Miocene mineralised centres in the Cajamarca and La Zanja districts, including both porphyry Cu and high-sulphidation centres.

Recognition of structural intersection zones between regional and oblique secondary faults is of fundamental importance for understanding controls on pluton emplacement and possible subsequent mineralisation in the Cajamarca region. Investigation of regional- and deposit-scale fault arrays and their relative timing suggests conjugate structural trends influenced formation of Miocene porphyry and high-sulphidation deposits in the Cajamarca region. A combined understanding of regionally significant structural trends and their relative timing combined with plate motions provides a powerful tool for exploration in hidden terrains or extending exposed structures beneath volcanic cover for exploring potentially hidden mineralised stocks.

SECTION C

Geochemistry of igneous suites from the Cajamarca district, northern Peru: Implications for magmatic controls on the formation of porphyry Cu-Au deposits

Section C. Geochemistry of igneous suites from the Cajamarca district, northern Peru: Implications for magmatic controls on the formation of porphyry Cu-Au deposits.

C.1 Abstract

Tertiary igneous rocks in the Cajamarca mining district range from medium to high-K, tholeiitic to calc-alkaline and are predominantly metaluminous. Palaeogene felsic rocks (57-43 Ma) are intermediate in composition (55.6–60.0 SiO_2 wt. %), contain hydrous and anhydrous mineral phases (plagioclase + amphibole + clinopyroxene), and have an average La_N/Yb_N ratio of 8.9. Partial melt modelling suggests these melts equilibrated with a garnet-poor residue that was dominated by pyroxene and olivine. Radiogenic isotope ratios indicate a low ε_{Nd} and high Sr_i material, possibly seawater, contaminated some Palaeogene magmas. Eocene volcanic melt compositions were controlled by fractionation of anhydrous minerals (plagioclase and pyroxene). It is inferred that this igneous suite developed during initial stages of magmatic arc formation and represents immature arc magmas. Oligocene mafic dykes (~29.5 Ma) are dominantly composed of anhydrous phases, have tholeiitic compositions, high $\sum$REE, and La_N/Yb_N ratios between 4 and 11 (mean = 7). These gabbroic dykes were derived from partial melting of a primitive mantle with an olivine-pyroxene dominated residual mineralogy. The third igneous suite includes Miocene intrusive and volcanic rocks (23.2-8.4 Ma) that were generated during periods of intense crustal thickening. These rocks are characterised by hydrous and anhydrous mineral phases (plagioclase + amphibole ± biotite ± quartz ± clinopyroxene), are intermediate to acidic in composition (57.7–68.8 SiO_2 wt. %) and have steep HREE-depleted profiles. Miocene synmineralisation intrusions are geochemically similar to coeval barren intrusions, but display minor relative enrichment in Th. Partial melting models and radiogenic isotopes indicate Miocene melts were derived from an amphibole-rich upper mantle to lower crust that assimilated minimal upper crustal material. Miocene melts were later strongly influenced by the fractionation of hornblende and biotite. Partial melting models of late Miocene rocks require higher residual garnet (up to 17%) than the early-middle Miocene magmas.

Results from this study suggest variations in residual mineralogy and subsequent fractionation processes are evident in the three igneous suites. These changes in residual mineralogy are inferred to result from an evolving magmatic arc undergoing extensive uplift, rapid increase in crustal thickness and deepening of the mantle-crust boundary. Early-middle Miocene synmineralisation intrusions are related to hydrous melts that were in equilibrium with an amphibole-rich residual, underwent minimal upper crustal contamination and late fractionation of hydrous minerals (i.e. biotite and minor hornblende). In contrast, late Miocene high-sulphidation deposits are linked to HREE-depleted magmas formed during the onset of a flattening subduction angle, cessation of rapid uplift and a progressive change in the residual mineralogy with greater garnet influence.

C.2 Introduction

Porphyry copper deposits form in magmatic arc environments and are related to magmatic fluids that typically exsolve from medium to high K, calc-alkaline magmas emplaced in subvolcanic environments (Sillitoe, 1972, 1988; Burnham, 1979). Numerous studies have characterised the geochemistry, source and evolution of Andean magmatic arc igneous rocks (Hawkesworth *et al*., 1979; Gill, 1981; Hildreth and Moorbath, 1988; Davidson *et al*., 1991; Kay *et al*., 1991; Macfarlane, 1999). In contrast, recent geochemical studies (Lang and Titley, 1998; Richards *et al*., 2001) of porphyry copper deposits have focussed on distinguishing mineralised from non-mineralised intrusive porphyry stocks, as well as defining the residual mineralogy of the source region from which synmineralisation magmas are derived (Kay and Mpodozis, 2001).

The Cajamarca region of northern Peru hosts several Miocene porphyry deposits, including the Michiquillay (Cu-Au-Mo), Minas Conga (Au-Cu), El Galeno (Cu-Au-Mo) Minas Carpa (Au-Cu) and Cerro Corona (Au-Cu) porphyry complexes. A number of high-sulphidation Au deposits are also located in the district, including the Yanacocha Au mine, Sipán, La Zanja and Tantahuatay. Recent studies have characterised mineralised and barren Miocene intrusive stocks in the Hualgayoc district (Macfarlane and Petersen, 1990; Macfarlane *et al*., 1994; James, 1998; Macfarlane, 1999). Whilst Turner (1997) presented major and some trace element data for middle to late Miocene volcanic rocks in the Yanacocha district. At present, no comprehensive geochemical studies have been reported for the mineralised porphyry centres or regional barren igneous units in the Cajamarca district.

This section presents a petrogenetic model for Tertiary magmatic units in the Cajamarca district. The section includes presentation of new major, trace element and radiogenic isotope data for magmatic units of varying age in the region. This section focuses on identification of different petrogenetic suites, modelling of residual mineralogy and fractionation processes, as well as investigating possible variations between synmineralisation and barren intrusive units. Finally, the petrogenesis of magmatic units in the Cajamarca region is compared with that of other porphyry copper regions located along the Andean belt.

C.3 Tectonic Setting and Regional Geology

The Cajamarca district is situated at an altitude between 2300 and 4400 m in the Western Cordillera of the northern Peruvian Andes where the present day maximum crustal thickness is ~45 km (Fukao *et al*., 1989). It is within one of three major Andean oroclines that is known as the Huancabamba Deflection (Mégard, 1984). The northern part of the deflection zone roughly coincides with the present change in subduction angle of the Nazca plate, from steep slab subduction north of the Peruvian-Ecuador border to shallow (~10^{o}) in central Peru (Fig. 1). The zone of flat subduction in northern and central Peru is defined by the distribution of earthquakes and absence of Quaternary volcanic activity (Barazangi and Isacks, 1979; James, 1981; Jordan *et al*., 1983; James and Sacks, 1999), and has been attributed to a lack of a mantle wedge between the subducting and overriding plate. Gutscher *et al*. (1999) argued that subduction of an ancient oceanic plateau beneath northern Peru occurred from 12 to 10 Ma and resulted in the present day low slab dip angle.

The Cajamarca district is characterised by Cretaceous marine sedimentary rocks that were deformed during Tertiary times by two orogenic episodes, known respectively as the Incaic and Quechua pulses (Mégard, 1984; Benavides, 1999). Initial

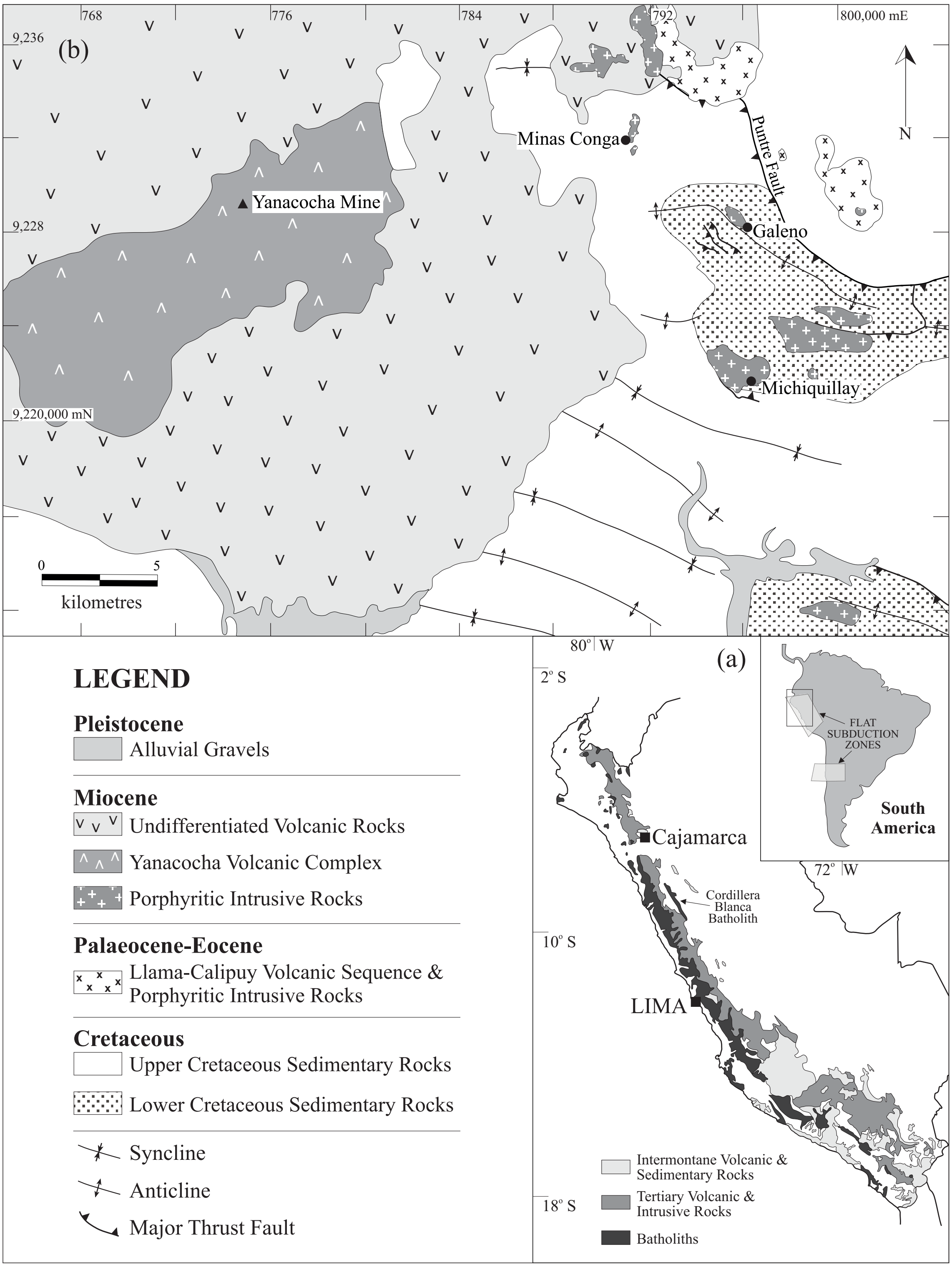

Fig. 1a. Simplified geology of Peruvian Andes showing the major Mesozoic and Cainozoic magmatic rocks. Insert, a map of South America illustrating zones of flat subduction. b. Simplified geological map of the Cajamarca study area (modified from Reyes, 1980).

fold-thrust development during Incaic orogenic pulses (Mégard, 1984) occurred during Eocene times over a reactivated margin of the Brazil shield (Macfarlane, 1999). Igneous rocks in the Cajamarca region are related to three major magmatic episodes that intrude and overlie the deformed Cretaceous sedimentary rocks and metamorphic basement. The first of these magmatic episodes occurred during Palaeogene times (57-35 Ma) and resulted in deposition of the Llama-Calipuy Volcanic Sequence, as well as the emplacement of several intrusive stocks (Noble *et al*., 1990; Section A). The Llama volcanic sequences form an aerially-extensive volcanic succession which is predominantly basaltic to andesitic and ranges in age from 54.8 to 35.4 Ma (Atherton *et al*., 1985; Noble *et al*., 1990; Section A). Oligocene mafic dykes also crop out throughout the region and have been recently dated at 29.4 Ma (Section A).

The second magmatic phase occurred during early-middle Miocene times (~23.2-15.8 Ma). Initiation of this magmatic period coincided with a number of important tectonic events that included a clockwise rotation of the Nazca plate, increased convergence rate, several deformation phases, and major uplift in northern Peru (Pardo-Casas and Molnar, 1987; Noble *et al*., 1990). Based on geophysical and geological data Kono *et al*. (1989) and James and Sacks (1999) concluded that the majority of Miocene crustal thickening in the Western Cordillera resulted from intense magmatism, as opposed to foreshortening in the Eastern Cordillera. This magmatic episode defines the main period of Cu-Au-Mo porphyry formation with the emplacement of several mineralised and barren intrusive units (Llosa *et al*., 1996; Section A). Volcanic rocks related to this magmatic episode are dominantly middle Miocene in age and appear to post-date intrusive activity and porphyry copper formation (Llosa *et al*., 1996; Turner, 1997). This early-middle Miocene magmatic episode in the Cajamarca region was followed by an apparent 3-4 m.y. magmatic hiatus during which extensive intrusive and hydrothermal activity took place to the north of Cajamarca and resulted in formation of the polymetallic deposits in the Hualgayoc mining district (Macfarlane *et al*., 1994; James, 1998).

The final magmatic phase identified near Cajamarca occurred during late Miocene times (12.3 – 8.4 Ma) and was characterised by widespread volcanism incorporating the Yanacocha Volcanic Complex, plus the Regalado and Huambos basalt to andesite volcanic sequences. Evidence for minor intrusive activity, such as emplacement of tonalite and rhyodacite stocks, has been observed at Yanacocha (Turner, 1997). Formation of the large high-sulphidation Yanacocha Au deposit occurred during this final magmatic interval. Magmatic activity ceased in both the Cajamarca and Hualgayoc districts at approximately 8 Ma (Macfarlane *et al*., 1994; Turner, 1997).

C.4 Analytical Methods

Samples collected and analysed include a diverse compositional range and unaltered or least altered samples were selected where possible. Major, trace and rare earth element analyses of 38 samples from five mineralised intrusive centres, and a variety of barren intrusive plus volcanic units in the Cajamarca region were used in this study (Fig. 2). Major elements and the majority of trace elements (Ba, V, Cr, Co, Ni, Zn, Ga, Rb, Sr, Y, Zr and Nb) were analysed by X-ray fluorescence (XRF) on a Siemens XRF sequential spectrometer (SRS303) and mineral analyses were performed on a Jeol JXA840 electron microprobe at the Advanced Analytical Centre, James Cook University Australia. REE and the remaining trace elements (Cs, Hf, Sc, Ta, Th and U) were analysed by instrumental neutron activation analysis (INAA) at the Becquerel Laboratories, Lucas Heights, New South Wales.

Where possible, unaltered samples were selected for Sr and Nd isotopic analyses. However, this was not always possible and the majority of samples were altered to some degree. Consequently, whole rock powders were leached in hot 6M HCl in a ultrasonicator followed by concentrated HNO_3 on the hotplate for 2 hours to remove any secondary carbonate material that may have perturbed the primary magmatic radiogenic value. The leached material was centrifuged, the HNO_3 removed and the residue was then rinsed with distilled water. Sr and Nd radiogenic isotope results were obtained in static multi-collector mode on a Finnigan-MAT 262 mass spectrometer at La Trobe University, Melbourne, Victoria. Sr isotope ratios were normalised to $^{86}Sr/^{87}Sr = 0.1194$, Nd isotope ratios to $^{146}Nd/^{144}Nd = 0.7219$. Sr isotope data are relative to SRM987-Sr = 0.71024 and Nd isotope data are reported relative to La Jolla-Nd = 0.511860.

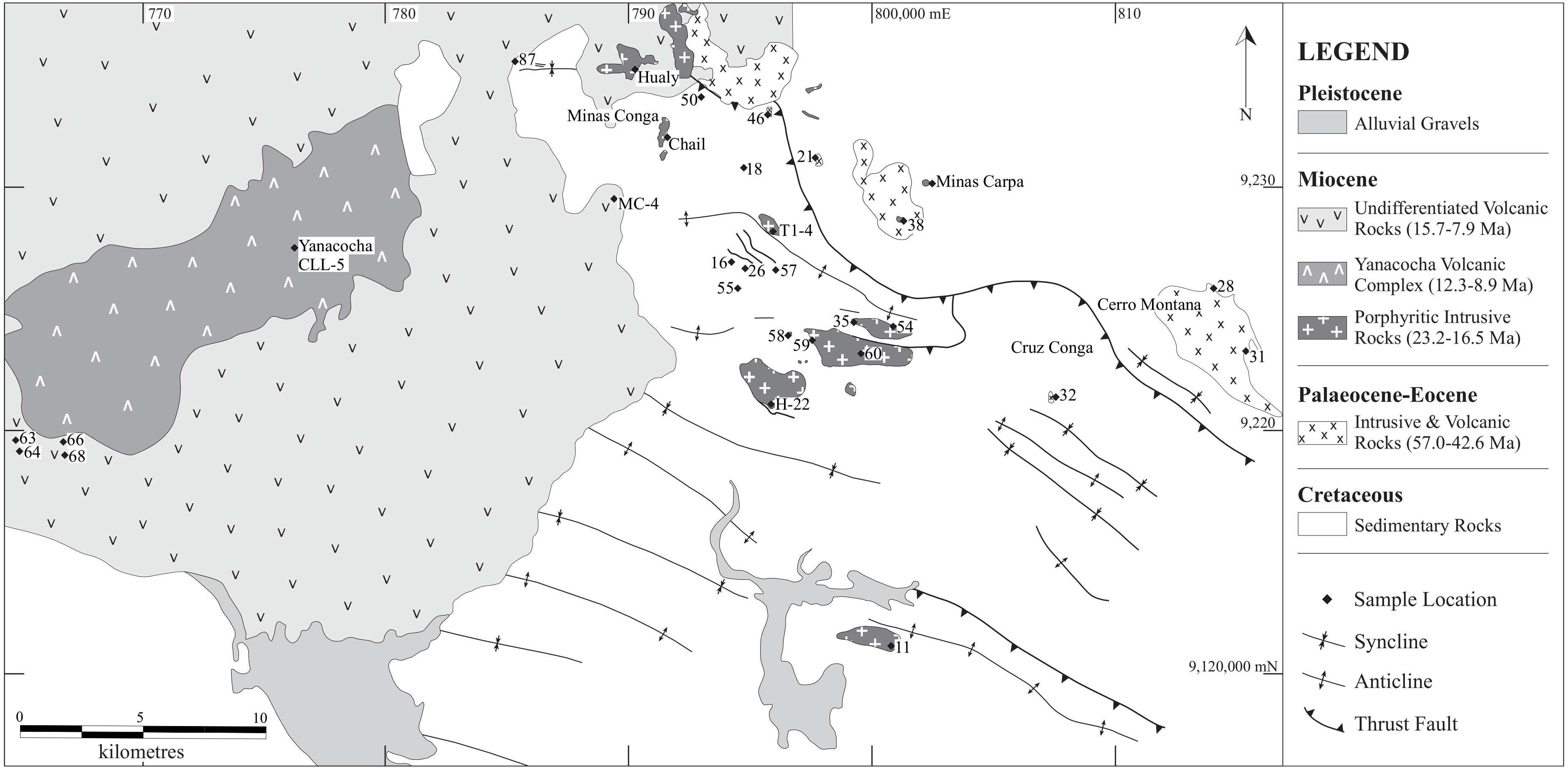

Fig. 2. Simplified geological map of the Cajamarca area showing the locations of the igneous rocks sampled and analysed.

C.5 Petrology - Rock Nomenclature

Tertiary intrusive rocks in the Cajamarca region range from gabbro (rare) to hornblende gabbro (minor) through to hornblende ± biotite diorite (most common). The gabbroic dykes are generally weakly porphyritic, whereas the diorite stocks are moderately to strongly porphyritic in texture. Volcanic sequences in the study area range from basaltic andesite to andesite and are strongly porphyritic. Clinopyroxene is common in the dykes and volcanic units, and generally defines an anhydrous mineral assemblage, i.e. plagioclase + clinopyroxene ± rare hornblende (Fig. 3). The felsic intrusive rocks are mostly characterised by a hydrous mineral assemblage of plagioclase + hornblende ± biotite ± quartz and rare clinopyroxene (Fig. 3). The majority of igneous rocks sampled in the region display weak to moderate alteration, with weak propylitic (sericite-carbonate-chlorite) alteration the most common and widespread.

C.5.1 Gabbroic Dykes

Plagioclase is the most abundant mineral phase in the gabbroic dykes and is present in two size populations with phenocrysts (1-3 mm) generally more abundant (25-75 vol.%, Fig. 3) than microphenocysts (0-50 vol.%; <1 mm). Euhedral plagioclase phenocrysts display both normal (Ca-rich cores) plus reverse (Ca-rich rims) zoning, and are mostly bytownite to labradorite in composition (An_{90-51}, Fig. 4). Euhedral clinopyroxene grains are less abundant (6-8 vol.%), present as phenocrysts (1-3 mm) and microphenocrysts (<1 mm), plus contain reverse zoning textures with Mg-rich rims (Appendix C1). Clinopyroxene grains are dominantly augite (Wo_{40-45}), with the exception of one dyke (S-87) that has augite grains with small, patchy Fe-rich zones (Wo_{39-40}, Fig. 4). Amphibole is present in only two of the samples (S-16 and S-55) and in low abundances (0.5-1.9 vol.%). Amphibole phenocrysts are magnesiohastingsite in composition (Fig. 4) and characterised by high Al_2O_3 and Mg # (67-68), plus low Fe_2O_3(T). These two samples (S-16 and S-55) also contain minor fine-grained phlogopite. The groundmass is feldspathic with fine-grained Fe-Ti oxides (titanomagnetite) and minor apatite present as accessory mineral phases.

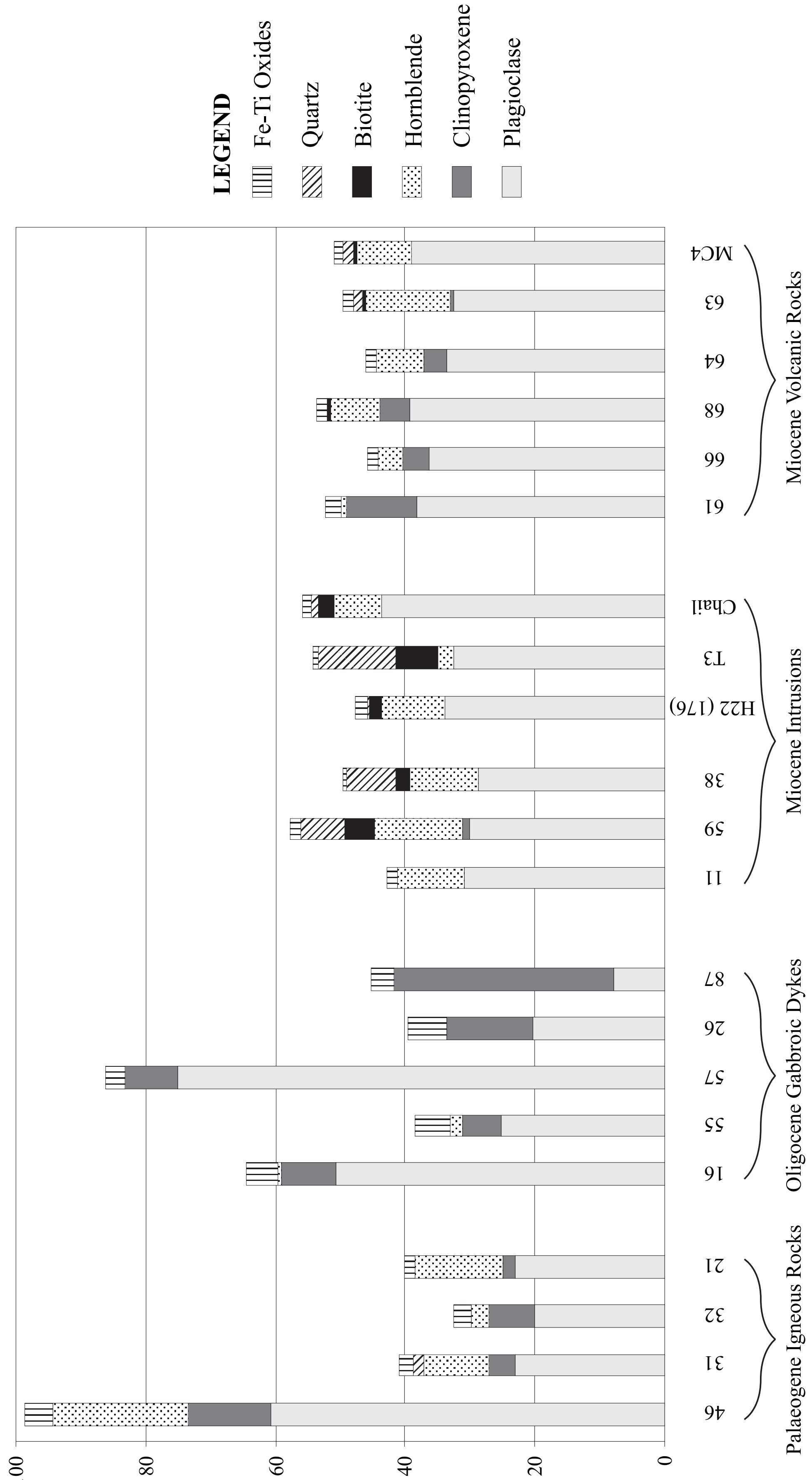

Fig. 3. Phenocryst abundance for the different igneous suites.

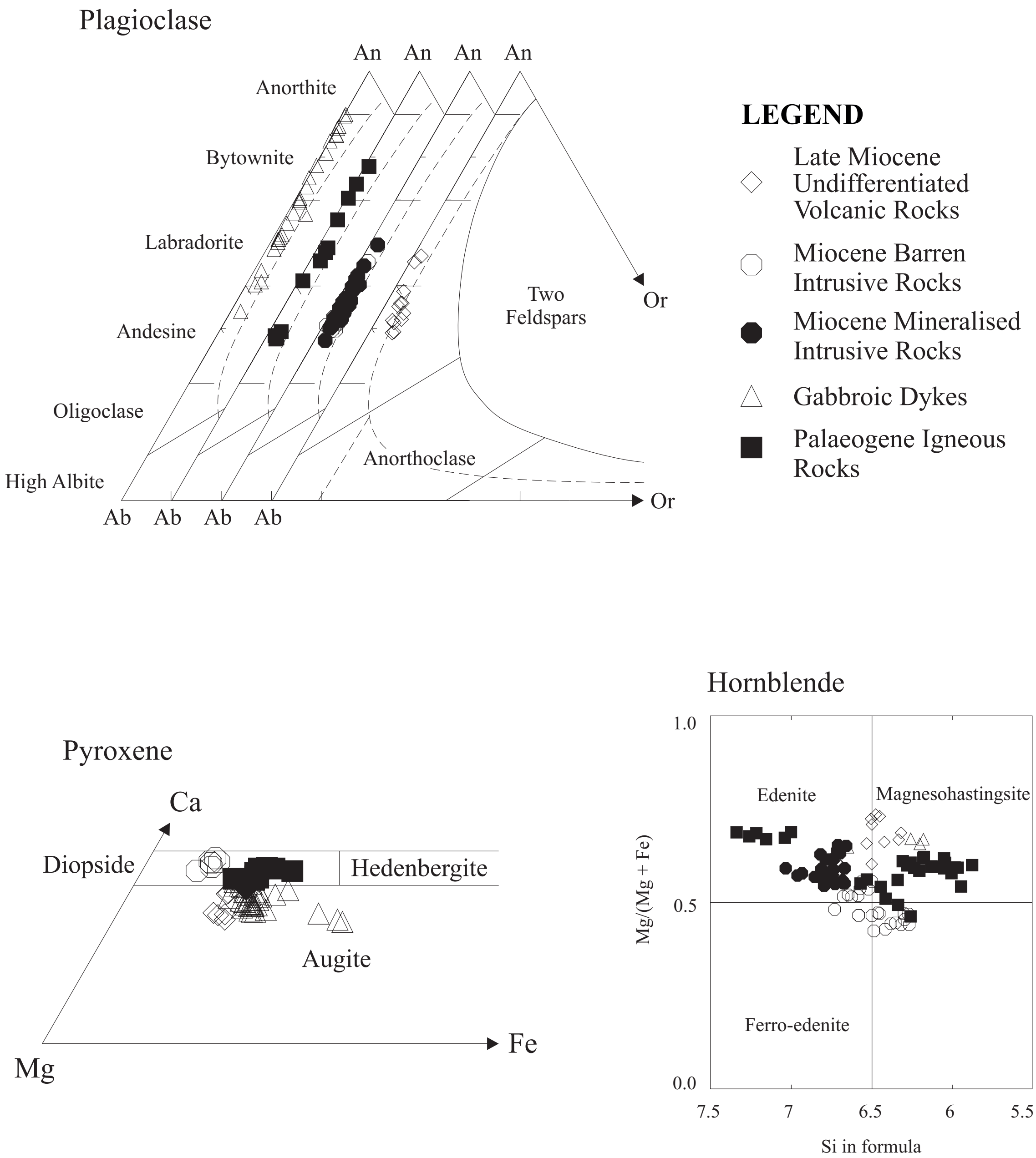

Fig. 4. Mineral chemistry and classification diagrams for pyroxene, hornblende and plagioclase phenocrysts.

C.5.2 Felsic Intrusive Units

Palaeogene and Miocene felsic intrusive bodies display similar petrographic characteristics with euhedral plagioclase the most abundant phenocryst (1-7 mm; 23-61 vol.%, Fig. 3). Plagioclase is characterised by normal, reverse and oscillatory zoning (Fig. 5), and some grains from mineralised centres have albite-sericite altered rims. Plagioclase phenocrysts from Palaeogene intrusive units range from bytownite to andesine (An_{74-34}; 23-61 vol.%), whereas phenocrysts from Miocene intrusive centres are dominantly less calcic and plot between labradorite and andesine (An_{57-38}; 25-44 vol.%, Fig. 4). Calcic amphibole phenocrysts (1-8 mm) in the felsic intrusive rocks are predominantly euhedral, light yellow to light brown or green in thin section and may contain minor feldspar inclusions. Amphiboles from barren Palaeogene intrusions are dominantly magnesiohastingsite to pargasite (Mg # = 51-69; 10-21 vol.%). Amphibole phenocrysts from barren Miocene intrusive centres tend to have lower SiO_2, MgO and higher Fe_2O_3(T) (Mg # = 42-56; 11-13 vol.%) than amphiboles from mineralised centres that are commonly edenites (Mg # = 47-65; 1-9 vol.%). Euhedral magmatic biotite phenocrysts (Mg # = 57-66; 2-6 vol.%) are present in all mineralised centres and range in size from 0.5 to 3 mm. Biotite phenocrysts have a low abundance in barren intrusive units (0-5 vol.%) and are strongly chloritised. Rounded quartz phenocrysts (1-4 mm) are present in some rocks and contain minor embayments. Euhedral clinopyroxene grains (0.5-2.0 mm) in samples S-59, S-31 and S-28 are present in minor amounts (1-4 vol.%). Clinopyroxenes from one hornblende-biotite quartz diorite (S-59) are diopsides (Wo_{47-49}) and have higher Mg # (Mg # = 81-86) than those from the gabbroic dykes (Appendix C1). Phenocrysts are set in a feldspathic groundmass. Zircon, apatite and Fe-Ti oxide (titanomagnetite) are present as accessory phases.

C.5.3 Volcanic Sequences

Rocks from the Lower Llama Volcanic Formation (~43 Ma; S-21 and S-32) contain euhedral plagioclase, hornblende and clinopyroxene phenocrysts set in a feldspathic groundmass with a trachytic texture. Euhedral plagioclase phenocrysts (0.3-1.0 mm; 20-23 vol.%) are the dominant phenocryst phase in S-32 and range in composition from An_{78} to An_{57}. Euhedral clinopyroxene phenocrysts (Mg # = 62-71; 2–7 vol.%) are less abundant, characterised by very high TiO_2 and Al_2O_3 contents (Appendix C1), and are diopsides (Wo_{45-47}). Some clinopyroxene grains display zoned and/or twinned textures. Amphibole phenocrysts from S-32 (Mg # = 59-62; 3 vol.%) are

THIS IMAGE HAS BEEN REMOVED DUE TO COPYRIGHT RESTRICTIONS

Fig. 5. Backscattered image of a plagioclase phenocryst from a mineralised centre (Sample S-T2: GN-39 214m). The image illustrates the oscillatory zonation of some plagioclase phenocrysts with Ca-rich zones appearing grey and the Ca-Na-rich zones having a light grey appearance. The phenocryst is set in a feldspathic groundmass with spotted quartz (dark grey) and K-feldspar (light grey). Width of image is 950 µm.

pargasites with high TiO_2 and Al_2O_3 plus low SiO_2 (Appendix C1). Amphiboles in S-21 are magnesiohastingsite to hastingsite and characterised by high Fe_2O_3(T) and Al_2O_3, plus low SiO_2 and Mg # (Mg # <62; 13 vol.%). Apatite microphenocrysts (0.1-0.3 mm; 1 vol.%) are also present in both samples.

Basaltic andesite rocks of the Regalado Volcanic Formation (~12.3 Ma; S-61, S-64, S-66, S-68) contain plagioclase (0.3-5.0 mm), clinopyroxene (0.2-1.5 mm) and amphibole (0.2-6.0 mm) phenocrysts. Euhedral plagioclase (34-39 vol.%; An_{58-41}) phenocrysts are characterised by normal, reverse and strong oscillatory zonation patterns. Amphibole phenocrysts (1-7 vol.%) have generally low Fe_2O_3(T) and high MgO, which reflect relatively high Mg # (58 to 74) compared with the felsic intrusive units. Amphibole phenocrysts are commonly poikilitic with feldspar, clinopyroxene and Fe-Ti oxide inclusions. Rims of amphibole grains have been altered to hematite. Euhedral clinopyroxene phenocrysts are generally less abundant (4–10 vol.%), commonly twinned and have high Mg # (> 75). They are typically diopside (Wo_{43-39}) and slightly depleted in Al_2O_3 plus Fe_2O_{3T}. The groundmass is felspathic and glassy with euhedral apatite microphenocrysts (0.1 mm) present in minor amounts (0.2-0.3 vol.%).

Andesite rocks from the Huambos volcanic sequences (~8 Ma; S-63 and S-MC4) consist of plagioclase, biotite, hornblende, quartz and clinopyroxene phenocrysts set in a feldspathic groundmass. Plagioclase phenocrysts (33-39 vol.%) display complex zoning patterns and are andesine in composition (An_{50-43}). Euhedral amphibole phenocrysts (8.5-13.0 vol.%) tend to have rims partially altered to hematite, low Fe_2O_3(T) and high MgO with Mg # of 56-73. Quartz phenocrysts (1.6 vol.%) are rounded and generally have minor embayments. Euhedral biotite phenocrysts (Mg# = 57-64; 0.6-0.7 vol.%) are enriched in Na_2O but depleted in K_2O compared with biotite phenocrysts from mineralised intrusive centres (Appendix C1). Clinopyroxene phenocrysts are rare, subhedral to euhedral, have low TiO_2 and are augites (Mg # = 72).

In summary, the rocks from the Eocene Llama Volcanic Sequence (S-21 and S-32) are characterised by amphiboles and clinopyroxenes that are enriched in TiO_2 and Al_2O_3 but depleted in SiO_2 compared to minerals from the Miocene Regalado and Huambos Formations.

C.6 Major Elements

The igneous rocks show a broad range in SiO_2 concentration (47.9–68.8 wt% SiO_2) and a large range in loss on ignition (11.3–0.9 wt% LOI; Appendix C2). Major component analyses have been normalised 100% on a volatile-free basis to facilitate comparison (Table 1). The gabbroic dykes are dominantly more basic [47.9–52.4 wt% $SiO_{2(N)}$] than the Palaeogene igneous units that are intermediate in composition [55.6–60.0 wt% $SiO_{2(N)}$] and the Miocene units range from intermediate to acidic [57.7-68.8 wt% $SiO_{2(N)}$]. The majority of intrusive and volcanic samples plot in the medium to high-K field (Fig. 6), range from weakly alkaline to subalkaline, and are metaluminous. The gabbroic dykes straddle the tholeiite - calc-alkaline boundary displaying a high Fe_2O_3(T) content, whereas the other igneous rocks show calc-alkaline affinity (Fig. 6).

The gabbroic dykes display increasing TiO_2, Na_2O and K_2O with fractionation, as monitored by SiO_2 (Fig. 7) and MgO. Fe_2O_3(T), CaO and MgO decrease with increasing SiO_2 for the gabbroic units, with Al_2O_3 and P_2O_5 displaying minor scatter. In general, the gabbros display a large amount of scatter that is possibly related to the moderate alteration and element mobility. Palaeogene felsic rocks show negative correlations of silica with TiO_2, Fe_2O_3(T), CaO and MgO. One volcanic sample (S-32) has anomalously high TiO_2. The remaining major elements, Al_2O_3, Na_2O, K_2O, MnO and P_2O_5, increase with increasing fractionation. Miocene intrusive and volcanic units show linear negative correlations between TiO_2, MgO and P_2O_5 and silica, whereas CaO, Fe_2O_3(T) and possibly Na_2O show curvilinear negative correlations. SiO_2 and K_2O display a positive curvilinear correlation, whereas Al_2O_3 shows no clear correlation with silica. Mineralised Miocene centres display similar major element trends and contents to barren intrusive centres of similar age with the exception of K_2O, which shows slight enrichment in the mineralised systems. This enrichment is probably due to hydrothermal alteration as evident from a K-feldspar-biotite altered sample from the El Galeno prospect (S-T1) that has an abnormally high K_2O/Al_2O_3 ratio. Fractionation trends are difficult to accurately determine due to the amount of scatter associated with phenocryst-rich units and partial alteration overprint. However, trends for CaO, K_2O

Table 1. Whole rock geochemistry of Tertiary igneous rocks in the Cajamarca region. Major components have been normalised on a volatile-free basis.

Suite	Gabbroic Dykes						Palaeocene-Eocene Intrusions				Eocene - Llama Volcanic			
Locality	S Galeno	S Galeno	S Galeno	N Galeno	E Galeno	N Galeno	Cerro Montana		East Minas Conga		La Carpa	Cruz Conga	Aurora Patricia	La Carpa
Sample No.	S-16	S-55	S-57	S-18	S-26	S-87	S-28	S-31	S-46	S-50	S-21	S-32	S-11	S-38
Rock Type	Hbl Gabbro	Hbl Gabbro	Gabbro	Gabbro	Gab Diorite	Gab Diorite	Hbl Diorite	Hbl Diorite	Hbl MD	Hbl MD	Hbl Andesite	Hbl Bas Andesite	Hbl Diorite	Hbl Qtz Diorite
wt. %														
SiO_2	48.88	47.89	50.35	48.65	52.11	52.41	59.99	58.23	55.88	55.60	57.57	56.37	62.87	65.33
TiO_2	1.26	1.15	1.30	1.34	1.55	1.12	0.59	0.66	0.71	0.71	0.65	1.13	0.53	0.49
Al_2O_3	19.08	18.23	20.17	18.47	17.34	18.59	18.01	19.04	17.84	18.24	19.00	18.92	17.88	17.08
Fe_2O_3(T)	12.18	13.18	10.07	11.48	11.40	10.37	7.19	7.66	7.40	8.02	6.61	7.06	4.95	3.99
MnO	0.17	0.23	0.21	0.14	0.66	0.15	0.30	0.27	0.17	0.17	0.22	0.25	0.11	0.08
MgO	5.11	5.08	3.88	7.02	3.91	3.40	1.90	2.05	3.69	4.06	2.11	1.66	1.85	1.84
CaO	9.89	10.83	9.60	9.06	7.11	9.41	5.54	5.15	8.20	7.84	6.92	6.59	5.85	4.63
Na_2O	2.26	2.40	3.29	3.25	3.22	3.31	3.94	4.86	3.82	3.98	4.51	4.67	3.77	3.84
K_2O	0.99	0.79	0.95	0.21	2.17	0.96	2.13	1.72	2.06	1.14	2.09	2.86	1.95	2.51
P_2O_5	0.18	0.22	0.18	0.38	0.53	0.26	0.40	0.37	0.23	0.25	0.31	0.47	0.24	0.21
$Total_{(N)}$	100.00	100.00	100.00	100.00	100.00	100.00	100.00	100.00	100.00	100.00	100.00	100.00	100.00	100.00
LOI	5.66	7.71	2.60	11.31	3.10	3.18	3.94	2.89	0.92	4.65	2.06	3.15	3.08	2.92
ppm														
Cr	19	9	5	39	36	3	9	19	31	10	0	0	26	21
Ni	13	13	14	32	28	8	9	6	15	16	6	5	6	11
Co	40	33	29	30	32	24	12	11	27	22	19	17	13	17
Sc	25	18	21	25	22	18	6	7	18	18	8	5	7	7
V	332	291	222	247	185	184	42	62	174	187	114	82	70	79
Rb	35	14	24	<1	67	18	61	39	62	27	59	74	60	76
Cs	8	1	2	<1	8	<1	<1	1	6	1	2	<1	1	3
Ba	375	366	621	829	701	373	1228	580	803	648	902	1073	827	864
Sr	514	582	711	625	472	571	898	799	635	816	775	967	584	623
Ga	17	17	23	18	21	16	16	16	20	19	20	23	21	21
Ta	<1	<1	1.04	<1	1.77	<1	<1	1.05	<1	<1	<1	2.17	<1	<1
Nb	1	2	9	11	21	4	3	7	5	4	5	29	5	5
Hf	1.9	1.8	2.1	2.4	5.1	3.5	3.6	3.3	2.9	2.6	3.6	5.0	3.1	3.0
Zr	51	57	81	88	241	128	112	97	86	83	111	189	110	92
Y	19	19	17	18	37	27	73	27	21	19	25	28	17	16
Th	1.5	1.7	3.4	3.5	9.6	3.0	3.2	4.7	6.9	5.5	7.3	12.0	4.6	3.0
U	<2	<2	<2	<2	3.1	<2	<2	<2	<2	<2	2.1	2.4	<2	2.2
La	10.60	12.70	18.40	24.30	43.20	20.00	34.00	25.80	25.90	23.60	34.10	58.40	20.70	15.00
Ce	22.70	25.30	36.10	47.10	82.40	46.00	60.70	51.00	48.00	44.30	65.10	106.00	37.30	26.70
Nd	13.10	13.00	16.90	na	35.10	na	32.20	25.30	23.00	na	26.60	41.50	18.00	14.70
Sm	3.15	3.26	3.39	4.32	7.14	5.07	7.54	5.42	4.09	3.96	5.50	7.26	3.66	3.40
Eu	1.11	1.02	1.33	1.26	1.71	1.42	2.50	1.74	1.17	0.84	1.58	2.07	1.03	0.75
Tb	0.62	0.54	0.65	0.60	1.10	0.88	1.32	0.90	0.69	0.64	0.78	0.94	0.51	0.48
Ho	0.74	0.69	0.77	na	1.28	na	1.78	1.07	0.85	na	0.98	1.13	0.58	na
Yb	1.77	1.67	1.60	1.48	3.16	2.64	4.45	2.59	2.05	1.88	2.70	2.42	1.27	0.86
Lu	0.24	0.23	0.22	0.21	0.45	0.40	0.66	0.35	0.29	0.28	0.34	0.31	<0.20	<0.20
Rb/Sr	0.07	0.02	0.03	0.00	0.14	0.03	0.07	0.05	0.10	0.03	0.08	0.08	0.10	0.12
Sr/Y	27.1	30.6	41.8	34.7	12.8	21.1	12.3	29.6	30.2	42.9	31.0	34.5	34.4	38.9
Zr/Nb	51.0	28.5	9.0	8.0	11.5	32.0	37.3	13.9	17.2	20.8	22.2	6.5	22.0	18.4
La_N/Yb_N	4.0	5.1	7.7	11.0	9.1	5.1	5.1	6.7	8.4	8.4	8.4	16.1	10.9	11.7

$Total_{(N)}$ = Volatile-free normalised; <2 = below detection limit; na = not analysed
Gab Diorite = Gabbroic Diorite; MD = Microdiorite; Bas Andesite = Basaltic Andesite; Hbl = Hornblende; Bt = Biotite

Table 1. cont.

Suite	Miocene Barren Intrusions							Miocene Synmineralisation Intrusions							
Locality	Michiquillay Region						Galeno Prospect	Michiquillay Prospect			Minas Conga Prospect		Galeno Prospect		
Sample No.	S-35	S-36	S-54	S-58	S-59	S-60	S-T4	S-H22(244)	S-H22(176)	S-H22(180)	S-Chail	S-Hualy	S-T1	S-T2	S-T3
Rock Type	Hbl-Bt Diorite	Hbl-Bt Diorite	Hbl-Bt Diorite	Hbl-Bt Diorite	Hbl-Bt Qtz Diorite	Hbl-Bt Diorite	Hbl-Bt Diorite	Hbl-Bt Diorite	Hbl-Bt Diorite	Hbl-Bt Diorite	Hbl-Bt Diorite	Hbl-Bt Diorite	Hbl-Bt Diorite	Hbl-Bt Diorite	Hbl-Bt Qtz Diorite
wt. %															
SiO_2	61.05	63.45	63.83	60.69	60.74	62.95	59.56	64.39	62.74	63.92	63.34	63.26	66.40	68.08	65.24
TiO_2	0.62	0.58	0.56	0.64	0.66	0.57	0.61	0.56	0.57	0.57	0.51	0.58	0.50	0.49	0.47
Al_2O_3	17.57	16.99	16.99	17.38	17.42	17.78	16.55	18.18	17.18	16.70	17.42	17.30	18.13	17.74	16.81
Fe_2O_3(T)	5.54	4.88	4.83	5.77	5.71	5.06	7.97	4.87	5.24	5.72	4.78	5.15	3.64	2.36	4.49
MnO	0.12	0.11	0.10	0.12	0.12	0.12	0.07	0.25	0.08	0.00	0.09	0.18	0.00	0.00	0.10
MgO	2.50	1.98	1.96	2.74	2.72	1.59	4.50	0.98	2.29	2.30	1.74	2.47	1.70	1.40	1.60
CaO	6.62	6.25	5.93	6.31	6.28	5.88	4.76	5.12	5.55	4.41	5.07	5.99	0.61	2.38	4.29
Na_2O	3.77	3.33	3.28	4.09	4.10	3.90	3.62	2.64	3.74	3.72	4.33	3.61	2.74	3.55	3.39
K_2O	1.98	2.20	2.29	2.04	2.02	1.92	2.15	2.78	2.37	2.41	2.48	1.23	6.10	3.77	3.39
P_2O_5	0.23	0.24	0.23	0.23	0.23	0.23	0.20	0.24	0.23	0.23	0.23	0.22	0.18	0.24	0.21
$Total_{(N)}$	100.00	100.00	100.00	100.00	100.00	100.00	100.00	100.00	100.00	100.00	100.00	100.00	100.00	100.00	100.00
LOI	2.22	5.08	5.63	4.47	2.50	3.62	2.12	7.80	1.40	1.84	1.32	5.06	4.31	3.83	2.60
ppm															
Cr	29	12	7	43	28	7	175	5	45	42	33	41	35	35	46
Ni	12	8	7	20	12	6	46	4	13	12	9	11	10	5	8
Co	24	15	19	17	22	15	23	24	23	22	21	14	21	20	21
Sc	10	8	8	13	13	7	18	10	10	10	8	8	6	6	6
V	103	95	93	123	118	87	146	79	90	94	72	116	80	79	68
Rb	58	64	66	60	60	52	90	100	51	75	72	33	165	81	88
Cs	<1	2	4	3	2	-1	3	3	1	2	<1	1	4	5	2
Ba	708	893	1065	622	671	766	344	529	668	582	723	473	630	606	794
Sr	793	625	580	619	708	774	532	230	690	600	643	615	295	491	528
Ga	20	18	19	19	19	20	20	21	18	20	19	20	18	18	20
Ta	<1	<1	<1	<1	<1	<1	<1	<1	1.46	1.18	1.21	<1	<1	1.26	<1
Nb	5	6	5	4	4	6	4	6	7	7	5	6	6	7	7
Hf	2.5	2.9	3.4	2.3	2.7	2.8	2.5	3.0	3.0	3.1	3.4	3.0	2.7	3.2	2.4
Zr	78	82	89	84	81	87	67	95	70	82	93	63	99	85	62
Y	12	11	16	12	15	11	16	16	14	12	13	13	13	11	10
Th	4.2	4.3	4.1	3.7	4.5	4.1	3.8	6.2	5.8	6.1	6.1	5.8	3.8	4.6	5.1
U	<2	2.7	<2	<2	<2	<2	<2	<2	<2	<2	<2	<2	<2	<2	<2
La	15.90	16.70	19.90	15.10	17.20	17.50	14.70	17.50	16.90	16.90	19.30	17.20	14.40	19.60	16.40
Ce	36.10	32.90	37.60	31.40	36.40	37.10	29.70	37.40	35.60	33.90	37.70	33.90	30.40	39.90	32.50
Nd	na	na	na	na	16.90	na	15.60	na	16.90	15.80	17.40	16.30	16.20	20.10	15.50
Sm	3.82	3.54	4.16	3.41	3.49	4.01	3.46	3.56	3.40	2.91	3.28	3.18	3.40	3.77	2.97
Eu	1.23	1.06	1.23	1.03	0.98	1.16	1.17	0.94	1.03	0.89	0.95	0.80	0.98	0.96	0.89
Tb	0.53	0.52	0.60	0.50	0.53	0.53	0.55	0.52	0.45	0.38	0.47	0.48	0.48	0.48	0.43
Ho	na	na	na	na	0.62	na	0.65	na	0.49	0.45	0.57	0.54	0.48	0.46	0.44
Yb	0.86	0.91	1.14	1.12	1.21	0.88	1.32	1.21	0.96	0.93	1.20	1.11	0.91	0.79	0.78
Lu	<0.20	<0.20	<0.20	<0.20	<0.20	<0.20	<0.20	<0.20	<0.20	<0.20	<0.20	<0.20	<0.20	<0.20	<0.20
Rb/Sr	0.07	0.10	0.11	0.10	0.08	0.07	0.17	0.43	0.07	0.13	0.11	0.05	0.56	0.16	0.17
Sr/Y	66.1	56.8	36.3	51.6	47.2	70.4	33.3	14.4	49.3	50.0	49.5	47.3	22.7	44.6	52.8
Zr/Nb	15.6	13.7	17.8	21.0	20.3	14.5	16.8	15.8	10.0	11.7	18.6	10.5	16.5	12.1	8.9
La_N/Yb_N	12.4	12.3	11.7	9.0	9.5	13.3	7.4	9.7	11.8	12.2	10.8	10.4	10.6	16.6	14.1

Table 1. cont.

Suite			Regalado Volcanic Units (M-L Mio)				Huambos Volcanics (L Mio)	
Locality	Minas Carpa	Yanacocha	North Cajamarca					W M Conga
Sample No.	S-M Carpa	S-CLL5	S-61	S-64	S-66	S-68	S-63	S-MC4
Rock Type	Hbl-Bt Diorite	Hbl-Bt Diorite	Hbl Bas Andesite	Hbl Bas Andesite	Hbl Bas Andesite	Hbl Bas Andesite	Hbl-Bt Andesite	Hbl-Bt Andesite
wt. %								
SiO_2	65.03	68.78	57.74	62.49	59.66	57.86	60.05	62.93
TiO_2	0.51	0.38	0.71	0.58	0.69	0.76	0.71	0.55
Al_2O_3	17.04	17.07	18.47	17.46	18.09	18.37	17.98	17.12
Fe_2O_3(T)	5.88	2.08	6.43	5.46	5.98	6.82	5.78	5.08
MnO	0.07	0.00	0.14	0.11	0.10	0.21	0.10	0.16
MgO	1.81	1.13	3.35	1.97	2.84	2.68	2.47	2.27
CaO	2.99	2.71	7.27	5.84	6.67	7.59	6.51	5.20
Na_2O	3.55	4.74	4.11	3.67	3.92	3.80	4.25	4.09
K_2O	2.89	2.92	1.52	2.17	1.77	1.63	1.88	2.38
P_2O_5	0.23	0.18	0.25	0.24	0.27	0.29	0.27	0.22
$Total_{(N)}$	100.00	100.00	100.00	100.00	100.00	100.00	100.00	100.00
LOI	4.06	1.18	1.18	3.95	1.58	2.55	1.21	2.72
ppm								
Cr	35	44	22	13	10	11	25	0
Ni	6	5	16	10	12	11	14	9
Co	22	26	23	20	19	18	19	21
Sc	8	5	17	13	13	13	10	9
V	87	68	132	102	120	129	123	101
Rb	87	83	33	64	46	42	47	70
Cs	3	<1	<1	<1	1	<1	2	<1
Ba	617	895	620	610	534	488	560	1973
Sr	433	805	838	660	718	759	820	594
Ga	20	20	21	19	22	21	22	20
Ta	<1	1.04	<1	<1	<1	<1	<1	<1
Nb	7	2	1	4	3	3	3	5
Hf	3.2	3.6	2.7	2.9	3.2	3.2	2.8	2.5
Zr	93	94	83	86	101	95	105	84
Y	14	7	18	20	15	14	16	12
Th	6.3	6.1	2.5	3.7	3.8	3.2	5.9	6.3
U	<2	<2	<2	<2	<2	<2	2.2	2.2
La	18.30	20.20	18.20	20.50	18.60	17.90	22.30	18.20
Ce	36.80	39.00	36.10	42.00	37.80	38.40	41.60	35.50
Nd	17.10	16.50	17.60	na	na	na	19.70	na
Sm	3.28	2.62	3.81	4.00	4.00	3.98	3.90	3.41
Eu	1.06	0.78	1.11	1.05	1.01	0.81	1.15	0.57
Tb	0.45	0.33	0.62	0.61	0.62	0.50	0.60	<0.50
Ho	0.52	0.35	0.77	na	na	na	0.74	na
Yb	1.12	0.62	1.65	1.23	1.37	1.29	1.56	0.99
Lu	<0.20	<0.20	0.21	<0.20	0.20	<0.20	0.22	<0.20
Rb/Sr	0.20	0.10	0.04	0.10	0.06	0.06	0.06	0.12
Sr/Y	30.9	115.0	46.6	33.0	47.9	54.2	51.3	49.5
Zr/Nb	13.3	47.0	83.0	21.5	33.7	31.7	35.0	16.8
La_N/Yb_N	10.9	21.8	7.4	11.1	9.1	9.3	9.6	12.3

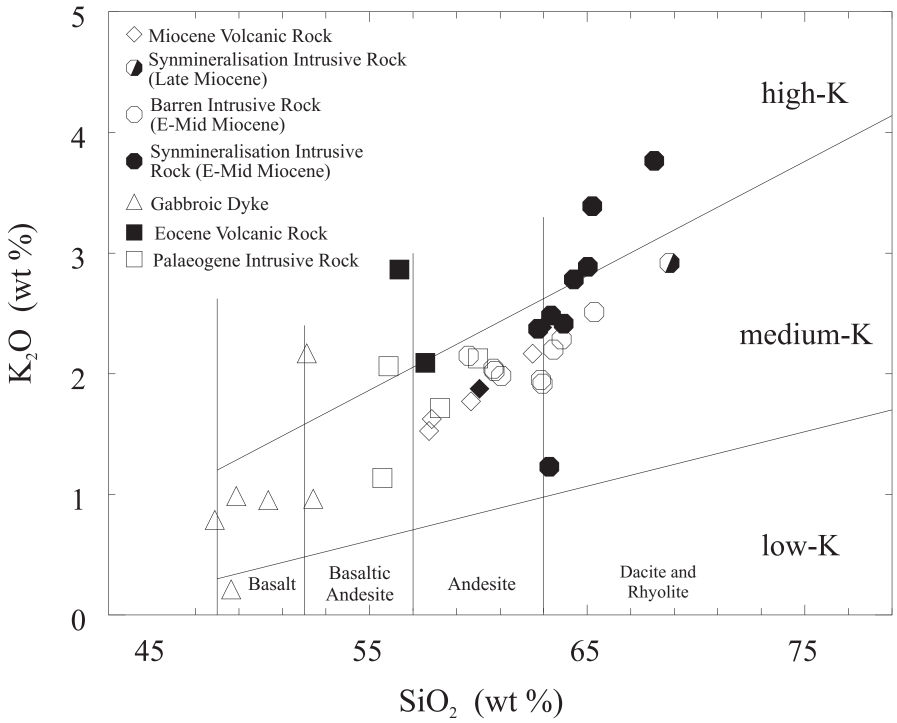

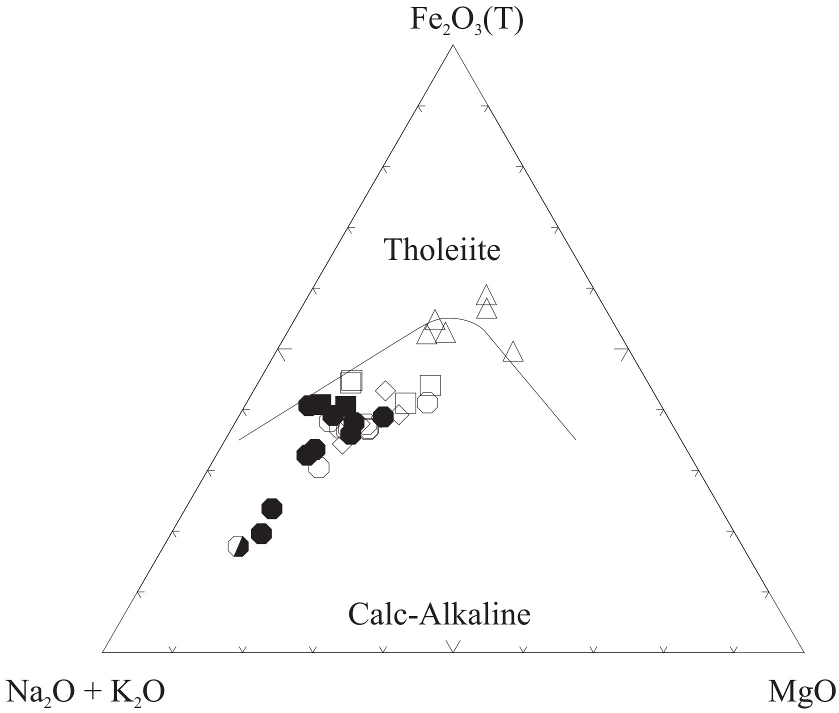

Fig. 6. K_2O vs. SiO_2 variation diagram for subalkaline rocks (Le Maitre *et al*., 1989). Tholeiite vs. calc-alkaline plot from Irvine and Baragar (1971).

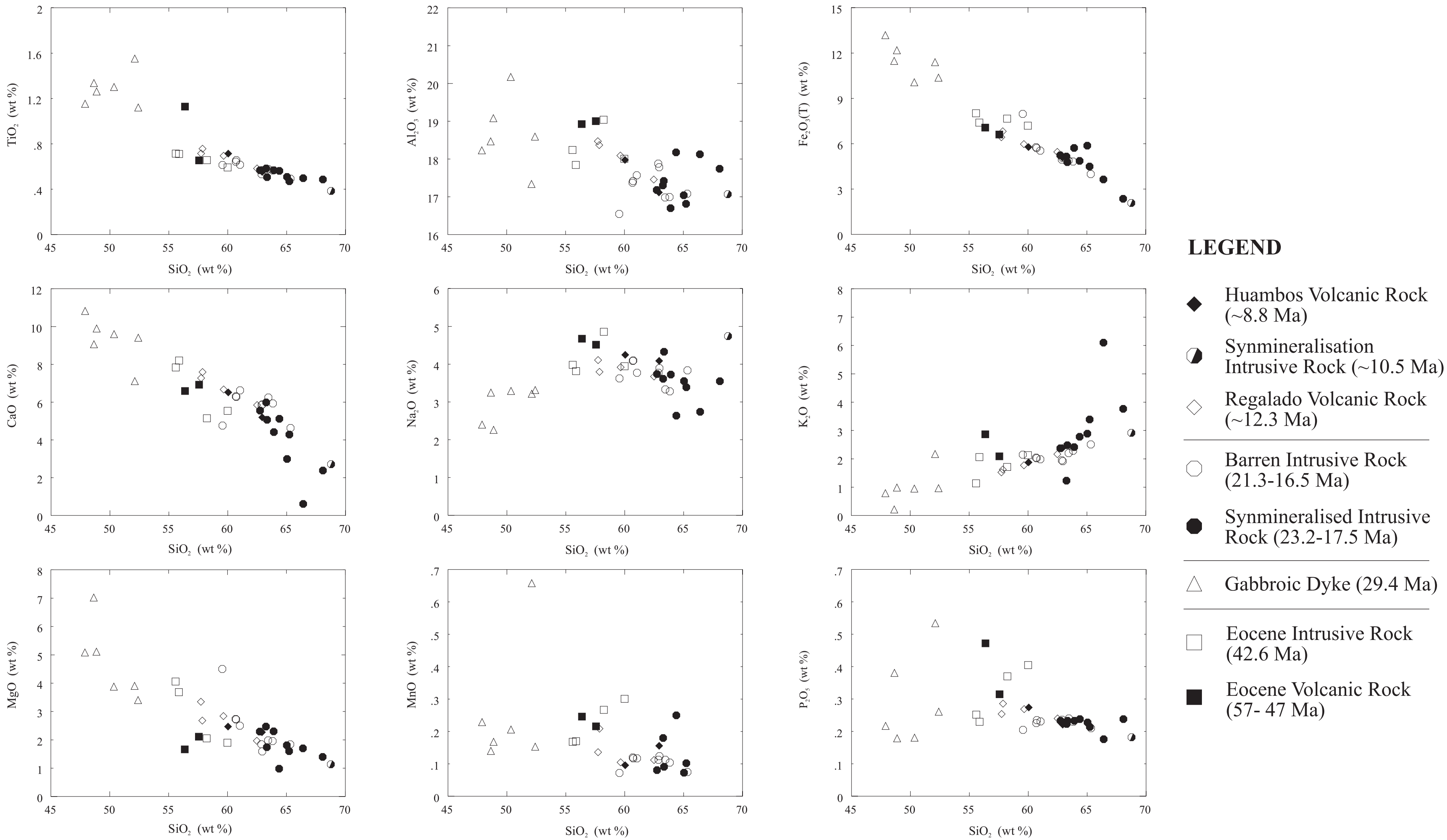

Fig. 7. Major element vs. SiO_2 variation diagrams for igneous rocks in the Cajamarca region.

and MgO against SiO_2 in all the igneous units are suggestive of fractionation of clinopyroxene, plagioclase, amphibole and titanomagnetite.

C.7 Trace Elements

The igneous units as a whole display an overall decrease in compatible elements Ni, Sc and V with increasing fractionation (as monitored by SiO_2; Fig. 8). One sample (S-T4) has anomalously high Cr and Ni contents (Table 1). Palaeogene felsic units display significantly steeper trends of decreasing Ni and Co than the other igneous suites. Large ion lithophile elements (LILE) Rb and Ba increase with fractionation in all igneous suites. High Rb content in sample S-T1 is due probably to alteration of plagioclase phenocrysts and an anomalously high Ba content is also evident in a late Miocene volcanic sample (S-MC4). Samples from mineralised centres are slightly depleted in Ba compared to coeval barren intrusive units, which possibly reflects Ba mobility during hydrothermal activity. Palaeogene felsic rocks display a slight increase in Sr content with fractionation compared to the Miocene units that show a steep decrease. A plot of Rb/Sr vs SiO_2 (Fig. 8) for all the igneous units displays moderate scatter but an overall increase in the Rb/Sr ratio associated with increasing silica content. Palaeogene felsic and Oligocene basic rocks display an overall increase in high field strength elements (HFSE) Nb, Hf and Zr with fractionation. Two samples (S-26 and S-32) display anomalously high HFSE values. Th and SiO_2 correlate negatively in the Palaeogene units. With the exception of the three samples from El Galeno, synmineralisation intrusions are typically enriched in Th compared with coeval barren intrusive units. Samples from El Galeno contain slightly lower Th than other samples from mineralised centres. La and SiO_2 show positive correlations in both the dykes and Palaeogene felsic rocks. However, the more evolved Miocene units display limited variation with increasing SiO_2. Heavy rare earth elements (HREE) and Y also display a positive correlation with increasing fractionation for the dykes and Palaeogene felsic units, but the Miocene units display a negative correlation. MORB normalised trace element diagrams dominantly show depletion in HFSE relative to LILE, as well as marked troughs for Nb, Ti and Rb (Fig. 9).

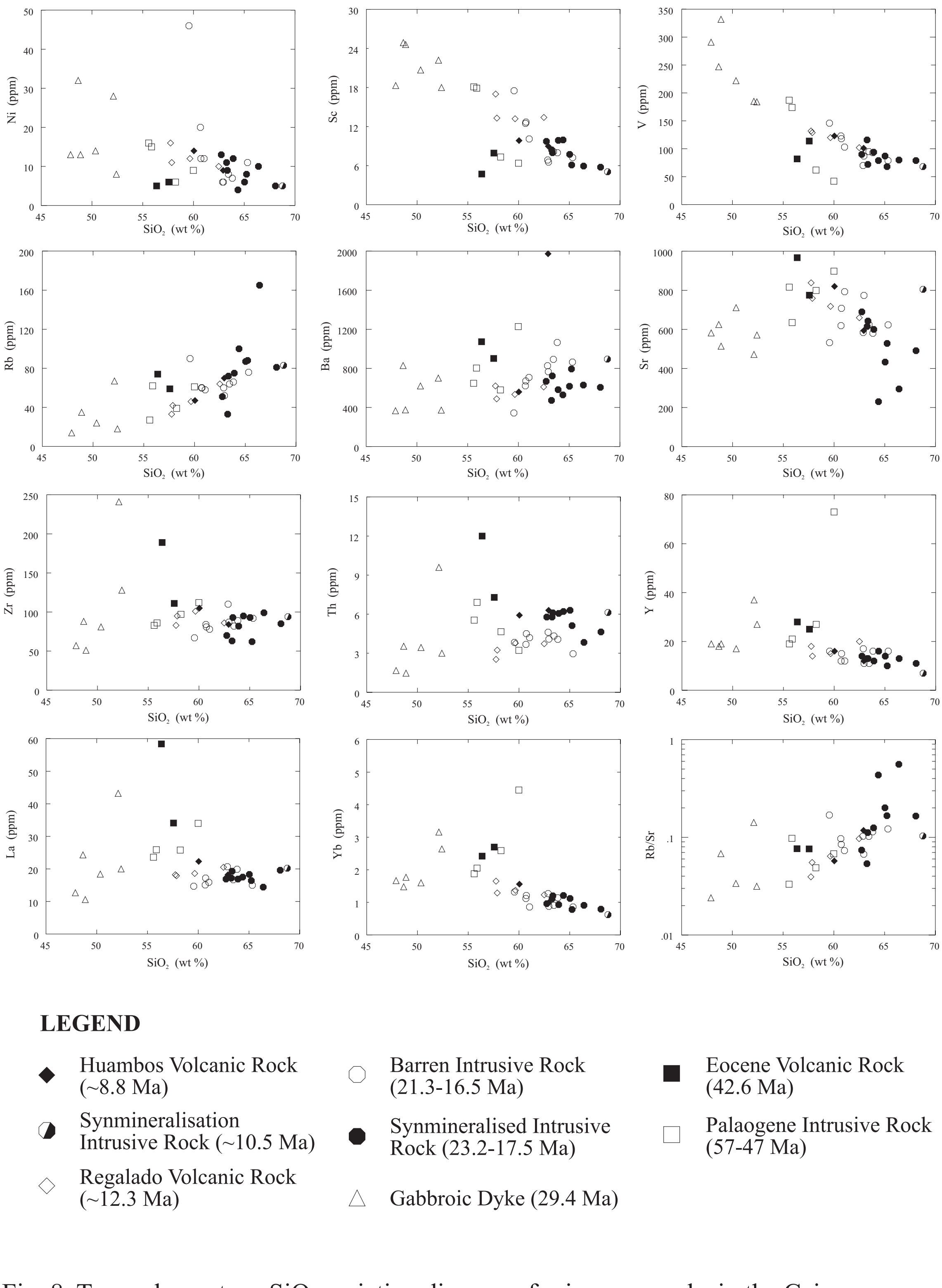

Fig. 8. Trace element vs. SiO_2 variation diagrams for igneous rocks in the Cajamarca region.

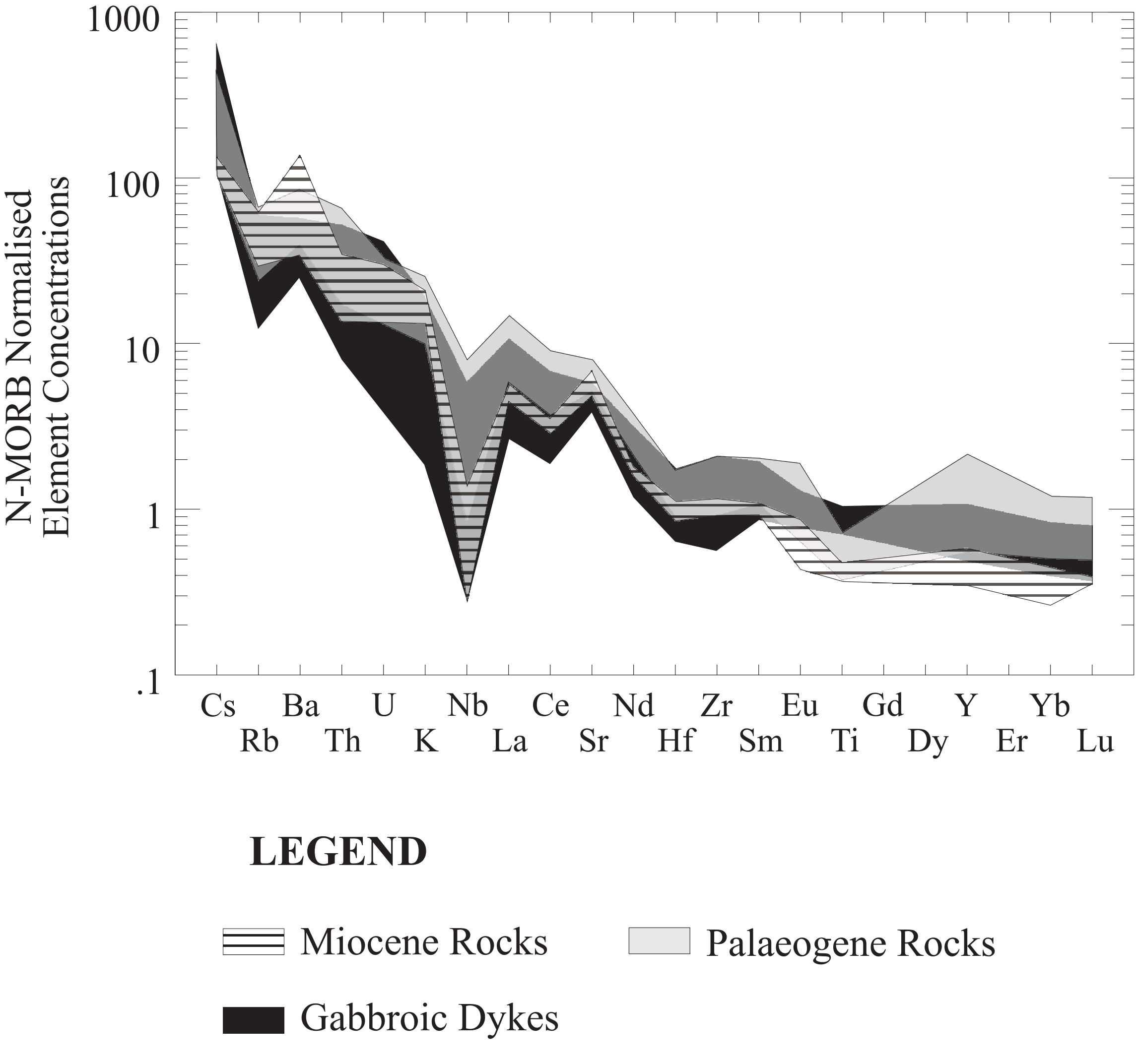

Fig. 9. N-MORB normalised incompatible trace element plots for the different rock suites. Normalising values from Sun and McDonough (1989).

C.8 Rare Earth Elements

All the igneous units display enrichment in LREE on chondrite-normalised plots (Fig. 10). The majority of samples lack an Eu anomaly, with only a few displaying weak negative Eu anomalies. A hornblende diorite dyke southeast of El Galeno (S-16) has the lowest LREE/HREE ratio, La_N/Yb_N, of 4.0, as well as the lowest total REE abundances. The Yanacocha intrusive porphyry sample has the highest La_N/Yb_N ratio at 21.8, but a sample from the Llama-Calipuy Volcanic Sequences (S-32) has the highest total REE abundances.

Gabbroic dykes sampled from the region have the flattest REE profiles (Fig. 10) with La_N/Yb_N between 4.0 and 11.0, at an average of 7.0 (Table 2). The dykes have a wide range in REE abundances and show a decrease in total REE with fractionation. Decreased La_N/Yb_N also accompanies the decrease in total REE from gabbro to hornblende diorite units. The two basic intrusive units with hornblende phenocrysts lack depletion in the middle to heavy REE.

Palaeogene felsic rocks have the highest REE abundances of all the igneous rocks. Increased REE abundances are associated with higher SiO_2 content. Palaeogene felsic units have La_N/Yb_N ranging from 5.1 to 16.1 with an average of 8.9. The intrusive samples from the Cerro Montana region have relatively flat patterns compared to the other Palaeogene samples (Fig. 10). An Eocene volcanic unit (S-21) from the Lower Llama Volcanic Formation displays a moderate depletion in the MREE to HREE compared to the other Palaeogene units.

Barren Miocene intrusive rocks display linear and steep REE profiles. They have a range in the La_N/Yb_N ratio from 7.4 to 13.3, at an average of 10.9, and show limited variation in both LREE and HREE content (Fig. 10). Synmineralisation intrusions tend to display even steeper REE trends and a slight depletion in Sm. These intrusive units have a La_N/Yb_N from 9.7 to 21.8, with the highest average of 12.9. The Yanacocha porphyry was the youngest intrusive unit sampled and has the highest La_N/Yb_N ratio (Table 2). REE profiles of samples from Miocene mineralised systems also display moderate variation in HREE content compared to the uniform LREE content. Late Miocene volcanic units display similar trends to the Miocene intrusions and have a

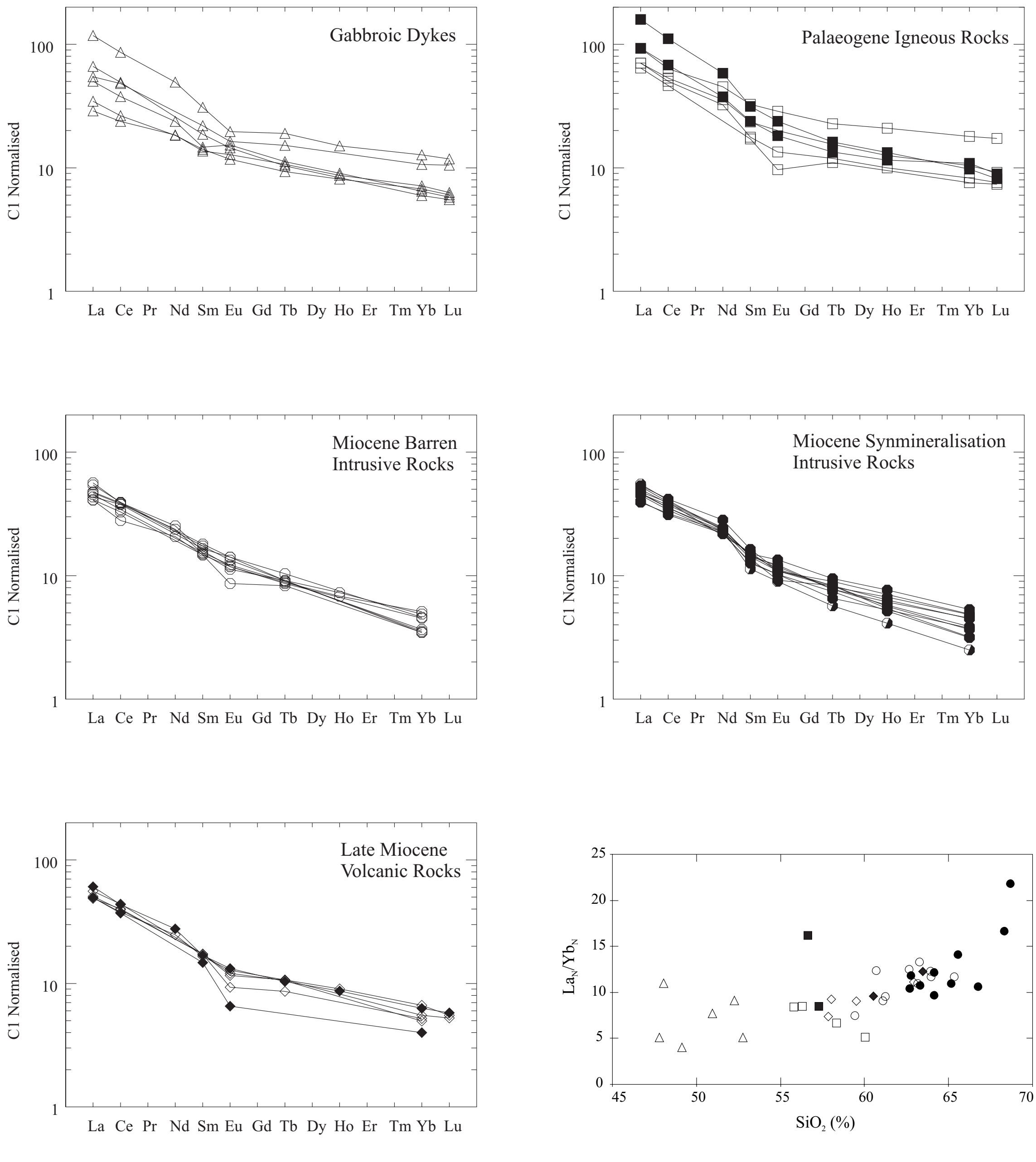

Fig. 10. Chondrite normalised REE profiles and La_N/Yb_N vs. SiO_2 plot for igneous suites in the Cajamarca region. Chondrite normalised values from Taylor and McLennan (1985).

Table 2. La_N/Yb_N ratios of igneous suites in the Cajamarca region. Chondritic values of Taylor and McLennan (1985).

Suites	**La_N/Yb_N Ratio**		
	Minimum	**Maximum**	**Average**
Suite 1 - Gabbroic Dykes	4.0	11.0	7.0
Suite 2 - Palaeogene Igneous Units	5.1	16.1	8.9
Suite 3a - Miocene Intrusive Units			
- *Barren Stocks*	7.4	13.3	10.9
- *Synmineralisation Stocks*	9.7	21.8	12.9
Suite 3b - Miocene Volcanic Units	7.4	12.3	9.8

La_N/Yb_N from 7.4 to 12.3, with an average of 9.8. Total REE for both the Regalado and Huambos formations decrease with increasing fractionation. The late Miocene volcanic samples display a slight Sm depletion and two samples (S-MC4 and S-68) also display negative Eu anomalies.

C.9 Rb-Sr and Sm-Nd Isotope Compositions

Sr and Nd isotopic compositions of selected magmatic rocks were also conducted during the study. However, several of the magmatic rocks were altered by later hydrothermal fluids. Hydrothermal fluids exsolved from a magma chamber may contain different isotopic compositions to the host intrusion (Skewes and Stern, 1996). Such variations may result from hydrothermal fluids interacting with wall rock during ascent from the magma chamber, or alternatively hydrothermal fluids may have been released from a compositionally different magma chamber. A pilot study including two samples was performed to detect any disturbances to the Sr and Nd isotopic system that resulted from the fluxing of hydrothermal fluids through the host intrusive rock. A moderately to strongly altered gabbroic dyke (S-16) and a weakly altered quartz diorite (S-59) were chosen based on degree of alteration and known age. These samples were analysed both as bulk whole rock powders and leached residual material. Leached samples were washed with hot 6M HCl prior to analysis to remove secondary carbonate material. The residual leached material is inferred to represent the original isotopic composition of the intrusive rock before hydrothermal fluxing. The results show a large amount of REE material was removed from the altered dyke (S-16) during the leaching process (Table 3). For the dyke, $^{143}Nd/^{144}Nd$ and $^{143}Sm/^{144}Nd$ ratios for the residual material are higher than the bulk powders. In contrast, the same isotopic ratios for the quartz diorite bulk powder are higher than the residual material. However, the difference in $^{143}Nd/^{144}Nd$ for both the bulk powder and residual material is minimal. Sr isotopic ratios are lower in both samples for the residual material than the bulk powder. These results suggest primary Sr, Rb and REE located along lattice edges of accessory minerals may have been removed during the leaching process, or, alternatively the majority of the REE are located in the secondary carbonate material. The large amounts of REE removed from the altered dyke suggest the latter. This indicated hydrothermal fluids have probably perturbed the original isotopic ratio for the intrusive rocks. Based

Table 3. Results from radiogenic Sr and Nd isotope analyses.

Sample no.	Sm ppm	Nd ppm	Rb ppm	Sr ppm	$(^{147}Sm/^{144}Nd)_m$	$(^{143}Nd/^{144}Nd)_m$	$\varepsilon_{Nd(0)}$	Age (Ma)	TDM (Ga)	$(^{87}Rb/^{86}Sr)_m$	$(^{87}Sr/^{86}Sr)_m$	$(^{87}Sr/^{86}Sr)_i$	Bulk weight (g)	Residue weight (g)
Palaeocene-Eocene Intrusive & Volcanic Rocks														
S-46 (Intr)	3.29	14.43	56.2	699	0.1361	0.512779	2.76	57.0	0.731	0.233	0.70422	0.70403	0.0408	0.0216
S-31 (Intr)	4.51	21.07	58.1	1246	0.1294	0.512781	2.79	47.0	0.670	0.135	0.70556	0.70547	0.0411	0.0197
S-32 (Volc)	2.95	14.89	82.5	925	0.1197	0.512814	3.44	43(?)	0.547	0.258	0.70399	0.70383	0.0414	0.0200
S-21 (Volc)	2.38	12.17	67.6	938	0.1180	0.512803	3.22	42.6	0.556	0.209	0.70483	0.70470	0.0431	0.0214
Oligocene Gabbroic Dykes														
S-16	1.12	3.74	23.4	322	0.1812	0.512751	2.20	29.4	1.870	0.211	0.70465	0.70455	0.0316	0.0212
S-57	2.54	11.24	29.9	516	0.1364	0.512742	2.03	29.4	0.808	0.168	0.70436	0.70428	0.0409	0.0186
Barren Miocene Intrusions														
S-11	1.42	5.98	59.8	559	0.1436	0.512691	1.04	21.3	1.000	0.310	0.70482	0.70473	0.0403	0.0342
S-59	1.75	8.89	62.4	392	0.1189	0.512695	1.10	20.6	0.740	0.461	0.70458	0.70445	0.0351	0.0299
S-38	1.06	6.01	80.1	784	0.1061	0.512728	1.76	17.9	0.600	0.296	0.70463	0.70456	0.0404	0.0238
S-T4	2.89	13.87	56.8	586	0.1261	0.512770	2.57	16.5	0.665	0.281	0.70478	0.70471	0.0422	0.0209
Synmineralised Early-Mid Miocene Intrusions														
S-Chail	1.21	5.65	54.9	693	0.1291	0.512715	1.50	23.2	0.787	0.229	0.70472	0.70464	0.0419	0.0303
S-H22 (176)	2.37	11.87	42.8	672	0.1205	0.512791	2.98	19.8	0.591	0.184	0.70429	0.70424	0.0431	0.0316
S-T2	0.44	2.87	53.4	530	0.0916	0.512684	0.89	17.5	0.585	0.291	0.70508	0.70501	0.0419	0.0345
Miocene Volcanic Rock														
S-MC4	1.79	8.90	75.1	632	0.1212	0.512728	1.75	9(?)	0.699	0.344	0.70472	0.70468	0.0408	0.0319
Mineralised Late Miocene Intrusion														
S-CLL5	0.92	7.60	84.4	881	0.0728	0.512667	0.56	10.0	0.525	0.278	0.70500	0.70496	0.0429	0.0357
S-11 (repeat)			64.8	622						0.302	0.70476		0.0400	0.0316
Pilot Study														
S-16 bulk	3.16	13.41	31.8	510	0.1426	0.512708	1.37		0.950	0.181	0.70474		0.0191	na
S-16 res-HCl	1.12	3.74	23.4	322	0.1812	0.512751	2.20		1.870	0.211	0.70465		0.0316	0.0212
S-59 bulk	3.32	15.87	57.4	1288	0.1264	0.512729	1.80		0.740	0.129	0.70512		0.0224	na
S-59 res-HCl	1.75	8.89	62.4	392	0.1189	0.512695	1.10		0.740	0.461	0.70458		0.0351	0.0299

all $^{143}Nd/^{144}Nd$ are relative to La Jolla-Nd = 0.511860; all $^{87}Sr/^{86}Sr$ are relative to SRM987-Sr = 0.71024

$\varepsilon_{Nd(0)}$ calculated for present-day CHUR = 0.512638

m = measured; *i* = initial; TDM - Depleted Mantle Age; na = not analysed

Bulk weight - weight of whole rock powder; Residual weight - weight of residual material after leaching on these results, the remaining 13 samples analysed were leached in hot 6M HCl to remove any secondary material that may have resulted in a bias related to hydrothermal fluxing of the host intrusive rock. This was considered to deliver the most accurate determination for the original primary isotopic ratio.

Igneous rocks from the Cajamarca district display a broad array of both initial $^{87}Sr/^{86}Sr$ (Sr_i) values that range between 0.7038 and 0.7055, and epsilon Nd [$\varepsilon_{Nd(0)}$] that range from +3.44 to +0.56 (Table 3, Fig. 11). The samples display an overall change from high $\varepsilon_{Nd(0)}$ and low Sr_i, through to high Sr_i and low ε_{Nd}. The Palaeogene magmas have higher $\varepsilon_{Nd(0)}$ values (+3.44 to +2.76) and a larger range of Sr_i (0.7038-0.7055) than the younger Miocene igneous units. The Cerro Montana sample (S-31) has anomalously high Sr_i but similar $\varepsilon_{Nd(0)}$ values to the other Palaeogene units. The gabbroic dykes have Sr_i ranging from 0.7043 to 0.7046 and lower $\varepsilon_{Nd(0)}$ values than the Palaeogene felsic rocks. Barren intrusive units have Sr_i between 0.7045 and 0.7047, with $\varepsilon_{Nd(0)}$ values that increase with age from +2.57 to +1.04. The mineralised centres have large $\varepsilon_{Nd(0)}$ and Sr_i ranges ($\varepsilon_{Nd(0)}$ = +2.98 to +0.56; Sr_i = 0.7043-0.7050), which overlap with coeval barren intrusions. However, the isotopic compositions of a synmineralisation stock from Michiquillay ($\varepsilon_{Nd(0)}$ = +2.98; Sr_i = 0.7042) and a post-mineralisation magmatic breccia at El Galeno ($\varepsilon_{Nd(0)}$ = +2.57; Sr_i = 0.7047) are considerably more primitive with more radiogenic Nd than intrusive units of similar or slightly older age. The late Miocene volcanic rock has $\varepsilon_{Nd(0)}$ of +1.75 and Sr_i of 0.70468.

Sr_i for the gabbroic units decreases with increasing silica, whereas the Palaeogene felsic rocks show a steep positive trend. The Miocene igneous units display a slight increase in Sr_i with fractionation. A plot of $\varepsilon_{Nd(0)}$ vs. SiO_2 shows a negative correlation between $\varepsilon_{Nd(0)}$ and increasing SiO_2 content for all of the igneous units. Sr_i vs. age displays an overall increase in Sr_i with time. In contrast, $\varepsilon_{Nd(0)}$ vs. age illustrates a general decrease in radiogenic Nd with time. However, the two Miocene intrusions with primitive compositions (S-H22 and S-T4) contain elevated Nd values compared to coeval intrusions.

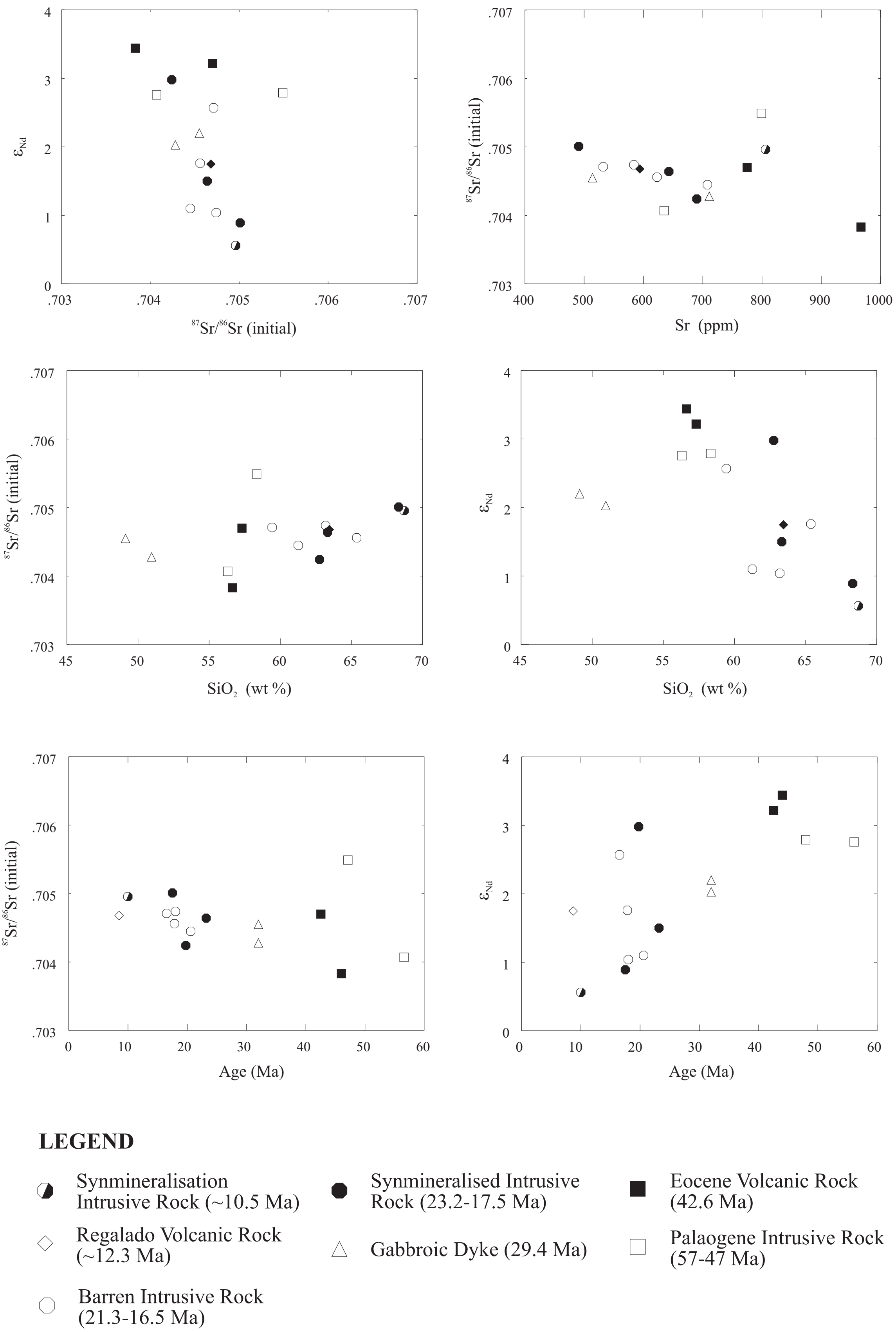

Fig. 11. Radiogenic isotope plots for selected igneous rocks from the Cajamarca region.

C.10 Petrogenetic Modelling of the Cajamarca Igneous Units

C.10.1 REE Partial Melting Models

Chondrite-normalised REE profiles of igneous units from a range of magmatic compositions have previously been modelled using partial melting, fractional crystallisation and assimilation-fractional crystallisation calculations (e.g. Petford and Atherton, 1996; Lang and Titley, 1998; Caffe *et al*., 2002). Macfarlane (1999) documented the isotopic homogeneity of Miocene igneous rocks from the Hualgayoc region and concluded the magmas represent upper sub-Andean mantle or lower sub-Andean crust melts that assimilated limited shallow crust material. Macfarlane (1999) suggested the rocks were isotopically homogenised prior to emplacement. Igneous rocks that have undergone minimal upper crustal contamination closely represent the geochemistry of their source regions. Most Miocene igneous rocks from the Cajamarca are compositionally similar to units from the Hualgayoc region (Fig. 5 in Macfarlane, 1999) and are also inferred to have undergone minimal contamination. Therefore, these rocks can be used to model source regions and possible subsequent fractional crystallisation processes. An attempt has been made to model some rocks from the Cajamarca region that are inferred to best represent unaltered and uncontaminated (low Sr_i) magmas for each of the igneous suites.

Trace element modelling presented in this paper involves two main stages, namely: (1) modelling the generation of a parent melt by partial melting of a mafic mantle source, and (2) modelling subsequent batch melting of the parent melt modelled in stage 1. Wood and Fraser (1976) defined batch melting as “continuous re-equilibration of melt with residual solid phases throughout partial melting until removal of melt”. Modal mantle- and batch-melting calculations of REE, Rb, Sr, Zr and Y have been modelled for selected magmatic units. Magmatic units were chosen based on age, suite type and observed geochemistry. Batch melting models were calculated using the equation of Shaw (1970):

$$C_m = C_i / [K_D + F_m * (1-K_D)]$$

Where C_m is the trace element concentration in the partial melt, C_i is the initial trace element concentration in the source, K_D is the bulk partition coefficient and F_m is the melt fraction. No studies to date have produced a set of internally consistent partition coefficients for all minerals coexisting with a single melt. Therefore, partition coefficients used for this study (Appendix C3) were adopted from Martin (1987), who modelled partial melting of tholeiitic basalt for the generation of tonalites and granodiorites.

Stage 1 – Generation of a primitive/parent mafic melt

For modelling of a parental melt, an Oligocene hornblende gabbro (S-16) that has the lowest concentrations of SiO_2, Rb and total REE abundances, as well as a relatively low La_N/Yb_N ratio (~4) has been used to represent a primitive/parent composition for magmas found in the Cajamarca region. Primitive mantle values from McDonough *et al*. (1992) have been used to represent the source composition.

Modal mantle-melting calculations indicate a melt of similar composition to the sample S-16 can be modelled by between 4 to 7% partial melting of a primitive mantle source (Table 4; Fig. 12). The modelled residue was dominated by >50% olivine, with subordinate amounts of orthopyroxene, clinopyroxene, amphibole and garnet. Whilst the deduced REE values are consistent with analytical values, the modelled LIL and Zr contents are significantly lower than the analytical results. Elevated concentrations of LIL might occur in gabbroic differentiates derived from a feldspar depleted upper mantle-lower crust due to their compatibility with feldspar.

Stage 2 – Generation of felsic melts

The primitive melt generated in stage 1 is now used as the source to model Palaeogene and Miocene melts.

Palaeogene Magmatism

Palaeogene intrusive and volcanic rocks have high REE abundances and flat REE profiles. Sample S-46 is a microdiorite with a low Sr_i that suggests minimal crustal

Table 4. Table showing whole rock geochemistry against modelled partial melt compositions.

	Mantle Melting		**Batch Melting Models**									
Suite	**Oligocene Dyke**		**Paleocene Intrusion**		**Early-Mid Miocene Intrusions**				**Miocene Volcanic Rock**		**Late Miocene Intrusion**	
Elements	**Sample 16**		**Sample 46**		**Sample Chail**		**Sample 59**		**Sample 61**		**Yanacocha**	
	Analytical Results	5% Melt	**Analytical Results**	40% Melt	**Analytical Results**	50% Melt	**Analytical Results**	55% Melt	**Analytical Results**	50% Melt	**Analytical Results**	45% Melt
Rb	35	9	62	60	72	55	60	56	33	60	83	67
Sr	514	229	635	633	643	645	708	705	838	734	805	881
Zr	51	31	86	90	93	76	81	71	83	75	94	75
Y	19	20	21	28	13	14	15	15	18	20	7	8
La	10.60	10.31	25.90	23.85	19.30	19.05	17.20	17.33	18.20	18.65	20.20	20.13
Ce	22.70	23.84	48.00	47.94	37.70	37.79	36.40	34.77	36.10	36.93	39.00	39.51
Nd	13.10	11.90	23.00	23.64	17.40	17.01	16.90	16.57	17.60	17.12	16.50	17.32
Sm	3.15	3.22	4.09	5.00	3.28	3.49	3.49	3.47	3.81	3.57	2.62	3.33
Eu	1.11	1.07	1.17	1.18	0.95	0.99	0.98	1.11	1.11	1.12	0.78	1.11
Tb	0.62	0.55	0.69	0.80	0.47	0.48	0.53	0.50	0.62	0.56	0.33	0.34
Yb	1.77	1.71	2.05	2.08	1.20	1.20	1.21	1.21	1.65	1.62	0.62	0.59
Lu	0.24	0.24	0.29	0.29	-0.20	0.17	-0.20	0.17	0.21	0.23	-0.20	0.08
La_N/Yb_N	4.05	4.07	8.45	7.67	10.75	10.61	9.51	9.59	7.38	7.72	21.79	22.68
Modelled Residual Mineralogy												
Olivine		55		15		-		-		-		-
Orthopyroxene		23		20		-		-		-		-
Clinopyroxene		15		42		36		50		55		30
Garnet		3		1.5		4		5		1		17
Amphibole		4		10		50		40		38		50
K-Feldspar		-		11		7		3		3		-
Ilmenite		-		-		2		1		2		2
Magnetite		-		-		1		1		1		1

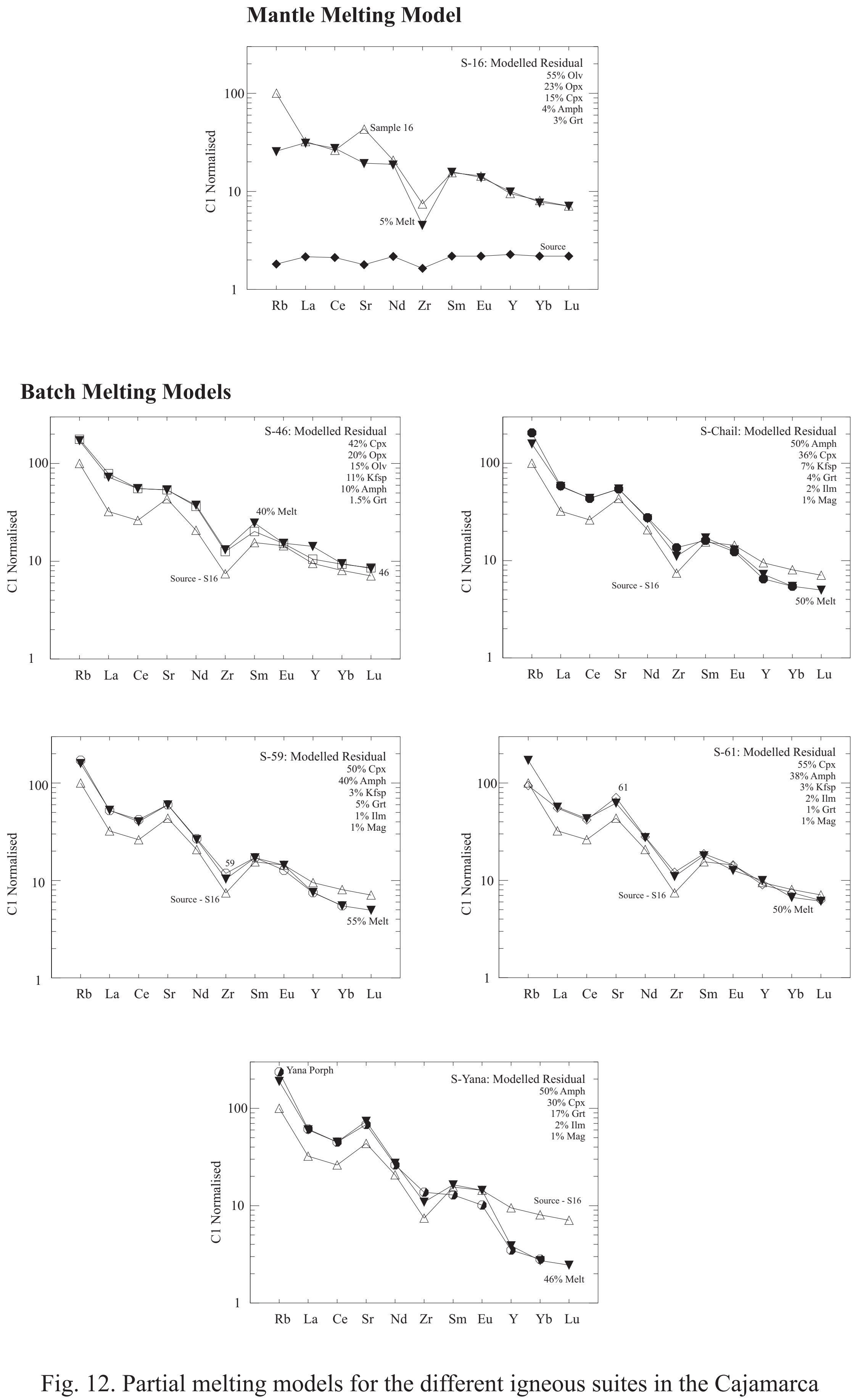

Fig. 12. Partial melting models for the different igneous suites in the Cajamarca region of northern Peru. Partition coefficient values are from Martin (1987).

contamination. This intrusion is the oldest igneous rock dated in the region at 57 Ma and is interpreted to be the most primitive and least contaminated of the Palaeogene felsic rocks. This sample is therefore used as the baseline melt composition for Palaeogene magmatic activity.

Batch-melting calculations for sample S-46 produced a dry residue composed of pyroxene, olivine, K-feldspar, minor amphibole and possibly garnet (Table 4, Fig. 12). Partial melting calculations suggest melt compositions related to development of Palaeogene magmatic units were strongly influenced by the presence of clinopyroxene compared to the olivine-dominated residue for the gabbroic dykes. Alternatively, Palaeogene units may have been derived from a different parental material or source region.

Early-Middle Miocene Magmatism

Early to middle Miocene intrusive units are predominantly diorites to quartz diorites that have moderately steep REE patterns. Barren and mineralised Miocene intrusions are both modelled. The oldest Miocene intrusion is a synmineralisation hornblende-biotite diorite (Chail) from the Minas Conga prospect at 23.2 Ma (Llosa *et al*., 1996). The barren Miocene intrusion (S-59) is slightly younger at 20.6 Ma (Section A) and can be modelled by high degrees of partial melting (~55% melt) with residues dominated by clinopyroxene, amphibole, plus minor garnet and K-feldspar (Table 4, Fig. 12). Modelled residue for the synmineralisation intrusion (Chail) has more amphibole and K-feldspar, but less clinopyroxene and garnet.

Late Miocene Magmatism

Miocene volcanic rocks show a wide range in SiO_2 and display flat to moderately steep REE patterns. This change from flat to steep trends is also accompanied by a progressive change in the modal mineralogy that probably reflects fractional crystallisation in shallow level magma chambers. Regalado volcanic rocks, of late Miocene age (12 Ma, Turner, 1997), can be modelled from a garnet-poor residue containing amphibole, clinopyroxene and K-feldspar (Table 4, Fig. 12). This modelled residual is very similar to that modelled for the early to middle Miocene intrusions.

The Yanacocha porphyritic intrusion (~10 Ma) has the steepest REE pattern of all the igneous units sampled in the region. It has strong depletion in HREE and can be modelled by ~45% melting of the parent mafic material. The modelled residue consists dominantly of amphibole with subordinate garnet, clinopyroxene and K-feldspar (Table 4). The modelled REE profile also displays a positive Eu anomaly in contrast with the observed REE pattern. The difference in Eu content between the modelled and observed trend may be explained through shallow-level fractionation of plagioclase. Similar changes in Eu anomalies have been observed and modelled at numerous porphyry copper complexes, such as Santa Rosa, Peru (Le Bel, 1985), Wushan, China (Zhitian and Kezhang, 1989), as well as in the Ray and Christmas Districts, Arizona (Lang and Titley, 1998). This model requires significantly higher residual garnet compared to the Miocene volcanic rocks suggesting a rapid change in the physical conditions of the source region, different source regions or that the rocks are of different age.

C.10.2 Sm vs. Th Bivariate Plot

Fractionation Trends

A Sm vs. Th log-log bivariate plot has been used to determine variations in trace element partitioning for the different igneous rock units sampled in the Cajamarca region. Th is highly incompatible throughout differentiation and generally immobile during hydrothermal processes (Kerrich and Wyman, 1997). Therefore, Th will be used as a fractionation index. Sm has a higher K_D value for amphibole/liquid compared with pyroxene/liquid thus highlighting differences between hydrous and anhydrous crystallisation assemblages (Aldanmaz *et al*., 2000). The Sm K_D value for amphibole increases with increasing fractionation (from basic to acidic melt compositions), thereby further highlighting magma compositions controlled by the fractionation of amphibole. Sm and Th K_D values for andesitic melt compositions have been adapted from Gill (1981), Green and Pearson (1985), and Nash and Creecraft (1985) to generate theoretical Rayleigh vectors (Appendix C4).

Samples of varying ages plot along different trends on a log Sm vs. log Th plot of igneous rocks from the Cajamarca region (Fig. 13). Gabbroic dykes display a linear

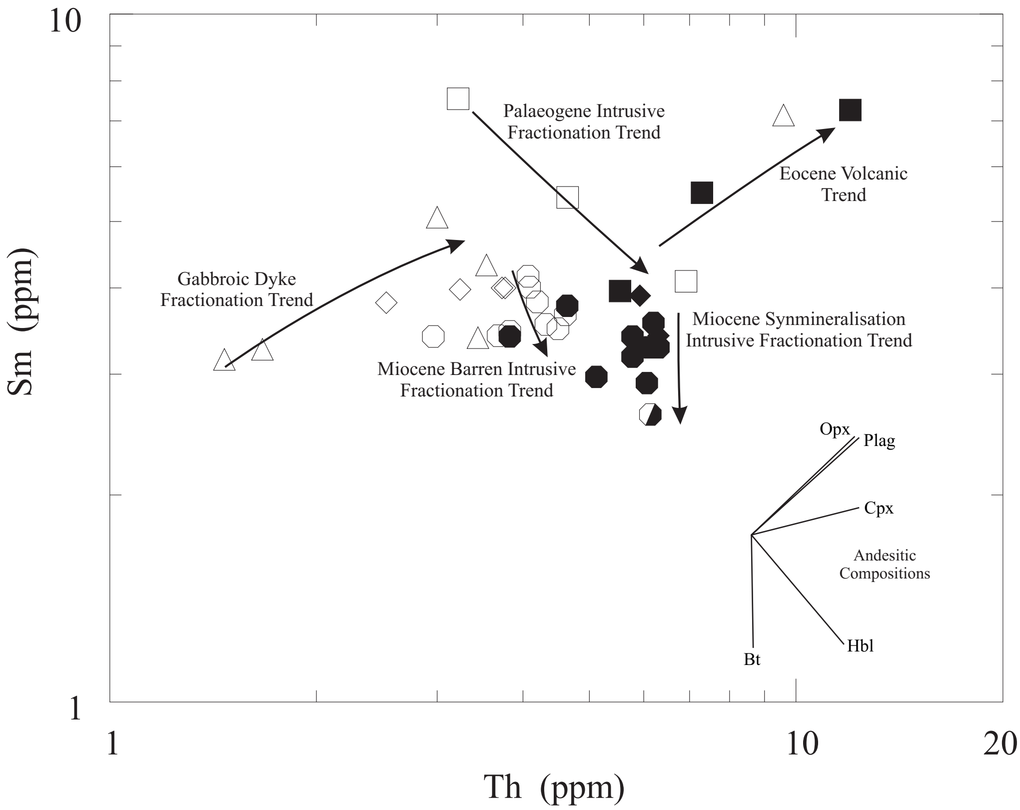

Fig. 13. Log Th vs. log Sm diagram showing theoretical Rayleigh vectors modelled for fractional crystallisation trends of an andestic melt. Partition coefficients for the fractionation model are from Gill (1981), Sm in hornblende from Green and Pearson (1985) and biotite for acidic magmas from Nash and Creecraft (1985).

increase in Sm with Th. Theoretical Rayleigh vectors suggest the compositions of these rocks were dominantly controlled by the fractionation of anhydrous minerals, such as plagioclase, orthopyroxene and clinopyroxene. Palaeocene-Eocene intrusive samples decrease in Sm with increasing Th. Significantly, Th decreases with increasing SiO_2 for these samples (Fig. 8) possibly suggesting Th saturation. Therefore, inferred hornblende fractionation from the theoretical vector trend is not applicable. In contrast, Sm and Th in Eocene volcanic samples display a positive correlation, suggesting an anhydrous mineral-dominated fractionation trend.

Miocene intrusive rocks show a general decrease in Sm with increasing Th. The barren Miocene intrusions display similar but slightly steeper trend than the Palaeocene intrusions indicating strong hornblende and minor biotite fractionation. Synmineralisation samples show minimal variation in Th with decreasing Sm. Theoretical Rayleigh vectors combined with petrographic evidence indicate melt compositions of Miocene synmineralisation stocks were strongly influenced by biotite and minor hornblende fractionation. In contrast, Miocene volcanic rocks tend to display a flat trend with minimal variation of Sm content with increasing Th. This suggests melt composition for the Miocene volcanic sequences was controlled by the fractionation of both hydrous and anhydrous minerals.

C.11 Discussion

C.11.1 Geochemistry of the Cajamarca Igneous Rocks

Petrographic and geochemical features have been used to characterise three igneous suites in the Cajamarca region; these include (1) gabbroic dykes, (2) Palaeogene felsic and (3) Miocene igneous rocks. All three suites are depleted in HFSE relative to LILE and LREE, a characteristic of subduction-related magmas that is considered to result from metasomatism of the source by LILE-rich hydrous fluids or a residual HFSE-bearing phase such as Ti-phases or amphibole (Pearce, 1983; Hawkesworth *et al*., 1993; Thirlwall *et al*., 1994).

The gabbroic dykes are tholeiitic with compositional trends that suggest clinopyroxene and possibly olivine fractionation. The dykes display primitive arc characteristics with increasing Zr, Y, REE content with increasing SiO_2 (Pearce and Norry, 1979). With the exception of two samples that contain hornblende phenocrysts, most gabbroic dykes contain anhydrous mineral assemblages. At shallow depths outside the stability field of amphibole, fractionation of basaltic melts will be dominantly controlled by anhydrous mineral assemblages (e.g. plagioclase, orthopyroxene, clinopyroxene and magnetite) and follow tholeiitic lines of descent (Wilson, 1989). Palaeogene felsic units display similar major and trace element trends to the gabbroic dykes. Palaeogene rocks increase in Al_2O_3, MnO, P_2O_5, Zr, Y and REE contents with fractionation. These trends suggest Zr and P were incompatible. Palaeogene units also display a decrease in Th content with increasing SiO_2. Trace element models suggest anhydrous and possibly hydrous mineral fractionation occurred. In comparison, Miocene igneous units display negative correlations between Na_2O, P_2O_5, Sr and LREE with SiO_2. Samples from mineralised Miocene intrusive complexes are enriched in K_2O and Th, and depleted in Ba, compared to barren intrusive units of similar age. The mobility of K_2O and Ba during hydrothermal alteration (Kerrich and Wyman, 1997) possibly explains variations of these elements. Miocene volcanic rocks display similar trends to the Miocene intrusions but some rocks have negative Eu anomalies. Major and trace (including rare earth) element data of Miocene igneous rocks suggest both hydrous and anhydrous mineral fractionation. These fractionation processes took place outside the stability field of plagioclase for all of the Miocene intrusive and most of the volcanic rocks.

C.11.2 Source Interpretation

Petrogenetic models for arc magmas developed prior to intensive crustal thickening suggest olivine-pyroxene-oxide mineral phases controlled fractionation near the base of the crust (Atherton *et al.*, 1985; Hildreth and Moorbath, 1988). Rare earth element partial melt modelling suggests Palaeogene melts equilibrated with anhydrous mineral phases (i.e. pyroxene and olivine) and an amphibole- and garnet-poor residue. Palaeogene felsic and Oligocene mafic igneous rocks from the Cajamarca region display a large variation in Sr_i (0.7038-0.7055) across a narrow silica and ε_{Nd} range. Th displays a steep negative correlation with increasing SiO2 possibly suggesting Th saturation or upper crustal contamination (Richards and Villeneuve, 2002). Isotope compositions suggest a low radiogenic Nd - high radiogenic Sr, possibly such as seawater or upper crustal, contaminated the source region of some Palaeogene magmas. Radiogenic isotope ratios and partial melting models suggest these melts were derived from a young magmatic arc environment in which the base of the crust was shallower than at present, and dominated by olivine and pyroxene mineral residues.

Atherton *et al*. (1985) concluded that the Eocene Calipuy volcanic rocks in northern Peru were derived from partial melting of garnet-free peridotite mantle and underwent later fractionation of anhydrous minerals. Trace element models of Palaeogene magmas indicate anhydrous mineral assemblages (plagioclase and pyroxene) controlled fractionation of the volcanic melts, whereas intrusive melts follow hornblende fractionation trends. This suggests intrusive melt compositions were characterised by slightly higher magmatic water.

The Cajamarca and Hualgayoc igneous rocks have higher Sr_i than Cretaceous igneous rocks of the northern Coastal batholith (on average 0.7040-0.7043; Beckinsale *et al*., 1985) but lower Sr_i values than younger Miocene intrusive units from the Cordillera Blanca Batholith (0.7041-0.7057; Petford *et al*. 1996). Such increases in radiogenic Sr with time are observed throughout the entire Andean belt and inferred to be the result of increased crustal contamination due to thickening of the crust (Davidson *et al*., 1991) or variations in the source (Petford *et al*., 1996). Macfarlane (1999) documented the isotopic homogeneity (Pb, Nd and Sr) of igneous rocks and ores from the Hualgayoc district concluding that the isotope data supported a model of subducted sediment enriching the mantle wedge to generate the parental magmas. Such a model does not require assimilation and contamination of the Cretaceous sedimentary rocks or metamorphic basement. Miocene igneous rocks from both the Cajamarca and Hualgayoc regions have similar isotopic compositions (Fig. 14). Miocene igneous units from Cajamarca (0.7043-0.7050) and Hualgayoc (0.7043–0.7048; Macfarlane, 1999) have overlapping Sr_i compositions (Fig. 14), although most rocks from the Cajamarca contain slightly more radiogenic Nd. The Miocene rocks from both regions display a slight increase in Sr_i with time. Two samples from mineralised centres in the Cajamarca region (H-22 – synmineralisation; T4 – post-mineralisation) and a dioritic dyke from the Hualgayoc region have primitive isotopic compositions compared to intrusions of similar or older age. These primitive compositions possibly reflect replenishment of the mantle or magma chamber with new parental mafic melts. Isotopic compositions of

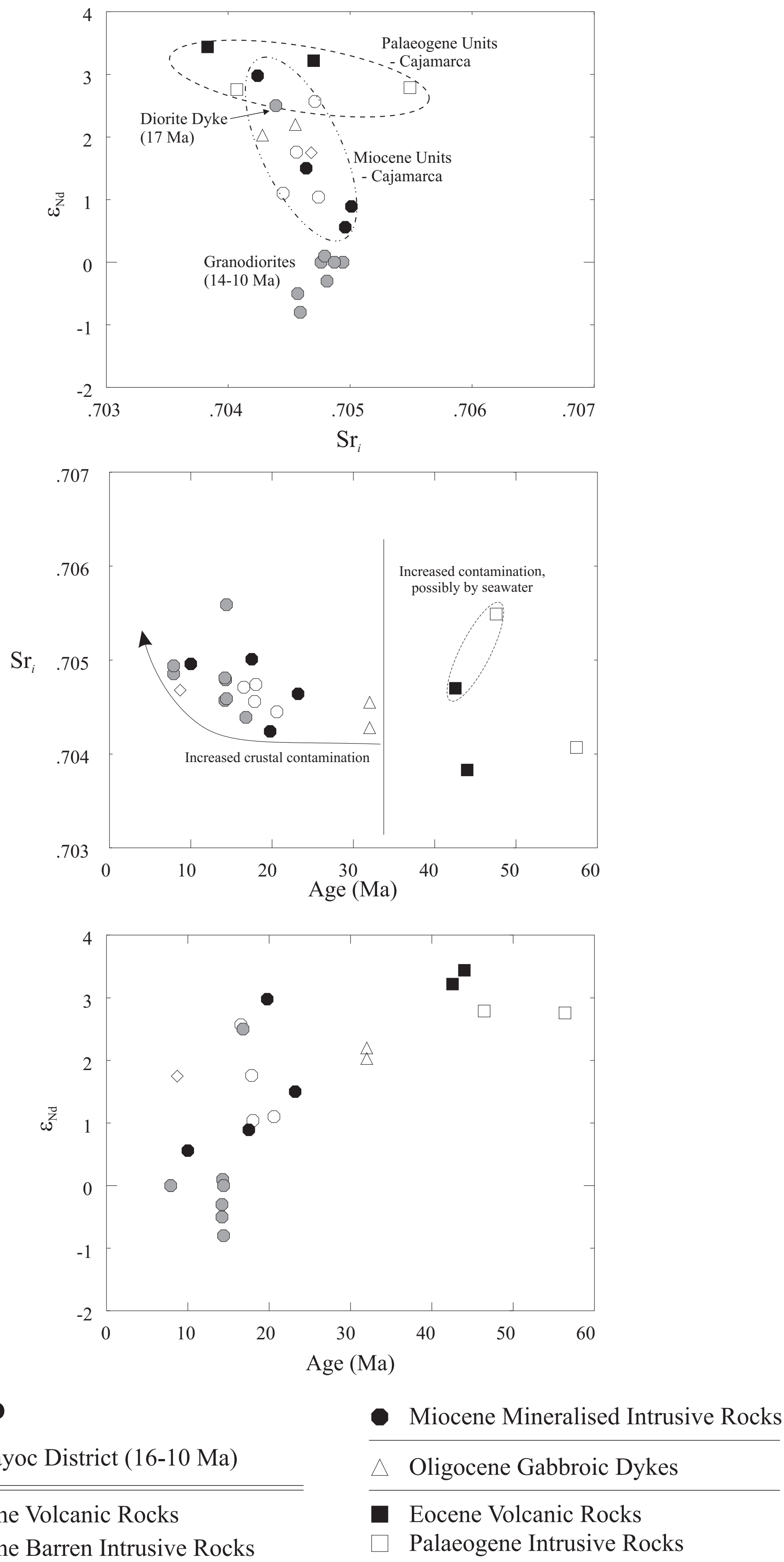

Fig. 14. ε_{Nd} and Sr$_i$ plots showing isotopic values for magmatic rocks from the Cajamarca and Hualgayoc district (Macfarlane, 1999).

Miocene igneous rocks from the Cajamarca and Hualgayoc regions indicate these magmas were derived from an enriched mantle that homogenised at deep levels, possibly in the upper mantle, and underwent minimal assimilation or contamination.

Based on outcrop evidence, early to middle Miocene times in the Cajamarca region were characterised by the emplacement of numerous intrusive stocks and were followed by extensive late Miocene volcanic activity. Miocene igneous rocks show a general depletion in both middle and heavy rare earth elements with increasing silica content. Some of the late Miocene volcanic rocks have a slight Eu anomaly, whereas the majority of Miocene intrusions lack negative Eu anomalies. The absence of a negative Eu anomaly may result from high magmatic oxidation states and/or suppression of plagioclase fractionation (e.g. Frey *et al*., 1978; Lopez, 1982; Lang and Titley, 1998). Magmatic trends for rocks of intermediate to acidic composition, such as observed in the Miocene igneous units, are commonly attributed to the increasing abundance of residual garnet in the source (Arth *et al*., 1978; Kay *et al*., 1991; Petford and Atherton, 1996; Kay and Mpodozis, 2001), and/or the fractionation of hornblende (Lang and Titley, 1998; Aldanmaz *et al*., 2000). Partial melting models suggest Miocene magmas were derived from an amphibole-rich residue but garnet content increased with time. This interpretation is supported by xenoliths in tuffs from SW Columbia that indicate hornblende-bearing assemblages dominate the deep crust of the northern Andes (Weber *et al*., 2002). The modelled amphibole-rich assemblage contrasts with the deduced Palaeogene olivine-pyroxene-rich residue (Fig. 15a). This major change in residual mineralogy coincided with intense crustal thickening in northern Peru, possibly indicating partial melting occurred at depths similar to those observed today, i.e. ~45 km (Fukao *et al*., 1989), and at greater temperature-pressure regimes to Palaeogene times. Trace element models also indicate that fractionation of hydrous minerals (e.g. hornblende and biotite) controlled melt compositions of the Miocene intrusions. In contrast, clinopyroxene and plagioclase fractionation influenced the composition of late Miocene volcanic rocks.

C.11.3 Model for Porphyry Cu Formation

Kay and Mpodozis (2001) proposed a three-stage model for generation of magmas related to the formation of giant Miocene Andean ore deposits in Chile. This

Fig. 15. Schematic magmatic and tectonic reconstruction of a section through the northern Peruvian Andes and Cajamarca region from Eocene to late Miocene times. (A) Eocene magmas are characterised by an olivine-pyroxene residual mineralogy, intruded the metamorphic basement and deformed Cretaceous sedimentary rocks and host no known mineralisation. (B) Early-middle Miocene magmas developed beneath a thickened crust, equilibrated with a wet amphibole-rich residue and are associated with a number of porphyry Cu deposits. Barren Miocene stocks underwent hornblende fractionation, whereas the composition of coeval synmineralisation stocks was controlled by biotite fractionation. (C) Formation of late Miocene high-sulphidation deposits occurred during termination of crustal thickening and onset of a flattening of the subduction zone. Late Miocene magmas equilibrated with a residual mineralogy that contained a higher garnet content than earlier magmas.

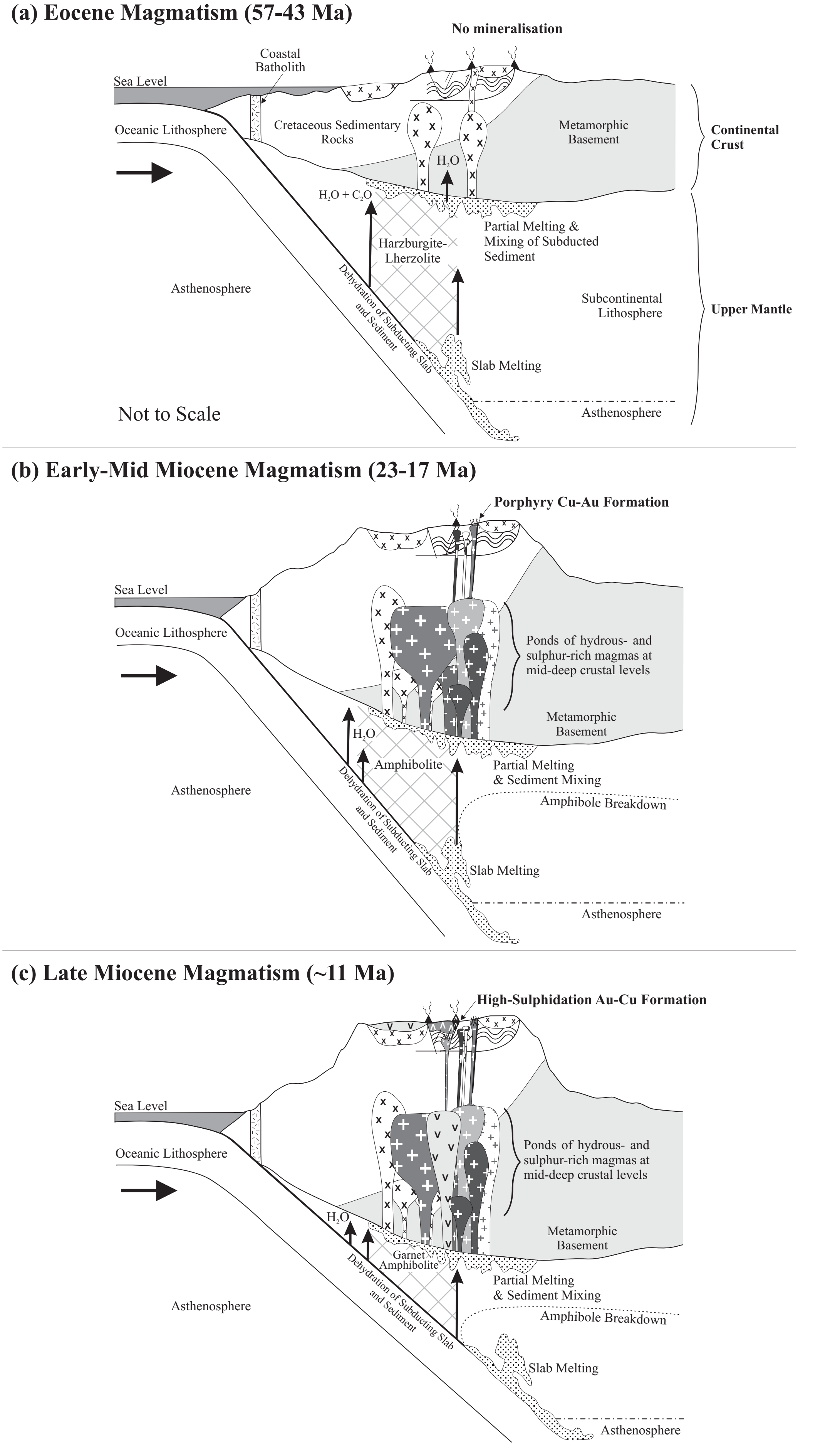
(a) Eocene Magmatism (57-43 Ma)
No mineralisation
Coastal Batholith
Sea Level
Oceanic Lithosphere
Cretaceous Sedimentary Rocks
Metamorphic Basement
Continental Crust
H_2O
$H_2O + C_2O$
Partial Melting & Mixing of Subducted Sediment
Harzburgite-Lherzolite
Asthenosphere
Dehydration of Subducting Slab and Sediment
Subcontinental Lithosphere
Upper Mantle
Slab Melting
Not to Scale
Asthenosphere
(b) Early-Mid Miocene Magmatism (23-17 Ma)
Porphyry Cu-Au Formation
Sea Level
Oceanic Lithosphere
Ponds of hydrous- and sulphur-rich magmas at mid-deep crustal levels
Metamorphic Basement
H_2O
Amphibolite
Partial Melting & Sediment Mixing
Asthenosphere
Amphibole Breakdown
Dehydration of Subducting Slab and Sediment
Slab Melting
Asthenosphere
(c) Late Miocene Magmatism (~11 Ma)
High-Sulphidation Au-Cu Formation
Sea Level
Oceanic Lithosphere
Ponds of hydrous- and sulphur-rich magmas at mid-deep crustal levels
H_2O
Metamorphic Basement
Garnet Amphibolite
Partial Melting & Sediment Mixing
Asthenosphere
Amphibole Breakdown
Dehydration of Subducting Slab and Sediment
Slab Melting
Asthenosphere

model incorporates shallowing of the subduction zone beneath a thickening crust and a progressive change from pyroxene- to amphibole- and finally garnet-bearing mineral residues. Large amounts of fluids released during the breakdown of the amphibole-bearing source resulted in development of hydrous oxidised melts. Storage of these hydrous melt at the lithosphere-crust interface in a compressive tectonic regime could have promoted fractional crystallisation, crustal contamination and melting-assimilation-storage-homogenisation (MASH) processes as outlined by Hildreth and Moorbath (1988). Generation and homogenisation of hydrous melts beneath a thickening crustal have been proposed as influential processes for the formation of porphyry copper deposits in Chile (Campos *et al*., 2002; Richards *et al*., 2001, Kay and Mpodozis, 2001; Oyarzun *et al*., 2001).

Geochemical and petrological data from the Cajamarca region suggest a different mode of porphyry Cu formation to that proposed in northern Chile. Porphyry Cu deposits in the Cajamarca region are inferred to have formed as a result of the following processes. Dehydration of the subducted slab released H_2O-rich fluids from the breakdown of hydrous minerals (e.g. Na-amphibole, lawsonite, chlorite) and caused decarbonation of subducted pelagic sediment, large-scale hydration of the lithospheric wedge and generated large volumes of partial melt (c.f. Peacock, 1993; Peacock *et al*., 1994). Experimental studies suggest silica and incompatible elements would also have been removed from both the subducted slab and sediments, and would then have ascended with H_2O-rich fluids to enrich the mantle wedge (Nakamura and Kushiro, 1974; Stern and Wyllie, 1978). These wet fluids induced development of parental mafic melts and supported continued crystallisation of hydrous mineral phases, in particular amphibole, in the mantle (Peacock, 1993). These primitive mafic melts may have undergone differentiation and possibly assimilation-fractional crystallisation (AFC) or MASH-type processes in an amphibole-rich upper mantle to lower crust interface. However, these later processes do not appear to have significantly influenced the generation of synmineralisation magmas in the Cajamarca district. Such processes are likely to occur during compressional regimes and beneath a thickened crust where melts preferentially pond and evolve at depth rather than migrate upwards into the mid or upper crust (Davidson *et al*., 1991; Campos *et al*., 2002).

Clusters of porphyry Cu deposits in Chile overlie large-scale magnetic anomalies that Behn *et al*. (2001) have interpreted as deep mafic to intermediate parental intrusive bodies of batholithic size. Highly oxidised, water-rich mafic melts have high sulphur solubility and are effective carries of chalcophile elements (Burnham, 1979). The content of sulphur and chalcophile elements in mafic melts is likely to increase with increased partial melting in the upper mantle (Burnham, 1981). Repeated injection of primitive hydrous melts into mid to deep crustal level magma chambers would further increase the concentration of sulphur.

During stages of high magmatic water content (in excess of 4 wt % H_2O) hornblende fractionation and suppression of plagioclase crystallisation may also occur, and result in segregation of hornblende (Naney, 1983: Merzbacher and Eggler, 1984; Rutherford and Devine, 1988). Continued fractionation and segregation of hornblende lowers the CaO, MREE-HREE and magmatic H_2O content in the melt. If the CaO content drops below the level required for amphibole crystallisation, biotite will replace hornblende as the dominant cotectic mafic phase (Naney, 1983; Candela, 1997; Richards *et al*., 2001). Such a change from hornblende- to biotite-dominated fractionation is observed between barren and synmineralisation stocks in the Cajamarca region and deposits in northern Chile (Richards *et al*., 2001). Oyarzun *et al*. (2001) proposed that giant porphyry Cu deposits in Chile are associated with hydrous melts that retained high sulphur levels and were emplaced in the upper crust during a low volcanic/intrusive ratio period as “closed or near-closed porphyry system”. Such systems have the potential to generate large concentrations of sulphides during plutonic crystallisation and hydrothermal processes.

As the water content in the mantle declined to due the breakdown of hydrous minerals, such as amphiboles and micas, high temperature/pressure anhydrous mineral phases crystallised (e.g. garnet and clinopyroxene). Kay and Mpodozis (2001) suggested that major Miocene ore deposits in Chile formed during progressive flattening of the subducting slab, which coincided with a change in the residual mineralogy from amphibole- to garnet-dominated They further argued the potential for significant mineralisation decreases as a dry, garnet-dominated source evolves. Trace element models of Miocene igneous rocks in the Cajamarca district suggest porphyry Cu-Au-Mo mineralisation occurred during the transition from a garnet-poor amphibole-dominated residue (50% amphibole, 5% garnet) in the early Miocene to an amphibole-garnet residue (50% amphibole, 17% garnet) during the late Miocene (Fig. 15b). The increasing presence of garnet as a residual mineral is linked to the cessation of crustal thickening (Noble *et al*., 1990) and the onset of a flattening subduction angle in northern Peru approximately 12 to 10 Ma (Gutscher *et al*., 1999). Formation of high-sulphidation Au deposits in the late Miocene were therefore temporally linked to flattening of the subduction angle, cessation of crustal thickening and a further change in residual mineralogy (Fig. 15c).

C.12 Conclusion

Porphyry Cu and high-sulphidation Au deposits in the Cajamarca region formed during early-middle Miocene and late Miocene magmatic events, respectively. Synmineralisation stocks are geochemically similar from coeval barren intrusions, but both differ significantly from barren Palaeogene magmatic rocks. Miocene mineralisation resulted from the culmination of progressive changes in the tectonomagmatic setting of the Cajamarca region during Tertiary times. The following features have important implications for Tertiary arc magmatism and magmatic related ore-forming fluids in northern Peru:

1. Palaeogene magmatic rocks were generated within an immature volcanic arc and derived from a residue characterised by anhydrous minerals (i.e. olivine and pyroxene). These magmas contained a magmatic water content of ~3 wt % H_2O, and underwent anhydrous and possibly hydrous mineral fractionation. A lack of mineralisation during this interval possibly relates to the dry nature of the mantle and melts.

2. Porphyry Cu deposits are associated with early-middle Miocene hornblende-biotite diorite stocks. These magmas were derived from large degrees of partial melting (~50%). The hydrous melts (> 3 wt % H_2O) equilibrated in the upper mantle with an amphibole-dominated residue. Replenishment of deep crustal ponds by primitive parental melts contributed significant amounts of magma and sulphur to the evolving

magma chamber. These hydrous sulphur-rich melts rose rapidly through the crust, which resulted in minimal crustal assimilation.

3. Late Miocene high-sulphidation deposits formed during cessation of uplift and crustal thickening in the Peruvian Andes that caused lowering of the crust-mantle boundary to present day depths (i.e. ~40 km). This resulted in a change of the residual mineralogy from amphibole to amphibole + garnet. The onset of a flat subduction zone also coincided with formation of the epithermal systems.

SECTION D

Geology of the El Galeno and Michiquillay Cu-Au-Mo deposits and a comparison with the Au-rich Minas Conga porphyry deposit in the Cajamarca mining district, northern Peru

Section D. Geology of the El Galeno and Michiquillay Cu-Au-Mo deposits and a comparison with the Au-rich Minas Conga porphyry deposit in the Cajamarca mining district, northern Peru.

D.1 Abstract

El Galeno and Michiquillay are Miocene Cu-Mo-Au porphyry-related deposits located in the Au-rich Cajamarca district of northern Peru. The El Galeno deposit (486 Mt at 0.57 % Cu, 0.14 g/t Au and 150 ppm Mo) is associated with multiple dioritic intrusions hosted within Lower Cretaceous quartzites and shales. Emplacement of the porphyry stocks (17.5 – 16.5 Ma) in a hanging wall anticline was structural controlled by oblique faults superimposed on early WNW-trending fold-thrust structures. Early K-feldspar-biotite-magnetite (potassic) alteration was associated with pyrite and chalcopyrite precipitation. A quartz-magnetite assemblage that occurs at depth has completely replaced potassically-altered rocks. Late- and post-mineralisation stocks are spatially and temporally related to a weak quartz-muscovite (phyllic) alteration. High Au grades are associated with early intrusive phases located near the centre of the deposit. Highest grade Cu (~0.9 % Cu) is mostly associated with a supergene enrichment blanket, whilst high Mo grades are restricted to contacts with the sedimentary rocks. The Michiquillay Cu-Au-Mo deposit (631 Mt at 0.69% Cu, 0.15 g/t Au, 100-200 ppm Mo) is associated with a Miocene (19.8 Ma) dioritic complex that was emplaced within the hanging wall of a back thrust fault. The intrusive complex is hosted in quartzites and limestones. The NE-trending deposit is crosscut by NNW-trending prospect-scale faults that influenced both alteration and metal distribution. In the SW and NE of the deposit, potassic alteration zones contain moderate hypogene grades (0.14 g/t Au and 0.8 % Cu) and are characterised by chalcopyrite and pyrite mineralisation. The core of the deposit is defined by a lower grade (0.08 g/t Au and 0.57 % Cu) phyllic alteration that overprinted early potassic alteration. Michiquillay contains a supergene enrichment blanket of 45 to 80 m thickness with an average Cu grade of 1.15 %, which is overlain by a deep leached cap (up to 150 m). In contrast to these Cu-Au-Mo deposits, the Au-rich Minas Conga deposit (~23.2 Ma) contains a well-developed potassic alteration associated with strong bornite + chalcopyrite mineralisation.

Sulphide Pb isotope ratios from these Cu-Au-Mo deposits and the Au-rich Minas Conga deposit scatter slightly but suggest a common mantle-dominated source. Similarities between these deposits include age (early-middle Miocene), intrusive rock type (dioritic) and metal source (deep mantle). Despite these similarities, results from this study suggest variation in metal grade between the Au-rich and hybrid-type deposits resulted from a combination of processes. These include temperature and oxygen fugacity conditions during hypogene mineralisation, late fluid flow resulting in a well-developed phyllic alteration zone, precipitation of ubiquitous hydrothermal magnetite, and complexity of intrusive history.

D.2 Introduction

The Cajamarca mining district, located in northern Peru, has one of the largest gold inventories in South America with the economic high-sulphidation Yanacocha Au mine, plus several smaller Au epithermal and porphyry Cu-Au deposits that include the Minas Conga (Au-Cu), Michiquillay (Cu-Au-Mo) and El Galeno (Cu-Au-Mo) prospects. Gold reserves for Minera Yanacocha are approximately 36.6 Moz (Newmont, 2002) and the three intrusion-related systems have a combined mineral resource in excess of 1600 Mt (Llosa and Veliz, 2000; McInnes, 1997; Cordova and Hoyos, 2000). Several barren intrusions of older or similar age and composition also crop out in the region. To the north of the Cajamarca district are a number of high-sulphidation Au deposits that include Sipán, La Zanja, Tantahuatay, and the porphyry-skarn-manto polymetallic Hualgayoc district (Fig. 1).

Previous work at mineralised centres in the Cajamarca region includes several studies at the Michiquillay deposit by Laughlin *et al*. (1968), Hollister and Sirvas (1974), and reports by the Metal Mining Agency, Japan International Cooperation Agency (1975) and McInnes (1997). Turner (1997, 1999) discussed the volcanic setting and styles of mineralisation of the Yanacocha deposits as well as other high-sulphidation systems (Sipán, La Zanja and Tantahuatay). Recent work by Longo (2000) provided a detailed discussion on the San Jose-Charachugo-Chaquicocha gold trend within the Yanacocha district, whilst Llosa and Veliz (2000) documented alteration and

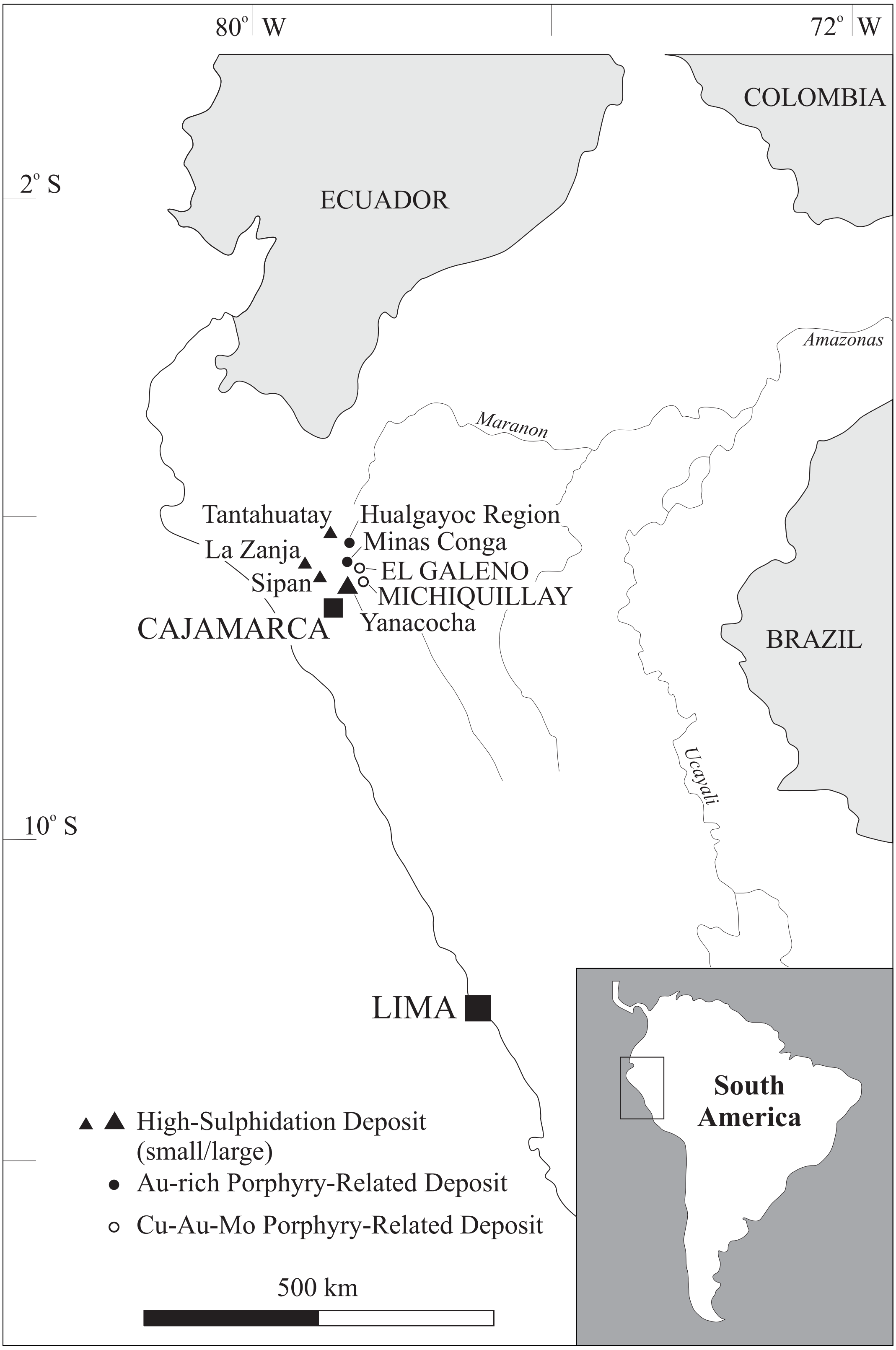

Fig. 1. Map of Peru showing the major mineralised centres near the township of Cajamarca.

mineralisation styles at the Au-Cu Minas Conga prospect. Unpublished reports (Hammond, 1998; Garcia, 1999; Sillitoe, 2000a; Davies, 2000) and published work by Cordova and Hoyos (2000) describe the geology of El Galeno.

This section presents a detailed geological description of the El Galeno (Cu-Mo-Au) prospect with emphasis on documentation of the relative timing of the different intrusive phases, as well as characterisation of the alteration, mineralisation and vein infill paragenesis. Revised intrusive, structural, alteration and mineralisation data from the Michiquillay prospect are also presented. New Pb isotope compositions for sulphide minerals from mineralised intrusions at the El Galeno, Michiquillay, Minas Conga and Yanacocha deposits are also presented. Finally, El Galeno and Michiquillay are compared with the relatively well-documented Au-rich Minas Conga porphyry complex.

D.3 Regional Geological Setting

The Cajamarca district is located in the Western Cordillera of northern Peru. The region is characterised by deformed Cretaceous marine sedimentary rocks that have undergone several phases of compressive deformation since Palaeogene time and been intruded by multiple magmatic phases (Fig. 2). Hydrothermal and mineralisation events were temporally related to two major magmatic episodes, i.e. early to middle Miocene porphyry Cu-Au-Mo formation and late Miocene epithermal activity (refer to Section A). The geological setting of northern Peru and the Cajamarca region is outlined in Benavides (1956), Reyes (1980), Wilson (1985a, 1985b), Cobbing *et al*., (1981), Turner (1997) and Wilson (2000).

D.3.1 Cretaceous to Oligocene Rocks

The oldest rocks that crop out in the Cajamarca region are a thick package of Lower- to Upper-Cretaceous platform sedimentary rocks. These sedimentary units include Lower-Cretaceous sandstone and quartzite sequences at the base of the package that fine upward to Upper-Cretaceous limestone, marl and shale sequences (Benavides, 1956). Intense folding and thrusting of the marine sediments from 59 to 55 Ma resulted

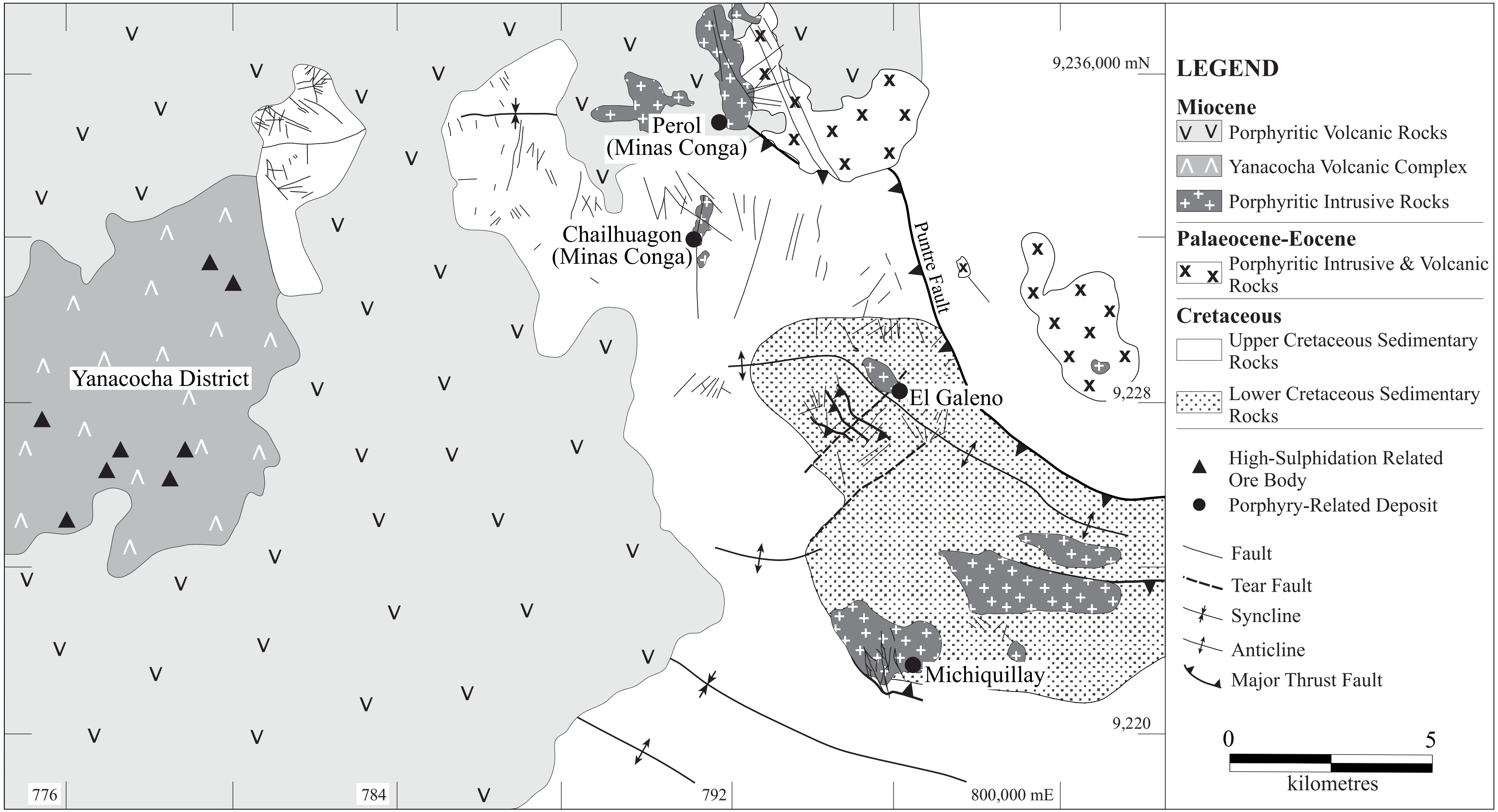

Fig. 2. Simplified geological map of the Cajamarca region showing the distribution of the major mineralised centres (modified from Reyes, 1980).

in emergence of the Cretaceous sedimentary units and development of open, upright folds and imbricate thrust sheets (Mégard, 1984, 1987).

The deformed sedimentary rocks are unconformably overlain by predominantly basaltic to andesitic volcanic sequences known as the Llama Formation (Noble *et al*., 1990; Atherton *et al*., 1985). The Lower Llama Volcanic Sequence forms an aerially-extensive volcanic succession that range in age from 54.8 to 42.6 Ma (Atherton *et al*., 1985; Noble *et al*., 1990; Section A). Intrusions in the Minas Conga, Cerro Perol and Cruz Conga regions indicate several stocks were emplaced between 57 and 43 Ma (Llosa *et al*., 1996; Section A).

D.3.1 Miocene Rocks

Early to middle Miocene magmatic units (23.2 – 15.8 Ma) are composed of intermediate, calc-alkaline porphyritic intrusive and volcanic rocks that contain plagioclase, mafic ± quartz phenocrysts. Geochronological studies of mineralised porphyry systems indicate emplacement, main stage alteration and mineralisation at these centres occurred during this magmatic interval (Llosa *et al*., 1996; Section A). Coeval barren porphyritic stocks of similar composition display weak propylitic alteration (Section A and C). The youngest intrusive age for this second magmatic interval is defined by an $^{40}Ar/^{39}Ar$ date of 16.5 Ma from a post-mineralisation intrusion at El Galeno (Section A), whilst the Upper Llama Volcanic Sequence has been dated at 15.8 Ma also using $^{40}Ar/^{39}Ar$ age dating (Turner, 1997). An interval from *ca*. 16 to 12 Ma is defined by an apparent decrease in magmatic and deformation activity in the Cajamarca region. However, the period between 14 and 10 Ma corresponded with major magmatic and hydrothermal activity in the polymetallic Hualgayoc district to the north (Macfarlane *et al*., 1994). Several mineralised centres developed in the Hualgayoc region during this period, including those at Cerro Corona and Tantahuatay (Fig. 1).

Deposition of andesitic lava flows of the Regalado Formation (12.3 to 11.6 Ma; Turner, 1997) represented the initiation of middle to late Miocene magmatic activity. Economically, the most productive interval for the Cajamarca region occurred between 12 and 10 Ma with formation of the high-sulphidation Yanacocha Au deposit. Main stage mineralisation at Yanacocha took place between 11.5 and 10.9 Ma (Turner, 1997).

Magmatic and hydrothermal activity in the region ceased in the late Miocene (~8 Ma) with the onset of a shallowing subduction zone (Gutscher *et al*., 1999).

D.4 Regional Structure

The Cajamarca area is located within the southern part of the Huancabamba Deflection zone where Andean structural fabric rotates from NNW to near E-W (Mégard, 1984). The reader is referred to Section B of this thesis for a detailed structural synthesis of the Cajamarca region.

Structural features observed in the deformed Cretaceous sedimentary rocks include large wavelength (>5 km) open folds that plunge gently WNW or ESE. In the northeastern part of the study area, a thrust fault known as the Puntre Fault is spatially associated with numerous magmatic units of both Palaeogene and Miocene age (Fig. 2). The thrust fault displays a major deflection in trend from near E-W to near N-S (see below). To the east and west of the deflection, the Puntre fault has a NW trend consistent with local regional structures. Faults and fractures in the Cretaceous sedimentary rocks are generally subvertical with dominantly normal slip ranging from a few to tens of metres. In the study area, subvertical fault planes plot in three general domains, which include N-S, E-W and ESE-trending. N-striking faults are the most abundant orientation recognised from aerial-photo interpretation (Section B).

D.5 El Galeno

El Galeno is a Cu-Au-Mo porphyry deposit with an estimated geological resource of 486 Mt at 0.57 % Cu, 0.14 g/t Au and 150 ppm Mo (Cordova and Hoyos, 2000). It is exposed at an altitude between 3,850 and 4,100 m. Multiple intrusive stocks were emplaced between *ca*. 17.50 and 16.53 Ma (Section A). The intrusions are hosted by folded Lower Cretaceous sedimentary rocks and were emplaced in a hanging wall anticline (Fig. 3). Mineralisation is characterised a hypogene zone overlain by a supergene enrichment blanket up to 120 m thick. Several unmineralised gabbroic dykes crop out to the southwest and northwest of the mineralised centre, and display weak to

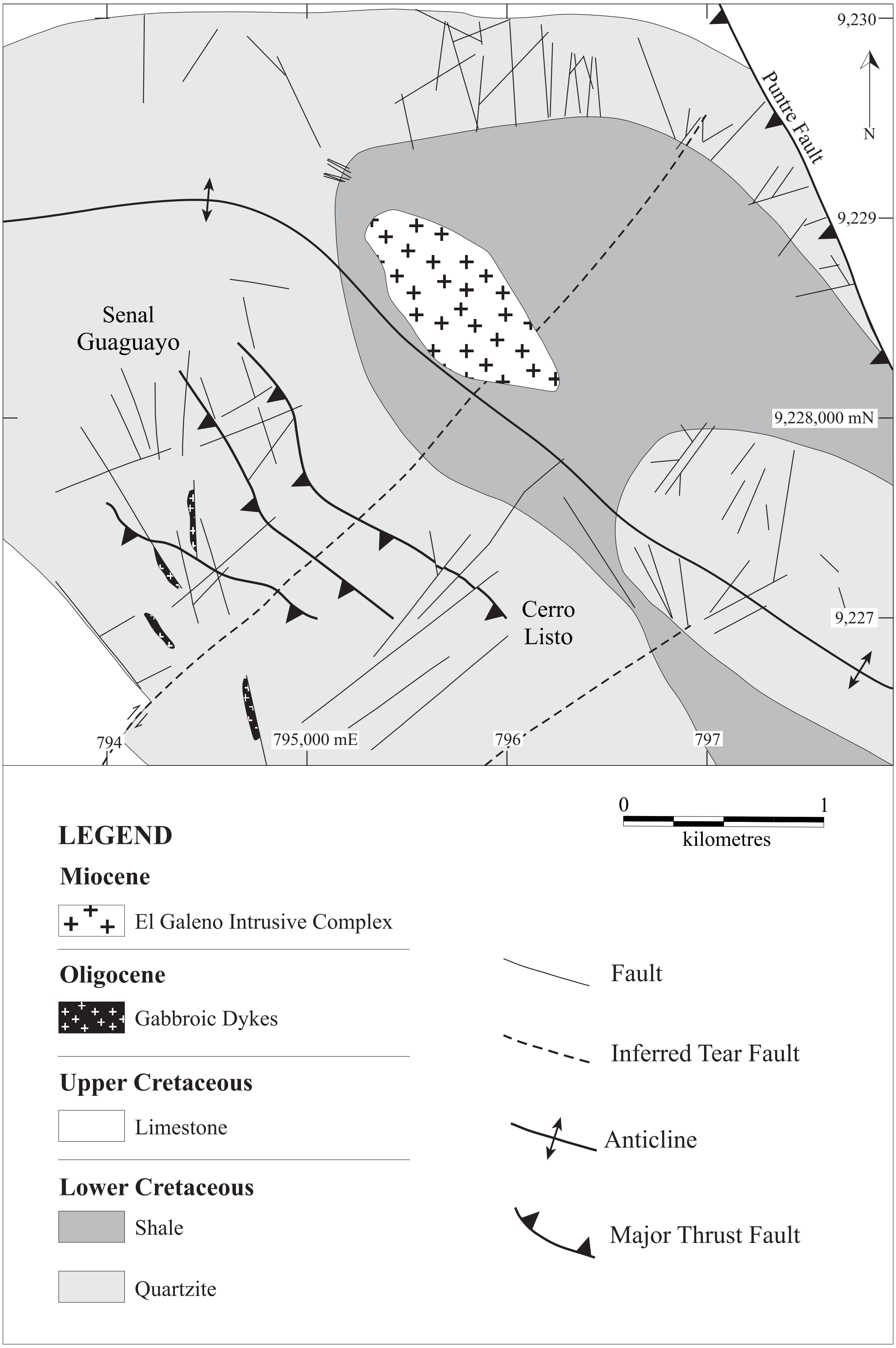

Fig. 3. Simplified structural map of El Galeno displaying the localisation of the intrusive complex within the hanging wall of the Puntre Fault and at the intersection of the NW-plunging El Galeno Anticline and a NE-trending dextral tear fault.

moderate chlorite alteration. The dykes intruded both subvertical N- to NW-trending fault planes and steeply dipping bedding planes. $^{40}Ar/^{39}Ar$ age dating of hornblende phenocrysts from a gabbroic dyke (S-16) yielded an approximate age of 29.4 ± 1.4 Ma (Section A), indicating the dykes are Oligocene in age and intruded prior to emplacement of the El Galeno porphyry complex.

D.5.1 Lithology

Field evidence indicates that the El Galeno porphyry complex is mainly hosted within quartzite and siltstone sedimentary units (Fig. 4). Observed contacts between intrusions and sedimentary host rocks are subvertical. Furthermore, drilling indicates the intrusive complex does not extend laterally beyond the outcrop limit (Appendix D1). The intrusive complex is elliptical in shape, ~1250 m in length by 600 m wide, and its long axis is oriented NW-SE. This orientation is roughly parallel to the WNW trend of the hanging wall anticline (El Galeno Anticline) that hosts the mineralised centre. The complex comprises at least four intrusive phases (Fig. 5), three of which are identifiable in outcrop and the other from drill core logging (Appendix D1).

P1 Porphyry - The oldest intrusive phase is a crowded medium-grained porphyritic diorite mostly composed of euhedral to subhedral plagioclase, with less abundant euhedral biotite, hornblende and rounded quartz phenocrysts (Fig. 6a). Plagioclase phenocrysts (An_{44-46}; 35-45 vol. %) range between 0.3 and 5.0 mm in length and show multiple twinning plus oscillatory zoning. Magmatic biotite and hornblende phenocrysts (1 vol. %) of 0.5 to 2.0 mm length are mostly replaced by secondary biotite. This is the largest body of the four recognised phases and later intrusive units were emplaced toward the core of this stock.

P2 Porphyry - The second intrusive phase is also a porphyritic diorite but texturally heterogeneous. It is dominantly characterised by a crowded porphyritic texture (Fig. 6b) with fine-grained plagioclase (0.5-1.0 mm; An_{42-60}) and less abundant rounded quartz grains, but varies to a medium-grained (1.5-3.0 mm) weakly porphyritic rock. Backscattered images of plagioclase phenocrysts illustrate compositional zoning (Fig. 5 in Section C). Phenocrysts show similar characteristics to magmatic grains in the

Fig. 4. Geological map of El Galeno with the major lithological units and prospect-scale structures. Outcrops of the intrusive complex were mostly created by road construction. Also, shown are the outer limits of Cu grade zones and the locations of drill core logged.

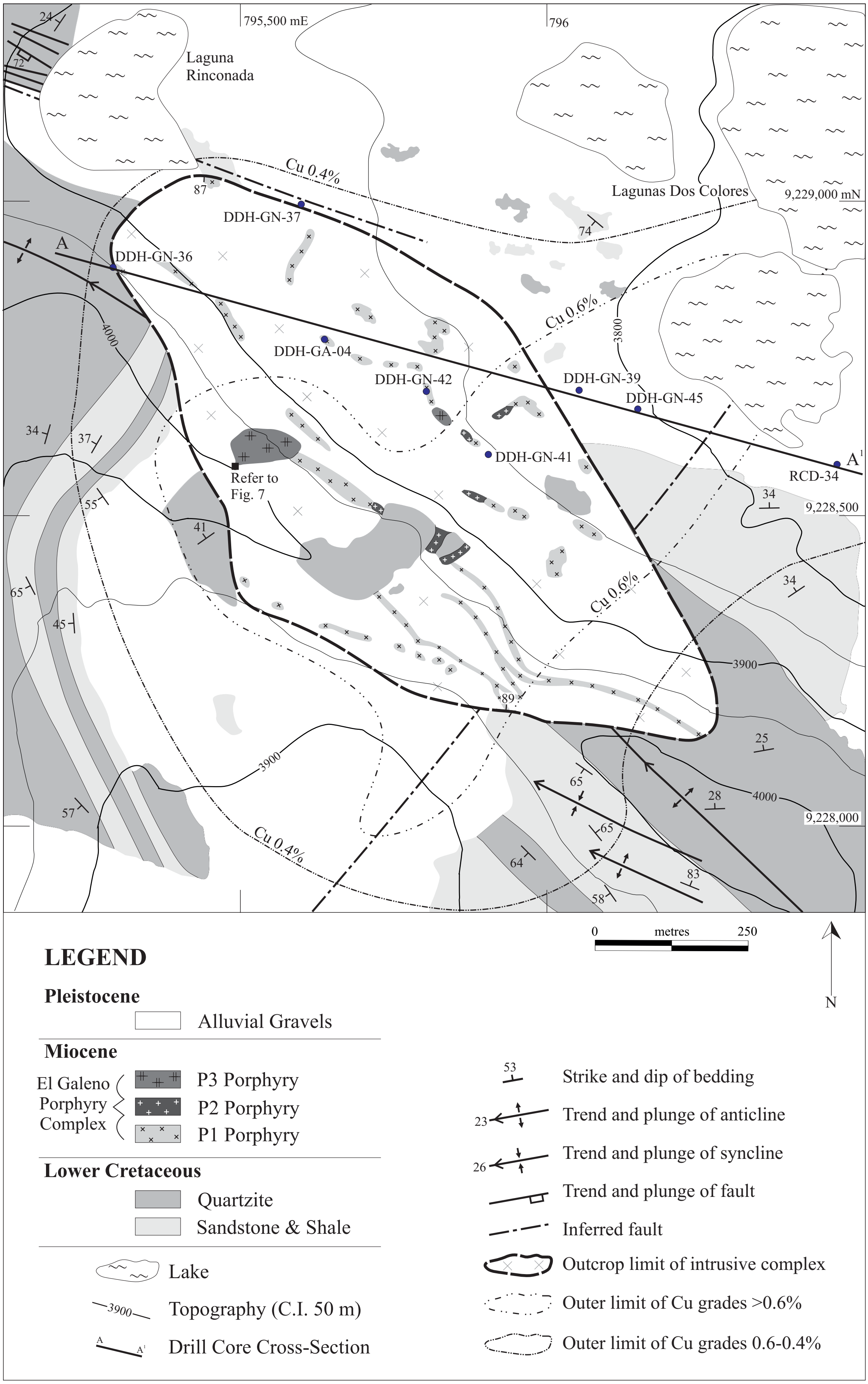
795,500 mE
796
Laguna Rinconada
Lagunas Dos Colores
9,229,000 mN
9,228,500
9,228,000
Cu 0.4%
Cu 0.6%
Cu 0.6%
Cu 0.4%
A
A1
DDH-GN-37
DDH-GN-36
DDH-GA-04
DDH-GN-42
DDH-GN-39
DDH-GN-45
DDH-GN-41
RCD-34
Refer to Fig. 7
4000
3800
3900
3900
4000
0 metres 250
N
LEGEND
Pleistocene
Alluvial Gravels
Miocene
El Galeno Porphyry Complex
P3 Porphyry
P2 Porphyry
P1 Porphyry
Lower Cretaceous
Quartzite
Sandstone & Shale
Lake
Topography (C.I. 50 m)
Drill Core Cross-Section
Strike and dip of bedding
Trend and plunge of anticline
Trend and plunge of syncline
Trend and plunge of fault
Inferred fault
Outcrop limit of intrusive complex
Outer limit of Cu grades >0.6%
Outer limit of Cu grades 0.6-0.4%

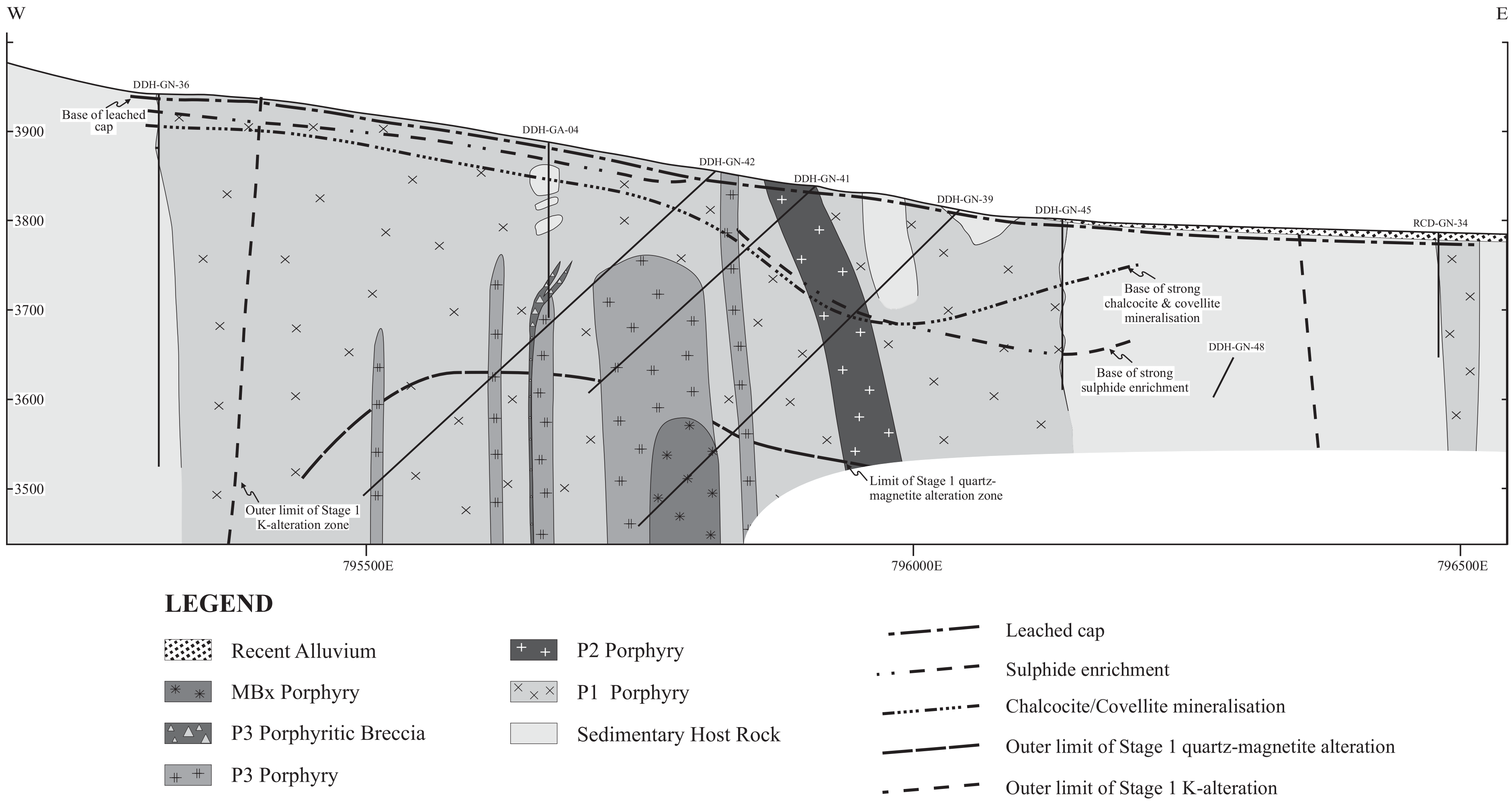

Fig. 5. Near E-W section through the El Galeno porphyry complex showing the distribution of the major lithological units and outer limits of alteration assemblages [based on drill core logging by Sillitoe (2000a) and the author (Appendix D1)]. The lower limits of the leached cap, chalcocite-covellite zone and sulfide enrichment blanket are also shown.

Fig. 6. Photographs of the different intrusive phases within the Galeno complex. (a) P1 porphyry composed dominantly of plagioclase (PL), hornblende (Hbl), biotite (Bt) and quartz (Qtz) phenocrysts. Plagioclases (yellow-orange colour) have been partially replaced by muscovite and illite. DDH-GN-42 96.6 m. (b) P2 porphyry with a medium to fine-grained crowded porphyritic texture consisting of plagioclase, biotite phenocrysts and fine-grained hornblende. Crosscutting quartz - K-feldspar veins (pink) and minor sulphides (dusty yellow centre) are related to dark K-feldspar-biotite alteration that is overprinted by weak propylitic alteration (light green spots upper left). DDH-GN-39 214 m. (c) P3 porphyry with coarse-grained plagioclase, biotite and hornblende and quartz phenocrysts. DDH-GN-42 246 m. (d) Biotised MBx porphyry with plagioclase (PL) and biotite (Bt) phenocrysts. MBx contains fragments of altered and mineralised P3 porphyry. Dark, fine-grained selvages composed of hydrothermal biotite rim some fragments. DDH-GN-39 400 m.

THE IMAGES ON THIS PAGE HAVE BEEN REMOVED DUE TO COPYRIGHT RESTRICTIONS

P1 porphyry. Hydrothermal biotite from this intrusion yielded an age of 17.5 ± 0.3 Ma using $^{40}Ar/^{39}Ar$ (Section A).

P3 Porphyry – The P3 porphyry is a coarse-grained crowded quartz-diorite porphyry with euhedral plagioclase, quartz, biotite and hornblende phenocrysts (Fig. 6c). Plagioclase phenocrysts (An_{42-51}; 30-35 vol. %) display oscillatory zoning and range in length from 1.0 up to 8.0 mm. Rounded quartz phenocrysts are 2.0 to 10.0 mm in length and may have minor embayments. Euhedral biotite books (6 vol. %) range from 1.0 to 10.0 mm in length and hornblende (~3 vol. %) phenocrysts are between 1.0 to 5.0 mm. This porphyry contains rare xenoliths of quartz-magnetite altered fragments. In drill core the occurrence of these intrusions is sporadic, varies in thickness from a few metres to tens of metres and was mainly intersected toward the centre of the P1 porphyry (Fig. 5). In outcrop (Fig. 4), contacts of a P3 porphyry body are near vertical (Fig. 7) from which it is inferred that this intrusive phase occurs as a number of small-sized vertical dykes.

P3 Porphyritic Breccia - Hydrothermal breccias (P3 porphyritic breccia) are located along the contacts of some of the P3 porphyry bodies (Fig. 5). Xenoliths observed within the hydrothermal breccia include angular to subrounded quartz and quartz-magnetite vein fragments that range in size from millimetres up to several centimetres (refer to Fig. 11a). The matrix is dominantly composed of quartz, muscovite and pyrite.

Thin (0.3-2.0 m wide) dioritic dykes are characterised by crowded porphyritic texture with abundant feldspar (0.6–2.5 mm) and minor mafic phenocrysts set within a light grey feldspathic groundmass. The dykes were not observed in outcrop and rarely intersected in drill core. The dykes are considered to have formed late in the evolution of the intrusive complex, probably following emplacement of the third intrusive phase. However, their exact timing is unclear.

MBx Porphyry - The youngest intrusive phase is a magmatic breccia that is weakly porphyritic, with phenocrysts and xenoliths set in a feldspar-rich matrix (Fig. 6d). Euhedral plagioclase phenocrysts (An_{40-56}; ~10 vol. %; 0.5 to 9.0 mm) show multiple twinning textures and generally contain sieve-textured rims that suggest

THE IMAGE ON THIS PAGE HAS BEEN REMOVED DUE TO COPYRIGHT RESTRICTIONS

Fig. 7. Photograph of a quartz-muscovite altered P3 porphyritic dyke that has intrude the P1 porphyry. Note the low vein density of the dyke compared to the earlier porphyry.

plagioclase instability (refer to insert of Fig. 11b). Biotite books (~2 vol. %) are euhedral and vary from 0.3 to 3.0 mm in size. Rounded quartz phenocrysts (~1 vol. %) are ~3.0 mm in length and acicular hornblende grains (0.3-2.0 mm) are partially replaced by secondary biotite. This unit was intersected at depth in the northern central part of the P1 porphyry (e.g. drill holes logged in Appendix D1). Xenoliths are generally rounded and range in size from a few to tens of centimetres. Altered and mineralised xenoliths of the previous three intrusive phases are the dominant clasts. Many clasts have thin (~1 mm) fine-grained dark selvages composed of hydrothermal biotite. Magmatic biotite books from this intrusion yielded a $^{40}Ar/^{39}Ar$ plateau age of 16.53 ± 0.18 Ma (Section A).

D.5.2 Structural Geology

El Galeno is situated at the intersection of a hanging wall anticline and a NE-striking tear fault (Fig. 3). The hanging wall anticline, called El Galeno Anticline, has a gentle plunge to the NW ($25^o \rightarrow 303^o$) and is located immediately above the Puntre Thrust fault. The Lower Cretaceous Chimú and Santa Formations in the hanging wall of the fault are juxtaposed against the Middle-Upper Cretaceous Yumagual Formation in the footwall, indicating over 2000 m of reverse offset based on unit thicknesses measured by Benavides (1956). To the east and northwest of the intrusive system, the reverse fault strikes approximately WNW and dips at a low angle (~30^o) to the SSW, suggesting that the fault forms a low-angle thrust ramp. However, to the northeast of the complex the reverse fault deflects in a clockwise direction to near NNW (Fig. 3). Within this NNW-trending zone of the fault, argillic-altered sedimentary rocks have a subvertical dip and display polyphase deformation. These features include early WNW shallowly plunging folds and subhorizontal calcite veins that are both crosscut by later extensional structures including subvertical calcite veins and small-scale normal faults (Section B.4.1). Other features observed in near proximity to the thrust zone include a bend in the hanging wall anticline axis towards the deflection zone and abundant fractures in Goyllarisquizga Group quartzites on the northern limb of the anticline. These features suggest a change from a low-angle frontal ramp, to the east and northwest of El Galeno, to a high-angle oblique ramp within the zone of deflection.

Southwest of the intrusive complex, exposures on Senal Guaguayo contain subvertical normal faults that range from NW- to near E-trending. Displacement along the fault planes varies from roughly two to five metres. Fault breccias and altered Oligocene gabbroic dykes (1–3 m wide) occur along some of these fault planes. Normal faults measured at Cerro Listo have a uniform orientation with a general NE trend and offsets up to 10 m. These subvertical faults are characterised by minor brecciation along fault planes, although gabbroic dykes are noticeably absent at Cerro Listo. Aerial photo interpretation suggests a NE-trending tear fault bisects the valley between topographic peaks of Senal Guaguayo and Cerro Listo (Fig. 3). This tear fault is interpreted to crosscut the El Galeno Anticline.

West of Laguna Rinconada (Fig. 4) a series of small-scale normal faults were observed within the Farrat Formation. These subvertical faults have an approximate E-W strike and display minor (0.5-2.0 m) displacement. Drill cores along strike of these faults (e.g. DDH-GN-37) are strongly fractured and characterised by intense clay alteration to depths in excess of 300 m (Appendix D1). It is inferred that the fault set west of Laguna Rinconada extends into the intrusive centre. The nature and history of this fault with respect to pluton emplacement, controls on mineralisation plus possible post-mineralisation offset is uncertain.

D.5.3 Alteration, Mineralisation and Vein Paragenesis

Four separate alteration events are identifiable at the El Galeno prospect based on drill core logging and petrographic studies. The first of these is temporally and spatially related to the earliest two intrusive phases. P3 porphyry truncates mineralised P1 and P2 porphyries indicating hydrothermal events occurred prior to its emplacement. Altered P3 porphyry is in turn crosscut by P3 hydrothermal breccias, with MBx porphyry containing mineralised xenoliths of all earlier intrusive phases. Alteration assemblages associated with each of the intrusive phases display zoned distributions.

Mineralisation is divided into two main phases, namely hypogene mineralisation, which includes up to three separate stages, and secondly supergene mineralisation (Fig. 8). Hypogene mineralisation occurs in all four generations of

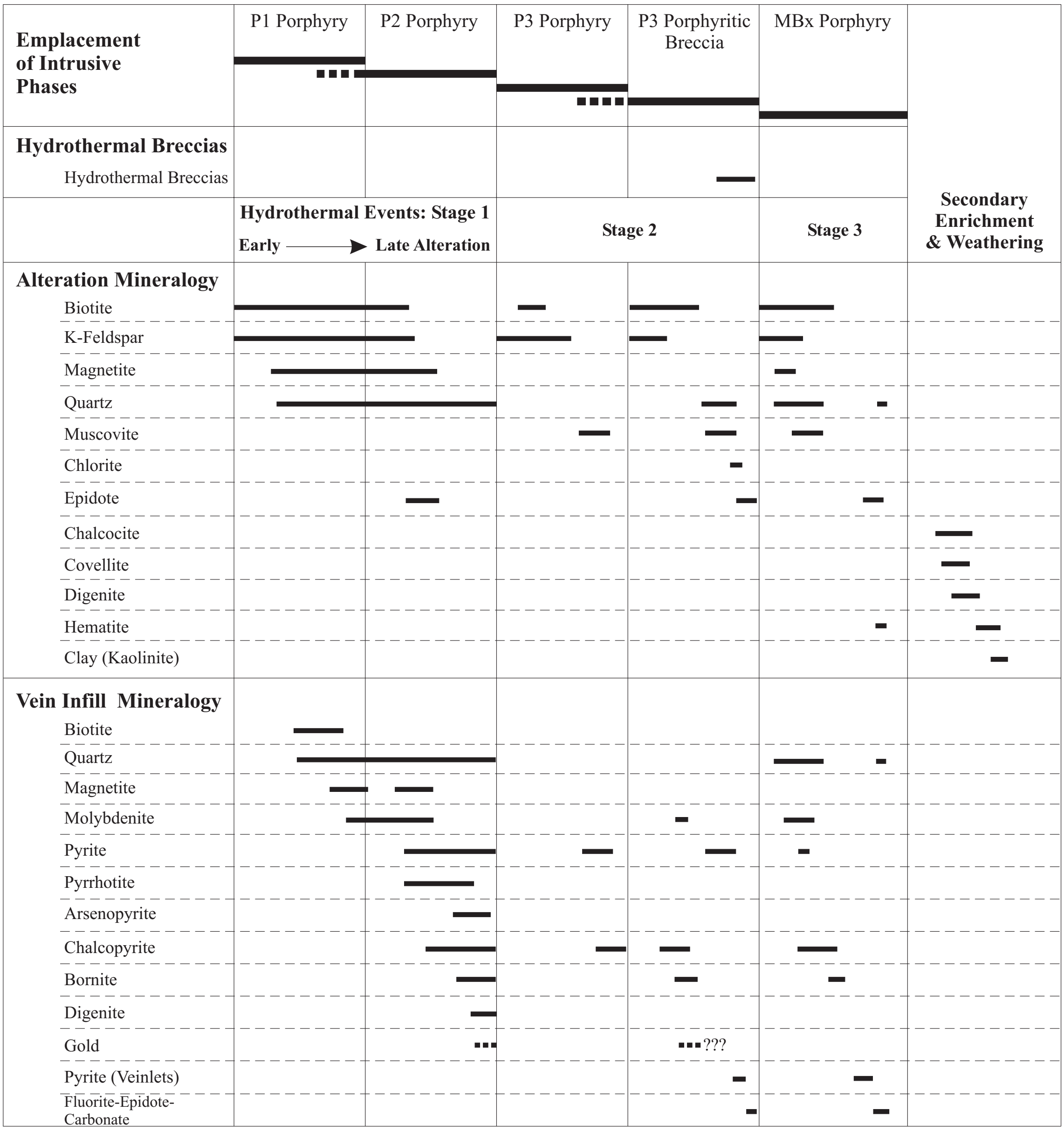

Fig. 8. Alteration and vein paragenesis at El Galeno.

porphyry intrusions as well as extending tens to a few hundreds of metres into the host sedimentary rocks.

Stage 1

Alteration - The oldest and most widespread alteration identified in drill core is observed within the earliest two intrusions. The dominant assemblage consists of K-feldspar and biotite (potassic alteration). This is characterised by replacement of plagioclase phenocrysts by K-feldspar (Fig. 9a), while primary hornblende and biotite phenocrysts are replaced by hydrothermal biotite, plus formation of fine-grained secondary biotite within the matrix. Minor amounts of fine-grained magnetite occur along the rims of altered mafic minerals and disseminated within the matrix. The earliest vein types include biotite-quartz fracture infillings (Fig. 9b), followed by quartz veins of varying thickness (0.5 mm up to 10 cm). The highest density of quartz stockwork is related to this alteration stage and generally extends about 200 m below the current surface (Appendix D1). Stockwork density generally decreases with depth and toward the periphery of the intrusive system, although quartz stockwork locally extends up to 100 m in to the host rocks. Minor silicification and a weak propylitic alteration are also evident along the contact margins with sedimentary host rocks and in localised zones of the P1 porphyry.

Pervasive magnetite-quartz alteration (Fig. 9c) occurs at depth and toward the central zone of the P1 porphyry (Fig. 5). Quartz-magnetite-altered fragments occur as xenoliths in the P3 porphyry, although a weak magnetite alteration is evident along its contacts. These relationships indicate this quartz-magnetite alteration dominantly occurred at depth and prior to emplacement of the third intrusive phase.

Hypogene Sulphides - Hypogene mineralisation identified at El Galeno is both fracture infill and disseminated in character. The earliest mineralisation was molybdenite (Fig. 9d) deposited in re-opened early quartz veins within both the P1 porphyry and host sedimentary rocks. These quartz veins range in thickness from a few millimetres to centimetres. The highest molybdenite abundances occur along the contacts between the host sedimentary rocks and P1 porphyry (Fig. 10a). This oldest mineralisation phase was followed by the deposition of magnetite and pyrite (Fig. 9d) with varying proportions of arsenopyrite and pyrrhotite. Later chalcopyrite (Fig. 9d) and

Fig. 9. Photographs of alteration and mineralisation features at El Galeno. (a) Photomicrograph of a zoned plagioclase phenocryst crosscut and partially replaced by early Stage 1 potassic alteration. (b) Stage 1 early biotite (Bt) vein in the P1 porphyry crosscut by a quartz (Qtz) vein (middle left of image). Thin magnetite (Mag) veins post-date both the biotite and quartz veins. DDH-GN-42 96.6 m. (c) Stage 1 quartz-magnetite alteration crosscut by quartz and quartz-magnetite veins. Magnetite infill of reopened veins and late pyrite (Pyr) veinlets are also evident. DDH-GN-42 465 m. (d) Photomicrograph of Stage 1 mineralisation with early molybdenite, followed by pyrite and finally chalcopyrite. DDH-GN-39 166m. (e) Photomicrograph showing Stage 2 K-feldspar (bottom left to top centre) has partially replaced a plagioclase phenocryst. Fine-grained hydrothermal biotite (pink, top right) also precipitated during this alteration stage. Both of these minerals are partially replaced by muscovite/illite. DDH-GN-41 258 m. (f) Stage 2 pyrite vein with a quartz-muscovite halo in a P3 dioritic dyke. DDH-GN-39 215 m.

THE IMAGES ON THIS PAGE HAVE BEEN REMOVED DUE TO COPYRIGHT RESTRICTIONS

Fig. 10. Section A-A[1] showing metal grade distributions. High Au and Cu grades are located in the upper eastern section of the porphyry complex. Moderate Cu grades also occur on the western flank of the complex. High Mo grades are mostly located on the edges of the complex. The quartz-magnetite alteration and late porphyries (P3 and MBx) are poorly mineralised.

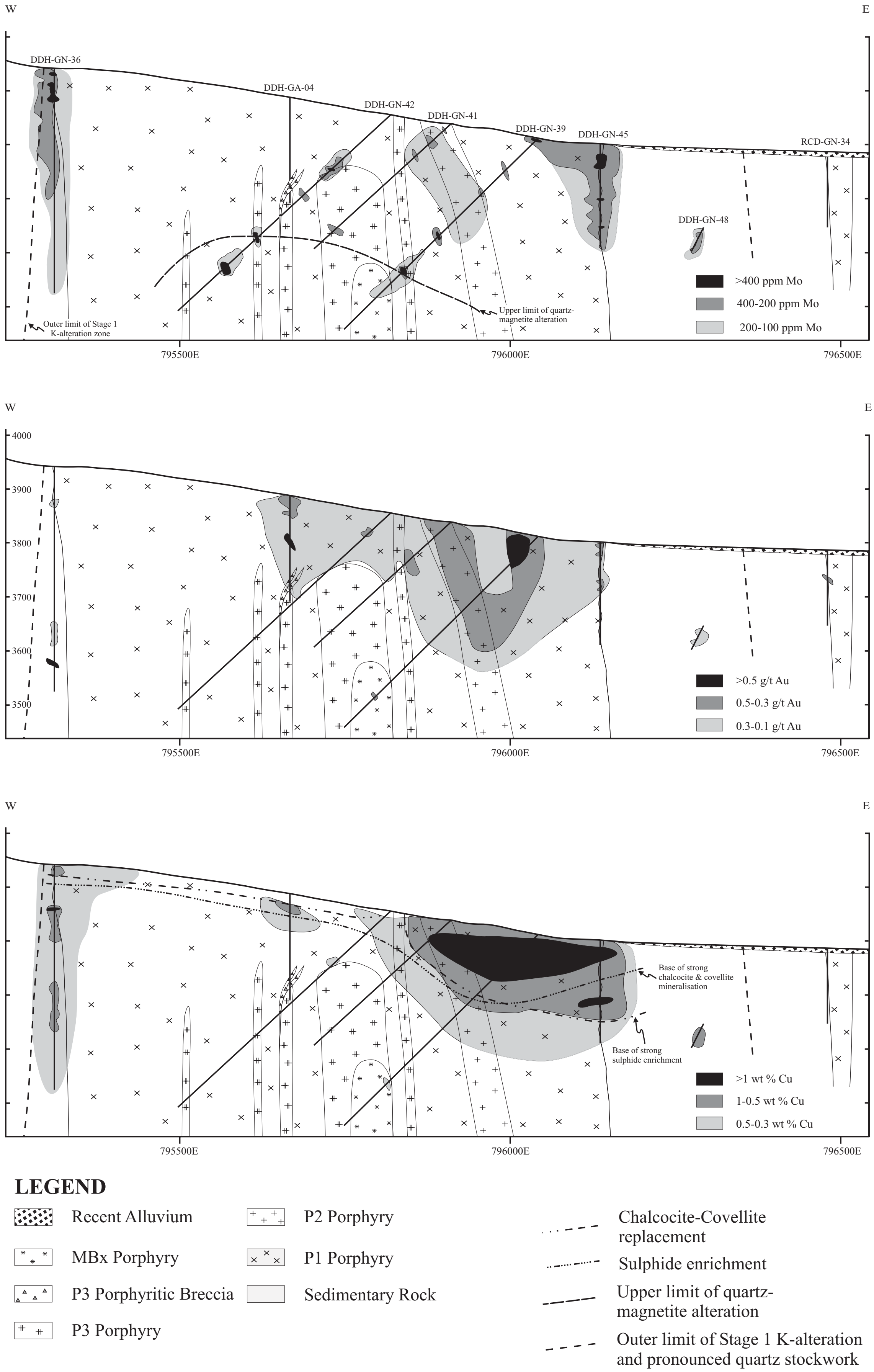
W
E
DDH-GN-36
DDH-GA-04
DDH-GN-42
DDH-GN-41
DDH-GN-39
DDH-GN-45
RCD-GN-34
DDH-GN-48
Outer limit of Stage 1 K-alteration zone
Upper limit of quartz-magnetite alteration
>400 ppm Mo
400-200 ppm Mo
200-100 ppm Mo
795500E
796000E
796500E
4000
3900
3800
3700
3600
3500
>0.5 g/t Au
0.5-0.3 g/t Au
0.3-0.1 g/t Au
Base of strong chalcocite & covellite mineralisation
Base of strong sulphide enrichment
>1 wt % Cu
1-0.5 wt % Cu
0.5-0.3 wt % Cu
LEGEND
Recent Alluvium
MBx Porphyry
P3 Porphyritic Breccia
P3 Porphyry
P2 Porphyry
P1 Porphyry
Sedimentary Rock
Chalcocite-Covellite replacement
Sulphide enrichment
Upper limit of quartz-magnetite alteration
Outer limit of Stage 1 K-alteration and pronounced quartz stockwork

minor amounts of bornite crosscut these earlier phases. These later mineralisation phases are evident in both the P1 and P2 intrusions. Hypogene pyrite, chalcopyrite and molybdenite also extend into the sedimentary host rocks. Based on logging and assay data (Appendix D2), high-grade hypogene zones are associated with intense hydrothermal biotite alteration zones and localised contacts between the host units and P1 porphyry (Fig. 10b-c).

Stage 2

Alteration - The second alteration stage was temporally related to emplacement of the P3 porphyry, P3 hydrothermal breccias and possibly the diorite dykes (Fig. 8). The earliest alteration identified with this stage involved intense K-feldspar replacement of the groundmass and primary plagioclase grains, and hydrothermal biotite replacement of primary mafic minerals. This potassic alteration has a smoky, light grey appearance that is particularly characteristic within P3 porphyries (Fig. 6c). The diorite dykes have a similar alteration assemblage but a slightly darker appearance. Development of new quartz veins and reopening of older veins was also related to this alteration phase. This alteration has a substantially lower vein density than the Stage 1 alteration (Fig. 7; Appendix D1).

A quartz-muscovite/illite ± pyrite (phyllic) alteration assemblage overprints the potassic-silicate alteration and early quartz ± molybdenite veins. The quartz-muscovite/illite alteration is defined by muscovite replacement of feldspar grains (Fig. 9e; Appendix D3), silicification of the groundmass and quartz infill in new or reopened fractures. Weak quartz-muscovite alteration is evident within the first three intrusive phases and dominantly restricted to the upper 150 m of the intrusive centre.

Hypogene Sulphides - Late quartz-muscovite-pyrite veins and thin pyrite veinlets overprint earlier stockwork. The quartz-pyrite veins with muscovite halos (Fig. 9f) are related to the weak phyllic alteration and veins mostly comprise pyrite infill. Minor chalcopyrite, bornite and molybdenite also precipitated along fracture planes. These veins are dominantly found within, or in close proximity, to the third intrusive phase. The P3 hydrothermal breccias have a quartz-muscovite-pyrite matrix with xenoliths of quartz-magnetite (Fig. 11a). This mineralisation event is distinguishable from stage 1 by a substantial decrease in Au, Cu and to a lesser extent Mo, but produced

Fig. 11. Photographs of alteration and mineralisation features at El Galeno. (a) Xenolith fragments of P1, P2, P3 and quartz-magnetite veins in the P3 hydrothermal breccia. The matrix of the breccia dominantly comprises quartz, muscovite and pyrite. DDH-GA-04 192.3 m. (b) Biotised MBx porphyry that contains thin quartz veins related to Stage 3 alteration. These veins have been reopened and infilled with molybdenite (Mo) and chalcopyrite (Ccp). Insert, plagioclase phenocryst with sieved-texture rim. DDH-GN-39 432 m. (c) Phyllic altered MBx porphyry with P1 porphyry fragment. Late pyrite veinlets crosscuts contact between the P1 fragment and MBX porphyry. Fine-grained plagioclase grains have been near completely replaced by muscovite/illite. DDH-GN-39 (435.8 m). (d) Photomicrograph of Stage 3 molybdenite and hematite (Hem; orange-brown). DDH-GN-39 432 m. (e) Photomicrograph of Stage 3 molybdenite, chalcopyrite and bornite (Bn). Late hematite partially replacing the copper-iron sulphide minerals, which are chalcopyrite and bornite. DDH-GN-39 432 m. (f) Chalcopyrite grain rimmed by late chalcocite (Cc) during secondary enrichment. DDH-GN-39 166.1 m.

zones with anomalously high Zn and Pb content (see below). Anomalously high Ag, Pb, and Zn grades are also associated with the hydrothermal breccia (Appendix D2). It is inferred that main stage deposition of Au, Cu and Mo occurred prior to emplacement of this phase.

Stage 3

Alteration - The youngest alteration event identified was temporally and spatially related to the emplacement of the final intrusive phase, i.e. MBx porphyry. Alteration is dark grey in appearance (Fig. 11b) and dominantly characterised by intense fine-grained hydrothermal biotitisation of magmatic mafic minerals plus the groundmass. Weak K-feldspar replacement of plagioclase and the groundmass was also associated with this event. Quartz-muscovite-pyrite (phyllic) alteration is evident near contacts between xenoliths and the magmatic breccia. This phyllic alteration is characterised by a high abundance (up to 15 vol. %) of disseminated fine-grained pyrite and intense muscovite replacement of feldspar (Fig. 11c).

Hypogene Sulphides - Several late veining events are temporally related with this alteration phase and contain similar mineralogy to the previous phases. The xenoliths display barren and mineralised veins that terminate at the fragment boundaries, which suggest that this mineralisation phase represents a new hypogene mineral deposition phase. However, as shown below metal grades associated with this intrusive-hydrothermal phase are the lowest of all the mineralising phases.

Sulphide minerals are commonly associated with zones of intense biotite and K-feldspar alteration. Early magnetite precipitation was followed by development of thin (~3 mm), wavy quartz veins. Quartz veins were later reopened and molybdenite, followed by pyrite, then chalcopyrite and bornite were deposited (Fig. 11b-e). These assemblages are crosscut by hairline pyrite veinlets (Fig. 11c). This late stage alteration also involved partial to complete hematite replacement of chalcopyrite and bornite (Fig. 11d-e). This was possibly associated with late fluorite-epidote-carbonate-quartz infill.

Secondary Enrichment & Weathering

Weak clay (argillic) alteration mostly occurs within the upper 10 m of the intrusive complex or zones with abundant fractures. In these zones, relict feldspar and mafic minerals have been replaced by kaolinite (Appendix D3).

Secondary mineralisation is restricted to a supergene blanket that extends *ca.* 120 m below the current surface (Fig. 5; Sillitoe, 2000a). Sulphide minerals present within the supergene blanket include chalcocite and minor covellite. Chalcocite replacement is mostly observed along the rims of both hypogene chalcopyrite and bornite (Fig. 11f). Metal grades within the supergene blanket range from 0.7 up to 1.2 % Cu. These grades are considerably higher than those related to hypogene mineralisation, which generally range between 0.2 and 0.3 % Cu. El Galeno also contains a leached cap that extends approximately 10 m below the surface.

D.5.4 Metal Grade versus Lithology

Average metal grades for the major lithological units identified in logged drill core have been calculated to help understand metal distribution. Contacts between the five major lithological units, i.e. the host sedimentary rocks and the four intrusive phases, were used to divide seven logged drill cores (GA-04, GN-36, GN-37, GN-39, GN-41, GN-42, GN-50) in to the five major rock units. Au, Cu, Mo, Ag, Pb and Zn assay data (Appendix D2) for each of the lithological units were added. The average and standard deviation of the five rock types were calculated for the six metals (Table 1). The total length of each lithological unit intersected in core was also added. The dyke and hydrothermal breccia units were rare in drill core and represent only a few metres of assay data analyses. Therefore, average metals grades for these units have been ignored due to a lack of data for comparison to the other rock units. Drill core GN-39 intersects all five lithological units and has been used to assess the correlation between the metals.

There is a considerable variation in metal grades between the five lithological units (Fig. 12). The standard deviations are mostly high and illustrate the heterogeneity of metal grade throughout each of the units. The highest average Au grades are associated with the P2 porphyry, followed by the P1 porphyry and host rock, and finally

Table 1: Average metal grades and standard deviation for identified lithological units in section A-A[1] at Galeno

	Host Rock		**P1 Porphyry**		**P2 Porphyry**		**P3 Porphyry**		**MBx Porphyry**		
	694 m		922 m		108 m		288 m		104 m		Total Length of Core
Metals	Avg	Std Dev	Avg	Std Dev	Avg	Std Dev	Avg	Std Dev	Avg	Std Dev	
Au (g/t)	0.10	0.10	0.11	0.13	0.14	0.11	0.04	0.03	0.05	0.05	
Cu (%)	0.49	0.26	0.22	0.25	0.32	0.28	0.06	0.04	0.10	0.06	
Mo (ppm)	128.6	89.3	82.6	111.6	61.1	46.3	43.8	107.7	48.3	37.4	
Ag (ppm)	3.75	3.97	1.66	1.61	1.34	0.79	2.16	5.23	1.81	0.99	
Pb (ppm)	90.1	401.0	37.1	65.1	17.9	17.7	100.1	357.9	11.8	8.5	
Zn (ppm)	191.7	661.6	76.7	121.7	44.1	34.4	121.3	195.5	41.1	21.0	

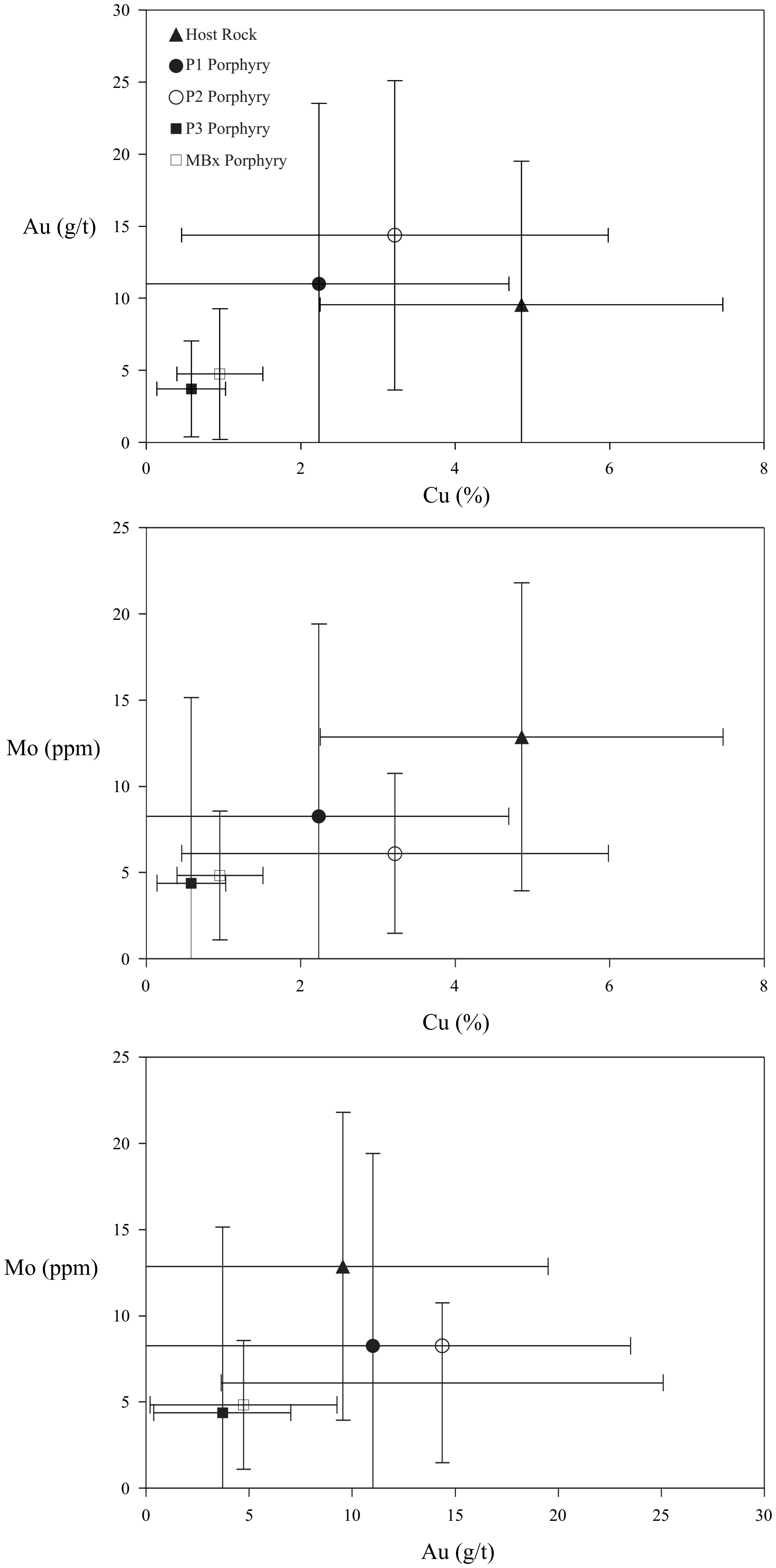

Fig. 12. Plots of average Au vs. Cu and Mo vs. Cu with standard deviation bars from assay data of drill core DDH-GN-39 (refer to Fig. 5).

by the youngest two intrusive phases that are generally poorly mineralised. High Au grades in the P2 porphyry were dominantly intersected toward the centre of the porphyry system. However, high grades are not observed within the same intrusive phase along the outer margins of the complex. High average Cu grades are associated with the oldest two intrusive units (P1 and P2) and extend a few metres into the host rock (Fig. 10), with the final two intrusive phases containing substantially lower grades. A large proportion of the highest Cu grades are located within a supergene enrichment blanket (Fig. 10), although the younger intrusions (P3 and MBx) contain only slightly lower hypogene Cu grades than P1 and P2 intrusions. Low Cu grades were intersected in all lithological units at depth. The host sedimentary rocks contain the highest Mo grades that tend to be spatially restricted along its contacts with the P1 porphyry (see D.5.3), which also contains elevated Mo. The remaining intrusions (P2 – MBx) contain less than half the average Mo grade of the mineralised sedimentary units. The host rocks and P3 porphyry contain the highest Ag, Pb and Zn grades (Appendix D2).

D.5.5 Interpretation of the El Galeno Deposit

Previous interpretations of El Galeno geology include a complex series of stratigraphically controlled sills and laccoliths that intruded along bedding planes or zones of weakness (Hammond, 1998). Recently, Sillitoe (2000a) suggested that several small, vertical, annular dykes intruded an early porphyry body that contains the majority of hypogene mineralisation. Based on observations from this study a revised version of the Sillitoe (2000a) model is presented for the El Galeno deposit.

Emplacement of the principal and earliest porphyry occurred at the intersection of a regional structure crosscut by an oblique secondary structure. The P1 porphyry is elliptical in plan with a northwest trend, similar to the localised structural fabric. Contacts between the intrusion and host rocks are vertical suggesting the intrusive body is an elongate vertical stock. These features indicate that emplacement of the principal El Galeno porphyry (P1) was dominantly structurally-controlled.

Early Mo precipitation occurred along the contacts of the P1 porphyry and host rocks. Candela and Piccoli (1995) showed that at low initial water content and a low

Cl/water ratio, Mo is preferentially partitioned from the melt into exsolved fluid compared to Cu. This suggests early Mo mineralisation is temporally associated with emplacement of the oldest and driest porphyry. Main stage Cu and Au deposition occurred during, or shortly after emplacement of the P2 porphyry, towards the core of the complex where temperatures would have been elevated. A pervasive quartz-magnetite alteration at depth and towards the core of the P1 porphyry possibly developed contemporaneously with emplacement of the P2 porphyry. Both the P1 and P2 porphyries have well-developed potassic alteration hosting modest hypogene mineralisation. The younger intrusions (P3 and MBx porphyries) are mostly evident in drill core, have potassic and phyllic alteration phases, and contain the lowest metal grades. These stocks are poorly mineralised and have a lower abundance of quartz stockwork than the earlier P1 and P2 porphyries. These intrusions are inferred to be late- to post-mineralisation. A substantial proportion of the higher Cu grades are associated with a supergene enrichment zone that extends up to 150 m beneath a thin leached cap. Sillitoe (2000a) suggested late glaciation might have removed a significant proportion of the leached cap and possibly a section of the immediately underlying sulphide enrichment zone.

D.6 Michiquillay

Michiquillay is a Cu-Au-Mo intrusive porphyry system with an indicated resource of 631 Mt at 0.69 % Cu, 0.15 g/t Au and between 100 to 200 ppm Mo with a supergene enrichment zone containing an estimated resource of 46.2 Mt at 1.15 % Cu (McInnes, 1997). The Michiquillay porphyry contains a leached cap (varying from a few metres up to 150 m thick) that overlies a secondary enrichment blanket (1.15 % Cu) extending up to a further 80 m. Exposures of the mineralised complex occur at altitudes from 3,500 to 3,750 m (Fig. 13).

Extensive mapping and drilling in the mid 1970’s by the Metal Mining Agency (MMA) defined the dimensions of the intrusive complex as being approximately 5 km in length and 1.5 km wide (Fig. 13). The main intrusive body is roughly parallel to the local NW structural trend. Laughlin *et al*. (1968) dated two intrusions in the Michiquillay region using the K-Ar technique. These include a quartz-biotite monzonite

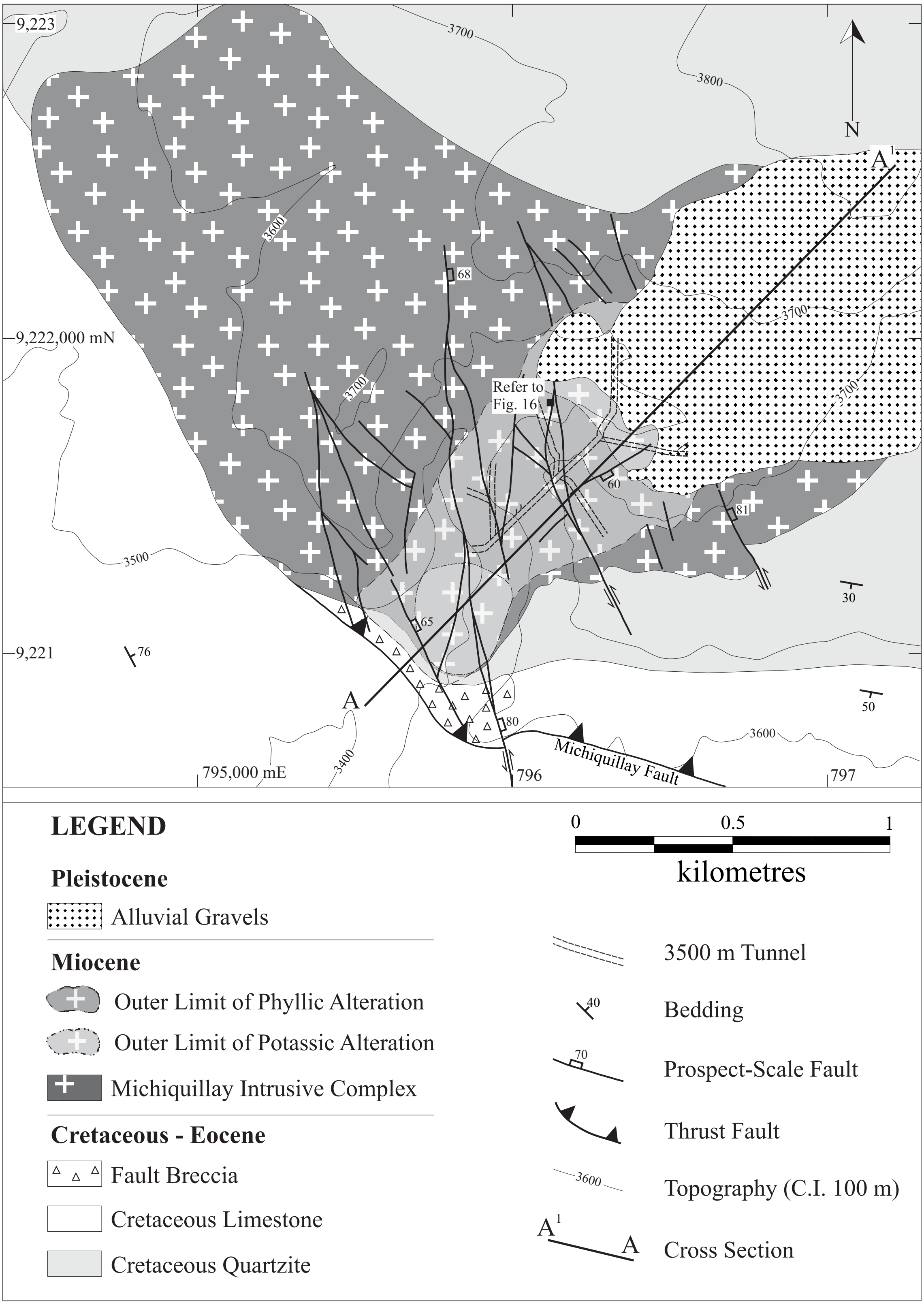

Fig. 13. Simplified geological map of the Michiquillay prospect [modified from previous mapping by MMA (1975)].

from the Michiquillay prospect that yielded an age of 20.6 ± 0.6 Ma (biotite) and a quartz-hornblende monzonite from the Michiquillay suite to the north that produced an age of 46.4 ± 1.8 Ma (hornblende). Llosa *et al*. (1996) obtained an age date of 18.8 ± 1.6 Ma (magmatic biotite) from an intrusion at the Michiquillay prospect also using the K-Ar technique. New $^{40}Ar/^{39}Ar$ age data (Section A) indicate emplacement of a synmineralisation stock at the Michiquillay prospect occurred at 19.77 ± 0.05 Ma. Whilst to the north of the prospect, a barren intrusion was emplaced at 20.6 ± 0.14 Ma (Section A). This indicates synmineralisation stocks at the deposit are slightly younger than unmineralised intrusions to the north.

D.6.1 Lithology

The Michiquillay intrusive centre is hosted within quartzite units to the north and limestone units to the south (Fig.13). At least two major intrusive phases were recognised during drill core logging based on textural evidence. The most common lithology is a medium-grained crowded porphyritic diorite (termed D1) with plagioclase, biotite and hornblende phenocrysts set in a feldspathic groundmass (Fig. 14a). Quartz phenocrysts are rounded, have a low abundance (between 0.5 and 4.0 vol. %) and occur in localised zones. Euhedral plagioclase phenocrysts (An_{42-52}) range from 0.3 to 5.0 mm and are the most abundant mineral (~35-45 vol %). Book-shaped euhedral biotite phenocrysts (~3 vol %) vary from 0.5 to 8 mm and generally contain minor feldspar inclusions. Hornblende phenocrysts (~1-3 vol %) are acicular and mostly 0.3 – 1.0 mm in length. Slight variations in grain-size and mineral abundance occur throughout the intrusive body, although no clear truncations or crosscutting relationships were observed making it difficult to distinguish discrete intrusive phases. Hollister and Sirvas (1974) referred to this as a quartz-biotite monzonite. However, petrographic evidence indicates primary feldspar phenocrysts are plagioclase and primary hornblende grains have been replaced by secondary biotite. Therefore, it is suggested this intrusive unit be classified as a biotite-hornblende diorite.

The second intrusive phase is weakly porphyritic and characterised by low vein abundance and intense biotite alteration (Fig. 14b-c). This medium- to fine-grained intrusive phase dominantly contains euhedral plagioclase phenocrysts (~15 vol %), plus

Fig. 14. Photographs of intrusive units, alteration and mineralisation features at Michiquillay. (a) The D1 porphyry consists of plagioclase, biotite and hornblende phenocrysts with a feldspathic groundmass. The groundmass has been partially to strongly overprinted by hydrothermal biotite (dark grey bottom left). Minor chalcopyrite (middle top) and pyrite (top right) is also present. H-22 176 m. (b) Medium-grained crowded D1 porphyry (left) truncated by a fine-grained dyke (right). Both intrusions contain minor quartz stockwork. J-20 170 m. (c) A dyke with plagioclase and biotite phenocrysts set in a groundmass that has been intensely replaced by hydrothermal biotite. Late pyrite and hematite veins crosscut the dyke. J-20 178.5 m. (d) Chalcopyrite and molybdenite mineralisation in a quartz vein. J-20 333.3 m. (e) Late pyrite veins with quartz-sericite halos crosscut the potassic altered D1 porphyry. I-23 268 m. (f) Quartz-sericite alteration has destructively replaced most primary igneous textures, although some grain boundaries are evident. Late thick pyrite veins are associated with the quartz-sericite alteration. L17.5 288 m.

biotised hornblende phenocrysts and euhedral biotite books (Fig. 14b). This second intrusive phase form sheets that range in thickness from 1 to 6 m (Fig. 15a). The dykes crosscut and truncate the potassic-altered main intrusion and contain xenoliths of the altered biotite-hornblende diorite (Fig. 14b). The dykes generally lack a well-developed stockwork. No quenched margins were observed along the rims of xenoliths. The dykes were only observed in the northeastern and southwestern zones of the complex. This phase is inferred to be a series of syn- to late-mineralisation vertical diorite dykes.

D.6.2 Structural Geology

The Michiquillay intrusive complex is located in the hanging wall of a NW-trending back thrust (Fig. 13) that was interpreted by Hollister and Sirvas (1974) to be crosscut by the NE-trending Encañada Fault. The latter fault was not recognised during aerial photo analysis or fieldwork by the author and its existence is suspect. The thrust dips at ~60^{o} towards the NE and is referred to as the Michiquillay Fault (Hollister and Sirvas, 1974; MMA, 1975). It is characterised by a matrix-supported breccia that contains both quartzite and limestone fragments, though no intrusive fragments were observed. The Michiquillay Fault was not intersected in drill core. However, in the southern zone of the deposit the reoccurrence of stockwork and change from potassic to phyllic alteration toward the bottom of some drill holes is interpreted to indicate the Michiquillay Fault is nearby (Appendix D4). In outcrop, oblique prospect-scale faults crosscut the porphyry deposit and were previously mapped by MMA (1975). These dominantly occur toward the centre of the deposit (Fig. 13) and are recognisable in outcrop by an increase in fracture density toward the central part of the fault zone. The faults are subvertical and dominantly strike either to the NNW or NNE (Section B.5.2).

The NNW-striking prospect-scale faults separate potassic alteration zones in the NE and SW of the complex, and define the outer limit of a strong phyllic alteration zone. An increase in stockwork density was noted along these fault planes (Fig. 16a). Some NNW fault planes contain localised zones of vuggy quartz that are spatially-associated with strong gossan-like oxidation features (Fig. 16b). The NNW-striking faults are the dominant fault set at the deposit and inferred to have strongly influenced

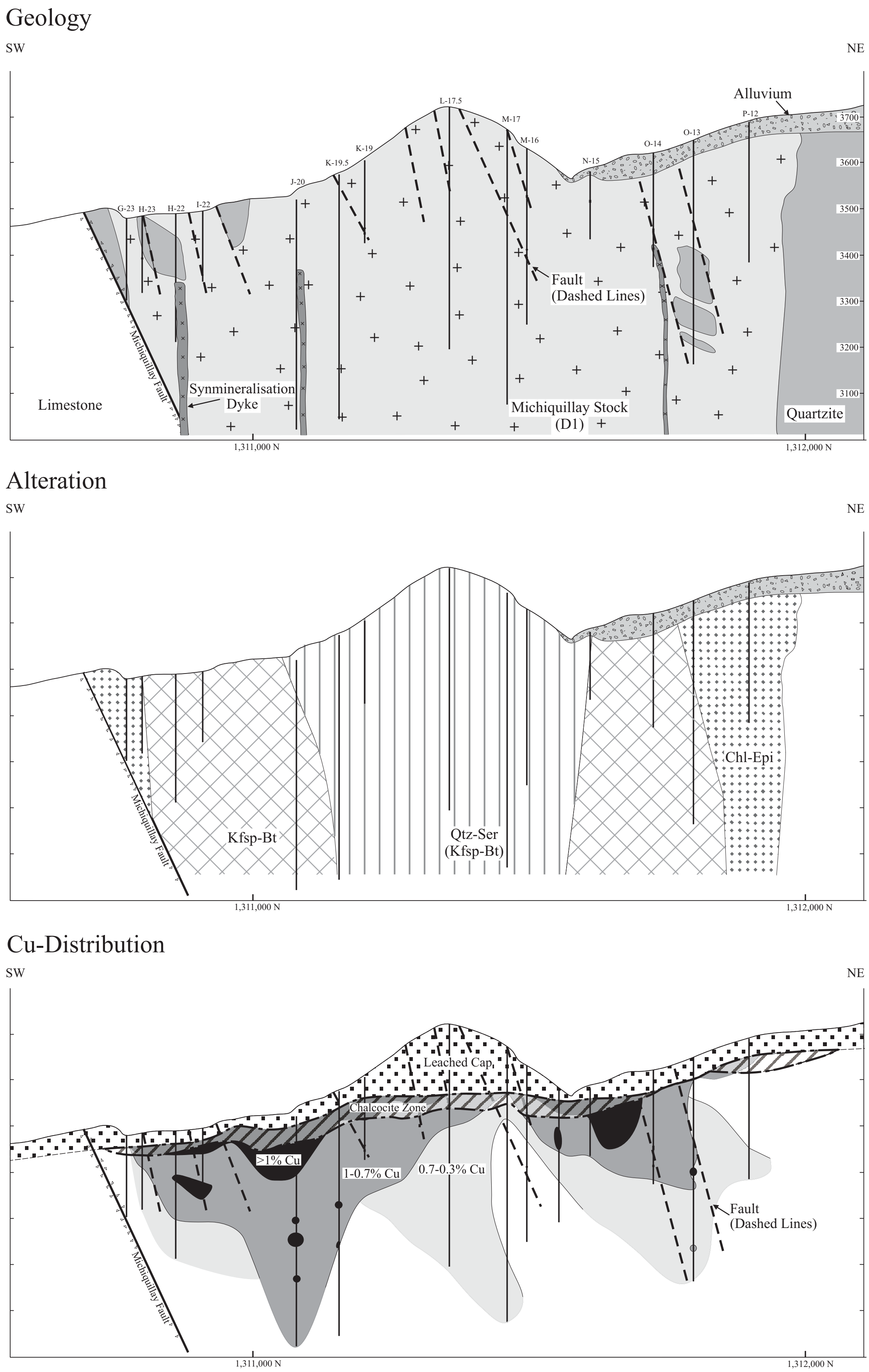

Fig. 15. Section A-A[1] looking NW, showing the major lithological units, alteration and Cu distribution at Michiquillay. Lithology and alteration distribution maps are based on logged drill cores and Cu grade map from assay data (see Appendix D4).

Fig. 16. Images of fault zones observed at Michiquillay. Refer to Fig. 13 for location. (a) Image of a fault plane showing strong quartz stockwork. Late subvertical slickenlines are also evident (centre). (b) A strongly oxidised fault within the D1 porphyry. The centre of the fault zone (bound by dotted lines) contains abundant hematite. Outside the hematite-rich zone, the silicic altered intrusive is strongly fractured.

both alteration and mineralisation. Steeply plunging slickenlines on some fault planes (Fig. 16a) indicate late subvertical displacement.

D.6.3 Alteration and Mineralisation

Both intrusive phases contain a well-developed K-feldspar-biotite-quartz-magnetite alteration assemblage. The potassic alteration is strongest in the northeastern and southwestern parts of the prospect (Fig. 15b), but extends only a few metres in the host rock. Surface expressions of the potassic alteration zones have a NE trend (Fig. 13). This alteration is characterised by the replacement of plagioclase by K-feldspar and the precipitation of fine-grained hydrothermal biotite that is strongly developed in the southwestern zone. The northeastern zone contains only moderate biotitisation but stronger K-feldspar-quartz alteration. Despite these slight variations, both the southwestern and northeastern zones display very similar alteration styles. Veins associated with the K silicate alteration include early thin (1-2 mm) wavy magnetite and biotite veins that are crosscut by quartz veins. Hypogene sulphides associated with the potassic alteration include chalcopyrite, molybdenite (Fig. 14d), pyrite and minor bornite. These minerals occur as infill in veins and fractures, as well as disseminated in the groundmass. Microscopic studies by MMA (1975) reported that pyrrhotite and sphalerite also precipitated during this stage. Based on logging results and corresponding assay data (Appendix D4), average hypogene grades for these zones are approximately 0.14 g/t Au and 0.8 % Cu.

Intense quartz-muscovite-pyrite (phyllic) and late kaolinite (argillic) alteration zones occupy the core of the complex (Fig. 15b). Quartz-pyrite veins with muscovite/illite (Appendix D3) halos are observed throughout the intrusive complex and crosscut all veins (Fig. 14e). Intense phyllic alteration has destructively overprinted older textures (Fig. 14f). Intensity of the quartz-muscovite alteration however weakens toward the edges of the core where it has partially replaced potassic-altered rocks. As mentioned above, NNW-striking faults are inferred to have controlled the distribution of these alteration assemblages. Sulphides precipitated during this alteration include large amounts of pyrite (Fig. 14f), plus minor molybdenite and chalcopyrite (McInnes, 1997). MMA (1975) also identified enargite, luzonite and tetrahedrite-tennantite within the central upper parts of the phyllic alteration zone. Au and Cu grades in this zone (0.08 g/t Au and 0.57 % Cu; Appendix D4) are lower than in the potassic alteration zones.

Michiquillay contains a supergene enrichment zone characterised by covellite and chalcocite replacement of hypogene chalcopyrite (Fig. 15c). Grades associated with this enrichment zone range from 2.2 to 0.5 % Cu, at an average of ~1.09 % Cu (McInnes, 1997). In parts, late clay (argillic) alteration partially to moderately overprints the quartz-muscovite alteration. Clay alteration is spatially associated with fault zones and extends to depths of 100 m below the surface. The composition of the clays was determined as kaolinite from X-ray diffraction analysis (Appendix D3). Late development of malachite is evident in both outcrop and on drill core.

D.6.4 Interpretation of the Michiquillay Complex

Based on the findings from this study combined with previous work (Hollister and Sirvas, 1974; MMA, 1975; McInnes, 1997) a revised model of the Michiquillay deposit is presented. Emplacement of the Michiquillay porphyry during early to middle Miocene times (~19.8 Ma) was structurally controlled by the Michiquillay Fault. The existence or significance of the Encañada Fault proposed by Hollister and Sirvas (1974) is unclear. Early potassic alteration developed along a NE trend and was associated with chalcopyrite, pyrite, magnetite, bornite and minor molybdenite mineralisation. Significant hypogene Cu and Au grades are preserved in the northeastern and southwestern potassic alteration zones. Late hydrothermal fluids related to phyllic and argillic alteration were transported along the NNW fault planes and overprinted earlier potassic alteration. An intense phyllic alteration zone located toward the centre of the deposit defines a pyritic-rich, low-grade zone. It is inferred that these late fluids remobilised some Cu and Au associated with early potassic alteration. The deposit contains a supergene enrichment zone located beneath a leached cap of varying thickness.

D.7 Pb Isotope Composition Of Sulphide Minerals

Pb isotope compositions of ores and igneous rocks have been used to infer the source of metals associated with central Andean (6^oS to 32^oS) magmatic-hydrothermal ore deposits [refer to Macfarlane (1999) and references therein]. Based on these compositions, Macfarlane *et al*. (1990) and Petersen *et al*. (1993) presented maps of the central Andes that identified three main Pb isotope provinces (Fig. 17). Pb isotope data defining province I are generally less radiogenic and interpreted to reflect a well-mixed sub-Andean mantle enriched by subducted sediment (Barriero, 1984; Macfarlane, 1999). Province III has elevated $^{207}Pb/^{204}Pb$ and $^{206}Pb/^{204}Pb$ values characteristic of upper crustal lead and is inferred to represent melting of an old felsic crust (Pichavant *et al*., 1988). Province II Pb isotope ratios lie between the two previous provinces. Macfarlane *et al*. (1990) interpreted these values to represent varying degrees of mixing between mantle-type (province I) and crustal-type (province III) sources. The Pb isotope compositions of chalcopyrite and pyrite separates from potassic altered synmineralisation intrusions at El Galeno, Michiquillay and Minas Conga were determined to assess for any systematic variation in the source of metals throughout the Cajamarca region. Additionally, chalcopyrite separates from the late poorly mineralised MBx porphyry at El Galeno and pyrite from a quartz-sericite altered intrusion at the Yanacocha mine were also analysed. Duplicate samples were also run for some of the samples. These analyses were conducted at the University of British Columbia and analytical procedures are reported in Appendix D5.

Pb isotope ratios of the sulphide minerals from the deposits display moderate scatter but tend to plot in steep linear trends (Fig. 18a; Table 2). Pyrite from Yanacocha has the least radiogenic Pb, whilst pyrite grains from Minas Conga generally are the most radiogenic. Of particular note, duplicate samples of sulphides show some variation (Table 2) but are generally within analytical error (Appendix D5). These variations in Pb isotope ratios may reflect either sample heterogeneity or thermal fractionation. Heterogeneity between the grains may result from mineral inclusions within the analysed grains. Alternatively, an external fluid or source, possibly from the host carbonate rocks, may cause heterogeneous grain compositions. Variations in Pb isotope compositions due to external fluid contributions, such as the host rocks, have been documented in late-stage sulphides at the Potrerillos deposit in Chile (see Tosdal *et al*.,

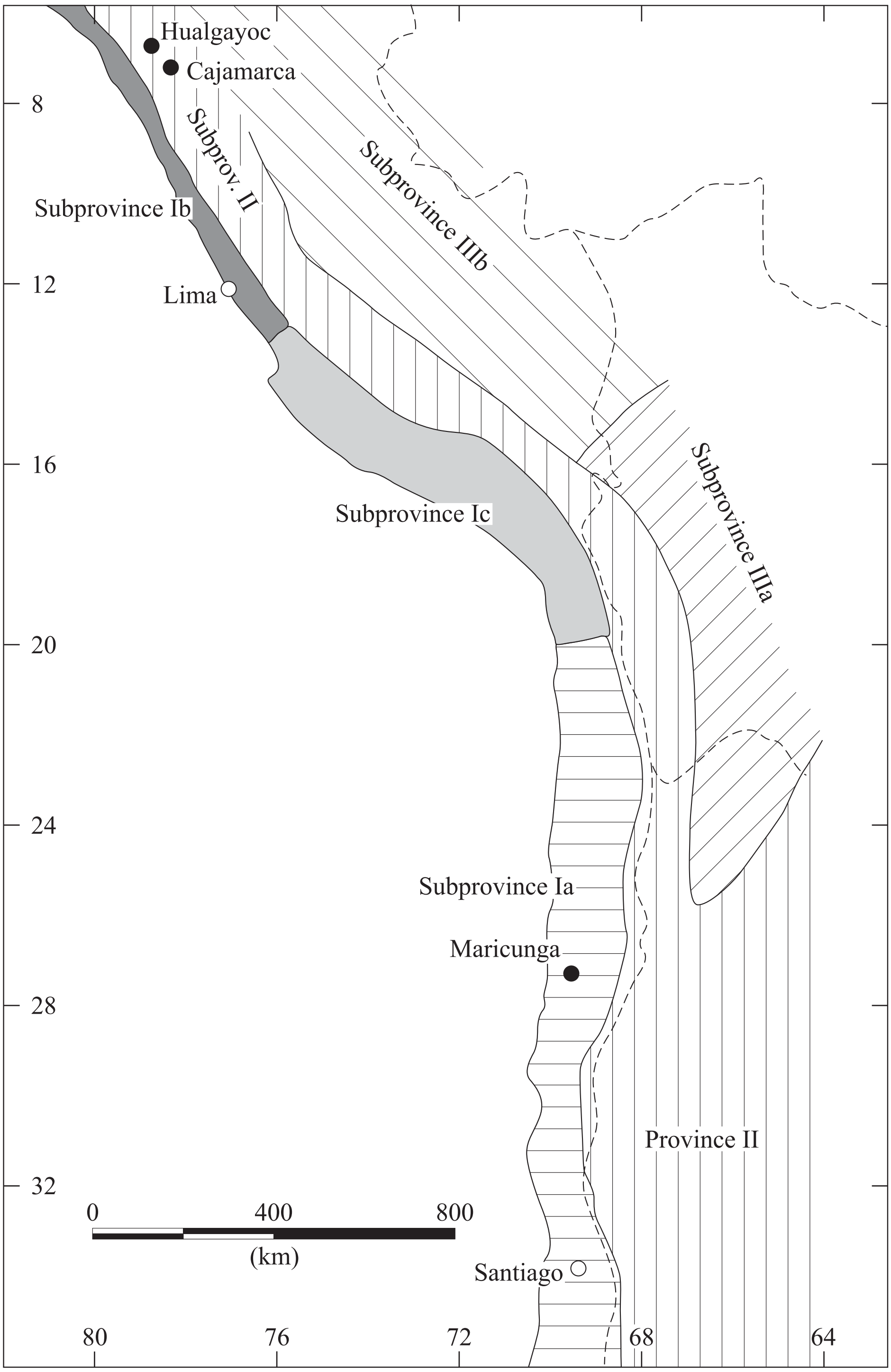

Fig. 17. Pb isotope map of the central Andes showing the provinces as proposed by Macfarlane *et al*. *(1990)* and Petersen *et al*. *(1993)*.

Fig. 18. A. Plots of Pb isotope ratios for sulphides from mineralised intrusions at the El Galeno (G), Michiquillay (MY), Minas Conga (MC) and Yanacocha deposits in the Cajamarca region. PYR = Pyrite; CCP = Chalcopyrite. B. Pb isotope compositions from previous studies of ores and igneous rocks from the Hualgayoc district (Macfarlane and Petersen, 1990) and fields for the various Andean Pb isotope provinces and subprovinces as defined by Macfarlane *et al*. (1990) and Petersen *et al*. (1993). S/K = average crustal growth curve of Stacey and Kramers (1975).

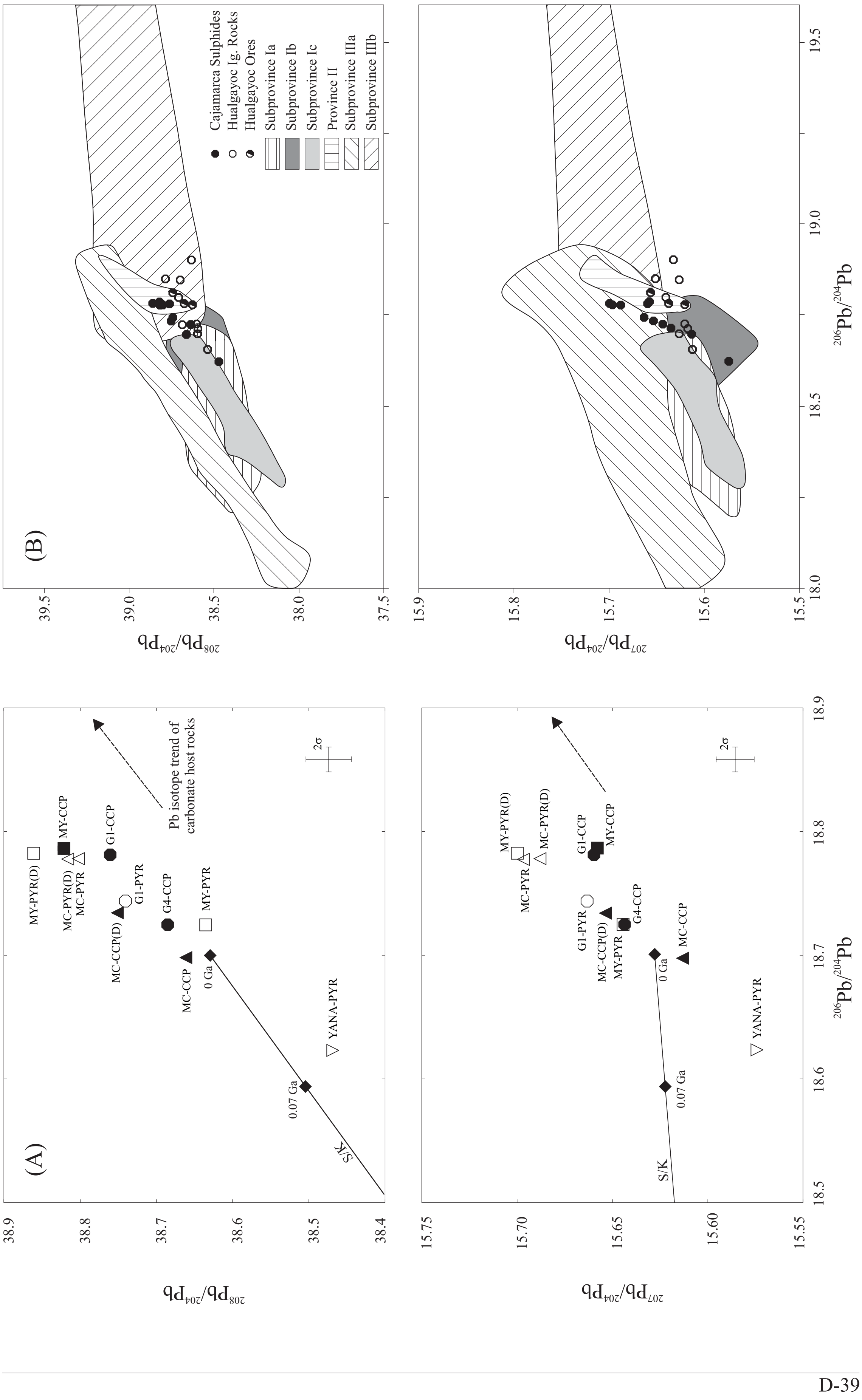

(A)
(B)
208Pb/204Pb
207Pb/204Pb
206Pb/204Pb
S/K
0 Ga
0.07 Ga
2σ
Pb isotope trend of carbonate host rocks
MY-PYR(D)
MC-PYR(D)
MC-PYR
MY-CCP
G1-CCP
G1-PYR
MC-CCP(D)
G4-CCP
MY-PYR
MC-CCP
YANA-PYR
Cajamarca Sulphides
Hualgayoc Ig. Rocks
Hualgayoc Ores
Subprovince Ia
Subprovince Ib
Subprovince Ic
Province II
Subprovince IIIa
Subprovince IIIb

Table 2. Pb isotope compositions of pyrites (PYR) and chalcopyrites (CCP) from mineralised porphyritic intrusions in the Cajamarca region.

Sample No.	Deposit	Drill Core	Depth (m)	Intrusion	Alteration Zone	Sulphide	$^{206}Pb/^{204}Pb$	$^{207}Pb/^{204}Pb$	$^{208}Pb/^{204}Pb$	$^{207}Pb/^{206}Pb$	$^{208}Pb/^{206}Pb$
G1-CCP	Galeno	GN-39	166.1	P1 Porphyry	Potassic	Chalcopyrite	18.7813	15.6597	38.7608	0.8338	2.0638
G1-PYR	Galeno	GN-39	166.1	P1 Porphyry	Potassic	Pyrite	18.7440	15.6633	38.7405	0.8356	2.0668
G4-CCP	Galeno	GN-39	432.0	MBx Porphyry	Potassic	Chalcopyrite	18.7071	15.6348	38.6853	0.8358	2.0680
MY-PYR	Michiquillay	J-20	346.7	D1 Porphyry	Potassic	Pyrite	18.7248	15.6439	38.6349	0.8355	2.0633
MY-PYR(D)	Michiquillay	J-20	346.7	D1 Porphyry	Potassic	Pyrite	18.7826	15.7000	38.8606	0.8359	2.0690
MY-CCP	Michiquillay	J-20	346.7	D1 Porphyry	Potassic	Chalcopyrite	18.7865	15.6577	38.8215	0.8335	2.0665
YANA-PYR	Yanacocha	CLL-05	569.0	Tonalite	Quartz-Sericite	Pyrite	18.6234	15.5742	38.4688	0.8363	2.0656
MC-CCP	Minas Conga	H-1	151.5	Main Diorite	Potassic	Chalcopyrite	18.6980	15.6132	38.6605	0.8350	2.0676
MC-CCP(D)	Minas Conga	H-1	151.5	Main Diorite	Potassic	Chalcopyrite	18.7342	15.6536	38.7507	0.8356	2.0685
MC-PYR	Minas Conga	H-1	151.5	Main Diorite	Potassic	Pyrite	18.7778	15.6968	38.8161	0.8359	2.0672
MC-PYR(D)	Minas Conga	H-1	151.5	Main Diorite	Potassic	Pyrite	18.7781	15.6878	38.8013	0.8355	2.0664

Results have been normalized using a fractionation factor of 0.15% based on multiple analyses of NBS981 standard lead, and the values in Thirlwall (2000).

(D) = duplicate samples

1999 and references therein). Sedimentary host rocks in the Cajamarca region have more radiogenic Pb and flatter Pb ratio trends compared to sulphides (Fig. 18a: Macfarlane, 1999). Therefore, the host rock compositions cannot solely account for the sulphide steep linear trend (Fig. 18a). Finally, analytical error, such as thermal fractionation in the mass spectrometer, may also account for some of the variation in the data (Tosdal, *pers. commun.*, 2002).

Regionally, pyrite from Yanacocha has the least radiogenic Pb and plots toward the nonradiogenic end of the province Ib array (Fig. 18b). Pyrite from Michiquillay, and chalcopyrite from the MBx porphyry at El Galeno also lie at the nonradiogenic end of the data and within the province Ib array. Chalcopyrites from the main intrusions at El Galeno, Michiquillay and Minas Conga have very similar Pb isotope compositions that plot between the end members of the province I and II arrays. In contrast, pyrites from Minas Conga and possibly Michiquillay have elevated $^{208}Pb/^{204}Pb$ and $^{207}Pb/^{204}Pb$ values. These samples plot toward the radiogenic end of the province II array (Fig.18b). With the exception of pyrite from Minas Conga and Michiquillay(?), these results overlap with Pb isotope compositions of ores and igneous rocks from the Hualgayoc region (Macfarlane and Petersen, 1990).

D.8 Discussion

D.8.1 Variations in Mineralised Porphyry Complexes

The Cajamarca district hosts a number of mineralised porphyry and high-sulphidation systems that display varying mineralisation and alteration styles. Three mineralised porphyry associations, El Galeno (Cu-Au-Mo porphyry), Michiquillay (Cu-Au-Mo porphyry) and the Chailhuagon-Perol (Au-Cu) porphyry complexes at Minas Conga (Llosa and Veliz, 2000) were emplaced within 6 m.y. of each other but have significantly different metal grades (Table 3). Turner (1999) suggested one of the principal differences between the various high-sulphidation systems in the Cajamarca region relates to level of erosion. He argued that the Yanacocha Au mine represents a high-level epithermal system characterised by phreatic breccias and has a poorly-understood structural control, whereas Sipán and La Zanja are relatively deeply-eroded

Table 3: Summary of the El Galeno, Michiquillay and Minas Conga porphyry centres.

	El Galeno[1]	**Michiquillay**[1, 2]	**Chailhuagon (Minas Conga)**[3, 1]	**Perol (Minas Conga)**[3]
Metal Association	Cu-Au-Mo	Cu-Au-Mo	Au-Cu	Au-Cu
Resource	486Mt @ 0.57% Cu + 0.14g/t Au	631Mt @ 0.69% Cu + 0.15g/t Au	102Mt @ 0.9g/t Au + 0.30% Cu	428 Mt @ 0.8g/t Au + 0.31% Cu
Age (Ma)	17.5 – 16.5	20.6 – 19.8	23.2 – 17.1	23.2 – 17.1
Intrusion Type	Hornblende-Biotite Diorite	Hornblende-Biotite Diorite	Hornblende-Biotite Diorite	Hornblende-Biotite Diorite
No. Intrusions Recognised	4	2	2	3
Dimensions of Principal Intrusive	1250 x 600 m (NW oriented)	5000 x 1500 m (NW oriented)	2000 x 500 m (N-S oriented)	1600 x 650 m (NW oriented)
Host Rock Type	Qtzte, Sst and Sh	Lst and Qtzte	Lst and Marl	Lst, Marl and MGD
Elevation (m.a.s.l.)	3,850 – 4,000	3,500 – 3,750	3,840 – 3,900	3,870 – 3,960
Structural Control of Porphyry Emplacement	Located at the intersection of several structures	Emplaced within the hanging wall of reverse fault	Located at the intersection of N- and NW-trending faults	NW-trending Perol Thrust Fault
Brecciation	Minor hydrothermal breccia, post-mineralisation magmatic breccia	Minor magmatic breccia, generally absent	Absent	Absent
Principal Alteration Phases	K, QM, QS, CbEF	K, M, QS, E, Cl	K(+M), QS, Skn, Q, CbE	K(+M), QS, Skn, AA
Quartz Stockwork	Moderate – Strong	Moderate – Strong	Strong	Strong-moderate
Controls on Mineralisation	Dominantly Intrusion Related	NNW faults and NE alteration trend	Intrusion and Vein Related	Intrusion and Vein Related
Main Hypogene Sulphides	Py, Ccp, Mo	Ccp, Pyr, Mo	Ccp, Bn, Py	Ccp, Bn, Py
Supergene Blanket	Present (0-120 m)	Present (0-40 m)	Absent	Poorly Developed (<50 m)
Supergene Sulphides	Cc, Cv	Cc, Cv	Cc, Cv	Cc, Cv
Leached Cap	Thin (<10 m)	Moderate-Thick (up to 80 m)	Absent	Absent

Rock Types: Qtzte = quartzite; Sst = sandstone; Sh = shale; Lst = limestone; MGD = microgranodiorite
Alteration Phases: K = potassic; Q = quartz/silicic; M = magnetite; S = sericite; Skn = skarn; AA = advanced argillic; Cb = carbonate; E = epidote; F = fluorite; Cl = clay
Sulphides: Py = pyrite; Ccp = chalcopyrite; Mo = molybdenite; Bn = bornite; Cc = chalcocite; Cv = Covellite
1 = This Study; 2 = MMA (1975), McInnes, (1997); 3 = Llosa and Veliz (2000)

systems where magmatic plus hydrothermal breccias predominate and structural controls are more clearly recognised. The following paragraphs compares and contrasts early Miocene porphyry-related deposits in the Cajamarca region. The aim of this is to identify the key process that caused the variation in metal grades amongst the deposits.

El Galeno is dominantly hosted in quartzites, Michiquillay in both quartzites and limestones, whereas the Minas Conga systems are mostly hosted in limestones and marls. Host rocks with low permeability, such as marbleised limestone, minimise lateral flow of hydrothermal fluids, thereby focusing metalliferous fluids to the host intrusion and possibly increasing metal concentrations (Sillitoe, 2000b). El Galeno, Michiquillay and Chailhuagon deposits consist of early to middle Miocene hornblende-biotite diorites that are geochemically very similar (Section C.12.1). Chailhuagon is the oldest complex and the main porphyritic stock was emplaced ~23.2 Ma (Llosa *et al*., 1996). Drilling at both Chailhuagon and Perol has defined post-mineralisation stocks at depth that significantly reduces the Au-Cu grade of both deposits (Llosa and Veliz, 2000). Michiquillay contains two recognisable synmineralisation intrusions that were emplaced at approximately 19.8 Ma (Section A). El Galeno is the youngest system (17.5 – 16.5 Ma) and has the most complex intrusive history, with at least four intrusive phases present. The earliest two intrusions at El Galeno are synmineralisation, whilst the final two represent late- to post-mineralisation porphyries. Post-mineralisation low-grade or barren stocks are however common features of both Au-rich and Cu-Au-Mo porphyry deposits (e.g. Maricunga belt, Vila and Sillitoe, 1991; Bajo de la Alumbrera, Ulrich and Heinrich, 2001; Sillitoe, 2000b).

Multiple alteration stages at El Galeno were temporally related to the emplacement of different intrusions. The earliest two porphyries are characterised by K-feldspar-biotite alteration and an intense quartz-magnetite alteration at depth. Potassic alteration is weakly overprinted by quartz-muscovite alteration associated with emplacement of later intrusions. At Michiquillay, the distribution of the two dominant alteration assemblages, i.e. potassic and phyllic, was controlled by NNW-trending prospect-scale faults. Intense potassic alteration consisting of K-feldspar, biotite and widespread magnetite defines the Chailhuagon main porphyritic stock. Both Galeno and Michiquillay lack widespread hydrothermal magnetite throughout the deposit. Au-rich porphyry deposits, such as Grasberg (Meinert *et al*., 1997; Pollard and Taylor, 2002), Far South East (Hedenquist *et al*., 1998) and Bajo de la Alumbrera (Ulrich and Heinrich, 2001), are commonly characterised by abundant hydrothermal magnetite associated with an early potassic alteration (Clark and Arancibia, 1995; Sillitoe, 2000b). All three mineralised centres in the Cajamarca district contain weak silicic, propylitic and late carbonate alteration. Skarn alteration is also evident at Perol and to a lesser extent at Chailhuagon.

Significant differences between the three mineralised porphyry centres relate to the hypogene sulphide assemblage and the presence or absence of a well-developed phyllic alteration. At El Galeno, hypogene Cu and Au grades are temporally and spatially associated with the two earliest intrusions. Potassic alteration zones in these intrusions have a high quartz stockwork density. Pyrite, molybdenite and to a slightly lesser extent chalcopyrite largely form the hypogene sulphide assemblage. At Michiquillay, high hypogene grades occupy zones of intense potassic alteration and are associated with chalcopyrite, pyrite, molybdenite and minor bornite. Late-stage fluids transported along NNW-trending faults at the prospect resulted in development of a low-grade, pyrite-rich phyllic core that overprinted the early potassic alteration. Gammons and Williams-Jones (1997) suggest late-stage fluids associated with phyllic overprinting have the potential to remobilise significant quantities of Au and Cu. Such a scenario is proposed for Michiquillay, where late-stage fluids remobilised early potassic alteration-related Cu and Au mineralisation away from the centre of the deposit. In contrast to Michiquillay and El Galeno, high metal grades at Chailhuagon are deficient in molybdenum. High hypogene Au and Cu grades are characterised by abundant bornite, magnetite and chalcopyrite. A strong association between gold and bornite mineralisation has been documented at other Au-rich porphyry deposits such as Bingham (Ballantyne *et al*., 1997) and Grasberg (Rubin and Kyle, 1997). However, where bornite is absent or chalcopyrite is more abundant than bornite, gold distribution is generally closely associated with chalcopyrite (Ballantyne *et al*., 1997, Ulrich and Heinrich, 2002; Kesler *et al*., 2002). Experimental studies of Au distribution for high temperature (400^{o} to 700^{o}C) porphyry copper deposits indicate that bornite is the dominant host of Au at temperatures of 700^{o}C or greater (Fig. 19; Simon *et al*., 2000). Additionally, chalcopyrite preferentially precipitates over bornite and magnetite at lower temperatures and oxygen fugacity. These authors also showed that when

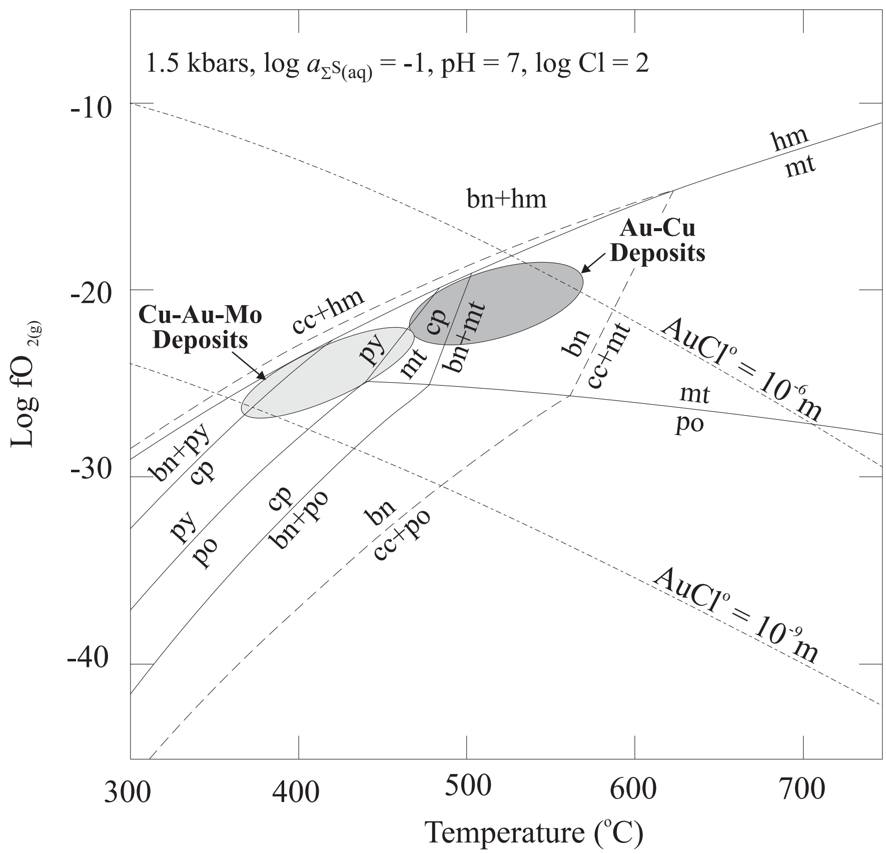

Fig. 19. Temperature-oxygen fugacity diagram for the Fe-Cu-S-O system with contours for solubility AuCl° (adapted from Simon *et al*. 2000). Main stage mineralisation at the Au-Cu type deposits, such as Chailhuagon and Perol, are inferred to have formed at higher temperatures and oxygen fugacity than Cu-Au-Mo type deposits, such as Michiquillay and El Galeno.

experimentally equilibrated with Au, chalcopyrite was found to contain one order of magnitude less Au than bornite.

The highest Cu grades at El Galeno are spatially-restricted to a secondary enrichment blanket that may have been partially removed during glaciation. Michiquillay also contains supergene enrichment zone of ~45 m thickness that is located beneath a moderately thick (up to 80 m) leached cap. In contrast, supergene enrichment and chalcocite-covellite replacement is very rare at Minas Conga.

Pb isotope compositions of sulphides from potassic alteration zones at three of the deposits, El Galeno, Michiquillay and Chailhuagon, plot on steep linear trend that suggests a common deep source. Pb isotope ratios of chalcopyrite from the Au-rich Chailhuagon deposit lie toward the centre of the Andean province I array. Sulphide Pb ratios from El Galeno and Michiquillay plot within the radiogenic end of the province I isotope array and overlap with previous Pb isotope compositions of ores and igneous rocks from the Hualgayoc region (Macfarlane and Petersen, 1990). Chalcopyrite from the Chailhuagon intrusion extends in to the radiogenic end of the Andean province II array. These results are consistent with a deep, possibly upper sub-Andean mantle, source that has been enriched by subducted sediment and undergone limited mixing of upper crustal material (Macfarlane, 1999).

D.9 Conclusion

The Cajamarca region hosts a number of significant Miocene porphyry-related deposits, including El Galeno (Cu-Au-Mo), Michiquillay (Cu-Au-Mo) and Minas Conga (Au-Cu). Despite significantly varying in Au and Cu concentrations, synmineralisation intrusions at these deposits have similar geochemical compositions and trends (Section C). New sulphide Pb isotope data show some variation but are consistent with a common mantle-dominated source. Based on observations presented in this section, a key difference between Au and Cu concentrations at the deposits is proposed to be the physio-chemical conditions associated with early stage hypogene mineralisation. Deposits at the Au-rich Minas Conga centre have a well-developed potassic alteration zone comprised of ubiquitous hydrothermal magnetite and a high temperature-oxygen fugacity hypogene sulphide assemblage dominated by bornite and chalcopyrite. These features conform to a generalised model for most Au-rich porphyry-related deposits found along the Andes and worldwide (Sillitoe, 2000b). Michiquillay and El Galeno are Cu-Au-Mo deposits that fit to generalised model for Andean porphyry Cu deposits proposed by Sillitoe (1988). These deposits contain an early potassic alteration overprinted by phyllic alteration, and in contrast to Minas Conga, lower temperature hypogene sulphide assemblages characterised by chalcopyrite and pyrite. Other factors that influenced metal grades between the deposits may include the occurrence of late-stage fluids resulting in development of an intense phyllic alteration and remobilisation of early potassic alteration-related metals, presence of widespread hydrothermal magnetite, complexity of intrusive history and host rock type.

SECTION E

Controls on formation of Miocene porphyry and high-sulphidation deposits in the Cajamarca Au District, northern Peru

Section E: Controls on formation of Miocene porphyry and high-sulphidation deposits in the Cajamarca Au District, northern Peru

E.1 Abstract

This section presents a model for the formation of Miocene mineralised centres in the Cajamarca region. Geochemical data for Miocene mineralised centres indicate metals and hydrous magmas were derived from partial melting of deep, amphibole-rich source, most likely upper mantle to lower crust. These magmas ascended rapidly along deeply tapping faults during brief changes in the tectonic stress and were emplaced in a highly fractured upper crust. The locations of magmatic and hydrothermal centres were controlled by zones of weakness in the upper crust, such as structural intersections between regional-scale faults and superimposed oblique faults. Fracture, vein and fault trends in the mineralised dioritic intrusions developed as a response to a regionally-extensive stress regime. Variations in metal grades at the early Miocene (23-17 Ma) porphyry deposits reflect differences in temperature and oxygen fugacity conditions during the precipitation of early-stage hypogene sulphides. Development of late Miocene (12.5-11 Ma) high-sulphidation deposits coincided with subduction of the Inca plateau, as well as cessation of crustal thickening and uplift. The timing of these Miocene deposits shows no direct correlation with either the Incaic or Quechua orogenic events, but a strong association with high plate convergence rates. It is suggested that porphyry-related and high-sulphidation deposits formed as a result of a combination of geological processes triggered by changes in the tectonic stress.

E.2 Introduction

Gold-rich porphyry deposits tend to cluster in geographically restricted belts or districts (Sillitoe, 2000b). The Cajamarca mining district of northern Peru and the Central Andean transect (24^{o} to 30^{o}S), as defined by Sasso and Clark (1998), are two such districts that host an unusually high concentration of Au-rich deposits compared to other Andean metalliferous districts. The Cajamarca district hosts a number of significant late Miocene (12.5-10.9 Ma) high-sulphidation deposits, including South America's largest Au mine at Yanacocha, and early Miocene (23.2-16.5 Ma) porphyry-related deposits (Fig. 1). Porphyry deposits include the Au-rich Minas Conga (Chailhuagon and Cerro Perol) and Cerro Corona deposits, as well as the Cu-Au-Mo Michiquillay and El Galeno deposits. The Au-rich deposits, Minas Conga and Cerro Corona (Hualgayoc region), have amongst the lowest Cu/Au atomic ratios (~8,500-15,500) of known porphyry copper deposits throughout the world (Kesler *et al*., 2002).

Both the Au-rich central Andes and Cajamarca districts host significant Tertiary epithermal and porphyry-related deposits. However, the central Andes also contain a number of giant Tertiary porphyry Cu deposits characterised by economically significant supergene enrichment zones. Clusters of gold-rich and copper-dominated deposits within the Central Andean transect show a common deep-level tectonomagmatic evolution. Geochemical modelling and structural observations reveal magmas formed during mineralisation episodes equilibrated with amphibole- to amphibole-garnet-bearing mineral residues and ascended along deeply tapping structures to shallow crustal levels (Kay *et al*., 1999; Richards *et al*., 2001; Chernicoff *et al*., 2002). Additionally, the geology, alteration and mineralisation styles of these central Andean deposits have been well documented. Compared to the central Andes, the tectonic, magmatic and upper crustal ore-forming processes that operated during the formation of mineralised centres in the Cajamarca district are poorly understood. This section presents a top-to-bottom model for the formation of Miocene deposits in the Cajamarca region based on geochronological, geochemical, structural and deposit geology studies.

E.3 Geological Setting

Cajamarca is located in the Western Cordillera of the northern Peruvian Andes, ~685 km north of Lima. This region is situated in the southern section of the Huancabamba Deflection where there is a significant change in the structural grain from the dominant NW Andean trend to near E-W. Cajamarca is located above a present day zone of flat subduction (Fig. 1). During Tertiary times, Cretaceous sedimentary rocks were folded and thrusted by several compressive orogenic events (Mégard, 1984).

Fig. 1. Location of Miocene deposits in the Cajamarca region of northern Peru, situated at the southern tip of the Huancabamba deflection and above the present day flat subduction zone where the dip of the subducting slab is ~10^{o} (Barazangi and Isacks, 1979). Also shown are some of the significant Tertiary porphyry and high-sulphidation deposits in the central Andean transect (24^{o}S-30^{o}S; adapted from Sillitoe, 1991; Noble and McKee, 1999).

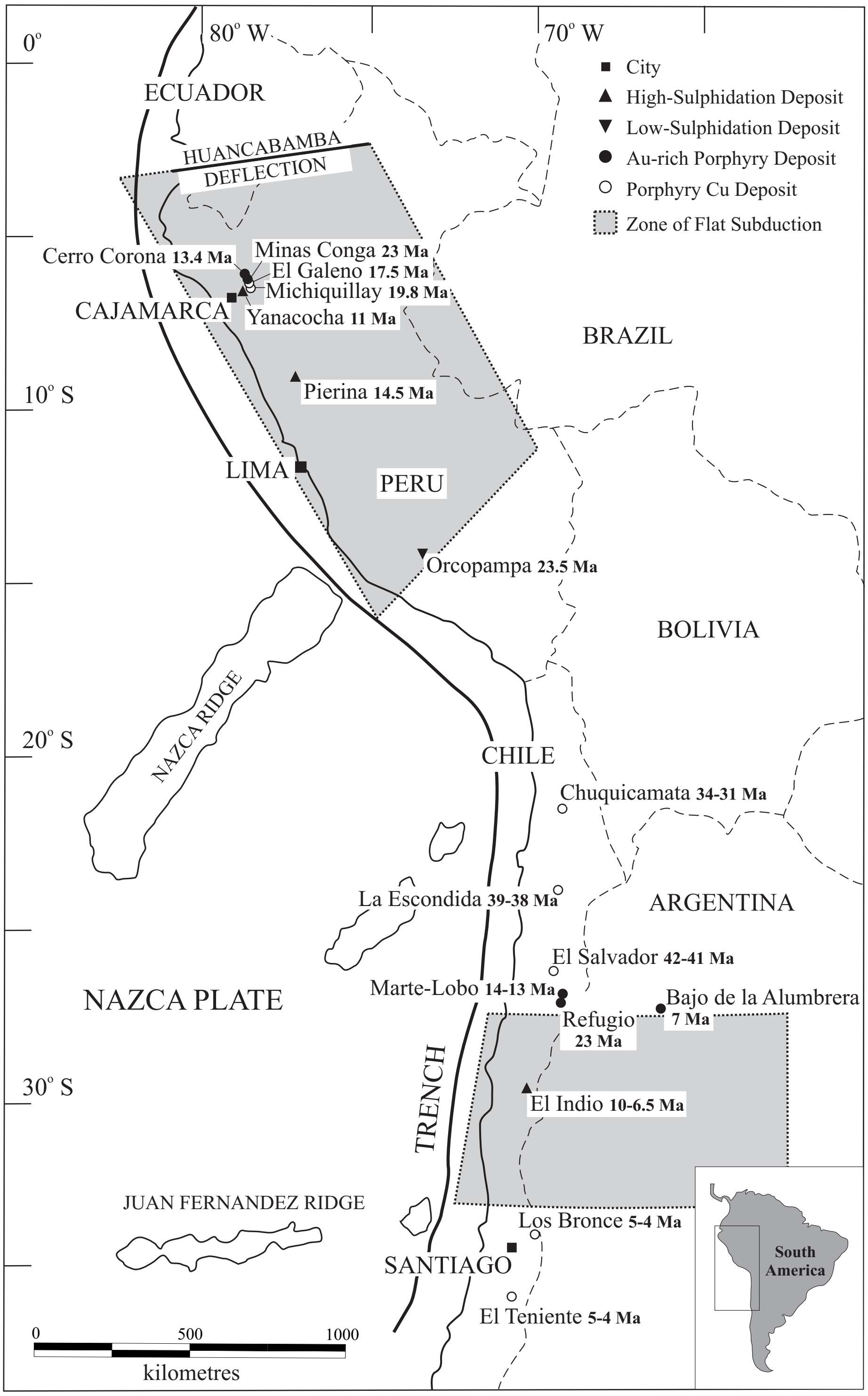
0°
80° W
70° W
City
High-Sulphidation Deposit
Low-Sulphidation Deposit
Au-rich Porphyry Deposit
Porphyry Cu Deposit
Zone of Flat Subduction
ECUADOR
HUANCABAMBA DEFLECTION
Cerro Corona 13.4 Ma
Minas Conga 23 Ma
El Galeno 17.5 Ma
Michiquillay 19.8 Ma
CAJAMARCA
Yanacocha 11 Ma
BRAZIL
10° S
Pierina 14.5 Ma
LIMA
PERU
Orcopampa 23.5 Ma
BOLIVIA
NAZCA RIDGE
20° S
CHILE
Chuquicamata 34-31 Ma
La Escondida 39-38 Ma
ARGENTINA
El Salvador 42-41 Ma
Marte-Lobo 14-13 Ma
NAZCA PLATE
Bajo de la Alumbrera 7 Ma
Refugio 23 Ma
30° S
El Indio 10-6.5 Ma
TRENCH
JUAN FERNANDEZ RIDGE
Los Bronce 5-4 Ma
SANTIAGO
El Teniente 5-4 Ma
0
500
1000
kilometres
South America

Palaeocene-Miocene magmas were channelled along deeply tapping faults and emplaced in zones of weakness in the highly fractured upper crust. Palaeogene igneous rocks commonly crop out in the footwall of the thrust fault, whereas most Neogene rocks are located in the hanging wall.

E.4 Re-evaluation of the Magmatic History of the Cajamarca Region

Tertiary igneous rocks intrude and unconformably overlie a deformed package of Cretaceous sedimentary rocks. The igneous rocks formed over two major magmatic intervals; these include Palaeogene (57.0-35.4 Ma) and Miocene magmatism (23.2-7.2 Ma). Palaeogene magmatic rocks comprise intermediate volcanic rocks belonging to the lower Llama Formation and coeval porphyritic intrusions. Peak Palaeogene magmatism (~43 Ma) roughly coincided with both the Incaic II orogenic event (43-42 Ma, Benavides, 1999) and the end of a high convergence rate period (49-42 Ma, Pardo-Casas and Molnar, 1987). This magmatic interval persisted until middle Oligocene times (~35 Ma, Noble *et al*., 1990), after which low convergence and magmatic quiescence characterised northern Peru. Gabbroic dykes were however emplaced at high crustal levels at *ca*. 29.5 Ma.

Commencement of early Miocene (23.2 Ma) magmatism roughly corresponded with the Incaic IV orogenic pulse (22 Ma, Benavides, 1999) and a change back to high convergence rates (Pardo-Casas and Molnar, 1987). Synmineralisation intrusions at porphyry-related deposits and regional coeval barren stocks were emplaced during the initial 7 m.y. of this magmatic interval (23.2-16.5 Ma; Llosa *et al*., 1996; Section A). Interestingly, no volcanic rocks have yet been dated for this interval. A cluster of age dates between 17.9 and 16.5 Ma signifies the termination of both early Miocene magmatism and prolific porphyry Cu formation. This 1.4 m.y. period coincided with the Quechua I orogenic event (17 Ma, Benavides, 1999). The locus of magmatic activity shifted to the polymetallic Hualgayoc district between 16.8 and 12.5 Ma (Borroden, 1982; Macfarlane *et al*., 1994; James, 1998; Noble and McKee, 1999). Widespread alteration and mineralisation near Hualgayoc occurred from 14.5 to 13.0 Ma (Macfarlane *et al*., 1994). The locus of magmatic activity changed back to near Cajamarca between 12.3 and 8.4 Ma. This late Miocene magmatism was characterised by widespread volcanism and formation of the high-sulphidation Yanacocha Au district (Turner, 1997). Significantly, formation of the Yanacocha Au district correlates with subduction of the Inca plateau (12-10 Ma) and flatting of the subduction dip angle (Gutscher *et al*., 1999). Magmatic activity terminated following the Quechua II orogenic event (7-8 Ma, Benavides, 1999).

Based on dates from Miocene mineralised centres in central and northern Peru, Noble and McKee (1999) argued magmatic-hydrothermal activity in the arc occurred over short-lived pulses with periods from 13 to 15.5 Ma and 7 to 10 Ma relating to intervals of increased mineralisation. Geochronological results from this study indicate that both prolonged (~7 m.y. during the early Miocene) and short-lived (at *ca*. 13.5-12.5 and 11.5-10.9 Ma in the middle-late Miocene) mineralisation intervals took place in northern Peru. These new $^{40}Ar/^{39}Ar$ dates also show mineralisation events did not necessarily coincide with the either the Inca or Quechua orogenic events, as previously proposed by Noble and McKee (1999).

E.5 Petrogenesis of Tertiary Igneous Rocks

Tertiary igneous rocks in the Cajamarca region are predominantly medium- to high-K calc-alkaline rocks that show typical magmatic arc affinity with enrichment of large ion lithophile elements (LILE) and light rare earth elements (LREE) relative to high field strength elements (HFSE). The oldest of these are Palaeocene-Eocene intrusive and volcanic rocks (57-43 Ma) of intermediate composition with moderate to flat REE profiles (average La_N/Yb_N ratio of 9). These rocks have primitive isotope compositions (Fig. 2a, Table 1), although some appear to have been contaminated by material with a low ε_{Nd} and high Sr_i, possibly seawater. Partial melt modelling suggests these melts were derived from a garnet-poor residue dominated by pyroxene and olivine, whilst mineral assemblages indicate magmas were dry melts (<3 wt % H_2O). Oligocene gabbroic dykes (29 Ma) have tholeiitic compositions and relatively flat REE profiles (La_N/Yb_N ratios of 4 to 11). Rare earth element modelling indicates these gabbros were derived from partial melting of a primitive mantle that was in equilibrium with olivine and pyroxene residue minerals. The dykes have primitive isotopic ratios (Fig. 2a) and display no clear evidence of upper crustal contamination. At present, no

Fig. 2. (A) Sr and Nd isotope plot of Tertiary igneous rocks in the Cajamarca-Hualgayoc region and Miocene mineralised districts in Chile. Igneous rocks from Cajamarca display limited evidence of upper crustal contamination. Note that synmineralisation rocks from Cajamarca and the Los Bronce-El Teniente regions have relatively primitive isotope compositions compared to other deposits of similar age. (B) Sulphide Pb isotope trends from mineralised Miocene intrusions in Cajamarca compared to Pb isotope trends of Au-rich and Ag-rich deposits in northern Chile and southern Peru (adapted from Tosdal *et al*., 1999). Tosdal (1995) proposed Au-rich deposits in northern Chile contained lower $^{208}Pb/^{204}Pb$ at any given $^{206}Pb/^{204}Pb$ value than Ag-rich deposits indicating greater crustal influence. Sulphides from Cajamarca plot to the right of the Chilean Au-rich deposits, suggesting even greater crustal influence. These isotope compositions and trends are consistent with deposits in the Pb isotope province II defined by Macfarlane *et al*. (1990) and suggest an upper mantle to lower crustal source. S/K = average crustal growth curve of Stacey and Kramers (1975).

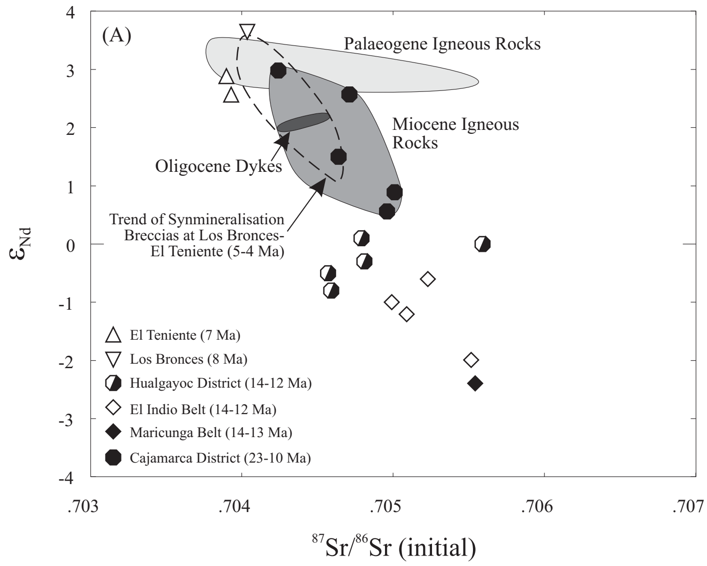
(A)
Palaeogene Igneous Rocks
Miocene Igneous Rocks
Oligocene Dykes
Trend of Synmineralisation Breccias at Los Bronces-El Teniente (5-4 Ma)
El Teniente (7 Ma)
Los Bronces (8 Ma)
Hualgayoc District (14-12 Ma)
El Indio Belt (14-12 Ma)
Maricunga Belt (14-13 Ma)
Cajamarca District (23-10 Ma)
ε_{Nd}
$^{87}Sr/^{86}Sr$ (initial)

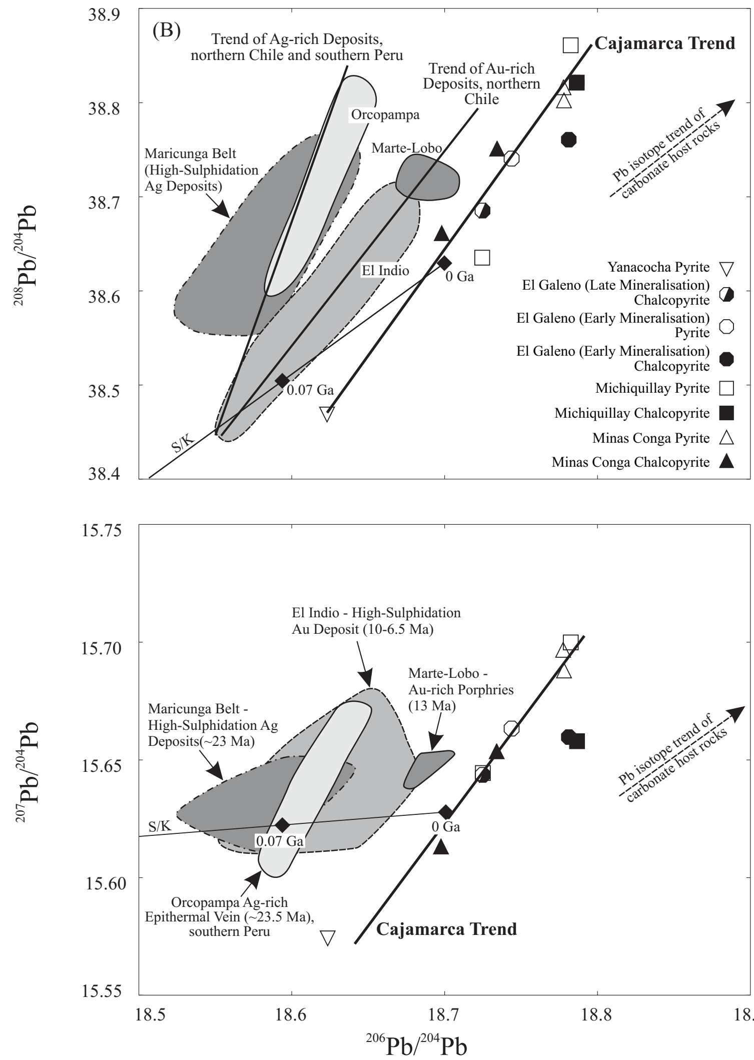
(B)
Trend of Ag-rich Deposits, northern Chile and southern Peru
Trend of Au-rich Deposits, northern Chile
Cajamarca Trend
Orcopampa
Marte-Lobo
Maricunga Belt (High-Sulphidation Ag Deposits)
El Indio
0 Ga
0.07 Ga
S/K
Pb isotope trend of carbonate host rocks
Yanacocha Pyrite
El Galeno (Late Mineralisation) Chalcopyrite
El Galeno (Early Mineralisation) Pyrite
El Galeno (Early Mineralisation) Chalcopyrite
Michiquillay Pyrite
Michiquillay Chalcopyrite
Minas Conga Pyrite
Minas Conga Chalcopyrite
$^{208}Pb/^{204}Pb$
El Indio - High-Sulphidation Au Deposit (10-6.5 Ma)
Marte-Lobo - Au-rich Porphries (13 Ma)
Maricunga Belt - High-Sulphidation Ag Deposits(~23 Ma)
Orcopampa Ag-rich Epithermal Vein (~23.5 Ma), southern Peru
$^{207}Pb/^{204}Pb$
$^{206}Pb/^{204}Pb$

Table 1. Results from radiogenic Sr, Nd (Section C) and Pb (Section D) analyses. Sample numbers in bold represent intrusions from mineralised centres

Sample No.	Location	Rock Type	Age (Ma)	Rb ppm	Sr ppm	$(^{87}Rb/^{86}Sr)_m$	$(^{87}Sr/^{86}Sr)_m$	$(^{87}Sr/^{86}Sr)_i$	Sm ppm	Nd ppm	$(^{147}Sm/^{144}Nd)_m$	$(^{143}Nd/^{144}Nd)_m$	$\varepsilon_{Nd(0)}$		$^{206}Pb/^{204}Pb$	$^{207}Pb/^{204}Pb$	$^{208}Pb/^{204}Pb$
S-46	Co Perol East	Intrusion	57.0	56.2	699	0.233	0.70422	0.70403	3.29	14.43	0.1361	0.512779	2.76				
S-31	Co Montana	Intrusion	47.0	58.1	1246	0.135	0.70556	0.70547	4.51	21.07	0.1294	0.512781	2.79				
S-32	Cruz Conga	Volcanic	43(?)	82.5	925	0.258	0.70399	0.70383	2.95	14.89	0.1197	0.512814	3.44				
S-21	La Carpa	Volcanic	42.6	67.6	938	0.209	0.70483	0.70470	2.38	12.17	0.1180	0.512803	3.22				
S-16	South Galeno	Dyke	29.4	23.4	322	0.211	0.70465	0.70455	1.12	3.74	0.1812	0.512751	2.20				
S-57	South Galeno	Dyke	29.4	29.9	516	0.168	0.70436	0.70428	2.54	11.24	0.1364	0.512742	2.03				
S-Chail	Minas Conga	Intrusion	23.2	54.9	693	0.229	0.70472	0.70464	1.21	5.65	0.1291	0.512715	1.50	ccp	18.6980-18.7342	15.6132-15.6536	38.6605-38.7507
														pyr	18.7778-18.7781	15.6878-15.6968	38.8013-38.8161
S-11	Aurora Patricia	Intrusion	21.3	59.8	559	0.310	0.70482	0.70473	1.42	5.98	0.1436	0.512691	1.04				
S-H22	Michiquillay	Intrusion	19.8	42.8	672	0.184	0.70429	0.70424	2.37	11.87	0.1205	0.512791	2.98	ccp	18.7865	15.6577	38.8215
														pyr	18.7248-18.7826	15.6439-15.7000	38.6349-38.8608
S-59	Michiquillay North	Intrusion	20.6	62.4	392	0.461	0.70458	0.70445	1.75	8.89	0.1189	0.512695	1.10				
S-T2	El Galeno	Intrusion	17.5	53.4	530	0.291	0.70508	0.70501	0.44	2.87	0.0916	0.512684	0.89	ccp	18.7813	15.6597	38.7608
S-38	La Carpa	Intrusion	17.9	80.1	784	0.296	0.70463	0.70456	1.06	6.01	0.1061	0.512728	1.76				
S-T4	El Galeno	Intrusion	16.5	56.8	586	0.281	0.70478	0.70471	2.89	13.87	0.1261	0.512770	2.57	ccp	18.7071	15.6348	38.6853
S-CLL5	Yanacocha	Intrusion	10.0	84.4	881	0.278	0.70500	0.70496	0.92	7.60	0.0728	0.512667	0.56	pyr	18.6234	15.5742	38.4688
S-MC4	South Minas Conga	Volcanic	9(?)	75.1	632	0.344	0.70472	0.70468	1.79	8.90	0.1212	0.512728	1.75				

All $^{143}Nd/^{144}Nd$ are relative to La Jolla-Nd = 0.511860; all $^{87}Sr/^{86}Sr$ are relative to SRM987-Sr = 0.71024; m = measured; i = initial

$\varepsilon_{Nd(0)}$ calculated for present-day CHUR = 0.512638

Pb isotope reactor of 0.15% based on muliple analyses of NBS981 standard lead, and the values in Thrilwall (2000) mineralisation is known to have been associated with Palaeogene magmatism.

Miocene intrusive and volcanic rocks (23-7 Ma) are intermediate to acidic in composition and have steep, HREE-depleted profiles (La_N/Yb_N ratios ranging from 7-21). Miocene synmineralisation intrusions have similar geochemistry to coeval barren stocks indicating a common origin. However, synmineralisation stocks are slightly enriched in Th suggesting greater fractionation. Partial melting models and isotope compositions (Fig. 2a) indicate early-middle Miocene magmas were derived from partial melting of an amphibole-rich source that was in equilibrium with minor amounts of garnet (possibly upper mantle to lower crust). These magmas assimilated minimal upper crustal material. Two early Miocene intrusions (S-T4 and S-H22) have considerably less radiogenic Nd and Sr compositions than intrusions of similar age. Sulphide Pb isotope compositions from mineralised deposits form steep trends consistent with an upper sub-Andean mantle source (Fig. 2b, Table 1). Late Miocene igneous rocks have more evolved Sr and Nd isotope compositions that are interpreted to signify crustal thickening. Partial melting models of these rocks also imply higher garnet content (up to 17%) in the residue than the early-middle Miocene magmas. Differences in isotopic compositions and modelled residual mineralogy between early and late Miocene rocks are inferred to reflect an evolving magmatic arc undergoing extensive uplift, rapid increase in crustal thickness and deepening of the mantle-crust boundary. Similar modelled changes in residual mineralogy (clinopyroxene $\Rightarrow$ amphibole $\Rightarrow$ garnet) have been linked with periods of crustal thickening and formation of Miocene hydrothermal deposits in the Central Andes (Kay *et al.*, 1991; Kay and Mpodozis, 2001).

E.6 Structural Controls at Mineralised Centres

Structural investigations reveal the dominant fault arrays in the Cajamarca region have progressively rotated in a clockwise direction from NE-trending during Eocene times to NNW-trending in the early-middle Miocene and finally NW in the late Miocene. Rotation of these fault arrays was temporally related to counterclockwise rotation of the subducting Nazca plate relative to the South America plate. This suggests changes in plate motion induced rotation of the horizontal principal stress field from

SW-oriented during most of the Palaeogene to near E-oriented since early Miocene times. Rotation of the principal stress direction resulted in NNW and NW-trending Miocene faults superimposed on Eocene NE-trending faults. Fault intersections generated by superimposed faults on pre-existing structures provided important channelways for later magmatic and hydrothermal fluids.

Both mineralised and barren Miocene intrusions are elliptical in plan with the long axes roughly parallel to local large-scale structure(s). Similar alignment of pre-existing local structures and the long axes of elliptical intrusions suggest the stocks intruded a highly fractured, anisotropic crust (Nakamura, 1977; Takada, 1994). The majority of these Miocene intrusions are spatially associated with the Puntre Thrust Fault. Structural observations along sections of the fault suggest normal displacement along the fault plane during the flow of mineralising fluids. During periods of relaxation or extension in subvolcanic environments, structural intersections between deeply-tapping faults and subordinate oblique faults provide favourable channelways for ascending magma melt and hydrothermal fluids (Gow and Ord, 1999; Tosdal and Richards, 2001; Richards *et al*., 2001). Since late Oligocene times, the high Peruvian Andes have been dominated by an extensional regime (Sebrier and Soler, 1991) providing favourable conditions for ascent of magmas. Though Bellier *et al*. (1989) showed that the maximum principal stress direction in the high Andes oscillated from vertical to horizontal throughout Neogene times. Plate tectonic data combined with field relationships indicate that Miocene intrusions were emplaced at structural intersections in a highly fractured upper crust during changes in the tectonic stress.

Fracture arrays at porphyry Cu deposits are influenced by either regional and/or localised tectonic stresses that result in linear fracture-vein arrays, or by magmatic influenced stress that produces concentric and radial fracture-vein arrays (c.f. Tosdal and Richards, 2001). Three distinct fault-fracture-vein arrays (NE, N-S and NW striking) have been identified at Minas Conga and Michiquillay (Llosa and Veliz, 2000; Section B). These regular array orientations are interpreted to have resulted from a tectonic influenced stress regime. In contrast, fractures at El Galeno have a random orientation and no clear preferred orientation. These arrays may have resulted either from overprinting of multiple fracture events, or alternatively indicate a dominantly magmatic stress field. Significantly, the most common fractures at El Galeno (NNW-trending) are subparallel to arrays at Minas Conga and Michiquillay. These results suggest a regionally extensive stress field influenced fault-fracture arrays at all three porphyry complexes. In the Laramide region of North America, similar regional systematic fracture patterns in plutons and their wall rocks have been related to regional stress fields (Heidrick and Titley, 1982).

Conjugate structural relationships are observed in both early Miocene porphyry-related and late Miocene high-sulphidation deposits. Both the Michiquillay and Yanacocha deposits have overall NE trends that are crosscut by ore-controlling NW-striking faults. At these deposits, subvertical NW-striking faults display sinistral movement whereas NE-trending faults are dextral, with both fault orientations also displaying late vertical movement (Longo, 2000; Section B). This implies the maximum principal stress direction during formation of this deposit rotated, possibly numerous times, between horizontal E-directed (strike-slip) and vertical (extension). Tosdal and Richards (2001) suggest episodic rotations of the regional stress field are unlikely during short time spans in which porphyry Cu deposits form (<1 m.y.). Therefore, rotations of the stress direction during hydrothermal activity are inferred to result from a low-differential stress field and fluctuating fluid pressures.

E.7 Deposit Geology

Porphyry-related deposits near Cajamarca formed during early to middle Miocene times (23.2 to 16.5 Ma) are associated with dioritic intrusions. These deposits are mostly located in the hanging wall of Puntre Thrust Fault. Synmineralisation intrusions share similar geochemical and sulphide Pb isotope compositions indicating a common origin (probably upper mantle to lower crust) for both the intrusions and metals. Mineralisation at the porphyry deposits occurs as both disseminated and in stockwork. However, despite these similarities the deposits display a number of significant differences that include variations in the Au/Cu ratio.

The Au-rich Minas Conga (23.2 Ma) and Minas Carpa (~17.5 Ma?) deposits are hosted in limestones, contain abundant hydrothermal magnetite, display a strong Au-Cu association with bornite-chalcopyrite mineralisation, lack a well-developed phyllic alteration and have preserved quartz-alunite lithocaps. These deposits have characteristics consistent with generalised Au-rich porphyry models (Sillitoe, 2000b, Kesler *et al.*, 2002), and close similarities to Au-rich dioritic porphyries in the Maricunga Belt in Chile (Vila and Sillitoe, 1991). In contrast, Michiquillay (19.8 Ma) and El Galeno (17.5-16.5 Ma) are Cu-Au-Mo deposits hosted in quartzites ± limestones and contain modest (45-100 m thick) supergene enrichment zones with Cu grades of >1 %. Hypogene pyrite-chalcopyrite mineralisation was associated with potassic alteration. Late, pyritic phyllic alteration zones that are slightly gold depleted overprint the potassic alteration zones. These Cu-Au-Mo deposits have characteristics typical of generalised porphyry Cu systems (Titley and Beane, 1981).

Deposits with high-sulphidation systems in the region include Tantahuatay (12.4 Ma; Macfarlane *et al.*, 1994), Sipán and Yanacocha (11.5-10.9 Ma, Turner, 1997). These formed *ca*. 10-5 m.y. after development of the major porphyry Cu deposits. A synmineralisation intrusion beneath the Yanacocha epithermal systems has slightly elevated SiO_2 (69 wt% SiO_2) compared to early Miocene synmineralisation stocks (avg. 65 wt% SiO_2). These deposits are characterised by acid-sulphate (alunite) alteration, but their settings and mineralisation styles vary significantly (Turner, 1999). In contrast to the structurally controlled caldera-related Sipán and La Zanja deposits, Yanacocha displays a greater degree of brecciation, lithological control and resurgent magmatic-hydrothermal activity (Turner, 1999). Intriguingly, pyrite from a mineralised intrusion at the Yanacocha Au mine has a less radiogenic Pb isotope composition than sulphides from early Miocene porphyry deposits reflecting an enriched mantle source (Fig. 2b).

Tosdal (1995) showed Au-rich deposits in northern Chile generally contained lower $^{208}Pb/^{204}Pb$ at any given $^{206}Pb/^{204}Pb$ value than Ag-rich deposits, which he interpreted to indicate a higher crustal influence (Fig. 2b). Sulphide Pb isotope results from this study show even lower $^{208}Pb/^{204}Pb$ values than the Chilean Au-rich deposits suggesting even greater crustal influence or alternatively mixing with subducted sediments (Macfarlane, 1999). Cajamarca is located within a Pb isotope province defined by a mantle source region mixed with either subducted sediment or crustal rocks (province II, Macfarlane *et al.*, 1990), compared to the Chilean deposits that are situated in province I characterised by a mantle-dominated source. Additionally, metamorphic basement rocks in northern Peru have much higher $^{206}Pb/^{204}Pb$ values than their equivalents in southern Peru and northern Chile (Macfarlane, 1999). Pb isotope compositions from Cajamarca might be expected to display higher $^{206}Pb/^{204}Pb$ had they been crustally contaminated. However, Sr-Nd-Pb isotope compositions from the Cajamarca-Hualgayoc region provide limited evidence of crustal contamination (Macfarlane, 1999; Section C). Therefore, Au enrichment in the Cajamarca region does not appear to have been influenced by crustal contamination.

E.8 Tectonomagmatic Model for Formation of Miocene Deposits

Recently, Shatwell (2002) proposed that Miocene Au-Cu deposits in the Cajamarca region formed due to subduction of the Inca Plateau (12-10 Ma). He proposed this led to shallowing of the slab dip angle and rapid erosion that caused fluctuations in the lithostatic-hydrostatic pressure boundaries. However, this argument ignores the fact that the early Miocene porphyry-related deposits formed 5-11 m.y. earlier. In addition, erosion surfaces observed in central Peru are noticeably absent in the Cajamarca region.

Initiation of mineralisation during early-middle Miocene times was triggered by an increase in plate convergence rates that resulted in the generation of hydrous (>3 wt % H_2O) melts from the breakdown of an amphibole-rich upper mantle (Fig. 3). Highly oxidised, H_2O-rich mafic melts have high sulphur solubility and are effective carriers of chalcophile elements (Burnham, 1979). In contrast, Palaeogene melts derived from an olivine-pyroxene residuum were relatively dry (<3 wt % H_2O) and poor carriers of chalcophile elements. This change from a pyroxene- to amphibole-dominated magma source occurred in the Cajamarca region is unclear. A similar correlation between periods of prolific mineralisation and magmas derived from an amphibole-rich source has also been proposed for formation of Miocene deposits in Chile (Kay *et al*., 1991; Kay *et al*., 1999; Kay and Mpodozis, 2001).

Commencement of high convergence rates in early Miocene times would have induced an E-W directed horizontal maximum principal stress on the magmatic arc. The lower crust would have been characterised by horizontal compression, whilst principal stress directions in the upper crust rotated between horizontal and vertical. Hydrous

Fig. 3. Schematic cross section through the northern Peruvian Andes illustrating the proposed tectonomagmatic model for Miocene deposits in the Cajamarca Au district. (A) Early-middle Miocene magmas developed beneath a thickening crust during the breakdown of amphibole-bearing mineral assemblages in the upper mantle. Deep level ponds of hydrous- and sulphur-rich magmas developed and were recharged by melts with primitive isotope compositions. Magmas ascended rapidly along deeply tapping faults, underwent minimal contamination and emplaced in a highly fractured upper crust. Host rock type, temperature and oxygen fugacity conditions during early potassic alteration, and presence of late-stage fluids strongly influenced the type (Au-rich vs. Cu-Au-Mo) of porphyry deposits formed. (B) Late Miocene high-sulphidation deposits formed during termination of crustal thickening and uplift, as well as the onset of a flattening of the subduction zone due subduction of the Inca plateau. Late Miocene magmas have slightly more evolved isotope compositions and modelling indicates higher garnet mineral residue content than the early Miocene magmas. Intriguingly though, ore pyrite from the Yanacocha deposit has less Pb isotope compositions than sulphides from early Miocene deposits. The high-sulphidation deposits all contain acid-sulphate alteration but show significantly different settings and mineralisation styles.

(A) Early-Mid Miocene Magmatism (23.2-16.5 Ma)

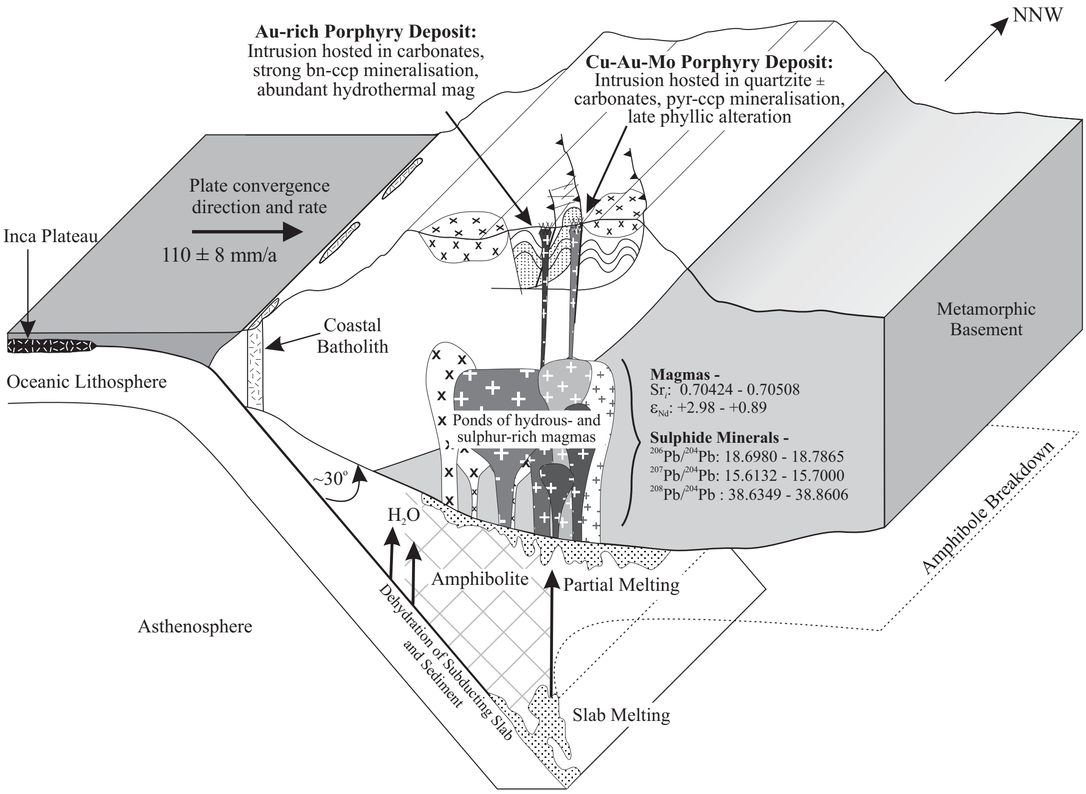

(B) Late Miocene Magmatism (12.5-10.9 Ma)

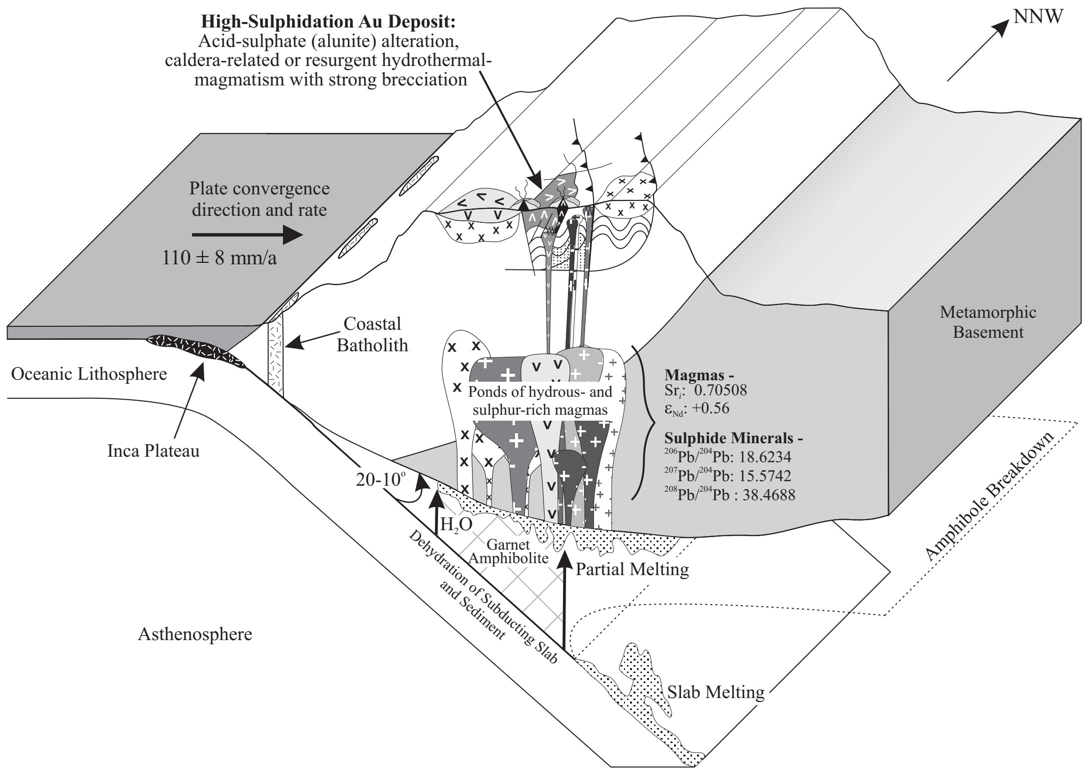

parental melts generated from partial melting of the amphibolite mantle ascended into deep levels of the thickening crust and formed large magma ponds (Fig. 3). Under compressional conditions, magmas would not easily migrate upwards and would have evolved at depth (Campos *et al*., 2002). Behn *et al*. (2001) suggest batholithic, deep crustal ponds of mafic to intermediate melts underlie metalliferous regions in Chile. Primitive isotopic compositions of some early Miocene magmas and late Miocene sulphides suggests these deep crustal ponds were replenished with newly generated oxidised melts that contributed significant amounts of magmatic water and sulphur. Or alternatively, primitive zones in an isotopically zoned pond or deep magma chamber were tapped during magma release. Water-rich primitive magmas were released from the ponds and ascended rapidly along deeply tapping faults during brief changes in the tectonic stress. Rapid ascent of the magmas minimised upper crustal contamination or mid-upper crustal ponding, thereby preventing potential loss of their Au and Cu content (c.f. Clark, 1993; Zentilli and Maksaev, 1995; Oyarzun *et al*., 2001). These uncontaminated magmas were emplaced in the hanging wall of the Puntre Thrust Fault (Fig. 3), commonly at structural intersections and during normal displacement along the fault plane.

Country rock type influenced the duration of solidification or development of an outer shell for the dioritic stocks. Highly fractured quartzite host rocks had a high permeability and metal-bearing hydrothermal fluids flowed both laterally and vertically. In contrast, contacts of carbonate rocks were marbleised thereby lowering permeability. Rocks with low permeability inhibit lateral fluid and heat flow thereby focussing metalliferous fluids within the intrusion and minimising metal loss into the host rock (Sillitoe, 2000b). Synmineralisation intrusions hosted in carbonates, such as Minas Conga (Au-Cu) and Minas Carpa (Au-Cu), have well-developed potassic alteration zones with high hydrothermal magnetite content. Bornite and chalcopyrite are the dominant sulphides associated with main stage mineralisation at these Au-rich deposits. These features suggest both high temperature and oxygen fugacity conditions during mineralisation. This is consistent with recent analytical and experimental data on Au-rich porphyry deposits (Kesler *et al*., 2002). In contrast, Cu-Au-Mo deposits (e.g. El Galeno and Michiquillay) are mainly hosted in quartzite rocks and have relatively magnetite-poor potassic alteration zones. Pyrite, chalcopyrite and molybdenite dominate hypogene mineralisation at these deposits. The deposits also contain well-developed phyllic alteration zones that are noticeably absent from the Au-rich deposits.

High-sulphidation deposits, such as Yanacocha (12-10 Ma) and Sipán (Miocene), are hosted by andesitic to dacitic rocks and exhibit intense acid-sulphate alteration (Fig. 3; Turner, 1999). Formation of these deposits was temporally linked to the cessation of uplift, crustal thickening and subduction of the Inca Plateau (Noble *et al*., 1979; Gutscher *et al*., 1999). Uplift and thickening caused lowering of the crust-mantle boundary to present day depths, i.e. ~45 km for northern Peru (Fukao *et al*., 1989), resulting in a significant change of the mantle mineralogy from amphibole+clinopyroxene to amphibole + clinopyroxene + garnet (Fig. 3). The onset of flat subduction, possibly due to subduction of the Inca plateau (12-10 Ma, Gutscher *et al*., 1999), also coincided with formation of the epithermal systems. An association between crustal thickening, shallowing of the subduction angle and changes in the residual mineral assemblage has also been suggested for formation of the El Indio and Los Bronce-El Teniente districts in Chile (Skewes and Stern, 1994; Kay *et al*., 1999).

E.9 Conclusion

In contrast to central Andean Miocene deposits, no extraordinary tectonic changes or features, such as slab rupture (Sasso and Clark, 1998) or change in slab inclination (Kay *et al*., 1999), are directly linked to the formation of the Miocene porphyry-related deposits in the Cajamarca region. Instead, these deposits formed due to a combination of rapid plate convergence, partial melting of a deep source containing amphibole – clinopyroxene ± garnet, short residence time in the deep crustal magma ponds that were recharged by newly generated oxidised melts, and rapid ascent of uncontaminated hydrous magmas along deeply tapping faults. Hypogene mineralisation at these deposits was strongly influenced by temperature and oxygen fugacity conditions during early potassic alteration.

Late Miocene epithermal deposits in the Cajamarca region share similar tectonic and magmatic histories to central Andean deposits. Formation of the high-sulphidation deposits occurred during periods of the cessation of crustal thickening and uplift, which was possibly related to increased garnet in the magma source. These features appear to be temporally linked to shallowing the slab angle and subduction of an oceanic plateau.

REFERENCE LIST

REFERENCE LIST

Abels, A. and Bischoff, L., 1999. Clockwise block rotations in northern Chile: Indications for a large-scale domino mechanism during the middle- to late Eocene. Geology, 27: 751-754.

Aldanmaz, E., Pearce, J.A., Thirlwall, M.F. and Mitchell, J.G., 2000. Petrogenetic evolution of late Cenozoic, post-collision volcanism in western Anatolia, Turkey. Journal of Volcanology and Geothermal Research, 102: 67-95.

Arth, J.G., Barker, F., Peterman, Z.E. and Friedman, I., 1978. Geochemistry of the gabbro-diorite-tonalite trondhjemite suite of southwest Finland and its implications for the origin of tonalitic and trondhjemitic magmas. Journal of Petrology, 19: 289-316.

Atherton, M.P., Sanderson, L.M., Warden, V. and McCourt, W.J., 1985. The volcanic cover: chemical composition and the origin of the magmas of the Calipuy Group. In: W.S. Pitcher, M.P. Atherton, E.J. Cobbing and R.A. Beckingsale (Editors), Magmatism at a Plate Edge: The Peruvian Andes. Blackie, Glasgow and London, pp. 973-984.

Ballantyne, G.H., Smith, T.W. and Redmond, P.B., 1997. Distribution and mineralogy of gold and silver in the Bingham Canyon porphyry copper deposit, Utah. Society of Economic Geologists Guidebook 29: 147-153.

Barazangi, M. and Isacks, B.L., 1979. Subduction of the Nazca plate beneath Peru: evidence from spatial distribution of earthquakes. Geophysical Journal of the Royal Astronomical Society, 57: 537-555.

Barreiro, B.A., 1984. Lead isotopes and Andean magmagenesis. In: R.S. Harmon and B.A. Barreiro (Editors), Andean Magmatism, Chemical and Isotopic Constraints. Shiva, Cheshire, pp. 21-30.

Beckinsale, R.D., Sanchez-Fernandez, A.W., Brook, M., Cobbing, E.J., Taylor, W.P. and Moore, N.D., 1985. Rb-Sr whole-rock isochron and K-Ar age determinations for the Coastal Batholith of Peru. In: W.S. Pitcher, M.P. Atherton, E.J. Cobbing and R.A. Beckingsale (Editors), Magmatism at a Plate Edge: The Peruvian Andes. Blackie, Glasgow and London, pp. 177-202.

Behn, G., Camus, F., Carrasco, P. and Ware, H., 2001. Aeromagnetic signature of porphyry copper systems in northern Chile and its geological implications. Economic Geology, 96: 239-248.

Bellier, O., Sebrier, M., Fourtanier, E., Gasse, F. and Robles, I., 1989. Late Cenozoic evolution of the E-W striking Cajamarca deflection in the Namora basin (Andes of Northern Peru). Annales Tectonicae, 3: 77-98.

Benavides, C.V., 1999. Orogenic evolution of the Peruvian Andes: the Andean cycle. In: B.J. Skinner (Editor), Geology and ore deposits of the Central Andes. Society of Economic Geologists, Special publication No. 7: 61-107.

Benavides, V., 1956. Cretaceous system in northern Peru. American Museum of Natural History Bulletin, 108: 355-493.

Borredon, R., 1982. Etude geologique et metallgenique du district minier de Hualgayoc (Perou Septentrional) a plomb-zinc-cuivre-argent. Unpub. Ph.D. Thesis, University of Paris VI.

Burnham, W.C., 1979. Magmas and hydrothermal fluids. In: H.L. Barnes (Editor), Geochemistry of hydrothermal ore deposits (Second Edition). Wiley-Interscience, New York, pp. 71-137.

Burnham, W.C., 1981. Convergence and mineralisation - Is there a relation? Geological Society of America, Memoir 154: 761-768.

Caffe, P.J., Trumbull, R.B., Coira, B.I. and Romer, R.L., 2002. Petrogenesis of Early Neogene magmatism in the northern Puna; implications for magma genesis and crustal processes in the Central Andean Plateau. Journal of Petrology, 43: 907-942.

Campos, E., Touret, J.L.R., Nikogosian, I. and Delgado, J., 2002. Overheated, Cu-bearing magmas in the Zaldivar porphyry-Cu deposit, Northern Chile. Geodynamic consequences. Tectonophysics, 345: 229-251.

Candela, P.A., 1997. A review of shallow, ore-related granites: Textures, volatiles, and ore metals. Journal of Petrology, 38: 1619-1633.

Candela, P.A. and Piccoli, P.M., 1995. Model ore-metal partitioning from melt into vapour and vapour/brine mixtures. Mineralogical Association of Canadian Short Course, 23: 101-127.

Chernicoff, C.J., Richards, J.P. and Zappettini, E.O., 2002. Crustal lineament control on magmatism and mineralisation in northwestern Argentina: geological, geophysical, and remote sensing evidence. Ore Geology Reviews, 21: 127-155.

Clark, A.H., 1993. Are outsized porphyry copper deposits either anatomically or environmentally distinctive? In: B.H. Whiting, C.J. Hodgson and R. Mason (Editors), Giant Ore Deposits. Society of Economic Geologists, Special Publication 2, pp. 213-283.

Clark, A.H. and Arancibia, O.N., 1995. The occurrence, paragenesis and implications of magnetite-rich alteration-mineralisation in calc-alkaline porphyry copper deposits. In: A.H. Clark (Editor), Giant ore deposits II: Controls on the scale of orogenic magmatic-hydrothermal mineralisation. Queen's University, Kingston, ON, pp. 583-640.

Cobbing, E.J., Pitcher, W.S., Wilson, J.J., Baldock, J.W., Taylor, W.P., McCourt, W. and Snelling, N.J., 1981. The geology of the Western Cordillera of northern Peru. Institute of Geological Sciences, Overseas Memoir 5.

Cordova, J.R. and Hoyos, D.J., 2000. Geologia del porfido de Cu-(Au-Mo) el Galeno, Cajamarca, Peru. X Congresso Peruano de Geologia Resumenes, Sociedad Geologica del Peru, Lima, 2000: 246.

Dalrymple, G.B. and Lanphere, M.A., 1974. $^{40}Ar/^{39}Ar$ age spectra of some undisturbed terrestrial samples. Geochemica et Cosmochimica Acta, 38: 715-738.

Davidson, J.P., Harmon, R.S. and Worner, G., 1991. The source of central Andean magmas; some considerations. In: R.S. Harmon and C.W. Rapela (Editors), Andean magmatism and its tectonic setting. Boulder, Colorado, Geological Society of America Special Paper 265, pp. 233-243.

Davies, C., 2000. Structural controls and magmatic evolution of the Cajamarca region, northern Peru. Unpubl. Internal Report for North Ltd., May 2000.

Fournier, R.O., 1999. Hydrothermal processes related to movement of fluid from plastic into brittle rock in the magmatic-epithermal environment. Economic Geology, 94: 1193-1212.

Frey, F.A., Chappell, B.W. and Roy, S.D., 1978. Fractionation of rare earth elements in the Tuolumme Intrusive Series, Sierra Nevada batholith, California. Geology, 6: 239-242.

Fukao, Y., Yamamoto, A. and Kono, M., 1989. Gravity anomaly across the Peruvian Andes. Journal of Geophysical Research, 94: 3867-3890.

Gammons, C.H. and Williams-Jones, A.E., 1997. Chemical mobility of gold in the porphyry-epithermal environment. Economic Geology, 92: 45-59.

Garcia, J.B., 1999. Estudio petrografico, mineralogico y de alteraciones en los sondeos DDH-GN-35 a DDH-GN-44, proyecto El Galeno, Cajamarca. Unpubl. Internal Report for North Ltd., 1999.

Gill, J.B., 1981. Orogenic Andesites and Plate Tectonics. Springer-Verlag, Berlin.

Glazner, A., 1991. Plutonism, oblique subduction, and continental growth: an example from the Mesozoic of California. Geology, 19: 784-786.

Gow, P. and Ord, A., 1999. Numerical modelling of deformation and fluid-flow in shallow plutonic compressional environments. Halls Gap, Victoria; Specialist Group in Tectonic and Structural Geology Conference: 86-87.

Green, T.H. and Pearson, N.J., 1985. Experimental determination of REE partition coefficients between amphibole and basaltic liquids at high pressure. Geochemica et Cosmochimica Acta, 49: 1465-1468.

Gustafson, L.B. and Hunt, J.P., 1975. The porphyry copper deposit of El Salvador, Chile. Economic Geology, 70: 857-912.

Gutscher, M.A., Olivet, J.L., Aslanian, D., Eissen, J.P. and Maury, R., 1999. The "lost Inca Plateau"; cause of flat subduction beneath Peru? The "lost Inca Plateau"; cause of flat subduction beneath Peru? Earth and Planetary Science Letters, 171: 335-341.

Hammond, R., 1998. El Galeno project, northern Peru: Observations and their implications. Unpubl. Internal Report for North Ltd, August 1998.

Harvey, B.A., Myers, S.A. and Klein, T., 1999. Yanacocha gold district, northern Peru. *Pacrim '99*, Bali, Indonesia, 10-13 October 1999: 445-459.

Hawkesworth, C.J., Gallagher, K., Hergt, J.M. and McDermott, F., 1993. Mantle and slab contributions in arc magmas. Annual Review of Earth Planetary Science, 21: 175-204.

Hawkesworth, C.J. Norry, M.J., Roddick, J.C., Baker, P.E., Francis, P.W. and Thorpe, R.S., 1979. $^{143}Nd/^{144}Nd$, $^{87}Sr/^{86}Sr$, and incompatible element variations in calc-alkaline andesites and plateau lavas from South America. Earth and Planetary Science Letters, 42: 45-57.

Hedenquist, J.W., Arribas, A.J. and Reynolds, J.T., 1998. Evolution of an intrusion-centred hydrothermal system: Far Southeast-Lepanto porphyry and epithermal Cu-Au deposits, Philippines. Economic Geology, 93: 373-404.

Heidrick, T.L. and Titley, S.R., 1982. Fracture and dyke patterns in Laramide plutons and their structural and tectonic implications: American southwest. In: S.R. Titley (Editor), Advances in Geology of the Porphyry Copper Deposits. University of Arizona, Tuscon, pp. 73-91.

Hildreth, W. and Moorbath, S., 1988. Crustal contributions to arc magmatism in the Andes of Central Chile. Contributions to Mineralogy and Petrology, 98: 455-489.

Hollister, V.F. and Sirvas, E.B., 1974. The Michiquillay porphyry copper deposit. Mineralium Deposita, 9: 261-269.

Irvine, T.N. and Baragar, W.R.A., 1971. A guide to chemical classification of the common volcanic rocks. Canadian Journal of Earth Science, 8: 523-548.

Jaillard, E. and Soler, P., 1996. Cretaceous to early Paleaogene tectonic evolution of the northern Central Andes (0-18^{o}S) and its relations to geodynamics. Tectonophysics, 259: 41-53.

James, D.E., 1981. Role of subducted continental material in the genesis of calc-alkaline volcanics of the central Andes. Geological Society of America, Memoir 154: 769-790.

James, D.E. and Sacks, I.S., 1999. Cenozoic formation of the Central Andes: A geophysical perspective. In: B.J. Skinner (Editor), Geology and Ore Deposits of the Central Andes. Society of Economic Geologists, Special Publication No. 7: 1-25.

James, J., 1998. Geology, alteration, and mineralisation of the Cerro Corona porphyry copper-gold deposit, Cajamarca Province, Peru. Unpubl. MSc Thesis, University of British Columbia, Vancouver, Canada.

Jordon, T.E., Isacks, B.L., Allmendinger, R.W., Brewer, J.A., Ramos, V.A. and Ando, C.J., 1983. Andean tectonics related to geometry of subducted Nazca plate. Geological Society of America Bulletin, 94: 341-361.

Kay, S.M. and Mpodozis, C., 2001. Central Andean ore deposits linked to evolving shallow subduction systems and thickening crust. GSA Today, 11: 4-9.

Kay, S.M., Mpodozis, C. and Coira, B.I., 1999. Magmatism, tectonism, and mineral deposits of the Central Andes (22°S-33°S). In: B.J. Skinner (Editor), Geology and Ore Deposits of the Central Andes. Society of Economic Geologists, Special Publication No. 7: 27-59

Kay, S.M., Mpodozis, C., Ramos, V.A. and Munizaga, F., 1991. Magma source variations for mid-late Tertiary magmatic rocks associated with a shallowing subduction zone and a thickening crust in the central Andes (28 to 33°S). In: R.S. Harmon and C.W. Rapela (Editors), Andean magmatism and its tectonic setting. Boulder, Colorado, Geological Society of America Special Paper 265, pp. 113-137.

Kerrich, R. and Wyman, D.A., 1997. Review of developments in trace-element fingerprinting of geodynamic settings and their implications for mineral exploration. Australian Journal of Earth Science, 44: 465-487.

Kesler, S.E., Chryssoulis, S.L. and Simon, G., 2002. Gold in porphyry copper deposits: its abundance and fate. Ore Geology Reviews, 21: 103-124.

Kissel, C., Laj, C., Surmont, J., Macedo-Sanchez, O. and Mitouard, P., 1992. South American active margin; Andean deflections and crustal thickening. Bulletin de la Societe Geologique de France, 163: 371-380.

Kono, M., Fukao, Y. and Yamamoto, A., 1989. Mountain building in the Central Andes. Journal of Geophysical Research, 94: 3891-3905.

Laj, C., Mitourad, P., Roperch, P., Kissel, C., Mourier, T. and Farfan Medrano, A., 1989. Paleomagnetic rotations in the coastal areas of Ecuador and northern Peru. In: C.

Kissel and C. Laj (Editors), Paleomagnetic Rotations and Continental Deformation. Kluwer, Amsterdam.

Lang, J.R. and Titley, S.R., 1998. Isotopic and geochemical characteristics of Laramide magmatic systems in Arizona and implications for the genesis of porphyry copper deposits. Economic Geology, 93: 138-170.

Laughlin, A.W., Damon, P.E. and Watson, B.N., 1968. Potassium-Argon dates from Toquepala and Michiquillay, Peru. Economic Geology, 63: 166-168.

Le Bel, L.M., 1985. Mineralisation in the Arequipa segment: The porphyry-Co deposit of Cerro Verde/Santa Rosa. In: W.S. Pitcher, M.P. Atherton, E.J. Cobbing and R.A. Beckingsale (Editors), Magmatism at a Plate Edge: The Peruvian Andes. Blackie, Glasgow and London, pp. 250-260.

Le Maitre, R.W., Bateman, P., Dudek, A., Keller, J., Lameyre Le Bas, M.J., Sabine, P.A., Schmid, R., Sorensen, H., Streckeisen, A., Woolley, A.R. and Zanettin, B., 1989. A classification of igneous rocks and glossary of terms. Blackwell, Oxford.

Lindsay, D.D., Zentilli, M. and Rojas de la Rivera, J., 1995. Evolution of an active ductile to brittle shear system controlling mineralisation at the Chuquicamata porphyry copper deposit, northern Chile. International Geology Review, 37: 945-958.

Llosa, F., Lescuyer, J.L. and Milesi, J.P., 1996. Minas Conga: descubrimiento, exploracion y marco geologico de los porfidos Au-Cu en la region de Cajamarca. Segundo Simposio Internacional del Oro, Comite Aurifero, Sociedad Nacional de Mineria y Petroleo, Lima: 275-283.

Llosa, F. and Veliz, J., 2000. Geologia, alteracion y mineralisacion de los porfidos de Au-Cu de Minas Conga, norte del Peru (Cajamarca). X Congresso Peruano de Geologia Resumenes, Sociedad Geologica del Peru, Lima, 2000: 248.

Longo, A.A., 2000. The San Jose-Charachugo-Chaquicocha gold trend, Yanacocha district, northern Peru. In: J.K. Cluer, J.G. Price, E.M. Struhsacker, R.F. Hardyman and

C.L. Morris (Editors), Geology and Ore Deposits 2000: The Great Basin and Beyond. Geological Society of Nevada Symposium Proceedings, May 15-18, 2000: 1-20.

Lopez, L., 1982. Carateristicas geoquimicas de rocas igneous asociadas con porfidos cupriferos chilenos. Revista Geologica de Chile, 17: pp. 3-19.

Macfarlane, A.W., 1999. Isotopic studies of northern Andean crustal evolution and ore metal sources. In: B.J. Skinner (Editor), Geology and Ore Deposits of the Central Andes. Society of Economic Geologists, Special Publication No. 7: 195-216.

Macfarlane, A.W., Marcet, P., LeHuray, A.P. and Petersen, U., 1990. Lead isotope provinces of the central Andes inferred from ores and crustal rocks. Economic Geology, 85: 1857-1880.

Macfarlane, A.W. and Petersen, U., 1990. Pb isotopes of the Hualgayoc area, northern Peru: Implications for metal provenance and genesis of a cordilleran polymetallic mining district. Economic Geology, 85: 1303-1327.

Macfarlane, A.W., Prol-Ledesma, R.-M. and Conrad, M.E., 1994. Isotope and fluid inclusion studies of geological and hydrothermal processes, northern Peru. International Geology Review, 36: 645-677.

Marsh, T.M., Einaudi, M.T. and McWilliams, M., 1997. $^{40}Ar/^{39}Ar$ geochronology of Cu-Au and Au-Ag mineralisation in the Poterillos district, Chile. Economic Geology, 92: 784-806.

Martin, H., 1987. Petrogenesis of Archean trondhjemites, tonalites, and granodiorites from eastern Finland; Major and trace element geochemistry. Journal of Petrology, 28: 921-953.

McInnes, P., 1997. A geological appraisal of the Michiquillay porphyry copper deposit and regional potential. Unpubl. Internal Report for North Ltd, October 1997.

McNulty, B.A., Farber, D.L., Wallace, G.S., Lopez, R. and Palacios, O., 1998. Role of plate kinematics and plate-slip-vector partitioning in continental magmatic arcs: Evidence from the Cordillera Blanca, Peru. Geology, 26: 827-830.

Mégard, F., 1984. The Andean orogenic period and its major structures in central and northern Peru. Journal of the Geological Society of London, 141: 892-900.

Mégard, F., 1987. Structure and evolution of the Peruvian Andes. In: Schaer and Rogers (Editors), Anatomy of Mountain Ranges. Princeton University Press, Princeton, New Jersey, pp. 179-210.

Meinert, L.D., Hefton, K.K., Mayes, D. and Tasiran, I., 1997. Geology, zonation, and fluid evolution of the Big Gossan Cu-Au skarn deposit, Erstberg district, Irian Jaya. Economic Geology, 92: 509-534.

Merzbacher, C. and Eggler, D.H., 1984. A magmatic geohygromteter: Application to Mount St. Helens and other dacitic magmas. Geology, 12: 587-590.

Metal Mining Agency, 1975. Report on geological survey of the Michiquillay area, Republic of Peru. Unpubl. Internal Report for Metal Mining Agency, Japan International Cooperation Agency and Government of Japan, November 1975.

Metal Mining Agency, 1975. Report on geological survey of the Michiquillay area, Republic of Peru. Unpubl. Internal Report for Metal Mining Agency, Japan International Cooperation Agency and Government of Japan, November 1975.

Mitouard, P., Kissel, C. and Laj, C., 1990. Post-Oligocene rotations in southern Ecuador and northern Peru and the formation of the Huancabamba deflection in the Andean Cordillera. Earth and Planetary Science Letters, 98: 329-339.

Mitouard, P., Laj, C., Mourier, T. and Kissel, C., 1992. Paleomagnetic study of an arcuate fold belt developed on a marginal orogen; the Cajamarca deflection, northern Peru. Earth and Planetary Science Letters, 112: 41-52.

Nakamura, K., 1977. Volcanoes as possible indicators of tectonic stress orientation - Principal and proposal. Journal of Volcanology and Geothermal Research, 2: 1-16.

Nakamura, Y. and Kushiro, I., 1974. Composition of the gas phase in Mg_2SiO_4-SiO_2-H_2O at 15 kbar, Geophysical Laboratory; Igneous petrology, experimental and field studies; Volatiles in ultrabasic and derivative rock systems. Carnegie Institution of Washington, pp. 255-259.

Naney, M.T., 1983. Phase equilibria of rock-forming ferromagnesian silicates in granitic systems. American Journal of Science, 283: 993-1033.

Nash, W.P. and Creecraft, H.R., 1985. Partition coefficients for trace elements in silicic magmas. Geochemica et Cosmochimica Acta, 49: 2309-2322.

Newmont, 2002. Newmont Mining Corporation web page: http://www.newmont.com/

Noble, D.C. and McKee, E.H., 1999. The Miocene metallogenic belt of Central and Northern Peru. In: B.J. Skinner (Editor), Geology and Ore Deposits of the Central Andes, Society of Economic Geologists, Special Publication No. 7: 155-193.

Noble, D.C., McKee, E.H. and Mégard, F., 1979. Early Tertiary "Incaic" tectonism, uplift, and volcanic activity, Andes of central Peru. Geological Society of America Bulletin, 90: 903-907.

Noble, D.C., McKee, E.H., Mourier, T. and Mégard, F., 1990. Cenozoic stratigraphy, magmatic activity, compressive deformation, and uplift in northern Peru. Geological Society of American Bulletin, 102: 1105-1113.

Noble, D.C., Sébrier, M., Mégard, F. and McKee, E.H., 1985. Demonstration of two pulses of Palaeogene deformation in the Andes of Peru. Earth and Planetary Science Letters, 73: 345-349.

Orton, J., 1874. The silver mines of Peru. Engineering Mining Journal, 17: 83.

Oyarzun, R., Márquez, A., Lillo, J., López, I. and Rivera, S., 2001. Giant versus small porphyry copper deposits of Cenozoic age in northern Chile: adakitic versus normal calc-alkaline magmatism. Mineralium Deposita, 36: 794-798.

Pardo-Casas, F. and Molnar, P., 1987. Relative motion of the Nazca (Farallon) and South American plates since Late Cretaceous time. Tectonics, 6: 233-248.

Peacock, S.M., 1993. Large-scale hydration of the lithosphere above the subducting slabs. Chemical Geology, 108: 49-59.

Peacock, S.M., Rushmer, T. and Thompson, A.B., 1994. Partial melting of subducting oceanic crust. Earth and Planetary Science Letters, 121: 227-244.

Pearce, J.A., 1983. Role of the sub-continental lithosphere in magma genesis at active continental margins. In: C.J. Hawkesworth and M.J. Norry (Editors), Continental basalts and mantle xenoliths. Shiva, Nantwich, pp. 230-249.

Pearce, J.A. and Norry, M.J., 1979. Petrogenetic implications of Ti, Zr, Y, and Nb variations in volcanic rocks. Contributions to Mineralogy and Petrology, 69: 33-47.

Petersen, U., 1999. Magmatic and metallogenic evolution of the Central Andes. In: B.J. Skinner (Editor), Geology and Ore Deposits of the Central Andes, Society of Economic Geologists, Special Publication No. 7: 109-153.

Petersen, U., Macfarlane, A.W. and Danielsen, A., 1993. Lead isotopic provinces in Peru, Bolivia and northern Chile. Second International Symposium on Andean Geodynamics: 477-480.

Petersen, U. and Vidal, C.E., 1996. Magmatic and tectonic controls on the nature and distribution of copper deposits in Peru. In: F. Camus, R.H. Sillitoe and R. Petersen (Editors), Andean Copper Deposits: New Discoveries, Mineralisation, Styles and Metallogeny. Society of Economic Geologists Special Publication No 5: 1-18.

Petford, N. and Atherton, M.P., 1992. Granitoid emplacement and deformation along a major crustal lineament: the Cordillera Blanca, Peru. Tectonophysics, 205: 171-185.

Petford, N. and Atherton, M.P., 1996. Na-rich partial melts from newly underplated basaltic crust: the Cordillera Blanca batholith, Peru. Journal of Petrology, 37: 1491-1521.

Petford, N., Atherton, M.P. and Halliday, A.N., 1996. Rapid magma production rates, underplating and remelting in the Andes: isotopic evidence from northern-central Peru (9-11^{o}S). Journal of South American Earth Science, 9: 69-78.

Petford, N., Lister, J.R. and Kerr, R.C., 1994. The ascent of felsic magmas in dykes. Lithos, 32: 161-168.

Pichavant, M., Kontak, D.J., Briqueu, L., Valencia Herrera, J. and Clark, A.H., 1988. The Miocene-Pliocene Macusani volcanics, SE Peru: II. Geochemistry and origin of a felsic peraluminous magma. Contributions to Mineral Petrology, 100: 325-388.

Pilger, R.H.J., 1984. Cenozoic plate kinematics, subduction and magmatism: South American Andes. Journal of the Geological Society of London, 141: 793-802.

Pitcher, W.S., 1997. The nature, ascent and emplacement of granitic magmas (2nd Edition). London, Chapman and Hall.

Pollard, P.J. and Taylor, R.G., 2002. Paragenesis of the Grasberg Cu-Au deposit, Irian Jaya, Indonesia: results from logging section 13. Mineralium Deposita, 37: 117-136.

Quiroz, A., 1997. El corredor estructural Chicama-Yanacocha y su importancia en la metalogenia del norte del Peru. IX Congreso Peruano de Geologia, Resumenes Extendidos. Sociedad Geologica del Peru, Vol. Esp. 1: 149-159.

Reyes, L.R., 1980. Mapa geologica del cuadrangulo de Cajamarca, Sheet 15f. Sector Energia y Minas, Instituto Geologico Minera y Metalurgico, Republica del Peru.

Richards, J.P. and Villeneuve, M., 2002. Characteristics of late Cenozoic volcanism along the Archibarca lineament from Cerro Llullaillaco to Corrida de Cori, northwest Argentina. Journal of Volcanology and Geothermal Research, 116: 161-200.

Richards, J.P., Boyce, A.J. and Pringle, M.S., 2001. Geological evolution of the Escondida area, northern Chile: A model for spatial and temporal localisation of porphyry Cu mineralisation. Economic Geology, 96: 271-305.

Rubin, J.N. and Kyle, J.R., 1997. Precious metal mineralogy in porphyry-, skarn-, and replacement-type ore deposits of the Erstberg (Gunung Bijih) Districtm Irian Jaya, Indonesia. Economic Geology, 92: 535-550.

Rutherford, M.J. and Devine, J.D., 1988. The May 18, 1980, eruption of Mount St. Helens: 3. Stability and chemistry of amphibole in the magma chamber. Journal of Geophysical research, 93: 11949-11959.

Sasso, A. and Clark, A.H., 1998. The Farallon Negro group, northwest Argentina: Magmatic, hydrothermal, and tectonic evolution and implications for Cu-Au metallogeny in the Andean backarc. Society of Economic Geologists Newsletter, 34: 1-18.

Sebrier, M. and Soler, P., 1991. Tectonics and magmatism in the Peruvian Andes from late Oligocene time to the Present. Geological Society of America, Special Paper 265: 259-278.

Shatwell, D., 2002. Miocene gold and copper mineralisation and the lost Inca Plateau in Peru. AIG News: 14-17.

Shaw, D.M., 1970. Trace element fractionation during anatexis. Geochemica et Cosmochimica Acta, 34: 237-243.

Sibson, R.H., 1985. A note on fault reactivation. Journal of Structural Geology, 7: 751-754.

Sibson, R.H., 2001. Seismogenic framework for hydrothermal transport and ore deposition. Society of Economic Geologists Reviews, 14: 25-50.

Sillitoe, R.H., 1972. Relation of metal provinces in western Americas to subduction of oceanic lithosphere. Geological Society of American Bulletin, 83: 813-818.

Sillitoe, R.H., 1988. Epochs of intrusion-related copper mineralisation in the Andes. Journal of South American Earth Science, 1: 89-107.

Sillitoe, R.H., 1991. Gold metallogeny of Chile - an introduction. Economic Geology, 86: 1155-1173.

Sillitoe, R.H., 2000a. Geological models and exploration potential of El Galeno and Carpa porphyry copper prospects, northern Peru. Unpubl. Internal Report for North Ltd., July 2000.

Sillitoe, R.H., 2000b. Gold-rich deposits: Descriptive and genetic models and their role in exploration and discovery. Society of Economic Geologists Reviews, 13: 315-345.

Simon, G., Kesler, S.E., Essene, E.J. and Chryssoulis, S.L., 2000. Gold in porphyry copper deposits: Experimental determination of the distribution of gold in the Cu-Fe-S system at 400^o to 700^{o}C. Economic Geology, 95: 259-270.

Skewes, A.M. and Stern, C.R., 1994. Tectonic trigger for the formation of late Miocene Cu-rich breccia pipes in the Andes of central Chile. Geology, 22: 551-553.

Skewes, A.M. and Stern, C.R., 1996. Late Miocene mineralised breccias in the Andes of Central Chile: Sr- and Nd-isotopic evidence for multiple magmatic sources. In: F. Camus, R.H. Sillitoe and R. Petersen (Editors), Andean Copper Deposits: New Discoveries, Mineralisation, Styles and Metallogeny. Society of Economic Geologists Special Publication No 5: 33-42.

Soler, P. and Bonhomme, M.G., 1990. Relation of magmatic activity to plate dynamics in central Peru from Late Cretaceous to present. In: S.M. Kay and C.W. Rapela

(Editors), Plutonism from Antarctica to Alaska. Special Paper - Geological Society of America, 173-190.

Stakey, J. S. and Kramers, J. D., 1975. Approximation of terrestrial lead isotope evolution by a two-stage model: Earth and Planetary Science Letters, 26: 207-221.

Stern, C.R. and Wyllie, P.J., 1978. Phase compositions through crystallisation intervals in basalt-andesite-H_2O at 30 kb with implications for subduction zone magmas. American Mineralogist, 63: 641-663.

Sun, S.S. and McDonough, W.F., 1989. Chemical and isotopic systematics of oceanic basalts: Implications for mantle composition and processes. Geological Society London Special Publication 42, 313-345.

Takada, A., 1994. The influence of regional stress and magmatic input on styles of monogenetic and polygenetic volcanism. Journal of Geophysical Research, 99: 13,563-13,573.

Taylor, S.R. and McLennan, S.M., 1985. The continental crust: Its composition and evolution. Oxford, Blackwell Scientific Publications Ltd.

Thirlwall, M.F., 2000. Interlaboratory and other errors in Pb-isotope analyses investigated using a ^{207}Pb-^{204}Pb double spike. Chemical Geology, 163: 299-322.

Thirlwall, M.F., Smith, T.E., Graham, A.M., Theodorou, N., Hollings, P., Davidson, J.P. and Arculus, R.J., 1994. High field strength anomalies in arc lavas: source or process? Journal of Petrology, 35: 819-838.

Titley, S.R. and Heidrick, T.L., 1978. Intrusion and fracture styles of some mineralised porphyry systems of the southwestern Pacific and their relationship to plate interactions. Economic Geology, 73: 891-903.

Titley, S.R. Thompson, R.C., Haynes, F.M., Manske, S.L., Robison, L.C. and White, J.L., 1986. Evolution of fractures and alteration in the Sierrita-Esperanza Hydrothermal System, Pima County, Arizona. Economic Geology, 81: 343-370.

Tosdal, R.M., 1995. Metal differences in Cenozoic porphyry Cu-Au-Mo deposits in the central Chilean Andes between 26^o and 28^o: An influence on the size of porphyry deposits? In: A.H. Clark (Editor), Giant Ore Deposits II: Controls on the scale of orogenic magmatic-hydrothermal mineralisation. Proceedings of the Second Giant Ore Deposits Workshop: Queens University, Ontario: 124-138.

Tosdal, R.M. and Richards, J.P., 2001. Magmatic and structural controls on the development of porphyry Cu ± Mo ± Au deposits. In: J.P. Richards and R.M. Tosdal (Editors), Structural controls on ore genesis. Society of Economic Geologists Reviews, 14: 157-181.

Tosdal, R. M., Wooden, J. L., and Bouse, R. M., 1999. Pb isotopes, ore deposits, and metallogenic terranes. In Lambert, D. D., and Ruiz, J. (Editors), Application of Radiogenic Isotopes to Ore Deposit Research and Exploration, Reviews in Economic Geology, 12: 1-28.

Turner, S.J., 1997. The Yanacocha epithermal gold deposits, northern Peru: high-sulphidation mineralisation in a flow dome setting. Unpubl. Ph.D. Thesis, Colorado School of Mines, Colorado, USA.

Turner, S.J., 1999. Settings and styles of high-sulphidation gold deposits in the Cajamarca region, northern Peru. *Pacrim '99*, Bali, Indonesia, 10-13 October 1999: 461-468.

Ulrich, T. and Heinrich, C.A., 2001. Geology and alteration geochemistry of the porphyry Cu-Au deposit at Bajo de la Alumbrera, Argentina. Economic Geology, 96: 1719-1742.

Vidal, C.E. and Noble, D.C., 1994. Yacimientos hidrotermales controlados por magmatismo y estructuras en la region central del Peru. Resumenes Extendidos, VIII

Congreso Peruano de Geologica, Sociedad Geologica del Peru, Publicacion Especial no.1: 48-52.

Vila, T. and Sillitoe, R.H., 1991. Gold-rich porphyry systems in the Maricunga Belt, northern Chile. Economic Geology, 86: 1238-1260.

von Humboldt, A., 1827. Ensayo politico sobre la Nueva Espana, 2nd Edition.

Weber, M.B.I., Tarney, J., Kempton, P.P.D. and Kent, R.W., 2002. Crustal make-up of the northern Andes: evidence based on deep crustal xenolith suites, Mercaderes, SW Columbia. Tectonophysics, 345: 49-82.

Wilson, J.J., 1985a. Mapa geologica del cuadrangulo de Celendin, Sheet 14g. Sector Energia y Minas, Instituto Geologico Minera y Metalurgico, Republica del Peru.

Wilson, J.J., 1985b. Mapa geologica del cuadrangulo de Chota, Sheet 14f. Sector Energia y Minas, Instituto Geologico Minera y Metalurgico, Republica del Peru.

Wilson, J.J., 2000. Structural development of the northern Andes of Peru. X Congresso Peruano de Geologia Resumenes, Sociedad Geologica del Peru, Lima, 2000.

Wilson, M., 1989. Igneous Petrogeneous: a Global Tectonic Approach. Chapman & Hall, London.

Wood, B.J. and Fraser, D.G., 1976. Elementary thermodynamics for geologists. Oxford, Oxford University Press: 218.

Zentilli, M. and Maksaev, V., 1995. Metallogenetic model for the Late Eocene-Early Oligocene supergiant porphyry event, northern Chile. In: A.H. Clark (Editor), Giant Ore Deposits II: Controls on the scale of orogenic magmatic-hydrothermal mineralisation. Proceedings of the Second Giant Ore Deposits Workshop: Queens University, Ontario: 152-165.

Zhitian, W. and Kezhang, Q., 1989. REE geochemistry character of porphyry copper molybdenite multimetal metallogenic series and its application to distinguishing ore-bearing quality of porphyies in Manzhouli-Xinbaerhuyouqi area of Inner Mongolia, International Geological Congress, 28th, Washington, D.C., Progress in Geoscience of China (1985-1988) – Papers: 125-128.

APPENDIX A1

Rock sample locations and descriptions

JCU No.	Sample No.	Northing (m)	Easting (m)	Location	Thin Section	Microprobe	XRD	Majors	Traces	REE	$^{40}Ar/^{39}Ar$	Sr Isotopes	Nd Isotopes	Pb Isotope
67720	S-16	9227017	794204	El Galeno Region	X	X		X	X	X	X	X	X	
67721	S-26	9226745	794774	El Galeno Region	X	X		X	X	X				
67722	S-55	9225913	794465	El Galeno Region	X	X		X	X	X				
67723	S-57	9226680	796058	El Galeno Region	X	X		X	X	X		X	X	
67724	S-18	9230960	794720	El Galeno Region	X			X	X	X				
67725	S-87	9235216	784989	Mishacocha	X	X		X	X	X				
67726	S-11	9211157	800904	Aurora Patricia	X	X		X	X	X	X	X	X	
67727	S-38	9228798	801199	La Carpa Region	X	X		X	X	X	X	X	X	
67728	S-35	9224490	799321	Michiquillay North	X			X	X	X				
67729	S-36	9224565	799745	Michiquillay North	X			X	X	X				
67730	S-54	9224321	800967	Michiquillay North	X			X	X	X				
67731	S-58	9224008	796602	Michiquillay North	X			X	X	X				
67732	S-59	9223743	797582	Michiquillay North	X	X		X	X	X	X	X	X	
67733	S-60	9223187	799620	Michiquillay North	X			X	X	X				
67734	S-MCarpa	9230300	802600	Minas Carpa (CP012)	X			X	X	X				
67735	S-Chail	9232500	791300	Chailhuagon	X	X		X	X	X		X	X	
67736	H-1 (152m)	9232130	791250	Chailhuagon	X									X
67737	S-Hual	9235440	790840	Hualyamachay Sur	X			X	X	X				
67738	S-H22 (244)	9221145	795729	Michiquillay Prospect	X	X		X	X	X				
67739	S-H22(176)	9221140	795725	Michiquillay Prospect	X	X		X	X	X	X	X	X	
67740	S-H22(180)	9221140	795725	Michiquillay Prospect	X	X		X	X	X				
67741	H-22 (176m)	9221140	795725	Michiquillay Prospect	X									
67742	I-23 (269m)	9221046	795833	Michiquillay Prospect	X		X							
67743	L-17.5 (180m)	9221594	796143	Michiquillay Prospect	X		X							
67744	L-17.5 (288m)	9221594	796143	Michiquillay Prospect	X									
67745	J-20 (170m)	9221335	795920	Michiquillay Prospect	X									
67746	J-20 (178m)	9221335	795920	Michiquillay Prospect	X									
67747	J-20 (333m)	9221335	795920	Michiquillay Prospect	X									
67748	J-20 (347m)	9221335	795920	Michiquillay Prospect	X									X
67749	S-T1	9228264	795871	El Galeno GN-46 (57m)	X	X		X	X	X				
67750	S-T2	9229000	795598	El Galeno GN-37 (310m)	X	X		X	X	X	X	X	X	
67751	S-T3	9228695	795763	El Galeno GN-42 (246m)	X	X		X	X	X				
67752	S-T4	9228700	796044	El Galeno GN-39 (432m)	X	X		X	X	X	X	X	X	
67753	GA-04 (192m)	9228780	795640	El Galeno	X									

JCU No.	Sample No.	Northing (m)	Easting (m)	Location	Thin Section	Microprobe	XRD	Majors	Traces	REE	$^{40}Ar/^{39}Ar$	Sr Isotopes	Nd Isotopes	Pb Isotope
67754	GN-41 (258m)	9228597	795899	El Galeno	X									
67755	GN-42 (96m)	9228695	795763	El Galeno	X									
67756	GN-42 (465m)	9228695	795763	El Galeno	X									
67757	GN-39 (400m)	9228700	796044	El Galeno	X									
67758	GN-39 (166m)	9228700	796044	El Galeno	X									X
67759	GN-39 (432m)	9228700	796044	El Galeno	X									X
67760	GN-39 (436m)	9228700	796044	El Galeno	X									
67761	GA-04 (174m)	9228780	795640	El Galeno	X		X							
67762	GN-39 (215m)	9228700	796044	El Galeno	X		X							
67763	GN-43 (14.9m)	9228400	795950	El Galeno	X		X							
67764	GN-43 (14.9m)	9228400	795950	El Galeno	X		X							
67765	S-Yana	9227200	777600	Yanacocha CLL-5 (795m)	X			X	X	X		X	X	X
67766	Yana	9227200	777600	Yanacocha CLL-5 (569m)	X									X
67767	S-46	9233180	795720	Cerro Perol East	X	X		X	X	X	X	X	X	
67768	S-50	9233920	792940	Cerro Perol	X			X	X	X				
67769	S-28	9225911	814373	Cerro Montana	X			X	X	X		X	X	
67770	S-31	9223290	815725	Cerro Montana	X	X		X	X	X	X	X	X	
67771	S-32	9221344	807480	Cruz Conga	X	X		X	X	X	X	X	X	
67772	S-21	9231380	797708	La Carpa Region	X	X		X	X	X	X	X	X	
67773	S-61	9218321	762720	Yanacocha Rd	X			X	X	X	X	X	X	
67774	S-64	9219230	764453	Yanacocha Rd	X	X		X	X	X				
67775	S-66	9219490	766253	Yanacocha Rd	X			X	X	X				
67776	S-68	9218935	766313	Yanacocha Rd	X			X	X	X				
67777	S-MC4	9229470	788645	Minas Conga Region	X	X		X	X	X	X	X	X	
67778	S-63	9219560	764260	Yanacocha Rd	X			X	X	X				

ROCK DESCRIPTIONS FOR GEOCHEMICAL SAMPLES

MAFIC DYKES

Sample 18 (Galeno)

In thin section, this sample is characterised by abundant acicular or needle-like feldspar grains. The feldspar grains are plagioclase, approximately 0.2 mm in length and display minor twinning. No zoning in the plagioclase grains was observed. The fine-grained, acicular feldspar have a trachytic texture appearance and are slightly aligned. Minor clinopyroxene grains and possibly hornblende are evident but are strongly replaced by carbonate plus chlorite. Calcite infill is evident in amygdule-like features that are angular in shape. Calcite infill is rimmed by light green chlorite. Amygdules are suggestive of suggest of shallow level emplacement. This idea of a shallow level emplacement is supported by the trachytic texture of the matrix, possible the result of a flow system. The groundmass has been strongly-pervasively replaced by secondary carbonate and chlorite. Chlorite alteration is pervasive throughout the sample. Very fine-grained opaque minerals, dominantly magnetite, are euhedral-subhedral shape and abundant. This sample is inferred to be a gabbroic dyke.

Sample 55 (Galeno)

In hand specimen, the sample contains cloudy white feldspar phenocrysts that display minor sericite replacement, 0.5-2.5 mm in length and euhderal-subhedral. Pyroxene grains appear moderately altered, are dusty in appearance and 0.6-3.0 mm in length. Veins composed of feldspar-calcite crosscut all other features. The matrix is dark grey to black in colour.

In thin section, the plagioclase phenocrysts are dominantly euhedral, display both zoning and twinning features and exhibit minor-moderate sericite replacement. Sericite alteration occurs toward the cores of the feldspar grains. Clinopyroxene phenocrysts exhibit primary euhedral grain boundaries, however the grains have undergone moderate-pervasive sericite replacement. Sericite replacement is strongest along and around intragranular fractures. Hornblende phenocrysts are rare and have jagged grain boundaries. The groundmass is composed of fine-grained plagioclase grains that display twinning and weak zoning textures. Strong-moderate carbonate and sericite replacement has overprinted some of the primary groundmass. Medium-grain magnetite is also present, as well as very weak chalcopyrite mineralisation. This sample is inferred to be a hornblende gabbroic dyke.

Sample 57 (Galeno)

This rock is characterised by coarse (2-8 mm) equigranular feldspar grains that are generally clear-cloudy white, 1-2 mm and mostly euhedral-subhedral. Pyroxene grains are ~2 mm in size, dominantly anhedral and appear in close association with chlorite minerals.

In thin section, the holocrystalline sample is dominantly composed of euhedral-subhedral plagioclase phenocrysts that display both twining and zoning textures. Large, phenocryst-size, plagioclase grains are euhedral in shape, whereas the smaller grains are dominantly anhedral. Both plagioclase grain populations exhibit minor-moderate sericite replacement that is commonly well developed along fracture planes. Clinopyroxene phenocrysts are subhedral-euhedral and may display simple twinning. Grain boundaries between pyroxene grains are undulose. Medium-grained magnetite grains are often angular to euhedral. Chlorite alteration is evident throughout the sample and appears to have preferentially replaced certain minerals. Pervasive chlorite alteration of the minerals has made is difficult to determine its primary composition. Weak secondary muscovite is also present. Minor carbonate alteration is generally found within late fractures as an infill mineral. This rock is inferred to be a gabbroic diorite dyke.

Sample 16 (Galeno)

This weakly porphyritic sample contains phenocrysts of clinopyroxene and plagioclase. The groundmass is medium-grained and composed of angular feldspar grains. Plagioclase grains display both simple twinning and oscillatory zoning. Some grains have been affected by minor-moderate sericite replacement. Some of the clinopyroxene grains display zoning and twinning and contain feldspar ± Fe-Ti oxides. Grains are generally euhedral-subhedral. Rare hornblende phenocrysts are evident. Minor sericite-carbonate-chlorite alteration is evident, and contains minor amounts of pyrite and chalcopyrite. Overall the sample is generally fresh with a weak propylitic alteration and is inferred to be a hornblende gabbro.

Sample 87 (Laguna Mishacocha)

In hand specimen this sample is characterised by feldspar phenocrysts that are ~0.3-2.0 mm in size, euhedral-subhedral in shape and generally clear in appearance. Relict mafic minerals(?) are evident, often bordered by a magnetite or hematite and probably undergone strong alteration. Wormy silicic vein(s) are evident, these are ~1-2 mm thick and are crosscut by late brittle fractures. The fractures appear to be infilled with hematite and have a thin selvage of magnetite. The matrix is black-dark grey and trachytic in appearance.

In thin section, there are two populations of plagioclases, a phenocryst group (greater than 1 mm) that are subhedral in shape, display both twinning and zoning textures and show evidence of weak sericite replacement towards the cores. A second population of feldspar grains are less than 1 mm in size and define the groundmass. The feldspar groundmass grains are elongate-acicular in shape, subhedral-anhedral and exhibit minor zoning textures. Euhedral-subhedral, fine-grained pyroxene grains also define the groundmass. The groundmass has undergone moderate carbonate and sericite replacement. Fine-grained primary magnetite is present, along with weak chalcopyrite mineralisation. No quartz grains were observed and possible mafic minerals are pervasively replaced. This sample is inferred to be a gabbroic diorite.

Sample 26

In hand sample, this rock contains acicular plagioclase grains (0.5 mm) and calcite amygdules. The sample is dark grey to dull green. The dull green appearance suggests chlorite alteration. This is confirmed in thin section, where the groundmass has been partially replaced by chlorite. Plagioclase grains display simple twinning and oscillatory zoning. Chlorite and minor calcite has pervasively replaced pyroxene(?) grains that are ~0.5 mm in length. Overall, the sample displays a moderate-strong chlorite alteration.

INTRUSIVE ROCKS

Sample 28 (Co Montana)

This porphyritic sample contains phenocrysts of plagioclase and hornblende, with minor amounts of magnetite, apatite and zircon. Plagioclase phenocrysts are euhedral-subhedral, display oscillatory zoning and twinning features, some grains display evidence of K-feldspar and minor sericite replacement. Hornblende phenocrysts range from euhedral-subhedral and show moderate chlorite replacement around the rims or along fracture planes. Accessory minerals include fine to medium-grained magnetite, apatite and zircon, although no quartz grains are evident. The groundmass has a trachytic-mosaic texture and feldspathic composition. Minor amounts of sericite-carbonate-chlorite alteration are evident, especially within the groundmass. The sample is inferred to be hornblende diorite.

Sample 31 (Co Montana)

This sample has a crowded porphyritic texture and contains phenocrysts of plagioclase, clinopyroxene and hornblende. Minor amounts of apatite and zircon are also present. The plagioclase grains display moderate-strong sericite-carbonate-chlorite alteration and some of the grains display oscillatory zoning and twinning. Subhedral-euhedral hornblende grains are moderately cracked and contain Fe-Ti oxide plus feldspar inclusions. Clinopyroxene grains are generally fractured with moderate-minor sericite replacement. Overall the sample contains moderate-strong chlorite-sericite alteration and is classified as a hornblende diorite.

Sample 11 (Aurora Patricia)

This moderately crowded porphyritic sample contains phenocrysts of hornblende and plagioclase that are set in a feldspathic groundmass. Euhedral-subhedral hornblende grains commonly contain small feldspar and/or magnetite inclusions, and are light green to green in colour. Some hornblende grains display fractures and weak chlorite alteration. Plagioclase grains display oscillatory zoning and simple or crosshatched twinning, some grains have minor fractures. Rounded quartz grains are rare. Sericite-carbonate replacement of plagioclase grains is particularly evident near the core or along fractures. The sample also contains minor apatite and zircon grains, as well as a moderate amount of medium-fine grained magnetite as accessory minerals. Overall, the sample appears to be generally unaltered and is inferred to be a hornblende granodiorite.

Sample 38 (La Carpa)

This sample is characterised by large feldspar phenocrysts, 1-4 mm in size, that are cloudy white-clear in colour and subhedral-anhedral. Euhedral hornblende grains are moderately abundant, mostly 1-2mm in length, acicular in shape and contain minor inclusions. Quartz grains are sub-anhedral, generally well rounded and ~2 mm in size. The matrix is light grey, feldspathic in appearance.

In thin section, plagioclase grains exhibit oscillatory zoning and twinning are generally unaltered. Some plagioclases contain intragranular fractures with minor carbonate and muscovite replacement. Hornblende grains are a yellowish green to green in colour, in parts show replacement textures that are associated with fractures, and grains often have chlorite, hematite and magnetite spots around the rim. Most quartz grains are well rounded and have a fine-grained recrystallised boundary. Biotite phenocrysts have a piokilitic texture with inclusions of feldspar, light brownish green-dark brown in colour and also rimmed with hematite and magnetite, they also exhibit minor chloritic replacement. Fine apatite and zircon crystals also occur throughout the slide. The sample is relatively unaltered, although contains very minor amount of sericitic, carbonate and chlorite alteration.

Sample 35 (Michiquillay North)

This sample is characterised by moderately abundant cloudy feldspar phenocrysts, they are generally subhedral, 0.7-4.0 mm in size. Hornblende phenocrysts occur in two populations, small (0.3 mm) dominant population and a larger (~2 mm) less abundant population. Quartz grains are generally rounded and range is size from 0.5-2.0 mm. The matrix is grey to light grey in colour.

In thin section, plagioclase grains show twinning and oscillatory zoning, occasionally have minor fracture and in places have minor-moderate sericitic alteration. Hornblende grains are mostly unaltered and green-dirty brown in colour. Quartz grains are often rounded, some grains contains good fluid inclusion trails, dominantly brine and vapour inclusions and have a thin recrystallised rim. Others minerals include minor amounts of apatite, zircon and magnetite. The occurrence of carbonates and epidote indicates minor propylitic alteration. This sample is inferred to be a hornblende granodiorite.

Sample 36 (Michiquillay North)

In thin section, plagioclase grains show strong zoning and twinning, grains are generally euhedral with minor intragranular fractures filled with sericite, chlorite and calcite. Relict biotite and hornblende grains have undergone intense chlorite and carbonate alteration with only the original grain shape preserved, plus very fine-grained opaque minerals are located within zones of chlorite alteration. These strongly altered grains appear to have a higher proportion of opaque minerals in comparison with the rest of the sample. Other minerals present within the sample include epidote, apatite, zircon and minor quartz (with few inclusions). Minor amounts of subangular opaques are found throughout the sample and range from fine to medium-grained. The matrix is equigranular, of feldspathic composition and shows very little evidence of alteration (possibly some K-feldspar alteration). The main alteration features are calcite and chlorite replacement that is mostly restricted to hornblende and biotite grains. This sample is a hornblende-biotite granodiorite.

Sample 54 (Michiquillay North)

Sample is characterised by a moderate abundance of sub-euhedral feldspars, dominantly with a cloudy to white appearance and ~0.5-2 mm in length. Mafic minerals are present in two populations a) (~3mm) euhedral, slightly dirty population with small inclusions possibly biotite and b) a smaller (~0.5mm) population with euhedral-subhedral boundaries, probably hornblende. Rounded quartz grains occur and are ~3-5mm in diameter. The matrix is a clear, light grey and feldspathic.

In thin section, the plagioclase grains are moderate-strongly replaced by sericite and carbonate material, with replacement occurring both along the grain boundaries as well as in the core. Biotite and hornblende grains have been completely replaced by carbonate and chlorite minerals, with only the original grain boundary remaining. Quartz crystals are generally rounded, some with embayment features and in parts contain small brine-vapour fluid inclusion and trails (although not particularly large or abundant inclusions). Small, euhedral fine-grained apatite and zircon crystals are also apparent within the rock. The matrix is feldspathic and contains minor amounts of carbonate replacement. There also rare amygdules with calcite infill. The rock has a porphyritic texture and has undergone strong sericite-chlorite-carbonate alteration. Muscovite alteration is dominantly associated with the replacement of plagioclase, while chlorite and carbonate alteration appear to be have replaced biotite and hornblende grains. Minor amounts of opaques (magnetite) are present. This is an altered hornblende-biotite granodiorite.

Sample 58 (Michiquillay North)

Moderately abundantly feldspar phenocrysts (0.7-4 mm) are clear-cloudy white in colour and sub-euhedral. Mafic grains are subhedral-euhedral, often have a dusty black colour and range in size from 0.4-2 mm. Occasional quartz grains are rounded and ~1.5-2.0 mm in diameter. The matrix is a dark grey-black.

In thin section, the porphyritic rock has euhedral plagioclase phenocrysts showing strong oscillatory zoning. Most grains are unaltered although some grains show sericitic replacement. A minor amount of carbonate infill is also apparent in some cores. Quartz grains are unaltered and are often rounded-globular in shape. Grain boundaries often have a fine-grained recrystallised rim and crystals also contain small fluid inclusion trails (inclusions are mostly brine or brine-vapour). Hornblende grains have been pervasively replaced by chlorite-carbonate-sericite alteration with most retaining their euhedral crystal shape. Grains often have a rim of magnetite and/or hematite. Randomly throughout the matrix are regions rich in carbonate minerals (probably calcite), epidote, apatite and fine-medium grained magnetite. The matrix is a very fine-grained feldspathic composition. This sample is moderately altered and has undergone carbonate-chlorite-sericite alteration. The sample is a inferred to be a hornblende granodiorite.

Sample 59 (Michiquillay North)

This sample is characterised by cloudy white-clear feldspar phenocrysts, 0.5-4.0 mm in size and subhedral in shape. Quartz grains are rounded and range in size from 0.3-3.0 mm. Biotite grains are evident (~5 mm). Hornblende crystals are moderately abundant, acicular and elongate in shape, euhedral, 0.8-2.5 mm in size with the larger grains occasionally having inclusions. The matrix is a light grey colour with a slightly green tinge.

In thin section, the plagioclase phenocrysts exhibit some intracrystalline fractures and are weakly-strongly replaced by sericite. Grains are dominantly euhedral, show good oscillatory zoning plus multiple twinning, and may contain minor-moderate sieve textures toward the rim. Abundant hornblende grains are euhedral-subhedral, green-yellowish green in colour and occasionally show zoning. Quartz grains are globular in shape, occasionally contain embayments and have very small, rare inclusions. Biotite grains have been pervasively replaced by chlorite and muscovite but retained their original crystal shape. The replaced grains often have a fine-grained magnetite/hematite rich rim. Minor amount of clinopyroxene, apatite and zircon are also evident in thin section. The matrix is of felspathic composition. This sample is inferred to be a hornblende-biotite granodiorite.

Sample 60 (Michiquillay North)

In hand specimen, this sample is characterised by subhedral-euhedral feldspar grains, dominantly cloudy white in colour and range in size from ~0.5-3.0 mm in length. Minor amounts of mafic minerals are present, grains are generally very small (~0.3 mm) in size but have a wide distribution throughout the sample. Grains have a dull black appearance. Minor amounts of quartz and fine-grained pyrite are also present. Pyrite grains occur both within other minerals and as individual spots throughout the matrix. The matrix is a light grey in colour with a slightly green tinge.

In thin section, plagioclases contain abundant intragranular fractures that are filled with carbonate, muscovite and occasionally epidote. Plagioclase grains are euhedral and show moderate twinning. Rounded quartz grains are relatively common, subhedral in shape, medium to coarse grained and generally clean with small inclusions (brine-vapour inclusions, rare salt crystals). Hornblende grains have been totally replaced by chlorite and calcite. Fine magnetite crystals often rim the replaced hornblende grains. The sample also contains large calcite crystals that have an infill appearance. Other minerals evident within the slide are epidote and minor amounts of sulphide minerals. The sample has undergone strong chlorite and carbonate alteration. It is inferred to be a hornblende granodiorite.

VOLCANIC ROCKS

Sample 21 (La Carpa)

Sample contains moderate-abundant feldspar grains that are generally 0.5-3 mm, subhedral, cloudy white-dirty green in colour. Hornblende grains are euhedral, occasionally subhedral in shape, range in size from 0.5-7.0 mm, larger grains may contain fine inclusions of white grains (possibly feldspar). Quartz phenocrysts are rounded in shape and ~2 mm in size. The matrix is a greenish grey colour with patches of abundant green minerals (probably epidote or chlorite).

In thin section, the sample has a crowded porphyritic texture with phenocrysts of plagioclase and hornblende. Plagioclase crystals are moderately altered showing varying degrees in sericitic replacement and intragranular fractures, fractures are often filled with muscovite and epidote, some grains have a vague melting rim with twinning and oscillating zoning is common. Hornblende grains are green-dark green in colour, with occasional inclusions of feldspar and opaque minerals. Clinopyroxene and apatite grains are also evident. The matrix is feldspathic and has a slightly trachytic texture. Overall, sample 21 is a crowded porphyritic volcanic that has undergone a moderate chlorite-sericite-carbonate alteration and is inferred to be a hornblende andesite.

Sample 32 (Cruz Conga)

In hand sample, this weakly porphyritic volcanic sample contains plagioclase, hornblende and pyroxene phenocrysts that are set within a pinkish red matrix. The plagioclase grains are generally clear whilst the hornblende grains are dusty-dull in appearance.

In thin section, the plagioclase phenocrysts are mostly euhedral-subhedral in shape, display simple-multiple twinning features and in parts has been replaced by K-feldspar. Some of the grains have undergone moderate muscovite alteration. Euhedral hornblende phenocrysts have a brown and have hazy iron oxidations rim characteristic of calc-alkaline igneous rocks. Opaque rims result from the formation of magnetite by oxidation of iron in ferro-magnesium minerals, which is common for hornblende in volcanic rocks. Clinopyroxene grains are subhedral-euhedral in shape, weakly pleochroic from light orange to light yellow, some display oscillatory zoning and twinning, and occur both freely within the groundmass as well as inclusions in hornblende phenocrysts. The sample contains fine to medium-grained, euhedral apatite minerals that are slight blue in colour. The sample also contains minor-moderate amounts of magnetite. The groundmass has a very fine-grained trachytic texture and is of feldspathic composition. The sample displays very weak chlorite alteration. The sample is inferred to be basaltic andesite volcanic rock.

Sample 50 (C^{o} Perol)

In thin section the slide exhibits a chlorite-epidote vein that has resulted in an alteration selvage. Away from the vein and related features, feldspar phenocrysts are euhedral and range from little-intense sericite replacement. Feldspar grains close to the veins have a considerably strong alteration appearance with intense-pervasive sericite-chlorite replacement. Throughout the entire slide, hornblende grains have been totally replaced by chlorite and minor amounts of carbonate material, but the original grain shape has been preserved. Amygdules are often filled with carbonate material and range in size from 4-1mm in length. The matrix is felspathic in composition with slight-moderate chlorite alteration and has a quasi-trachytic texture. The matrix texture as well as the presence of amygdules is suggestive of a volcanic or extrusive system. The chlorite-epidote vein is ~0.3mm thick and resulted in an alteration selvage that ranges in thickness from 1-5mm thick. The vein is dominantly composed of epidote that appears to have been partially destroyed by late calcite infill. The selvage is epidote and chlorite rich, dirty in appearance and destroyed most the original wall rock features. Very little opaque minerals are found within or around the vein-selvage area.

Sample 61 (Cajamarca)

Sample contains abundant sub-euhedral feldspar grains of 0.5-2 mm size, white-clear in colour with rare inclusions of a dark mineral. Pyroxene minerals are also present, rose in colour, euhedral and ~1 mm in size. Hornblende grains are dominantly acicular, 1-4 mm, occasional inclusions are evident and few grains have a corroded hematite rim. The sample is brown in colour with abundant feldspar and pyroxene grains. Calcite rich fragments are also present and have a dark rim.

Eu-subhedral plagioclase grains show strong twinning and zoning, grains are abundant and most are unaltered although some have a sericitic rim. Pyroxene minerals are moderately abundance, occasionally exhibit zoning and twinning, are euhedral-subhedral in shape. Few hornblende grains are present, often display a thick hematite rim and are acicular in shape. The matrix is composed of fine, elongate felspar minerals and has a slight trachytic texture. This sample is a hornblende andesite.

Sample 64 (Cajamarca)

In outcrop exposure and in hand specimen the sample is characteristic of a porphyritic basalt lava flow. Subhedral-euhedral feldspar phenocrysts range in size from

0.5-3 mm, with the larger grains (~3-5 mm) having a cloudy white colour and the smaller grains being generally translucent. Mafic grains are dominantly subhedral, 1-5 mm, often contain inclusions and have a corroded hematite rim. Minor amounts of pyroxene is visible, they are often rose-olive in colour and ~1-2 mm in size. The sample is dark-dirty brown in colour and in places small feldspar grains appear to be aligned. Flow layers vary in thickness from millimetres to several centimetres.

In thin section, abundant plagioclase grains are mostly clean, occasionally with minor sericite, often show good twinning and zoning. Some grains are slightly fractured and may have thin boiling rims. Clinopyroxene are dominantly fine grained (~1 mm or less in size, rarely larger) and lack twinning or zoning textures. Hornblende grains have a corroded rim of magnetite and/or hematite. Often they appear poikilitic in texture with numerous feldspar and occasional pyroxene inclusions. The matrix is feldspathic in composition and granular in appearance (not necessarily trachytic). Flow layer boundaries are subtle to discrete and evident by minor changes in the appearance of the matrix and abundance of phenocrysts. These rocks are inferred to be hornblende andesite flows.

Sample 66 (Cajamarca)

In hand specimen the rock is dark brown in colour, has a weak fine-grained porphyritic texture and appears to be part of a possible massive flow unit. Few phenocrysts of mafic minerals are present and ~2-6 mm long and appear to be slightly altered with a corroded hematite rim. Feldspar grains are generally equigranular and ~1 mm in size. The sample contains a moderate amount of anastomosing fractures that are possibly filled with quartz-feldspar-calcite type minerals.

In thin section, plagioclase grains are euhedral-subhedral, mostly unaltered although minor-moderate sericite replacement is evident. There is a semi-preferred orientation of grains and most have a strong zoning or twinning texture. Hornblende grains have a thick hematite rim but are generally have a fresh core. Minor amounts of fine-grained clinopyroxene grains are present, they are generally euhedral and in places have a thin corroded rim. The matrix is dominantly composed of felspathic material with minor amounts of clay. Its texture is granular-glassy, possibly tuffaceous. This is inferred to be a hornblende andesite.

Sample 68 (Cajamarca)

In this sample feldspars are characterised by a large phenocryst population that is 4-6 mm in size, clear-cloudy white and dominantly euhedral. The smaller population is more abundant, ~1 mm or smaller in size, elongate and euhedral in shape, appear to have a preferred orientation and a light hazy white in colour. Hornblende grains are often euhedral, ~2 mm in length, commonly contain small white inclusions and have a brown hematite rim. The matrix is a dirty grey-brownish grey.

In thin section, euhedral plagioclase grains are clear-dusty in appearance, occasional zoning and twinning is apparent, grains show minor sericite alteration and the smaller grains have a slight-moderate alignment. Pyroxene grains are often fine grained (~0.5 mm or smaller), mostly clean and subhedral-euhedral in shape. Some pyroxene grains may have feldspar or magnetite overgrowths. Corroded hornblende phenocrysts have a slight piokilitic texture with fine grains of feldspar. The matrix is of feldspathic composition and is generally dirty in appearance.

APPENDIX A2

Laboratory analytical procedures for $^{40}Ar/^{39}Ar$ analyses

LABORATORY ANALYTICAL PROCEDURES

New Mexico Geochronology Research Lab

NMGRL Analytical Procedures - Hornblende separates were obtained using heavy liquid separation and handpicking techniques. The samples were loaded into a Al disc and irradiated for seven hours in the D-3 position at the Nuclear Science Centre reactor, Texas A&M University. The irradiated samples were monitored with a 27.84 Ma sanidine NMGRL standard (FC-1).

Irradiated hornblende grains were placed in a Mo furnace crucible and step-heated for three minutes by a 50W CO_2 laser at the NMGRL. During heating, gases evolved from the samples heated in the furnace react with the first stage getter, i.e. a SAES GP-50 getter heated at 450^{o}C. Following heating the gas expanded into a second stage for two minutes. The second stage is comprised of a SAES GP-50 getter operated at 20^{o}C and a tungsten filament operated at ~2000^{o}C. During second stage cleaning, the furnace and the first stage are pumped out. After gettering in the second stage, the gas is expanded into a MAP-215-50 mass spectrometer. Gases evolved from the samples heated in the laser are expanded via a cold finger operated at –140^{o}C directly into the second stage. Following cleanup, the gas in the second stage and laser chamber is expanded in the mass spectrometer for analysis. Isotopes are detected on a Johnston electron multiplier operated at ~2.1 kV. Blanks for the furnace are run every three to six heating steps and between every four analyses for the laser system.

Argon Geochronology Laboratory (University of Queensland)

Hornblende and biotite separates were obtained using heavy liquid separation and handpicking techniques Ten to twenty pure grains from each sample were loaded into irradiation disks along with Fish Canyon (nominal age of 28.02 Ma) and Cobb Mountain sanidine (nominal age of 1.194 Ma) standards (Renne *et al*., 1998). The disks were wrapped in Al-foil, vacuum sealed in silica glass tubes and irradiated for 14 hours at the B-1 CLICIT facility at the Radiation Centre, Oregon State University, USA.

Sample and flux monitor irradiation geometry followed those of Vasconcelos (1999). After a two-month cooling period, the samples were analysed by the laser incremental-heating $^{40}Ar/^{39}Ar$ method at the UQ-AGES (University of Queensland Argon Geochronology in Earth Sciences) laboratory following procedures detailed by Vasconcelos (1999). Air pipettes and full system blanks were analysed before and after each grain, yielding $^{40}Ar/^{36}Ar$ discrimination values ranging from 0.9845 ± 0.0026 to 1.0139 ± 0.0022, with an average value of 0.9996 ± 0.0024. Average blank value for the analyses was 0.0069 ± 0.0001 nA of current in the electron multiplier. All dates are reported using 5.543 x 10^{-10} a-1 as the total decay constant for 40^{K} (Steiger and Jäger, 1977) and the following values for the reactor correction factors: (2.64 ± 0.02) x 10^{-4} for $(^{36}Ar/^{37}Ar)Ca$, (7.04 ± 0.06) x 10^{-4} for $(^{39}Ar/^{37}Ar)Ca$ and (8 ± 3) x 10^{-4} for $(^{40}Ar/^{36}Ar)K$. J-factors for each sample are shown in Appendix A3.

References

Renne, R., Swisher, C.C., Deino, A.L., Karner, D.B., Owens, T.L. and DePaolo, D.J., 1998. Intercalibration of standards, absolute ages and uncertainties in $^{40}Ar/^{39}Ar$ dating. Chemical Geology, 145: 117–152.

Steiger, R.H. and Jäger, E., 1977. Subcommission on geochronology: Convention on the use of decay constants in geo- and cosmochronology. Earth and Planetary Science Letters, 36: 359-362.

Vasconcelos, P.M., 1999. $^{40}Ar/^{39}Ar$ geochronology of supergene processes in ore deposits. In: J.P. Richards and R.M. Tosdal (Editors), Structural controls on ore genesis. Society of Economic Geologists Reviews, 14: 157-181.

APPENDIX A3

$^{40}Ar/^{39}Ar$ incremental step heating data

ID	Temp (°C)	$^{37}Ar/^{39}Ar$	$^{40}Ar/^{39}Ar$	$^{36}Ar/^{39}Ar$ (x 10^{-3})	$^{39}Ar_K$ (x 10^{-6} mol)	K/Ca	^{40}Ar (%)	^{39}Ar (%)	Age (Ma)	Error (1σ) (Ma)
21, 17.19 mg hornblende, J=0.0007388										
A	5	295.60	1.998	985.70	5.72	0.26	1.5	0.9	6.00	4.50
B	10	673.60	17.930	2172.80	2.40	0.03	4.9	1.3	44.00	17.00
C	15	385.50	15.300	1207.50	1.64	0.03	7.8	1.6	40.00	14.10
D	20	66.88	14.130	124.10	6.24	0.04	46.9	2.6	41.90	1.20
E	25	37.38	6.088	20.02	41.60	0.08	85.5	9.3	42.33	0.21
F	30	34.07	5.816	8.00	118.40	0.09	94.5	28.5	42.62	0.12
G	35	33.36	5.815	5.38	181.30	0.09	96.7	57.8	42.70	0.11
H	40	33.30	5.899	5.95	173.60	0.09	96.2	85.9	42.42	0.10
I	45	30.88	5.124	14.32	66.50	0.10	87.7	96.6	35.90	0.15
J	50	12.29	0.371	28.55	12.80	1.40	31.6	98.7	5.17	0.33
K	50	12.34	0.177	32.55	8.12	2.90	22.2	100.0	3.64	0.49
total gas age					618.30	0.15			40.21	0.58#
Plateau (steps B-H)		MSWD = 0.90			525.10	0.09		84.9	**42.55**	**0.12#**
59, 0.2 mg hornblende, J=0.0007399										
A	5	315.00	4.366	1025.10	5.73	0.12	4.0	1.5	16.60	5.30
B	10	87.23	4.561	252.30	14.20	0.11	15.0	5.2	17.40	1.00
C	15	40.66	2.943	87.33	16.10	0.17	37.1	9.4	20.09	0.50
D	20	23.73	5.124	28.71	90.60	0.10	66.0	33.1	20.89	0.14
E	25	20.26	4.868	17.56	150.70	0.10	76.4	72.4	20.63	0.10
F	30	22.70	4.568	26.33	76.50	0.11	67.4	92.4	20.39	0.15
G	35	26.55	3.526	40.73	9.92	0.14	55.8	95	19.72	0.42
H	40	28.48	2.924	40.86	2.63	0.17	58.5	95.7	22.10	1.40
I	45	28.26	2.998	42.85	2.92	0.17	56.1	96.4	21.10	1.20
J	50	26.98	4.078	41.08	10.90	0.13	56.3	99.3	20.22	0.51
K	50	27.61	4.072	41.10	2.73	0.13	57.2	100.0	21.00	1.30
total gas age					372.90	0.11			20.42	0.6#
Plateau (steps C-K)		MSWD = 1.7			363.00	0.11		94.8	**20.61**	**0.14#**
38, 19.76 mg hornblende, J=0.0007392										
A	5	414.40	2.354	1368.70	7.29	0.22	2.4	1.0	13.50	5.60
B	10	155.10	1.174	479.50	13.90	0.43	8.7	3.0	17.90	1.70
C	15	41.41	2.033	94.10	14.30	0.25	33.3	5.0	18.31	0.50
D	20	17.92	5.023	16.38	76.30	0.10	75.3	15.6	17.99	0.12
E	25	15.64	4.804	8.64	207.80	0.11	86.2	44.7	17.98	0.07
F	30	14.60	5.357	5.79	229.00	0.10	91.3	76.6	17.77	0.06
G	35	14.16	5.435	4.27	143.00	0.09	94.3	96.6	17.80	0.06
H	40	16.03	5.132	10.30	16.70	0.10	83.7	98.9	17.88	0.21
I	45	20.94	5.168	35.22	4.09	0.10	52.3	99.5	14.62	0.79
J	50	24.87	5.357	40.52	2.76	0.10	52.6	99.9	17.80	1.10
K	50	51.60	5.056	155.50	0.72	0.10	11.8	100.0	8.10	4.70
total gas age					715.90	0.11			17.81	0.38#
Plateau (steps A-H)		MSWD = 1.2			708.30	0.11		98.9	**17.85**	**0.06#**

= 2σ error; J = error in neutron flux

ID	$^{40}Ar/^{39}Ar$	$^{38}Ar/^{39}Ar$ (x 10^{-2})	$^{37}Ar/^{39}Ar$ (x 10^{-2})	$^{36}Ar/^{39}Ar$ (x 10^{-3})	^{40}Ar (moles) (x 10^{-15})	$^{40}Ar/^{39}Ar$	% Rad	Age (Ma)	Error (1σ) (Ma)
S-46, hornblende, J=0.003688									
A	224.83	0.05	0.00	0.53	1.37	68.62	30.50	407.00	49.19
B	18.22	0.04	19.34	0.04	25.42	8.90	48.20	58.26	22.77
C	9.48	0.03	6.99	0.00	73.87	9.01	94.60	58.96	4.05
E	7.69	0.02	6.41	0.00	64.09	8.51	110.20	55.78	3.35
D	13.28	0.03	31.49	0.01	12.32	14.13	104.10	91.64	30.07
F	12.75	0.02	0.00	n/a	10.80	21.24	166.70	136.07	32.61
G	35.75	n/a	20.18	n/a	924.24	42.80	118.00	264.39	102.53
H	19.11	n/a	3.93	n/a	174.64	290.23	1514.90	1312.87	167.77
I	5.23	n/a	0.00	n/a	2409.66	455.34	8715.00	1778.01	646.57
total gas age								87.00	4.00#
Plateau (steps B-E)								**57.00**	**3.00#**
S-31, hornblende, J=0.003688									
A	43.62	n/a	0.00	0.01	15.88	41.71	95.60	258.15	77.85
B	23.43	0.00	132.25	0.25	338.06	-43.10	-166.90	-312.33	276.96
C	7.92	0.02	14.50	0.01	55.82	6.15	77.00	40.49	4.74
D	7.03	0.02	10.21	0.00	1.32	6.93	97.90	45.53	1.79
E	7.30	0.03	11.74	0.00	97.56	7.78	105.80	51.07	2.65
F	8.46	n/a	0.00	0.07	360.60	-11.59	-137.00	-78.83	74.80
G	8.75	n/a	0.00	n/a	157.75	60.50	691.70	363.34	125.61
H	8.01	n/a	5.38	0.00	677.44	9.63	119.70	62.93	32.43
I	7.30	n/a	2.93	0.06	284.38	-9.07	-124.10	-61.39	71.14
total gas age								47.00	2.00#
Plateau (steps B-F)								**47.00**	**3.00#**
S-16, hornblende, J=0.003688									
A	352.38	0.26	7.68	1.34	0.12	-44.36	-12.50	-322.31	99.21
B	79.23	0.06	9.74	0.27	0.25	1.56	2.00	10.35	10.18
C	32.16	0.03	10.94	0.10	0.21	4.12	12.70	27.20	3.75
D	8.84	0.02	2.53	0.02	0.13	4.41	49.80	29.11	1.19
E	7.10	0.02	4.04	0.01	4.39	4.93	69.10	32.48	1.96
F	7.86	0.02	5.91	0.01	5.29	4.87	61.80	32.14	2.02
G	6.24	0.01	26.98	0.01	4.57	4.03	63.30	26.59	1.80
H	5.63	0.01	57.86	0.02	3.45	3.11	53.10	20.61	2.01
I	6.67	0.02	197.36	0.07	2.79	2.72	35.10	18.02	4.12
J	7.69	0.04	608.04	0.17	57.05	7.79	58.00	51.09	29.07
K	7.06	0.13	771.35	0.23	967.27	-4.34	-28.10	-29.11	190.74
total gas age								24.60	1.20#
Plateau (steps C-H)								**29.40**	**1.40#**
S-11, hornblende, J=0.003688									
A	59.29	0.03	22.36	0.18	40.80	7.05	11.70	46.31	47.90
B	10.58	0.01	34.59	0.06	11.77	-3.11	-28.70	-20.82	26.72
C	3.63	0.02	7.69	0.00	35.18	3.76	103.10	24.87	2.96
E	2.98	0.02	7.01	0.00	1.34	3.25	108.50	21.49	0.73
D	3.05	0.02	7.42	0.00	1.22	3.16	102.90	20.88	0.85
F	5.04	0.03	14.26	0.01	20.07	1.87	36.70	12.39	7.22
G	4.72	n/a	7.57	n/a	218.03	19.49	410.60	125.24	40.22
H	5.36	n/a	79.39	n/a	n/a	149.65	2635.10	792.86	135.35
I	12.93	n/a	0.00	n/a	2033.25	1205.22	9324.90	3057.32	348.02
total gas age								24.70	0.80#
Plateau (steps A-F)								**21.30**	**0.80#**
H-22, biotite, J=0.003688									
A	31.23	-6.97	0.00	n/a	49.30	131.28	420.30	712.35	60.33
B	29.38	1.67	2.00	28.70	2.84	20.91	71.10	133.99	13.91
C	8.34	1.91	11.80	n/a	1.66	9.24	110.80	60.43	6.84
D	4.70	1.42	9.33	0.43	3.26	4.58	97.50	30.24	2.03
E	4.16	1.27	1.48	n/a	2.62	4.38	105.10	28.88	2.16

ID	$^{40}Ar/^{39}Ar$	$^{38}Ar/^{39}Ar$ (x 10^{-2})	$^{37}Ar/^{39}Ar$ (x 10^{-2})	$^{36}Ar/^{39}Ar$ (x 10^{-3})	^{40}Ar (moles) (x 10^{-15})	$^{40}Ar/^{39}Ar$	% Rad	Age (Ma)	Error (1σ) (Ma)
F	4.18	1.53	8.04	n/a	3.36	4.62	110.60	30.50	1.75
G	3.25	1.53	3.63	0.37	3.67	3.15	96.70	20.82	1.20
H	3.19	1.49	2.09	n/a	5.86	3.25	101.80	21.50	0.71
I	3.01	1.48	1.51	n/a	8.61	3.18	105.60	21.01	0.51
J	3.02	1.49	1.38	0.71	0.13	2.81	93.10	18.62	0.33
K	2.99	1.46	1.05	0.37	0.22	2.88	96.30	19.08	0.21
L	2.98	1.47	1.23	0.37	0.33	2.87	96.30	19.02	0.14
M	2.99	1.50	1.80	0.13	0.42	2.95	98.70	19.54	0.13
N	3.02	1.45	2.02	0.16	0.58	2.98	98.50	19.70	0.12
O	3.05	1.50	2.25	0.17	0.79	3.00	98.40	19.86	0.10
P	3.05	1.46	2.92	0.45	0.98	3.01	99.60	19.92	0.08
Q	3.07	1.47	3.55	0.34	0.57	2.97	96.80	19.66	0.10
R	3.03	1.51	3.41	0.38	0.33	2.92	96.40	19.35	0.14
S	3.02	1.51	2.07	0.26	0.98	2.95	97.50	19.51	0.53
total gas age								20.02	0.05#
Plateau (steps M-Q)								**19.77**	**0.05#**
T-2, hydorthermal biotite, J=0.003688									
A	56.61	7.07	15.90	20.20	11.10	-3.11	-5.50	-20.79	14.63
B	6.61	1.66	2.77	4.96	2.89	5.14	77.80	33.90	3.67
C	3.26	1.33	0.89	1.95	4.49	2.69	82.40	17.80	1.33
D	2.98	1.52	1.34	0.57	4.79	2.81	94.30	18.63	1.01
E	2.84	1.48	1.55	0.34	5.78	2.74	96.60	18.14	0.83
F	2.77	1.53	2.30	0.68	6.52	2.57	92.90	17.03	0.67
G	2.75	1.45	1.54	0.61	8.25	2.57	93.50	17.03	0.51
H	2.79	1.46	1.62	0.93	9.43	2.52	90.20	16.88	0.52
I	2.96	1.54	7.48	0.39	4.82	2.85	96.10	18.83	0.94
total gas age								17.50	0.30#
Plateau (steps C-I)								**17.50**	**0.30#**
T-4, magmatic biotite, J=0.003688									
A	10.11	2.07	12.00	19.50	2.17	4.36	43.10	28.77	6.42
B	3.32	1.60	3.05	n/a	4.46	3.58	107.80	23.64	1.11
C	2.71	1.40	1.42	n/a	6.32	2.93	108.30	19.40	0.68
D	2.66	1.46	0.83	0.30	9.38	2.57	96.70	17.03	0.44
E	2.63	1.43	1.09	0.62	0.11	2.45	93.00	16.23	0.34
F	2.64	1.40	1.36	0.33	0.15	2.54	96.30	16.83	0.29
G	2.63	1.44	1.87	0.71	0.11	2.42	92.10	16.02	0.38
H	2.66	1.45	2.46	0.78	6.73	2.43	91.40	16.09	0.59
I	2.67	1.36	0.35	0.18	5.20	2.62	98.00	17.35	0.77
J	2.70	1.35	0.28	1.27	1.89	2.33	86.10	15.41	1.89
K	2.68	1.34	1.43	0.45	2.05	2.55	95.10	16.87	1.73
total gas age								17.24	0.18#
Plateau (steps D-K)								**16.53**	**0.18#**

= 2σ error; J = error in neutron flux; n/a = no detection

APPENDIX C1

Electron microprobe analyses

Electron microprobe analyses of feldspar grains

	Gabbroic Dyke																											
	Hbl Gabbro										Hbl Gabbro					Gabbro										Gabbroic Diorite		
Sample No.	16	16	16	16	16	16	16	16	16	16	55	55	55	55	55	57	57	57	57	57	57	57	57	57	57	87	87	87
Analysis No.	1r	1c	1r1	1c1	2r	2c	3r	3c	4r	4c	1r	2c	2r	3c	3r	1r	1c	2r	2c	3c	4r	4c	5r	6r	6c	1c	1r	2c
Oxide Weight Percent																												
SiO_2	50.48	47.52	57.12	49.43	53.21	49.95	55.84	46.89	47.53	45.77	46.27	48.55	51.71	47.22	46.85	51.09	52.58	51.79	54.81	64.47	53.88	52.78	53.04	52.54	50.35	51.49	52.85	50.41
TiO_2	<0.20	<0.20	<0.20	<0.20	<0.20	<0.20	<0.20	<0.20	<0.20	<0.20	<0.20	<0.20	<0.20	<0.20	<0.20	<0.20	<0.20	<0.20	<0.20	<0.20	<0.20	<0.20	<0.20	<0.20	<0.20	<0.20	<0.20	<0.20
Al_2O_3	29.84	32.85	26.02	31.40	28.52	30.52	27.12	33.40	32.79	34.35	32.92	31.30	29.32	32.85	33.32	30.39	29.04	29.10	27.60	21.44	28.34	29.27	28.51	28.50	30.02	29.62	29.09	30.64
Fe_2O_3(T)	0.72	0.49	0.74	0.76	0.97	0.97	0.46	0.71	0.53	0.48	0.52	0.57	0.98	0.63	0.63	0.76	0.76	0.88	0.80	0.37	0.65	0.69	0.75	0.81	0.42	0.72	0.82	0.72
MnO	<0.20	<0.20	<0.20	<0.20	<0.20	<0.20	<0.20	<0.20	<0.20	<0.20	<0.20	<0.20	<0.20	<0.20	<0.20	<0.20	<0.20	<0.20	<0.20	<0.20	<0.20	<0.20	<0.20	<0.20	<0.20	<0.20	<0.20	<0.20
MgO	0.21	0.39	<0.20	0.40	0.66	0.43	0.41	0.42	0.64	0.56	0.61	0.43	0.49	0.71	0.64	0.44	0.52	0.29	0.47	<0.20	0.27	0.68	<0.20	0.63	0.28	0.60	0.63	0.66
CaO	14.12	16.90	8.78	15.46	12.40	14.65	10.36	17.66	17.01	18.20	17.42	15.90	13.71	17.03	17.08	13.78	12.27	12.56	10.57	3.20	11.09	12.46	11.93	12.31	14.19	12.77	12.98	15.01
Na_2O	3.21	1.80	5.97	2.38	4.28	2.91	5.47	1.41	1.56	1.16	1.05	1.99	3.21	1.43	1.57	3.63	4.03	4.25	5.34	10.06	5.17	4.30	4.52	4.37	3.28	3.13	3.83	2.73
K_2O	<0.20	<0.20	<0.20	<0.20	<0.20	<0.20	<0.20	<0.20	<0.20	<0.20	<0.20	<0.20	<0.20	<0.20	<0.20	0.21	0.23	0.23	0.48	0.31	0.25	0.23	0.26	0.26	<0.20	0.60	<0.20	<0.20
Cl	<0.20	<0.20	<0.20	<0.20	<0.20	<0.20	<0.20	<0.20	<0.20	<0.20	<0.20	<0.20	<0.20	<0.20	<0.20	<0.20	<0.20	<0.20	<0.20	<0.20	<0.20	<0.20	<0.20	<0.20	<0.20	<0.20	<0.20	<0.20
Total	98.77	100.02	99.46	99.88	100.36	99.61	100.17	100.58	100.50	100.82	98.93	99.16	99.72	100.11	100.42	100.34	99.45	99.26	100.25	100.07	99.81	100.48	99.35	99.77	98.81	99.20	100.51	100.50
Number of atoms per formula unit (32 oxygens)																												
Si	9.34	8.74	10.34	9.07	9.66	9.19	10.07	8.60	8.72	8.40	8.62	8.99	9.46	8.69	8.61	9.31	9.61	9.52	9.92	11.41	9.80	9.56	9.71	9.61	9.31	9.46	9.58	9.19
Ti	<0.20	<0.20	<0.20	<0.20	<0.20	<0.20	<0.20	<0.20	<0.20	<0.20	<0.20	<0.20	<0.20	<0.20	<0.20	-	-	-	-	-	-	-	-	-	-	-	-	-
Al	6.50	7.12	5.55	6.79	6.10	6.62	5.77	7.22	7.09	7.43	7.22	6.83	6.32	7.12	7.21	6.53	6.25	6.30	5.89	4.47	6.07	6.25	6.15	6.14	6.54	6.42	6.21	6.58
Fe^{2+}	0.11	0.07	0.11	0.12	0.15	0.15	0.07	0.11	0.08	0.07	0.08	0.09	0.15	0.10	0.10	0.11	0.12	0.13	0.12	0.05	0.10	0.10	0.11	0.12	0.06	0.11	0.12	0.11
Mn	-	-	-	-	-	-	-	-	-	-	-	-	-	-	-	-	-	-	-	-	-	-	-	-	-	-	-	-
Mg	0.06	0.11	-	0.11	0.18	0.12	0.11	0.12	0.18	0.15	0.17	0.12	0.13	0.20	0.17	0.12	0.14	0.08	0.13	-	0.07	0.18	-	0.17	0.08	0.16	0.17	0.18
Ca	2.80	3.33	1.70	3.04	2.41	2.89	2.00	3.47	3.34	3.58	3.48	3.15	2.69	3.35	3.36	2.69	2.40	2.47	2.05	0.60	2.16	2.42	2.34	2.41	2.81	2.51	2.52	2.93
Na	1.15	0.64	2.09	0.84	1.51	1.03	1.91	0.50	0.55	0.41	0.38	0.71	1.14	0.51	0.56	1.28	1.42	1.51	1.87	3.45	1.82	1.51	1.60	1.55	1.18	1.12	1.34	0.96
K	-	-	-	-	-	-	-	-	-	-	-	-	-	-	-	0.05	0.05	0.05	0.11	0.07	0.06	0.05	0.06	0.06	-	0.14	-	-
Cl	-	-	-	-	-	-	-	-	-	-	-	-	-	-	-	-	-	-	-	-	-	-	-	-	-	-	-	-
Total	20.00	20.04	19.99	19.98	20.06	20.04	20.04	20.04	20.05	20.09	19.97	19.98	19.96	20.01	20.07	20.11	20.00	20.11	20.13	20.12	20.10	20.10	20.04	20.12	20.04	19.99	20.01	20.00
An	0.71	0.84	0.45	0.78	0.62	0.74	0.51	0.87	0.86	0.90	0.90	0.82	0.70	0.87	0.86	0.67	0.62	0.61	0.51	0.15	0.53	0.61	0.58	0.60	0.71	0.67	0.65	0.75
Ab	0.29	0.16	0.55	0.22	0.38	0.26	0.49	0.13	0.14	0.10	0.10	0.18	0.30	0.13	0.14	0.32	0.37	0.37	0.46	0.84	0.45	0.38	0.40	0.39	0.29	0.30	0.35	0.25
Or	0.00	0.00	0.00	0.00	0.00	0.00	0.00	0.00	0.00	0.00	0.00	0.00	0.00	0.00	0.00	0.01	0.01	0.01	0.03	0.02	0.01	0.01	0.02	0.01	0.00	0.04	0.00	0.00

r = analysis at grain rim; c = analysis at grain core; <0.20 = below detection limit; - = below detection limit

Feldspar analyses cont.

	Palaeogene Igneous Units														Miocene Barren Intrusive Units							
	Hbl Diorite						Hbl Microdiorite			Basaltic Andesite					Hbl Diorite				Hbl-Bt Qtz Diorite			
Sample No.	31	31	31	31	31	31	46	46	46	32	32	32	32	32	11	11	11	11	59	59	59	59
Analysis No.	1c	2c	2r	2r1	2r2	3r	1c	2r	2c	1c	2c	3c	4r	4r	1r	1c	2r	2c	1c	2c	2r	3c
SiO_2	58.64	59.51	59.07	67.14	58.19	59.52	54.22	51.82	48.70	49.10	53.41	50.43	53.82	52.91	55.64	56.81	55.33	55.98	58.52	57.60	57.94	57.66
TiO_2	<0.20	<0.20	<0.20	<0.20	<0.20	<0.20	<0.20	<0.20	<0.20	<0.20	<0.20	<0.20	<0.20	<0.20	<0.20	<0.20	<0.20	<0.20	<0.20	<0.20	<0.20	<0.20
Al_2O_3	25.84	25.33	25.24	20.47	25.90	24.22	27.14	29.81	31.18	31.89	27.96	30.13	27.75	27.95	26.99	26.16	27.09	26.77	25.39	25.27	25.78	26.22
Fe_2O_3(T)	0.41	0.37	0.47	0.35	0.41	0.70	0.29	0.27	0.49	0.55	0.51	0.43	0.64	0.70	<0.20	<0.20	0.32	0.33	<0.20	<0.20	<0.20	<0.20
MnO	<0.20	<0.20	<0.20	<0.20	<0.20	<0.20	<0.20	<0.20	<0.20	<0.20	<0.20	<0.20	<0.20	<0.20	<0.20	<0.20	<0.20	<0.20	<0.20	<0.20	<0.20	<0.20
MgO	0.45	0.52	0.37	0.44	0.40	0.38	0.59	0.57	0.37	0.28	0.20	0.36	0.20	0.59	<0.20	0.23	0.21	0.45	0.47	0.43	0.51	0.46
CaO	8.13	7.78	7.71	1.39	7.91	6.76	10.55	13.13	15.04	15.23	11.37	13.63	11.20	12.09	9.57	8.85	9.91	9.11	8.83	8.33	8.78	8.88
Na_2O	6.67	6.74	6.84	10.44	6.94	7.16	5.48	3.77	2.92	2.32	4.38	3.13	4.68	4.45	5.43	5.93	5.25	5.93	6.43	6.22	5.84	5.73
K_2O	0.41	0.28	0.38	0.31	0.40	0.49	<0.20	<0.20	<0.20	<0.20	0.35	<0.20	0.34	0.36	0.27	0.25	0.26	0.26	0.20	0.32	0.36	0.32
Cl	<0.20	<0.20	<0.20	<0.20	<0.20	<0.20	<0.20	<0.20	<0.20	<0.20	<0.20	<0.20	<0.20	<0.20	<0.20	<0.20	<0.20	<0.20	<0.20	<0.20	<0.20	<0.20
Total	100.65	100.54	100.25	100.75	100.22	99.28	98.53	99.68	98.90	99.58	98.39	98.41	98.80	99.21	98.39	98.50	98.51	98.85	100.36	98.47	99.48	99.59
Si	10.46	10.58	10.56	11.72	10.43	10.73	9.95	9.46	9.03	9.02	9.83	9.33	9.87	9.71	10.16	10.34	10.11	10.18	10.46	10.48	10.43	10.37
Ti	-	-	-	-	-	-	-	-	-	-	-	-	-	-	-	-	-	-	-	-	-	-
Al	5.43	5.31	5.31	4.21	5.47	5.14	5.87	6.41	6.81	6.91	6.06	6.57	6.00	6.05	5.81	5.61	5.83	5.74	5.35	5.42	5.47	5.56
Fe^{2+}	0.06	0.05	0.07	0.05	0.06	0.10	0.05	0.04	0.08	0.08	0.08	0.07	0.10	0.11	-	-	0.05	0.05	-	-	-	-
Mn	-	-	-	-	-	-	-	-	-	-	-	-	-	-	-	-	-	-	-	-	-	-
Mg	0.12	0.14	0.10	0.11	0.11	0.10	0.16	0.16	0.10	0.08	0.06	0.10	0.06	0.16	-	0.06	0.06	0.12	0.12	0.12	0.14	0.12
Ca	1.55	1.48	1.48	0.26	1.52	1.30	2.07	2.57	2.99	3.00	2.24	2.70	2.20	2.38	1.87	1.72	1.94	1.77	1.69	1.62	1.69	1.71
Na	2.30	2.32	2.37	3.53	2.41	2.50	1.95	1.33	1.05	0.82	1.56	1.12	1.66	1.58	1.92	2.09	1.86	2.09	2.22	2.19	2.04	2.00
K	0.09	0.06	0.09	0.07	0.09	0.11	-	-	-	-	0.08	-	0.08	0.08	0.06	0.06	0.06	0.06	0.04	0.07	0.08	0.07
Cl	-	-	-	-	-	-	-	-	-	-	-	-	-	-	-	-	-	-	-	-	-	-
Total	20.03	19.95	19.99	20.00	20.09	20.00	20.11	20.03	20.11	19.97	19.95	19.95	20.00	20.10	19.91	19.92	19.93	20.02	19.98	19.97	19.90	19.89
An	0.39	0.38	0.38	0.07	0.38	0.33	0.52	0.66	0.74	0.78	0.58	0.71	0.56	0.59	0.49	0.45	0.50	0.45	0.43	0.42	0.44	0.45
Ab	0.58	0.60	0.60	0.92	0.60	0.64	0.48	0.34	0.26	0.22	0.40	0.29	0.42	0.39	0.50	0.54	0.48	0.53	0.56	0.56	0.53	0.53
Or	0.02	0.02	0.02	0.02	0.02	0.03	0.00	0.00	0.00	0.00	0.02	0.00	0.02	0.02	0.02	0.02	0.02	0.02	0.01	0.02	0.02	0.02

Feldspar analyses cont.

	Early-Mid Miocene Mineralised Intrusive Centres																						
	Hbl-Bt Diorite																	Hbl-Bt Diorite					
Sample No.	Chail	Chail	Chail	Chail	Chail	Chail	Chail	Chail	Chail	Chail	Chail	Chail	Chail	Chail	Chail	Chail	Chail	H22	H22	H22	H22	H22	H22
Analysis No.	1r	1c	2r	2c	3r	3c	3r	4r	4c	5r	5c	6r	6c	7r	7c	7c1	7c2	1c	2c	3c	3r	4r	4c
SiO_2	55.80	57.16	56.82	56.18	58.17	58.58	57.52	58.60	57.12	57.42	57.18	55.86	57.58	58.23	56.11	54.09	56.53	59.16	58.00	56.56	57.60	58.59	59.24
TiO_2	<0.20	<0.20	<0.20	<0.20	<0.20	<0.20	<0.20	<0.20	<0.20	<0.20	<0.20	<0.20	<0.20	<0.20	<0.20	<0.20	<0.20	<0.20	<0.20	<0.20	<0.20	<0.20	<0.20
Al_2O_3	27.05	26.07	26.40	26.76	25.60	25.30	26.11	25.71	26.38	26.28	26.22	27.13	26.01	25.48	26.81	27.80	26.58	26.06	25.99	27.36	26.29	25.97	25.76
Fe_2O_3(T)	0.25	0.33	0.21	0.30	0.36	0.35	0.25	<0.20	0.24	0.19	0.28	0.26	0.35	0.22	0.32	0.43	<0.20	<0.20	<0.20	<0.20	0.24	0.42	<0.20
MnO	<0.20	<0.20	<0.20	<0.20	<0.20	<0.20	<0.20	<0.20	<0.20	<0.20	<0.20	<0.20	<0.20	<0.20	<0.20	<0.20	<0.20	<0.20	<0.20	<0.20	<0.20	<0.20	<0.20
MgO	0.54	0.40	0.41	0.39	0.20	0.30	0.38	0.43	0.22	0.59	0.46	0.25	0.48	0.42	0.35	0.51	0.22	0.63	0.61	0.41	0.61	0.46	0.44
CaO	9.54	8.79	8.89	9.57	8.14	7.77	8.47	8.35	9.00	8.62	8.79	9.82	8.93	8.11	9.42	10.68	9.14	8.76	8.81	10.39	9.33	8.92	8.34
Na_2O	5.73	6.41	6.00	5.65	6.36	6.97	6.35	6.18	5.99	6.26	6.33	5.33	6.09	6.49	5.80	5.23	5.97	6.07	5.96	5.27	5.78	6.09	6.04
K_2O	0.23	0.23	0.29	0.32	0.29	0.36	0.29	0.32	0.21	0.25	0.31	0.21	0.38	0.27	0.28	<0.20	0.34	0.32	0.43	<0.20	0.28	0.31	0.44
Cl	<0.20	<0.20	<0.20	<0.20	<0.20	<0.20	<0.20	<0.20	<0.20	<0.20	<0.20	<0.20	<0.20	<0.20	<0.20	<0.20	<0.20	<0.20	<0.20	<0.20	<0.20	<0.20	<0.20
Total	99.18	99.52	99.12	99.22	99.24	99.91	99.52	99.83	99.29	99.75	99.76	98.97	99.87	99.55	99.24	99.11	99.02	101.30	100.14	100.40	100.42	100.87	100.53
Si	10.12	10.32	10.29	10.19	10.49	10.52	10.36	10.50	10.32	10.33	10.30	10.15	10.34	10.48	10.17	9.87	10.24	10.46	10.39	10.13	10.31	10.42	10.53
Ti	-	-	-	-	-	-	-	-	-	-	-	-	-	-	-	-	-	-	-	-	-	-	-
Al	5.78	5.55	5.63	5.72	5.44	5.35	5.54	5.43	5.61	5.57	5.56	5.81	5.51	5.40	5.73	5.98	5.67	5.43	5.49	5.78	5.54	5.45	5.40
Fe^{2+}	0.04	0.05	0.03	0.05	0.05	0.05	0.04	-	0.04	0.03	0.04	0.04	0.05	0.03	0.05	0.07	-	-	-	-	0.04	0.06	-
Mn	-	-	-	-	-	-	-	-	-	-	-	-	-	-	-	-	-	-	-	-	-	-	-
Mg	0.14	0.11	0.11	0.10	0.05	0.08	0.10	0.11	0.06	0.16	0.12	0.07	0.13	0.11	0.09	0.14	0.06	0.17	0.16	0.11	0.16	0.12	0.12
Ca	1.85	1.70	1.72	1.86	1.57	1.49	1.63	1.60	1.74	1.66	1.70	1.91	1.72	1.56	1.83	2.09	1.77	1.66	1.69	1.99	1.79	1.70	1.59
Na	2.01	2.24	2.11	1.99	2.22	2.43	2.22	2.14	2.10	2.18	2.21	1.87	2.12	2.26	2.04	1.85	2.09	2.08	2.07	1.83	2.00	2.10	2.08
K	0.05	0.05	0.07	0.07	0.07	0.08	0.07	0.07	0.05	0.06	0.07	0.05	0.09	0.06	0.06	-	0.08	0.07	0.10	-	0.07	0.07	0.10
Cl	-	-	-	-	-	-	-	-	-	-	-	-	-	-	-	-	-	-	-	-	-	-	-
Total	20.01	20.04	19.98	19.98	19.92	20.05	19.98	19.89	19.93	20.01	20.03	19.91	19.96	19.97	20.00	20.08	19.95	19.92	19.96	19.92	19.96	19.95	19.87
An	0.47	0.43	0.44	0.47	0.41	0.37	0.42	0.42	0.45	0.43	0.43	0.50	0.44	0.40	0.47	0.53	0.45	0.44	0.44	0.52	0.46	0.44	0.42
Ab	0.51	0.56	0.54	0.51	0.58	0.61	0.57	0.56	0.54	0.56	0.56	0.49	0.54	0.58	0.52	0.47	0.53	0.55	0.54	0.48	0.52	0.54	0.55
Or	0.01	0.01	0.02	0.02	0.02	0.02	0.02	0.02	0.01	0.01	0.02	0.01	0.02	0.02	0.02	0.00	0.02	0.02	0.03	0.00	0.02	0.02	0.03

Feldspar analyses cont.

	Early-Mid Miocene Mineralised Intrusive Centres																								
	Hbl-Bt Diorite				Hbl-Bt Diorite							Hbl-Bt Qtz Diorite						Hbl-Bt Diorite							
Sample No.	T1 Gal	T1 Gal	T1 Gal	T1 Gal	T2 Gal	T2 Gal	T2 Gal	T2 Gal	T2 Gal	T2 Gal	T2 Gal	T3 Gal	T3 Gal	T3 Gal	T3 Gal	T3 Gal	T3 Gal	T4 Gal	T4 Gal	T4 Gal	T4 Gal	T4 Gal	T4 Gal	T4 Gal	T4 Gal
Analysis No.	1r	1c	2c	3c	1r	1c	2r	2c	2c	3c	3r	1c	1r	2r	2c	3c	3r	1c	1r	2c	2r	3r	3c	4r	4c
SiO_2	58.84	60.04	59.09	58.78	58.58	59.51	54.41	59.37	55.64	59.55	58.28	58.55	58.72	57.58	58.63	57.98	57.05	57.37	57.46	57.32	54.45	55.71	56.29	58.05	55.82
TiO_2	<0.20	<0.20	<0.20	<0.20	<0.20	<0.20	<0.20	<0.20	<0.20	<0.20	<0.20	<0.20	<0.20	<0.20	<0.20	<0.20	<0.20	<0.20	<0.20	<0.20	<0.20	<0.20	<0.20	<0.20	<0.20
Al_2O_3	24.88	24.31	24.59	24.14	25.24	24.30	27.03	24.20	26.06	24.40	24.99	25.18	24.62	25.34	24.68	24.71	25.37	25.44	25.33	25.70	27.81	25.49	25.16	24.97	26.35
Fe_2O_3(T)	<0.20	<0.20	<0.20	<0.20	<0.20	0.26	<0.20	0.32	0.28	<0.20	0.23	0.20	0.23	<0.20	0.29	<0.20	<0.20	<0.20	0.43	0.20	0.32	0.30	0.21	<0.20	0.30
MnO	<0.20	<0.20	<0.20	<0.20	<0.20	<0.20	<0.20	<0.20	<0.20	<0.20	<0.20	<0.20	<0.20	<0.20	<0.20	<0.20	<0.20	<0.20	<0.20	<0.20	<0.20	<0.20	<0.20	<0.20	<0.20
MgO	<0.20	<0.20	<0.20	<0.20	0.26	<0.20	0.24	0.27	<0.20	0.25	<0.20	0.39	<0.20	0.23	0.29	<0.20	<0.20	0.32	0.33	0.44	0.39	0.20	<0.20	0.29	0.45
CaO	8.86	8.49	8.47	8.75	9.13	8.13	12.38	8.37	10.90	8.09	8.92	8.76	8.67	10.07	8.96	9.48	9.71	8.47	8.19	8.43	11.17	9.13	8.95	7.95	9.54
Na_2O	5.46	5.73	5.55	5.73	5.75	5.94	4.46	5.93	4.85	5.84	5.32	5.28	5.77	5.23	5.59	5.58	5.03	6.29	6.52	6.35	4.74	5.79	5.88	6.44	5.69
K_2O	0.30	0.38	0.32	0.26	0.20	0.38	0.27	0.46	0.20	0.45	0.29	0.40	0.41	0.36	0.45	0.31	0.40	0.41	0.50	0.44	0.26	0.39	0.38	0.35	0.36
Cl	<0.20	<0.20	<0.20	<0.20	<0.20	<0.20	<0.20	<0.20	<0.20	<0.20	<0.20	<0.20	<0.20	<0.20	<0.20	<0.20	<0.20	<0.20	<0.20	<0.20	<0.20	<0.20	<0.20	<0.20	<0.20
Total	98.80	99.31	98.30	98.12	99.36	98.72	99.15	99.04	98.15	98.89	98.21	98.84	98.81	99.12	98.97	98.63	97.92	98.53	98.91	99.03	99.49	97.16	97.13	98.26	98.63
Si	10.63	10.78	10.71	10.70	10.55	10.75	9.94	10.72	10.22	10.74	10.59	10.57	10.63	10.43	10.60	10.54	10.44	10.44	10.44	10.39	9.90	10.32	10.41	10.57	10.20
Ti	-	-	-	-	-	-	-	-	-	-	-	-	-	-	-	-	-	-	-	-	-	-	-	-	-
Al	5.30	5.15	5.23	5.18	5.35	5.17	5.82	5.15	5.64	5.18	5.35	5.36	5.25	5.41	5.26	5.30	5.47	5.46	5.42	5.49	5.96	5.56	5.48	5.36	5.67
Fe^{2+}	-	-	-	-	-	0.04	-	0.05	0.04	-	0.03	0.03	0.03	-	0.04	-	-	-	0.07	0.03	0.05	0.05	0.03	-	0.05
Mn	-	-	-	-	-	-	-	-	-	-	-	-	-	-	-	-	-	-	-	-	-	-	-	-	-
Mg	-	-	-	-	0.07	-	0.07	0.07	-	0.07	-	0.10	-	0.06	0.08	-	-	0.09	0.09	0.12	0.10	0.06	-	0.08	0.12
Ca	1.71	1.64	1.69	1.71	1.76	1.57	2.43	1.62	2.14	1.56	1.74	1.69	1.68	1.95	1.74	1.85	1.90	1.65	1.59	1.64	2.18	1.81	1.77	1.55	1.87
Na	1.91	2.04	1.92	2.02	2.00	2.08	1.58	2.07	1.72	2.04	1.87	1.85	2.02	1.83	1.96	1.97	1.79	2.22	2.29	2.23	1.67	2.08	2.10	2.27	2.02
K	0.07	0.09	0.09	0.06	0.05	0.09	0.06	0.11	0.05	0.10	0.07	0.09	0.09	0.08	0.10	0.07	0.09	0.10	0.12	0.10	0.06	0.09	0.09	0.08	0.08
Cl	-	-	-	-	-	-	-	-	-	-	-	-	-	-	-	-	-	-	-	-	-	-	-	-	-
Total	19.70	19.80	19.72	19.74	19.82	19.75	19.96	19.80	19.85	19.75	19.69	19.72	19.79	19.82	19.80	19.84	19.77	19.99	20.05	20.02	19.99	19.99	19.96	19.93	20.02
An	0.46	0.43	0.46	0.45	0.46	0.42	0.60	0.43	0.55	0.42	0.47	0.47	0.44	0.50	0.46	0.48	0.50	0.42	0.40	0.41	0.56	0.45	0.45	0.40	0.47
Ab	0.52	0.54	0.52	0.53	0.53	0.56	0.39	0.55	0.44	0.55	0.51	0.51	0.53	0.47	0.52	0.51	0.47	0.56	0.57	0.56	0.43	0.52	0.53	0.58	0.51
Or	0.02	0.02	0.02	0.02	0.01	0.02	0.02	0.03	0.01	0.03	0.02	0.03	0.02	0.02	0.03	0.02	0.02	0.02	0.03	0.03	0.02	0.02	0.02	0.02	0.02

Feldspar analyses cont.

	Miocene Volcanic Units											
	Hbl Basaltic Andesite						Hbl-Bt Andesite					
Sample No.	64	64	64	64	64	64	63	63	63	63	63	63
Analysis No.	1r	1c	2c	2r	3c	3r	1r	1c	2c	2r	3r	3c
SiO_2	55.78	55.90	59.46	60.27	59.79	57.99	58.41	58.56	58.16	58.27	59.11	58.00
TiO_2	<0.20	<0.20	<0.20	<0.20	<0.20	<0.20	<0.20	<0.20	<0.20	<0.20	<0.20	<0.20
Al_2O_3	27.50	27.87	25.38	25.26	25.28	26.24	24.94	26.10	25.29	25.79	25.69	26.36
Fe_2O_3(T)	0.49	0.79	0.25	0.26	0.42	0.38	0.43	0.25	0.56	<0.20	0.47	0.13
MnO	<0.20	<0.20	<0.20	<0.20	<0.20	<0.20	<0.20	<0.20	<0.20	<0.20	<0.20	<0.20
MgO	0.45	0.48	0.53	0.44	0.52	0.54	<0.20	0.40	0.54	0.42	0.39	0.50
CaO	11.21	11.19	8.30	7.73	8.04	9.09	8.21	8.91	8.25	8.90	8.28	9.54
Na_2O	4.52	4.86	5.45	6.09	6.43	5.61	6.02	5.46	5.73	5.67	5.98	5.33
K_2O	0.26	<0.20	0.75	0.81	0.80	0.47	0.64	0.53	0.81	0.49	0.54	0.35
Cl	<0.20	<0.20	<0.20	<0.20	<0.20	<0.20	<0.20	<0.20	<0.20	<0.20	<0.20	<0.20
Total	100.31	101.33	100.10	101.04	101.43	100.34	99.12	100.23	99.45	99.73	100.71	100.38
Si	10.03	9.98	10.61	10.66	10.58	10.37	10.57	10.45	10.50	10.46	10.52	10.35
Ti	-	-	-	-	-	-	-	-	-	-	-	-
Al	5.83	5.86	5.33	5.26	5.27	5.53	5.32	5.49	5.38	5.45	5.39	5.55
Fe^{2+}	0.07	0.12	0.04	0.04	0.06	0.06	0.07	0.04	0.08	-	0.07	0.02
Mn	-	-	-	-	-	-	-	-	-	-	-	-
Mg	0.12	0.13	0.14	0.12	0.13	0.14	-	0.10	0.14	0.11	0.10	0.13
Ca	2.16	2.14	1.59	1.46	1.52	1.74	1.59	1.70	1.59	1.71	1.58	1.82
Na	1.57	1.68	1.88	2.08	2.20	1.94	2.11	1.89	2.00	1.97	2.06	1.84
K	0.06	-	0.17	0.18	0.18	0.11	0.15	0.12	0.19	0.11	0.12	0.08
Cl	-	-	-	-	-	-	-	-	-	-	-	-
Total	19.86	19.95	19.75	19.84	19.98	19.89	19.91	19.80	19.91	19.85	19.88	19.83
An	0.57	0.56	0.44	0.39	0.39	0.46	0.41	0.46	0.42	0.45	0.42	0.49
Ab	0.42	0.44	0.52	0.56	0.56	0.51	0.55	0.51	0.53	0.52	0.55	0.49
Or	0.02	0.00	0.05	0.05	0.05	0.03	0.04	0.03	0.05	0.03	0.03	0.02

Electron microprobe analyses of hornblende grains

	Gabbroic Dyke			Palaeogene Igneous Units																							
	Sth Galeno			Co Montana - Hbl Diorite														East Minas Conga - Hbl Microdiorite									
Sample No.	55	55	55	31	31	31	31	31	31	31	31	31	31	31	31	31	31	46	46	46	46	46	46	46	46	46	46
Analysis No.	1r	1r	1c	1r	1c	1c1	2r	2c	2r1	2c1	2c2	2c3	3c	4r	4c	4r1	4r2	1c	1r	2c	3c	4r	4c	Stk 1c	Stk 2c	Stk 2r	Stk 3c
Oxide Weight Percent																											
SiO_2	42.46	42.16	41.94	42.23	42.46	42.10	42.12	40.49	44.03	40.37	40.56	42.64	42.75	43.18	43.02	43.82	43.83	49.85	50.47	41.89	46.01	48.12	47.14	45.06	43.22	49.42	48.03
TiO_2	2.15	2.65	2.68	2.45	2.56	2.65	2.68	2.64	2.22	2.66	2.57	2.49	2.36	2.53	3.14	1.99	2.44	1.46	1.21	2.23	2.07	1.60	1.99	1.60	1.97	1.60	2.08
Al_2O_3	13.07	13.44	13.45	12.61	11.91	11.98	12.41	14.39	9.73	14.45	14.41	11.59	11.67	10.67	10.45	9.05	9.66	5.99	5.15	12.72	8.70	5.76	6.68	9.55	10.41	6.01	6.86
Fe_2O_3(T)	11.92	12.16	11.68	15.02	14.78	15.87	14.43	14.62	17.26	14.90	15.14	14.75	16.41	18.64	15.51	20.21	19.69	12.15	12.09	13.87	13.87	12.65	11.89	15.61	15.64	11.95	12.42
MnO	0.31	0.20	<0.20	0.39	0.34	0.36	0.29	<0.20	0.29	<0.20	0.33	0.22	0.49	0.40	0.33	0.69	0.75	0.47	0.60	0.33	0.47	0.46	0.57	0.73	0.39	0.59	0.56
MgO	13.67	13.10	13.31	12.29	12.81	12.56	13.14	12.03	11.90	12.22	11.69	13.00	11.77	10.92	12.58	10.42	10.92	14.36	15.00	11.69	12.49	14.43	14.79	11.38	11.26	14.68	14.39
CaO	11.01	10.92	10.83	10.85	10.98	10.73	11.05	11.02	10.20	11.10	11.17	10.62	10.59	10.28	10.56	10.22	9.97	11.06	11.03	11.10	11.93	11.05	10.86	10.83	10.99	10.81	10.60
Na_2O	2.20	2.45	2.94	2.22	2.39	2.65	2.55	2.80	1.98	2.42	2.23	2.39	2.12	2.33	2.29	2.01	2.52	1.37	1.32	2.21	1.61	1.25	1.38	1.61	2.06	1.43	1.71
K_2O	0.38	0.49	0.47	0.52	0.56	0.51	0.51	0.51	0.52	0.42	0.56	0.53	0.51	0.54	0.47	0.64	0.51	0.57	0.44	0.66	0.76	0.57	0.57	0.59	0.70	0.59	0.51
Cl	<0.20	<0.20	<0.20	<0.20	<0.20	<0.20	<0.20	<0.20	0.25	<0.20	<0.20	<0.20	<0.20	0.20	<0.20	0.32	0.22	0.22	<0.20	<0.20	<0.20	<0.20	<0.20	<0.20	<0.20	<0.20	<0.20
O=Cl									0.06					0.05		0.07	0.05	0.05									
Total	97.24	97.66	97.37	98.71	98.82	99.51	99.24	98.78	98.30	98.68	98.72	98.25	98.82	99.61	98.51	99.29	100.46	97.43	97.48	96.73	98.04	96.04	96.04	97.09	96.79	97.22	97.28
Number of atoms per formula unit (23 oxygens)																											
Si	6.26	6.20	6.18	6.13	6.05	5.88	6.24	6.26	6.21	6.18	5.99	6.57	5.97	6.01	6.31	6.34	6.42	7.26	7.34	6.28	6.79	7.16	7.00	6.75	6.53	7.22	7.04
Ti	0.24	0.29	0.30	0.40	0.44	0.40	0.27	0.28	0.29	0.30	0.29	0.25	0.30	0.29	0.28	0.26	0.28	0.16	0.13	0.25	0.23	0.18	0.22	0.18	0.22	0.17	0.23
Al	2.27	2.33	2.34	2.14	2.27	2.51	2.19	2.07	2.08	2.15	2.51	1.71	2.52	2.52	2.02	2.04	1.87	1.03	0.88	2.25	1.51	1.01	1.17	1.68	1.85	1.03	1.19
Fe^{2+}	1.47	1.50	1.44	1.80	1.72	1.73	1.85	1.82	1.96	1.77	1.81	2.15	1.84	1.87	1.83	2.03	2.32	1.48	1.47	1.74	1.71	1.57	1.48	1.95	1.98	1.46	1.52
Mn	0.04	0.02	-	0.03	0.02	0.03	0.05	-	0.05	-	0.02	0.04	0.02	0.04	0.03	0.06	0.05	0.06	0.07	0.04	0.06	0.06	0.07	0.09	0.05	0.07	0.07
Mg	3.00	2.87	2.92	2.66	2.66	2.61	2.70	2.81	2.76	2.87	2.65	2.64	2.69	2.58	2.87	2.60	2.42	3.11	3.25	2.61	2.74	3.20	3.27	2.54	2.53	3.19	3.14
Ca	1.74	1.72	1.71	1.80	1.82	1.85	1.72	1.73	1.69	1.74	1.75	1.63	1.76	1.77	1.68	1.68	1.64	1.72	1.72	1.78	1.88	1.76	1.73	1.74	1.78	1.69	1.66
Na	0.63	0.70	0.84	0.66	0.65	0.71	0.63	0.68	0.76	0.72	0.80	0.57	0.69	0.64	0.69	0.61	0.67	0.39	0.37	0.64	0.46	0.36	0.40	0.47	0.60	0.40	0.48
K	0.07	0.09	0.09	0.19	0.18	0.22	0.10	0.10	0.10	0.10	0.10	0.10	0.08	0.11	0.10	0.10	0.10	0.11	0.08	0.13	0.14	0.11	0.11	0.11	0.13	0.11	0.10
Cl	-	-	-	-	-	-	-	-	0.03	-	-	-	-	0.02	-	0.04	0.05	0.05	-	-	-	-	-	-	-	-	-
Total	15.73	15.76	15.83	15.84	15.82	15.94	15.80	15.82	15.91	15.88	15.94	15.72	15.86	15.84	15.80	15.77	15.80	15.37	15.36	15.73	15.56	15.44	15.48	15.55	15.72	15.39	15.46
# Mg	67.13	65.76	67.01	59.72	60.66	60.05	59.32	60.70	58.51	61.87	59.45	55.12	59.37	57.92	61.10	56.11	51.07	67.81	68.85	60.02	61.58	67.02	68.90	56.51	56.19	68.64	67.37
Al^{VI}	1.74	1.80	1.82	1.87	1.95	2.12	1.76	1.74	1.79	1.82	2.01	1.43	2.03	1.99	1.69	1.66	1.58	0.74	0.66	1.72	1.21	0.84	1.00	1.25	1.47	0.79	0.96

r = analysis at grain rim; c = analysis at grain core; <0.20 = below detection limit; - = below detection limit

Hornblende analyses cont.

											Miocene Barren Intrusive Units																			
	Cruz Conga - Basaltic Andesite						Carpa - Hbl Andesite					Michiquillay Region - Hbl-Bt Qtz Diorite											Aurora Patricia - Hbl Diorite					Carpa - Hbl Qtz Diorite		
Sample No.	32	32	32	32	32	32	21	21	21	21	21	59	59	59	59	59	59	59	59	59	59	59	11	11	11	11	11	38	38	38
Analysis No.	1c	2c	3c	3r	4c	5c	1c	2c	2r	3c	4c	1c	2c	3c	4c	4r	5c	5r	6c	6r	7c	7r	1c	2c	3r	3c	4c	1c	2c	3c
SiO_2	41.34	40.84	40.87	41.73	41.00	39.52	39.32	41.61	40.93	40.28	42.86	41.09	43.03	42.15	44.33	44.60	43.65	44.19	43.50	43.58	42.07	43.15	43.02	42.91	42.59	41.85	41.82	41.17	41.51	41.37
TiO_2	3.65	3.93	3.86	3.65	3.94	3.56	2.08	2.41	2.37	2.11	1.84	1.24	1.22	1.05	1.21	1.17	1.88	1.95	1.57	1.45	1.18	1.31	1.00	1.03	1.10	1.06	1.15	1.46	1.15	1.24
Al_2O_3	12.23	12.84	12.62	12.38	13.06	14.34	14.17	10.97	11.24	13.07	10.17	12.27	11.19	12.38	10.11	10.18	11.21	10.68	11.38	11.21	12.05	11.43	10.69	10.84	11.14	11.84	12.07	12.31	11.56	11.96
Fe_2O_3(T)	14.76	13.29	14.64	14.62	13.99	13.94	16.40	18.12	19.30	13.35	16.29	19.21	19.01	20.03	17.32	18.35	16.00	15.76	16.63	16.76	19.88	20.69	19.41	20.00	19.72	20.50	20.42	18.24	19.68	18.69
MnO	0.26	0.33	0.23	0.25	<0.20	0.21	<0.20	0.75	1.01	<0.20	1.07	0.79	0.59	0.43	0.53	0.52	0.21	0.22	0.31	0.57	0.51	0.53	0.39	0.70	0.61	0.64	0.45	0.41	0.57	0.62
MgO	12.24	12.29	11.94	12.16	12.10	11.76	10.95	9.95	9.34	12.18	10.83	8.52	9.48	9.99	10.39	9.59	11.29	11.08	10.78	10.13	8.37	8.56	9.52	9.79	9.94	9.16	9.23	9.06	8.71	8.76
CaO	11.30	11.54	11.59	11.44	11.50	11.58	11.33	10.68	10.88	13.00	12.35	12.65	12.15	10.59	10.95	10.78	10.81	11.00	10.63	10.47	10.97	10.82	10.77	10.75	10.78	10.75	10.57	12.49	12.60	12.67
Na_2O	2.33	2.44	2.25	2.33	2.28	2.45	2.51	2.15	1.90	2.38	2.05	1.27	1.57	2.10	1.84	1.43	2.23	2.57	2.04	1.78	1.50	1.75	1.23	1.54	1.22	1.17	1.64	1.48	1.79	1.81
K_2O	0.93	0.98	0.98	0.99	0.96	1.14	0.81	0.99	1.06	0.88	0.95	1.31	1.01	1.14	0.72	0.74	0.63	0.73	0.61	0.85	1.33	1.12	0.59	0.66	0.73	0.94	0.85	1.21	1.20	1.28
Cl	<0.20	<0.20	<0.20	<0.20	<0.20	<0.20	<0.20	<0.20	<0.20	<0.20	<0.20	0.24	<0.20	0.27	<0.20	<0.20	0.30	0.22	<0.20	<0.20	<0.20	<0.20	<0.20	<0.20	<0.20	<0.20	<0.20	<0.20	<0.20	<0.20
O=Cl												0.05		0.06			0.07	0.05												
Total	99.08	98.54	99.00	99.64	99.05	98.54	97.77	97.70	98.13	97.39	98.44	98.51	99.36	100.05	97.48	97.42	98.11	98.33	97.47	97.00	98.00	99.44	96.72	98.30	97.93	97.93	98.30	97.94	98.86	98.46
Si	6.11	6.18	6.05	6.13	6.05	5.88	5.95	6.34	6.26	6.05	6.45	6.27	6.45	6.30	6.68	6.73	6.50	6.57	6.52	6.59	6.42	6.49	6.58	6.50	6.46	6.38	6.36	6.27	6.32	6.30
Ti	0.41	0.45	0.43	0.40	0.44	0.40	0.24	0.28	0.27	0.24	0.21	0.14	0.14	0.12	0.14	0.13	0.21	0.22	0.18	0.16	0.13	0.15	0.11	0.12	0.13	0.12	0.13	0.17	0.13	0.14
Al	2.13	2.29	2.20	2.14	2.27	2.51	2.52	1.97	2.03	2.32	1.80	2.21	1.98	2.18	1.79	1.81	1.97	1.87	2.01	2.00	2.17	2.03	1.93	1.93	1.99	2.13	2.16	2.21	2.07	2.15
Fe^{2+}	1.83	1.68	1.81	1.80	1.72	1.73	2.07	2.31	2.47	1.68	2.05	2.45	2.38	2.50	2.18	2.32	1.99	1.96	2.08	2.12	2.53	2.60	2.48	2.53	2.50	2.61	2.59	2.32	2.50	2.38
Mn	0.03	0.04	0.03	0.03	-	0.03	-	0.10	0.13	-	0.14	0.10	0.07	0.05	0.07	0.07	0.03	0.03	0.04	0.07	0.07	0.07	0.05	0.09	0.08	0.08	0.06	0.05	0.07	0.08
Mg	2.69	2.77	2.63	2.66	2.66	2.61	2.47	2.26	2.13	2.73	2.42	1.94	2.12	2.22	2.33	2.16	2.50	2.45	2.41	2.28	1.90	1.92	2.17	2.21	2.25	2.08	2.09	2.06	1.98	1.99
Ca	1.79	1.87	1.84	1.80	1.82	1.85	1.84	1.74	1.78	2.09	1.99	2.07	1.95	1.70	1.77	1.74	1.72	1.75	1.71	1.69	1.79	1.74	1.76	1.74	1.75	1.76	1.72	2.04	2.05	2.07
Na	0.67	0.71	0.64	0.66	0.65	0.71	0.74	0.63	0.56	0.69	0.60	0.38	0.45	0.61	0.54	0.42	0.64	0.74	0.59	0.52	0.44	0.51	0.37	0.45	0.36	0.35	0.48	0.44	0.53	0.53
K	0.18	0.19	0.19	0.19	0.18	0.22	0.16	0.19	0.21	0.17	0.18	0.25	0.19	0.22	0.14	0.14	0.12	0.14	0.12	0.16	0.26	0.22	0.12	0.13	0.14	0.18	0.16	0.23	0.23	0.25
Cl	-	-	-	-	-	-	-	-	-	-	-	0.06	-	0.07	-	-	0.08	0.05	-	-	-	-	-	-	-	-	-	-	-	-
Total	15.84	16.21	15.84	15.84	15.82	15.94	16.02	15.83	15.87	15.99	15.85	15.86	15.78	15.97	15.65	15.53	15.76	15.77	15.66	15.65	15.76	15.74	15.60	15.73	15.69	15.70	15.78	15.82	15.92	15.90
# Mg	59.62	62.23	59.23	59.72	60.66	60.05	54.34	49.46	46.32	61.91	54.21	44.13	47.05	47.06	51.65	48.21	55.70	55.61	53.61	51.86	42.87	42.44	46.63	46.57	47.31	44.34	44.60	46.96	44.10	45.49
Al^{VI}	1.89	1.82	1.95	1.87	1.95	2.12	2.05	1.66	1.74	1.95	1.55	1.73	1.55	1.70	1.32	1.27	1.50	1.43	1.48	1.41	1.58	1.51	1.42	1.50	1.54	1.62	1.64	1.73	1.68	1.70

Hornblende analyses cont.

	Early-Mid Miocene Mineralised Intrusive Centres																							
	Minas Conga - Hbl-Bt Diorite										Michiquillay Prospect - Hbl-Bt Diorite										Galeno - Hbl-Bt Diorite			
Sample No.	Chail	Chail	Chail	Chail	Chail	Chail	Chail	Chail	Chail	Chail	H22	H22	H22	H22	H22	H22	H22	H22	H22	H22	T4	T4	T4	T4
Analysis No.	1r	1c	2r	2c	3r	3c	4r	4c	4r1	5c	1c	1r	2c	2r	3c	3r	4c	4r	5r	5c	1r	1c	2r	2c
SiO_2	45.34	44.80	46.61	45.97	45.13	45.66	45.62	44.92	45.73	44.88	47.47	46.15	45.88	47.32	45.54	47.44	44.81	46.19	45.38	45.72	42.93	43.69	43.74	43.45
TiO_2	1.41	1.29	1.20	1.31	1.34	1.11	1.40	1.41	1.54	1.31	1.07	1.17	1.23	0.94	1.26	1.07	1.14	1.19	1.34	1.26	1.35	1.22	1.26	1.25
Al_2O_3	8.78	9.01	8.59	8.59	8.56	8.14	9.01	9.27	9.11	9.66	8.65	9.26	9.68	8.73	9.66	7.89	9.94	9.10	10.45	9.28	10.25	10.16	9.86	10.07
Fe_2O_3(T)	15.71	15.72	14.48	15.03	14.25	15.86	13.13	17.03	13.75	13.19	15.84	15.90	16.54	15.83	16.84	15.21	16.51	15.92	14.79	16.89	17.92	17.13	17.08	17.38
MnO	0.51	0.56	0.66	0.78	0.75	0.52	0.67	0.64	0.55	0.64	0.43	0.42	0.38	0.39	0.50	0.57	0.57	0.45	0.49	0.42	0.64	0.65	0.57	0.35
MgO	12.62	12.79	13.80	13.57	13.76	12.80	13.94	11.74	13.68	13.88	11.93	11.82	11.67	12.20	11.57	12.37	11.43	11.78	11.27	11.36	10.48	11.16	10.42	10.38
CaO	10.75	10.78	10.69	11.03	11.26	10.93	11.24	10.91	10.79	10.81	11.05	10.98	10.83	10.84	10.98	10.59	10.92	10.92	10.83	10.87	11.08	11.09	11.19	11.01
Na_2O	2.13	2.25	1.97	2.18	2.05	1.92	1.97	1.90	2.28	1.87	1.40	1.75	2.02	1.80	1.75	1.48	2.01	1.40	1.88	1.47	1.79	1.71	1.74	1.66
K_2O	0.66	0.74	0.63	0.76	0.81	0.68	0.92	0.93	0.83	0.78	0.69	0.66	0.67	0.66	0.70	0.48	0.81	0.75	0.79	0.80	0.90	0.98	0.95	0.91
Cl	<0.20	<0.20	<0.20	<0.20	<0.20	<0.20	<0.20	<0.20	<0.20	<0.20	<0.20	<0.20	<0.20	<0.20	<0.20	<0.20	0.23	0.21	<0.20	<0.20	<0.20	0.20	<0.20	<0.20
O=Cl																	0.05	0.05				0.05		
Total	98.10	98.08	98.79	99.33	98.00	97.67	98.05	98.85	98.43	97.18	98.64	98.31	99.05	98.81	98.89	97.22	98.33	97.85	97.35	98.25	97.45	97.95	96.86	96.59
Si	6.74	6.67	6.82	6.74	6.70	6.81	6.71	6.67	6.72	6.66	6.96	6.82	6.75	6.93	6.73	7.03	6.68	6.85	6.74	6.80	6.57	6.65	6.63	6.58
Ti	0.16	0.14	0.13	0.14	0.15	0.12	0.15	0.16	0.17	0.15	0.12	0.13	0.14	0.10	0.14	0.12	0.13	0.13	0.15	0.14	0.14	0.14	0.14	0.11
Al	1.54	1.58	1.48	1.48	1.50	1.43	1.56	1.62	1.58	1.69	1.49	1.61	1.68	1.51	1.68	1.38	1.74	1.59	1.83	1.63	1.80	1.76	1.81	1.93
Fe^{2+}	1.95	1.96	1.77	1.84	1.77	1.98	1.61	2.11	1.69	1.64	1.94	1.97	2.04	1.94	2.08	1.88	2.06	1.97	1.84	2.10	2.16	2.17	2.22	2.48
Mn	0.06	0.07	0.08	0.10	0.09	0.07	0.08	0.08	0.07	0.08	0.05	0.05	0.05	0.05	0.06	0.07	0.07	0.06	0.06	0.05	0.08	0.07	0.04	0.05
Mg	2.79	2.84	3.01	2.96	3.04	2.85	3.06	2.60	2.99	3.07	2.61	2.60	2.56	2.66	2.55	2.73	2.54	2.60	2.50	2.51	2.50	2.36	2.36	2.17
Ca	1.71	1.72	1.67	1.73	1.79	1.75	1.77	1.73	1.70	1.72	1.74	1.74	1.71	1.70	1.74	1.68	1.74	1.73	1.72	1.73	1.79	1.82	1.80	1.76
Na	0.62	0.65	0.56	0.62	0.59	0.56	0.56	0.55	0.65	0.54	0.40	0.50	0.58	0.51	0.50	0.43	0.58	0.40	0.54	0.42	0.50	0.51	0.49	0.37
K	0.13	0.14	0.12	0.14	0.15	0.13	0.17	0.18	0.15	0.15	0.13	0.12	0.13	0.12	0.13	0.09	0.15	0.14	0.15	0.15	0.19	0.18	0.18	0.12
Cl	-	-	-	-	-	-	-	-	-	-	-	-	-	-	-	-	0.06	0.05	-	-	-	0.01	-	-
Total	15.74	15.80	15.68	15.79	15.80	15.70	15.72	15.72	15.76	15.72	15.47	15.60	15.66	15.55	15.63	15.45	15.75	15.54	15.57	15.58	15.78	15.69	15.70	15.60
# Mg	58.87	59.18	62.93	61.67	63.26	58.99	65.43	55.13	63.93	65.21	57.31	56.99	55.69	57.86	55.03	59.18	55.22	56.87	57.58	54.49	53.73	52.10	51.56	46.63
Al^{VI}	1.26	1.33	1.18	1.26	1.30	1.19	1.29	1.33	1.28	1.34	1.04	1.18	1.25	1.07	1.27	0.97	1.32	1.15	1.26	1.20	1.43	1.35	1.37	1.42

Hornblende analyses cont.

	Miocene Volcanic Units													
	Regalado Voclanic Sequence - Hbl Basaltic Andesite									Huambos Fm - Hbl-Bt Andesite				
Sample No.	64	64	64	64	64	64	64	64	64	63	63	63	63	63
Analysis No.	1r	1c	2c	2r	3r	3c	4r	4c	5c	1r	1c	2c	2r	3c
SiO_2	45.10	43.97	44.53	44.69	43.67	45.64	45.65	45.51	43.34	44.44	44.16	45.11	44.61	43.98
TiO_2	1.71	1.86	1.93	1.89	2.13	1.87	2.05	1.98	2.08	2.40	1.80	1.72	1.76	1.85
Al_2O_3	12.11	13.56	11.92	11.98	11.20	9.94	9.62	9.35	12.99	11.32	11.77	9.58	9.64	11.75
Fe_2O_3(T)	12.37	11.91	9.73	9.56	12.39	15.39	15.01	14.56	11.31	10.57	9.85	15.37	16.02	14.02
MnO	0.48	<0.20	0.25	0.22	<0.20	0.37	0.31	0.32	<0.20	<0.20	0.21	0.61	0.40	0.52
MgO	13.40	13.52	14.39	14.95	13.67	12.06	12.56	12.67	13.96	14.48	15.06	11.66	11.67	11.97
CaO	10.95	11.45	11.22	11.29	11.37	10.70	10.67	10.74	11.29	11.09	11.08	10.64	10.59	10.96
Na_2O	2.01	2.20	2.33	2.47	2.72	1.65	2.00	2.04	2.34	2.15	2.61	1.47	1.65	2.01
K_2O	0.37	0.57	0.62	0.62	0.54	0.96	0.89	1.00	0.56	0.47	0.56	1.05	1.01	0.65
Cl	<0.20	<0.20	<0.20	<0.20	<0.20	0.24	0.24	<0.20	<0.20	<0.20	<0.20	0.22	<0.20	<0.20
O=Cl						0.06	0.05					0.05		
Total	98.51	99.19	96.93	97.73	97.99	98.74	98.92	98.32	97.86	97.07	97.16	97.38	97.53	97.83
Si	6.53	6.33	6.50	6.48	6.42	6.71	6.70	6.71	6.32	6.50	6.45	6.74	6.68	6.50
Ti	0.19	0.20	0.21	0.21	0.24	0.21	0.23	0.22	0.23	0.26	0.20	0.19	0.20	0.21
Al	2.07	2.30	2.05	2.05	1.94	1.72	1.66	1.62	2.23	1.95	2.03	1.69	1.70	2.05
Fe^{2+}	1.50	1.43	1.19	1.16	1.52	1.89	1.84	1.79	1.38	1.29	1.20	1.92	2.01	1.73
Mn	0.06	-	0.03	0.03	-	0.05	0.04	0.04	-	-	0.03	0.08	0.05	0.07
Mg	2.89	2.90	3.13	3.23	3.00	2.64	2.74	2.78	3.03	3.15	3.28	2.59	2.60	2.64
Ca	1.70	1.77	1.76	1.75	1.79	1.68	1.67	1.70	1.76	1.74	1.73	1.70	1.70	1.73
Na	0.56	0.61	0.66	0.69	0.77	0.47	0.57	0.58	0.66	0.61	0.74	0.43	0.48	0.58
K	0.07	0.10	0.12	0.11	0.10	0.18	0.17	0.19	0.10	0.09	0.11	0.20	0.19	0.12
Cl	-	-	-	-	-	0.06	0.06	-	-	-	-	0.06	-	-
Total	15.57	15.68	15.65	15.72	15.84	15.61	15.67	15.68	15.72	15.62	15.77	15.59	15.66	15.65
# Mg	65.88	66.90	72.49	73.59	66.29	58.26	59.85	60.80	68.73	70.94	73.15	57.47	56.48	60.33
Al^{VI}	1.47	1.67	1.50	1.52	1.58	1.29	1.30	1.29	1.68	1.50	1.55	1.26	1.32	1.50

Electron microprobe analyses of pyroxene grains

Gabbroic Dyke — South Galeno - Hbl Gabbro

Sample No.	16	16	16	16	16	16	16	16	16	16	16	16	16	16	16
Analysis No.	1r	1c	1r	1r1	2c	3c	3r	4r	4c	4r2	5c	5r	7r	7c	7r2
Oxide Weight Percent															
SiO_2	51.48	50.46	50.05	49.14	51.41	51.02	51.86	50.50	52.56	50.87	51.95	50.73	49.90	51.24	50.47
TiO_2	0.53	0.61	0.87	0.96	0.62	0.61	0.60	0.76	0.24	0.54	0.39	0.81	0.88	0.72	0.96
Al_2O_3	1.54	3.86	3.60	4.22	2.61	2.95	1.83	3.99	1.75	2.56	2.04	3.70	4.69	3.32	3.68
Fe_2O_3(T)	10.89	9.45	10.56	10.34	9.62	10.03	10.12	10.97	10.26	10.14	10.28	11.06	9.71	9.57	10.78
MnO	<0.20	0.28	0.39	0.27	0.38	0.20	<0.20	<0.20	0.30	0.30	0.45	<0.20	<0.20	0.31	0.30
MgO	14.40	13.99	13.20	13.41	14.44	13.73	14.45	13.55	14.91	13.87	14.39	13.30	13.58	13.75	13.40
CaO	20.10	20.72	20.61	20.46	20.11	20.40	20.33	20.12	20.12	19.95	19.98	20.34	21.54	20.50	20.30
Na_2O	<0.40	<0.40	<0.40	<0.40	<0.40	<0.40	<0.40	<0.40	<0.40	<0.40	<0.40	<0.40	<0.40	<0.40	<0.40
K_2O	<0.20	<0.20	<0.20	<0.20	<0.20	<0.20	<0.20	<0.20	<0.20	<0.20	<0.20	<0.20	<0.20	<0.20	<0.20
Cl	<0.20	<0.20	<0.20	<0.20	<0.20	<0.20	<0.20	<0.20	<0.20	<0.20	<0.20	<0.20	<0.20	<0.20	<0.20
Total	99.12	99.83	99.75	98.85	99.30	99.06	99.47	100.44	100.58	98.36	99.97	100.41	100.80	99.86	100.32
Number of atoms per formula unit (6 oxygens)															
Si	1.95	1.89	1.89	1.87	1.93	1.92	1.95	1.89	1.95	1.93	1.94	1.90	1.86	1.92	1.89
Ti	0.02	0.02	0.02	0.03	0.02	0.02	0.02	0.02	0.01	0.02	0.01	0.02	0.02	0.02	0.03
Al	0.07	0.17	0.16	0.19	0.12	0.13	0.08	0.18	0.08	0.11	0.09	0.16	0.21	0.15	0.16
Fe^{2+}	0.34	0.30	0.33	0.33	0.30	0.32	0.32	0.34	0.32	0.32	0.32	0.35	0.30	0.30	0.34
Mn	-	0.01	0.01	0.01	0.01	0.01	-	-	0.01	0.01	0.01	-	-	0.01	0.01
Mg	0.81	0.78	0.74	0.76	0.81	0.77	0.81	0.75	0.83	0.79	0.80	0.74	0.75	0.77	0.75
Ca	0.81	0.83	0.83	0.83	0.81	0.82	0.82	0.81	0.80	0.81	0.80	0.81	0.86	0.82	0.81
Na	-	-	-	-	-	-	-	-	-	-	-	-	-	-	-
K	-	-	-	-	-	-	-	-	-	-	-	-	-	-	-
Cl	-	-	-	-	-	-	-	-	-	-	-	-	-	-	-
Total	4.01	4.03	4.02	4.01	4.00	4.00	4.00	4.02	4.02	4.00	4.02	4.01	4.03	4.01	4.02
En	41.18	40.73	38.64	39.36	41.83	40.23	41.59	39.65	42.25	40.72	41.38	38.98	39.34	40.40	39.17
Fs	17.48	15.91	17.99	17.47	16.26	16.81	16.34	18.01	16.79	17.19	17.32	18.17	15.79	16.29	18.18
Wo	41.34	43.36	43.37	43.17	41.91	42.96	42.06	42.34	40.96	42.09	41.30	42.84	44.88	43.31	42.64
# Mg	70.21	72.51	69.02	69.81	72.78	70.93	71.79	68.77	72.15	70.92	71.38	68.20	71.36	71.92	68.91

Gabbroic Dyke — South Galeno - Hbl Gabbro

Sample No.	55	55	55	55	55	55
Analysis No.	1r	1c	2c	2r	3c	3r
Oxide Weight Percent						
SiO_2	51.44	50.23	52.21	51.83	51.49	50.71
TiO_2	0.71	0.65	0.52	0.63	0.71	0.81
Al_2O_3	3.89	5.12	2.58	3.70	3.95	4.65
Fe_2O_3(T)	8.46	8.55	8.22	8.17	8.00	8.50
MnO	0.36	0.29	0.41	0.20	0.23	0.29
MgO	13.54	13.28	14.54	13.92	13.88	13.59
CaO	20.50	20.06	19.82	20.67	21.05	21.37
Na_2O	0.64	0.63	0.72	0.63	0.74	0.58
K_2O	<0.20	<0.20	<0.20	<0.20	<0.20	<0.20
Cl	<0.20	<0.20	<0.20	<0.20	<0.20	<0.20
Total	99.59	98.87	99.09	99.84	100.08	100.56
Number of atoms per formula unit (6 oxygens)						
Si	1.92	1.89	1.95	1.92	1.91	1.88
Ti	0.02	0.02	0.01	0.02	0.02	0.02
Al	0.17	0.23	0.11	0.16	0.17	0.20
Fe^{2+}	0.26	0.27	0.26	0.25	0.25	0.26
Mn	0.01	0.01	0.01	0.01	0.01	0.01
Mg	0.75	0.74	0.81	0.77	0.77	0.75
Ca	0.82	0.81	0.79	0.82	0.84	0.85
Na	0.05	0.05	0.05	0.05	0.05	0.04
K	-	-	-	-	-	-
Cl	-	-	-	-	-	-
Total	4.00	4.01	4.01	4.00	4.01	4.02
En	40.76	40.65	43.24	41.57	41.26	40.10
Fs	14.89	15.18	14.40	14.03	13.75	14.58
Wo	44.35	44.17	42.36	44.40	44.99	45.32
# Mg	74.05	73.46	75.92	75.23	75.54	74.01

Gabbroic Dyke — East Galeno - Gabbroic Diorite

Sample No.	57	57	57	57	57	57	57	57	57	57
Analysis No.	1r	1c	1r1	1c1	2r	2c	2r1	3r	3c	4c
Oxide Weight Percent										
SiO_2	51.67	51.31	52.29	51.56	51.64	51.64	51.43	51.24	51.31	51.49
TiO_2	0.78	0.80	0.41	0.64	0.76	0.71	0.75	0.75	0.65	0.72
Al_2O_3	2.47	2.23	1.93	2.17	1.66	1.84	2.03	2.07	2.18	1.80
Fe_2O_3(T)	10.65	10.54	12.04	11.37	11.18	10.66	10.95	10.99	10.69	10.77
MnO	0.31	<0.20	0.35	0.30	0.29	0.34	0.38	0.46	0.38	0.33
MgO	13.84	14.14	13.43	14.10	13.86	14.22	13.99	14.17	13.81	14.29
CaO	19.72	19.67	19.37	19.39	19.85	20.03	19.69	19.25	19.45	19.40
Na_2O	<0.40	<0.40	<0.40	<0.40	<0.40	0.52	<0.40	0.45	<0.40	<0.40
K_2O	<0.20	<0.20	<0.20	<0.20	<0.20	<0.20	<0.20	<0.20	<0.20	<0.20
Cl	<0.20	<0.20	<0.20	<0.20	<0.20	<0.20	<0.20	<0.20	<0.20	<0.20
Total	99.73	99.30	99.89	99.89	99.52	100.02	99.44	99.41	98.61	98.88
Number of atoms per formula unit (6 oxygens)										
Si	1.94	1.93	1.96	1.94	1.95	1.94	1.94	1.93	1.95	1.95
Ti	0.02	0.02	0.01	0.02	0.02	0.02	0.02	0.02	0.02	0.02
Al	0.11	0.10	0.09	0.10	0.07	0.08	0.09	0.09	0.10	0.08
Fe^{2+}	0.33	0.33	0.38	0.36	0.35	0.33	0.35	0.35	0.34	0.34
Mn	0.01	-	0.01	0.01	0.01	0.01	0.01	0.01	0.01	0.01
Mg	0.77	0.79	0.75	0.79	0.78	0.79	0.79	0.80	0.78	0.81
Ca	0.79	0.79	0.78	0.78	0.80	0.80	0.79	0.78	0.79	0.79
Na	-	-	-	-	-	0.04	-	-	-	-
K	-	-	-	-	-	-	-	-	-	-
Cl	-	-	-	-	-	-	-	-	-	-
Total	4.00	4.01	3.99	4.01	4.01	4.02	4.00	4.02	3.99	4.00
En	40.50	41.36	39.15	40.78	40.08	40.86	40.54	41.16	40.61	41.45
Fs	18.00	17.30	20.27	18.93	18.62	17.75	18.43	18.67	18.27	18.08
Wo	41.50	41.35	40.58	40.29	41.29	41.40	41.03	40.18	41.12	40.47
# Mg	69.85	70.51	66.53	68.86	68.83	70.39	69.47	69.68	69.72	70.27

r = analysis at grain rim; c = analysis at grain core; <0.20 = below detection limit; - = below detection limit

Pyroxene analyses cont.

	Palaeogene Igneous Units															Miocene Barren Intrusions						Miocene Volcanic Units							
	North Galeno - Gabbroic Diorite					East M Conga - Hbl MD			Cruz Conga - Basltic Andesite							Michiquillay Region - Hbl-Bt Qtz Diorite						Regalado Voclanic Sequence - Hbl Basaltic Andesite						Huambos Fm	
Sample No.	87	87	87	87	87	46	46	46	32	32	32	32	32	32	32	59	59	59	59	59	59	64	64	64	64	64	64	63	63
Analysis No.	1c	1r	1c1	2r	2c	1r	1c	2c	1c	2c	3c	4c	5c	6c	7c	1c	2c	3c	3r	4c	5c	1c	2c	2r	3c	3r	4r	1c	1r
SiO_2	52.09	50.14	51.90	51.02	52.62	51.79	51.35	52.48	50.06	50.36	49.97	49.73	49.01	47.79	50.05	51.13	50.89	50.23	50.64	53.13	50.79	52.62	54.22	54.15	54.94	52.58	54.09	54.54	53.77
TiO_2	0.21	1.02	0.23	0.93	0.28	0.27	0.20	<0.20	1.22	0.91	1.03	0.86	1.26	1.71	1.10	0.60	0.69	0.82	0.60	0.35	0.77	0.53	0.30	0.34	0.32	0.57	0.40	0.24	<0.20
Al_2O_3	0.64	3.58	0.62	3.50	0.88	1.60	1.34	0.64	4.44	3.78	4.12	4.47	4.92	6.02	3.66	5.39	5.35	5.90	5.37	2.85	5.19	2.28	0.97	1.13	1.24	2.47	1.31	1.35	1.10
Fe_2O_3(T)	18.20	12.27	17.88	11.56	16.16	9.16	9.73	8.00	9.38	9.78	10.47	12.01	9.35	9.94	9.54	5.23	5.18	5.71	5.30	4.43	4.95	8.19	8.93	7.86	8.50	7.94	9.09	9.34	9.26
MnO	0.40	0.46	0.36	0.28	0.56	0.84	1.11	0.89	0.46	0.31	0.49	0.97	0.21	<0.20	0.42	<0.20	<0.20	<0.20	<0.20	<0.20	<0.20	0.36	0.55	0.36	0.50	0.36	0.37	0.69	0.94
MgO	9.81	11.27	10.07	12.04	10.82	13.15	12.70	14.25	12.88	13.34	11.59	10.86	12.43	12.02	13.00	13.94	14.39	13.85	14.23	15.36	14.26	14.78	15.50	15.87	16.02	14.63	15.55	13.60	13.35
CaO	17.72	19.74	18.03	19.58	18.58	21.35	21.37	21.88	21.97	21.81	21.81	21.60	22.05	21.97	21.78	22.41	22.31	22.21	21.65	21.93	22.17	20.64	19.08	19.04	19.23	20.26	18.54	20.52	20.42
Na_2O	<0.40	<0.40	0.60	0.72	0.87	0.83	0.60	0.46	0.49	0.64	0.61	0.65	0.47	0.53	<0.40	<0.40	0.91	0.54	0.61	<0.40	0.79	0.83	0.55	<0.40	0.57	<0.40	0.62	0.56	<0.40
K_2O	<0.20	<0.20	<0.20	<0.20	<0.20	<0.20	<0.20	<0.20	<0.20	<0.20	<0.20	<0.20	<0.20	<0.20	<0.20	<0.20	<0.20	<0.20	<0.20	<0.20	<0.20	<0.20	<0.20	<0.20	<0.20	<0.20	<0.20	<0.20	<0.20
Cl	<0.20	<0.20	<0.20	<0.20	<0.20	<0.20	<0.20	<0.20	<0.20	<0.20	<0.20	<0.20	<0.20	<0.20	<0.20	<0.20	<0.20	<0.20	<0.20	<0.20	<0.20	<0.20	<0.20	<0.20	<0.20	<0.20	<0.20	<0.20	<0.20
Total	99.44	98.94	99.77	99.69	100.81	99.04	98.50	98.76	101.02	100.98	100.13	101.29	99.81	100.13	99.83	99.24	99.85	99.50	98.59	98.52	99.08	100.30	100.18	99.14	101.40	99.20	100.09	100.87	99.50
Si	2.02	1.92	2.00	1.92	2.00	1.96	1.96	1.98	1.86	1.88	1.88	1.87	1.85	1.80	1.88	1.89	1.87	1.86	1.88	1.96	1.88	1.95	2.00	2.01	2.00	1.96	1.99	2.01	2.01
Ti	0.01	0.03	0.01	0.03	0.01	0.01	0.01	-	0.03	0.03	0.03	0.02	0.04	0.05	0.03	0.02	0.02	0.02	0.02	0.01	0.02	0.01	0.01	0.01	0.01	0.02	0.01	0.01	-
Al	0.03	0.16	0.03	0.16	0.04	0.07	0.06	0.03	0.19	0.17	0.18	0.20	0.22	0.27	0.16	0.23	0.23	0.26	0.24	0.12	0.23	0.10	0.04	0.05	0.05	0.11	0.06	0.06	0.05
Fe^{2+}	0.59	0.39	0.58	0.36	0.51	0.29	0.31	0.25	0.29	0.30	0.33	0.38	0.29	0.31	0.30	0.16	0.16	0.18	0.16	0.14	0.15	0.25	0.28	0.24	0.26	0.25	0.28	0.29	0.29
Mn	0.01	0.01	0.01	0.01	0.02	0.03	0.04	0.03	0.01	0.01	0.02	0.03	0.01	-	0.01	-	-	-	-	-	-	0.01	0.02	0.01	0.02	0.01	0.01	0.02	0.03
Mg	0.57	0.64	0.58	0.68	0.61	0.74	0.72	0.80	0.71	0.74	0.65	0.61	0.70	0.67	0.73	0.77	0.79	0.76	0.79	0.85	0.79	0.81	0.85	0.88	0.87	0.81	0.85	0.75	0.74
Ca	0.73	0.81	0.75	0.79	0.76	0.87	0.88	0.89	0.88	0.87	0.88	0.87	0.89	0.89	0.88	0.89	0.88	0.88	0.86	0.87	0.88	0.82	0.75	0.76	0.75	0.81	0.73	0.81	0.82
Na	-	-	0.05	0.05	0.06	0.06	0.04	0.03	0.04	0.05	0.04	0.05	0.03	0.04	-	-	0.07	0.04	0.04	-	0.06	0.06	0.04	-	0.04	-	0.04	0.04	-
K	-	-	-	-	-	-	-	-	-	-	-	-	-	-	-	-	-	-	-	-	-	-	-	-	-	-	-	-	-
Cl	-	-	-	-	-	-	-	-	-	-	-	-	-	-	-	-	-	-	-	-	-	-	-	-	-	-	-	-	-
Total	3.98	3.99	4.00	4.00	4.01	4.03	4.03	4.02	4.03	4.04	4.02	4.03	4.03	4.04	4.02	3.99	4.03	4.01	4.01	3.98	4.01	4.02	3.99	3.98	3.99	3.99	3.99	3.98	3.98
En	29.74	34.55	30.28	36.74	32.23	38.53	37.19	40.74	37.64	38.46	34.67	32.23	36.95	35.99	37.96	42.25	43.16	41.94	43.43	45.69	43.24	42.93	44.87	46.45	45.90	43.21	45.46	40.02	39.55
Fs	31.64	21.93	30.76	20.29	27.96	16.47	17.83	14.29	16.16	16.32	18.41	21.65	15.94	16.70	16.33	8.91	8.72	9.70	9.08	7.40	8.41	13.95	15.41	13.49	14.48	13.75	15.53	16.57	16.97
Wo	38.62	43.52	38.96	42.98	39.81	45.00	44.99	44.97	46.20	45.22	46.92	46.12	47.11	47.31	45.72	48.85	48.12	48.35	47.49	46.91	48.35	43.12	39.72	40.06	39.62	43.04	39.01	43.41	43.48
# Mg	48.99	62.06	50.11	64.97	54.39	71.88	69.94	76.04	70.97	70.85	66.35	61.69	70.32	68.30	70.83	82.59	83.19	81.21	82.71	86.06	83.71	76.27	75.56	78.27	77.06	76.65	75.30	72.18	71.99

APPENDIX C2

Raw whole rock geochemical data

ANALYTICAL TECHNIQUES FOR X-RAY FLUORESCENCE

Samples selected for X-ray fluorescence (XRF) were crushed in a clean tungsten-carbide bowl using a Rocklabs tema mill. Splits of the samples were analysed by the Advanced Analytical Centre (AAC) at James Cook University. Approximately 10 g of each sample was weighed into a porcelain crucible and heated at 1000^{o}C for 10 hours to determine the loss on ignition (LOI). Approximately 0.6 g of the heated samples were then pressed into disks and analysed using the Siemens SRS-3000 X-ray fluorescence (XRF) spectrometer. Two duplicate samples of S-59 were run to establish variance and analytical error. One of these (S-59 Duplicate 1) was also crushed in a tungsten-carbide bowl, whereas the other (S-59 Duplicate 2) was crushed in a chromium-steel bowl. Duplicate samples show minimal variations and are within analytical error.

Suite	Gabbroic Dykes						Palaeocene-Eocene Intrusions				Eocene - Llama Volcanic					
Locality	S Galeno	S Galeno	S Galeno	N Galeno	E Galeno	N Galeno	Cerro Montana		East Minas Conga		La Carpa	Cruz Conga	Aurora Patricia	La Carpa		
Sample No.	S-16	S-55	S-57	S-18	S-26	S-87	S-28	S-31	S-46	S-50	S-21	S-32	S-11	S-38	S-35	S-36
Rock Type	Hbl Gabbro	Hbl Gabbro	Gabbro	Gabbro	Gab Diorite	Gab Diorite	Hbl Diorite	Hbl Diorite	Hbl MD	Hbl MD	Hbl Andesite	Basaltic Andesite	Hbl Diorite	Hbl Qtz Diorite	Hbl-Bt Diorite	Hbl-Bt Diorite
wt.%																
SiO_2	46.49	44.37	49.67	43.17	50.70	51.13	57.80	56.70	55.80	53.34	56.16	54.90	61.30	63.52	59.38	60.85
TiO_2	1.20	1.07	1.28	1.19	1.51	1.09	0.57	0.64	0.71	0.69	0.64	1.10	0.52	0.48	0.60	0.55
Al_2O_3	18.15	16.89	19.90	16.39	16.87	18.14	17.35	18.54	17.82	17.50	18.54	18.43	17.43	16.61	17.09	16.29
Fe_2O_3(T)	11.59	12.21	9.93	10.19	11.09	10.12	6.93	7.46	7.39	7.69	6.45	6.88	4.83	3.88	5.39	4.68
MnO	0.16	0.21	0.20	0.12	0.64	0.15	0.29	0.26	0.17	0.16	0.21	0.24	0.11	0.07	0.11	0.11
MgO	4.86	4.71	3.82	6.23	3.80	3.32	1.83	2.00	3.68	3.90	2.06	1.62	1.80	1.79	2.43	1.90
CaO	9.41	10.03	9.47	8.04	6.92	9.18	5.34	5.01	8.19	7.52	6.75	6.42	5.70	4.50	6.44	5.99
Na_2O	2.15	2.22	3.25	2.88	3.13	3.23	3.80	4.73	3.81	3.82	4.40	4.55	3.68	3.73	3.67	3.20
K_2O	0.94	0.73	0.94	0.19	2.11	0.94	2.05	1.67	2.06	1.09	2.04	2.79	1.90	2.44	1.93	2.11
P_2O_5	0.17	0.20	0.18	0.34	0.52	0.26	0.39	0.36	0.23	0.24	0.31	0.46	0.23	0.20	0.23	0.23
LOI	5.66	7.71	2.60	11.31	3.10	3.18	3.94	2.89	0.92	4.65	2.06	3.15	3.08	2.92	2.22	5.08
Total	100.78	100.35	101.24	100.06	100.39	100.74	100.29	100.26	100.78	100.60	99.61	100.54	100.58	100.14	99.49	100.99
ppm																
Cr	19	9	5	39	36	3	9	19	31	10	0	0	26	21	29	12
Ni	13	13	14	32	28	8	9	6	15	16	6	5	6	11	12	8
Co	40	33	29	30	32	24	12	11	27	22	19	17	13	17	24	15
Sc	25	18	21	25	22	18	6	7	18	18	8	5	7	7	10	8
V	332	291	222	247	185	184	42	62	174	187	114	82	70	79	103	95
Rb	35	14	24	<1	67	18	61	39	62	27	59	74	60	76	58	64
Cs	8	1	2	<1	8	<1	<1	1	6	1	2	<1	1	3	<1	2
Ba	375	366	621	829	701	373	1228	580	803	648	902	1073	827	864	708	893
Sr	514	582	711	625	472	571	898	799	635	816	775	967	584	623	793	625
Ga	17	17	23	18	21	16	16	16	20	19	20	23	21	21	20	18
Ta	<1.0	<1.0	1.0	<1.0	1.8	<1.0	<1.0	1.1	<1.0	<1.0	<1.0	2.2	<1.0	<1.0	<1.0	<1.0
Nb	1.0	2.0	9.0	11.0	21.0	4.0	3.0	7.0	5.0	4.0	5.0	29.0	5.0	5.0	5.0	6.0
Hf	1.9	1.8	2.1	2.4	5.1	3.5	3.6	3.3	2.9	2.6	3.6	5.0	3.1	3.0	2.5	2.9
Zr	51.0	57.0	81.0	88.0	241.0	128.0	112.0	97.0	86.0	83.0	111.0	189.0	110.0	92.0	78.0	82.0
Y	19.0	19.0	17.0	18.0	37.0	27.0	73.0	27.0	21.0	19.0	25.0	28.0	17.0	16.0	12.0	11.0
Th	1.5	1.7	3.4	3.5	9.6	3.0	3.2	4.7	6.9	5.5	7.3	12.0	4.6	3.0	4.2	4.3
U	<2.0	<2.0	<2.0	<2.0	3.1	<2.0	<2.0	<2.0	<2.0	<2.0	2.1	2.4	<2.0	2.2	<2.0	2.7
La	10.60	12.70	18.40	24.30	43.20	20.00	34.00	25.80	25.90	23.60	34.10	58.40	20.70	15.00	15.90	16.70
Ce	22.70	25.30	36.10	47.10	82.40	46.00	60.70	51.00	48.00	44.30	65.10	106.00	37.30	26.70	36.10	32.90
Nd	13.10	13.00	16.90	na	35.10	na	32.20	25.30	23.00	na	26.60	41.50	18.00	14.70	na	na
Sm	3.15	3.26	3.39	4.32	7.14	5.07	7.54	5.42	4.09	3.96	5.50	7.26	3.66	3.40	3.82	3.54
Eu	1.11	1.02	1.33	1.26	1.71	1.42	2.50	1.74	1.17	0.84	1.58	2.07	1.03	0.75	1.23	1.06
Tb	0.62	0.54	0.65	0.60	1.10	0.88	1.32	0.90	0.69	0.64	0.78	0.94	0.51	0.48	0.53	0.52
Ho	0.74	0.69	0.77	na	1.28	na	1.78	1.07	0.85	na	0.98	1.13	0.58	na	na	na
Yb	1.77	1.67	1.60	1.48	3.16	2.64	4.45	2.59	2.05	1.88	2.70	2.42	1.27	0.86	0.86	0.91
Lu	0.24	0.23	0.22	0.21	0.45	0.40	0.66	0.35	0.29	0.28	0.34	0.31	<0.20	<0.20	<0.20	<0.20
Rb/Sr	0.07	0.02	0.03	0.00	0.14	0.03	0.07	0.05	0.10	0.03	0.08	0.08	0.10	0.12	0.07	0.10
Sr/Y	27.05	30.63	41.82	34.72	12.76	21.15	12.30	29.59	30.24	42.95	31.00	34.54	34.35	38.94	66.08	56.82
La_N/Yb_N	4.00	5.09	7.69	10.98	9.14	5.07	5.11	6.66	8.45	8.39	8.45	16.14	10.90	11.66	12.36	12.27

<2.0 = below detection limit; na = not analysed
Gab Diorite = Gabbroic Diorite; MD = Microdiorite; Bas Andesite = Basaltic Andesite; Hbl = Hornblende; Bt = Biotite

Suite	Miocene Barren Intrusive Units							Miocene Mineralised Centres							
Locality	Michiquillay Region						Galeno Prospect	Michiquillay Prospect			Minas Conga Prospect		Galeno Prospect		
Sample No.	S-54	S-58	S-59	S-59 (Duplicate 1)	S-59 (Duplicate 2)	S-60	S-T4	S-H22(244)	S-H22(176)	S-H22(180)	S-Chail	S-Hualy	S-T1	S-T2	S-T3
Rock Type	Hbl-Bt Diorite	Hbl-Bt Diorite	Hbl-Bt Qtz Diorite	Hbl-Bt Qtz Diorite	Hbl-Bt Qtz Diorite	Hbl-Bt Diorite	Hbl-Bt Diorite	Hbl-Bt Diorite	Hbl-Bt Diorite	Hbl-Bt Diorite	Hbl-Bt Diorite	Hbl-Bt Diorite	Hbl-Bt Diorite	Hbl-Bt Diorite	Hbl-Bt Qtz Diorite
wt.%															
SiO_2	60.58	58.51	59.77	59.50	59.84	61.09	58.20	59.51	61.90	63.00	62.50	59.70	64.00	65.80	63.90
TiO_2	0.54	0.62	0.65	0.63	0.64	0.55	0.60	0.52	0.56	0.56	0.50	0.55	0.48	0.47	0.46
Al_2O_3	16.13	16.75	17.14	17.06	17.17	17.26	16.17	16.80	16.95	16.46	17.19	16.33	17.47	17.15	16.47
Fe_2O_3(T)	4.58	5.56	5.62	5.59	5.73	4.91	7.79	4.50	5.17	5.64	4.72	4.86	3.51	2.28	4.40
MnO	0.10	0.12	0.12	0.12	0.12	0.12	0.07	0.23	0.08	0.00	0.09	0.17	0.00	0.00	0.10
MgO	1.86	2.64	2.68	2.66	2.69	1.55	4.40	0.91	2.26	2.27	1.72	2.33	1.64	1.35	1.57
CaO	5.63	6.08	6.18	6.17	6.16	5.71	4.65	4.73	5.48	4.35	5.00	5.65	0.59	2.30	4.20
Na_2O	3.11	3.94	4.03	3.97	3.88	3.78	3.54	2.44	3.69	3.67	4.27	3.41	2.64	3.43	3.32
K_2O	2.17	1.97	1.99	1.97	1.98	1.86	2.10	2.57	2.34	2.38	2.45	1.16	5.88	3.64	3.32
P_2O_5	0.22	0.22	0.23	0.22	0.22	0.22	0.20	0.22	0.23	0.23	0.23	0.21	0.17	0.23	0.21
				0.01	0.00										
LOI	5.63	4.47	2.50	2.45	2.46	3.62	2.12	7.80	1.40	1.84	1.32	5.06	4.31	3.83	2.60
Total	100.54	100.87	100.91	100.33	100.89	100.67	99.84	100.22	100.06	100.40	99.99	99.43	100.69	100.48	100.55
ppm															
Cr	7	43	28	24	103	7	175	5	45	42	33	41	35	35	46
Ni	7	20	12	13	14	6	46	4	13	12	9	11	10	5	8
Co	19	17	22	32	12	15	23	24	23	22	21	14	21	20	21
Sc	8	13	13	13	13	7	18	10	10	10	8	8	6	6	6
V	93	123	118	119	117	87	146	79	90	94	72	116	80	79	68
Rb	66	60	60	60	60	52	90	100	51	75	72	33	165	81	88
Cs	4	3	2	1	2	<1	3	3	1	2	<1.0	1	4	5	2
Ba	1065	622	671	660	658	766	344	529	668	582	723	473	630	606	794
Sr	580	619	708	711	705	774	532	230	690	600	643	615	295	491	528
Ga	19	19	19	18	19	20	20	21	18	20	19	20	18	18	20
Ta	<1.0	<1.0	<1.0	<1.0	<1.0	<1.0	<1.0	<1.0	1.5	1.2	1.2	<1.0	<1.0	1.3	<1.0
Nb	5.0	4.0	4.0	4.0	5.0	6.0	4.0	6.0	7.0	7.0	5.0	6.0	6.0	7.0	7.0
Hf	3.4	2.3	2.7	2.3	3.2	2.8	2.5	3.0	3.0	3.1	3.4	3.0	2.7	3.2	2.4
Zr	89.0	84.0	81.0	87.0	84.0	87.0	67.0	95.0	70.0	82.0	93.0	63.0	99.0	85.0	62.0
Y	16.0	12.0	15.0	14.0	15.0	11.0	16.0	16.0	14.0	12.0	13.0	13.0	13.0	11.0	10.0
Th	4.1	3.7	4.5	4.3	4.1	4.1	3.8	6.2	5.8	6.1	6.1	5.8	3.8	4.6	5.1
U	<2.0	<2.0	<2.0	<2.0	<2.0	<2.0	<2.0	<2.0	<2.0	<2.0	<2.0	<2.0	<2.0	<2.0	<2.0
La	19.90	15.10	17.20	16.80	16.00	17.50	14.70	17.50	16.90	16.90	19.30	17.20	14.40	19.60	16.40
Ce	37.60	31.40	36.40	35.40	32.20	37.10	29.70	37.40	35.60	33.90	37.70	33.90	30.40	39.90	32.50
Nd	na	na	16.90	na	na	na	15.60	na	16.90	15.80	17.40	16.30	16.20	20.10	15.50
Sm	4.16	3.41	3.49	3.47	3.59	4.01	3.46	3.56	3.40	2.91	3.28	3.18	3.40	3.77	2.97
Eu	1.23	1.03	0.98	0.92	0.99	1.16	1.17	0.94	1.03	0.89	0.95	0.80	0.98	0.96	0.89
Tb	0.60	0.50	0.53	0.59	0.57	0.53	0.55	0.52	0.45	0.38	0.47	0.48	0.48	0.48	0.43
Ho	na	na	0.62	na	na	na	0.65	na	0.49	0.45	0.57	0.54	0.48	0.46	0.44
Yb	1.14	1.12	1.21	1.14	1.32	0.88	1.32	1.21	0.96	0.93	1.20	1.11	0.91	0.79	0.78
Lu	<0.20	<0.20	<0.20	<0.20	<0.20	<0.20	<0.20	<0.20	<0.20	<0.20	<0.20	<0.20	<0.20	<0.20	<0.20
Rb/Sr	0.11	0.10	0.08	0.08	0.09	0.07	0.17	0.43	0.07	0.13	0.11	0.05	0.56	0.16	0.17
Sr/Y	36.25	51.58	47.20	50.79	47.00	70.36	33.25	14.38	49.29	50.00	49.46	47.31	22.69	44.64	52.80
La_N/Yb_N	11.67	9.02	9.51	9.85	8.11	13.30	7.45	9.67	11.77	12.15	10.75	10.36	10.58	16.59	14.06

Suite			Regalado Volcanic Units (M-L Mio)				Huambos Volcanics (L Mio)	
Locality	Minas Carpa	Yanacocha			North Cajamarca			W M Conga
Sample No.	S-M Carpa	S-CLL5	S-61	S-64	S-66	S-68	S-63	S-MC4
Rock Type	Hbl-Bt Diorite	Hbl-Bt Diorite	Hbl Andesite	Hbl Andesite	Hbl Andesite	Hbl Andesite	Hbl-Bt Andesite	Hbl-Bt Andesite
wt.%								
SiO_2	62.62	67.90	57.18	60.53	58.57	56.57	59.82	61.77
TiO_2	0.49	0.38	0.71	0.57	0.68	0.74	0.71	0.54
Al_2O_3	16.41	16.85	18.29	16.91	17.76	17.96	17.91	16.80
Fe_2O_3(T)	5.66	2.05	6.37	5.29	5.87	6.67	5.76	4.99
MnO	0.07	0.00	0.14	0.11	0.10	0.20	0.10	0.15
MgO	1.74	1.12	3.31	1.91	2.79	2.62	2.46	2.23
CaO	2.88	2.68	7.20	5.66	6.55	7.42	6.49	5.10
Na_2O	3.42	4.68	4.07	3.56	3.85	3.71	4.23	4.01
K_2O	2.78	2.88	1.51	2.10	1.74	1.59	1.87	2.34
P_2O_5	0.22	0.18	0.25	0.23	0.26	0.28	0.27	0.22
LOI	4.06	1.18	1.18	3.95	1.58	2.55	1.21	2.72
Total	100.35	99.90	100.20	100.81	99.75	100.32	100.83	100.88
ppm								
Cr	35	44	22	13	10	11	25	0
Ni	6	5	16	10	12	11	14	9
Co	22	26	23	20	19	18	19	21
Sc	8	5	17	13	13	13	10	9
V	87	68	132	102	120	129	123	101
Rb	87	83	33	64	46	42	47	70
Cs	3	<1	<1	<1	<1	<1	2	<1
Ba	617	895	620	610	534	488	560	1973
Sr	433	805	838	660	718	759	820	594
Ga	20	20	21	19	22	21	22	20
Ta	<1.0	1.0	<1.0	<1.0	<1.0	<1.0	<1.0	<1.0
Nb	7.0	2.0	1.0	4.0	3.0	3.0	3.0	5.0
Hf	3.2	3.6	2.7	2.9	3.2	3.2	2.8	2.5
Zr	93.0	94.0	83.0	86.0	101.0	95.0	105.0	84.0
Y	14.0	7.0	18.0	20.0	15.0	14.0	16.0	12.0
Th	6.3	6.1	2.5	3.7	3.8	3.2	5.9	6.3
U	<2.0	<2.0	<2.0	<2.0	<2.0	<2.0	2.2	2.2
La	18.30	20.20	18.20	20.50	18.60	17.90	22.30	18.20
Ce	36.80	39.00	36.10	42.00	37.80	38.40	41.60	35.50
Nd	17.10	16.50	17.60	na	na	na	19.70	na
Sm	3.28	2.62	3.81	4.00	4.00	3.98	3.90	3.41
Eu	1.06	0.78	1.11	1.05	1.01	0.81	1.15	0.57
Tb	0.45	0.33	0.62	0.61	0.62	0.50	0.60	<0.50
Ho	0.52	0.35	0.77	na	na	na	0.74	na
Yb	1.12	0.62	1.65	1.23	1.37	1.29	1.56	0.99
Lu	<0.20	<0.20	0.21	<0.20	0.20	<0.20	0.22	<0.20
Rb/Sr	0.20	0.10	0.04	0.10	0.06	0.06	0.06	0.12
Sr/Y	30.93	115.00	46.56	33.00	47.87	54.21	51.25	49.50
La_N/Yb_N	10.93	21.79	7.38	11.14	9.08	9.28	9.56	12.29

APPENDIX C3

Partial melting modelling calculations and partition coefficients

Starting composition and partition coefficents used for partial melting models.

Element	Basaltic Source* (ppm)	Olv[1]	Opx[1]	Cpx[1]	Grt[1]	Amp[1]	Kfs[1]	Ilm[1]	Mag[1]
La	10.60	0.0004	0.002	0.10	0.04	0.2	0.10	0.005	0.22
Ce	22.70	0.0005	0.003	0.20	0.08	0.3	0.06	0.006	0.26
Nd	13.10	0.0010	0.007	0.40	0.20	0.8	0.04	0.008	0.30
Sm	3.15	0.0013	0.010	0.60	1.00	1.1	0.04	0.010	0.35
Eu	1.11	0.0016	0.013	0.60	0.98	1.3	4.60	0.007	0.26
Tb	0.62	0.0016	0.019	0.70	7.50	2.0	0.06	0.022	0.28
Yb	1.77	0.0015	0.049	0.60	21.00	1.7	0.04	0.077	0.18
Lu	0.24	0.0015	0.058	0.60	21.00	1.5	0.03	0.100	0.18
Rb	35	0.0100	0.022	0.03	0.03	0.2	2.40		
Sr	514	0.0140	0.017	0.20	0.01	0.4	5.10		
Zr	51	0.4000	0.100	0.35	0.50	0.5	0.02		
Y	19	0.0015	0.030	0.03	16.00	1.9			

* Data from this study (Sample S16)

[1] Martin (1987)

Olv = Olivine; Opx = Orthopyroxene; Cpx = Clinopyroxene; Grt = Garnet; Amp = Amphibole

Kfs = K-feldspar; Ilm = Ilmenite; Mag = Magnetite

Mantle Melting Model To Generate S-16

%	Residual mineralogy	
4	0.04	Amphibole
15	0.15	Clinopyroxene
23	0.23	Orthopyroxene
55	0.55	Olivine
3	0.03	Garnet
0	0.00	Plagioclase

Mantle KD Values for partial melting calculation (Martin, 1987)

	Olivine	Orthopyroxene	Clinopyroxene	Garnet	Amphibole	Plagioclase
La	0.0004	0.002	0.070	0.015	0.20	0.130
Ce	0.0005	0.003	0.098	0.021	0.30	0.110
Nd	0.0010	0.007	0.210	0.087	0.80	0.070
Sm	0.0013	0.010	0.260	0.217	1.10	0.050
Eu	0.0016	0.013	0.310	0.320	1.30	1.300
Tb	0.0016	0.019	0.315	0.779	2.00	0.037
Yb	0.0015	0.049	0.280	4.030	1.70	0.024
Lu	0.0015	0.058	0.270	5.050	1.50	0.023
Rb	0.0100	0.022	0.030	0.040	0.22	0.060
Sr	0.0140	0.017	0.120	0.012	0.36	2.000
Zr	0.4000	0.100	0.350	0.500	0.45	0.250
Y	0.0015	0.030	0.300	2.000	1.90	0.600

Prim. Mantle (McDonough et al. 1992)		Calculated bulk partition coefficient	
La	0.71	La	0.01963
Ce	1.83	Ce	0.02830
Nd	1.37	Nd	0.06822
Sm	0.44	Sm	0.09253
Eu	0.17	Eu	0.11197
Tb	0.11	Tb	0.15587
Yb	0.48	Yb	0.24300
Lu	0.07	Lu	0.26617
Rb	0.64	Rb	0.02506
Sr	21.10	Sr	0.04437
Zr	11.20	Zr	0.32850
Y	4.55	Y	0.18873

1% Batch Melt		2% Batch Melt		5% Batch Melt		S-16	6% Batch Melt		10% Batch Melt		20% Batch Melt		35% Batch Melt		50% Melt	
La	24.05	La	18.04	La	10.31	10.60	La	9.02	La	6.02	La	3.28	La	1.95	La	1.39
Ce	48.22	Ce	38.40	Ce	23.84	22.70	Ce	21.17	Ce	14.61	Ce	8.23	Ce	4.98	Ce	3.57
Nd	17.62	Nd	15.73	Nd	11.90	13.10	Nd	11.00	Nd	8.46	Nd	5.37	Nd	3.46	Nd	2.56
Sm	4.37	Sm	4.01	Sm	3.22	3.15	Sm	3.02	Sm	2.42	Sm	1.62	Sm	1.08	Sm	0.81
Eu	1.39	Eu	1.29	Eu	1.07	1.11	Eu	1.02	Eu	0.84	Eu	0.58	Eu	0.40	Eu	0.30
Tb	0.66	Tb	0.63	Tb	0.55	0.62	Tb	0.52	Tb	0.45	Tb	0.33	Tb	0.24	Tb	0.19
Yb	1.92	Yb	1.86	Yb	1.71	1.77	Yb	1.67	Yb	1.51	Yb	1.22	Yb	0.95	Yb	0.77
Lu	0.27	Lu	0.26	Lu	0.24	0.24	Lu	0.24	Lu	0.22	Lu	0.18	Lu	0.14	Lu	0.12
Rb	18.24	Rb	14.25	Rb	8.60	35.00	Rb	7.60	Rb	5.18	Rb	2.89	Rb	1.73	Rb	1.24
Sr	391.27	Sr	332.37	Sr	228.97	514.00	Sr	207.46	Sr	150.79	Sr	89.60	Sr	55.70	Sr	40.41
Zr	33.41	Zr	32.76	Zr	30.93	51.00	Zr	30.37	Zr	28.31	Zr	24.20	Zr	19.87	Zr	16.86
Y	23.12	Y	22.20	Y	19.84	19.00	Y	19.17	Y	16.86	Y	12.96	Y	9.63	Y	7.66

Batch Melting Model To Generate S-46

%	Residual mineralogy	
15	0.15	Olivine
20	0.20	Orthopyroxene
42	0.42	Clinopyroxene
1.5	0.02	Garnet
10	0.10	Amphibole
11	0.11	K-Feldspar
0	0.00	Ilmenite
0	0.00	Magnetite
0	0.00	Quartz

Archean Tholeiitic KD Values for partial melting calculation (Martin, 1987)

	Olivine	Orthopyroxene	Clinopyroxene	Garnet	Amphibole	K feldspar	Ilmenite	Magnetite	Quartz
La	0.0004	0.002	0.10	0.04	0.20	0.10	0.005	0.22	0.018
Ce	0.0005	0.003	0.20	0.08	0.30	0.06	0.006	0.26	0.014
Nd	0.0010	0.007	0.40	0.20	0.80	0.04	0.008	0.30	0.016
Sm	0.0013	0.010	0.60	1.00	1.10	0.04	0.010	0.35	0.017
Eu	0.0016	0.013	0.60	0.98	1.30	4.60	0.007	0.26	0.080
Tb	0.0016	0.019	0.70	7.50	2.00	0.06	0.022	0.28	0.019
Yb	0.0015	0.049	0.60	21.00	1.70	0.04	0.077	0.18	0.017
Lu	0.0015	0.058	0.60	21.00	1.50	0.03	0.100	0.18	0.011
Rb	0.0100	0.022	0.03	0.03	0.22	2.40			
Sr	0.0140	0.017	0.20	0.01	0.36	5.10			
Zr	0.4000	0.100	0.35	0.50	0.45	0.02			
Y	0.0015	0.030	0.03	16.00	1.90				

Primitive Basaltic Source (S16)		Calculated bulk partition coefficient	
La	10.60	La	0.07406
Ce	22.70	Ce	0.12248
Nd	13.10	Nd	0.25691
Sm	3.15	Sm	0.38360
Eu	1.11	Eu	0.90554
Tb	0.62	Tb	0.61714
Yb	1.77	Yb	0.75143
Lu	0.24	Lu	0.73213
Rb	35.00	Rb	0.30501
Sr	514.00	Sr	0.68670
Zr	51.00	Zr	0.28170
Y	19.00	Y	0.44883

1% Batch Melt		2% Batch Melt		5% Batch Melt		10% Batch Melt		25% Batch Melt		29% Batch Melt		40% Batch Melt		Sample 46	50% Melt	
La	127.22	La	114.50	La	88.07	La	63.60	La	34.69	La	30.94	La	23.85	25.90	La	19.74
Ce	172.95	Ce	162.11	Ce	136.46	Ce	107.98	Ce	66.40	Ce	60.22	Ce	47.94	48.00	Ce	40.45
Nd	49.56	Nd	48.20	Nd	44.55	Nd	39.55	Nd	29.59	Nd	27.73	Nd	23.64	23.00	Nd	20.84
Sm	8.08	Sm	7.96	Sm	7.60	Sm	7.07	Sm	5.86	Sm	5.60	Sm	5.00	4.09	Sm	4.55
Eu	1.22	Eu	1.22	Eu	1.22	Eu	1.21	Eu	1.19	Eu	1.19	Eu	1.18	1.17	Eu	1.17
Tb	1.00	Tb	0.99	Tb	0.97	Tb	0.95	Tb	0.87	Tb	0.85	Tb	0.80	0.69	Tb	0.77
Yb	2.35	Yb	2.34	Yb	2.32	Yb	2.28	Yb	2.18	Yb	2.15	Yb	2.08	2.05	Yb	2.02
Lu	0.33	Lu	0.33	Lu	0.32	Lu	0.32	Lu	0.30	Lu	0.30	Lu	0.29	0.29	Lu	0.28
Rb	112.19	Rb	109.75	Rb	103.01	Rb	93.46	Rb	73.11	Rb	69.09	Rb	60.03	62.00	Rb	53.64
Sr	745.11	Sr	741.74	Sr	731.82	Sr	715.85	Sr	671.88	Sr	661.05	Sr	632.99	635.00	Sr	609.48
Zr	176.54	Zr	172.26	Zr	160.57	Zr	144.26	Zr	110.56	Zr	104.08	Zr	89.63	86.00	Zr	79.58
Y	41.82	Y	41.32	Y	39.88	Y	37.70	Y	32.39	Y	31.22	Y	28.39	21.00	Y	26.23

Batch Melting Model To Generate Chail

%	Residual Mineralogy	
36	0.36	Clinopyroxene
4	0.04	Garnet
50	0.50	Amphibole
7	0.07	K-Feldspar
2	0.02	Ilmenite
1	0.01	Magnetite
0	0.00	Quartz

Archean Tholeiitic KD Values for partial melting calculation (Martin, 1986)

	Olivine	Orthopyroxene	Clinopyroxene	Garnet	Amphibole	K feldspar	Ilmenite	Magnetite	Quartz
La	0.0004	0.002	0.10	0.04	0.20	0.10	0.005	0.22	0.018
Ce	0.0005	0.003	0.20	0.08	0.30	0.06	0.006	0.26	0.014
Nd	0.0010	0.007	0.40	0.20	0.80	0.04	0.008	0.3	0.016
Sm	0.0013	0.010	0.60	1.00	1.10	0.04	0.010	0.35	0.017
Eu	0.0016	0.013	0.60	0.98	1.30	4.60	0.007	0.26	0.080
Tb	0.0016	0.019	0.70	7.50	2.00	0.06	0.022	0.28	0.019
Yb	0.0015	0.049	0.60	21.00	1.70	0.04	0.077	0.18	0.017
Lu	0.0015	0.058	0.60	21.00	1.50	0.03	0.100	0.18	0.011
Rb	0.0100	0.022	0.03	0.03	0.22	2.40			
Sr	0.0140	0.017	0.20	0.01	0.36	5.10			
Zr	0.4000	0.100	0.35	0.50	0.45	0.02			
Y	0.0015	0.030	0.03	16.00	1.90				

Primitive Basaltic Source (S-16)		Calculated bulk partition coefficient	
La	10.60	La	0.14690
Ce	22.70	Ce	0.23212
Nd	13.10	Nd	0.55796
Sm	3.15	Sm	0.81250
Eu	1.11	Eu	1.22994
Tb	0.62	Tb	1.55944
Yb	1.77	Yb	1.91214
Lu	0.24	Lu	1.81190
Rb	35.00	Rb	0.29016
Sr	514.00	Sr	0.60952
Zr	51.00	Zr	0.37240
Y	19.00	Y	1.60080

1% Batch Melt		2% Batch Melt		5% Batch Melt		10% Batch Melt		20% Batch Melt		35% Batch Melt		50% Melt		Sample Chail
La	68.20	La	64.65	La	55.92	La	45.65	La	33.38	La	23.79	La	19.05	19.30
Ce	94.66	Ce	91.73	Ce	83.91	Ce	73.48	Ce	58.85	Ce	45.32	Ce	37.79	37.70
Nd	23.29	Nd	23.11	Nd	22.58	Nd	21.75	Nd	20.27	Nd	18.38	Nd	17.01	17.40
Sm	3.87	Sm	3.86	Sm	3.83	Sm	3.79	Sm	3.71	Sm	3.59	Sm	3.49	3.28
Eu	0.90	Eu	0.91	Eu	0.91	Eu	0.92	Eu	0.94	Eu	0.97	Eu	0.99	0.95
Tb	0.40	Tb	0.40	Tb	0.40	Tb	0.41	Tb	0.43	Tb	0.45	Tb	0.48	0.47
Yb	0.93	Yb	0.93	Yb	0.95	Yb	0.97	Yb	1.02	Yb	1.11	Yb	1.20	1.20
Lu	0.13	Lu	0.13	Lu	0.14	Lu	0.14	Lu	0.15	Lu	0.16	Lu	0.17	-0.20
Rb	117.74	Rb	115.00	Rb	107.48	Rb	96.91	Rb	80.99	Rb	64.98	Rb	55.48	72.00
Sr	837.92	Sr	832.62	Sr	817.11	Sr	792.52	Sr	747.51	Sr	688.83	Sr	644.96	643.00
Zr	134.68	Zr	132.48	Zr	126.31	Zr	117.20	Zr	102.43	Zr	86.14	Zr	75.71	93.00
Y	11.91	Y	11.96	Y	12.10	Y	12.33	Y	12.83	Y	13.66	Y	14.48	13.00

<u>Batch Melting Model To Generate S-59</u>

%	**Residual mineralogy**	
0	0.00	Olivine
0	0.00	Orthopyroxene
50	0.50	Clinopyroxene
5	0.05	Garnet
40	0.40	Amphibole
3	0.03	K-Feldspar
1	0.01	Ilmenite
1	0.01	Magnetite
0	0.00	Quartz

Archean Tholeiitic KD Values for partial melting calculation (Martin, 1987)

	Olivine	Orthopyroxene	Clinopyroxene	Garnet	Amphibole	K feldspar	Ilmenite	Magnetite	Quartz	Kfs	Plag
La	0.0004	0.002	0.10	0.04	0.20	0.10	0.005	0.22	0.018	0.10	0.140
Ce	0.0005	0.003	0.20	0.08	0.30	0.06	0.006	0.26	0.014	0.06	0.100
Nd	0.0010	0.007	0.40	0.20	0.80	0.04	0.008	0.30	0.016	0.04	0.069
Sm	0.0013	0.010	0.60	1.00	1.10	0.04	0.010	0.35	0.017	0.04	0.052
Eu	0.0016	0.013	0.60	0.98	1.30	4.60	0.007	0.26	0.080	4.60	0.790
Tb	0.0016	0.019	0.70	7.50	2.00	0.06	0.022	0.28	0.019	0.06	0.060
Yb	0.0015	0.049	0.60	21.00	1.70	0.04	0.077	0.18	0.017	0.04	0.012
Lu	0.0015	0.058	0.60	21.00	1.50	0.03	0.100	0.18	0.011	0.03	0.009
Rb	0.0100	0.022	0.03	0.03	0.22	2.40				2.40	2.400
Sr	0.0140	0.017	0.20	0.01	0.36	5.10				5.10	2.000
Zr	0.4000	0.100	0.35	0.50	0.45	0.02				0.02	0.010
Y	0.0015	0.030	0.03	16.00	1.90						

Basaltic Source (S16)		Calculated bulk partition coefficient	
La	10.60	La	0.13725
Ce	22.70	Ce	0.22846
Nd	13.10	Nd	0.53428
Sm	3.15	Sm	0.79480
Eu	1.11	Eu	1.00967
Tb	0.62	Tb	1.52982
Yb	1.77	Yb	2.03377
Lu	0.24	Lu	1.95370
Rb	35.00	Rb	0.17670
Sr	514.00	Sr	0.39765
Zr	51.00	Zr	0.38060
Y	19.00	Y	1.57500

1% Batch Melt		2% Batch Melt		5% Batch Melt		10% Batch Melt		20% Batch Melt		35% Batch Melt		55% Melt		S-59
La	72.66	La	68.61	La	58.76	La	47.42	La	34.22	La	24.13	La	17.33	17.20
Ce	96.12	Ce	93.07	Ce	85.01	Ce	74.28	Ce	59.30	Ce	45.54	Ce	34.77	36.40
Nd	24.31	Nd	24.10	Nd	23.49	Nd	22.55	Nd	20.88	Nd	18.79	Nd	16.57	16.90
Sm	3.95	Sm	3.94	Sm	3.91	Sm	3.86	Sm	3.77	Sm	3.63	Sm	3.47	3.49
Eu	1.10	Eu	1.10	Eu	1.10	Eu	1.10	Eu	1.10	Eu	1.10	Eu	1.11	0.98
Tb	0.41	Tb	0.41	Tb	0.41	Tb	0.42	Tb	0.44	Tb	0.46	Tb	0.50	0.53
Yb	0.87	Yb	0.88	Yb	0.89	Yb	0.92	Yb	0.97	Yb	1.06	Yb	1.21	1.21
Lu	0.12	Lu	0.12	Lu	0.13	Lu	0.13	Lu	0.14	Lu	0.15	Lu	0.17	-0.20
Rb	189.26	Rb	181.19	Rb	160.65	Rb	135.12	Rb	102.53	Rb	75.29	Rb	55.60	60.00
Sr	1273.31	Sr	1254.59	Sr	1201.59	Sr	1122.55	Sr	992.05	Sr	844.74	Sr	705.13	708.00
Zr	131.85	Zr	129.77	Zr	123.92	Zr	115.24	Zr	101.09	Zr	85.37	Zr	70.71	81.00
Y	12.11	Y	12.15	Y	12.29	Y	12.52	Y	13.01	Y	13.83	Y	15.09	15.00

Batch Melting Model To Generate S-61

%	Residual mineralogy	
0	0.00	Olivine
0	0.00	Orthopyroxene
55	0.55	Clinopyroxene
1	0.01	Garnet
38	0.38	Amphibole
3	0.03	K-Feldspar
2	0.02	Ilmenite
1	0.01	Magnetite
0	0.00	Quartz

Archean Tholeiitic KD Values for partial melting calculation (Martin, 1987)

	Olivine	Orthopyroxene	Clinopyroxene	Garnet	Amphibole	K feldspar	Ilmenite	Magnetite	Quartz	Kfs	Plag
La	0.0004	0.002	0.10	0.04	0.20	0.10	0.005	0.22	0.018	0.10	0.140
Ce	0.0005	0.003	0.20	0.08	0.30	0.06	0.006	0.26	0.014	0.06	0.100
Nd	0.0010	0.007	0.40	0.20	0.80	0.04	0.008	0.30	0.016	0.04	0.069
Sm	0.0013	0.010	0.60	1.00	1.10	0.04	0.010	0.35	0.017	0.04	0.052
Eu	0.0016	0.013	0.60	0.98	1.30	4.60	0.007	0.26	0.080	4.60	0.790
Tb	0.0016	0.019	0.70	7.50	2.00	0.06	0.022	0.28	0.019	0.06	0.060
Yb	0.0015	0.049	0.60	21.00	1.70	0.04	0.077	0.18	0.017	0.04	0.012
Lu	0.0015	0.058	0.60	21.00	1.50	0.03	0.100	0.18	0.011	0.03	0.009
Rb	0.0100	0.022	0.03	0.03	0.22	2.40				2.40	2.400
Sr	0.0140	0.017	0.20	0.01	0.36	5.10				5.10	2.000
Zr	0.4000	0.100	0.35	0.50	0.45	0.02				0.02	0.010
Y	0.0015	0.030	0.03	16.00	1.90						

Basaltic Source (S16)		Calculated bulk partition coefficient	
La	10.60	La	0.13670
Ce	22.70	Ce	0.22932
Nd	13.10	Nd	0.53036
Sm	3.15	Sm	0.76290
Eu	1.11	Eu	0.97454
Tb	0.62	Tb	1.22504
Yb	1.77	Yb	1.19054
Lu	0.24	Lu	1.11470
Rb	35.00	Rb	0.17244
Sr	514.00	Sr	0.39993
Zr	51.00	Zr	0.36910
Y	19.00	Y	0.89850

	1% Batch Melt	2% Batch Melt	5% Batch Melt	10% Batch Melt	20% Batch Melt	35% Batch Melt	50% Melt	Sample 61
La	72.94	68.85	58.93	47.53	34.26	24.15	18.65	18.20
Ce	95.77	92.75	84.75	74.09	59.20	45.49	36.93	36.10
Nd	24.48	24.27	23.65	22.69	20.98	18.86	17.12	17.60
Sm	4.12	4.10	4.07	4.00	3.89	3.72	3.57	3.81
Eu	1.14	1.14	1.14	1.14	1.13	1.13	1.12	1.11
Tb	0.51	0.51	0.51	0.52	0.53	0.54	0.56	0.62
Yb	1.49	1.49	1.50	1.51	1.54	1.57	1.62	1.65
Lu	0.22	0.22	0.22	0.22	0.22	0.22	0.23	0.21
Rb	193.67	185.19	163.69	137.15	103.57	75.74	59.70	33.00
Sr	1266.23	1247.78	1195.53	1117.54	988.57	842.69	734.32	838.00
Zr	135.85	133.61	127.29	118.00	102.97	86.45	74.50	83.00
Y	21.12	21.10	21.03	20.91	20.68	20.34	20.02	18.00

Batch Melting Model To Generate Yana

%	Residual mineralogy	
30	0.30	Clinopyroxene
17	0.17	Garnet
50	0.50	Amphibole
0	0.00	K-Feldspar
2	0.02	Ilmenite
1	0.01	Magnetite
0	0.00	Quartz

Archean Tholeiitic KD Values for partial melting calculation (Martin, 1987)

	Olivine	Orthopyroxene	Clinopyroxene	Garnet	Amphibole	K feldspar	Ilmenite	Magnetite	Quartz
La	0.0004	0.002	0.10	0.04	0.20	0.10	0.005	0.22	0.018
Ce	0.0005	0.003	0.20	0.08	0.30	0.06	0.006	0.26	0.014
Nd	0.0010	0.007	0.40	0.20	0.80	0.04	0.008	0.30	0.016
Sm	0.0013	0.010	0.60	1.00	1.10	0.04	0.010	0.35	0.017
Eu	0.0016	0.013	0.60	0.98	1.30	4.60	0.007	0.26	0.080
Tb	0.0016	0.019	0.70	7.50	2.00	0.06	0.022	0.28	0.019
Yb	0.0015	0.049	0.60	21.00	1.70	0.04	0.077	0.18	0.017
Lu	0.0015	0.058	0.60	21.00	1.50	0.03	0.100	0.18	0.011
Rb	0.0100	0.022	0.03	0.03	0.22	2.40			
Sr	0.0140	0.017	0.20	0.01	0.36	5.10			
Zr	0.4000	0.100	0.35	0.50	0.45	0.02			
Y	0.0015	0.030	0.03	16.00	1.90				

Basaltic Source (S16)		Calculated bulk partition coefficient	
La	10.60	La	0.13910
Ce	22.70	Ce	0.22632
Nd	13.10	Nd	0.55716
Sm	3.15	Sm	0.90370
Eu	1.11	Eu	0.99934
Tb	0.62	Tb	2.48824
Yb	1.77	Yb	4.60334
Lu	0.24	Lu	4.50380
Rb	35.00	Rb	0.12478
Sr	514.00	Sr	0.24221
Zr	51.00	Zr	0.41500
Y	19.00	Y	3.67900

1% Batch Melt		2% Batch Melt		5% Batch Melt		10% Batch Melt		20% Batch Melt		45% Batch Melt		S-Yana	50% Melt	
La	71.76	La	67.81	La	58.20	La	47.07	La	34.05	La	20.13	20.20	La	18.61
Ce	96.99	Ce	93.88	Ce	85.66	Ce	74.75	Ce	59.57	Ce	39.51	39.00	Ce	37.02
Nd	23.33	Nd	23.14	Nd	22.61	Nd	21.78	Nd	20.29	Nd	17.32	16.50	Nd	16.83
Sm	3.48	Sm	3.48	Sm	3.47	Sm	3.45	Sm	3.41	Sm	3.33	2.62	Sm	3.31
Eu	1.11	Eu	1.11	Eu	1.11	Eu	1.11	Eu	1.11	Eu	1.11	0.78	Eu	1.11
Tb	0.25	Tb	0.25	Tb	0.26	Tb	0.27	Tb	0.28	Tb	0.34	0.33	Tb	0.36
Yb	0.39	Yb	0.39	Yb	0.40	Yb	0.42	Yb	0.46	Yb	0.59	0.62	Yb	0.63
Lu	0.05	Lu	0.05	Lu	0.06	Lu	0.06	Lu	0.06	Lu	0.08	-0.20	Lu	0.09
Rb	262.11	Rb	245.99	Rb	207.66	Rb	164.86	Rb	116.74	Rb	67.49	83.00	Rb	62.23
Sr	2057.75	Sr	1997.16	Sr	1835.06	Sr	1616.41	Sr	1305.34	Sr	881.32	805.00	Sr	827.56
Zr	121.18	Zr	119.52	Zr	114.80	Zr	107.71	Zr	95.86	Zr	75.19	94.00	Zr	72.08
Y	5.20	Y	5.24	Y	5.36	Y	5.57	Y	6.04	Y	7.68	7.00	Y	8.12

APPENDIX C4

Fractional crystallisation modelling using partition coefficients

Fractional Crystallisation Modelling Using Partition Coefficients

	Opx	Cpx	Hbl	Plag	Bt
Sm	0.100	0.750	2.000	0.110	2.117
Th	0.050	0.010	0.150	0.010	0.997

Partition Coefficients taken from Gill (1981), Sm in Hbl from Green and Pearson (1985) and Bt from Nash and Creecraft (1985)

Initial Composition (S-46)					
Sm	4.09				
Th	6.90				
5% fractional crystallisation					
Sm	4.28	4.14	3.89	4.28	3.86
Th	7.24	7.26	7.21	7.26	6.90
10% fractional crystallisation					
Sm	4.50	4.20	3.68	4.49	3.64
Th	7.63	7.66	7.55	7.66	6.90
20% fractional crystallisation					
Sm	5.00	4.32	3.27	4.99	3.19
Th	8.53	8.61	8.34	8.61	6.90
30% fractional crystallisation					
Sm	5.64	4.47	2.86	5.62	2.75
Th	9.68	9.82	9.34	9.82	6.91
50% fractional crystallisation					
Sm	7.63	4.86	2.05	7.58	1.89
Th	13.33	13.70	12.44	13.70	6.91

APPENDIX D1

El Galeno drill core geology

DRILL CORE LOGGING PROCEDURES

A total of 15 drill cores that were logged by the author are presented in the following appendix. Seven of these are from the El Galeno deposit (Appendix D1-D2) and eight from the Michiquillay deposit (Appendix D4). Logged drill cores ranged in length from 120 to 530 m. Previous logging of the El Galeno drill cores had been completed and compiled by North Ltd (Peru) geologists prior to initiation of the Ph.D. study. North Ltd. geologists logged intrusive type, alteration assemblage and intensity, vein abundance, plus sulphide type and abundance. Drill core logging by the author focussed on identification of the various lithological units with particular emphasis on documenting and re-evaluating the intrusive history. Drill core logging by the author also involved revising fault/gouge zones, alteration phases and distribution, vein density and sulphide minerals paragenesis. Drill core log sheets by the author were later combined with the logged data from the North geologists in a database format. At Michiquillay, the majority of the drill core logging focussed on identifying the main lithological units, fault/gouge zones and alteration phases. In Appendix D4, Cu grades under column Cu_%$_1$ were obtained from drill core assay data compiled by ASRARCO between 1963 and 1965. The remaining metals grades Au(ppb)$_2$ to Mo(ppm)$_2$ were obtained from assayed samples run by North Ltd in 1997. Samples assayed were taken at 15 m intervals from the following drill cores; H-22, J-20, K-19.5, M-17 and N-15.5.

ABBREVIATIONS

El Galeno

Grv = gravels

P1 = P1 porphyry

P2 = P2 porphyry

P3 = P3 porphyry

P3 Bx = P3 porphyritic breccia

P3 dykes = P3 dykes

MBx = MBx porphyry

Michiquillay

D1 = Michiquillay porphyry

Dyke = synmineralisation dyke

Common

Qz = quartzites

Sltst = siltstones

Bx = breccia

Flt = fault

Mag = magmatic breccia

Hydro Bx = hydrothermal breccia

Altn = dominant alteration

Altn2 = subordinate alteration

K = potassic

Mt = magnetite

Prop = propylitic

Silf = silicic

Phyl = phyllic

Arg = argillic

1 = weak

2 = moderate

3 = strong

4 = intense

Hole_Id	From	To	Rock	Bx	Altn	Altn 2	K	Phyl	Silc	Prop	qz_a/b_%	Pyr	Mag	Ccp	Cc	Cv	Bn	Mo
DDH-GN-36	0	2	grv															
DDH-GN-36	2	20	P1		phyl	arg		4	1	1	16	2			2	1		1
DDH-GN-36	20	38	qz		phyl			2			19	2			2	1		1
DDH-GN-36	38	54	P1		phyl	arg		4		1	12	2						2
DDH-GN-36	54	56	P1		phyl	arg		4		1	12	1						2
DDH-GN-36	56	69	P1		phyl	arg		4		1	12	1						1
DDH-GN-36	69	74	P1		phyl	arg		4		1	12	1						1
DDH-GN-36	74	76	qz		phyl			2			12	1			1	1		1
DDH-GN-36	76	83	qz		phyl			2			15	1			1	1		1
DDH-GN-36	83	92	qz		phyl			2			14	1						1
DDH-GN-36	92	95	qz		phyl			2			14	1						1
DDH-GN-36	95	107	qz		phyl			2			13	1						1
DDH-GN-36	107	114	qz		phyl			2			11	2			1	1		1
DDH-GN-36	114	118	qz		phyl			2			16	2			1	1		1
DDH-GN-36	118	123	qz		phyl			2			8	1						
DDH-GN-36	123	124	P1		phyl			4			16	1						
DDH-GN-36	124	131	qz		phyl			2			7	2			1	1		1
DDH-GN-36	131	145	qz		phyl			2			12	2			1	1		1
DDH-GN-36	145	148	qz		phyl			2			12	2			1	1		1
DDH-GN-36	148	152	qz		phyl			2			7	2			1			
DDH-GN-36	152	156	qz		phyl			2			7	2			1			
DDH-GN-36	156	162	qz		phyl			2			9	2			1			
DDH-GN-36	162	163	P1		phyl	k	3	4		1	9	2			1			
DDH-GN-36	163	164	qz		phyl			2			12	2			1			1
DDH-GN-36	164	166	qz		phyl			2			12	2			1			1
DDH-GN-36	166	169	qz		phyl			2			14	2			1			1
DDH-GN-36	169	170	qz		phyl			2			18	2			1			1
DDH-GN-36	170	171	P1		phyl			2		1	18	2			1			1
DDH-GN-36	171	175	qz		phyl			2			18	2			1			1
DDH-GN-36	175	175	P1		phyl			2		1	18	2			1			1
DDH-GN-36	175	177	qz		phyl			1			18	2			1			1
DDH-GN-36	177	180	qz		phyl			1			18	2			1			1
DDH-GN-36	180	195	qz		phyl			1			5	2			1			1
DDH-GN-36	195	198	P1		phyl	prop		4	1	1	13	2						
DDH-GN-36	198	204	qz		phyl			1				2						
DDH-GN-36	204	205	P1		phyl	prop		4	1	1		2						
DDH-GN-36	205	210	qz		phyl			1				2						
DDH-GN-36	210	211	P1		phyl	prop		4	1	1		2						
DDH-GN-36	211	213	qz		phyl			1				2			1			1
DDH-GN-36	213	215	P1		phyl	prop		4	1	1		2			1			1
DDH-GN-36	215	222	qz		phyl			1				2			1			
DDH-GN-36	222	226	qz		phyl			1			11	2			1			
DDH-GN-36	226	230	qz		phyl			1			13	2			1			1
DDH-GN-36	230	235	qz		phyl			1			14	2			1			
DDH-GN-36	235	236	qz		phyl			1			11	2			1			
DDH-GN-36	236	238	qz		phyl			1			11	2			1			
DDH-GN-36	238	250	qz		phyl			1			11	2			1			
DDH-GN-36	250	251	P1		phyl			4			13	2			1			
DDH-GN-36	251	253	qz		phyl			1			11	2			1			
DDH-GN-36	253	257	P1		phyl			4			14	1			1			
DDH-GN-36	257	265	qz		phyl			1			18	2			1	1		
DDH-GN-36	265	270	qz		phyl			1			15	2			1	1		
DDH-GN-36	270	275	qz		phyl			1			12	2			1	1		
DDH-GN-36	275	283	qz		phyl			1			17	2			1	1		
DDH-GN-36	283	285	qz		phyl			1			11	2			1	1		
DDH-GN-36	285	286	qz		phyl			1			11	2			1	1		
DDH-GN-36	286	287	qz		phyl			1			11	2			1	1		
DDH-GN-36	287	287	qz		phyl			1			11	2			1	1		
DDH-GN-36	287	289	qz		phyl			1			11	2			1	1		
DDH-GN-36	289	292	qz		phyl			1			11	2			1	1		
DDH-GN-36	292	298	qz		phyl			1			18	2		1	1	1		
DDH-GN-36	298	300	qz		phyl			1			18	2		1	1	1		
DDH-GN-36	300	304	qz		phyl			1			26	2		1	1	1		
DDH-GN-36	304	305	qz		phyl			1			26	2			1			
DDH-GN-36	305	309	qz		phyl			1			26	2						
DDH-GN-36	309	315	qz		phyl			1			17	2						
DDH-GN-36	315	320	qz		phyl			1			17	1			1			
DDH-GN-36	320	332	qz		phyl			1				2			1			
DDH-GN-36	332	335	P1		phyl			4			18	1			1			
DDH-GN-36	335	340	qz		phyl			1				2			1			
DDH-GN-36	340	349	qz		phyl			1			27	2						
DDH-GN-36	349	352	qz		phyl			1				2						
DDH-GN-36	352	357	P1		phyl			4			18	1						
DDH-GN-36	357	361	qz		phyl			1				2		1	1	1		1
DDH-GN-36	361	362	qz		phyl	k	2	1			13	1						
DDH-GN-36	362	365	qz		phyl	k	2	1			13	2			1			
DDH-GN-36	365	367	qz		phyl	k	2	1			13	2			1			
DDH-GN-36	367	368	P1		phyl	k	2	4			13	2			1			
DDH-GN-36	368	369	qz		phyl			1			13	2			1			
DDH-GN-36	369	379	qz		phyl			1			16	2		1	1	1		
DDH-GN-36	379	383	qz		phyl			1			16	1			1			1
DDH-GN-36	383	387	qz		phyl			1			19	1			1			
DDH-GN-36	387	388	qz		phyl			1			19	1			1			
DDH-GN-36	388	399	qz		phyl			1			26	2		1	1	1		

Hole_Id	From	To	Rock	Bx	Altn	Altn 2	K	Phyl	Silc	Prop	qz_a/b_%	Pyr	Mag	Ccp	Cc	Cv	Bn	Mo
DDH-GN-36	399	402	qz		phyl			1			28	2		1	1	1		
DDH-GN-36	402	408	qz		phyl			1			28	2		1	1	1		
DDH-GN-36	408	419	qz		phyl			1		1	31	2		1				

Hole_Id	From	To	Rock	Bx	Altn	Altn 2	K	Phyl	Silc	Prop	qz_a/b_%	Pyr	Mag	Ccp	Cc	Cv	Bn	Mo
DDH-GN-37	0	8	grv															
DDH-GN-37	8	45	? P1	Flt	phyl-arg			4			12	2			2	1		1
DDH-GN-37	45	69	? P1	Flt	phyl-arg			4			12	2			2			1
DDH-GN-37	69	93	? P1	Flt	phyl-arg			4			12	2			2			
DDH-GN-37	93	143	? P1	Flt	phyl-arg			4			12	2			2			1
DDH-GN-37	143	151	P1		arg	phyl		1			10	2			2			1
DDH-GN-37	151	175	? P1	Flt	k		4	1			8	2			2			1
DDH-GN-37	175	181	P1		phyl	phyl	2	4			8	2			2			1
DDH-GN-37	181	205	? P1	Flt	phyl		2	4			8	1		1	1	1		1
DDH-GN-37	205	219	P2		k	phyl	4	1			8	1		1	1	1		1
DDH-GN-37	219	286	P2		k	phyl	4	1			8	1			1	1		
DDH-GN-37	285	289	? P1	Flt	k	prop	4	1		2	23	1			1	1		
DDH-GN-37	289	295	? P1	Flt	k	prop	4	1		2	23	1	1	1	1			1
DDH-GN-37	295	304	? P1	Flt	k	prop	4	1		2	23	1	1	1	1			1
DDH-GN-37	304	315	P2		k	prop	4			1	17	1	1	1	1			1
DDH-GN-37	315	325	? P1	Flt	k	prop	4			2	17	1	1	1				1
DDH-GN-37	325	328	P2		k	phyl		1			20	1	1	1				1
DDH-GN-37	328	348	P2		k	phyl	3	1			10	1	1	1				1
DDH-GN-37	348	358	P2		k	phyl	2	1			7	1	1	1				1
DDH-GN-37	358	360	P3		k	phyl	2	1			7	1	1	1				1
DDH-GN-37	360	373	P2		k	phyl	3	1			16	1	1	1				1
DDH-GN-37	373	373	P2		k	phyl	2	1			7	1	1	1				1
DDH-GN-37	373	391	P2		k	phyl	3	1			16	1	1	1				1

Hole_Id	From	To	Rock	Bx	Altn	Altn 2	K	Phyl	Silc	Prop	qz_a/b_%	Pyr	Mag	Ccp	Cc	Cv	Bn	Mo
DDH-GN-39	0	5	grv															
DDH-GN-39	5	6	grv															
DDH-GN-39	6	14	qz		k	phyl	1	1			12	2			1	2		1
DDH-GN-39	14	20	qz		k	phyl	1	1			12	2			2	1		1
DDH-GN-39	20	28	P1		k		4	1			16	2			2	2		1
DDH-GN-39	28	54	P1		k		4	1			16	2			2	2		1
DDH-GN-39	54	69	P1		k		4	1			18	2			2	2		1
DDH-GN-39	69	71	qz		k	phyl	1	1			17	2			2			
DDH-GN-39	71	91	qz		k	phyl	1	1			17	2			2	1		1
DDH-GN-39	91	99	qz		k	phyl	1	1		2	18	2			2	1		1
DDH-GN-39	99	100	qz		k	phyl	1	4			16	2			2	1		1
DDH-GN-39	100	104	qz		k	phyl	1	1			15	2			2	1		1
DDH-GN-39	104	108	qz		k	phyl	1	1	4		15	2			2	1		1
DDH-GN-39	108	113	qz		k	phyl	1	1			15	2			2	1		1
DDH-GN-39	113	124	qz		k	phyl	1	1			13	2			2	1		1
DDH-GN-39	124	139	P1		k		4	1			21	2		1	2	1		1
DDH-GN-39	139	157	P2		k		4	1			16	2		1	2	1		1
DDH-GN-39	157	160	P2		k		4	1			14	2		1	2	1		1
DDH-GN-39	160	169	P2		k		4	1			14	2		1				1
DDH-GN-39	169	189	P2		k		4	1		2	14	2		1				1
DDH-GN-39	189	193	P1		k		4	1			16	2		1				1
DDH-GN-39	193	201	P2		k		4	1			15	2		1				1
DDH-GN-39	201	210	P1		k		3	1			11	2		1				1
DDH-GN-39	210	222	P1		k		3	1			10	2		1				1
DDH-GN-39	222	235	P1		k		3	1			13	2		1				1
DDH-GN-39	235	237	P3 Dyke		k		4	1			10	2		1				1
DDH-GN-39	237	253	P1		k		3	1			13	2		1				1
DDH-GN-39	253	257	P3 Dyke		k		4	1			10	2		1				1
DDH-GN-39	257	271	P1		k		3	1			13	2		1				1
DDH-GN-39	271	290	P1		k		3	1			18	2		1				1
DDH-GN-39	290	311	P1		k		3	1			16	2		1				1
DDH-GN-39	311	317	P3		k		3	1			13	2		1				1
DDH-GN-39	317	322	P1		k		3	1			16	1						1
DDH-GN-39	322	333	P1		k		3	1			20	2		1				1
DDH-GN-39	333	348	P1		k		3	1		1	20	2	1	1				1
DDH-GN-39	348	359	P1		k		3	1			14	2	2	1				
DDH-GN-39	359	367	MBx	Mag	k	phyl	4	1			4	2	2	1				1
DDH-GN-39	367	374	MBx	Mag	k	phyl	2	1			4	2	2	1				1
DDH-GN-39	374	375	MBx	Mag	k	phyl	4	1			4	2	2	1				1
DDH-GN-39	375	389	MBx	Mag	k	phyl	2	1			5	2	1	1				1
DDH-GN-39	389	399	MBx	Mag	k	phyl	2	2		1	5	2	1	1				1
DDH-GN-39	399	407	MBx	Mag	k	phyl	2	2		1	4	2	1	1				1
DDH-GN-39	407	408	MBx	Mag	k		4				4	2	1	1				1
DDH-GN-39	408	410	MBx	Mag	k	phyl	2	1			4	2	1	1				
DDH-GN-39	410	422	MBx	Mag	k		4				4	2	1	1				1
DDH-GN-39	422	425	MBx	Mag	k	phyl	2	1			4	2	1	1				1
DDH-GN-39	425	428	MBx	Mag	k		4				4	2	1					1
DDH-GN-39	428	431	MBx	Mag	k		2	1			4	2	1					1
DDH-GN-39	431	433	MBx	Mag	k		4				4	2		1				
DDH-GN-39	433	456	MBx	Mag	k		2	1			6	2	1					
DDH-GN-39	456	465	MBx	Mag	k		2				7	2	1					
DDH-GN-39	465	475	P3		k		2				7	2	1	1				

Hole_Id	From	To	Rock	Bx	Altn	Altn 2	K	Phyl	Silc	Prop	qz_a/b_%	Pyr	Mag	Ccp	Cc	Cv	Bn	Mo

Hole_Id	From	To	Rock	Bx	Altn	Altn 2	K	Phyl	Silc	Prop	qz_a/b_%	Pyr	Mag	Ccp	Cc	Cv	Bn	Mo
DDH-GN-41	0	1	grv															
DDH-GN-41	1	12	P2		k		4	1			20	1			1			
DDH-GN-41	12	16	P2		k		4	1			20	2	1		2	2		
DDH-GN-41	16	25	P2		k		4	1			20	2	1		2	2		
DDH-GN-41	25	28	P2		k		4	1		1	20	2	1		2	2		1
DDH-GN-41	28	33	P2		k		4	1			20	2	1		2	2		
DDH-GN-41	33	40	P2		k		4	1			20	2	1		2	2		
DDH-GN-41	40	46	P2		k		4	1			20	2	1		2	2		
DDH-GN-41	46	48	P2		k		4	1			5	2	1		3	2		
DDH-GN-41	48	56	P2		k	phyl	4	3			21	2	1		1	2		
DDH-GN-41	56	59	P2		k	phyl	4	3			15	2	1		2	1		
DDH-GN-41	59	65	P2		k	phyl	4	3			15	2			2	1		
DDH-GN-41	65	67	P2		k	phyl	4	3		1	15	1			1	1		
DDH-GN-41	67	69	P2		k	phyl	4	3			14	1			2	1		
DDH-GN-41	69	75	P2		k		3	2			16	1			2	1		
DDH-GN-41	75	83	P2		k		4	1			16	1			2			
DDH-GN-41	83	92	P2		k		3	1			16	1		1	1	1		
DDH-GN-41	92	102	P1		k		3	1			19	1	2		1			
DDH-GN-41	102	120	P3		k		2	1			6	2	1	1	1			1
DDH-GN-41	120	124	P3		k		2	1			6	2	1		1			
DDH-GN-41	124	128	P3		k		3	2			6	2	1					
DDH-GN-41	128	132	P3		k		2	1			6	2	2		1			
DDH-GN-41	132	137	P1		k		3	1			16	2	2		1			
DDH-GN-41	137	146	P1		k		3	1			16	2	1		1			1
DDH-GN-41	146	153	P1		k		3	1			16	2	1	1	1			
DDH-GN-41	153	160	P3		k		2	1			6	2	2	1				1
DDH-GN-41	160	166	P3		k		2	1			6	2	2					
DDH-GN-41	166	169	P3		k		2	1			6	2	2					2
DDH-GN-41	169	172	P3		k		2	1			6	2	2	1	1			1
DDH-GN-41	172	176	P3		k		2				6	2	2	1	1			1
DDH-GN-41	176	188	P3		k		2				6	2	1					
DDH-GN-41	188	199	P3		k		2				6	2	2					
DDH-GN-41	199	200	P3		phyl		2	3			5	2	2					
DDH-GN-41	200	208	P3		k		2	3			5	2	1					
DDH-GN-41	208	220	P3		k		2				5	2	1					
DDH-GN-41	220	240	P3		k		2				6	2	1					
DDH-GN-41	240	260	P3		k		2				5	2	1	1				
DDH-GN-41	260	263	P3		k		2				6	2	2					
DDH-GN-41	263	269	P3		k		2				15	2	2					
DDH-GN-41	269	280	P3		k		2				6	2	2					
DDH-GN-41	280	296	P3		k		2				6	2	2					1
DDH-GN-41	296	307	P1		k		3				11	2	3					
DDH-GN-41	307	320	P1		k		3				11	2	3					

Hole_Id	From	To	Rock	Bx	Altn	Altn 2	K	Phyl	Silc	Prop	qz_a/b_%	Pyr	Mag	Ccp	Cc	Cv	Bn	Mo
DDH-GN-42	0	3	grv															
DDH-GN-42	3	14	P2		phyl	k	3	4			9	1	1					
DDH-GN-42	14	29	P2		k		3	2			10	1	1					
DDH-GN-42	29	63	P2		k		3	2			10	2	2	1	2			
DDH-GN-42	63	66	P2		silf	k	3	1	4		10	2	1	1	1			
DDH-GN-42	66	68	P2		silf				4		10	2	1	1	1			
DDH-GN-42	68	97	P2		k		3	2			9	2	1					1
DDH-GN-42	97	98	P2		k		3	2			9	2	1					1
DDH-GN-42	98	103	P2		k		3	2			9	2	1					1
DDH-GN-42	103	104	P2		k		3	2			9	2	1					1
DDH-GN-42	104	117	P2		k		3	2			12	2	1					1
DDH-GN-42	117	128	P2		k		3	2			12	2	1					1
DDH-GN-42	128	142	P2		k		3	2			12	2	1					1
DDH-GN-42	142	148	P2		phyl	silf		4	3		12	2	1					1
DDH-GN-42	148	158	P2		k		3	2	2		12	2	1					1
DDH-GN-42	158	172	P3		k		2			1	4	2	2					1
DDH-GN-42	172	180	P1		k		4			1	10	2	1					1
DDH-GN-42	180	184	P1		silf				4		10	2	1					1
DDH-GN-42	184	195	P1		k		2			1	10	2	1					1
DDH-GN-42	195	206	P1		k		2	1	2	2	12	2	1					1
DDH-GN-42	206	208	P1		k		2	1			12	2	2	1		1		1
DDH-GN-42	208	210	P1		phyl			1			12	2	2	1		1		1
DDH-GN-42	210	220	P1		k		2	1			12	2	2	1		1		1
DDH-GN-42	220	234	P1		k		2			2	12	2	2	1		1		1
DDH-GN-42	234	257	P3		k		2				5	2	2	2				1
DDH-GN-42	257	261	P3		k		2				5	2	2	2				1
DDH-GN-42	261	284	P1		silf	k	3		4	2	8	2	2	1	1	1		1
DDH-GN-42	284	306	P1		k		3	1		2	8	2	2	1		1		1
DDH-GN-42	306	315	P3		k		2				5	2	2	2				1
DDH-GN-42	315	317	P1		phyl		2	3			8	2	2	1		1		1
DDH-GN-42	317	320	P3		silf	k	3	1	4	2	5	2	2	1		1		1
DDH-GN-42	320	341	P1		k		3	1		2	8	2	2	1		1		1
DDH-GN-42	341	344	P3		k		2				5	2	2	1				1
DDH-GN-42	344	356	P1		mt	phyl	2	3	4		8	2	3	1				1
DDH-GN-42	356	360	P3		phyl		2	3		2	5	2	2	1				1

Hole_Id	From	To	Rock	Bx	Altn	Altn 2	K	Phyl	Silc	Prop	qz_a/b_%	Pyr	Mag	Ccp	Cc	Cv	Bn	Mo
DDH-GN-42	360	369	P1		mt		2		4	2	9	2	4	1				
DDH-GN-42	369	370	P3		silf		2		4	2	5	2	2	1				
DDH-GN-42	370	378	P1		mt		2		4	2	10	2	4	1				
DDH-GN-42	378	382	P3		k		2			2	5	1	2					1
DDH-GN-42	382	387	P1		mt		2		4	2	7	2	4	1				1
DDH-GN-42	387	394	P3		k		2			2	5	2	2	1				1
DDH-GN-42	394	401	P1		mt		2		4	2	8	2	4					1
DDH-GN-42	401	422	P1		mt		2		4	2	9	2	4	1				1
DDH-GN-42	422	474	P1		mt		2		4	2	9	2	4					
DDH-GN-42	474	476	P1		mt		2			2	9	2	4					
DDH-GN-42	476	480	P3		k		2			2	5	2	2					
DDH-GN-42	480	481	P3		k		2				5	2	2					1
DDH-GN-42	481	485	P3		k		2			2	5	2	2					1
DDH-GN-42	485	488	P1		mt		2			2	5	2	3	1				
DDH-GN-42	488	499	P1		mt		2		4	2	5	2	3	1				

Hole_Id	From	To	Rock	Bx	Altn	Altn 2	K	Phyl	Silc	Prop	qz_a/b_%	Pyr	Mag	Ccp	Cc	Cv	Bn	Mo
DDH-GN-45	0	4	grv															
DDH-GN-45	4	8	P1		k	phyl	4	3			5	1						
DDH-GN-45	8	14	P1		k	phyl	4	3			5	1			1	1		1
DDH-GN-45	14	20	P1		k		4	2			18	2			2	1		1
DDH-GN-45	20	27	P1		k		4	2			18	2			2	1		1
DDH-GN-45	27	31	P1		k		4	2			18	2			2	1		2
DDH-GN-45	31	40	P1		k		4	2			18	2			2	1		1
DDH-GN-45	40	42	P1		k		4	2			18	1		1	1	1		2
DDH-GN-45	42	54	P1		k		4	2			18	1		1	1	1		2
DDH-GN-45	54	57	qz		k		1					1		1	1	1		1
DDH-GN-45	57	60	qz		k		1				7	1	2	1	2	1		1
DDH-GN-45	60	64	qz		k		1				12	2		1	1	1		1
DDH-GN-45	64	69	qz		k		1					2		1	1	1		1
DDH-GN-45	69	79	qz		k		1					2		1	1	1		1
DDH-GN-45	79	80	qz		k		1					2		1	1	1		1
DDH-GN-45	80	85	qz		k		1					2		1	2	1		1
DDH-GN-45	85	86	qz		k		1					2		2	2	1		1
DDH-GN-45	86	88	P1		k		4			1	5	3		2	2	1		1
DDH-GN-45	88	92	qz		k		1					1		1	2	1		1
DDH-GN-45	92	95	P1		k		4			1		2		1	2	1		1
DDH-GN-45	95	100	qz		k		1				12	2		1	1	1		1
DDH-GN-45	100	102	qz		k		1				12	1		1	1			1
DDH-GN-45	102	102	qz		k		1				12	2		1	2			2
DDH-GN-45	102	110	qz		k		1				12	1		1	1			2
DDH-GN-45	110	114	qz		k		1				12	1		1	1			2
DDH-GN-45	114	116	qz		k		1				12	1		1	1			1
DDH-GN-45	116	117	qz		k		1				12	1		1	1			1
DDH-GN-45	117	121	qz		k		1				12	2		2	2			1
DDH-GN-45	121	122	qz		k		1				12	2		2	2			1
DDH-GN-45	122	124	qz		k		1				12	2		2	2			1
DDH-GN-45	124	126	qz		k		1				12	2		2	2			1
DDH-GN-45	126	134	qz		k		1				12	2		2	1			1
DDH-GN-45	134	137	P1		k		4	2			22	1		1	1			1
DDH-GN-45	137	138	qz		k		1	1			22	1		1	1			1
DDH-GN-45	138	147	P1		k		4	2			22	1		1	1			1
DDH-GN-45	147	152	qz		k		1				13	2		1	1			
DDH-GN-45	152	155	P1		k		4				9	2	1	1				
DDH-GN-45	155	158	P1		k		4	1			17	2		1				1
DDH-GN-45	158	161	qz		k		1	1			17	2		1	1			2
DDH-GN-45	161	162	P1		k		4	1			17	1	1	1	1			1
DDH-GN-45	162	167	qz		k		1				7	2		1	1			1
DDH-GN-45	167	177	qz		k		1		4		7	2		1	1			1
DDH-GN-45	177	179	qz		k		1				10	2		2	1	1		1
DDH-GN-45	179	182	qz		k		1				10	2		2	1			1
DDH-GN-45	182	187	qz		k		1				10	2		2				
DDH-GN-45	187	192	qz		k		1				10	2		2	1			

Hole_Id	From	To	Rock	Bx	Altn	Altn 2	K	Phyl	Silc	Prop	qz_a/b_%	Pyr	Mag	Ccp	Cc	Cv	Bn	Mo
DDH-GN-46	0	12	P1		k		3	2		2			1					
DDH-GN-46	12	17	P1		k		3	1		2	9	1	2		1			
DDH-GN-46	17	22	P1		k		3	1		2	9	2	2		1	1		1
DDH-GN-46	22	22	P1		k		3	1		2	9	2						
DDH-GN-46	22	24	P1		k		3	1		2	9	2	1					
DDH-GN-46	24	26	P1		k		3	1		2	9	2						
DDH-GN-46	26	28	P1		k		4	1		2	9	2						
DDH-GN-46	28	30	P1		k		4	1		2	17	1	1		1			
DDH-GN-46	30	55	P1		k		4	1		2	17	2	1		1	1		
DDH-GN-46	55	57	P1		k		4	1		2	17	2	1					
DDH-GN-46	57	61	P1		k		4	1		2	17	2	2		1			1
DDH-GN-46	61	69	qz-sltst		k		1				26	2			2	1		
DDH-GN-46	69	70	qz-sltst		k		1				26	2			1	1		
DDH-GN-46	70	78	qz-sltst		k		1				26	2			2			
DDH-GN-46	78	79	qz-sltst		k		1				26	2			1			
DDH-GN-46	79	84	qz-sltst		k		1				26	2			2			
DDH-GN-46	84	86	qz-sltst		k		1				17	2			1	1		

Hole_Id	From	To	Rock	Bx	Altn	Altn 2	K	Phyl	Silc	Prop	qz_a/b_%	Pyr	Mag	Ccp	Cc	Cv	Bn	Mo
DDH-GN-46	86	93	qz-sltst		k		1				17	2			2	1		
DDH-GN-46	93	94	qz-sltst		k		1				10	1						
DDH-GN-46	94	98	qz-sltst		k		1				17	2			1			
DDH-GN-46	98	101	qz-sltst		k		1				17	2			1	1		
DDH-GN-46	101	120	qz-sltst		k		1				17	2						1
DDH-GN-46	120	123	qz-sltst		k		1				17	2		1	1			
DDH-GN-46	123	139	qz-sltst		k		1				20	2	1		1			1
DDH-GN-46	139	141	qz-sltst		k		1				20	2						
DDH-GN-46	141	141	qz-sltst		k		1				20	2		1	1			
DDH-GN-46	141	143	qz-sltst		k		1				20	2						2
DDH-GN-46	143	146	qz-sltst		k		1				20	2			1			
DDH-GN-46	146	147	qz-sltst		k		1				10	1			1			
DDH-GN-46	147	152	qz-sltst		k		1				14	2	1	1	2			
DDH-GN-46	152	154	qz-sltst		k		1				14	2		1				1
DDH-GN-46	154	165	P1		k		4				5	2		1	1			1
DDH-GN-46	165	172	P1		k		4				5	2		2	1			
DDH-GN-46	172	173	P1		k		4				5	2		2	2			1
DDH-GN-46	173	179	P1		k		4				5	2		2	1			
DDH-GN-46	179	181	P1		k		4				5	2		2	1			
DDH-GN-46	181	182	P1		k		4				5	2		2	2			1
DDH-GN-46	182	183	P1		k		4				5	2		2	1			1
DDH-GN-46	183	191	P1		k		4				5	2		2	1			
DDH-GN-46	191	194	qz-sltst		k		1				20	2		2	1			2
DDH-GN-46	194	195	qz-sltst		k		1				20	2		2	1			
DDH-GN-46	195	196	qz-sltst		k		1				18	2	1					
DDH-GN-46	196	198	qz-sltst		k		1				13	2		1				1
DDH-GN-46	198	204	qz-sltst		k		1				13	2		1	2			1
DDH-GN-46	204	207	qz-sltst		k		1				13	2						
DDH-GN-46	207	216	qz-sltst		k		1				13	2		1	1			
DDH-GN-46	216	225	qz-sltst		k		1				13	2		2	1			
DDH-GN-46	225	238	qz-sltst		k		1				21	2		2				
DDH-GN-46	238	243	qz-sltst		k		1				13	2		2				
DDH-GN-46	243	247	P1		k		4				14	2	2	1				1
DDH-GN-46	247	250	qz-sltst		k		1				15	2	1	2	1			1

APPENDIX D2

El Galeno drill core assay data

Hole_Id	From	To	Rock	Au_g/t	Cu_%	Mo_ppm	Ag_ppm	As_ppm	Bi_ppm	Pb_ppm	Sb_ppm	Zn_ppm
DDH-GH-04	0	2	P1	0.17	0.03							
DDH-GH-04	2	4	P1	0.25	0.19							
DDH-GH-04	4	6	P1	0.30	0.30							
DDH-GH-04	6	8	P1	0.45	0.16							
DDH-GH-04	8	10	P1	0.36	0.05							
DDH-GH-04	10	12	P1	0.37	0.28							
DDH-GH-04	12	14	P1	0.33	0.11							
DDH-GH-04	14	16	P1	0.42	0.19							
DDH-GH-04	16	18	P1	0.24	0.12							
DDH-GH-04	18	20	P1	0.31	0.19							
DDH-GH-04	20	22	P1	0.29	0.45							
DDH-GH-04	22	24	P1	0.22	0.27							
DDH-GH-04	24	26	qz	0.16	0.36							
DDH-GH-04	26	28	qz	0.12	0.35							
DDH-GH-04	28	30	qz	0.12	0.62							
DDH-GH-04	30	32	qz	0.20	0.70							
DDH-GH-04	32	34	qz	0.22	0.62							
DDH-GH-04	34	36	qz	0.22	0.71							
DDH-GH-04	36	38	qz	0.32	0.57							
DDH-GH-04	38	40	qz	0.21	0.70							
DDH-GH-04	40	42	qz	0.13	0.50							
DDH-GH-04	42	44	qz	0.13	0.37							
DDH-GH-04	44	46	qz	0.14	0.33							
DDH-GH-04	46	48	qz	0.14	0.38							
DDH-GH-04	48	50	qz	0.10	0.35							
DDH-GH-04	50	52	qz	0.12	0.36							
DDH-GH-04	52	54	qz	0.11	0.26							
DDH-GH-04	54	56	qz	0.09	0.38							
DDH-GH-04	56	58	qz	0.11	0.26							
DDH-GH-04	58	60	qz	0.14	0.24							
DDH-GH-04	60	62	qz	0.15	0.35							
DDH-GH-04	62	64	P1	0.15	0.20							
DDH-GH-04	64	66	P1	0.17	0.16							
DDH-GH-04	66	68	qz	0.09	0.21							
DDH-GH-04	68	70	qz	0.11	0.21							
DDH-GH-04	70	72	qz	0.11	0.19							
DDH-GH-04	72	74	qz	0.08	0.24							
DDH-GH-04	74	76	P1	0.10	0.16							
DDH-GH-04	76	78	P1	0.13	0.12							
DDH-GH-04	78	80	P1	0.14	0.16							
DDH-GH-04	80	82	P1	0.15	0.13							
DDH-GH-04	82	84	P1	0.11	0.12							
DDH-GH-04	84	86	P1	0.08	0.10							
DDH-GH-04	86	88	qz	0.10	0.20							
DDH-GH-04	88	90	qz	0.07	0.21							
DDH-GH-04	90	92	qz	0.10	0.26							
DDH-GH-04	92	94	P1	1.28	0.12							
DDH-GH-04	94	96	qz	0.11	0.14							
DDH-GH-04	96	98	qz	0.13	0.20							
DDH-GH-04	98	100	qz	0.09	0.21							
DDH-GH-04	100	102	qz	0.13	0.30							
DDH-GH-04	102	104	qz	0.11	0.22							
DDH-GH-04	104	106	P1	0.09	0.12							
DDH-GH-04	106	108	P1	0.11	0.06							
DDH-GH-04	108	110	P1	0.14	0.13							
DDH-GH-04	110	112	P1	0.10	0.08							
DDH-GH-04	112	114	P1	0.10	0.12							
DDH-GH-04	114	116	P1	0.09	0.15							
DDH-GH-04	116	118	P1	0.08	0.06							
DDH-GH-04	118	120	P1	0.11	0.15							
DDH-GH-04	120	122	P1	0.20	0.20							
DDH-GH-04	122	124	P1	0.10	0.14							
DDH-GH-04	124	126	P3	0.02	0.03							
DDH-GH-04	126	128	P3	0.03	0.03							
DDH-GH-04	128	130	P1	0.05	0.06							
DDH-GH-04	130	132	P1	0.06	0.08							
DDH-GH-04	132	134	P1	0.11	0.12							
DDH-GH-04	134	136	P1	0.10	0.12							
DDH-GH-04	136	138	P1	0.14	0.13							
DDH-GH-04	138	140	P1	0.09	0.09							
DDH-GH-04	140	142	P1	0.06	0.07							
DDH-GH-04	142	144	P1	0.07	0.11							
DDH-GH-04	144	146	P1	0.07	0.12							
DDH-GH-04	146	148	P1	0.13	0.10							
DDH-GH-04	148	150	P3	0.05	0.02							
DDH-GH-04	150	152	P1	0.06	0.07							
DDH-GH-04	152	154	P1	0.06	0.07							
DDH-GH-04	154	156	P1	0.04	0.05							
DDH-GH-04	156	158	P1	0.07	0.08							
DDH-GH-04	158	160	P3 Bx	0.11	0.11							
DDH-GH-04	160	162	P3 Bx	0.17	0.22							
DDH-GH-04	162	164	P1	0.15	0.26							
DDH-GH-04	164	166	P1	0.11	0.14							
DDH-GH-04	166	168	P3 Bx	0.13	0.19							
DDH-GH-04	168	170	P1	0.11	0.05							
DDH-GH-04	170	172	P1	0.16	0.07							
DDH-GH-04	172	174	P3	0.10	0.13							
DDH-GH-04	174	176	P1	0.07	0.07							
DDH-GH-04	176	178	P1	0.04	0.09							
DDH-GH-04	178	180	P1	0.04	0.07							
DDH-GH-04	180	182	P1	0.06	0.09							
DDH-GH-04	182	184	P1	0.09	0.12							
DDH-GH-04	184	186	P1	0.08	0.14							
DDH-GH-04	186	188	P3	0.06	0.08							
DDH-GH-04	188	190	P3	0.04	0.09							
DDH-GH-04	190	192	P3	0.04	0.05							
DDH-GH-04	192	194	P3	0.07	0.05							
DDH-GH-04	194	196	P1	0.06	0.06							
DDH-GH-04	196	198	P1	0.04	0.05							
DDH-GH-04	198	200	P1	0.04	0.05							
DDH-GH-04	200	201	P1	0.05	0.03							

Hole_Id	From	To	Rock	Au_g/t	Cu_%	Mo_ppm	Ag_ppm	As_ppm	Bi_ppm	Pb_ppm	Sb_ppm	Zn_ppm
DDH-GN-36	0	2	P1	0.06	0.46	87	2	1640	3	28	37	203
DDH-GN-36	2	4	P1	0.06	0.59	187	7	2200	3	42	53	378
DDH-GN-36	4	6	P1	0.05	0.39	211	4	1370	3	59	29	358
DDH-GN-36	6	8	P1	0.06	0.57	501	1	776	3	84	3	60
DDH-GN-36	8	10	P1	0.06	0.56	318	3	1260	3	30	3	156
DDH-GN-36	10	12	P1	0.05	0.26	114	3	870	3	36	9	213

Hole_Id	From	To	Rock	Au_g/t	Cu_%	Mo_ppm	Ag_ppm	As_ppm	Bi_ppm	Pb_ppm	Sb_ppm	Zn_ppm
DDH-GN-36	12	14	P1	0.05	0.43	340	4	1570	3	35	9	300
DDH-GN-36	14	16	P1	0.04	0.31	370	1	688	3	51	3	98
DDH-GN-36	16	18	P1	0.04	0.58	314	1	790	3	36	3	88
DDH-GN-36	18	20	P1	0.04	0.42	144	1	788	3	48	3	47
DDH-GN-36	20	22	qz	0.07	0.43	125	1	441	3	77	3	156
DDH-GN-36	22	24	qz	0.03	0.44	158	1	638	3	59	3	86
DDH-GN-36	24	26	qz	0.02	0.28	110	1	534	3	54	3	80
DDH-GN-36	26	28	qz	0.02	0.30	113	1	337	3	36	3	58
DDH-GN-36	28	30	qz	0.02	0.30	461	1	327	3	49	3	60
DDH-GN-36	30	32	qz	0.02	0.31	489	1	408	3	48	3	73
DDH-GN-36	32	34	qz	0.02	0.30	197	1	282	3	22	3	45
DDH-GN-36	34	36	qz	0.02	0.51	181	2	560	3	43	3	108
DDH-GN-36	36	38	qz	0.02	0.31	388	1	840	3	24	3	29
DDH-GN-36	38	40	P1	0.08	0.44	434	1	688	3	42	3	196
DDH-GN-36	40	42	P1	0.03	0.29	215	1	664	3	20	3	142
DDH-GN-36	42	44	P1	0.03	0.28	207	1	653	3	21	3	179
DDH-GN-36	44	46	P1	0.03	0.33	192	1	782	3	22	3	180
DDH-GN-36	46	48	P1	0.06	0.30	161	1	428	3	25	3	109
DDH-GN-36	48	50	P1	0.04	0.26	223	1	255	3	42	3	71
DDH-GN-36	50	52	P1	0.03	0.31	554	1	970	3	29	3	250
DDH-GN-36	52	54	P1	0.04	0.40	575	1	1040	3	59	3	323
DDH-GN-36	54	56	P1	0.04	0.26	268	1	801	3	136	3	211
DDH-GN-36	56	58	P1	0.04	0.32	408	1	860	3	42	3	175
DDH-GN-36	58	60	P1	0.03	0.33	196	1	910	3	26	3	180
DDH-GN-36	60	62	Flt w/ P1	0.04	0.29	347	1	801	3	45	3	247
DDH-GN-36	62	64	Flt w/ P1	0.08	0.34	358	1	216	3	26	3	68
DDH-GN-36	64	66	Flt w/ P1	0.08	0.28	239	1	111	3	28	3	52
DDH-GN-36	66	68	Flt w/ P1	0.10	0.43	334	1	163	3	44	3	96
DDH-GN-36	68	70	Flt w/ P1	0.09	0.38	171	1	366	3	31	3	137
DDH-GN-36	70	72	Flt w/ P1	0.17	0.30	157	1	567	3	95	5	278
DDH-GN-36	72	74	P1	0.04	0.31	208	5	1070	3	225	32	517
DDH-GN-36	74	76	qz	0.02	0.38	135	1	202	3	103	3	99
DDH-GN-36	76	78	qz	0.01	0.33	288	1	189	3	50	3	108
DDH-GN-36	78	80	qz	0.02	0.34	251	1	765	3	72	3	188
DDH-GN-36	80	82	qz	0.03	0.38	302	1	339	3	38	3	101
DDH-GN-36	82	84	qz	0.04	0.55	195	1	209	3	28	3	45
DDH-GN-36	84	86	qz	0.06	1.06	130	5	810	9	36	3	137
DDH-GN-36	86	88	qz	0.06	0.83	80	4	632	3	30	3	90
DDH-GN-36	88	90	qz	0.02	0.41	90	3	641	3	16	3	99
DDH-GN-36	90	92	qz	0.03	0.47	99	3	1360	3	22	25	175
DDH-GN-36	92	94	qz	0.04	0.58	205	1	569	3	21	3	86
DDH-GN-36	94	96	qz	0.01	0.29	92	1	402	3	35	3	59
DDH-GN-36	96	98	qz	0.01	0.19	56	1	442	3	19	3	88
DDH-GN-36	98	100	qz	0.01	0.19	71	1	391	3	22	3	70
DDH-GN-36	100	102	qz	0.01	0.22	43	1	467	3	25	3	86
DDH-GN-36	102	104	qz	0.01	0.18	106	1	330	3	20	3	58
DDH-GN-36	104	106	qz	0.01	0.14	46	1	399	3	24	3	89
DDH-GN-36	106	108	qz	0.03	0.51	141	3	731	3	42	3	213
DDH-GN-36	108	110	qz	0.08	0.44	228	1	99	3	29	3	51
DDH-GN-36	110	112	qz	0.04	0.31	351	1	59	3	23	3	40
DDH-GN-36	112	114	qz	0.03	0.30	258	1	137	3	83	3	140
DDH-GN-36	114	116	qz	0.04	0.29	118	1	26	3	20	3	28
DDH-GN-36	116	118	qz	0.02	0.37	161	1	57	3	82	3	79
DDH-GN-36	118	120	qz	0.04	0.44	176	2	277	3	44	3	68
DDH-GN-36	120	122	qz	0.03	0.42	164	1	224	3	26	3	56
DDH-GN-36	122	124	P1	0.05	0.41	196	1	575	3	34	3	157
DDH-GN-36	124	126	P1	0.03	0.43	126	1	62	3	41	3	44
DDH-GN-36	126	128	qz	0.05	0.41	96	1	64	3	22	3	50
DDH-GN-36	128	130	qz	0.06	0.54	148	2	31	3	37	3	91
DDH-GN-36	130	132	qz	0.06	0.46	94	1	120	3	48	3	65
DDH-GN-36	132	134	qz	0.03	0.41	106	1	285	3	28	3	90
DDH-GN-36	134	136	qz	0.08	0.48	198	2	89	3	15	3	30
DDH-GN-36	136	138	qz	0.03	0.45	145	1	102	3	32	3	33
DDH-GN-36	138	140	qz	0.03	0.33	145	1	65	3	31	3	27
DDH-GN-36	140	142	qz	0.08	0.53	186	9	1120	3	102	162	401
DDH-GN-36	142	144	qz	0.02	0.38	116	2	610	3	41	3	114
DDH-GN-36	144	146	Flt Zone	0.08	0.50	206	8	2030	6	159	62	706
DDH-GN-36	146	148	qz	0.04	0.21	144	3	840	6	97	7	251
DDH-GN-36	148	150	qz	0.03	0.22	110	2	794	3	60	5	258
DDH-GN-36	150	152	qz	0.02	0.38	136	2	980	3	58	3	22
DDH-GN-36	152	154	qz	0.03	0.37	198	2	1130	3	18	3	263
DDH-GN-36	154	156	qz	0.03	0.37	130	2	970	3	27	3	207
DDH-GN-36	156	158	qz	0.01	0.36	216	1	58	3	25	3	40
DDH-GN-36	158	160	qz	0.03	0.45	274	2	280	3	38	3	81
DDH-GN-36	160	162	P1	0.06	0.46	139	1	51	3	14	3	19
DDH-GN-36	162	164	qz	0.04	0.34	58	1	744	3	17	3	86
DDH-GN-36	164	166	qz	0.03	0.32	121	2	752	5	55	5	127
DDH-GN-36	166	168	qz	0.03	0.25	75	2	781	3	42	8	164
DDH-GN-36	168	170	qz	0.02	0.27	116	2	459	3	100	3	204
DDH-GN-36	170	172	qz	0.04	0.44	106	1	380	3	23	3	109
DDH-GN-36	172	174	qz	0.04	0.32	98	1	61	3	19	3	41
DDH-GN-36	174	176	qz	0.07	0.42	80	2	75	3	25	3	34
DDH-GN-36	176	178	qz	0.07	0.51	115	1	96	3	22	3	35
DDH-GN-36	178	180	qz	0.05	0.41	47	3	589	3	41	3	148
DDH-GN-36	180	182	qz	0.08	0.36	55	5	1070	3	197	55	277
DDH-GN-36	182	184	qz	0.07	0.32	43	5	1060	3	149	74	261
DDH-GN-36	184	186	qz	0.03	0.23	82	3	679	3	60	27	186
DDH-GN-36	186	188	qz	0.05	0.31	98	6	990	3	74	78	260
DDH-GN-36	188	190	qz	0.03	0.32	87	5	970	3	52	66	231
DDH-GN-36	190	192	qz	0.03	0.27	61	6	950	3	97	100	260
DDH-GN-36	192	194	qz	0.02	0.25	54	4	880	3	49	54	190
DDH-GN-36	194	196	P1	0.06	0.36	165	14	1420	9	80	290	541
DDH-GN-36	196	198	P1	0.06	0.30	86	12	1110	8	140	285	476
DDH-GN-36	198	200	qz	0.02	0.28	55	4	1000	3	61	67	241
DDH-GN-36	200	202	qz	0.04	0.31	72	9	1050	6	61	198	302
DDH-GN-36	202	204	qz	0.02	0.35	65	3	1010	3	19	42	206
DDH-GN-36	204	206	qz	0.05	0.38	69	2	930	3	69	12	250
DDH-GN-36	206	208	qz	0.03	0.33	53	2	700	3	18	9	124
DDH-GN-36	208	210	qz	0.04	0.36	220	2	793	3	59	8	123
DDH-GN-36	210	212	P1	0.06	0.23	108	4	798	3	193	74	309
DDH-GN-36	212	214	P1	0.06	0.25	82	6	810	3	659	89	1180
DDH-GN-36	214	216	qz	0.05	0.34	79	9	1060	5	98	172	388
DDH-GN-36	216	218	qz	0.04	0.41	44	18	1420	11	106	375	478
DDH-GN-36	218	220	qz	0.03	0.22	30	4	781	3	53	43	206
DDH-GN-36	220	222	Flt Zone	0.07	0.56	55	10	1500	3	140	101	574
DDH-GN-36	222	224	qz	0.06	0.44	64	5	860	3	84	151	342
DDH-GN-36	224	226	qz	0.05	0.44	105	5	680	3	60	94	184
DDH-GN-36	226	228	qz	0.02	0.19	52	4	493	13	57	76	171
DDH-GN-36	228	230	Flt Zone	0.03	0.48	52	5	790	8	32	59	178
DDH-GN-36	230	232	qz	0.04	0.50	101	3	262	3	34	3	108

Hole_Id	From	To	Rock	Au_g/t	Cu_%	Mo_ppm	Ag_ppm	As_ppm	Bi_ppm	Pb_ppm	Sb_ppm	Zn_ppm
DDH-GN-36	232	234	qz	0.04	0.44	206	4	271	3	61	3	92
DDH-GN-36	234	236	qz	0.03	0.41	144	3	113	3	26	3	43
DDH-GN-36	236	238	qz	0.05	0.61	113	27	1180	25	129	708	514
DDH-GN-36	238	240	qz	0.04	0.43	88	15	1400	12	55	394	370
DDH-GN-36	240	242	qz	0.03	0.28	41	12	910	9	185	205	500
DDH-GN-36	242	244	qz	0.03	0.34	47	12	1130	6	132	241	488
DDH-GN-36	244	246	qz	0.02	0.28	43	7	1040	3	181	195	472
DDH-GN-36	246	248	qz	0.02	0.21	43	5	756	3	159	156	424
DDH-GN-36	248	250	qz	0.02	0.20	36	5	731	3	104	67	380
DDH-GN-36	250	252	qz	0.02	0.19	35	6	684	6	50	133	218
DDH-GN-36	252	254	qz	0.02	0.26	34	7	735	5	143	75	369
DDH-GN-36	254	256	qz	0.01	0.39	72	5	798	3	237	16	452
DDH-GN-36	256	258	qz	0.02	0.35	82	3	313	3	24	3	66
DDH-GN-36	258	260	qz	0.03	0.32	71	2	96	3	40	3	65
DDH-GN-36	260	262	qz	0.01	0.30	113	2	90	3	67	3	74
DDH-GN-36	262	264	qz	0.01	0.31	80	1	46	3	13	3	38
DDH-GN-36	264	266	qz	0.02	0.37	54	3	426	3	56	3	165
DDH-GN-36	266	268	qz	0.05	0.34	92	3	261	3	40	3	120
DDH-GN-36	268	270	qz	0.01	0.36	77	3	465	3	24	3	124
DDH-GN-36	270	272	qz	0.02	0.35	132	1	32	3	11	3	23
DDH-GN-36	272	274	qz	0.03	0.35	165	1	41	3	20	3	34
DDH-GN-36	274	276	qz	0.09	0.58	66	29	1300	8	5840	284	9590
DDH-GN-36	276	278	qz	0.05	0.39	45	2	125	3	25	3	130
DDH-GN-36	278	280	qz	0.01	0.40	91	2	463	3	27	3	581
DDH-GN-36	280	282	qz	0.01	0.41	49	4	423	3	30	6	112
DDH-GN-36	282	284	Flt w/ P1	0.12	0.91	76	80	3330	15	15200	592	26500
DDH-GN-36	284	286	Flt w/ P1	0.03	0.37	52	12	1140	3	406	65	675
DDH-GN-36	286	288	qz	0.02	0.43	55	4	435	3	40	8	122
DDH-GN-36	288	290	qz	0.03	0.40	39	9	1400	3	155	61	375
DDH-GN-36	290	292	qz	0.02	0.36	72	4	689	3	91	17	156
DDH-GN-36	292	294	qz	0.02	0.40	68	5	880	3	64	71	324
DDH-GN-36	294	296	Flt Zone	0.29	0.44	75	50	1310	12	10400	1020	14500
DDH-GN-36	296	298	Flt Zone	0.22	0.73	53	59	2350	12	9330	1220	17400
DDH-GN-36	298	300	qz	0.03	0.31	36	4	605	3	129	14	264
DDH-GN-36	300	302	qz	0.04	0.36	60	2	35	3	60	3	73
DDH-GN-36	302	304	qz	0.04	0.27	66	1	31	3	15	3	59
DDH-GN-36	304	306	qz	0.03	0.32	38	2	83	3	31	3	53
DDH-GN-36	306	308	qz	0.04	0.43	92	3	60	3	34	3	42
DDH-GN-36	308	310	qz	0.05	0.59	144	6	234	3	49	3	82
DDH-GN-36	310	312	qz	0.03	0.33	52	2	87	3	25	3	33
DDH-GN-36	312	314	qz	0.04	0.35	56	2	60	3	22	3	32
DDH-GN-36	314	316	qz	0.05	0.37	56	4	206	3	44	3	89
DDH-GN-36	316	318	Flt Zone	0.04	0.32	132	6	260	3	120	28	217
DDH-GN-36	318	320	Flt Zone	0.04	0.35	71	5	523	3	118	3	262
DDH-GN-36	320	322	qz	0.02	0.34	73	5	459	3	81	6	167
DDH-GN-36	322	324	qz	0.02	0.37	44	4	404	3	71	3	122
DDH-GN-36	324	326	qz	0.01	0.20	29	3	496	3	47	14	139
DDH-GN-36	326	328	qz	0.01	0.33	56	3	778	3	88	15	209
DDH-GN-36	328	330	qz	0.03	0.37	49	3	900	3	35	77	134
DDH-GN-36	330	332	qz	0.03	0.24	52	5	734	3	135	210	337
DDH-GN-36	332	334	Flt w/ P1	0.23	0.36	33	25	570	3	2300	797	1280
DDH-GN-36	334	336	qz	0.05	0.23	51	6	400	3	230	87	387
DDH-GN-36	336	338	qz	0.02	0.18	71	8	501	3	480	147	1150
DDH-GN-36	338	340	qz	0.01	0.23	30	3	720	3	70	29	154
DDH-GN-36	340	342	qz	0.03	0.38	109	4	666	3	94	33	242
DDH-GN-36	342	344	qz	0.04	0.30	71	6	368	5	84	31	169
DDH-GN-36	344	346	qz	0.07	0.35	67	3	53	3	12	3	18
DDH-GN-36	346	348	qz	0.07	0.32	75	6	570	3	114	62	188
DDH-GN-36	348	350	qz	0.04	0.27	35	7	724	3	166	58	422
DDH-GN-36	350	352	qz	0.02	0.23	26	4	554	3	95	20	185
DDH-GN-36	352	354	Flt w/ P1	0.03	0.30	39	3	460	3	50	6	95
DDH-GN-36	354	356	Flt w/ P1	0.09	0.29	67	1	103	3	28	3	53
DDH-GN-36	356	358	qz	0.05	0.24	108	6	292	3	191	30	418
DDH-GN-36	358	360	qz	0.01	0.22	146	8	622	3	135	98	278
DDH-GN-36	360	362	qz	0.03	0.18	62	2	106	3	46	6	76
DDH-GN-36	362	364	qz	0.02	0.32	36	6	285	3	90	3	125
DDH-GN-36	364	366	qz	0.03	0.23	51	6	275	3	322	3	405
DDH-GN-36	366	368	Flt w/ P1	1.29	0.55	77	95	3000	94	11000	181	25600
DDH-GN-36	368	370	qz	0.02	0.25	39	5	351	6	81	28	130
DDH-GN-36	370	372	qz	0.07	0.28	42	6	555	5	301	9	358
DDH-GN-36	372	374	qz	0.05	0.28	95	3	75	3	22	3	27
DDH-GN-36	374	376	qz	0.03	0.30	45	3	54	3	14	3	23
DDH-GN-36	376	378	qz	0.05	0.41	49	5	230	5	46	3	80
DDH-GN-36	378	380	qz	0.02	0.35	50	5	479	3	67	12	153
DDH-GN-36	380	382	qz	0.03	0.37	60	6	820	3	56	18	163
DDH-GN-36	382	384	qz	0.01	0.34	54	6	608	3	139	9	248
DDH-GN-36	384	386	qz	0.02	0.19	31	5	567	3	148	28	287
DDH-GN-36	386	388	P1	0.03	0.13	47	3	292	5	164	3	239
DDH-GN-36	388	390	qz	0.05	0.19	40	3	225	3	111	3	148
DDH-GN-36	390	392	P3 Bx	0.06	0.26	46	10	628	3	688	101	2480
DDH-GN-36	392	394	qz	0.05	0.33	69	5	247	3	48	3	100
DDH-GN-36	394	396	qz	0.05	0.32	73	5	436	3	42	3	439
DDH-GN-36	396	398	qz	0.03	0.25	49	4	481	3	211	14	425
DDH-GN-36	398	400	qz	0.02	0.22	81	3	206	3	108	5	430
DDH-GN-36	400	402	qz	0.06	0.27	61	1	47	3	20	3	33
DDH-GN-36	402	404	qz	0.03	0.25	57	5	386	3	217	22	430
DDH-GN-36	404	406	qz	0.04	0.31	81	4	178	3	158	3	263
DDH-GN-36	406	408	qz	0.05	0.28	37	4	255	3	102	3	150
DDH-GN-36	408	410	qz	0.04	0.37	90	5	314	3	55	3	110
DDH-GN-36	410	412	qz	0.07	0.35	50	38	1100	3	3040	291	4970
DDH-GN-36	412	414	qz	0.06	0.35	76	14	1070	3	427	87	820
DDH-GN-36	414	416	qz	0.06	0.24	43	5	645	3	163	45	324
DDH-GN-36	416	418	qz	0.03	0.28	92	2	293	3	23	3	55
DDH-GN-36	418	419.3	qz	0.02	0.35	45	2	219	3	13	3	25

Hole_Id	From	To	Rock	Au_g/t	Cu_%	Mo_ppm	Ag_ppm	As_ppm	Bi_ppm	Pb_ppm	Sb_ppm	Zn_ppm
DDH-GN-37	0	2	Flt Zone	0.03	0.01	14	1	70	3	60	3	14
DDH-GN-37	2	4	Flt Zone	0.01	0.01	6	1	38	3	12	3	18
DDH-GN-37	4	6	Flt Zone	0.01	0.01	8	1	31	3	12	3	8
DDH-GN-37	6	8	Flt Zone	0.09	0.18	57	1	176	3	22	3	17
DDH-GN-37	8	10	Flt Zone	0.18	0.90	63	2	633	3	33	3	10
DDH-GN-37	10	12	Flt Zone	0.16	0.80	52	1	226	3	27	3	7
DDH-GN-37	12	14	Flt Zone	0.17	0.80	68	1	332	3	30	3	14
DDH-GN-37	14	16	Flt Zone	0.10	0.45	92	1	43	3	22	3	13
DDH-GN-37	16	18	Flt Zone	0.22	0.90	108	2	242	3	25	3	16
DDH-GN-37	18	20	Flt Zone	0.07	0.45	74	1	205	6	21	3	20
DDH-GN-37	20	22	Flt Zone	0.14	0.38	146	1	242	3	31	3	20
DDH-GN-37	22	24	Flt Zone	0.17	0.53	91	2	194	3	35	3	19
DDH-GN-37	24	26	Flt Zone	0.16	0.48	88	2	249	3	34	3	26

Hole_Id	From	To	Rock	Au_g/t	Cu_%	Mo_ppm	Ag_ppm	As_ppm	Bi_ppm	Pb_ppm	Sb_ppm	Zn_ppm
DDH-GN-37	26	28	Flt Zone	0.16	0.63	27	1	195	5	28	3	31
DDH-GN-37	28	30	Flt Zone	0.22	0.66	103	2	363	3	37	3	21
DDH-GN-37	30	32	Flt Zone	0.23	0.49	68	1	415	3	32	3	20
DDH-GN-37	32	34	Flt Zone	0.21	0.61	85	2	166	3	31	3	37
DDH-GN-37	34	36	Flt Zone	0.19	0.34	60	2	265	3	33	3	29
DDH-GN-37	36	38	Flt Zone	0.16	0.46	33	1	130	3	28	3	20
DDH-GN-37	38	40	Flt Zone	0.16	0.40	45	1	210	3	26	3	12
DDH-GN-37	40	42	Flt Zone	0.24	0.41	51	1	525	3	22	3	43
DDH-GN-37	42	44	Flt Zone	0.21	0.41	50	1	278	3	23	3	22
DDH-GN-37	44	46	Flt Zone	0.16	0.30	54	1	366	3	23	3	16
DDH-GN-37	46	48	Flt Zone	0.16	0.42	38	1	298	3	19	3	18
DDH-GN-37	48	50	Flt Zone	0.19	0.33	236	2	324	3	21	3	23
DDH-GN-37	50	52	Flt Zone	0.15	0.33	76	1	203	3	20	3	29
DDH-GN-37	52	54	Flt Zone	0.10	0.24	39	1	51	3	19	3	26
DDH-GN-37	54	56	Flt Zone	0.09	0.20	63	1	182	3	18	3	20
DDH-GN-37	56	58	Flt Zone	0.08	0.20	55	1	156	3	21	3	21
DDH-GN-37	58	60	Flt Zone	0.07	0.18	58	1	45	3	19	3	39
DDH-GN-37	60	62	Flt Zone	0.12	0.35	305	1	83	3	24	3	56
DDH-GN-37	62	64	Flt Zone	0.14	0.37	80	1	149	5	22	3	53
DDH-GN-37	64	66	Flt Zone	0.14	0.41	53	1	85	3	20	3	15
DDH-GN-37	66	68	Flt Zone	0.11	0.52	54	1	90	6	20	3	14
DDH-GN-37	68	70	P1	0.07	0.24	38	1	101	3	21	3	30
DDH-GN-37	70	72	Flt Zone	0.17	0.25	171	1	121	3	22	3	27
DDH-GN-37	72	74	Flt Zone	0.11	0.38	50	1	142	3	20	3	26
DDH-GN-37	74	76	Flt Zone	0.14	0.41	81	2	179	3	20	3	29
DDH-GN-37	76	78	Flt Zone	0.16	0.36	79	1	80	3	15	3	20
DDH-GN-37	78	80	Flt Zone	0.17	0.40	53	1	56	3	16	3	25
DDH-GN-37	80	82	Flt Zone	0.16	0.34	67	2	121	3	15	3	8
DDH-GN-37	82	84	Flt Zone	0.16	0.33	66	1	102	3	13	3	14
DDH-GN-37	84	86	Flt Zone	0.11	0.26	130	1	127	9	17	3	14
DDH-GN-37	86	88	Flt Zone	0.18	0.35	29	1	250	3	19	3	22
DDH-GN-37	88	90	Flt Zone	0.20	0.51	39	1	113	3	16	3	18
DDH-GN-37	90	92	Flt Zone	0.16	0.48	68	2	288	3	17	3	26
DDH-GN-37	92	94	Flt Zone	0.11	0.31	95	1	357	3	19	3	31
DDH-GN-37	94	96	Flt Zone	0.21	0.37	36	2	179	3	15	3	39
DDH-GN-37	96	98	Flt Zone	0.19	0.31	76	1	213	3	16	3	55
DDH-GN-37	98	100	Flt Zone	0.14	0.20	20	2	230	7	18	3	57
DDH-GN-37	100	102	Flt Zone	0.18	0.24	39	2	218	3	14	3	64
DDH-GN-37	102	104	Flt Zone	0.20	0.32	3	1	10	3	10	3	5
DDH-GN-37	104	106	Flt Zone	0.19	0.39	43	2	274	3	13	3	40
DDH-GN-37	106	108	Flt Zone	0.24	0.41	54	2	138	3	19	3	71
DDH-GN-37	108	110	Flt Zone	0.22	0.49	133	2	149	3	15	3	35
DDH-GN-37	110	112	P1	0.22	0.60	179	2	92	3	16	3	54
DDH-GN-37	112	114	Flt Zone	0.14	0.37	38	2	219	3	16	3	85
DDH-GN-37	114	116	Flt Zone	0.16	0.39	92	2	65	3	15	3	63
DDH-GN-37	116	118	Flt Zone	0.14	0.29	128	2	147	5	18	3	57
DDH-GN-37	118	120	P1	0.13	0.36	76	2	85	6	15	3	45
DDH-GN-37	120	122	P1	0.11	0.32	80	2	39	8	15	3	28
DDH-GN-37	122	124	P1	0.12	0.34	60	2	81	3	42	3	121
DDH-GN-37	124	126	Flt Zone	0.24	0.55	77	3	160	3	15	3	244
DDH-GN-37	126	128	Flt Zone	0.30	0.90	68	3	336	3	13	3	290
DDH-GN-37	128	130	Flt Zone	0.17	0.43	22	3	196	3	55	3	1200
DDH-GN-37	130	132	Flt Zone	0.34	1.40	33	9	317	11	14	3	7430
DDH-GN-37	132	134	Flt Zone	0.14	0.34	37	4	116	40	26	3	750
DDH-GN-37	134	136	Flt Zone	0.09	0.14	28	1	28	3	17	3	119
DDH-GN-37	136	138	Flt Zone	0.12	0.27	41	1	33	3	16	3	114
DDH-GN-37	138	140	Flt Zone	0.08	0.20	70	1	67	3	14	3	63
DDH-GN-37	140	142	Flt Zone	0.11	0.19	30	1	93	3	14	3	83
DDH-GN-37	142	144	Flt Zone	0.10	0.20	28	1	55	3	13	3	111
DDH-GN-37	144	146	P1	0.10	0.21	55	1	60	3	15	3	55
DDH-GN-37	146	148	P1	0.15	0.31	86	1	56	3	15	3	28
DDH-GN-37	148	150	P1	0.11	0.28	52	2	43	3	15	3	91
DDH-GN-37	150	152	Flt Zone	0.15	0.30	71	3	125	5	17	3	112
DDH-GN-37	152	154	Flt Zone	0.12	0.25	55	2	149	5	16	3	47
DDH-GN-37	154	156	Flt Zone	0.11	0.26	144	2	120	3	13	3	68
DDH-GN-37	156	158	Flt Zone	0.10	0.28	56	2	86	3	15	3	74
DDH-GN-37	158	160	Flt Zone	0.12	0.26	29	2	68	3	15	3	90
DDH-GN-37	160	162	Flt Zone	0.10	0.22	10	2	67	3	12	3	73
DDH-GN-37	162	164	Flt Zone	0.12	0.29	31	1	61	3	16	3	75
DDH-GN-37	164	166	Flt Zone	0.07	0.23	163	1	47	3	15	3	73
DDH-GN-37	166	168	Flt Zone	0.15	0.36	228	2	147	3	17	3	80
DDH-GN-37	168	170	Flt Zone	0.24	0.32	132	2	206	3	15	3	97
DDH-GN-37	170	172	Flt Zone	0.13	0.37	258	3	87	3	14	3	113
DDH-GN-37	172	174	Flt Zone	0.13	0.30	300	3	110	3	18	3	93
DDH-GN-37	174	176	P1	0.10	0.30	78	1	57	3	13	3	74
DDH-GN-37	176	178	P1	0.09	0.24	47	1	96	3	15	3	81
DDH-GN-37	178	180	P1	0.19	0.56	150	2	37	3	14	3	63
DDH-GN-37	180	182	Flt Zone	0.12	0.40	122	2	35	3	14	3	87
DDH-GN-37	182	184	Flt Zone	0.12	0.33	92	2	49	3	16	3	77
DDH-GN-37	184	186	Flt Zone	0.09	0.25	61	1	69	3	16	3	69
DDH-GN-37	186	188	Flt Zone	0.10	0.30	184	1	57	3	14	3	72
DDH-GN-37	188	190	Flt Zone	0.08	0.25	84	1	59	5	15	3	40
DDH-GN-37	190	192	Flt Zone	0.04	0.15	68	1	56	3	14	3	60
DDH-GN-37	192	194	Flt Zone	0.03	0.14	67	1	35	3	15	3	57
DDH-GN-37	194	196	Flt Zone	0.06	0.21	117	1	34	3	14	3	113
DDH-GN-37	196	198	Flt Zone	0.08	0.23	69	2	53	6	15	3	36
DDH-GN-37	198	200	Flt Zone	0.05	0.17	47	1	26	3	16	3	66
DDH-GN-37	200	202	Flt Zone	0.05	0.17	51	1	23	3	14	3	74
DDH-GN-37	202	204	Flt Zone	0.05	0.20	99	1	30	3	13	3	73
DDH-GN-37	204	206	P2	0.04	0.10	30	1	54	3	11	3	71
DDH-GN-37	206	208	P2	0.04	0.15	16	1	57	3	12	3	43
DDH-GN-37	208	210	P2	0.12	0.35	43	1	35	3	13	3	58
DDH-GN-37	210	212	P2	0.09	0.26	48	1	40	3	13	3	37
DDH-GN-37	212	214	P2	0.08	0.25	188	1	47	3	13	3	28
DDH-GN-37	214	216	P2	0.11	0.26	55	2	243	3	14	3	38
DDH-GN-37	216	218	P2	0.09	0.24	51	1	104	3	13	3	29
DDH-GN-37	218	220	P2	0.06	0.15	28	1	30	3	13	3	31
DDH-GN-37	220	222	P2	0.08	0.18	30	1	54	3	13	3	42
DDH-GN-37	222	224	P2	0.05	0.12	28	1	28	3	12	3	50
DDH-GN-37	224	226	P2	0.02	0.09	35	1	34	3	11	3	63
DDH-GN-37	226	228	P2	0.02	0.05	37	1	59	3	12	3	38
DDH-GN-37	228	230	P2	0.04	0.13	55	1	46	3	12	3	33
DDH-GN-37	230	232	P2	0.08	0.20	47	1	43	3	13	3	34
DDH-GN-37	232	234	P2	0.13	0.21	63	1	49	3	14	3	38
DDH-GN-37	234	236	P2	0.06	0.15	41	1	49	3	13	3	36
DDH-GN-37	236	238	P2	0.08	0.24	52	2	64	3	13	3	22
DDH-GN-37	238	240	P2	0.07	0.22	46	2	46	3	15	3	37
DDH-GN-37	240	242	P2	0.06	0.16	31	1	53	3	17	3	35
DDH-GN-37	242	244	P2	0.07	0.21	46	2	68	3	16	3	55
DDH-GN-37	244	246	P2	0.09	0.22	61	3	103	5	15	3	49

Hole_Id	From	To	Rock	Au_g/t	Cu_%	Mo_ppm	Ag_ppm	As_ppm	Bi_ppm	Pb_ppm	Sb_ppm	Zn_ppm
DDH-GN-37	246	248	P2	0.09	0.27	79	1	44	3	12	3	36
DDH-GN-37	248	250	P2	0.08	0.19	20	1	41	3	12	3	40
DDH-GN-37	250	252	P2	0.08	0.20	20	1	39	3	14	3	36
DDH-GN-37	252	254	P2	0.06	0.22	32	2	32	3	15	3	54
DDH-GN-37	254	256	P2	0.17	0.23	39	2	48	3	19	3	62
DDH-GN-37	256	258	P2	0.09	0.20	28	2	70	3	31	3	71
DDH-GN-37	258	260	P2	0.08	0.17	12	1	47	3	13	3	54
DDH-GN-37	260	262	P2	0.09	0.15	39	1	126	3	16	3	52
DDH-GN-37	262	264	P2	0.04	0.14	20	1	89	3	15	3	50
DDH-GN-37	264	266	P2	0.07	0.15	31	1	48	3	13	3	49
DDH-GN-37	266	268	P2	0.10	0.21	44	1	76	3	11	3	55
DDH-GN-37	268	270	P2	0.12	0.26	30	1	62	3	12	3	61
DDH-GN-37	270	272	P2	0.09	0.22	40	2	35	3	12	3	59
DDH-GN-37	272	274	P2	0.07	0.14	19	1	67	3	11	3	52
DDH-GN-37	274	276	P2	0.11	0.16	16	1	77	3	10	3	45
DDH-GN-37	276	278	P2	0.08	0.16	54	1	73	3	11	3	59
DDH-GN-37	278	280	P2	0.04	0.06	8	1	89	5	12	3	44
DDH-GN-37	280	282	P2	0.03	0.08	8	1	42	3	12	3	51
DDH-GN-37	282	284	P2	0.08	0.10	8	1	37	3	10	3	28
DDH-GN-37	284	286	P2	0.06	0.12	20	1	37	3	10	3	46
DDH-GN-37	286	288	Flt Zone	0.03	0.05	9	1	46	3	11	3	33
DDH-GN-37	288	290	Flt Zone	0.02	0.05	20	1	28	3	8	3	44
DDH-GN-37	290	292	Flt Zone	0.02	0.05	16	1	24	3	9	3	26
DDH-GN-37	292	294	Flt Zone	0.02	0.06	13	2	25	3	94	3	147
DDH-GN-37	294	296	Flt Zone	0.05	0.10	19	1	80	5	11	3	30
DDH-GN-37	296	298	Flt Zone	0.04	0.11	27	1	61	3	13	3	39
DDH-GN-37	298	300	Flt Zone	0.06	0.12	25	1	51	3	10	3	43
DDH-GN-37	300	302	Flt Zone	0.06	0.13	27	1	57	3	10	3	41
DDH-GN-37	302	304	Flt Zone	0.08	0.13	39	1	71	3	9	3	31
DDH-GN-37	304	306	P2	0.07	0.14	40	1	51	3	13	3	41
DDH-GN-37	306	308	P2	0.06	0.15	31	1	28	3	9	3	31
DDH-GN-37	308	310	Flt Zone	0.07	0.17	82	1	24	3	9	3	40
DDH-GN-37	310	312	P2	0.06	0.18	78	1	24	3	9	3	36
DDH-GN-37	312	314	P2	0.09	0.17	35	1	45	3	11	3	38
DDH-GN-37	314	316	P2	0.08	0.20	46	1	44	5	11	3	51
DDH-GN-37	316	318	Flt Zone	0.11	0.17	62	1	25	5	11	3	78
DDH-GN-37	318	320	Flt Zone	0.07	0.16	31	1	29	3	11	3	70
DDH-GN-37	320	322	Flt Zone	0.07	0.16	37	1	24	3	9	3	37
DDH-GN-37	322	324	Flt Zone	0.03	0.13	36	1	182	3	21	3	86
DDH-GN-37	324	326	P2	0.02	0.07	8	1	138	3	27	51	68
DDH-GN-37	326	328	P2	0.04	0.13	20	1	111	5	21	21	57
DDH-GN-37	328	330	P2	0.02	0.06	14	1	115	3	15	7	58
DDH-GN-37	330	332	Flt Zone	0.06	0.14	40	1	34	3	11	16	73
DDH-GN-37	332	334	Flt Zone	0.06	0.11	65	1	10	3	11	3	47
DDH-GN-37	334	336	P2	0.06	0.16	54	1	33	3	11	3	41
DDH-GN-37	336	338	P2	0.06	0.10	38	1	10	5	8	3	27
DDH-GN-37	338	340	Flt Zone	0.05	0.11	36	1	30	3	10	3	36
DDH-GN-37	340	342	Flt Zone	0.06	0.15	62	1	20	3	11	3	37
DDH-GN-37	342	344	P2	0.09	0.24	83	1	10	3	12	3	55
DDH-GN-37	344	346	Flt Zone	0.07	0.18	73	1	10	3	10	3	31
DDH-GN-37	346	348	P2	0.04	0.06	20	2	89	12	201	3	390
DDH-GN-37	348	350	Flt Zone	0.04	0.07	69	1	10	3	9	3	42
DDH-GN-37	350	352	Flt Zone	0.07	0.11	128	1	10	3	10	3	47
DDH-GN-37	352	354	Flt Zone	0.02	0.05	58	1	10	3	7	3	55
DDH-GN-37	354	356	Flt Zone	0.03	0.09	106	1	10	3	9	3	56
DDH-GN-37	356	358	P2	0.06	0.09	38	1	10	3	9	3	48
DDH-GN-37	358	360	P3	0.04	0.07	21	1	10	3	9	3	61
DDH-GN-37	360	362	P2	0.04	0.13	93	1	10	3	17	3	64
DDH-GN-37	362	364	P2	0.04	0.11	31	1	23	3	13	3	82
DDH-GN-37	364	366	P2	0.06	0.13	44	1	10	3	10	3	43
DDH-GN-37	366	368	P2	0.05	0.14	47	1	21	3	10	3	40
DDH-GN-37	368	370	P2	0.05	0.14	42	1	25	3	9	3	51
DDH-GN-37	370	372	P2	0.05	0.14	82	1	10	3	9	3	56
DDH-GN-37	372	374	P2	0.04	0.15	40	1	10	3	9	3	44
DDH-GN-37	374	376	P2	0.08	0.22	43	1	10	3	10	3	46
DDH-GN-37	376	378	P2	0.06	0.14	108	1	20	3	17	3	50
DDH-GN-37	378	380	P2	0.05	0.15	76	1	10	3	14	3	45
DDH-GN-37	380	382	P2	0.03	0.07	35	1	10	3	11	3	37
DDH-GN-37	382	384	P2	0.07	0.16	57	1	10	3	10	3	38
DDH-GN-37	384	386	P2	0.05	0.11	29	1	20	3	10	3	36
DDH-GN-37	386	388	P2	0.05	0.09	25	1	10	3	9	3	35
DDH-GN-37	388	390	P2	0.04	0.13	39	1	10	3	10	3	34
DDH-GN-37	390	391	P2	0.05	0.18	141		24	3	11	3	41

Hole N°	From	To	Rock	Au_g/T	Cu_%	Mo_ppm	Ag_ppm	As_ppm	Bi_ppm	Pb_ppm	Sb_ppm	Zn_ppm
DDH-GN-39	5	7	Qz	0.08	0.04	20	1	154	3	76	3	12
DDH-GN-39	7	9	Qz	0.48	0.84	137	1	32	3	12	3	18
DDH-GN-39	9	11	Qz	0.11	0.63	348	1	27	3	14	3	10
DDH-GN-39	11	13	Qz	0.12	0.85	275	1	28	3	14	3	12
DDH-GN-39	13	15	Qz	0.08	0.73	78	1	35	3	30	3	18
DDH-GN-39	15	17	Qz	0.08	0.90	297	1	42	3	29	3	48
DDH-GN-39	17	19	Qz	0.11	0.99	410	1	81	3	19	3	12
DDH-GN-39	19	21	P1	0.13	0.98	133	1	141	3	23	3	27
DDH-GN-39	21	23	P1	0.22	0.94	97	1	25	3	17	3	13
DDH-GN-39	23	25	P1	0.15	0.81	87	1	38	3	33	3	26
DDH-GN-39	25	27	P1	0.27	0.87	40	1	55	3	22	3	14
DDH-GN-39	27	29	P1	0.16	1.06	38	1	57	3	37	3	24
DDH-GN-39	29	31	P1	0.28	0.90	93	1	39	3	22	3	14
DDH-GN-39	31	33	P1	0.37	1.03	41	1	22	3	19	3	12
DDH-GN-39	33	35	P1	0.47	1.15	55	1	28	3	17	3	11
DDH-GN-39	35	37	P1	0.83	0.80	34	1	22	3	16	3	9
DDH-GN-39	37	39	P1	0.44	1.25	74	1	47	3	15	3	10
DDH-GN-39	39	41	P1	0.10	0.84	29	1	221	3	20	3	27
DDH-GN-39	41	43	P1	0.38	0.97	51	1	45	3	24	3	15
DDH-GN-39	43	45	P1	0.35	0.77	36	1	39	3	26	3	285
DDH-GN-39	45	47	P1	0.53	1.14	29	1	43	3	20	3	21
DDH-GN-39	47	49	P1	0.23	0.90	47	1	172	3	35	3	31
DDH-GN-39	49	51	P1	0.28	0.76	37	1	179	3	29	3	34
DDH-GN-39	51	53	P1	0.14	0.11	29	3	254	3	30	3	45
DDH-GN-39	53	55	P1	0.25	0.66	77	4	25	3	19	3	19
DDH-GN-39	55	57	P1	1.01	0.64	19	1	23	3	16	3	29
DDH-GN-39	57	59	P1	0.39	0.75	29	1	37	3	18	3	21
DDH-GN-39	59	61	P1	0.31	0.71	61	1	24	3	20	3	16
DDH-GN-39	61	63	P1	0.21	1.28	16	1	25	3	16	3	10
DDH-GN-39	63	65	P1	0.99	1.24	20	1	31	3	16	3	14
DDH-GN-39	65	67	P1	0.50	1.05	27	1	26	3	21	3	16
DDH-GN-39	67	69	P1	0.38	0.78	44	1	26	3	19	3	16
DDH-GN-39	69	71	Qz	0.11	1.04	68	1	73	3	26	3	26
DDH-GN-39	71	73	Qz	0.08	1.04	45	2	62	3	19	3	33

Hole_Id	From	To	Rock	Au_g/t	Cu_%	Mo_ppm	Ag_ppm	As_ppm	Bi_ppm	Pb_ppm	Sb_ppm	Zn_ppm
DDH-GN-39	73	75	Qz	0.09	0.81	55	2	54	3	19	3	25
DDH-GN-39	75	77	Qz	0.06	1.00	52	5	188	3	27	3	59
DDH-GN-39	77	79	Qz	0.06	0.63	47	1	54	3	21	3	18
DDH-GN-39	79	81	Qz	0.10	0.93	52	4	394	5	40	28	45
DDH-GN-39	81	83	Qz	0.12	1.03	81	3	174	3	30	3	21
DDH-GN-39	83	85	Qz	0.13	1.11	110	2	240	3	29	3	24
DDH-GN-39	85	87	Qz	0.09	1.07	262	1	24	3	18	3	14
DDH-GN-39	87	89	Qz	0.10	0.65	64	3	142	3	23	3	36
DDH-GN-39	89	91	Qz	0.12	1.10	62	5	41	3	20	3	48
DDH-GN-39	91	93	Qz	0.12	1.06	93	5	103	3	24	3	73
DDH-GN-39	93	95	Qz	0.11	1.03	47	8	145	3	24	3	134
DDH-GN-39	95	97	Qz	0.06	1.38	36	9	197	3	22	3	79
DDH-GN-39	97	99	Qz	0.09	1.05	36	9	71	3	29	3	127
DDH-GN-39	99	101	Qz	0.12	1.01	28	12	236	3	288	3	410
DDH-GN-39	101	103	Qz	0.09	1.11	49	8	63	3	30	3	143
DDH-GN-39	103	105	Qz	0.09	1.24	47	8	122	3	33	3	127
DDH-GN-39	105	107	Qz	0.10	1.26	91	11	255	3	136	3	151
DDH-GN-39	107	109	Qz	0.12	1.13	35	7	146	3	49	3	101
DDH-GN-39	109	111	Qz	0.15	0.89	45	2	20	3	21	3	33
DDH-GN-39	111	113	Qz	0.10	0.91	36	1	20	3	21	3	30
DDH-GN-39	113	115	Qz	0.18	0.87	41	2	20	3	20	3	34
DDH-GN-39	115	117	Qz	0.09	0.94	39	2	70	3	28	3	48
DDH-GN-39	117	119	Qz	0.13	0.94	65	5	57	3	38	3	75
DDH-GN-39	119	121	Qz	0.12	0.95	35	8	320	3	159	3	140
DDH-GN-39	121	123	Qz	0.09	1.01	85	5	520	22	29	22	86
DDH-GN-39	123	125	P1	0.09	0.93	39	2	128	3	19	3	34
DDH-GN-39	125	127	P1	0.11	0.68	27	2	38	3	30	3	53
DDH-GN-39	127	129	P1	0.17	0.65	50	1	35	3	30	3	42
DDH-GN-39	129	131	P1	0.12	0.67	40	2	37	3	27	3	41
DDH-GN-39	131	133	P1	0.14	0.69	49	1	33	3	24	3	31
DDH-GN-39	133	135	P1	0.19	0.71	48	2	99	3	43	3	67
DDH-GN-39	135	137	P1	0.09	0.60	48	1	89	3	22	3	28
DDH-GN-39	137	139	P1	0.07	0.64	56	1	30	3	37	3	36
DDH-GN-39	139	141	P2	0.23	0.64	92	1	10	3	26	3	42
DDH-GN-39	141	143	P2	0.38	0.56	102	1	20	3	20	3	41
DDH-GN-39	143	145	P2	0.26	0.51	242	1	126	3	28	20	65
DDH-GN-39	145	147	P2	0.21	0.46	104	1	108	3	27	3	51
DDH-GN-39	147	149	P2	0.28	0.47	87	1	25	3	37	3	65
DDH-GN-39	149	151	P2	0.26	0.55	79	1	42	3	33	3	47
DDH-GN-39	151	153	P2	0.17	0.38	77	1	10	3	22	3	59
DDH-GN-39	153	155	P2	0.20	0.35	61	1	38	3	21	3	53
DDH-GN-39	155	157	P2	0.24	0.38	96	1	10	3	18	3	61
DDH-GN-39	157	159	P2	0.27	0.44	74	1	10	3	17	3	20
DDH-GN-39	159	161	P2	0.19	0.43	39	1	10	3	16	3	48
DDH-GN-39	161	163	P2	0.33	0.47	54	1	21	3	13	3	49
DDH-GN-39	163	165	P2	0.36	0.50	50	1	10	3	13	3	48
DDH-GN-39	165	167	P2	0.24	0.41	209	1	10	3	22	3	60
DDH-GN-39	167	169	P2	0.42	0.47	53	2	20	3	22	3	67
DDH-GN-39	169	171	P2	0.30	0.43	94	2	10	3	16	3	62
DDH-GN-39	171	173	P2	0.23	0.42	88	1	10	3	14	3	50
DDH-GN-39	173	175	P2	0.27	0.60	68	1	25	3	26	3	79
DDH-GN-39	175	177	P2	0.35	0.54	64	2	31	3	19	3	67
DDH-GN-39	177	179	P2	0.29	0.48	88	2	10	3	13	3	63
DDH-GN-39	179	181	P1	0.25	0.50	33	2	45	3	16	3	41
DDH-GN-39	181	183	P2	0.12	0.47	33	1	10	3	15	3	34
DDH-GN-39	183	185	P2	0.19	0.42	42	1	25	3	15	3	39
DDH-GN-39	185	187	P2	0.18	0.39	62	1	10	3	16	3	44
DDH-GN-39	187	189	P2	0.14	0.40	54	2	217	3	36	3	17
DDH-GN-39	189	191	P1	0.32	0.35	88	1	970	3	21	18	62
DDH-GN-39	191	193	P1	0.14	0.28	56	1	24	3	12	3	21
DDH-GN-39	193	195	P2	0.01	0.14	149	1	10	3	14	3	15
DDH-GN-39	195	197	P2	0.06	0.21	96	1	24	3	14	3	23
DDH-GN-39	197	199	P2	0.16	0.35	57	1	32	3	12	3	42
DDH-GN-39	199	201	P2	0.19	0.30	64	1	24	3	10	3	43
DDH-GN-39	201	203	P1	0.13	0.22	61	1	25	3	11	3	47
DDH-GN-39	203	205	P1	0.16	0.26	85	1	10	3	9	3	46
DDH-GN-39	205	207	P1	0.19	0.36	52	1	24	3	11	48	
DDH-GN-39	207	209	P1	0.22	0.45	128	1	22	3	10	3	38
DDH-GN-39	209	211	P1	0.16	0.25	47	1	22	3	12	3	46
DDH-GN-39	211	213	P1	0.15	0.28	44	1	27	3	16	3	59
DDH-GN-39	213	215	P1	0.16	0.25	50	1	24	3	13	3	46
DDH-GN-39	215	217	P3 Dyke	0.08	0.20	120	1	40	3	15	3	50
DDH-GN-39	217	219	P1	0.08	0.22	76	1	43	7	42	3	89
DDH-GN-39	219	221	P1	0.07	0.23	47	1	51	5	34	3	60
DDH-GN-39	221	223	P1	0.11	0.23	41	1	33	5	19	3	45
DDH-GN-39	223	225	P1	0.06	0.18	47	2	38	11	21	3	64
DDH-GN-39	225	227	P1	0.09	0.16	31	3	127	3	28	3	96
DDH-GN-39	227	229	P1	0.07	0.20	16	2	37	6	18	3	62
DDH-GN-39	229	231	P1	0.09	0.17	37	2	21	3	13	3	50
DDH-GN-39	231	233	P1	0.19	0.26	20	2	25	3	11	3	51
DDH-GN-39	233	235	P1	0.28	0.32	38	2	26	3	10	3	52
DDH-GN-39	235	237	P3 Dyke	0.29	0.34	27	3	28	3	12	3	57
DDH-GN-39	237	239	P1	0.10	0.14	15	3	36	3	14	3	48
DDH-GN-39	239	241	P1	0.08	0.10	21	2	148	3	14	3	47
DDH-GN-39	241	243	P1	0.05	0.08	18	2	326	3	20	3	63
DDH-GN-39	243	245	P1	0.11	0.07	10	2	1340	3	18	5	74
DDH-GN-39	245	247	P1	0.07	0.14	518	2	668	3	22	3	98
DDH-GN-39	247	249	P1	0.07	0.16	152	3	162	3	35	3	59
DDH-GN-39	249	251	P1	0.10	0.24	92	3	298	5	31	3	77
DDH-GN-39	251	253	P1	0.08	0.27	32	3	54	5	29	3	51
DDH-GN-39	253	255	P3 Dyke	0.06	0.13	22	2	30	3	17	3	46
DDH-GN-39	255	257	P3 Dyke	0.07	0.14	38	2	33	3	16	3	53
DDH-GN-39	257	259	P1	0.09	0.22	36	3	33	6	109	3	68
DDH-GN-39	259	261	P1	0.07	0.18	25	3	38	5	35	3	58
DDH-GN-39	261	263	P1	0.12	0.23	24	2	29	3	14	3	50
DDH-GN-39	263	265	P1	0.09	0.19	32	2	24	3	15	3	56
DDH-GN-39	265	267	P1	0.05	0.16	30	2	28	5	20	3	59
DDH-GN-39	267	269	P1	0.05	0.14	34	2	26	3	13	3	48
DDH-GN-39	269	271	P1	0.18	0.13	29	2	29	3	17	3	55
DDH-GN-39	271	273	P1	0.05	0.13	30	2	30	3	18	3	64
DDH-GN-39	273	275	P1	0.00	0.00							
DDH-GN-39	275	277	P1	0.04	0.11	20	1	24	3	13	3	62
DDH-GN-39	277	279	P1	0.04	0.08	18	1	22	3	9	3	49
DDH-GN-39	279	281	P1	0.04	0.09	17	1	27	3	10	3	30
DDH-GN-39	281	283	P1	0.01	0.07	11	1	27	3	12	3	31
DDH-GN-39	283	285	P1	0.02	0.18	13	3	138	3	21	3	84
DDH-GN-39	285	287	P1	0.01	0.06	9	1	37	3	13	3	60
DDH-GN-39	287	289	P1	0.05	0.19	146	1	29	3	13	3	37
DDH-GN-39	289	291	P1	0.03	0.10	16	1	46	3	10	3	34
DDH-GN-39	291	293	P1	0.01	0.04	5	1	54	3	9	3	37

Hole_Id	From	To	Rock	Au_g/t	Cu_%	Mo_ppm	Ag_ppm	As_ppm	Bi_ppm	Pb_ppm	Sb_ppm	Zn_ppm
DDH-GN-39	293	295	P1	0.02	0.08	7	1	99	3	12	3	55
DDH-GN-39	295	297	P1	0.06	0.11	10	1	38	3	10	3	38
DDH-GN-39	297	299	P1	0.02	0.07	7	1	27	3	10	3	35
DDH-GN-39	299	301	P1	0.04	0.08	6	1	25	3	10	3	40
DDH-GN-39	301	303	P1	0.03	0.05	13	1	35	3	8	3	34
DDH-GN-39	303	305	P1	0.03	0.06	30	1	29	3	9	3	32
DDH-GN-39	305	307	P1	0.10	0.13	14	1	32	3	9	3	30
DDH-GN-39	307	309	P1	0.04	0.07	149	1	32	3	11	3	27
DDH-GN-39	309	311	P1	0.06	0.18	137	2	37	3	12	3	36
DDH-GN-39	311	313	P3	0.06	0.06	8	1	31	3	6	3	38
DDH-GN-39	313	315	P3	0.03	0.04	9	1	33	3	7	3	37
DDH-GN-39	315	317	P3	0.02	0.03	8	1	30	3	3	3	34
DDH-GN-39	317	319	P1	0.02	0.11	55	2	79	3	13	3	49
DDH-GN-39	319	321	P1	0.06	0.12	158	1	29	3	9	3	26
DDH-GN-39	321	323	P1	0.09	0.15	14	2	33	3	9	3	33
DDH-GN-39	323	325	P1	0.07	0.11	32	2	32	3	7	3	29
DDH-GN-39	325	327	P1	0.07	0.10	20	2	31	3	8	3	25
DDH-GN-39	327	329	P1	0.14	0.15	82	1	31	3	9	3	27
DDH-GN-39	329	331	P1	0.06	0.11	96	1	30	3	9	3	30
DDH-GN-39	331	333	P1	0.03	0.10	585	1	98	3	12	3	33
DDH-GN-39	333	335	P1	0.05	0.07	39	1	31	3	7	3	31
DDH-GN-39	335	337	P1	0.06	0.06	15	1	33	3	5	3	29
DDH-GN-39	337	339	P1	0.05	0.08	75	2	105	3	8	3	37
DDH-GN-39	339	341	P1	0.03	0.08	15	1	43	3	3	3	38
DDH-GN-39	341	343	P1	0.02	0.15	64	2	175	3	17	3	61
DDH-GN-39	343	345	Flt Zone	0.05	0.06	36	1	33	3	5	3	29
DDH-GN-39	345	347	Flt Zone	0.08	0.11	170	2	42	3	7	3	41
DDH-GN-39	347	349	Flt Zone	0.07	0.13	78	2	45	3	9	3	31
DDH-GN-39	349	351	Flt Zone	0.04	0.14	125	2	45	3	10	3	32
DDH-GN-39	351	353	P1	0.04	0.09	34	2	51	3	9	3	36
DDH-GN-39	353	355	P1	0.03	0.10	70	2	122	3	11	3	50
DDH-GN-39	355	357	P1	0.02	0.10	52	4	255	3	29	3	101
DDH-GN-39	357	359	P1	0.04	0.10	41	3	106	3	12	3	58
DDH-GN-39	359	361	MBx	0.03	0.13	39	4	242	3	26	3	91
DDH-GN-39	361	363	MBx	0.10	0.18	57	3	88	3	14	3	60
DDH-GN-39	363	365	MBx	0.06	0.11	115	1	49	3	8	3	29
DDH-GN-39	365	367	MBx	0.09	0.16	42	2	49	3	12	3	44
DDH-GN-39	367	369	MBx	0.05	0.30	47	1	29	3	8	3	28
DDH-GN-39	369	371	MBx	0.05	0.11	127	1	33	3	12	3	35
DDH-GN-39	371	373	MBx	0.03	0.08	33	1	32	3	8	3	29
DDH-GN-39	373	375	MBx	0.07	0.33	72	7	418	3	66	35	138
DDH-GN-39	375	377	MBx	0.03	0.08	44	2	146	3	11	3	54
DDH-GN-39	377	379	MBx	0.04	0.11	51	2	33	3	15	3	35
DDH-GN-39	379	381	MBx	0.04	0.07	49	1	28	3	7	3	32
DDH-GN-39	381	383	MBx	0.02	0.07	40	2	43	3	9	3	38
DDH-GN-39	383	385	MBx	0.04	0.06	23	1	29	3	8	3	36
DDH-GN-39	385	387	MBx	0.06	0.08	181	1	31	3	6	3	51
DDH-GN-39	387	389	MBx	0.04	0.09	25	1	27	3	8	3	32
DDH-GN-39	389	391	MBx	0.04	0.10	36	1	35	3	10	3	44
DDH-GN-39	391	393	MBx	0.06	0.06	21	1	37	3	8	3	42
DDH-GN-39	393	395	MBx	0.12	0.16	98	3	35	3	9	3	36
DDH-GN-39	395	397	MBx	0.07	0.10	185	2	35	3	10	3	27
DDH-GN-39	397	399	MBx	0.14	0.12	57	2	34	3	8	3	52
DDH-GN-39	399	401	MBx	0.30	0.13	45	2	43	3	12	3	30
DDH-GN-39	401	403	MBx	0.07	0.10	28	2	94	3	13	3	36
DDH-GN-39	403	405	MBx	0.05	0.12	40	2	45	3	14	3	28
DDH-GN-39	405	407	MBx	0.06	0.12	68	3	37	3	11	3	25
DDH-GN-39	407	409	MBx	0.04	0.08	68	2	34	3	10	3	38
DDH-GN-39	409	411	MBx	0.02	0.08	71	2	44	3	17	3	54
DDH-GN-39	411	413	MBx	0.01	0.05	21	2	95	3	18	3	52
DDH-GN-39	413	415	MBx	0.04	0.12	21	2	32	3	16	3	48
DDH-GN-39	415	417	MBx	0.04	0.09	30	2	37	3	9	3	44
DDH-GN-39	417	419	MBx	0.03	0.08	18	1	37	3	8	3	47
DDH-GN-39	419	421	MBx	0.06	0.10	14	2	85	3	14	3	48
DDH-GN-39	421	423	MBx	0.04	0.07	34	2	60	3	19	3	35
DDH-GN-39	423	425	MBx	0.03	0.14	23	2	91	3	11	3	26
DDH-GN-39	425	427	MBx	0.03	0.05	20	2	73	3	8	3	36
DDH-GN-39	427	429	MBx	0.06	0.08	41	2	43	3	7	3	42
DDH-GN-39	429	431	MBx	0.05	0.06	21	1	35	3	8	3	30
DDH-GN-39	431	433	MBx	0.04	0.04	70	2	36	3	6	3	46
DDH-GN-39	433	435	MBx	0.03	0.06	14	2	27	3	9	3	32
DDH-GN-39	435	437	MBx	0.03	0.07	44	2	59	3	12	3	35
DDH-GN-39	437	439	MBx	0.02	0.05	17	2	41	3	9	3	31
DDH-GN-39	439	441	MBx	0.07	0.10	18	1	37	3	8	3	23
DDH-GN-39	441	443	MBx	0.03	0.07	31	1	55	3	11	3	40
DDH-GN-39	443	445	MBx	0.03	0.10	68	2	48	3	15	3	29
DDH-GN-39	445	447	MBx	0.03	0.07	53	1	83	3	9	3	25
DDH-GN-39	447	449	MBx	0.01	0.04	30	1	68	3	9	3	23
DDH-GN-39	449	451	MBx	0.01	0.10	26	2	127	3	12	3	27
DDH-GN-39	451	453	MBx	0.01	0.07	47	2	137	3	9	3	26
DDH-GN-39	453	455	MBx	0.01	0.07	55	1	164	3	10	3	115
DDH-GN-39	455	457	MBx	0.01	0.07	11	1	63	3	14	3	36
DDH-GN-39	457	459	MBx	0.01	0.04	91	1	40	3	8	3	33
DDH-GN-39	459	461	MBx	0.01	0.03	17	2	30	3	7	3	33
DDH-GN-39	461	463	MBx	0.01	0.03	13	1	37	3	8	3	32
DDH-GN-39	463	465	P3	0.03	0.04	12	1	36	3	7	3	33
DDH-GN-39	465	467	P3	0.02	0.03	15	1	46	3	6	3	32
DDH-GN-39	467	469	P3	0.05	0.09	35	2	86	3	9	3	36
DDH-GN-39	469	471	P3	0.01	0.03	13	1	36	3	5	3	33
DDH-GN-39	471	473	P3	0.01	0.02	8	2	47	3	9	3	34
DDH-GN-39	473	475	P3	0.01	0.03	9	2	94	3	12	3	42

Hole N°	From	To	Rock	Au_g/T	Cu_%	Mo_ppm	Ag_ppm	As_ppm	Bi_ppm	Pb_ppm	Sb_ppm	Zn_ppm
DDH-GN-41	0	2	P2	0.06	0.05	41	3	329	3	41	3	3
DDH-GN-41	2	4	P2	0.10	0.06	96	4	602	3	47	5	10
DDH-GN-41	4	6	P2	0.13	0.04	57	4	778	3	43	21	5
DDH-GN-41	6	8	P2	0.16	0.23	21	5	172	3	26	3	9
DDH-GN-41	8	10	P2	0.19	0.20	45	3	56	3	22	3	15
DDH-GN-41	10	12	P2	0.31	0.13	55	2	221	3	17	3	30
DDH-GN-41	12	14	P2	0.35	0.49	66	2	35	3	19	3	28
DDH-GN-41	14	16	P2	0.36	0.90	269	2	30	3	16	3	22
DDH-GN-41	16	18	P2	0.22	0.80	76	3	53	3	28	3	24
DDH-GN-41	18	20	P2	0.27	0.59	39	2	102	3	16	3	18
DDH-GN-41	20	22	P2	0.30	0.77	44	2	105	3	19	3	27
DDH-GN-41	22	24	P2	0.48	0.57	124	2	29	3	16	3	29
DDH-GN-41	24	26	P2	0.28	0.62	37	2	24	3	17	3	31
DDH-GN-41	26	28	P2	0.39	0.54	47	2	25	3	16	3	30
DDH-GN-41	28	30	P2	0.33	0.42	84	2	22	3	13	3	39
DDH-GN-41	30	32	P2	0.32	0.39	43	1	25	3	17	3	32

Hole_Id	From	To	Rock	Au_g/t	Cu_%	Mo_ppm	Ag_ppm	As_ppm	Bi_ppm	Pb_ppm	Sb_ppm	Zn_ppm
DDH-GN-41	32	34	P2	0.23	0.46	34	1	23	3	16	3	30
DDH-GN-41	34	36	P2	0.25	0.45	64	2	24	3	14	3	27
DDH-GN-41	36	38	P2	0.39	0.75	48	2	26	3	15	3	19
DDH-GN-41	38	40	P2	0.17	0.64	113	1	42	3	20	3	21
DDH-GN-41	40	42	P2	0.15	0.57	199	2	41	3	18	3	20
DDH-GN-41	42	44	P2	0.27	0.48	163	1	23	3	18	3	35
DDH-GN-41	44	46	P2	0.25	0.65	71	3	164	3	19	3	60
DDH-GN-41	46	48	P2	0.11	2.40	119	3	278	3	23	3	65
DDH-GN-41	48	50	P2	0.17	0.89	212	2	35	3	15	3	17
DDH-GN-41	50	52	P2	0.22	0.58	28	1	32	3	15	3	24
DDH-GN-41	52	54	P2	0.23	0.49	25	1	29	3	17	3	26
DDH-GN-41	54	56	P2	0.18	0.64	78	1	48	3	26	3	23
DDH-GN-41	56	58	Flt Zone	0.16	0.72	112	1	217	3	21	14	31
DDH-GN-41	58	60	Flt Zone	0.17	0.64	57	1	58	3	17	3	22
DDH-GN-41	60	62	Flt Zone	0.17	0.58	64	1	27	3	15	3	19
DDH-GN-41	62	64	Flt Zone	0.13	0.88	23	1	31	3	17	8	21
DDH-GN-41	64	66	Flt Zone	0.18	0.83	29	1	32	3	16	3	22
DDH-GN-41	66	68	Flt Zone	0.27	0.53	51	1	27	3	16	3	28
DDH-GN-41	68	70	P2	0.21	0.66	29	1	88	3	20	3	28
DDH-GN-41	70	72	P2	0.14	0.68	109	1	122	3	28	3	21
DDH-GN-41	72	74	P2	0.12	0.59	44	2	75	3	20	3	26
DDH-GN-41	74	76	P2	0.14	0.65	46	3	107	3	27	3	34
DDH-GN-41	76	78	Flt Zone	0.19	0.64	53	2	120	3	26	3	36
DDH-GN-41	78	80	Flt Zone	0.19	0.61	79	2	200	3	41	3	59
DDH-GN-41	80	82	Flt Zone	0.24	0.71	288	2	85	3	24	3	23
DDH-GN-41	82	84	Flt Zone	0.26	0.65	92	1	180	3	21	3	20
DDH-GN-41	84	86	Flt Zone	0.17	0.40	46	1	343	3	37	7	44
DDH-GN-41	86	88	Flt Zone	0.10	0.25	47	2	49	3	16	3	17
DDH-GN-41	88	90	Flt Zone	0.12	0.25	48	1	50	3	19	3	23
DDH-GN-41	90	92	P1	0.28	0.33	70	1	51	3	17	3	28
DDH-GN-41	92	94	P1	0.21	0.33	125	1	23	3	18	3	29
DDH-GN-41	94	96	P1	0.19	0.33	72	1	10	3	16	3	32
DDH-GN-41	96	98	P1	0.28	0.35	77	1	88	3	15	3	36
DDH-GN-41	98	100	P1	0.24	0.26	96	2	40	3	17	3	35
DDH-GN-41	100	102	P1	0.22	0.26	89	1	74	3	17	3	36
DDH-GN-41	102	104	P3	0.18	0.19	36	1	98	3	16	3	40
DDH-GN-41	104	106	P3	0.11	0.15	41	1	25	3	14	3	42
DDH-GN-41	106	108	P3	0.16	0.22	59	1	25	3	19	3	34
DDH-GN-41	108	110	P3	0.18	0.16	60	1	108	3	15	3	41
DDH-GN-41	110	112	P3	0.05	0.14	48	2	56	3	40	3	58
DDH-GN-41	112	114	P3	0.12	0.12	32	1	20	3	15	3	39
DDH-GN-41	114	116	P3	0.07	0.15	64	2	61	3	20	3	33
DDH-GN-41	116	118	P3	0.07	0.11	69	1	37	3	15	3	40
DDH-GN-41	118	120	P3	0.07	0.07	29	1	47	3	10	3	36
DDH-GN-41	120	122	P3	0.06	0.19	75	1	43	3	20	3	34
DDH-GN-41	122	124	P3	0.08	0.13	36	1	63	3	18	3	42
DDH-GN-41	124	126	P3	0.12	0.22	47	1	85	3	30	3	45
DDH-GN-41	126	128	P3	0.15	0.27	29	1	102	3	23	3	77
DDH-GN-41	128	130	P3	0.06	0.15	49	1	69	3	19	3	37
DDH-GN-41	130	132	P1	0.03	0.04	18	1	28	3	9	3	34
DDH-GN-41	132	134	P1	0.08	0.11	72	1	26	3	14	3	28
DDH-GN-41	134	136	P1	0.07	0.14	39	1	26	3	18	3	23
DDH-GN-41	136	138	P1	0.23	0.40	83	1	35	3	20	3	35
DDH-GN-41	138	140	P1	0.21	0.36	55	3	83	3	28	3	46
DDH-GN-41	140	142	P1	0.05	0.14	46	3	241	3	41	3	67
DDH-GN-41	142	144	P1	0.08	0.20	29	5	575	3	63	40	208
DDH-GN-41	144	146	P1	0.09	0.20	34	2	80	3	21	3	34
DDH-GN-41	146	148	P1	0.09	0.18	26	1	73	3	21	3	31
DDH-GN-41	148	150	P1	0.06	0.12	27	2	106	3	35	3	50
DDH-GN-41	150	152	P1	0.10	0.12	38	1	35	3	14	3	23
DDH-GN-41	152	154	P3	0.04	0.07	28	1	72	3	36	3	45
DDH-GN-41	154	156	P3	0.05	0.03	40	1	135	3	6	3	36
DDH-GN-41	156	158	P3	0.07	0.08	58	1	26	3	12	3	32
DDH-GN-41	158	160	P3	0.02	0.04	19	1	26	3	11	3	40
DDH-GN-41	160	162	P3	0.02	0.03	14	1	30	3	6	3	45
DDH-GN-41	162	164	P3	0.04	0.05	25	1	40	3	10	3	37
DDH-GN-41	164	166	P3	0.06	0.05	19	1	35	3	10	3	38
DDH-GN-41	166	168	P3	0.06	0.08	21	1	48	3	12	3	36
DDH-GN-41	168	170	P3	0.04	0.06	79	1	102	3	26	3	43
DDH-GN-41	170	172	P3	0.04	0.06	64	1	37	3	14	3	40
DDH-GN-41	172	174	P3	0.04	0.06	63	1	32	3	10	3	33
DDH-GN-41	174	176	P3	0.03	0.06	35	1	47	3	11	3	30
DDH-GN-41	176	178	P3	0.04	0.06	21	1	27	3	10	3	35
DDH-GN-41	178	180	P3	0.03	0.03	12	1	59	3	8	3	42
DDH-GN-41	180	182	P3	0.07	0.03	6	1	173	3	8	3	45
DDH-GN-41	182	184	P3	0.04	0.04	13	1	38	3	8	3	33
DDH-GN-41	184	186	P3	0.06	0.06	82	1	192	3	16	3	45
DDH-GN-41	186	188	P3	0.06	0.05	36	1	52	3	12	3	30
DDH-GN-41	188	190	P3	0.03	0.05	32	1	43	3	13	3	31
DDH-GN-41	190	192	P3	0.02	0.02	18	1	34	3	5	3	36
DDH-GN-41	192	194	P3	0.03	0.06	21	1	50	3	13	3	43
DDH-GN-41	194	196	P3	0.11	0.09	22	1	890	3	27	3	105
DDH-GN-41	196	198	P3	0.05	0.04	27	1	212	3	22	3	68
DDH-GN-41	198	200	P3	0.09	0.04	11	1	479	3	31	3	102
DDH-GN-41	200	202	P3	0.04	0.04	16	3	201	6	98	3	161
DDH-GN-41	202	204	P3	0.08	0.04	57	2	860	3	143	3	240
DDH-GN-41	204	206	P3	0.08	0.06	46	2	466	3	22	3	41
DDH-GN-41	206	208	P3	0.06	0.14	21	1	75	3	28	3	56
DDH-GN-41	208	210	P3	0.03	0.09	30	1	36	3	19	3	48
DDH-GN-41	210	212	P3	0.02	0.03	31	1	32	3	12	3	47
DDH-GN-41	212	214	P3	0.01	0.03	13	1	27	3	12	3	51
DDH-GN-41	214	216	P3	0.01	0.03	95	1	72	3	27	3	71
DDH-GN-41	216	218	P3	0.01	0.02	15	1	27	3	12	3	49
DDH-GN-41	218	220	P3	0.01	0.04	41	1	28	3	37	3	66
DDH-GN-41	220	222	P3	0.01	0.03	13	1	31	3	20	3	55
DDH-GN-41	222	224	P3	0.02	0.03	30	3	38	5	216	3	360
DDH-GN-41	224	226	P3	0.01	0.02	21	1	29	3	24	3	71
DDH-GN-41	226	228	P3	0.02	0.03	12	2	30	5	26	3	73
DDH-GN-41	228	230	P3	0.02	0.05	8	1	27	3	29	3	75
DDH-GN-41	230	232	P3	0.04	0.11	44	4	33	3	128	3	165
DDH-GN-41	232	234	P3	0.02	0.04	17	1	28	3	30	3	78
DDH-GN-41	234	236	P3	0.01	0.03	10	1	26	3	45	3	94
DDH-GN-41	236	238	P3	0.01	0.03	13	2	27	3	60	3	95
DDH-GN-41	238	240	P3	0.01	0.03	9	11	42	3	674	20	520
DDH-GN-41	240	242	P3	0.03	0.05	11	5	39	3	555	3	1010
DDH-GN-41	242	244	P3	0.07	0.14	28	12	52	3	772	43	740
DDH-GN-41	244	246	P3	0.04	0.09	16	39	62	3	2730	100	1050
DDH-GN-41	246	248	P3	0.02	0.05	3	24	38	3	1500	49	480
DDH-GN-41	248	250	P3	0.03	0.08	34	40	68	3	2540	107	1280
DDH-GN-41	250	252	P3	0.02	0.05	12	2	23	3	50	3	81

Hole_Id	From	To	Rock	Au_g/t	Cu_%	Mo_ppm	Ag_ppm	As_ppm	Bi_ppm	Pb_ppm	Sb_ppm	Zn_ppm
DDH-GN-41	252	254	P3	0.01	0.05	10	2	34	3	53	3	133
DDH-GN-41	254	256	P3	0.02	0.03	10	1	23	3	14	3	46
DDH-GN-41	256	258	P3	0.01	0.04	30	2	22	3	47	3	174
DDH-GN-41	258	260	P3	0.03	0.05	29	1	28	3	21	3	54
DDH-GN-41	260	262	P3	0.01	0.04	67	3	69	3	218	3	410
DDH-GN-41	262	264	P3	0.01	0.07	50	6	79	3	830	10	650
DDH-GN-41	264	266	P3	0.01	0.06	59	6	90	3	234	12	740
DDH-GN-41	266	268	P3	0.01	0.07	121	3	123	3	73	3	197
DDH-GN-41	268	270	P3	0.04	0.12	232	2	33	3	27	3	56
DDH-GN-41	270	272	P3	0.06	0.14	99	3	35	3	46	3	170
DDH-GN-41	272	274	P3	0.02	0.03	7	2	34	3	45	3	257
DDH-GN-41	274	276	P3	0.01	0.03	9	2	32	3	14	3	63
DDH-GN-41	276	278	P3	0.02	0.03	13	1	27	3	10	3	39
DDH-GN-41	278	280	P3	0.01	0.03	39	1	10	3	10	3	40
DDH-GN-41	280	282	P3	0.01	0.04	33	1	27	3	43	3	84
DDH-GN-41	282	284	P3	0.03	0.05	29	1	25	3	17	3	42
DDH-GN-41	284	286	P3	0.01	0.03	32	1	29	3	20	3	56
DDH-GN-41	286	288	P3	0.02	0.03	5	1	24	3	13	3	52
DDH-GN-41	288	290	P3	0.03	0.05	9	2	65	3	38	3	160
DDH-GN-41	290	292	P3	0.02	0.03	33	1	32	3	61	3	226
DDH-GN-41	292	294	P3	0.03	0.03	8	1	43	3	24	3	73
DDH-GN-41	294	296	P1	0.08	0.12	29	1	72	3	31	3	110
DDH-GN-41	296	298	P1	0.06	0.09	54	1	44	3	32	3	83
DDH-GN-41	298	300	P1	0.05	0.06	35	2	176	3	102	5	510
DDH-GN-41	300	302	P1	0.01	0.05	38	2	60	3	79	3	371
DDH-GN-41	302	304	P1	0.02	0.06	52	1	39	3	25	3	54
DDH-GN-41	304	306	P1	0.03	0.07	21	4	92	9	274	3	1380
DDH-GN-41	306	308	P1	0.03	0.06	21	2	58	3	96	3	121
DDH-GN-41	308	310	P1	0.04	0.09	38	2	124	3	69	3	184
DDH-GN-41	310	312	P1	0.05	0.12	41	1	35	3	59	3	127
DDH-GN-41	312	314	P1	0.05	0.07	22	1	41	3	55	3	97
DDH-GN-41	314	316	P1	0.04	0.06	27	1	86	3	42	3	78
DDH-GN-41	316	318	P1	0.06	0.06	18	1	533	3	120	3	195
DDH-GN-41	318	320	P1	0.04	0.07	25	2	426	3	92	3	110

Hole N°	From	To	Rock	Au_g/T	Cu_%	Mo_ppm	Ag_ppm	As_ppm	Bi_ppm	Pb_ppm	Sb_ppm	Zn_ppm
DDH-GN-42	3	6	P1	0.17	0.04	19	2	55	3	11	3	15
DDH-GN-42	6	8	P1	0.19	0.02	27	1	104	3	11	3	8
DDH-GN-42	8	10	P1	0.15	0.03	30	1	76	5	11	3	14
DDH-GN-42	10	12	P1	0.15	0.03	35	1	97	3	14	3	17
DDH-GN-42	12	14	P1	0.14	0.02	18	1	73	5	8	3	20
DDH-GN-42	14	16	P1	0.12	0.03	26	1	157	3	23	3	8
DDH-GN-42	16	18	P1	0.17	0.02	32	1	76	3	12	3	7
DDH-GN-42	18	20	P1	0.17	0.07	34	2	194	3	21	16	10
DDH-GN-42	20	22	P1	0.12	0.07	18	1	57	3	11	3	7
DDH-GN-42	22	24	P1	0.13	0.09	36	1	75	3	14	3	8
DDH-GN-42	24	26	P1	0.17	0.20	20	1	130	3	16	3	6
DDH-GN-42	26	28	P1	0.11	0.22	56	1	46	3	17	3	12
DDH-GN-42	28	30	P1	0.11	0.12	16	1	111	3	22	3	7
DDH-GN-42	30	32	P1	0.05	0.12	24	2	198	3	31	3	24
DDH-GN-42	32	34	P1	0.05	0.16	25	1	132	3	49	3	26
DDH-GN-42	34	36	P1	0.10	0.18	16	1	75	3	18	3	14
DDH-GN-42	36	38	P1	0.09	0.18	18	2	79	3	26	3	15
DDH-GN-42	38	40	P1	0.15	0.18	26	2	366	3	42	3	33
DDH-GN-42	40	42	P1	0.12	0.19	50	2	236	3	54	3	72
DDH-GN-42	42	44	P1	0.16	0.35	29	1	85	3	33	3	23
DDH-GN-42	44	46	P1	0.17	0.39	50	1	81	3	25	3	24
DDH-GN-42	46	48	P1	0.14	0.36	37	1	33	3	29	3	23
DDH-GN-42	48	50	P1	0.15	0.33	44	2	100	3	28	3	40
DDH-GN-42	50	52	P1	0.27	0.32	33	2	571	3	59	21	71
DDH-GN-42	52	54	P1	0.11	0.18	22	1	79	3	51	3	44
DDH-GN-42	54	56	P1	0.15	0.20	21	1	31	3	21	3	28
DDH-GN-42	56	58	P1	0.15	0.15	18	1	48	3	17	3	25
DDH-GN-42	58	60	Flt Zone	0.35	0.16	36	1	514	3	17	3	25
DDH-GN-42	60	62	Flt Zone	0.14	0.17	39	1	137	3	15	3	23
DDH-GN-42	62	64	P1	0.08	0.10	40	1	72	3	11	3	17
DDH-GN-42	64	66	P1	0.21	0.14	41	1	476	3	17	3	38
DDH-GN-42	66	68	P1	0.09	0.14	32	2	177	3	17	3	26
DDH-GN-42	68	70	P1	0.13	0.13	42	1	31	3	14	3	33
DDH-GN-42	70	72	P1	0.12	0.11	54	1	217	3	15	3	36
DDH-GN-42	72	74	P1	0.10	0.09	18	1	27	3	12	3	35
DDH-GN-42	74	76	P1	0.08	0.09	22	1	30	3	9	3	33
DDH-GN-42	76	78	P1	0.09	0.12	32	1	23	3	10	3	32
DDH-GN-42	78	80	P1	0.09	0.11	22	1	28	3	10	3	36
DDH-GN-42	80	82	P1	0.09	0.10	21	1	23	3	12	3	38
DDH-GN-42	82	84	P1	0.10	0.14	51	1	28	3	13	3	37
DDH-GN-42	84	86	P1	0.08	0.15	55	2	104	3	50	3	69
DDH-GN-42	86	88	P1	0.09	0.15	67	1	35	3	14	3	37
DDH-GN-42	88	90	P1	0.05	0.08	19	1	35	3	12	3	42
DDH-GN-42	90	92	P1	0.11	0.14	23	1	162	5	14	3	48
DDH-GN-42	92	94	P1	0.09	0.07	15	1	190	3	9	3	53
DDH-GN-42	94	96	P1	0.08	0.11	39	1	58	3	11	3	35
DDH-GN-42	96	98	P1	0.06	0.09	22	1	33	6	13	3	50
DDH-GN-42	98	100	P1	0.07	0.19	41	3	126	3	36	3	38
DDH-GN-42	100	102	P1	0.08	0.15	78	2	129	3	39	3	32
DDH-GN-42	102	104	P1	0.10	0.10	20	1	179	3	10	3	36
DDH-GN-42	104	106	P1	0.13	0.19	162	2	39	3	15	3	35
DDH-GN-42	106	108	P1	0.08	0.11	25	1	188	3	8	3	23
DDH-GN-42	108	110	P1	0.08	0.08	30	1	228	3	23	3	44
DDH-GN-42	110	112	P1	0.04	0.10	48	1	29	3	18	3	25
DDH-GN-42	112	114	P1	0.04	0.07	132	1	33	7	16	3	32
DDH-GN-42	114	116	P1	0.09	0.10	13	1	82	3	13	3	45
DDH-GN-42	116	118	P1	0.09	0.14	101	1	165	3	9	3	23
DDH-GN-42	118	120	P1	0.18	0.22	216	2	261	3	11	3	49
DDH-GN-42	120	122	P1	0.11	0.15	82	1	41	3	10	3	42
DDH-GN-42	122	124	P1	0.09	0.11	20	1	37	3	7	3	27
DDH-GN-42	124	126	P1	0.09	0.15	145	1	116	3	13	3	28
DDH-GN-42	126	128	P1	0.13	0.21	80	1	34	3	15	3	36
DDH-GN-42	128	130	P1	0.07	0.10	30	1	45	3	16	3	27
DDH-GN-42	130	132	P1	0.12	0.12	27	1	30	3	12	3	29
DDH-GN-42	132	134	P1	0.08	0.08	18	1	35	3	10	3	26
DDH-GN-42	134	136	P1	0.10	0.14	20	1	31	3	12	3	29
DDH-GN-42	136	138	P1	0.20	0.32	92	1	36	3	14	3	30
DDH-GN-42	138	140	P1	0.13	0.20	645	1	48	3	14	3	33
DDH-GN-42	140	142	P1	0.06	0.06	21	1	33	3	9	3	40
DDH-GN-42	142	144	P1	0.16	0.12	24	1	880	3	16	3	99
DDH-GN-42	144	146	P1	0.07	0.07	22	1	238	3	10	3	32
DDH-GN-42	146	148	P1	0.20	0.07	49	1	1100	3	14	3	28
DDH-GN-42	148	150	P1	0.10	0.11	38	1	89	3	13	3	30

Hole_Id	From	To	Rock	Au_g/t	Cu_%	Mo_ppm	Ag_ppm	As_ppm	Bi_ppm	Pb_ppm	Sb_ppm	Zn_ppm
DDH-GN-42	150	152	P1	0.07	0.09	136	1	62	3	12	3	31
DDH-GN-42	152	154	P1	0.11	0.13	257	3	514	3	20	16	48
DDH-GN-42	154	156	P1	0.14	0.09	365	2	566	5	16	12	45
DDH-GN-42	156	158	P1	0.09	0.10	101	2	315	3	16	3	44
DDH-GN-42	158	160	P3	0.04	0.04	26	1	39	5	20	3	74
DDH-GN-42	160	162	P3	0.03	0.05	110	1	41	3	33	3	86
DDH-GN-42	162	164	P3	0.03	0.06	32	1	79	3	33	3	80
DDH-GN-42	164	166	P3	0.03	0.04	42	2	36	3	145	3	155
DDH-GN-42	166	168	P3	0.02	0.04	5	1	35	3	38	3	115
DDH-GN-42	168	170	P3	0.02	0.04	10	1	32	3	27	3	73
DDH-GN-42	170	172	P3	0.03	0.10	10	1	33	3	33	3	55
DDH-GN-42	172	174	P1	0.07	0.19	63	2	118	3	29	3	109
DDH-GN-42	174	176	P1	0.05	0.16	38	2	89	3	18	3	235
DDH-GN-42	176	178	P1	0.03	0.08	37	1	24	3	21	3	28
DDH-GN-42	178	180	P1	0.03	0.14	30	2	21	3	27	3	32
DDH-GN-42	180	182	P1	0.02	0.18	19	2	69	3	38	3	145
DDH-GN-42	182	184	P1	0.04	0.15	15	2	98	3	28	3	141
DDH-GN-42	184	186	P1	0.05	0.15	36	1	39	3	22	3	41
DDH-GN-42	186	188	P1	0.02	0.09	25	3	138	3	103	21	110
DDH-GN-42	188	190	P1	0.04	0.09	28	1	20	3	19	3	32
DDH-GN-42	190	192	P1	0.04	0.07	13	1	30	3	21	3	24
DDH-GN-42	192	194	P1	0.06	0.09	14	2	175	3	19	18	78
DDH-GN-42	194	196	P1	0.05	0.14	34	2	27	3	17	3	26
DDH-GN-42	196	198	P1	0.02	0.08	14	1	43	3	28	3	45
DDH-GN-42	198	200	P1	0.03	0.14	31	2	54	3	49	3	70
DDH-GN-42	200	202	P1	0.03	0.08	33	2	177	3	45	3	90
DDH-GN-42	202	204	P1	0.04	0.10	35	1	24	3	24	3	29
DDH-GN-42	204	206	P1	0.05	0.18	187	2	33	3	18	3	59
DDH-GN-42	206	208	P1	0.02	0.08	101	1	32	3	13	3	22
DDH-GN-42	208	210	P1	0.04	0.10	220	1	20	3	12	3	23
DDH-GN-42	210	212	P1	0.04	0.10	15	1	10	3	16	3	29
DDH-GN-42	212	214	P1	0.06	0.11	30	2	23	3	18	3	27
DDH-GN-42	214	216	P1	0.08	0.17	24	1	29	3	13	3	32
DDH-GN-42	216	218	P1	0.09	0.13	39	2	62	3	15	3	31
DDH-GN-42	218	220	P1	0.12	0.13	38	2	291	3	16	3	32
DDH-GN-42	220	222	P1	0.05	0.08	62	1	73	3	11	3	48
DDH-GN-42	222	224	P1	0.06	0.08	13	1	86	3	17	3	31
DDH-GN-42	224	226	P1	0.04	0.10	50	2	53	3	18	3	34
DDH-GN-42	226	228	P1	0.07	0.10	24	1	30	3	13	3	30
DDH-GN-42	228	230	P1	0.08	0.14	64	1	29	3	16	3	28
DDH-GN-42	230	232	P1	0.07	0.10	20	1	27	3	15	3	33
DDH-GN-42	232	234	P1	0.12	0.13	15	1	25	3	19	3	45
DDH-GN-42	234	236	P3	0.02	0.04	3	1	30	3	15	3	77
DDH-GN-42	236	238	P3	0.02	0.06	34	1	53	3	43	3	250
DDH-GN-42	238	240	P3	0.02	0.03	17	1	25	3	32	3	122
DDH-GN-42	240	242	P3	0.04	0.06	86	1	26	3	24	3	87
DDH-GN-42	242	244	P3	0.01	0.02	5	1	29	5	14	3	83
DDH-GN-42	244	246	P3	0.01	0.03	10	1	31	5	21	3	81
DDH-GN-42	246	248	P3	0.01	0.03	15	1	29	3	57	3	280
DDH-GN-42	248	250	P3	0.03	0.07	12	1	93	3	33	3	99
DDH-GN-42	250	252	P3	0.01	0.02	8	1	32	3	7	3	55
DDH-GN-42	252	254	P3	0.01	0.03	3	1	26	3	10	3	54
DDH-GN-42	254	256	P3	0.01	0.02	3	1	27	3	8	3	58
DDH-GN-42	256	258	P3 Bx	0.01	0.02	3	1	32	3	10	3	65
DDH-GN-42	258	260	P3 Bx	0.01	0.03	3	1	28	3	15	3	69
DDH-GN-42	260	262	P1	0.02	0.06	10	1	33	5	23	3	42
DDH-GN-42	262	264	P1	0.02	0.04	10	1	31	3	53	3	27
DDH-GN-42	264	266	P1	0.02	0.05	14	1	34	3	40	3	32
DDH-GN-42	266	268	P1	0.04	0.06	25	1	36	3	14	3	27
DDH-GN-42	268	270	P1	0.02	0.03	69	1	31	3	97	3	42
DDH-GN-42	270	272	P1	0.03	0.04	6	1	32	5	15	3	32
DDH-GN-42	272	274	P1	0.02	0.03	11	1	35	3	10	3	30
DDH-GN-42	274	276	P1	0.01	0.03	12	1	42	3	15	3	31
DDH-GN-42	276	278	P1	0.01	0.03	8	1	37	3	9	3	32
DDH-GN-42	278	280	P1	0.01	0.03	16	1	132	3	14	3	37
DDH-GN-42	280	282	P1	0.01	0.04	14	1	49	3	11	3	40
DDH-GN-42	282	284	P1	0.01	0.04	20	1	107	5	24	3	42
DDH-GN-42	284	286	P1	0.03	0.07	26	2	63	3	43	3	46
DDH-GN-42	286	288	P1	0.02	0.06	20	2	153	3	43	3	67
DDH-GN-42	288	290	P1	0.02	0.02	5	1	45	3	32	3	51
DDH-GN-42	290	292	P1	0.01	0.02	23	1	36	3	35	3	41
DDH-GN-42	292	294	P1	0.02	0.04	15	1	34	3	31	3	47
DDH-GN-42	294	296	P1	0.04	0.06	27	1	38	7	16	3	28
DDH-GN-42	296	298	P1	0.02	0.08	29	1	86	5	20	3	27
DDH-GN-42	298	300	P1	0.01	0.05	15	1	130	3	28	3	45
DDH-GN-42	300	302	P1	0.03	0.05	14	1	58	5	12	3	29
DDH-GN-42	302	304	P1	0.01	0.05	155	1	52	6	42	3	60
DDH-GN-42	304	306	P1	0.02	0.03	29	1	39	3	20	3	35
DDH-GN-42	306	308	P3	0.03	0.05	39	1	36	3	21	3	45
DDH-GN-42	308	310	P3	0.02	0.04	13	1	32	3	14	3	37
DDH-GN-42	310	312	P3	0.02	0.04	17	1	33	3	15	3	25
DDH-GN-42	312	314	P3	0.02	0.05	14	1	46	3	24	3	30
DDH-GN-42	314	316	P3	0.01	0.04	512	1	81	3	23	3	26
DDH-GN-42	316	318	P3	0.01	0.04	82	1	46	3	13	3	30
DDH-GN-42	318	320	P3	0.02	0.05	41	1	43	3	13	3	38
DDH-GN-42	320	322	P1	0.06	0.07	30	1	407	3	17	3	37
DDH-GN-42	322	324	P1	0.04	0.04	19	1	49	3	27	3	39
DDH-GN-42	324	326	P1	0.02	0.03	10	1	43	5	18	3	42
DDH-GN-42	326	328	P1	0.03	0.04	26	1	78	3	39	3	58
DDH-GN-42	328	330	P1	0.02	0.06	47	1	57	6	33	3	51
DDH-GN-42	330	332	P1	0.03	0.06	27	1	49	5	12	3	29
DDH-GN-42	332	334	P1	0.03	0.07	31	1	186	3	38	3	57
DDH-GN-42	334	336	P1	0.02	0.04	26	1	127	6	25	3	49
DDH-GN-42	336	338	P1	0.02	0.07	34	2	202	37	41	5	78
DDH-GN-42	338	340	P1	0.03	0.03	7	1	41	3	9	3	24
DDH-GN-42	340	342	P1	0.03	0.06	25	1	36	3	19	3	35
DDH-GN-42	342	344	P3	0.03	0.04	34	1	34	5	17	3	37
DDH-GN-42	344	346	P1	0.04	0.04	47	1	33	3	9	3	24
DDH-GN-42	346	348	P1	0.03	0.06	18	1	36	3	16	3	21
DDH-GN-42	348	350	P1	0.04	0.07	14	1	30	5	12	3	23
DDH-GN-42	350	352	P1	0.04	0.11	24	2	48	5	20	3	34
DDH-GN-42	352	354	P1	0.03	0.11	98	3	67	3	51	3	74
DDH-GN-42	354	356	P1	0.02	0.08	112	2	56	5	52	3	51
DDH-GN-42	356	358	P3	0.02	0.04	115	1	30	6	35	3	65
DDH-GN-42	358	360	P3	0.02	0.06	43	1	26	3	20	3	50
DDH-GN-42	360	362	P1	0.01	0.04	29	1	29	3	23	3	30
DDH-GN-42	362	364	P1	0.04	0.07	19	2	99	3	16	3	29
DDH-GN-42	364	366	P1	0.02	0.05	23	1	62	3	6	3	36
DDH-GN-42	366	368	P1	0.03	0.04	31	1	164	3	26	3	71
DDH-GN-42	368	370	P1	0.03	0.05	33	1	48	3	24	3	56

Hole_Id	From	To	Rock	Au_g/t	Cu_%	Mo_ppm	Ag_ppm	As_ppm	Bi_ppm	Pb_ppm	Sb_ppm	Zn_ppm
DDH-GN-42	370	372	P3	0.02	0.03	56	1	122	3	8	3	26
DDH-GN-42	372	374	P1	0.04	0.05	25	1	205	3	8	3	20
DDH-GN-42	374	376	P1	0.05	0.05	10	1	141	3	6	3	17
DDH-GN-42	376	378	P1	0.03	0.04	67	1	173	3	8	3	34
DDH-GN-42	378	380	P3	0.04	0.03	28	1	200	3	11	3	85
DDH-GN-42	380	382	P3	0.07	0.07	92	9	518	3	1200	16	2300
DDH-GN-42	382	384	P1	0.05	0.03	10	1	422	3	15	3	202
DDH-GN-42	384	386	P1	0.02	0.04	3	1	316	3	13	3	72
DDH-GN-42	386	388	P3	0.04	0.08	17	2	241	3	24	6	80
DDH-GN-42	388	390	P3	0.05	0.04	1140	1	598	3	11	3	78
DDH-GN-42	390	392	P3	0.02	0.04	19	1	123	3	9	3	44
DDH-GN-42	392	394	P3	0.02	0.05	137	1	131	3	29	3	90
DDH-GN-42	394	396	P1	0.02	0.05	22	2	130	3	9	3	23
DDH-GN-42	396	398	P1	0.02	0.07	22	1	105	3	9	3	22
DDH-GN-42	398	400	P1	0.03	0.06	19	2	356	3	17	18	71
DDH-GN-42	400	402	P1	0.00	0.03	7	2	1620	3	96	18	410
DDH-GN-42	402	404	P1	0.04	0.09	43	17	584	30	300	160	430
DDH-GN-42	404	406	P1	0.02	0.05	18	1	276	3	13	5	60
DDH-GN-42	406	408	P1	0.05	0.04	9	1	732	3	16	3	55
DDH-GN-42	408	410	P1	0.06	0.04	15	3	262	3	38	33	47
DDH-GN-42	410	412	P1	0.02	0.03	12	1	63	3	11	3	26
DDH-GN-42	412	414	P1	0.02	0.08	24	1	89	3	21	3	24
DDH-GN-42	414	416	P1	0.02	0.12	63	5	286	3	86	3	104
DDH-GN-42	416	418	P1	0.01	0.03	10	1	164	3	11	3	28
DDH-GN-42	418	420	P1	0.02	0.08	20	2	198	3	12	3	26
DDH-GN-42	420	422	P1	0.02	0.05	18	1	113	3	7	3	20
DDH-GN-42	422	424	P1	0.03	0.05	6	1	173	3	97	3	172
DDH-GN-42	424	426	P1	0.03	0.04	3	2	309	3	110	3	123
DDH-GN-42	426	428	P1	0.04	0.06	9	1	183	3	15	3	28
DDH-GN-42	428	430	P1	0.06	0.04	10	2	344	3	69	8	80
DDH-GN-42	430	432	P1	0.03	0.03	13	1	122	3	7	3	25
DDH-GN-42	432	434	P1	0.02	0.04	6	1	53	3	6	3	17
DDH-GN-42	434	436	P1	0.02	0.02	6	1	63	3	12	3	21
DDH-GN-42	436	438	P1	0.03	0.10	14	1	139	3	15	3	30
DDH-GN-42	438	440	P1	0.02	0.06	3	1	102	3	10	3	23
DDH-GN-42	440	442	P1	0.02	0.03	5	1	171	3	6	3	19
DDH-GN-42	442	444	P1	0.02	0.02	3	1	177	3	7	3	27
DDH-GN-42	444	446	P1	0.04	0.03	3	3	271	3	46	13	112
DDH-GN-42	446	448	P1	0.02	0.03	6	1	134	3	8	3	25
DDH-GN-42	448	450	P1	0.01	0.03	5	1	92	3	3	3	20
DDH-GN-42	450	452	P1	0.02	0.03	5	2	146	3	13	3	29
DDH-GN-42	452	454	P1	0.01	0.03	3	1	60	3	8	3	33
DDH-GN-42	454	456	P1	0.01	0.03	3	1	84	3	16	3	79
DDH-GN-42	456	458	P1	0.02	0.03	3	2	99	3	10	3	42
DDH-GN-42	458	460	P1	0.03	0.02	3	1	59	3	5	3	29
DDH-GN-42	460	462	P1	0.03	0.03	3	1	79	3	7	3	24
DDH-GN-42	462	464	P1	0.01	0.01	3	1	62	3	5	3	30
DDH-GN-42	464	466	P1	0.04	0.03	7	2	260	3	14	3	70
DDH-GN-42	466	468	P1	0.02	0.01	8	1	123	3	7	3	30
DDH-GN-42	468	470	P1	0.03	0.03	8	1	350	3	11	3	64
DDH-GN-42	470	472	P1	0.01	0.02	6	1	118	3	22	3	54
DDH-GN-42	472	474	P1	0.01	0.03	8	3	93	3	27	13	44
DDH-GN-42	474	476	P1	0.01	0.02	8	2	108	3	14	3	39
DDH-GN-42	476	478	P3	0.03	0.02	3	1	181	3	50	3	171
DDH-GN-42	478	480	P3	0.01	0.01	3	1	37	3	38	3	160
DDH-GN-42	480	482	P3	0.01	0.02	3	3	186	3	106	12	199
DDH-GN-42	482	484	P3	0.01	0.01	3	1	41	3	8	3	144
DDH-GN-42	484	486	P3	0.01	0.03	8	3	63	3	63	11	157
DDH-GN-42	486	488	P1	0.02	0.05	11	6	256	3	50	39	90
DDH-GN-42	488	490	P1	0.03	0.02	15	2	91	3	22	3	67
DDH-GN-42	490	492	P1	0.02	0.02	7	2	86	3	13	3	34
DDH-GN-42	492	494	P1	0.01	0.01	10	1	46	3	6	3	29
DDH-GN-42	494	496	P1	0.01	0.02	7	1	85	3	9	3	28
DDH-GN-42	496	498	P1	0.02	0.02	7	1	57	3	10	3	45
DDH-GN-42	498	499	P1	0.01	0.01	5	1	46	3	5	3	38

Hole_Id	From	To	Rock	Au_g/t	Cu_%	Mo_ppm	Ag_ppm	As_ppm	Bi_ppm	Pb_ppm	Sb_ppm	Zn_ppm
DDH-GN-46	0	2	P1	0.23	0.03	197	1	23	3	13	3	38
DDH-GN-46	2	4	P1	0.17	0.11	218	1	23	3	35	3	38
DDH-GN-46	4	6	P1	0.17	0.03	117	1	10	3	17	3	41
DDH-GN-46	6	8	P1	0.16	0.03	169	1	10	3	14	3	34
DDH-GN-46	8	10	P1	0.29	0.11	351	4	40	3	158	3	74
DDH-GN-46	10	12	P1	0.22	0.05	152	1	22	3	40	3	28
DDH-GN-46	12	14	P1	0.07	0.62	349	4	45	3	363	3	513
DDH-GN-46	14	16	P1	0.30	0.22	162	2	35	3	141	3	85
DDH-GN-46	16	18	P1	0.15	0.19	486	2	27	3	119	3	87
DDH-GN-46	18	20	P1	0.10	0.42	243	3	24	3	255	3	214
DDH-GN-46	20	22	P1	0.06	0.49	114	2	53	3	398	3	515
DDH-GN-46	22	24	P1	0.15	0.43	187	1	27	3	103	3	110
DDH-GN-46	24	26	P1	0.13	0.51	463	2	31	3	146	3	268
DDH-GN-46	26	28	P1	0.26	0.43	124	1	10	3	90	3	96
DDH-GN-46	28	30	P1	0.28	0.36	185	1	21	3	44	3	175
DDH-GN-46	30	32	P1	0.28	0.38	150	1	10	3	28	3	57
DDH-GN-46	32	34	P1	0.26	0.44	163	1	39	3	37	3	43
DDH-GN-46	34	36	P1	0.08	0.31	210	3	92	3	185	3	248
DDH-GN-46	36	38	P1	0.09	0.40	216	3	118	3	363	3	525
DDH-GN-46	38	40	P1	0.18	0.58	222	7	453	3	705	15	544
DDH-GN-46	40	42	P1	0.25	0.58	163	1	51	3	125	3	95
DDH-GN-46	42	44	P1	0.31	0.39	312	1	10	3	28	3	79
DDH-GN-46	44	46	P1	0.15	0.26	227	1	23	3	54	3	93
DDH-GN-46	46	48	P1	0.15	0.30	149	1	26	3	88	3	141
DDH-GN-46	48	50	P1	0.09	0.34	153	1	30	3	135	3	161
DDH-GN-46	50	52	P1	0.20	0.47	185	1	52	3	71	3	79
DDH-GN-46	52	54	P1	0.26	0.44	297	1	23	3	45	3	70
DDH-GN-46	54	56	P1	0.27	0.30	210	1	51	3	112	3	37
DDH-GN-46	56	58	P1	0.30	0.46	623	1	25	3	48	3	72
DDH-GN-46	58	60	P1	0.22	0.35	178	1	31	3	63	3	106
DDH-GN-46	60	62	P1	0.23	0.67	184	1	45	3	132	3	97
DDH-GN-46	62	64	qz	0.09	0.61	139	1	57	3	118	3	88
DDH-GN-46	64	66	qz	0.25	1.05	251	2	392	3	100	6	85
DDH-GN-46	66	68	qz	0.10	0.97	218	1	112	3	71	3	45
DDH-GN-46	68	70	qz	0.13	1.16	116	3	150	3	54	3	62
DDH-GN-46	70	72	qz	0.13	0.73	128	1	98	3	41	3	31
DDH-GN-46	72	74	qz	0.11	0.96	259	2	104	3	31	3	32
DDH-GN-46	74	76	qz	0.08	0.55	151	1	40	3	26	3	17
DDH-GN-46	76	78	qz	0.23	0.40	196	1	24	3	23	3	17
DDH-GN-46	78	80	qz	0.35	0.50	207	1	10	3	19	3	38
DDH-GN-46	80	82	qz	0.28	0.49	358	1	10	3	21	3	21
DDH-GN-46	82	84	qz	0.11	0.52	230	2	67	3	25	3	42

Hole_Id	From	To	Rock	Au_g/t	Cu_%	Mo_ppm	Ag_ppm	As_ppm	Bi_ppm	Pb_ppm	Sb_ppm	Zn_ppm
DDH-GN-46	84	86	qz	0.12	0.88	153	2	76	3	18	3	26
DDH-GN-46	86	88	qz	0.13	0.64	180	2	62	3	18	3	32
DDH-GN-46	88	90	qz	0.22	0.68	138	1	26	3	22	3	21
DDH-GN-46	90	92	qz	0.19	0.94	200	2	69	3	38	3	33
DDH-GN-46	92	94	qz	0.19	0.54	186	1	40	3	19	3	32
DDH-GN-46	94	96	qz	0.46	0.73	285	3	52	3	22	3	51
DDH-GN-46	96	98	qz	0.32	0.38	223	1	32	3	16	3	25
DDH-GN-46	98	100	qz	0.19	0.59	171	3	95	3	20	3	67
DDH-GN-46	100	102	qz	0.08	0.52	136	3	77	3	28	3	77
DDH-GN-46	102	104	qz	0.09	0.60	252	3	67	3	28	3	83
DDH-GN-46	104	106	qz	0.13	0.55	176	3	68	3	21	3	49
DDH-GN-46	106	108	qz	0.09	0.45	191	2	48	3	57	3	110
DDH-GN-46	108	110	qz	0.13	0.41	163	2	32	3	22	3	71
DDH-GN-46	110	112	qz	0.14	0.58	177	4	136	3	28	3	77
DDH-GN-46	112	114	qz	0.18	0.56	202	4	99	3	28	3	57
DDH-GN-46	114	116	qz	0.18	0.50	326	2	43	3	18	3	43
DDH-GN-46	116	118	qz	0.16	0.56	168	3	115	3	21	3	62
DDH-GN-46	118	120	qz	0.07	0.62	140	4	236	3	29	3	107
DDH-GN-46	120	122	qz	0.08	0.64	196	4	244	3	22	3	72
DDH-GN-46	122	124	qz	0.10	0.66	300	4	64	3	34	3	236
DDH-GN-46	124	126	qz	0.19	0.93	243	6	108	3	32	3	172
DDH-GN-46	126	128	qz	0.07	0.67	257	3	51	3	29	3	410
DDH-GN-46	128	130	qz	0.16	0.71	278	3	62	3	37	3	159
DDH-GN-46	130	132	qz	0.17	0.54	240	3	30	3	27	3	62
DDH-GN-46	132	134	qz	0.16	0.49	252	2	20	3	18	3	73
DDH-GN-46	134	136	qz	0.18	0.51	279	2	10	3	16	3	86
DDH-GN-46	136	138	qz	0.29	0.55	290	2	10	3	16	3	68
DDH-GN-46	138	140	qz	0.28	0.82	400	4	52	3	70	3	303
DDH-GN-46	140	142	qz	0.20	1.06	311	7	112	3	37	3	132
DDH-GN-46	142	144	qz	0.47	0.84	227	4	34	3	18	3	86
DDH-GN-46	144	146	qz	0.40	0.61	268	3	29	3	17	3	107
DDH-GN-46	146	148	qz	0.36	0.67	246	3	24	3	17	3	50
DDH-GN-46	148	150	qz	0.40	1.10	209	5	39	3	22	3	101
DDH-GN-46	150	152	qz	0.34	0.98	276	5	48	3	16	3	81
DDH-GN-46	152	154	qz	0.30	0.55	247	3	20	3	17	3	44
DDH-GN-46	154	156	P1	0.10	0.60	696	4	64	3	47	3	60
DDH-GN-46	156	158	P1	0.08	0.54	386	8	145	3	68	3	79
DDH-GN-46	158	160	P1	0.14	0.56	277	5	89	3	33	3	86
DDH-GN-46	160	162	P1	0.10	0.52	248	4	70	3	65	3	129
DDH-GN-46	162	164	P1	0.22	0.82	320	6	31	3	46	3	121
DDH-GN-46	164	166	P1	0.15	0.48	201	4	24	3	31	3	106
DDH-GN-46	166	168	P1	0.10	0.83	307	6	133	3	37	3	94
DDH-GN-46	168	170	P1	0.20	0.87	224	5	103	3	41	3	92
DDH-GN-46	170	172	P1	0.11	1.08	114	5	76	3	39	3	82
DDH-GN-46	172	174	P1	0.10	0.75	350	4	54	3	39	3	82
DDH-GN-46	174	176	P1	0.13	0.65	138	4	97	3	55	3	78
DDH-GN-46	176	178	P1	0.07	0.50	197	3	58	3	41	3	66
DDH-GN-46	178	180	P1	0.26	0.64	144	3	28	3	22	3	67
DDH-GN-46	180	182	P1	0.23	0.78	206	4	43	3	54	3	104
DDH-GN-46	182	184	P1	0.16	1.14	188	7	205	3	89	3	157
DDH-GN-46	184	186	P1	0.16	0.70	270	5	62	3	32	3	65
DDH-GN-46	186	188	P1	0.16	0.39	142	2	44	3	31	3	134
DDH-GN-46	188	190	P1	0.34	0.43	130	2	10	3	27	3	64
DDH-GN-46	190	192	qz	0.29	0.43	153	2	23	3	25	3	51
DDH-GN-46	192	194	qz	0.12	0.44	213	2	75	3	64	3	105
DDH-GN-46	194	196	qz	0.08	0.34	86	3	82	3	39	3	249
DDH-GN-46	196	198	qz	0.07	0.42	174	4	231	3	46	3	70
DDH-GN-46	198	200	qz	0.09	0.53	180	3	95	3	20	3	45
DDH-GN-46	200	202	qz	0.07	0.42	155	3	92	3	28	3	43
DDH-GN-46	202	204	qz	0.28	0.56	278	2	28	3	17	3	57
DDH-GN-46	204	206	qz	0.35	0.71	226	6	333	3	113	3	108
DDH-GN-46	206	208	qz	0.04	0.33	120	2	30	3	22	3	34
DDH-GN-46	208	210	qz	0.13	0.43	179	2	26	3	18	3	40
DDH-GN-46	210	212	qz	0.11	0.54	93	3	33	3	15	3	40
DDH-GN-46	212	214	qz	0.16	0.45	169	3	40	3	17	3	46
DDH-GN-46	214	216	qz	0.30	0.46	257	2	25	3	14	3	43
DDH-GN-46	216	218	qz	0.10	0.66	89	6	135	3	119	3	209
DDH-GN-46	218	220	qz	0.12	0.34	198	2	28	3	17	3	106
DDH-GN-46	220	222	qz	0.03	0.26	167	3	114	3	46	3	71
DDH-GN-46	222	224	qz	0.14	0.30	95	2	10	3	17	3	22
DDH-GN-46	224	226	qz	0.34	0.70	112	4	89	3	22	3	80
DDH-GN-46	226	228	qz	0.17	0.56	150	4	339	3	99	3	145
DDH-GN-46	228	230	qz	0.06	0.31	109	1	10	3	19	3	21
DDH-GN-46	230	232	qz	0.16	0.51	148	2	32	3	16	3	39
DDH-GN-46	232	234	qz	0.25	0.65	179	4	192	3	21	3	57
DDH-GN-46	234	236	qz	0.13	0.65	327	4	136	3	50	13	49
DDH-GN-46	236	238	qz	0.31	0.95	216	8	267	3	29	24	87
DDH-GN-46	238	240	qz	0.51	0.91	149	6	61	3	14	3	75
DDH-GN-46	240	242	qz	0.20	0.72	127	4	31	3	19	3	65
DDH-GN-46	242	244	qz	0.37	0.71	162	3	31	3	14	3	78
DDH-GN-46	244	246	P1	0.31	0.59	143	3	28	3	17	3	124
DDH-GN-46	246	248	qz	0.58	0.96	177	4	46	3	13	3	65
DDH-GN-46	248	250	qz	0.50	0.88	127	4	42	3	14	3	70

Hole_Id	From	To	Rock	Au_g/t	Cu_%	Mo_ppm	Ag_ppm	As_ppm	Bi_ppm	Pb_ppm	Sb_ppm	Zn_ppm
DDH-GN-50	0	2	qz	0.02	0.01	1	10	59	-5	12	-5	13
DDH-GN-50	2	4	qz	0.03	0.03	0	28	15	-5	6	-5	10
DDH-GN-50	4	6	qz	0.01	0.02	0	10	5	-5	9	-5	7
DDH-GN-50	6	8	qz	0.01	0.00	0	24	5	-5	8	-5	8
DDH-GN-50	8	10	qz	0.01	0.01	0	10	7	-5	20	-5	6
DDH-GN-50	10	12	qz	0.01	0.00	0	6	6	-5	66	-5	7
DDH-GN-50	12	14	qz	0.01	0.00	0	7	4	-5	32	-5	8
DDH-GN-50	14	16	qz	0.01	0.01	0	70	9	-5	51	-5	9
DDH-GN-50	16	18	qz	0.01	0.01	0	58	3	-5	18	-5	8
DDH-GN-50	18	20	qz	0.01	0.01	1	26	8	-5	81	-5	6
DDH-GN-50	20	22	qz	0.05	0.21	0	35	307		56	-5	11
DDH-GN-50	22	24	qz	0.02	0.11	0	31	91		14	-5	8
DDH-GN-50	24	26	qz	0.03	0.19	1	36	186		15	-5	10
DDH-GN-50	26	28	qz	0.01	0.01	0	17	8	-5	66	-5	6
DDH-GN-50	28	30	qz	0.01	0.01	0	24	11	-5	7	-5	9
DDH-GN-50	30	32	qz	0.01	0.01	0	50	5	-5	41	-5	6
DDH-GN-50	32	34	qz	0.01	0.01	0	29	4	-5	58	-5	6
DDH-GN-50	34	36	qz	0.01	0.01	0	6	7	-5	28	-5	7
DDH-GN-50	36	38	qz	0.01	0.00	0	35	-3	-5	84	-5	6
DDH-GN-50	38	40	qz	0.01	0.00	0	16	-3	-5	3	-5	6
DDH-GN-50	40	42	qz	0.02	0.01	0	63	12	-5	7	-5	7
DDH-GN-50	42	44	qz	0.01	0.02	0	21	19	-5	19	-5	9
DDH-GN-50	44	46	qz	0.01	0.03	0	18	54	-5	38	-5	10
DDH-GN-50	46	48	qz	0.01	0.01	0	79	8	-5	17	-5	7

Hole_Id	From	To	Rock	Au_g/t	Cu_%	Mo_ppm	Ag_ppm	As_ppm	Bi_ppm	Pb_ppm	Sb_ppm	Zn_ppm
DDH-GN-50	48	50	qz	0.01	0.01	0	5	10	-5	8	-5	9
DDH-GN-50	50	52	qz	0.01	0.01	0	5	15	-5	28	-5	12
DDH-GN-50	52	54	qz	0.01	0.01	0	4	7	-5	7	-5	9
DDH-GN-50	54	56	qz	0.01	0.01	0	6	5	-5	6	-5	9
DDH-GN-50	56	58	qz	0.03	0.01	0	15	6	-5	7	-5	8
DDH-GN-50	58	60	qz	0.02	0.03	0	6	81	-5	22	6	8
DDH-GN-50	60	62	qz	0.02	0.02	0	15	14	-5	12	-5	7
DDH-GN-50	62	64	qz	0.02	0.02	0	7	14	-5	13	-5	6
DDH-GN-50	64	66	qz	0.03	0.18	0	15	185		14	5	9
DDH-GN-50	66	68	qz	0.03	0.07	0	14	196	-5	-2	7	7
DDH-GN-50	68	70	qz	0.03	0.13	0	26	215		11	-5	14
DDH-GN-50	70	72	qz	0.02	0.12	0	29	275		11	-5	7
DDH-GN-50	72	74	qz	0.03	0.09	0	12	201	-5	36	-5	10
DDH-GN-50	74	76	qz	0.03	0.05	0	9	137	-5	8	-5	8
DDH-GN-50	76	78	qz	0.02	0.21	0	20	546		9	-5	14
DDH-GN-50	78	80	qz	0.02	0.10	0	20	229		8	-5	10
DDH-GN-50	80	82	qz	0.01	0.01	0	22	16	-5	15	-5	6
DDH-GN-50	82	84	qz	0.01	0.01	0	12	18	-5	9	-5	6
DDH-GN-50	84	86	qz	0.01	0.01	0	8	19	-5	9	-5	5
DDH-GN-50	86	88	qz	0.01	0.01	0	11	8	-5	35	-5	7
DDH-GN-50	88	90	qz	0.02	0.02	0	4	27	-5	11	-5	8
DDH-GN-50	90	92	qz	0.01	0.03	0	21	35	-5	20	-5	10
DDH-GN-50	92	94	qz	0.01	0.02	0	10	19	-5	34	-5	8
DDH-GN-50	94	96	qz	0.02	0.03	0	9	26	-5	9	-5	8
DDH-GN-50	96	98	qz	0.01	0.04	0	21	101	-5	8	-5	6
DDH-GN-50	98	100	qz	0.02	0.06	0	9	87	-5	12	6	21
DDH-GN-50	100	102	qz	0.02	0.05	0	7	73	-5	12	-5	10
DDH-GN-50	102	104	qz	0.02	0.05	0	24	122	-5	15	-5	17
DDH-GN-50	104	106	qz	0.02	0.05	0	6	157	-5	40	-5	11
DDH-GN-50	106	108	qz	0.02	0.11	1	21	240		19	8	16
DDH-GN-50	108	110	qz	0.02	0.04	0	32	137	-5	18	-5	10
DDH-GN-50	110	112	qz	0.01	0.50	13	16	1560		61	136	111
DDH-GN-50	112	114	qz	0.02	0.06	1	49	149	-5	16	8	10
DDH-GN-50	114	116	qz	0.03	0.06	0	21	147	-5	10	-5	9
DDH-GN-50	116	118	qz	0.01	0.02	0	7	49	-5	16	-5	7
DDH-GN-50	118	120	qz	0.01	0.02	0	123	29	-5	-2	-5	6
DDH-GN-50	120	122	qz	0.01	0.02	0	11	39	-5	10	-5	7
DDH-GN-50	122	124	qz	0.01	0.03	0	50	61	-5	23	-5	13
DDH-GN-50	124	126	qz	0.01	0.06	0	58	111	-5	9	-5	9
DDH-GN-50	126	128	qz	0.01	0.08	0	15	208	-5	8	-5	11
DDH-GN-50	128	130	qz	0.01	0.05	0	94	37	-5	8	-5	7
DDH-GN-50	130	132	qz	0.01	0.03	1	61	76	-5	22	10	42
DDH-GN-50	132	134	qz	0.01	0.21	6	39	668		34	121	144
DDH-GN-50	134	136	qz	0.02	0.15	3	28	418		44	68	160
DDH-GN-50	136	138	qz	0.02	0.04	1	102	92	-5	28	23	87
DDH-GN-50	138	140	qz	0.03	0.06	1	104	179	-5	28	21	75
DDH-GN-50	140	142	qz	0.02	0.10	3	41	309		35	59	179
DDH-GN-50	142	144	qz	0.02	0.20	3	79	491		20	65	209
DDH-GN-50	144	146	qz	0.01	0.13	3	94	346		14	50	114
DDH-GN-50	146	148	qz	0.02	0.27	5	82	799		17	101	213
DDH-GN-50	148	150	qz	0.03	0.20	3	142	603		14	47	117
DDH-GN-50	150	152	qz	0.04	0.27	4	366	785		16	76	233
DDH-GN-50	152	154	qz	0.02	0.26	1	59	122		20	6	65
DDH-GN-50	154	156	qz	0.02	0.19	2	78	198		21	25	70
DDH-GN-50	156	158	qz	0.01	0.26	2	157	282		17	52	122
DDH-GN-50	158	160	qz	0.01	0.32	1	216	314		53	13	92
DDH-GN-50	160	162	qz	0.01	0.26	1	65	296		15	7	66
DDH-GN-50	162	164	qz	0.03	0.38	2	71	330		10	6	132
DDH-GN-50	164	166	qz	0.07	0.55	4	143	617		58	26	498
DDH-GN-50	166	168	qz	0.05	0.41	2	310	413		23	6	187
DDH-GN-50	168	170	qz	0.03	0.28	1	273	143		21	-5	88
DDH-GN-50	170	172	qz	0.02	0.24	1	126	24		15	-5	74
DDH-GN-50	172	174	qz	0.06	0.75	13	142	1340		26	303	486
DDH-GN-50	174	176	qz	0.03	0.35	1	193	105		10	6	63
DDH-GN-50	176	178	qz	0.03	0.33	1	154	24		12	-5	49
DDH-GN-50	178	180	qz	0.03	0.23	1	136	5		25	-5	80
DDH-GN-50	180	182	qz	0.02	0.20	1	242	4		8	-5	35
DDH-GN-50	182	184	qz	0.01	0.22	1	220	44		25	-5	41
DDH-GN-50	184	186	qz	0.04	0.31	8	192	925		53	125	396
DDH-GN-50	186	188	qz	0.03	0.27	4	166	736		64	40	236
DDH-GN-50	188	190	qz	0.03	0.27	1	93	15		17	-5	51
DDH-GN-50	190	192	qz	0.02	0.27	1	75	5		10	-5	50
DDH-GN-50	192	194	qz	0.02	0.25	1	96	91		42	-5	60
DDH-GN-50	194	196	qz	0.02	0.26	1	257	194		8	6	78
DDH-GN-50	196	198	qz	0.07	0.33	1	134	-3		17	-5	23
DDH-GN-50	198	200	qz	0.07	0.44	1	202	6		13	-5	51
DDH-GN-50	200	202	qz	0.12	0.48	1	784	-3		14	-5	57
DDH-GN-50	202	204	qz	0.02	0.25	2	174	402		25	10	92
DDH-GN-50	204	206	qz	0.01	0.24	1	210	321		29	6	59
DDH-GN-50	206	208	qz	0.03	0.26	1	185	205		36	10	95
DDH-GN-50	208	210	qz	0.03	0.41	1	305	22		21	-5	53
DDH-GN-50	210	212	qz	0.03	0.43	1	359	46		12	-5	42
DDH-GN-50	212	214	qz	0.02	0.44	1	432	56		22	-5	51
DDH-GN-50	214	216	qz	0.03	0.44	2	274	544		28	6	77
DDH-GN-50	216	218	Flt Zone	0.12	0.50	2	528	236		14	-5	38
DDH-GN-50	218	220	qz	0.03	0.38	3	124	842		23	16	125
DDH-GN-50	220	222	qz	0.06	0.53	2	114	406		36	5	63
DDH-GN-50	222	224	Flt Zone	0.11	0.69	3	246	28		40	-5	41
DDH-GN-50	224	226	Flt Zone	0.19	0.55	2	235	16		27	-5	35
DDH-GN-50	226	228	Flt Zone	0.03	0.61	2	416	120		30	-5	35
DDH-GN-50	228	230	Flt Zone	0.11	0.41	1	153	9		6	-5	20
DDH-GN-50	230	232	Flt Zone	0.11	0.56	2	218	159		5	-5	31

APPENDIX D3

X-ray diffraction analyses

Analytical Techniques for X-Ray Diffraction

Four samples from the El Galeno deposit and two from Michiquillay were selected for X-ray diffraction (XRD) analyses. Samples were crushed into a fine powder using in a clean agate bowl and a Rocklabs mill. Splits of the crushed samples were lightly pressed onto a glass disk and analysed using a Siemens D-5000 X-ray diffractometer in the Advance Analytical Centre (AAC) lab at James Cook University. Mineralogical phases were deduced using the computer software programme Eva. The programme matches diffraction patterns and peaks with reference patterns.

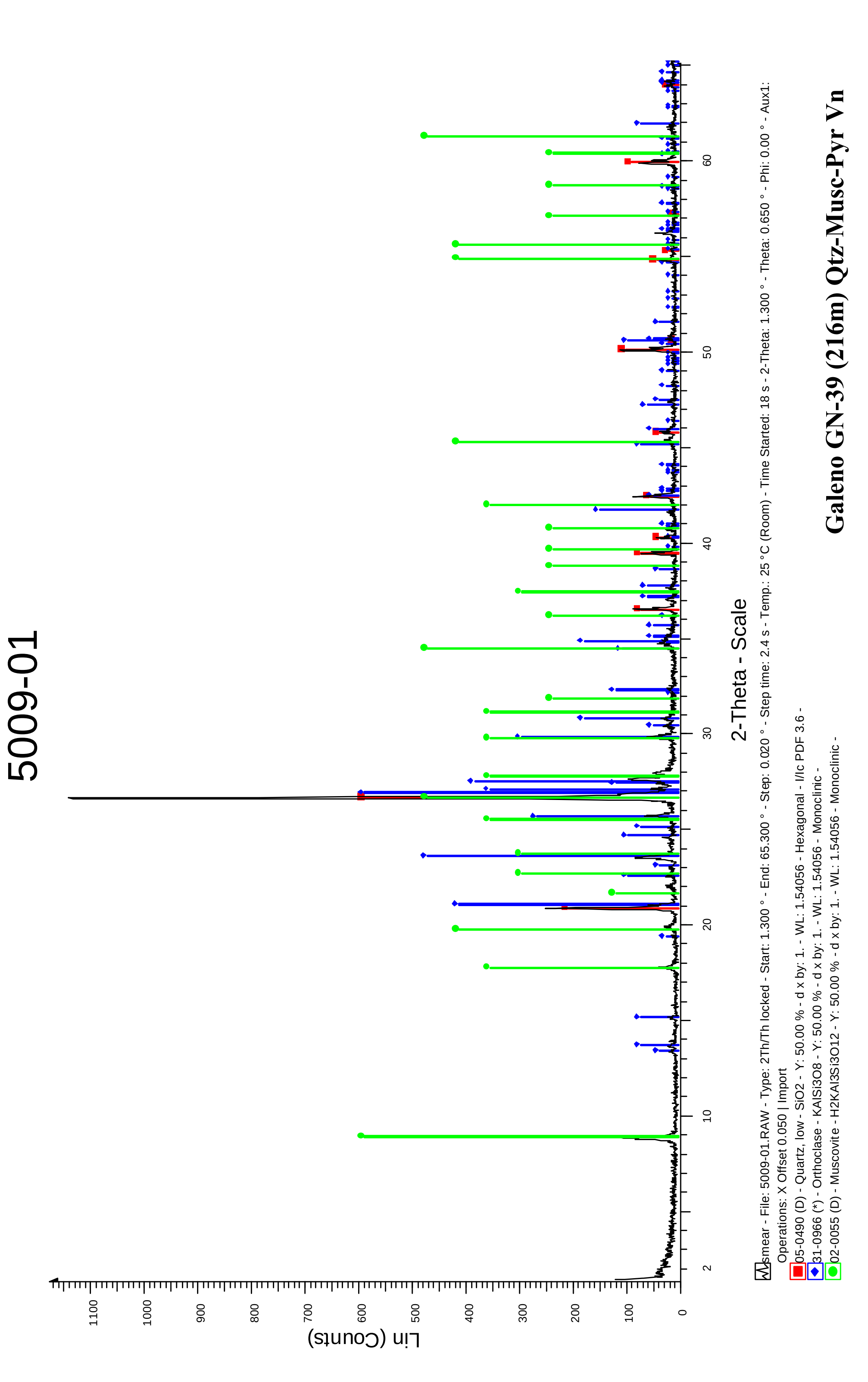
5009-01
Lin (Counts)
2-Theta - Scale
Galeno GN-39 (216m) Qtz-Musc-Pyr Vn
smear - File: 5009-01.RAW - Type: 2Th/Th locked - Start: 1.300 ° - End: 65.300 ° - Step: 0.020 ° - Step time: 2.4 s - Temp.: 25 °C (Room) - Time Started: 18 s - 2-Theta: 1.300 ° - Theta: 0.650 ° - Phi: 0.00 ° - Aux1:
Operations: X Offset 0.050 | Import
05-0490 (D) - Quartz, low - SiO2 - Y: 50.00 % - d x by: 1. - WL: 1.54056 - Hexagonal - I/Ic PDF 3.6 -
31-0966 (*) - Orthoclase - KAlSi3O8 - Y: 50.00 % - d x by: 1. - WL: 1.54056 - Monoclinic -
02-0055 (D) - Muscovite - H2KAl3Si3O12 - Y: 50.00 % - d x by: 1. - WL: 1.54056 - Monoclinic -

5009-02

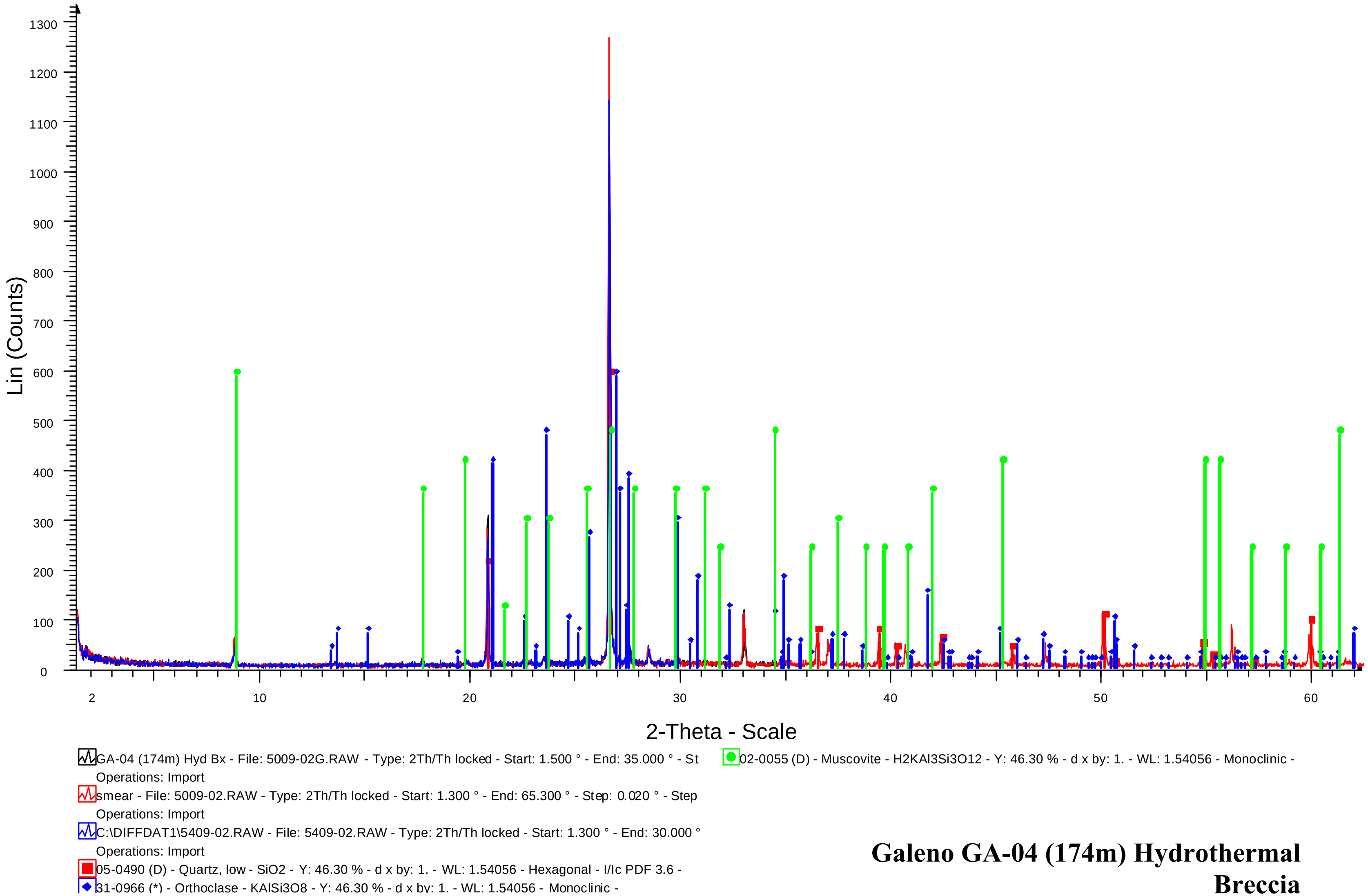

Galeno GA-04 (174m) Hydrothermal Breccia

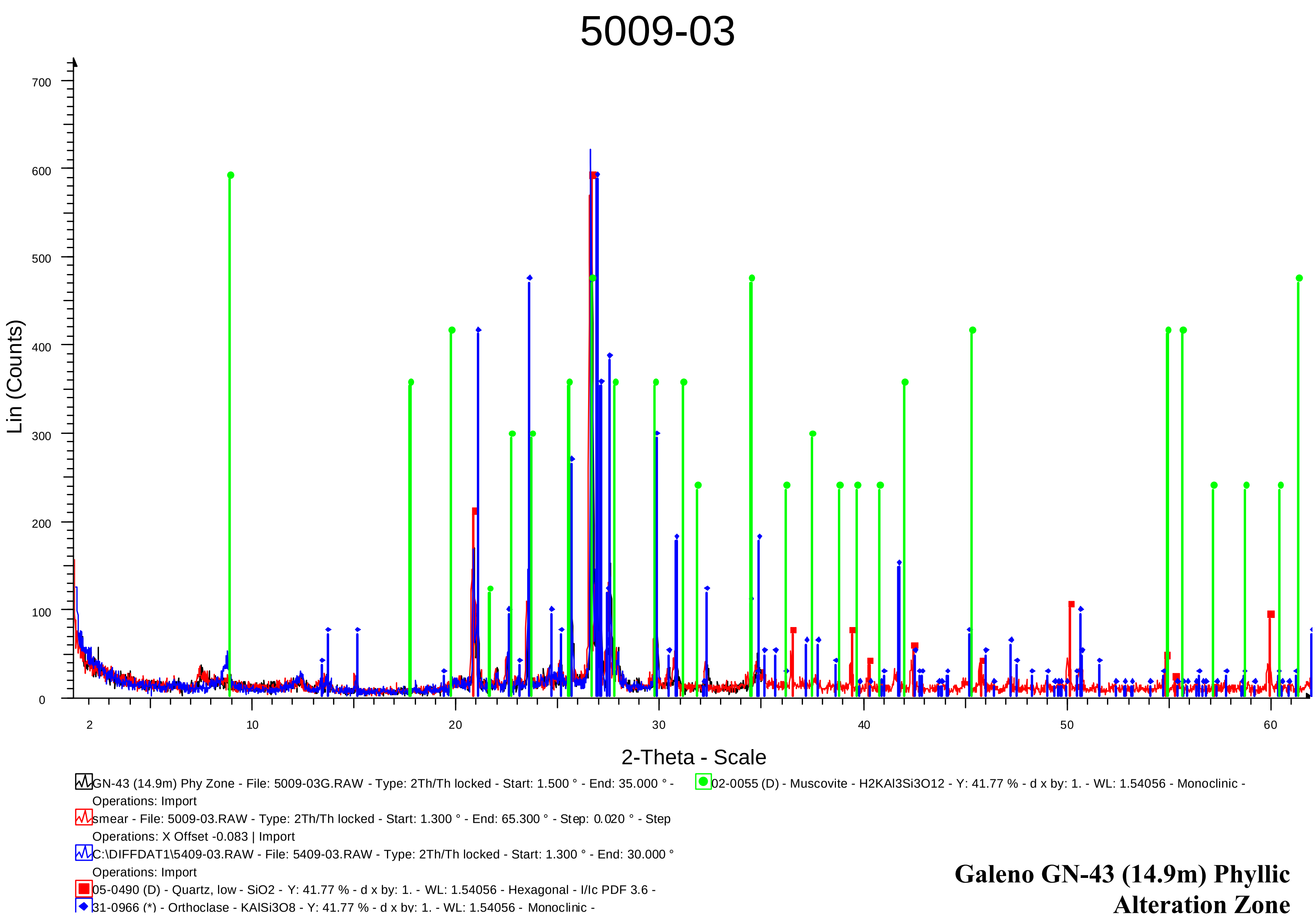

Galeno GN-43 (14.9m) Phyllic Alteration Zone

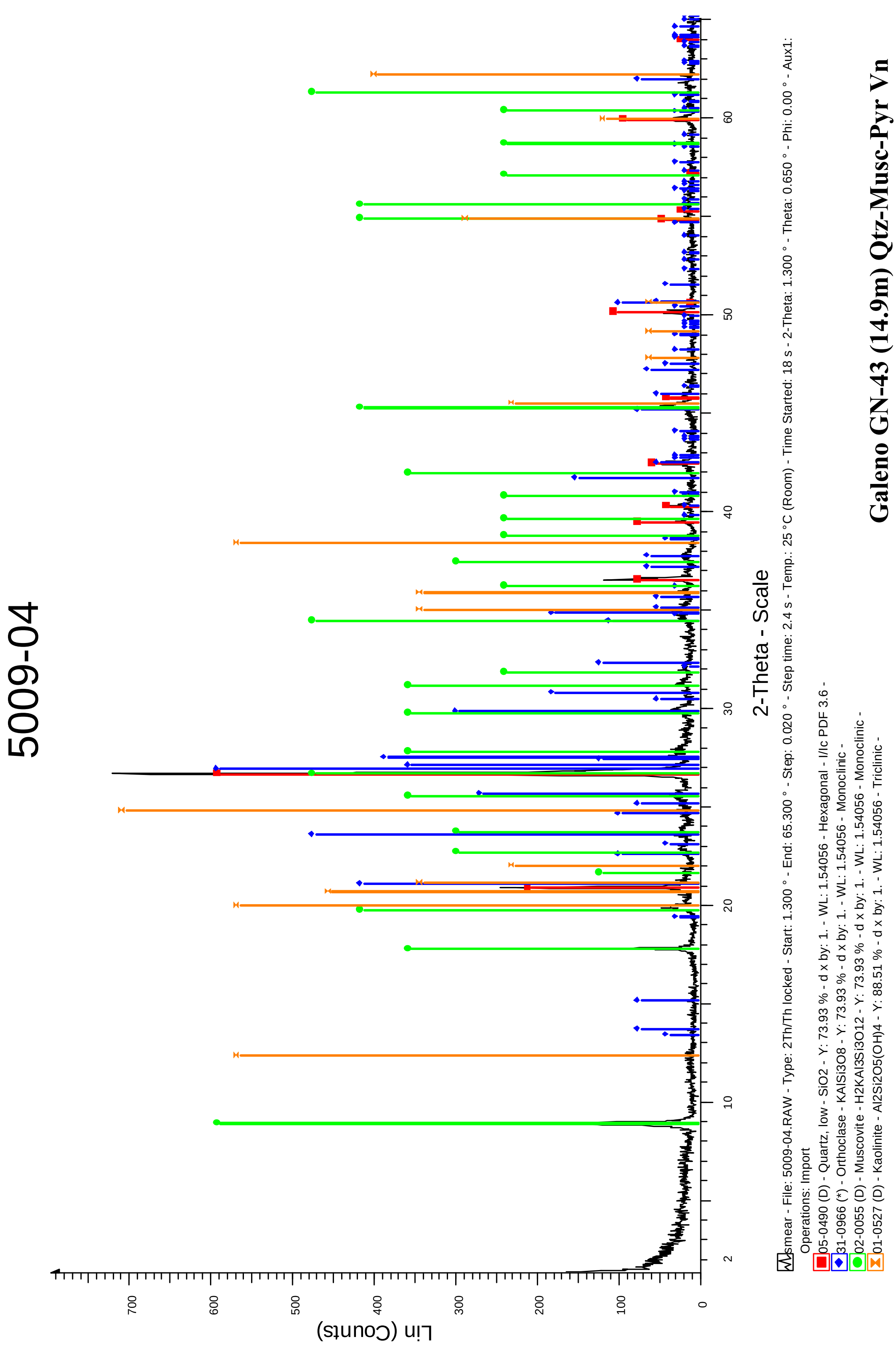
5009-04
Lin (Counts)
0
100
200
300
400
500
600
700
2
10
20
30
40
50
60
2-Theta - Scale
smear - File: 5009-04.RAW - Type: 2Th/Th locked - Start: 1.300 ° - End: 65.300 ° - Step: 0.020 ° - Step time: 2.4 s - Temp.: 25 °C (Room) - Time Started: 18 s - 2-Theta: 1.300 ° - Theta: 0.650 ° - Phi: 0.00 ° - Aux1:
Operations: Import
05-0490 (D) - Quartz, low - SiO2 - Y: 73.93 % - d x by: 1. - WL: 1.54056 - Hexagonal - I/Ic PDF 3.6 -
31-0966 (*) - Orthoclase - KAlSi3O8 - Y: 73.93 % - d x by: 1. - WL: 1.54056 - Monoclinic -
02-0055 (D) - Muscovite - H2KAl3Si3O12 - Y: 73.93 % - d x by: 1. - WL: 1.54056 - Monoclinic -
01-0527 (D) - Kaolinite - Al2Si2O5(OH)4 - Y: 88.51 % - d x by: 1. - WL: 1.54056 - Triclinic -
Galeno GN-43 (14.9m) Qtz-Musc-Pyr Vn

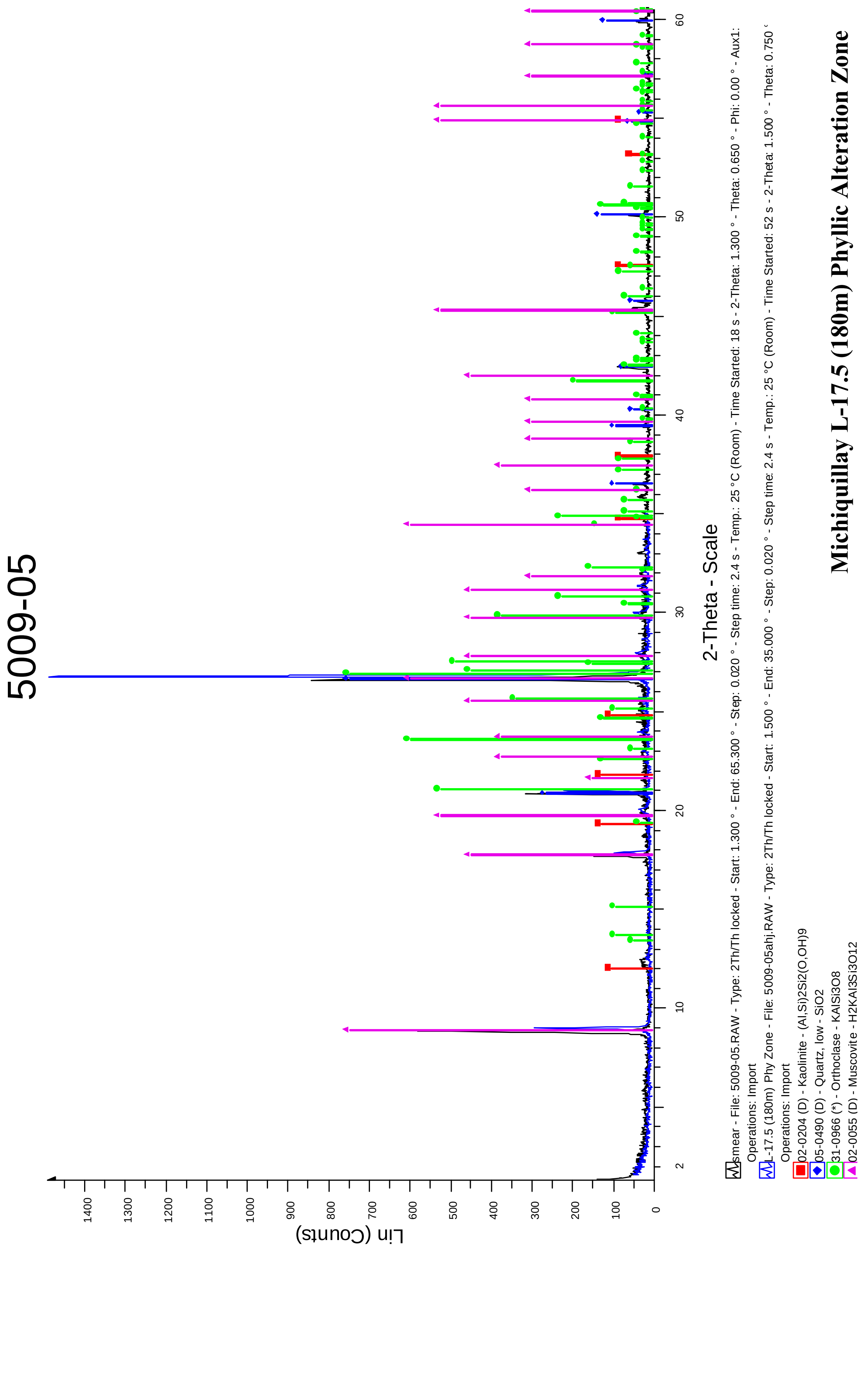

Michiquillay L-17.5 (180m) Phyllic Alteration Zone

5009-06

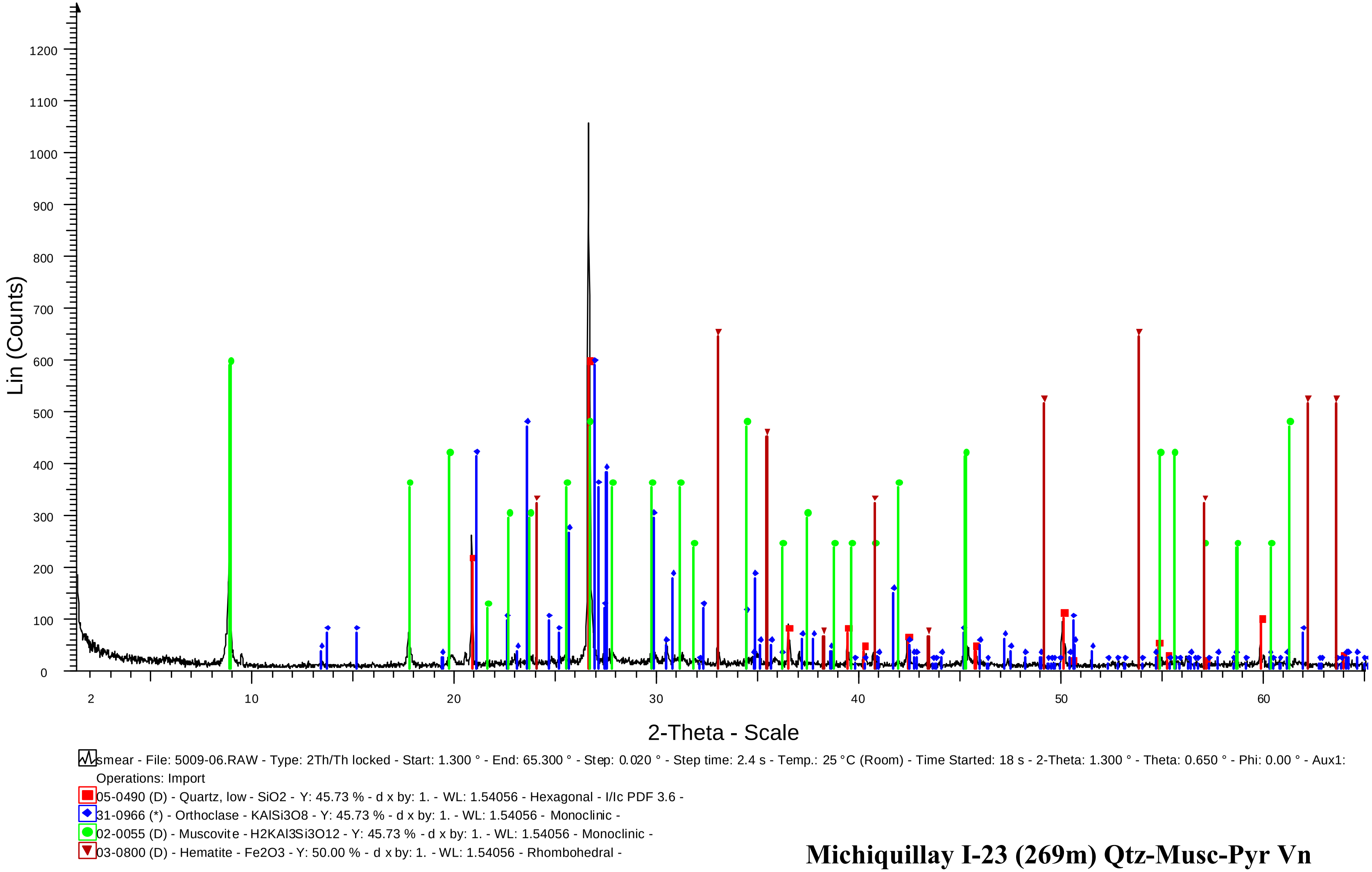

Michiquillay I-23 (269m) Qtz-Musc-Pyr Vn

Appendix D4

Michiquillay drill core geology and assay data

Hole N°	From	To	Rock	Altn	Altn 2	$Cu\_\%_1$	$Au(ppb)_2$	$Ag(ppm)_2$	$Cu\_\%_2$	$Zn(ppm)_2$	$Mo(ppm)_2$
H-22	3	5	D1	k	phyl	0.65	168	1.6	1.02	95	55
H-22	5	8	D1	k	phyl	0.76					
H-22	8	9	D1	k	phyl	0.66					
H-22	9	11	D1	k	phyl	0.64					
H-22	11	14	D1	k	phyl	1.35					
H-22	14	16	D1	k	phyl	1.09					
H-22	16	18	D1	k	phyl	1.15					
H-22	18	21	D1	k	phyl	1.33	177	2.6	1.04	206	54
H-22	21	24	D1	k	phyl	1.40					
H-22	24	27	D1	k	phyl	1.23					
H-22	27	29	D1	k	phyl	1.05					
H-22	29	32	D1	k	phyl	1.12					
H-22	32	34	D1	k	phyl	1.43	266	2.8	1.22	50	44
H-22	34	38	D1	k	phyl	1.40					
H-22	38	41	D1	k	phyl	1.70					
H-22	41	44	D1	k	phyl	1.35					
H-22	44	47	D1	k	phyl	1.29					
H-22	47	50	D1	k	phyl	1.27	94	3.4	0.87	89	35
H-22	50	52	qz	phyl	arg	0.93					
H-22	52	55	qz	phyl	arg	1.18					
H-22	55	58	qz	phyl	arg	0.81					
H-22	58	62	qz	phyl	arg	0.93					
H-22	62	65	qz	phyl	arg	0.88	77	3.2	0.81	91	36
H-22	65	67	qz	phyl	arg	0.78					
H-22	67	71	qz	phyl	arg	0.81					
H-22	71	75	qz	phyl	arg	1.06					
H-22	75	78	qz	phyl	arg	1.03					
H-22	78	81	qz	phyl	arg	0.88	80	1.8	0.81	54	36
H-22	81	84	qz	phyl	arg	0.80					
H-22	84	87	qz + Dyke	phyl	k	0.78					
H-22	87	88	qz	phyl	arg	0.93					
H-22	88	91	qz	phyl	arg	0.83					
H-22	91	94	qz	phyl	arg	0.87	86	2.3	0.82	65	25
H-22	94	98	qz	phyl	arg	0.88					
H-22	98	102	qz	phyl	arg	0.71					
H-22	102	105	qz + D1	phyl	arg	1.16					
H-22	105	108	qz	phyl	arg	0.89					
H-22	108	111	qz	phyl	arg	1.06	121	2.8	1.06	106	76
H-22	111	114	qz	phyl	arg	1.30					
H-22	114	115	qz	phyl	arg	1.17					
H-22	115	119	qz	phyl	arg	1.05					
H-22	119	122	qz	phyl	arg	1.16					
H-22	122	125	qz	phyl	arg	0.95	68	1.4	0.89	72	47
H-22	125	127	qz	phyl	arg	1.15					
H-22	127	131	qz	phyl	arg	1.07					
H-22	131	134	qz	phyl	arg	1.05					
H-22	134	137	qz	phyl	arg	0.88					
H-22	137	140	qz	phyl	arg	0.77	40	0.3	0.20	46	26
H-22	140	143	Dyke	k		0.82					
H-22	143	146	D1	k	phyl	0.29					
H-22	146	149	Dyke	k		0.15					
H-22	149	152	D1	k	phyl	0.08					
H-22	152	154	D1	k	phyl	0.14	66	0.4	0.11	47	12
H-22	154	158	Dyke	k		0.09					
H-22	158	161	Dyke	k		0.21					
H-22	161	164	Dyke	k		0.11					
H-22	164	167	Dyke	k		0.05					
H-22	167	170	D1	k	phyl	0.14	36	-0.3	0.05	40	8
H-22	170	173	D1	k	phyl	0.08					
H-22	173	176	D1	k	phyl	0.06					
H-22	176	178	D1	k	phyl	0.05					
H-22	178	181	Dyke	k		0.06					
H-22	181	184	Dyke	k		0.11					
H-22	184	186	Dyke	k		0.09	32	-0.3	0.06	31	22
H-22	186	189	Dyke	k		0.13					
H-22	189	191	D1	k	phyl	0.07					
H-22	191	194	D1	k	phyl	0.08					
H-22	194	197	D1	k	phyl	0.05					
H-22	197	200	D1	k	phyl	0.04	35	-0.3	0.07	24	6
H-22	200	203	D1	k	phyl	0.06					
H-22	203	205	D1	k	phyl	0.06					
H-22	205	208	Dyke	k		0.04					
H-22	208	210	Dyke	k		0.10					
H-22	210	213	Dyke	k		0.14					
H-22	213	216	Dyke	k		0.12	36	0.3	0.11	41	11
H-22	216	219	Dyke	k		0.07					
H-22	219	221	Dyke	k		0.12					
H-22	221	222	Dyke	k		0.12					
H-22	222	224	Dyke	k		0.17					
H-22	224	227	Dyke	k		0.26					
H-22	227	230	Dyke	k		0.15	33	-0.3	0.11	28	36
H-22	230	234	D1	k		0.17					
H-22	234	237	Dyke	k		0.13					
H-22	237	240	Dyke	k		0.11					
H-22	240	244	Dyke	k		0.12					
H-22	244	247	Dyke	k		0.36	87	0.9	0.51	36	59
H-22	247	249	Dyke	k		0.31					
H-22	249	252	Dyke	k		0.10					
H-22	252	255	Dyke	k		0.86					

Hole N°	From	To	Rock	Altn	Altn 2	Cu_%$_1$	Au(ppb)$_2$	Ag(ppm)$_2$	Cu_%$_2$	Zn(ppm)$_2$	Mo(ppm)$_2$
H-22	255	257	Dyke	k		0.77					
H-22	257	261	Dyke	k		0.95	143	1.2	0.72	22	127
H-22	261	264	D1	k		0.82					
H-22	264	267	D1	k		0.92					
H-22	267	270	D1	k		0.94					
H-22	270	273	D1	k		0.72					
H-22	273	276	Dyke	k		0.18					
H-22	276	278	Dyke	k		0.21					
H-22	278	281	Dyke	k		0.50					
H-22	281	284	D1	k	arg	0.44					

Hole N°	From	To	Rock	Altn	Altn 2	Cu_%$_1$	Au(ppb)$_2$	Ag(ppm)$_2$	Cu_%$_2$	Zn(ppm)$_2$	Mo(ppm)$_2$
I-21	23	27	D1	phyl	k	1.73					
I-21	27	30	D1	phyl	k	0.68					
I-21	30	34	D1	phyl	k	0.73					
I-21	34	36	D1	phyl	k	0.54					
I-21	36	38	D1	phyl	k	1.07					
I-21	38	41	Hydro Bx	phyl		0.45					
I-21	41	44	Hydro Bx	phyl		0.37					
I-21	44	46	Flt Zone	arg		0.49					
I-21	46	50	Flt Zone	arg		0.34					
I-21	50	52	D1	phyl	k	0.28					
I-21	52	55	D1	phyl	k	0.64					
I-21	55	58	D1	phyl	k	0.58					
I-21	58	61	D1	phyl	k	0.55					
I-21	61	66	D1	phyl	k	0.47					
I-21	66	69	D1	k	phyl	0.83					
I-21	69	71	D1	k	phyl	0.43					
I-21	71	74	D1	k	phyl	0.23					
I-21	74	76	D1	k	phyl	0.15					
I-21	76	79	D1	k	phyl	0.10					
I-21	79	80	D1	k	phyl	0.11					
I-21	80	83	D1	k		0.14					
I-21	83	87	D1	k		0.18					
I-21	87	89	D1	k		0.28					
I-21	89	92	D1	k		0.25					
I-21	92	93	D1	k		0.26					
I-21	93	96	D1	k		0.28					
I-21	96	99	D1	k		0.31					
I-21	99	102	D1	k		0.26					
I-21	102	104	D1	k		0.33					
I-21	104	106	D1	k		0.38					
I-21	106	109	D1	k		0.22					
I-21	109	111	D1	k		0.43					
I-21	111	114	D1	k		0.28					
I-21	114	117	D1	k		0.18					
I-21	117	120	D1	k		0.13					
I-21	120	121	D1	k		0.23					

Hole N°	From	To	Rock	Altn	Altn 2	Cu_%$_1$	Au(ppb)$_2$	Ag(ppm)$_2$	Cu_%$_2$	Zn(ppm)$_2$	Mo(ppm)$_2$
J-20	28	31	D1	phyl	k	1.20	164	1.2	0.83	24	76
J-20	31	32	D1	phyl	k	5.16					
J-20	32	35	D1	phyl	k	2.33					
J-20	35	39	D1	phyl	k	1.87					
J-20	39	42	D1	phyl	k	5.55					
J-20	42	45	D1	phyl	k	1.28	195	1.4	0.94	57	146
J-20	45	48	D1	phyl	k	1.15					
J-20	48	51	D1	phyl	k	0.79					
J-20	51	53	D1	phyl	k	0.93					
J-20	53	56	D1	phyl	k	0.84					
J-20	56	59	D1	phyl	k	0.88	161	1.3	0.68	42	25
J-20	59	62	D1	phyl	k	0.78					
J-20	62	64	D1	phyl	k	0.99					
J-20	64	68	D1	phyl	k	1.05					
J-20	68	70	D1	phyl	k	0.87					
J-20	70	73	D1	phyl	k	0.89					
J-20	73	76	D1	phyl	k	0.78	123	1.0	0.59	44	29
J-20	76	78	D1	phyl	k	1.01					
J-20	78	81	D1	phyl	k	1.53					
J-20	81	82	D1	phyl	k	1.28					
J-20	82	85	D1	phyl	k	1.00					
J-20	85	88	D1	phyl	k	0.94	182	1.1	0.84	33	16
J-20	88	91	D1	phyl	k	1.08					
J-20	91	94	D1	phyl	k	0.91					
J-20	94	97	D1	k	phyl	0.74					
J-20	97	98	D1	k	phyl	0.88					
J-20	98	100	D1	k	phyl	1.82					
J-20	100	104	D1	k	phyl	1.26	185	1.5	0.85	61	40
J-20	104	107	D1	k	phyl	0.90					
J-20	107	109	D1	k	phyl	0.65					
J-20	109	112	D1	k	phyl	0.78					
J-20	112	114	D1	k	phyl	1.18					
J-20	114	116	D1	k	phyl	1.11					
J-20	116	119	D1	k	phyl	1.02	198	1.5	0.94	53	40
J-20	119	121	D1	k	phyl	0.96					
J-20	121	124	D1	k	phyl	0.94					
J-20	124	127	D1	k	phyl	0.92					

Hole N°	From	To	Rock	Altn	Altn 2	Cu_%$_1$	Au(ppb)$_2$	Ag(ppm)$_2$	Cu_%$_2$	Zn(ppm)$_2$	Mo(ppm)$_2$
J-20	127	130	D1	k	phyl	1.19					
J-20	130	133	D1	k	phyl	1.16					
J-20	133	136	D1	k	phyl	1.05	228	1.5	1.04	35	97
J-20	136	139	D1	k	phyl	0.85					
J-20	139	141	D1	k	phyl	0.73					
J-20	141	145	D1	k	phyl	0.58					
J-20	145	147	D1	k	phyl	0.90					
J-20	147	150	D1	k	phyl	0.82	235	2.9	1.14	244	31
J-20	150	153	D1	k	phyl	0.85					
J-20	153	155	D1	k	phyl	1.08					
J-20	155	158	D1	k	phyl	0.79					
J-20	158	160	D1	k	phyl	1.14					
J-20	160	163	D1	k	phyl	1.14	92	1.1	0.63	82	87
J-20	163	166	D1	k	phyl	0.92					
J-20	166	169	D1 + Dyke	k		0.99					
J-20	169	172	D1	k	phyl	0.79					
J-20	172	175	D1	k	phyl	0.74					
J-20	175	179	Dyke	k		0.53	140	1.0	0.84	43	57
J-20	179	182	Dyke	k		0.71					
J-20	182	185	D1	k	phyl	0.87					
J-20	185	188	D1	k	phyl	0.77					
J-20	188	191	D1	k	phyl	1.48					
J-20	191	194	D1	k	phyl	1.12	142	1.2	0.74	41	64
J-20	194	198	Dyke	k		0.66					
J-20	198	201	Dyke	k		0.25					
J-20	201	203	D1	k	phyl	0.94					
J-20	203	206	D1	k	phyl	1.00					
J-20	206	209	D1	k		0.78	141	1.0	0.79	19	87
J-20	209	212	D1	k		0.99					
J-20	212	216	D1	k		0.88					
J-20	216	219	D1	k		1.05					
J-20	219	222	D1	k		0.99					
J-20	222	225	D1	k		0.89	162	1.2	0.92	31	58
J-20	225	228	D1	k		0.97					
J-20	228	232	D1	k	phyl	1.14					
J-20	232	235	D1	k	phyl	1.02					
J-20	235	238	D1	k	phyl	1.00					
J-20	238	241	D1	k		0.95	95	0.6	0.55	34	39
J-20	241	244	Dyke	k		0.68					
J-20	244	247	D1	k		1.10					
J-20	247	250	D1	k		0.84					
J-20	250	253	D1	k		1.12					
J-20	253	256	D1	k		0.95	94	0.9	0.72	33	67
J-20	256	259	D1	k		0.97					
J-20	259	262	D1	k		0.97					
J-20	262	265	D1	k		1.28					
J-20	265	268	D1	k		1.44					
J-20	268	271	D1	k		1.56	160	1.0	0.87	30	85
J-20	271	273	D1	k		1.53					
J-20	273	276	D1	k		1.22					
J-20	276	281	D1	k		0.72					
J-20	281	282	D1	k		0.35					
J-20	282	285	D1	k		0.48	91	1.2	0.88	61	69
J-20	285	288	D1	k		0.28					
J-20	288	290	D1	k		0.19					
J-20	290	293	D1	k		0.48					
J-20	293	296	D1	k		0.78					
J-20	296	298	D1	k		1.36	89	1.2	0.77	45	67
J-20	298	301	D1	k		0.93					
J-20	301	304	D1	k		1.00					
J-20	304	308	D1	k		0.83					
J-20	308	310	D1	k		0.88					
J-20	310	313	D1	k		0.82					
J-20	313	315	D1	k		0.80	82	0.8	0.56	34	75
J-20	315	318	D1	k		0.80					
J-20	318	321	D1	k		0.73					
J-20	321	324	D1	k		0.73					
J-20	324	327	D1	k		0.81					
J-20	327	329	D1	k		0.96	95	1.3	0.70	68	124
J-20	329	331	D1	k		0.92					
J-20	331	334	D1	k		1.27					
J-20	334	337	D1	k		1.19					
J-20	337	340	D1	k		0.89					
J-20	340	343	D1	k		0.90	63	0.6	0.53	20	91
J-20	343	346	D1	k		1.24					
J-20	346	349	D1	k		1.07					
J-20	349	352	D1	k		0.85					
J-20	352	353	D1	k		0.56					
J-20	353	357	D1	k		0.49					
J-20	357	359	D1	k		0.55					
J-20	359	364	D1	k		0.51					
J-20	364	367	D1	k		0.85					
J-20	367	369	D1	k		0.52					
J-20	369	372	D1	k		0.59					
J-20	372	375	D1	k		0.74					
J-20	375	377	D1	k		1.00					
J-20	377	380	D1	k		1.13					
J-20	380	382	D1	k		0.75					
J-20	382	386	D1	k		0.82					

Hole N°	From	To	Rock	Altn	Altn 2	Cu_%1	Au(ppb)2	Ag(ppm)2	Cu_%2	Zn(ppm)2	Mo(ppm)2
J-20	386	389	D1	k		1.01					
J-20	389	390	D1	k		0.93					
J-20	390	393	D1	k		1.07					
J-20	393	396	D1	k		0.84					
J-20	396	399	D1	k		0.99					
J-20	399	401	D1	k		0.76					
J-20	401	405	D1	k		1.14					
J-20	405	408	D1	k		0.93					
J-20	408	411	D1	k		0.68					
J-20	411	413	D1	k		0.61					
J-20	413	416	D1	k		0.70					
J-20	416	419	D1	k		1.14					
J-20	419	422	D1	k		0.95					
J-20	422	426	D1	k		0.60					
J-20	426	429	D1	k		0.46					
J-20	429	432	D1	k		0.49					
J-20	432	435	D1	k		0.66					
J-20	435	439	D1	k		0.54					
J-20	439	440	D1	k		0.79					
J-20	440	443	D1	k	phyl	0.55					
J-20	443	446	D1	k		0.71					
J-20	446	449	D1	k		0.65					
J-20	449	453	D1	k		0.85					
J-20	453	456	D1	k		0.65					
J-20	456	459	D1	k		0.64					
J-20	459	463	D1	k		0.49					
J-20	463	466	D1	k		0.59					
J-20	466	469	D1	k		0.41					
J-20	469	471	D1	k		0.48					
J-20	471	474	D1	k		0.46					
J-20	474	477	D1	k		0.70					
J-20	477	481	D1	k		0.70					
J-20	481	483	D1	k		0.69					
J-20	483	486	D1	k		0.60					
J-20	486	489	D1	k		0.59					
J-20	489	491	D1	k		0.58					
J-20	491	495	D1	k		0.72					
J-20	495	499	D1	k	phyl	0.83					
J-20	499	501	D1	k	phyl	0.93					

Hole N°	From	To	Rock	Altn	Altn 2	Cu_%1	Au(ppb)2	Ag(ppm)2	Cu_%2	Zn(ppm)2	Mo(ppm)2
K-19	47	50	D1	phyl	arg	1.32					
K-19	50	53	D1	phyl	arg	1.41					
K-19	53	56	D1	phyl	arg	1.28					
K-19	56	59	D1	phyl	arg	1.27					
K-19	59	62	D1	phyl	arg	1.44					
K-19	62	64	D1	phyl	arg	1.83					
K-19	64	67	D1	phyl	arg	1.61					
K-19	67	70	D1	phyl	arg	1.89					
K-19	70	73	D1	phyl	arg	1.70					
K-19	73	75	D1	phyl	arg	1.17					
K-19	75	78	D1	phyl	arg	1.42					
K-19	78	80	D1	phyl	arg	1.22					
K-19	80	84	D1	phyl	arg	1.06					
K-19	84	87	D1	phyl	arg	1.29					
K-19	87	90	D1	phyl	arg	1.09					
K-19	90	93	D1	phyl	arg	0.59					
K-19	93	96	D1	phyl	arg	0.47					
K-19	96	99	D1	phyl	arg	0.48					
K-19	99	102	D1	phyl	arg	0.80					
K-19	102	103	D1	phyl		0.56					
K-19	103	106	D1	phyl		0.60					
K-19	106	108	D1	phyl		0.55					
K-19	108	111	D1	phyl		0.63					
K-19	111	114	D1	phyl		0.73					
K-19	114	116	D1	phyl		0.64					
K-19	116	119	D1	phyl		0.63					
K-19	119	122	D1	phyl		0.65					
K-19	122	125	D1	phyl		0.81					
K-19	125	128	D1	phyl		0.72					
K-19	128	131	D1	phyl		0.62					
K-19	131	134	D1	phyl		0.69					
K-19	134	137	D1	phyl		0.66					
K-19	137	140	D1	phyl		0.72					
K-19	140	141	D1	phyl		0.60					
K-19	141	143	D1	phyl		0.56					
K-19	143	144	D1	phyl		0.64					
K-19	144	147	D1	phyl		0.69					
K-19	147	150	D1	phyl		0.68					
K-19	150	153	D1	phyl		0.54					
K-19	153	156	D1	phyl		0.67					
K-19	156	159	Flt Zone	arg	phyl	0.74					
K-19	159	162	Flt Zone	arg	phyl	0.90					
K-19	162	165	Flt Zone	arg	phyl	0.75					
K-19	165	166	Flt Zone	arg	phyl	0.69					
K-19	166	169	Flt Zone	arg	phyl	0.54					
K-19	169	171	Flt Zone	arg	phyl	0.48					
K-19	171	172	Flt Zone	arg	phyl	0.38					

Hole N°	From	To	Rock	Altn	Altn 2	$Cu\_\%_1$	$Au(ppb)_2$	$Ag(ppm)_2$	$Cu\_\%_2$	$Zn(ppm)_2$	$Mo(ppm)_2$
K-19	172	174	Flt Zone	arg	phyl	0.22					
K-19	174	175	Flt Zone	arg	phyl	n/a					
K-19	175	177	D1	phyl		0.38					
K-19	177	179	D1	phyl		0.58					
K-19	179	181	D1	phyl		0.64					

Hole N°	From	To	Rock	Altn	Altn 2	$Cu\_\%_1$	$Au(ppb)_2$	$Ag(ppm)_2$	$Cu\_\%_2$	$Zn(ppm)_2$	$Mo(ppm)_2$
K-19.5	0		D1	arg	phyl		122	1.7	1.04	71	304
K-19.5	15		D1	arg	phyl		119	0.8	1.20	26	621
K-19.5	30		D1	arg	phyl		170	1.0	1.09	20	625
K-19.5	45		D1	arg	phyl		133	0.9	0.59	63	536
K-19.5	60		D1 + Flt	arg	phyl		138	1.2	0.64	34	405
K-19.5	75		D1	arg	phyl		145	1.6	0.58	302	683
K-19.5	90		D1	arg	phyl		120	3.0	0.66	371	449
K-19.5	105		D1	arg	phyl		221	2.1	0.71	144	379
K-19.5	120		D1	arg	phyl		114	3.6	0.74	186	505
K-19.5	135		D1	arg	phyl		105	1.3	0.55	65	655
K-19.5	150		D1 + Flt	arg	phyl		138	1.5	0.71	21	669
K-19.5	165		D1	arg	phyl		137	1.3	0.65	75	586
K-19.5	180		D1	arg	phyl		125	1.5	0.68	29	505
K-19.5	195		D1	arg	phyl		382	1.4	0.82	66	864
K-19.5	210		D1	phyl	arg		164	1.8	0.98	55	468
K-19.5	228		D1	phyl	arg		129	1.4	0.79	29	407
K-19.5	245		D1	phyl	arg		180	1.2	0.68	23	452
K-19.5	260		D1	phyl	arg		96	1.1	0.66	32	452
K-19.5	275		D1	phyl	arg		45	2.8	0.33	206	96
K-19.5	290		D1	phyl	arg		69	1.4	0.71	149	216
K-19.5	305		D1	phyl	arg		115	1.5	0.90	497	412
K-19.5	320		D1	phyl	arg		95	1.0	0.76	39	303
K-19.5	335		D1	phyl	arg		81	0.8	0.60	18	209
K-19.5	350		D1	phyl	arg		35	0.6	0.32	53	44
K-19.5	365		D1	phyl	arg		60	0.8	0.47	120	49
K-19.5	380		D1	phyl	arg		68	0.8	0.60	34	47
K-19.5	395		D1	phyl			23	0.5	0.35	30	64
K-19.5	410		D1	phyl			72	0.5	0.37	32	95
K-19.5	425		D1	phyl			40	0.5	0.42	24	104
K-19.5	440		D1	phyl			46	0.6	0.46	30	117
K-19.5	455		D1	phyl			103	0.8	0.63	30	243
K-19.5	470		D1	phyl			76	0.8	0.70	33	196
K-19.5	485		D1	phyl			58	0.6	0.59	31	277
K-19.5	500		D1	phyl			51	0.6	0.61	39	250
K-19.5	515		D1	phyl			49	0.8	0.65	36	142
K-19.5	530		D1	phyl			52	0.9	0.64	69	148

Hole N°	From	To	Rock	Altn	Altn 2	$Cu\_\%_1$	$Au(ppb)_2$	$Ag(ppm)_2$	$Cu\_\%_2$	$Zn(ppm)_2$	$Mo(ppm)_2$
L-17.5	123	126	D1	phyl	arg	0.03					
L-17.5	126	128	D1	phyl	arg	0.05					
L-17.5	128	131	D1	phyl	arg	0.09					
L-17.5	131	137	D1	phyl	arg	0.06					
L-17.5	137	141	D1	phyl	arg	0.08					
L-17.5	141	144	D1	phyl	arg	0.10					
L-17.5	144	147	D1	phyl	arg	0.09					
L-17.5	147	151	D1	phyl	arg	0.09					
L-17.5	151	154	D1	phyl	arg	0.34					
L-17.5	154	157	D1	phyl	arg	0.57					
L-17.5	157	162	D1	phyl	arg	0.91					
L-17.5	162	164	D1	phyl	arg	0.40					
L-17.5	164	165	D1	phyl	arg	0.58					
L-17.5	165	168	D1	phyl	arg	0.85					
L-17.5	168	171	D1	phyl	arg	0.91					
L-17.5	171	173	D1	phyl		0.82					
L-17.5	173	176	D1	phyl		0.29					
L-17.5	176	179	D1	phyl		1.28					
L-17.5	179	182	D1	phyl		1.36					
L-17.5	182	184	D1	phyl		0.53					
L-17.5	184	186	D1	phyl		0.64					
L-17.5	186	190	D1	phyl		0.92					
L-17.5	190	193	D1	phyl		0.79					
L-17.5	193	195	D1	phyl		0.79					
L-17.5	195	196	D1	phyl		0.69					
L-17.5	196	200	D1	phyl		1.06					
L-17.5	200	204	D1	phyl		0.86					
L-17.5	204	207	D1	phyl		0.96					
L-17.5	207	210	D1	phyl		0.94					
L-17.5	210	212	D1	phyl		0.91					
L-17.5	212	215	D1	phyl		0.87					
L-17.5	215	218	D1	phyl		0.72					
L-17.5	218	221	D1	phyl		0.64					
L-17.5	221	224	D1	phyl		0.48					
L-17.5	224	228	D1	arg	phyl	0.44					
L-17.5	228	231	D1	phyl		0.53					
L-17.5	231	233	D1	phyl		0.65					
L-17.5	233	236	D1	phyl		0.68					
L-17.5	236	239	D1	phyl		0.73					
L-17.5	239	242	D1	phyl		0.64					
L-17.5	242	243	D1	phyl		0.44					
L-17.5	243	246	D1	phyl		0.59					

Hole N°	From	To	Rock	Altn	Altn 2	Cu_%1	Au(ppb)2	Ag(ppm)2	Cu_%2	Zn(ppm)2	Mo(ppm)2
L-17.5	246	248	D1	phyl		0.60					
L-17.5	248	251	D1	phyl		0.32					
L-17.5	251	255	D1	phyl		0.31					
L-17.5	255	258	D1	phyl		0.39					
L-17.5	258	262	D1	phyl		0.54					
L-17.5	262	265	D1	phyl		0.33					
L-17.5	265	269	D1	phyl		0.55					
L-17.5	269	273	D1	phyl		0.77					
L-17.5	273	276	D1	phyl		0.54					
L-17.5	276	279	D1	phyl		0.56					
L-17.5	279	281	D1	phyl		0.25					
L-17.5	281	283	D1	phyl		0.44					
L-17.5	283	286	D1	phyl		0.32					
L-17.5	286	289	D1	phyl		0.47					
L-17.5	289	292	D1	phyl		0.57					
L-17.5	292	294	D1	phyl		0.73					
L-17.5	294	296	D1	phyl		0.45					
L-17.5	296	298	D1	phyl		0.51					
L-17.5	298	301	D1	phyl		0.74					
L-17.5	301	302	D1	phyl		0.53					
L-17.5	302	306	D1	phyl		0.48					
L-17.5	306	309	D1	phyl		0.72					
L-17.5	309	314	D1	phyl		0.67					
L-17.5	314	317	D1	phyl		0.69					
L-17.5	317	320	D1	phyl		0.30					
L-17.5	320	323	D1	phyl		0.78					
L-17.5	323	327	D1	phyl		0.67					
L-17.5	327	329	D1	phyl		0.43					
L-17.5	329	332	D1	phyl		0.62					
L-17.5	332	335	D1	phyl		0.70					
L-17.5	335	337	D1	phyl		0.64					
L-17.5	337	339	D1	phyl		0.53					
L-17.5	339	325	D1	phyl		0.73					
L-17.5	325	346	D1	phyl	arg	0.77					
L-17.5	346	349	D1	phyl	arg	0.77					
L-17.5	349	352	D1	arg	phyl	0.86					
L-17.5	352	356	D1	arg	phyl	0.61					
L-17.5	356	357	D1	arg	phyl	0.71					
L-17.5	357	360	D1	arg	phyl	0.33					
L-17.5	360	362	D1	phyl	arg	0.85					
L-17.5	362	366	D1	phyl	arg	0.49					
L-17.5	366	370	D1	phyl	arg	0.51					
L-17.5	370	372	D1	phyl		0.58					
L-17.5	372	375	D1	phyl		0.36					
L-17.5	375	377	D1	phyl		0.31					
L-17.5	377	380	D1	phyl		0.26					
L-17.5	380	382	D1	phyl		0.42					
L-17.5	382	383	D1	phyl		0.37					
L-17.5	383	385	D1	phyl		0.39					
L-17.5	385	388	D1	phyl		0.36					
L-17.5	388	390	D1	phyl		0.30					
L-17.5	390	392	D1	phyl		0.29					
L-17.5	392	396	D1	arg	phyl	0.33					
L-17.5	396	399	D1	arg	phyl	0.27					
L-17.5	399	401	D1	arg	phyl	0.24					
L-17.5	401	403	D1	arg	phyl	0.29					
L-17.5	403	407	D1	arg	phyl	0.28					
L-17.5	407	410	D1	phyl	arg	0.38					
L-17.5	410	413	D1	arg	phyl	0.32					
L-17.5	413	415	D1	arg	phyl	0.32					
L-17.5	415	419	D1	arg	phyl	0.29					
L-17.5	419	422	D1	phyl	arg	0.30					
L-17.5	422	427	D1	phyl	arg	0.33					
L-17.5	427	429	D1	phyl	arg	0.37					
L-17.5	429	431	D1	arg	phyl	0.36					
L-17.5	431	434	D1	arg	phyl	0.30					
L-17.5	434	438	D1	arg	phyl	0.27					
L-17.5	438	441	D1	arg	phyl	0.61					
L-17.5	441	445	D1	arg	phyl	0.46					
L-17.5	445	447	D1	arg	phyl	0.39					
L-17.5	447	449	D1	arg	phyl	0.31					
L-17.5	449	453	D1	arg	phyl	0.36					
L-17.5	453	455	D1	arg	phyl	0.52					
L-17.5	455	459	D1	arg	phyl	0.39					
L-17.5	459	461	D1	arg	phyl	0.31					
L-17.5	461	465	D1	arg	phyl	0.36					
L-17.5	465	468	D1	arg	phyl	0.55					
L-17.5	468	470	D1	arg	phyl	0.63					
L-17.5	470	473	D1	arg	phyl	0.63					
L-17.5	473	477	D1	arg	phyl	0.53					
L-17.5	477	479	D1	arg	phyl	0.50					
L-17.5	479	482	D1	arg	phyl	0.63					
L-17.5	482	485	D1	arg	phyl	0.48					
L-17.5	485	488	D1	arg	phyl	0.44					
L-17.5	488	491	D1	arg	phyl	0.37					
L-17.5	491	494	D1	arg	phyl	0.48					
L-17.5	494	497	D1	arg	phyl	0.44					
L-17.5	497	500	D1	arg	phyl	0.64					
L-17.5	500	503	D1	phyl	arg	0.44					

Hole N°	From	To	Rock	Altn	Altn 2	Cu_%$_1$	Au(ppb)$_2$	Ag(ppm)$_2$	Cu_%$_2$	Zn(ppm)$_2$	Mo(ppm)$_2$
L-17.5	503	506	D1	phyl	arg	0.55					
L-17.5	506	509	D1	arg	phyl	0.69					
L-17.5	509	511	D1	arg	phyl	0.80					
L-17.5	511	515	D1	arg	phyl	0.50					
L-17.5	515	517	D1	arg	phyl	0.45					
L-17.5	517	520	D1	arg	phyl	0.54					
L-17.5	520	523	D1	arg	phyl	0.42					
L-17.5	523	525	D1	arg	phyl	0.25					

Hole N°	From	To	Rock	Altn	Altn 2	Cu_%$_1$	Au(ppb)$_2$	Ag(ppm)$_2$	Cu_%$_2$	Zn(ppm)$_2$	Mo(ppm)$_2$
M-17	0						59	0.3	0.31	-5	15
M-17	15						60	-0.3	0.28	12	10
M-17	30						76	0.7	0.55	162	24
M-17	45						156	0.4	0.31	17	12
M-17	60						62	-0.3	0.15	19	30
M-17	75						41	0.3	0.14	22	12
M-17	90						41	-0.3	0.13	28	12
M-17	105						52	-0.3	0.17	29	30
M-17	120						32	-0.3	0.11	32	15
M-17	135						46	-0.3	0.11	27	28
M-17	150						36	-0.3	0.11	29	27
M-17	165						33	-0.3	0.11	-5	35
M-17	180						41	-0.3	0.13	11	25
M-17	195						56	-0.3	0.19	17	63
M-17	210						35	-0.3	0.19	11	45
M-17	225						38	-0.3	0.19	5	95
M-17	240						36	0.4	0.18	8	84
M-17	255						43	0.4	0.20	14	146
M-17	270						46	0.3	0.19	14	55
M-17	285						39	0.3	0.21	19	34
M-17	300						37	-0.3	0.24	9	42
M-17	315						42	-0.3	0.23	18	43
M-17	330						43	0.3	0.27	12	25
M-17	345						39	0.5	0.32	19	18
M-17	360						36	0.6	0.24	141	105
M-17	375						46	0.5	0.33	89	51
M-17	390						66	0.4	0.34	14	112
M-17	405						63	0.4	0.42	25	27
M-17	420						63	0.8	0.44	18	26
M-17	435						46	0.5	0.38	51	58
M-17	450						66	1.6	0.44	104	24
M-17	465						41	4.5	0.33	232	127
M-17	480						50	1.3	0.35	371	96

Hole N°	From	To	Rock	Altn	Altn 2	Cu_%$_1$	Au(ppb)$_2$	Ag(ppm)$_2$	Cu_%$_2$	Zn(ppm)$_2$	Mo(ppm)$_2$
M-16	67	69	D1	phyl		N/A					
M-16	69	97	D1	phyl							
M-16	97	110	D1	phyl							
M-16	110	138	D1	phyl							
M-16	138	146	D1	k + Flt Zone	phyl						
M-16	146	149	D1	k	phyl						
M-16	149	195	D1	phyl							
M-16	195	197	D1	k							
M-16	197	203	D1	phyl							
M-16	203	207	D1	k	phyl						
M-16	207	214	D1	phyl							
M-16	214	227	D1	phyl							
M-16	227	232	Flt Zone	arg							
M-16	232	234	D1	arg	phyl						
M-16	234	240	D1	phyl							
M-16	240	242	D1	k							
M-16	242	247	D1	phyl							
M-16	247	260	D1	phyl							
M-16	260	288	D1	phyl	arg						
M-16	288	295	D1	phyl							
M-16	295	301	D1	phyl	arg						
M-16	301	306	D1	phyl							
M-16	306	313	D1	phyl							
M-16	313	321	D1	phyl							
M-16	321	324	Flt Zone	phyl							
M-16	324	339	D1	phyl							
M-16	339	343	Flt Zone	phyl							
M-16	343	383	D1	phyl							

Hole N°	From	To	Rock	Altn	Altn 2	Cu_%$_1$	Au(ppb)$_2$	Ag(ppm)$_2$	Cu_%$_2$	Zn(ppm)$_2$	Mo(ppm)$_2$
N-15	25	26	D1	phyl		2.46					
N-15	26	29	D1	phyl		2.76					
N-15	29	32	D1	phyl		2.76					
N-15	32	35	D1	k	phyl	1.59					
N-15	35	38	D1	k	phyl	1.61					
N-15	38	41	D1	k	phyl	1.71					
N-15	41	44	D1	k	phyl	1.62					
N-15	44	46	D1	k	phyl	2.01					
N-15	46	49	D1	k	phyl	1.57					
N-15	49	52	D1	k	phyl	1.82					
N-15	52	54	D1	k	phyl	1.70					

Hole N°	From	To	Rock	Altn	Altn 2	$Cu\_\%_1$	$Au(ppb)_2$	$Ag(ppm)_2$	$Cu\_\%_2$	$Zn(ppm)_2$	$Mo(ppm)_2$
N-15	54	57	D1	k	phyl	1.30					
N-15	57	61	Flt Zone	arg		1.41					
N-15	61	63	Flt Zone	arg		0.86					
N-15	63	65	D1	k	phyl	0.77					
N-15	65	68	D1	k	phyl	0.67					
N-15	68	71	D1	k	phyl	0.80					
N-15	71	74	D1	k	phyl	0.83					
N-15	74	77	D1	k	phyl	0.70					
N-15	77	81	D1	k	phyl	0.45					
N-15	81	84	Flt Zone	arg		0.45					
N-15	84	87	D1	k	phyl	0.41					
N-15	87	90	D1	k	phyl	0.63					
N-15	90	93	D1	k	phyl	0.98					
N-15	93	96	D1	k	phyl	0.88					
N-15	96	99	D1	k	phyl	0.85					
N-15	99	102	D1	k	phyl	0.77					
N-15	102	105	D1	k	phyl	0.66					
N-15	105	108	D1	k	phyl	0.72					
N-15	108	111	D1	k	phyl	0.75					
N-15	111	113	D1	k	phyl	1.14					
N-15	113	117	D1	k	phyl	1.17					
N-15	117	120	D1	k	phyl	1.20					
N-15	120	123	D1	k	phyl	0.98					
N-15	123	126	D1	k	phyl	1.06					
N-15	126	129	D1	k	phyl	1.01					
N-15	129	132	D1	k	phyl	1.30					
N-15	132	135	D1	k	phyl	1.50					
N-15	135	138	D1	k	phyl	1.13					
N-15	138	141	D1	k	phyl	0.98					
N-15	141	144	D1	k	phyl	1.44					
N-15	144	148	D1	k	phyl	1.19					
N-15	148	150	D1	k	phyl	1.24					

Hole N°	From	To	Rock	Altn	Altn 2	$Cu\_\%_1$	$Au(ppb)_2$	$Ag(ppm)_2$	$Cu\_\%_2$	$Zn(ppm)_2$	$Mo(ppm)_2$
N-15.5	0						457	1.3	2.26	12	-5
N-15.5	15						359	1.3	1.21	20	6
N-15.5	30						270	1.2	0.80	21	5
N-15.5	45						240	1.4	0.82	30	22
N-15.5	60						322	1.2	0.80	30	-5
N-15.5	75						309	1.7	0.85	27	-5
N-15.5	90						283	1.1	0.83	26	-5
N-15.5	105						225	1.4	0.63	28	-5
N-15.5	120						212	0.8	0.55	17	-5
N-15.5	135						221	1.1	0.67	24	-5
N-15.5	150						176	0.6	0.47	18	9
N-15.5	165						112	0.7	0.36	24	7
N-15.5	180						81	0.3	0.29	9	-5
N-15.5	195						49	0.5	0.20	12	25
N-15.5	210						50	-0.3	0.18	14	33
N-15.5	225						42	-0.3	0.17	16	14
N-15.5	240						43	-0.3	0.13	24	20
N-15.5	250.96						32	-0.3	0.17	21	15

Hole N°	From	To	Rock	Altn	Altn 2	$Cu\_\%_1$	$Au(ppb)_2$	$Ag(ppm)_2$	$Cu\_\%_2$	$Zn(ppm)_2$	$Mo(ppm)_2$
O-14	57	59	D1	phyl	k	0.42					
O-14	59	62	D1	phyl	k	0.28					
O-14	62	65	D1	phyl	k	0.26					
O-14	65	67	D1	phyl	k	0.38					
O-14	67	69	D1	phyl	k	0.45					
O-14	69	72	D1	phyl	k	0.73					
O-14	72	74	D1	phyl	k	0.62					
O-14	74	76	D1	phyl	k	0.31					
O-14	76	79	D1	phyl	k	0.43					
O-14	79	81	D1	phyl	k	0.38					
O-14	81	85	D1	phyl	k	0.48					
O-14	85	90	D1	phyl	k	0.37					
O-14	90	92	D1	phyl	k	0.30					
O-14	92	94	D1	phyl	k	0.47					
O-14	94	96	D1	phyl	k	0.50					
O-14	96	99	D1	phyl	k	0.46					
O-14	99	102	D1	phyl	k	0.44					
O-14	102	104	D1	phyl	k	0.52					
O-14	104	106	D1	phyl	k	0.48					
O-14	106	108	D1	phyl	k	0.50					
O-14	108	111	D1	phyl	k	0.56					
O-14	111	114	D1	phyl	k	0.45					
O-14	114	117	D1	k		0.36					
O-14	117	119	D1	k		0.79					
O-14	119	121	D1	k		0.68					
O-14	121	124	D1	k		0.83					
O-14	124	127	D1	k		0.65					
O-14	127	130	D1	k		0.53					
O-14	130	134	D1	k		0.48					
O-14	134	136	D1	k		0.48					
O-14	136	138	D1	k		0.41					
O-14	138	141	D1	k		0.29					
O-14	141	144	D1	k		0.39					

Hole N°	From	To	Rock	Altn	Altn 2	Cu_%$_1$	Au(ppb)$_2$	Ag(ppm)$_2$	Cu_%$_2$	Zn(ppm)$_2$	Mo(ppm)$_2$
O-14	144	146	D1	k		0.43					
O-14	146	147	D1	k		0.40					
O-14	147	150	D1	k		0.38					
O-14	150	153	D1	k		0.53					
O-14	153	157	D1	k		0.53					
O-14	157	160	D1	k		0.80					
O-14	160	163	D1	k		0.55					
O-14	163	165	Flt Zone	arg		0.65					
O-14	165	167	Flt Zone	arg		0.70					
O-14	167	171	D1	phyl		0.51					
O-14	171	173	D1	phyl		0.45					
O-14	173	175	D1	phyl		0.81					
O-14	175	177	D1	phyl	k	0.85					
O-14	177	180	D1	phyl	k	0.81					
O-14	180	182	D1	phyl	k	0.84					
O-14	182	184	D1	phyl	k	0.68					
O-14	184	186	D1	phyl	k	0.82					
O-14	186	187	D1	phyl	k	0.59					
O-14	187	190	D1	phyl	k	0.85					
O-14	190	191	D1	phyl	k	0.54					
O-14	191	193	D1	k	phyl	0.60					
O-14	193	195	D1	k	phyl	0.53					
O-14	195	197	D1	k	phyl	0.80					
O-14	197	199	D1	k	phyl	0.53					
O-14	199	202	D1	k	phyl	0.44					
O-14	202	205	Dyke	k		0.59					
O-14	205	206	Dyke	k		0.77					
O-14	206	208	D1	k	phyl	0.63					
O-14	208	210	D1	k	phyl	0.63					
O-14	210	213	D1	k	phyl	0.78					
O-14	213	215	D1	k	phyl	0.82					
O-14	215	217	D1	k	phyl	0.56					
O-14	217	218	D1	k	phyl	0.76					
O-14	218	221	D1	k	phyl	0.80					
O-14	221	223	D1	k	phyl	1.08					
O-14	223	225	D1	k	phyl	0.92					
O-14	225	228	D1	k	phyl	0.70					
O-14	228	230	D1	k	phyl	0.63					
O-14	230	232	D1	k	phyl	0.11					
O-14	232	235	D1	k	phyl	0.80					
O-14	235	237	D1	k	phyl	0.74					
O-14	237	239	D1	k	phyl	0.98					
O-14	239	242	D1	k	phyl	0.61					
O-14	242	245	D1	k	phyl	0.77					
O-14	245	247	D1	k	phyl	0.76					
O-14	247	248	D1	k	phyl	0.80					

APPENDIX D5

Pb isotope analytical procedures and raw data

ANALYTICAL TECHNIQUES FOR PB ISOTOPE ANALYSES

The following procedures for sulphide Pb isotope analyses were conducted at the University of British Columbia. Trace lead sulphide samples were prepared from 10-50 mg of handpicked pyrite or chalcopyrite crystals, which were leached in dilute hydrochloric acid to remove surface contamination before dissolution in nitric acid. Separation and purification of Pb employed ion exchange column techniques. The samples were converted to bromide, and the solution was passed through ion exchange columns in hydrobromic acid, and the lead eluted in 6N hydrochloric acid.

Approximately 10-25 ng of the lead in chloride form was loaded on a rhenium filament using a phosphoric acid-silica gel emitter, and isotopic compositions were determined in peak-switching mode using a modified VG54R thermal ionisation mass spectrometer. The measured ratios were corrected for instrumental mass fractionation of 0.12%/amu (Faraday collector) or 0.43%/amu (Daly collector) per mass unit based on repeated measurements of the N.B.S. SRM 981 Standard Isotopic Reference Material and the values recommended by Thirlwall (2000). Errors were numerically propagated including all mass fractionation and analytical errors, using the technique of Roddick (1987). All errors are quoted at the 2σ level. Age assignments follow the time scale of Harland *et al*. (1990).

References

Harland, W.B., Armstrong, R.L., Cox, A.V., Craig, L.E., Smith, A.G. and Smith, D.G., 1990. A geologic time scale: 1989. Cambridge University Press, Cambridge, pp. 263.

Roddick, J.C., 1987. Generalised numerical error analysis with application to geochronology and thermodynamics. Geochimica et Cosmochimica Acta, 51: 2129-2135.

Stacey, J.S. and Kramer, J.D., 1975. Approximation of terrestrial lead isotope evolution by a two-stage model. Earth and Planetary Science Letters, 26: 207-221.

Thirlwall, M.F., 2000. Interlaboratory and other errors in Pb-isotope analyses investigated using a ^{207}Pb-^{204}Pb double spike. Chemical Geology, 163: 299-322.

Lead isotope data from the University of British Columbia

Sample No.	$^{206}Pb/^{204}Pb$	Pb64 abs err	Pb64 % err	$^{207}Pb/^{204}Pb$	Pb74 abs err	Pb74 % err	$^{208}Pb/^{204}Pb$	Pb84 abs err	Pb84 % err	$^{207}Pb/^{206}Pb$	Pb76 abs err	Pb76 % err	$^{208}Pb/^{206}Pb$	Pb86 abs err	Pb86 % err	Deposit
G1-CCP	18.7813	0.0245	0.13	15.6597	0.0214	0.14	38.7608	0.0598	0.15	0.8338	0.0003	0.036	2.0638	0.0011	0.055	El Galeno
G1-PYR	18.7440	0.0084	0.04	15.6633	0.0103	0.07	38.7405	0.0338	0.09	0.8356	0.0002	0.023	2.0668	0.0009	0.043	El Galeno
G4-CCP	18.7071	0.0333	0.18	15.6348	0.0286	0.18	38.6853	0.0749	0.19	0.8358	0.0003	0.031	2.0680	0.0009	0.046	El Galeno
MY-PYR	18.7248	0.0623	0.33	15.6439	0.0522	0.33	38.6349	0.1329	0.34	0.8355	0.0004	0.047	2.0633	0.0013	0.063	Michiquillay
MY-PYR	18.7826	0.0274	0.15	15.7000	0.0239	0.15	38.8606	0.0640	0.16	0.8359	0.0003	0.031	2.0690	0.0009	0.045	Michiquillay
MY-CCP	18.7865	0.0159	0.08	15.6577	0.0128	0.08	38.8215	0.0447	0.12	0.8335	0.0005	0.057	2.0665	0.0010	0.049	Michiquillay
YANA-PYR	18.6234	0.0187	0.10	15.5742	0.0173	0.11	38.4688	0.0483	0.13	0.8363	0.0002	0.024	2.0656	0.0009	0.044	Yanacocha
MC-CCP	18.6980	0.0111	0.06	15.6132	0.0103	0.07	38.6605	0.0388	0.10	0.8350	0.0004	0.044	2.0676	0.0011	0.053	Minas Conga
MC-CCP	18.7342	0.0118	0.06	15.6536	0.0124	0.08	38.7507	0.0381	0.10	0.8356	0.0002	0.024	2.0685	0.0009	0.044	Minas Conga
MC-PYR	18.7778	0.0205	0.11	15.6968	0.0235	0.15	38.8161	0.0771	0.20	0.8359	0.0004	0.054	2.0672	0.0020	0.099	Minas Conga
MC-PYR	18.7781	0.0204	0.11	15.6878	0.0236	0.15	38.8013	0.0763	0.20	0.8355	0.0004	0.050	2.0664	0.0020	0.095	Minas Congaco

Analyses by Janet Gabites, Geochronology Laboratory, Department of Earth and Ocean Sciences, The University of British Columbia.
Results have been normalized using a fractionation factor of 0.15% based on multiple analyses of NBS981 standard lead, and the values in Thirlwall (2000).
Minerals analysed: pyr = pyrite, ccp = chalcopyrite